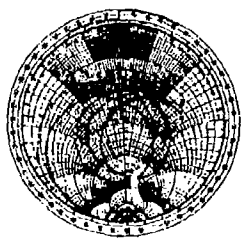

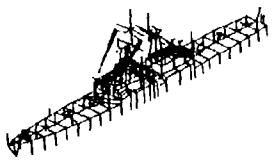

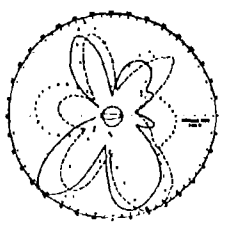

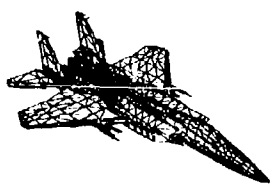

10th Annual Review of Progress in

Applied Computational Electromagnetics

at the
Doubletree Hotel & Convention Center
Monterey, California

March 21 - 26, 1994

CONFERENCE PROCEEDINGS

The 10th Anniversary ACES Conference

CONFERENCE PROCEEDINGS

VOLUME II

10th Annual Review of Progress in

APPLIED

COMPUTATIONAL

ELECTROMAGNETICS

at the

Doubletree Hotel and Convention Center

Monterey, California

March 21-26, 1994

CONFERENCE PROGRAM COMMITTEE CHAIRMAN

Andy Terzuoli

Library of Congress Catalog Card Number: 94-70636

Sponsored by

The Applied Computational Electromagnetics Society
and DOD and DOE in cooperation with IEEE, URSI, ASEE, SIAM and AMTA

VOLUME II

THE APPLIED COMPUTATIONAL ELECTROMAGNETICS SOCIETY

1995 CALL FOR PAPERS 1995

The 11th Annual Review of Progress in Applied Computational Electromagnetics

March 21-26 1995

Naval Postgraduate School, Monterey, CA

Share your knowledge and expertise with your colleagues

The Annual ACES Symposium is an ideal opportunity to participate in a large gathering of EM analysis enthusiasts. The purpose of the Symposium is to bring analysts together to share information and experience about the practical application of EM analysis using computational methods. The Symposium features four areas of interest: technical publication, demonstrations, vendor booths and short courses. All aspects of electromagnetic computational analysis are represented. The Symposium will also include invited speakers and interactive forums. Contact Ray Luebbers (814) 865-2362 for details.

1995 ACES Symposium Chairman
Ray Luebbers
Penn State University
320 EE East
University Park, PA 16802
Phone (814) 865-2362
Fax: (814) 865-7065
Email: LU4@psuvm.psu.edu

1995 ACES Symposium Administrator
Richard W. Adler
ECE Dept/Code ECAB
Naval Postgrad School
833 Dyer Rd, Room 437
Monterey, CA 93943-5121
Phone (408-646-1111)
Fax (408) 649-0300
Email: 5541304@mcimail.com

1995 ACES Symposium Co-Chairman
Richard K. Gordon
EE Dept. Univ of Mississippi
Anderson Hall, Box 41
University, MS 38677
Phone (601) 232-5388
Fax: (601) 232-7231
Email: eegordon@vm.cc.olemiss.edu

1995 ACES Symposium
Sponsored by: ACES, USAIESA, NCCOSC, NPS, DOE/LLNL, DOD/USA CECOM
In cooperation with: The IEEE Antennas and Propagation Society, the IEEE ElectromagneticCompatibility Society and USNC/URSI

1994 Conference Program Committee
for the
10th Annual Review of Progress in Applied Computational Electromagnetics
at the
Doubletree Hotel and Convention Center
Monterey, California

Conference Chairman:
Andy Terzuoli
Air Force Institute of Technology
School of Engineering
P.O. Box 3402
Dayton, OH 45401
Tel (513) 255-3636 X4717/Fax: 476-4055

Co-Chairman:
Jeff Fath and Dennis Andersh
Wright Laboratory/AARA
2010 Fifth St., Bldg 23
Wright Patterson AFB, OH 45433
Tel (916) 643-6935/Fax: 1053

Conference Advisor:
Dick Adler
ECE Dept. Code ECAB
Naval Postgraduate School
833 Dyer Rd., Room 437
Monterey, CA 93943
Tel (408) 646-1111/Fax: 649-0300

Conference/Vendor Facilitator: Jodi Nix
Veda Incorporated
5200 Springfield Pike,
Suite 200
Dayton, OH 45431
Tel (513) 476-3550/Fax: 3577

Short Course Chair:
Robert Lee
The Ohio State University
ElectroScience Laboratory
1320 Kinnear Rd.
Columbus, OH 43210-1272

Short Course Co-Chair: Jin-Fa Lee
Worcester Polytechnic Inst.
100 Institute Rd., EE Dept.
Worcester, MA 01609

1995 Conference Chairman:
Ray Luebbers
Penn-State University
320 Electrical Engineering East
University Park, PA 16802
Tel (814) 865-2362

Conference Secretary: Pat Adler

Advisory Committee:
Dick Adler, Naval Postgraduate School
Dennis Andersh, Major USAF, Wright Laboratory
Jeff Fath, Captain USAF, SM-ALC/QL
Pat Foster, Microwave and Antenna Systems
Richard K. Gordon, Univ. of Mississippi
Jim Logan, NRAD
Ray Luebbers, Penn State Univ.
Andy Peterson, Georgia Institute of Technology
John Rockway, NRAD
Andy Terzuoli, AF Institute of Technology
Frank Walker, Boeing Defense and Space Group
Perry Wheless, Univ. of Alabama

A•C•E•S 1994

10th Anniversary

Monterey, California
March 21-26, 1994

Conference Chairman:
Andy Terzuoli
Air Force Institute of Technology
School of Engineering
P.O. Box 3402 • Dayton, Ohio 45401
Tel: 513/255-3636x4717 • Fax: 513/476-4055

Conference Co-Chairmen:
Jeff Fath and Dennis Andersh
Wright Laboratory/AARA
2010 Fifth St., Bldg 23
Wright-Patterson AFB, Ohio 45433-7001
Tel: 513/255-1115 • Fax: 513/476-4414

Short Course Co-Chairman:
Rob Lee
The Ohio State University
ElectroScience Laboratory
1320 Kinnear Rd. • Columbus, Ohio 43212
Tel: 614/292-7981 • Fax: 614/292-7297

Conference Advisor:
Dick Adler
Naval Postgraduate School
ECE Dept. Code ECAB
833 Dyer Rd., Room 437
Monterey, California 93943-5121
Tel: 408/656-2352 • Fax: 408/656-2955
E-Mail: 5541304@mcimail.com

Conference Facilitator:
Jodi Nix
Veda Incorporated
5200 Springfield Pike, Suite 200
Dayton, Ohio 45431
Tel: 513/476-3550 • Fax: 513/476-3577
E-Mail: jodi@image.mbvlab.wpafb.af.mil

1995 Conference Chairman:
Ray Luebbers
The Pennsylvania State University
Electrical Engineering Dept.
University Park, Pennsylvania 16802
Tel: 814/865-2362 • Fax: 814/865-7065
E-Mail: lu4@psuvm.psu.edu

APPLIED COMPUTATIONAL ELECTROMAGNETICS SOCIETY

The Tenth Annual Review of Progress in Applied Computational Electromagnetics

From The Conference Chairman To All Attendees:

On behalf of the conference committee, welcome and thank you for coming to ACES '94. Also welcome (back) to Monterey, to California, and to the Naval Postgraduate School from which we have our roots. If you are from abroad, of course, welcome (back) to the USA. If this is your first time here, an extra welcome, and an invitation to ask any of us to give you our version of where to go and what to do, or how you can become involved--we do need you!

As I write this letter, the January '94 earthquake in the Los Angeles area, and its after shocks, are still very much in the news; as we plan this enjoyable week for us all, I cannot help but think of those affected, possibly some of you. I find it remarkable that despite the numerous calamities affecting ACES' beautiful host state of California, an atmosphere of energetic hope always prevails.

For this 10th Anniversary meeting, we have tried to make it special and memorable, and to give a distinct *thank you* to Dick and Pat Adler for their years of selfless service. We tried to centralize everything around the Doubletree/Convention Center so as to give Dick and Pat *somewhat* of a break this year. We have coordinated noteworthy social events, vendor exhibits, and short courses. We deliberately tried to expand the short courses and sessions so that those of you at home with ACES can reach out to other related areas like Wavelets, Time Frequency Analysis, and Measurement Validation. We also felt that with research money being tight, if ACES was the *one* conference you went to this year, you would be able to partially diversify while here.

By way of acknowledgments and thanks, once again Dick and Pat Adler, and Pat's team of dedicated ladies who work so hard behind the scenes, not only here during the conference, but all year. Jodi Nix, who I'm sure you all talked to at least once this past year, has been the hands and feet of ACES '94 for over a year. She attended ACES '93, visited the Doubletree, gave ACES publicity at numerous other conferences this past year, and contacted countless perspective participants in various capacities. She and her team at Veda designed our letterhead, poster, flyers, etc., coordinated all the mailings, and even kept me on schedule; please thank her *every* time you see her!

Thanks to Jeff Fath, Dennis Andersh, and the Air Force Wright Laboratories for support, advice, publicity, and help with every facet of this conference; to Rob Lee and Jin Fa Lee who, as you can see, did a super job in pulling together all the short course ideas into a working reality. Ray Luebbers, the ACES '95 (despite what it says in the January announcement) Conference Chairman, did a great job in helping us out this year providing overall help and paper review.

Last but not least to my friend God I simply say *thank you, sir, and please don't let the earth shake while we are here.*

Best Wishes,
Andy Terzuoli, Chairman,
1994 ACES Conference.

Dayton, Ohio
February, 1994

ACES PRESIDENT'S STATEMENT

It's nice to be here in California in March, especially considering the frigid weather we experienced in the Midwest this past winter.

It's especially nice, however, to be here for the tenth annual conference of ACES. It's hard to believe that nine years have gone by since Ed Miller and his colleagues at LLNL convened a meeting to determine if there was a need to form a society to cater to the needs of the computational electromagnetics community. The answer was a resounding 'yes' then, and so it remains today.

ACES is unique in its attitude to the profession. It has senior-level researchers, certainly, who publish significant papers, and yet much of the email I read comes from amateur radio operators who want to use NEC in their nonprofessional activities, and naturally look to ACES to give them support in their endeavors. Perhaps that's more of a credit to NEC, but ACES started as a virtual NEC user's group, and it's nice to see that we haven't lost our roots.

Andy Terzuoli and Jodi Nix have done a great job in organizing the conference. We owe them a great debt. And how about Dick and Pat Adler? You thought they were just a couple of names who wanted your money. Now that you've had a chance to meet them, and their support staff, you can do the right thing and thank them, too.

Let me tell you how to get the most out of this conference: meet colleagues, see the acquarium, go to the banquet, have a good time. The papers will be so much better if you're in a good mood. That's what we want for you.

Harold A. Sabbagh
ACES President

ACES 1994 SHORT COURSES

MONDAY MARCH 21 — FULL DAY COURSE

"WAVELET ELECTRODYNAMICS"
by Gerald Kaiser, Dept. of Mathematical Sciences, UMass-Lowell

MONDAY MARCH 21 — FULL DAY COURSE

"TIME-FREQUENCY ANALYSIS"
by Leon Cohen, Hunter College and Graduate Center of CUNY

MONDAY MARCH 21 — FULL DAY COURSE

"GEMACS FROM A-Z"
by Buddy Coffey, Advanced EM

MONDAY MARCH 21 — HALF DAY COURSE

"FDTD FOR ANTENNAS AND SCATTERING"
by Ray Luebbers, Penn State University

MONDAY MARCH 21 — HALF DAY COURSE

"MEASUREMENT VALIDATION FOR COMPUTATIONAL ELECTROMAGNETICS"
by Al Dominek, Ohio State University

MONDAY MARCH 21 — HALF DAY COURSE

"USING MODEL-BASED PARAMETER ESTIMATION TO INCREASE EFFICIENCY AND EFFECTIVENESS OF COMPUTATIONAL ELECTROMAGNETICS"
by Ed Miller, Los Alamos National Lab

SATURDAY MARCH 26 — FULL DAY COURSE

"FINITE ELEMENT METHODS FOR ELECTROMAGNETICS"
by Jin-Fa Lee, Worcester Polytechnic Institute; Robert Lee, Ohio State University; Tom Cwik, Jet Propulsion Laboratory; and John Brauer, MacNeal-Schwendler Corporation

SATURDAY MARCH 26 — FULL DAY COURSE

"WIRE ANTENNA MODELING USING NEC"
by Richard Adler, Naval Postgraduate School; James Breakall, Penn State University; and Gerald Burke, Lawrence Livermore National Lab

SATURDAY MARCH 26 — HALF DAY COURSE

"VOLUME-INTEGRAL EQUATIONS IN EDDY-CURRENT NONDESTRUCTIVE EVALUATION"
by Hal Sabbagh, Sabbagh Associates

SATURDAY MARCH 26 — HALF DAY COURSE

"ELECTROMAGNETIC CHARACTERIZATION OF ELECTRONIC PACKAGES"
by Andreas Cangellaris, University of Arizona

SESSION 12:

FINITE DIFFERENCE TIME DOMAIN II

Chair: Raymond Luebbers
Co-Chair: John Beggs

FD-TD Algorithm for the Nonlinear Maxwell's Equations with Applications to Femtosecond Soliton Propagation

Peter M. Goorjian
Mail Stop T27B-1
NASA-Ames Research Center
Moffett Field, CA 94035-1000
(415) 604-5547

Rose M. Joseph and Allen Taflove
EECS Dept., McCormick School of Engin.
Northwestern University
Evanston, Illinois 60208-3118
(708)491-4127

Experimentalists have produced all-optical switches capable of 100 femtosecond responses. Also, there are experimental observations of spatial soliton interactions. To model such effects, nonlinearities in optical materials mu be included. The behavior of electromagnetic fields in nonlinear dielectrics can be determined by solving the nonlinear Maxwell's equations. However currently, the standard method for determining the fields is to solve the nonlinear Schrodinger equation (NLSE), which is an approximation that neglects the optical carrier of the pulse. For modeling small scale engineered inhomogeneities in optical devices, on the order of 0.1 to 10 optical cycles, the assumptions in the NLSE become unjustified.

In this paper, solutions are presented of calculations of the 2-D vector nonlinear Maxwell's equations for propagating and scattering temporal and spatial solitons in material media having linear and nonlinear instantaneous and Lorentzian dispersive effects in the electric polarization. The optical carrier is retained in these calculations. A finite difference method is used to solve Maxwell's equations and the ordinary differential equations that determine the linear and nonlinear dispersive effects [1].

Figure 1 shows the electric field of a propagating optical soliton carrier pulse in a dielectric waveguide. Notice that the pulse is not dispersing due to the nonlinear effects. Figure 2 shows the collision of two equal-amplitude, counter-propagating solitons. After the collision, the two pulses regain their original shapes. The presentation will include a video of these calculations. Figure 3 shows the simulation of the parallel co-propagation of two in-phase, equal-amplitude spatial solitons. The separation provides the basis for an all-optical switching mechanism because, without the second beam, a single beam will travel undeflected.

This new approach enforces the vector field boundary conditions at all interfaces of dissimilar media in the time scale of the optical carrier. Therefore this approach is completely general. It assumes nothing about the homogeneity or isotropy of the optical medium, the magnitude of the nonlinearity, the nature of the materials's frequency dependence or the shape, duration and vector nature of the optical pulses. By retaining the optical carrier, this method solves for fundamental quantities, viz. the electric and magnetic fields in space and time, rather than a nonphysical envelope function. It has the potential to provide 2-D and 3-D modeling capability for millimeter scale integrated optical circuits having sub-μm engineered inhomogeneities.

1. Goorjian, P. M., Taflove, A., Joseph, R. M., and Hagness S. C., *IEEE J. Quantum Electronics*, Vol. 28, No. 10, pp. 2416-2422, Oct., 1992.
2. Joseph, R. M., Goorjian, P. M., and Taflove, A., *Optics Letters* , Vol. 18, No. 7, pp. 491-493, April 1, 1993.

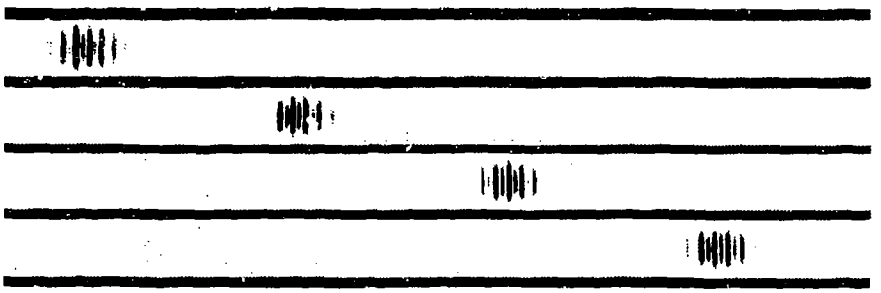

Fig. 1. Electric field of a propagating optical soliton carrier pulse with initial hyperbolic secant envelope ($\lambda = 2.19$ μm, $\tau = 14.6$ fs) in 1-μm thick Lorentz medium dielectric waveguide, including quantum effects such as the Kerr and Raman interactions.

Fig. 2. Electric field of colliding counter-propagating solitons corresponding to Fig. 1, (approaching, destructively interfering, constructively interfering, separating).

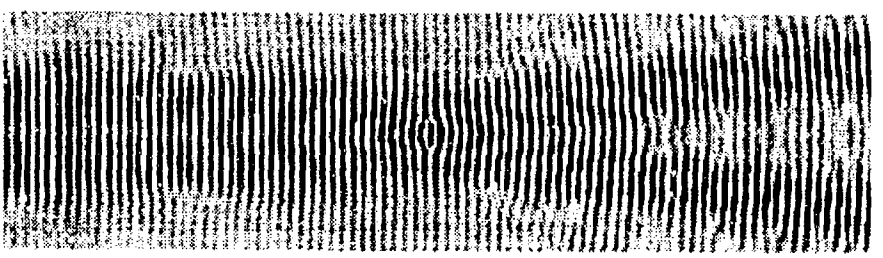

Fig. 3. Electric field of two parallel, in-phase, co-propagating spatial solitons showing alternating attraction and repulsion interactions for a uniform dielectric medium having a finite nonlinearity.

Finite Difference - Time Domain Tests of Random Media Propagation Theory

L. J. Nickisch
Mission Research Corporation
2900 Garden Road, Suite 2
Monterey, California 93940-5326
and
P. M. Franke
University of Illinois at Urbana-Champaign
Department of Electrical and Computer Engineering
323 CSRL MC-229
1308 W. Main Street
Urbana, IL 61801

Abstract

The recent extension of the Finite Difference - Time Domain (FDTD) method to frequency dependent media [*Nickisch and Franke*, 1992] allows FDTD to now be applied to ionospheric propagation. The FDTD method solves the Maxwell equations directly in the time domain by temporal integration. No approximations beyond that of finite differencing are necessary, although the direct enforcement of certain approximations is possible. By doing so, the method can be used to explore the effect of many standard propagation approximations. We consider certain approximations typically applied to the problem of propagation in randomly structured ionization such as the neglect of polarization coupling and the assumption of small angle scattering.

1. Introduction

Due to advances in the computational speed of modern processors and the availability of relatively inexpensive computer memory, the Finite Difference - Time Domain (FDTD) method is becoming increasingly viable as a calculational tool for physically realistic electromagnetic propagation problems. In the FDTD method, the Maxwell equations (or equations derived from them) are solved directly in the time domain by converting the continuum equations to discrete difference equations – approximating derivatives as finite differences. Until relatively recently, frequency dependent media (such as the ionospheric plasma) presented a problem to the FDTD approach since for such dispersive media the relation of the electric displacement to the electric field implies a convolution in the time domain. As we have reported [*Nickisch and Franke*, 1992], it is possible to fully account for the dispersive nature of the medium without resorting to convolutions. Our approach incorporates the absorptive and anisotropic nature of the ionospheric channel as well, and we have shown that the method is capable of extreme accuracy. Since the FDTD method requires no approximations

other than that implicit in the finite differencing, it is ideal for the application on which report here, that of examining the way in which the standard random media approximations degrade when applied outside their regime of strict validity.

Interest in the applicability of approximate propagation theory outside intended regimes arises, in particular, in the arena of HF communications and radar. Theoretical treatments for the calculation of signal decorrelation effects derived for satellite communications at substantially higher frequencies are commonly applied to the HF band (3 - 30 MHz) simply because no alternative exists. Yet certain of the approximations assumed in the derivation of the theoretical expressions are manifestly violated at HF frequencies for particular environments. For example, the derivation of the parabolic equation for the two-position mutual coherence function assumes (among other things) that the field correlation length remains large compared to the wavelength of the propagating field. Yet analysis of measured HF channel probe data for propagation through the naturally highly structured ionosphere of the earth's polar region indicates that the field correlation lengths are often smaller than a wavelength [*Nickisch*, 1992]. Since the predictions of the approximate propagation theory are used to design communication and radar systems for stressing environments, one would like to have some indication of how reliable such extrapolated results are.

In the following section we will review the approximations leading to the parabolic equation for the two-position mutual coherence function. In Section 3 we will compare results obtained using the FDTD method for the full vector wave equation to FDTD solutions of the scalar Helmholtz wave equation, and further compare these results to the predictions of the propagation theory of Section 2. Finally, in Section 4, we will briefly discuss the implications of our results.

2. Random Media Propagation Theory – the Parabolic Wave Equation and the Two-Position Mutual Coherence Function

The source free Maxwell equations are

$$\vec{\nabla} \cdot \vec{D} = 0 \tag{1}$$

$$\vec{\nabla} \cdot \vec{B} = 0 \tag{2}$$

$$\vec{\nabla} \times \vec{E} = -\frac{\partial \vec{B}}{\partial t} \tag{3}$$

$$\vec{\nabla} \times \vec{H} = \frac{\partial \vec{D}}{\partial t} \tag{4}$$

where for the medium we are concerned with, $\vec{B} = \mu_o \vec{H}$, and μ_o is the permeability of free space. The electric displacement $\vec{D}$ is related to the electric field $\vec{E}$ by the expression

$$\vec{D} = \epsilon_o \vec{E} + \vec{P} \quad , \tag{5}$$

where ϵ_o is the permittivity of free space and $\vec{P}$ is the electric polarization. The electric polarization accounts for the reaction of a medium to impressed electromagnetic fields (charge displacement), a [illegible]such is obtainable from a dynamical equation. For a charged cold plasma, this dynam[illegible]al equation is [*Budden*, 1985],

$$-e\vec{E} + \frac{1}{N_e}\frac{\partial \vec{P}}{\partial t} \times \vec{B}_E = \frac{m_e}{N_e e}\left(\frac{\partial^2 \vec{P}}{\partial t^2} + \nu_c \frac{\partial \vec{P}}{\partial t}\right) \quad . \tag{6}$$

Equation (6) is simpl[illegible]ewton's Second Law relating the forces on the charged plasma to the plasma acceleration, written in terms of the electric polarization $\vec{P}$. We have included in (6) the forces on a charge due to the applied field of our wave of interest and the external geomagnetic field $\vec{B}_E$ responsible for magneto-ionic splitting. The collisional forces responsible for signal absorption are incorporated through the electron collision frequency ν_c in the last term.

The vector wave equation is readily obtained from the Maxwell equations by applying the curl operator to (3) and applying (4), with the result

$$\frac{1}{c^2}\frac{\partial^2 \vec{E}}{\partial t^2} = \nabla^2 \vec{E} - \vec{\nabla}(\vec{\nabla} \cdot \vec{E}) - \mu_o \frac{\partial^2 \vec{P}}{\partial t^2} \quad . \tag{7}$$

Here $c = 1/\sqrt{\mu_o \epsilon_o}$ is the vacuum speed of light.

Thus far we have made no approximations aside from some modeling assumptions in Equation (6) regarding the simple collision frequency model for absorption and the neglect of the impressed magnetic field in deference to the stronger geomagnetic field; the vector wave equation is essentially exact.

In many cases the propagation medium can, to a high degree, be modeled as linear in its response to impressed fields. It is then useful to define a dielectric constant of the medium. Since our discussion of the parabolic wave equation will follow that of *Ishimaru* [1978, chapter 20], we will use his notion of a relative dielectric constant ϵ_r, so that in the frequency domain Equation (5) becomes

$$\vec{D}(\omega) = \epsilon_o \epsilon_r(\omega)\vec{E}(\omega) \quad . \tag{8}$$

Most generally the relative dielectric constant is a tensor and its product with $\vec{E}$ on the RHS of (8) is a tensor product, but the standard random media propagation theory we are about to discuss neglects anisotropy, so there is no need here to consider anything but the scalar case. (This is actually an approximation since the ionospheric plasma is indeed anisotropic due to the influence of the geomagnetic field.) In the frequency domain, the vector wave equation (7) becomes

$$0 = \nabla^2 \vec{E} + k_o^2 \epsilon_r \vec{E} \quad \vec{\nabla}(\vec{\nabla} \cdot \vec{E}) \quad , \tag{9}$$

where $k_o = \omega/c$ is the free space wavenumber. The last term on the RHS is the only term which can couple different field polarizations, and we will refer to it as the polarization coupling term. Neglecting this term results in the scalar Helmholtz wave equation.

When can the polarization coupling term be neglected? By Equation (1), we obtain the identity

$$0 = \vec{\nabla} \cdot (\epsilon_r \vec{E}) = \epsilon_r \vec{\nabla} \cdot \vec{E} + (\vec{\nabla} \epsilon_r) \cdot \vec{E} \quad , \tag{10}$$

and hence the vector wave equation (9) can be rewritten as

$$0 = \nabla^2 \vec{E} + k_o^2 \epsilon_r \vec{E} + \vec{\nabla} \left[\frac{\vec{\nabla} \epsilon_r}{\epsilon_r} \cdot \vec{E} \right] \quad . \tag{11}$$

In this form one can see that for media with structure scale sizes L_o which remain large compared to the field wavelength $\lambda = 2\pi/k_o$, the polarization coupling term may be neglected relative to the k_o^2 term (that is, by expanding the derivatives of the polarization coupling term and approximating, for example, $\partial \epsilon_r / \partial x$ with ϵ_r / L_o, one argues that each piece of the expanded polarization coupling term must remain smaller than the k_o^2 term and can therefore be neglected). Thus the standard random media propagation theory for strong scatter begins with the scalar Helmholtz wave equation

$$0 = \nabla^2 u(\vec{r}) + k_o^2 \epsilon_r u(\vec{r}) \quad , \tag{12}$$

where $u(\vec{r})$ stands for any component of the vector field $\vec{E}(\vec{r})$.

We now sketch the derivation of the parabolic wave equation, following *Ishimaru* [1978, chapter 20] in substantially reduced detail and placing emphasis on the approximations employed. First the propagation medium is assumed to consist of a smooth background contribution $\langle \epsilon_r(\vec{r}) \rangle$ with superimposed random structure $\epsilon_1(\vec{r})$,

$$\epsilon_r(\vec{r}) = \langle \epsilon_r \rangle [1 + \epsilon_1(\vec{r})] \quad . \tag{13}$$

Writing $k^2 = k_o^2 \langle \epsilon_r \rangle$, the Helmholtz wave equation becomes

$$0 = \left[\nabla^2 + k^2 (1 + \epsilon_1(\vec{r})) \right] u(\vec{r}) \quad . \tag{14}$$

The parabolic wave equation is obtained from (14) by neglecting backscatter and assuming that the propagation is confined to only small angular deflections from a preferred direction (here taken to be the $\hat{x}$ direction). Thus the field is written as

$$u(\vec{r}) = U(\vec{r}) e^{ikx} \quad , \tag{15}$$

where the exponential is assumed to contain the rapid field variations and its sign indicates that only forward propagating contributions are accounted for. $U(\vec{r})$ is assumed to be only slowly varying spatially. When this form is substituted into (14), one finds that the term containing $\partial^2 U(\vec{r}) / \partial x^2$ is negligible relative to the term which mixes the first derivative of U with the first derivative of the exponential, as long as the scale of variation of $U(\vec{r})$ in the propagation direction (denoted ℓ_x) remains large compared to a wavelength, $\ell_x \gg \lambda$. The resulting parabolic wave equation is

$$2ik\frac{\partial U(\vec{r})}{\partial x} + \nabla_\perp^2 U(\vec{r}) + k^2\epsilon_1(\vec{r})U(\vec{r}) = 0 \quad . \tag{16}$$

Here $\nabla_\perp^2$ is the Laplacian acting only on the spatial coordinates transverse to the assumed direction of propagation. The advantage of the parabolic wave equation is that it is first order in the direction of propagation, so that solutions can be obtained from it by simple integration. Its disadvantage is its restriction to small angle scatter (which is related to the neglect of backscatter, the assumption that all fast field variations are contained in the exponential of (15), and the neglect of the second derivative contributions of U in the direction of propagation). [It is worth noting that a simple geometrical calculation of the parallel correlation length based on a single phase-changing screen relates ℓ_x to the transverse correlation length ℓ_o as $\ell_x \approx \ell_o^2/\lambda$. Thus the restriction $\ell_x \gg \lambda$ requires that $\ell_o \gg \lambda$ as well. The transverse correlation length is itself inversely proportional to the standard deviation scattering angle, $\sigma_\theta \sim \lambda/\ell_o$. Thus the restriction $\ell_o \gg \lambda$ is actually a small angle scatter restriction.]

From the parabolic wave equation, it is useful to derive equations for various expectation values of field products, referred to as field moments. We will here consider the second moment, the two-position mutual coherence function $\Gamma(x, \Delta\vec{\rho})$ where $\vec{\rho}$ refers to the transverse spatial coordinates,

$$\Gamma(x, \Delta\vec{\rho}) = \langle U(x, \vec{\rho} + \Delta\vec{\rho})U^*(x, \vec{\rho})\rangle \quad . \tag{17}$$

The angle brackets refer to ensemble averaging (this averaging will be replaced with spatial averaging in our FDTD processing to be discussed in the next section) and the asterisk refers to complex conjugation. Implicit in the definition (17) is the assumption that the two positon mutual coherence function depends only on the transverse spatial *separation* of the field points, but not on their absolute positions. An equation for the two-position mutual coherence function can be derived from the parabolic wave equation. We will not reproduce that derivation here, but again refer the interested reader to *Ishimaru* [1978]. Its derivation requires use of the Markovian approximation, that the dielectric fluctuations of the medium are delta correlated in the propagation direction,

$$\langle \epsilon_1(\vec{r} + \Delta\vec{r})\epsilon_1(\vec{r})\rangle = \delta(\Delta x)A(x, \Delta\vec{\rho}) \quad . \tag{18}$$

The impact of this assumption is thought to be small for the calculation of the transverse correlation of the field, and we will not specifically address it further here. The resultant equation for the two-position mutual coherence function is

$$\left[\frac{\partial}{\partial x} + \frac{1}{2}d(x, \Delta\vec{\rho})\right]\Gamma(x, \Delta\vec{\rho}) = 0 \tag{19}$$

where

$$d(x, \Delta\vec{\rho}) = \frac{k^2}{2}[A(x, \vec{0}) - A(x, \Delta\vec{\rho})] \tag{20}$$

is the differential phase structure function. The solution of (19) is simply

$$\Gamma(x, \Delta\vec{\rho}) = e^{-\frac{1}{2}D(\Delta\vec{\rho})} \quad , \tag{21}$$

where $D(\Delta\vec{\rho})$, the phase structure function, is the integral of the differential structure function over the propagation path.

The dielectric fluctuations of (18) can be related to electron density fluctuations by making use of the relation $\epsilon_r = 1 - (r_e c^2/\pi)N_e/f^2$, valid for an isotropic collisionless cold plasma. Here r_e is the classical electron radius and f is the wave frequency. Let ξ represent the fractional electron density deviation,

$$\xi = \frac{\Delta N_e}{\langle N_e \rangle} \quad . \tag{22}$$

In Section 3 we will consider FDTD propagation orthogonal to elongated electron density structure described by a *Gaussian* autocorrelation function,

$$B_\xi(\rho) = \frac{\sigma_{N_e}^2}{\langle N_e \rangle^2} e^{-\frac{\rho^2}{L_o^2}} \quad , \tag{23}$$

where L_o characterizes the scale size of the electron density structures. For propagation through a structured slab of length L, the phase structure function for the Gaussian case is

$$D(\Delta y) = 2\sigma_\phi^2 \left[1 - e^{-\frac{\Delta y^2}{L_o^2}}\right] \quad , \tag{24}$$

where

$$\sigma_\phi^2 = \sqrt{\pi}(\lambda r_e)^2 L L_o \sigma_{N_e}^2 \quad , \tag{25}$$

and

$$\sigma_{N_e}^2 = \xi^2 \langle N_e \rangle^2 \quad . \tag{26}$$

This brings us another typically applied approximation, the so-called Quadratic Structure Function (QSF) approximation. Since the two-position mutual coherence function solution (21) is simply the exponential of the phase structure function, a Gaussian mutual coherence function is obtained when the phase structure function is quadratic. Indeed, if the exponential in (24) is expanded in a Taylor's series, such a quadratic structure function is obtained by neglecting terms of higher power than two. Such an approximation is valid, however, only under conditions of sufficiently strong scatter that the mutual coherence function is essentially zero for spatial separations exceeding L_o. Figure 1 shows the effect of the QSF approximation. Here the parameters of the ionized medium have been chosen to agree with those used in our FDTD runs to be discussed in the next section. The solid curves are the mutual coherence functions obtained from the parabolic equation (PE) solution (24) and the dotted curves are the corresponding QSF approximation results. Only in the strongest

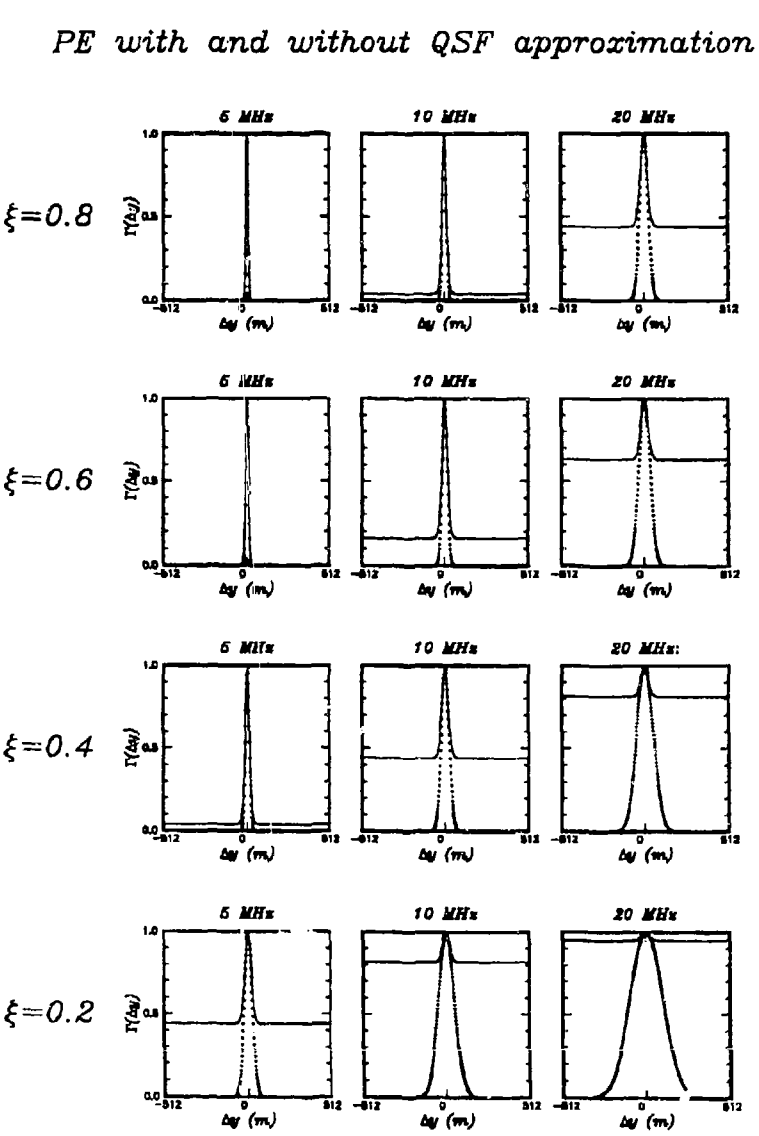

Figure 1: Mutual coherence functions obtained using the full parabolic equation result (solid curves) and the quadratic structure function approximation (dotted curves).

scattering cases do the two solutions agree. For moderate to weak scatter, the QSF approximation fails to exhibit the semi-coherent "wings" of the full PE solution. The QSF result does match the the central "Gaussian" portion of the full PE result.

One important result of the QSF approximation is the simple expression for the transverse correlation length, defined as the $1/e$ point of the (Gaussian-shaped) QSF mutual coherence function. For our case of interest (propagation orthogonal to infinitely elongated electron density structure) the field correlation length transverse to both the propagation direction and the elongation direction, ℓ_o, is given by,

$$\ell_o = \frac{L_o}{\sigma_\phi} \quad . \tag{27}$$

More general second moments are also of interest such as the case in which the fields in (17) are evaluated at separated frequencies as well as separated spatial points, and various approaches to the solution of the associated second moment equation exist. Notably, *Knepp* [1983, 1985] has obtained an analytic solution for the two-position two-frequency mutual coherence function for a spherical wave impinging on a randomly structured slab of background electron density. This solution can be reduced to the single frequency plane wave case discussed above by receding the spherical wave source to an infinite distance from the medium and setting the frequency separation to zero.

Let us summarize the above development for propagation in the strong scatter regime. First the true vector wave equation is reduced to the scalar Helmholtz wave equation by neglecting the polarization coupling contribution (generally valid when the field wavelength is small relative to the ionospheric structure scale size). Then it is assumed that the field is dominantly forward scattering; all backscattered contributions are ignored. It is further assumed that this forward scattered field is scattered through only small angles, resulting in the so-called parabolic approximation in which a second derivative contribution in the propagation direction is neglected relative to other terms (generally valid when the field correlation length is large relative to the field wavelength). From the parabolic wave equation, stochastic equations are formed for higher field moments, usually under the assumption that the fluctuations in the refractive index are small relative to the mean, and the Markov assumption is used (the propagation medium is assumed to be delta correlated in the propagation direction). From this point further analytical progress is made by assuming that the moments depend only on transverse spatial separations, not on absolute positions. Finally, it is often assumed that the scatter is sufficiently strong that the quadratic structure function (QSF) approximation is valid.

3. FDTD Propagation in Randomly Structured Ionization

The analysis we are about to present extends an earlier, very preliminary look into FDTD propagation in randomly structured ionization [*Nickisch and Franke*, 1993]. In that work we presented results based on FDTD computations performed with grid densities which ranged from minimally adequate at the lower frequencies considered (eight points per wavelength) to inadequately sparse at the higher frequencies (four points per wavelength). However, the

potential of the method was demonstrated and some indication of the nature of the discrepancy between the approximate theoretical results and full vector wave FDTD results was gleaned. The current work is based on significantly enhanced grid densities and additionally includes comparisons with FDTD-generated solutions of the Helmholtz wave equation.

The FDTD computations were performed on a 1024 by 512 point mesh, with the longer dimension in the direction transverse to the direction of propagation of the incident plane wave pulse. The grid spacing was taken to be 1 meter in each direction of the 2-D mesh, which allowed better than ten point per wavelength resolution for frequencies up to 30 MHz. The incident pulse form (in the propagation direction) was chosen to be a single cycle of a squared cosine (and planar in the transverse dimension), and its temporal width was adjusted so that its frequency spectrum was essentially zero at frequencies above 30 MHz. Thus the grid was able to support the full frequency content of the signal with excellent resolution. The incident pulse was polarized in the transverse ($\hat{y}$) direction.

The randomly structured medium consisted of a background slab of ionization at a plasma frequency of 4 MHz, 320 meters long in the propagation ($\hat{x}$) direction, with steep exponential tapering at the forward and backward edges, and extending the entire transverse dimension. The superimposed random structure had a Gaussian autocorrelation function characterized by an $L_o = 32$ meter scale, and the fractional electron density variance was varied between $\xi = 0.2 - 0.8$ for the different runs.

These 2-D computations actually represent 3-D propagation for a plane wave pulse incident normally on ionization structure infinitely elongated in the third ($\hat{z}$) direction. Periodic boundary conditions were employed at the transverse grid edges. Second order Mur absorbing boundary conditions were used at the forward and backward edges [*Mur*, 1981]. Only the forward propagating field was studied in detail; the signal time history was recorded at a plane beyond the structured slab of ionization.

Figure 2 displays the time history at the receiver plane of the principal polarization of the field for the vector wave case with $\xi = 0.8$. Angular scatter is evident in the contorted wavefronts. The corresponding cross-polarized field component is shown in Figure 3. Note that this cross-polarized energy would not appear for the scalar Helmholtz wave equation since no polarization coupling occurs there; the energy transferred to the cross-polarization in the vector wave equation case remains in the principal polarization in the Helmholtz case. In Figure 4, the frequency domain content of the principal polarization is displayed (magnitude only), illustrating one of the greatest advantages of the time domain approach over spectral approaches: In a single calculation we have computed the response a very large portion of the HF band. Frequency domain approaches would have required numerous calculations to obtain such coverage. We note that signal absorption due to electron collisions was accounted for in this calculation, and thus much of the lower frequency content of the incident signal has been removed by the medium. The geomagnetic field was turned off here, however, so there are no anisotropic effects.

In addition to the performing full vector wave FDTD computations, we also performed similar computations with the scalar Helmholtz wave equation by neglecting the polarization coupling term in Equation (7). Figure 5 displays the frequency domain content of the

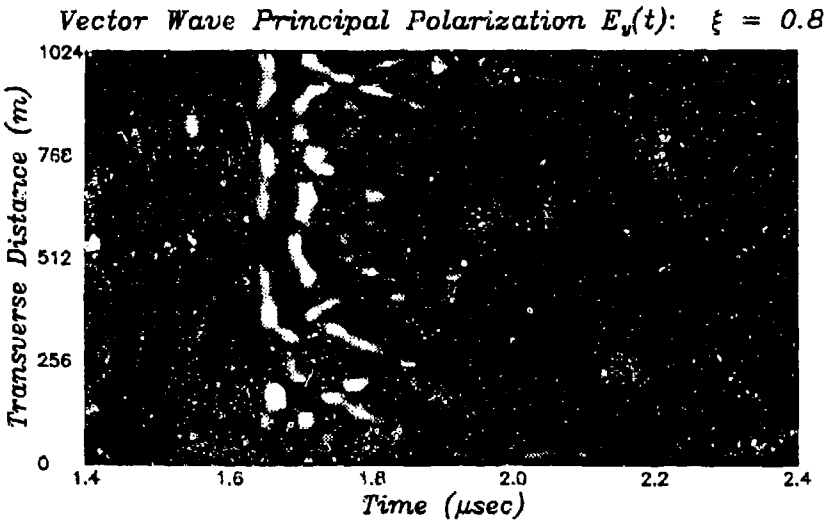

Figure 2: Time domain field of the principal polarization for the vector wave equation case.

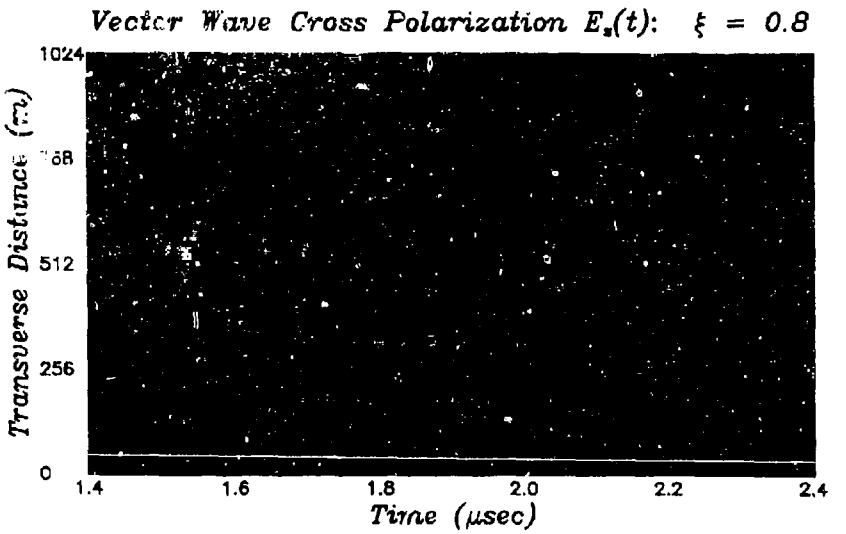

Figure 3: Time domain field of the cross-polarization for the vector wave equation case.

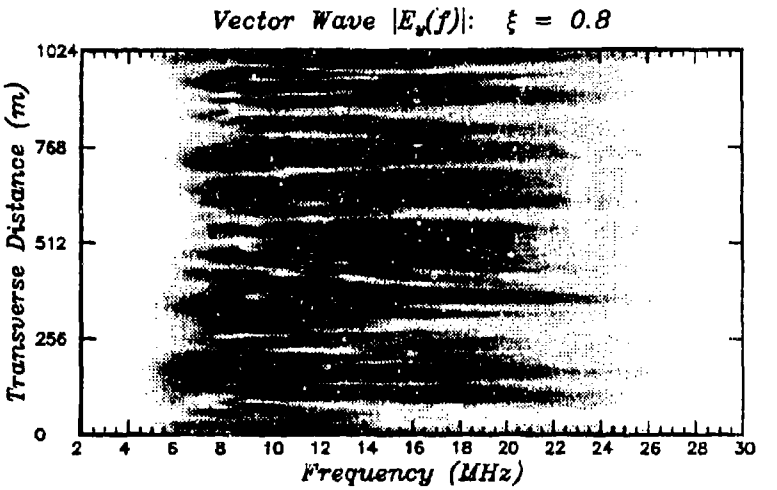

Figure 4: Frequency domain field magnitude for the vector wave equation case.

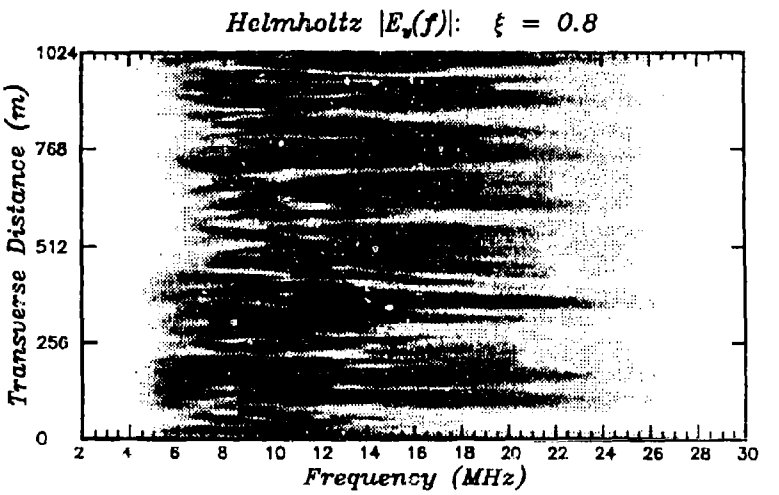

Figure 5: Frequency domain field magnitude for the Helmholtz wave equation case.

Helmholtz result. It is nearly indistinguishable from the principal polarization component of the corresponding vector wave equation case, Figure 4. The difference appears to be primarily one of amplitude as all the energy transferred to the cross-polarization in the vector wave equation case remains in this polarization in the Helmholtz case. Though we will not show specific examples here, we have noted substantially larger differences in the backscattered fields of the two cases.

The reader familiar with RF signal propagation in randomly structured ionization will note that the calculational parameters used in our FDTD computations (quoted above) are stressing to the validity of the standard random media propagation approximations. It is of interest, then, to see what the theory which makes use of all the approximations predicts in this case. To perform such a comparison, we computed the two-position mutual coherence function (MCF) of the received field across the frequency band for several realizations similar to Figure 4, but for varying fractional electron density variances ($\xi = 0.2, 0.4, 0.6, 0.8$). We then computed the correlation lengths of these MCFs and compared them to the results of the analytical calculation discussed at the end of Section 2.

Figure 6 displays a subset of the mutual coherence functions computed from the FDTD realizations (solid curves). Recall that the standard definition of the correlation length is the $1/e$ point of the mutual coherence function. In order to compare with the QSF approximate expression for the correlation length, we also fit the central peak of our FDTD generated MCFs with Gaussians (dotted curves in Figure 6). The correlation lengths quoted in Figure 6 represent the $1/e$ points of these fitted Gaussians. The correlation lengths so defined actually indicate the coherence scale of the random component of the field only.

The results of our correlation analysis are displayed in Figure 7. Here the FDTD vector wave equation results are shown as crosses, the Helmholtz results are indicated by circles, and the approximate propagation theory results appear as solid curves (denoted *QSF PE*). We point out that these computations were performed with superior FDTD grid resolution (60 points per wavelength at 5 MHz and ranging to 10 grid points per wavelength at 30 MHz).

The first thing to note about Figure 7 is the remarkable agreement of the methods considering how far away from the regime of validity the theoretical approximations were applied. The numerical values are at least of the same order of magnitude, and such accuracy is often all that is required when considering system performance issues in severely structured environments. One must bear in mind, however, that if the standard $1/e$ definition of the signal correlation length had been applied in computing the vector wave and Helmholtz results, their curves in Figure 7 would be arcing strongly toward infinity at the RHS of the figure. But at least in an intermediate regime, the FDTD curves closely approach the theoretical curves.

The second point of interest is that in all cases the vector wave correlation lengths are larger than the Helmholtz values. Thus, for the principal polarization, neglect of polarization coupling produces a somewhat more pessimistic result from a system performance point of view. We have found (but do not show here) that the correlation lengths of the cross-polarized fields for the vector wave equation case are substantially smaller than those of the

Vector Wave: Principal Polarization

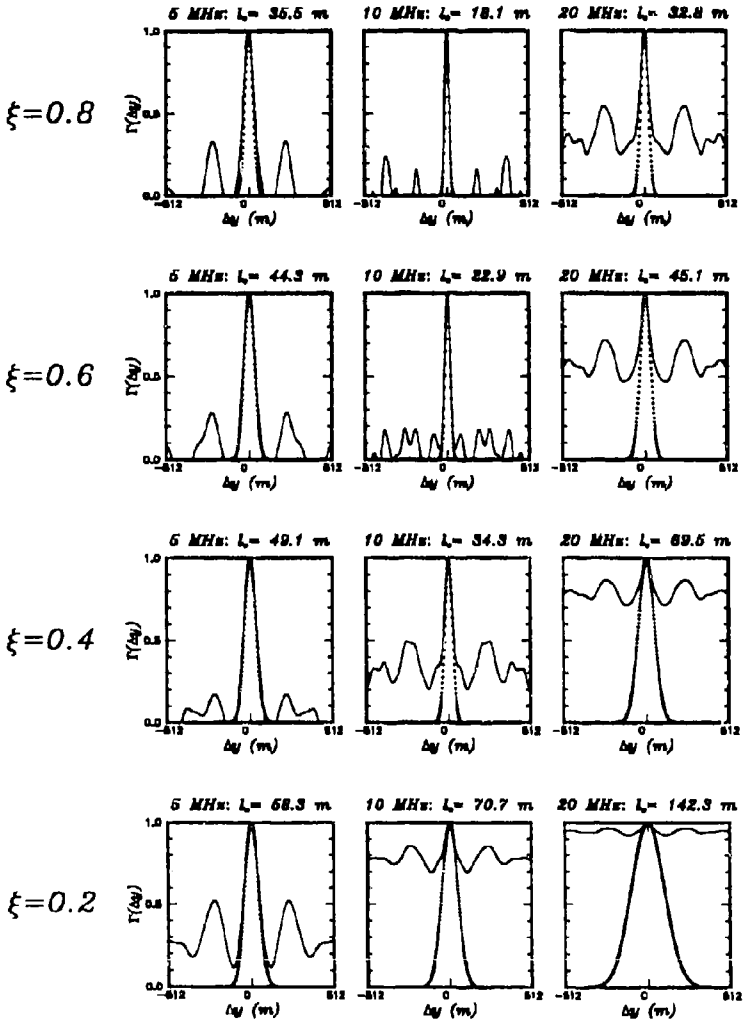

Figure 6: FDTD computed two-position mutual coherence functions and best fit Gaussians.

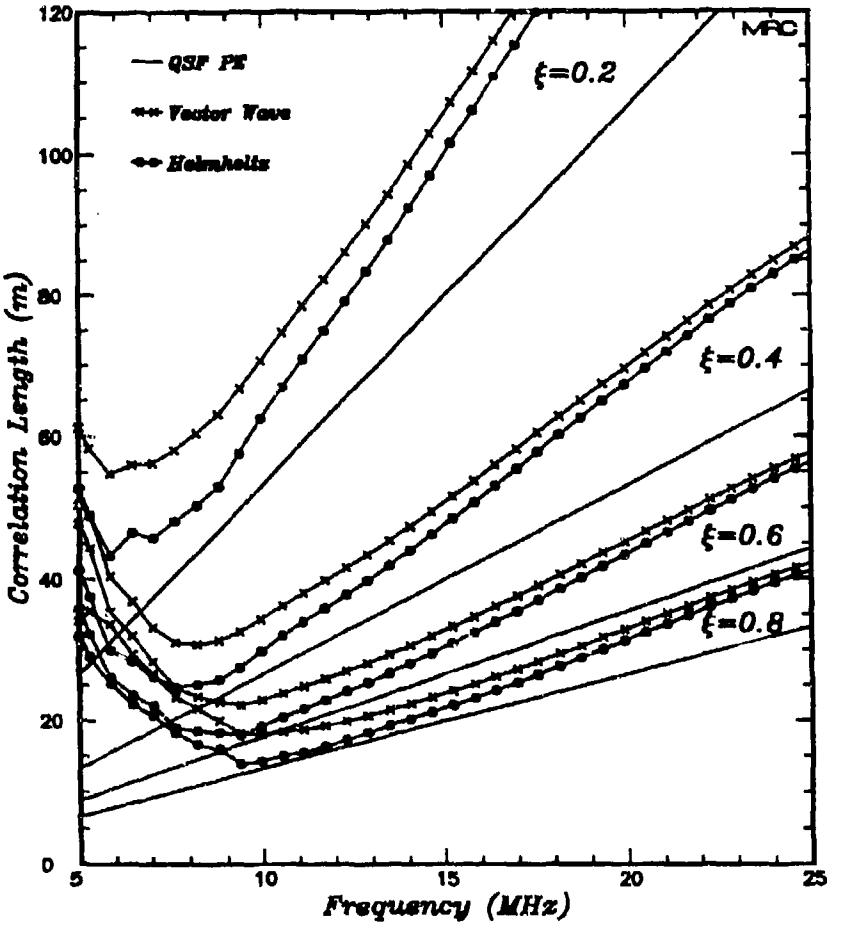

Figure 7: Correlation lengths of best fit Gaussians to the FDTD-computed vector wave equation (crosses) and the Helmholtz wave equation (circles), compared to the theoretical parabolic equation result under the QSF approximation (solid curves).

principal polarization. The smaller coherence scale of the cross-polarized field occurs in these cases because all field energy in the cross-polarized channel is the result of depolarizing scatter of the principal polarization field from the random structure; there is no incident coherent field in the cross-polarized channel.

Thirdly, there is a minimum frequency in each case below which the FDTD computed correlation lengths grow larger with declining frequency, in marked contrast to the predictions of the approximate theory. This is the regime where the most fundamental assumptions leading to the parabolic wave equation are being violated; the field correlation length and the structure scale size of the medium become smaller than the field wavelength. The effect is manifested in smoother, more coherent fields.

4. Discussion

Comparison of Figures 1 and 6 is quite illuminating. Because the FDTD-computed MCF is obtained by spatial averaging over a limited transverse dimension, as opposed to ensemble averaging with an infinite data base, the "wings" of the FDTD-computed MCFs are not smooth. Yet the agreement of Figures 1 and 6 is remarkable. This indicates that, at least for the limited parameter regime tested, the parabolic approximation holds pretty well for the principal polarization. The breakdown of the parabolic equation's approximations is primarily manifested at the lowest frequencies where the vector wave MCFs broaden relative to the PE MCFs. The quadratic structure function approximation, however, is seen in these figures to have a quite limited regime of applicability.

Our results, as summarized in Figures 6 and 7, indicate that when the approximate propagation theory is applied in the regime where the field correlation lengths and the scale size of medium structure approach or even get smaller than the field wavelength, it does not underestimate the level of signal decorrelation. Similarly, in the regime where the QSF approximation is invalid, at least the level of signal decorrelation is again not underestimated. This is good from the standpoint that systems designed under the more stressing conditions predicted by the approximate theory should be able to perform under the true, more benign conditions. However, there is a danger that systems could be over specified, resulting in more costly systems than necessary. Systems which might be predicted to fail by the predictions of the approximate propagation theory (when applied outside of its regime of strict validity) could possibly be able to operate in reality.

We must be careful in interpreting the increase of correlation length with declining frequency exhibited on the LHS of Figure 7. Both conditions $L_o \gg \lambda$ and $\ell_o \gg \lambda$ are being violated in the approximate propagation theory, and there is no way of ascertaining from the current set of FDTD data which violation is playing the dominant role in correlation length growth. It seems plausible, however, that it is the smallness of the ionization structure scale sizes with respect to the field wavelength which is most important; the structures are less effective at scattering wavelengths significantly larger than themselves.

The FDTD analysis presented here is very limited in scope. Only the forward propagating wave was examined in detail, and this only for a structured plasma slab of one fixed length

with a Gaussian autocorrelation function of one fixed scale size. One should be cautious about generalizing these results to other parameter regimes.

Acknowledgements

Dr. Nickisch's contributions to this work were supported by the Defense Nuclear Agency under contract DNA001-93-C-0168.

References

Budden, K. G., The Propagation of Radio Waves, Cambridge University Press, 1985.

Ishimaru, A., Wave Propagation and Scattering in Random Media, Academic Press, 1978.

Knepp, D. L., "Analytic solution for the two-frequency mutual coherence function for spherical wave propagation," *Radio Sci.*, **18**, no. 4, pp. 535-549, 1983.

Knepp, D. L., "Aperture Antenna Effects After Propagation Through Strongly Disturbed Random Media," *IEEE Ant. Propag.*, **AP-33**, no. 10, pp. 1074-1084, 1985.

Mur, G.,"Absorbing boundary conditions for the finite-difference approximation of the time domain electromagnetic-field equations," *IEEE Trans. Electromagn. Compat.*, **EMC-23**, no. 4, pp. 377-382, 1981.

Nickisch, L. J. and P. M. Franke, "Finite Difference - Time Domain Solution of Maxwell's Equations for the Dispersive Ionosphere," *IEEE Antennas and Propagation Magazine*, Vol. 34, No. 5, October 1992.

Nickisch, L. J. and P. M. Franke, "Toward an FDTD Analysis of the Standard Approximations for Propagation in Randomly Structured Ionization," *9th Annual Review of Progress in Applied Computational Electromagnetics - Conference Proceedings*, March 1993.

Nickisch, L. J., "Non-uniform motion and extended media effects on the mutual coherence function: An analytic solution for spaced frequency, position, and time," *Radio Sci.*, **27**, no. 1, pp. 9-22, 1992.

3D Analysis of Nonlinear Magnetic Diffusion by FDTD Techniques

Richard Holland
Shield Rite, Inc., P. O. Box 8250
Albuquerque, NM 87198
(505) 842-6018 or 0126

Abstract

The Finite-Difference Time-Domain (FDTD) approach is a particularly useful method for investigating nonlinear electromagnetics because the nonlinear relationships may be directly incorporated into the equation for advancing the electromagnetic fields. This approach is applicable to nonlinear magnetic materials with or without hysteresis (i.e., time dependence). Problems with geometric details that are very small compared to signal wavelengths, however, stress FDTD techniques. This occurs because the Courant-limited Δt can become small enough to require the use of $> 10^{11}$ time steps unless one is tricky. Tricky means observing that this sort of problem has a solution which seldom depends on the speed of light c. Here, we demonstrate successfully whacking the Courant stability condition senseless by defining c to be 100 m/s.

Introduction

In a previous publication,[1] we described the "reduced-c" technique for a magnetically linear 3D problem. The linear problem geometry is illustrated in Figure 1: It consists of an aluminum enclosure with walls 0.0127 m (.5 in) thick. The overall enclosure is 2.54m x 2.54m x 16.18m (100in x 100in x 637in). All of the walls are meshed into five cells, each 0.0051 m thick. Interior mesh count is 5 x 5 x 20 cells. The enclosure is driven by a current on the underlying conductor of

$$I = A\ (e^{-\alpha t} - e^{-\beta t}) \tag{1}$$

where

$$\begin{aligned} A &= 45.0\ kA \\ \alpha &= 22.2\ s^{-1} \\ \beta &= 6450\ s^{-1} \end{aligned} \tag{2}$$

In this paper, we shall discuss excitation of a steel enclosure. The dimensions of the steel enclosure differ in a minor way from the aluminum one: Its dimensions are 2.87m x 2.87m x 17.22m, and walls are .0118 m thick. The cell arrangement is identical to that shown in Figure 1 for the aluminum enclosure, so the actual cell sizes are proportionately altered in a minor way. In Figure 1, the thickness of the wall cells is greatly exaggerated to make them visible.

While the objective of our *study* was to evaluate the magnetic fields diffusing into the enclosure, the objective of this *article* is to illustrate a means for avoiding Courant-dictated Δt's which are ridiculously tiny. There has been FDTD work where one first makes a coarse pass to

determine the general nature of the EM fields over a large object. One can then finely rezone a small portion of the target and use the first-pass solution to drive the rezoned portion of the target on a second pass. This scheme is called the two-pass algorithm. On the second pass, the Courant-limited Δt can become onerously small, even though there are no electromagnetic effects that require fine temporal resolution. The reduced-c technique can however, be applied to the second pass. This is a novel concept, and should permit much more practical application of two-pass FDTD procedures.

The Nonlinear Constituent Relations

For B vs. H nonlinear, but not with hysteresis, we first expressed $\mu(H) = B/H$ in a three-range dependence:

$$\mu(H) = \begin{cases} \mu_0(\mu_i + \nu H) & H \le H_{low} \\ \nu_0 & H_{low} < H < H_{high} \\ \dfrac{1}{a + b(H - H_3)} + \mu_0 & H \ge H_{high} \end{cases} \tag{3}$$

If the nonlinear FDTD equations are used in this form, it is necessary to advance H by iteration: $\mu(H^{m+1})$ is first approximated by $\mu(H^m)$. The new H^{m+1} thus computed is then used to estimate $\mu(H^{m+1})$, and H is solved again. In the particular example we studied, one iteration was satisfactory, although we also tested five, two, and zero iterations. Table 1 shows some magnetization model parameters we used. Figure 2 shows the associated $B/H = \mu(B)$ vs. B curves.

Table 1. Table of Model Parameters

	a	b	ν	ν_0	B_{low}	B_{high}	H_3	μ_i
Tape 2.4	400	1.22	13.369	2.142×10^{-3}	.257	.535	194	100
Tape 2.5	162	0.61	6.35	2.136×10^{-3}	.52	1.07	0	100
Tape 2.6	163.26	.8107	8.471	2.115×10^{-3}	.39	.8025	0	100

Numerical Results

All results which we present are based on the speed of light being slowed to 5000 m/s in normal cells (see Figure 1), and to 100 m/s across the thin dimension of the skinny cells. This slowing is implemented by scaling ε. Normally, one could also scale μ, but we think that would cause problems here due to the assumed magnetic nonlinearities. The ε scaling factors required to reduce c to this degree are about $\varepsilon_r = 4 \times 10^9$ in ordinary cells and $\varepsilon_r = 10^{13}$ across the skinny cells. These scaling factors, for the given cell dimensions, result in a model where all cell edges, large and small, require about 20 ps for light to transit. On the order of 3×10^4, instead of 10^{11} time steps are thus required for calculations out to .5 s. Our calculation are all based on a steel bulk conductivity of 2.5×10^6 S/m.

The enclosure was divided up into measurement planes denoted 2 to 6, as illustrated in Figure 3. The transverse magnetic field was sampled at four points in each plane, located as Figure 4 shows. Experimental results we shall discuss were all taken at Cross-section 6. Figure 5 compares the experimentally observed magnetic field at Observation Point 1 and the calculated magnetic field based on the models parameterized in Table 1. The same data is compared at Point 3 in Figure 6, at Point 5 in Figure 7, and at Point 7 in Figure 8. Generally speaking, fields are overpredicted near the floor of the enclosure and underpredicted near the ceiling of the enclosure. The Tape 2.4 model permits part of the enclosure floor to saturate, which results in the major spike (i.e., shielding breach) predicted at early time at Observation Point 1.

Hysteretic Considerations

The steel enclosure walls actually exhibit considerable hysteresis. One model for B vs. H with hysteresis is the cubic representation shown in Figure 9:

$$H(B) = a_3B^3 + a_2B^2 + a_1B + a_0 \tag{4}$$

where, for the upper curve

$$(a_3,\ a_2,\ a_1,\ a_0) = (137.1,\ -242.2,\ 191.8,\ 700.) \tag{5}$$

and for the lower curve

$$(a_3,\ a_2,\ a_1,\ a_0) = (137.1,\ 242.2,\ 191.8,\ -700.) \tag{6}$$

If one is at some point (B^n, H^n) within the area enclosed by the curves, and if B^{n+1} is a ΔB change from B^n, then H^{n+1} is evaluated through an operation of the form

$$H^{n+1} = m_w(B^{n+1} - B^n) + H^n \tag{7}$$

where m_w is a multi-valued weighted slope defined to contain the hysteretic path within the prescribed hysteresis and to follow the appropriate curve as the fields move into the saturation region.

In general, the complexities of FDTD analysis with hysteresis present are outside the scope of this publication. Our intent is more to bedazzle the reader with the wonders of the Courant-eluding reduced-c concept than to get bogged down in the dreadful drudgery of FDTD characterization of hysteresis in 3D.

Conclusions

We have demonstrated that, for geometries where fields evolve very slowly compared to electromagnetic transit times, the Courant condition can be stretched many orders of magnitude by scaling ε and/or μ. The present article demonstrates a case where ε was scaled by 10^{13} to reduce c to 100 m/s. Usually, ε and μ are best scaled equally, so the free-space impedance E/H is not modified. Where ε is scaled by ε_r, μ is unscaled, and the input drive is a current or magnetic field, reduced-c computations will output E fields low by the factor $(\varepsilon_r)^{1/2}$.

Acknowledgement

The author wishes to thank Ray Luebbers, who has also examined magnetically nonlinear problems by FDTD,[2] for recognizing the full significance of the reduced-c concept as it pertains to mitigating Courant limitations. Without his enthusiastic reaction, it is unlikely we would be promoting application of this concept to the entire FDTD/FVTD community, as opposed to a limited magnetic diffusion audience.

References

1. R. Holland, "Finite-difference-time-domain (FDTD) analysis of magnetic diffusion," *IEEE Trans. Electromagn. Compat.*, vol. EMC-36, pp. xx-xx, February 1994.

2. R. Luebbers, K. K. Kumagai, and S. Adachi, "FDTD calculation of transient pulse through a nonlinear steel sheet," *IEEE Trans. Electromagn. Compat.*, vol. EMC-35, pp. 90-94, February 1993.

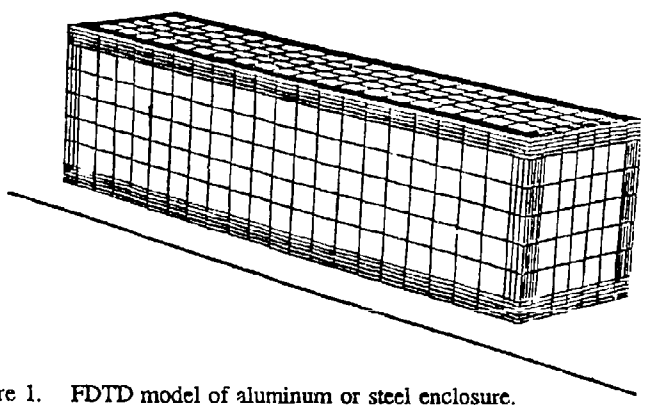

Figure 1. FDTD model of aluminum or steel enclosure.

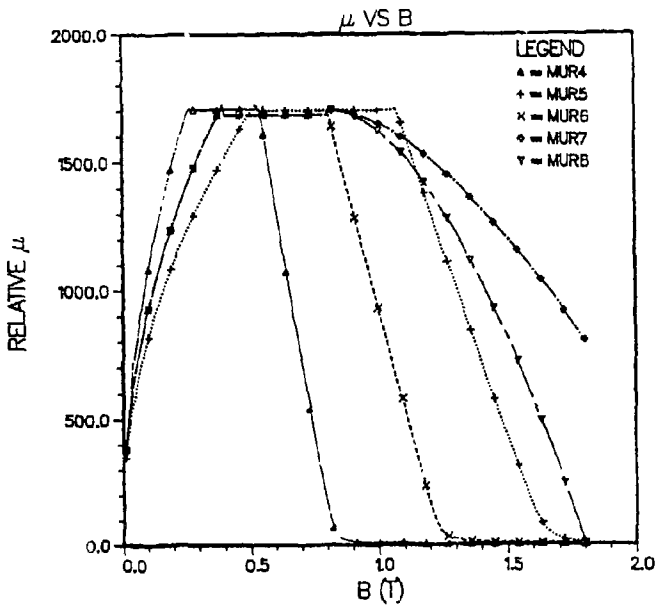

Figure 2. μ vs. B curves based on the parameters defined in (3), and given the Table 1 values.

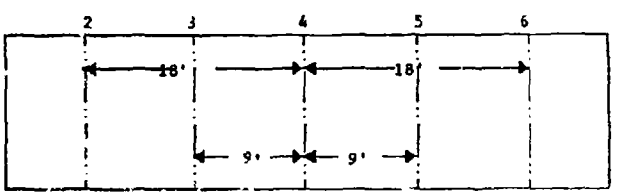

Figure 3. Measurement Planes 2 - 6 of the enclosure.

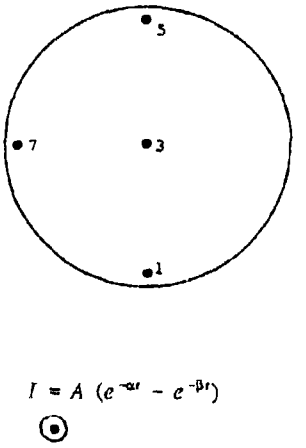

Figure 4. Location of transverse magnetic field observation points in each measurement plane.

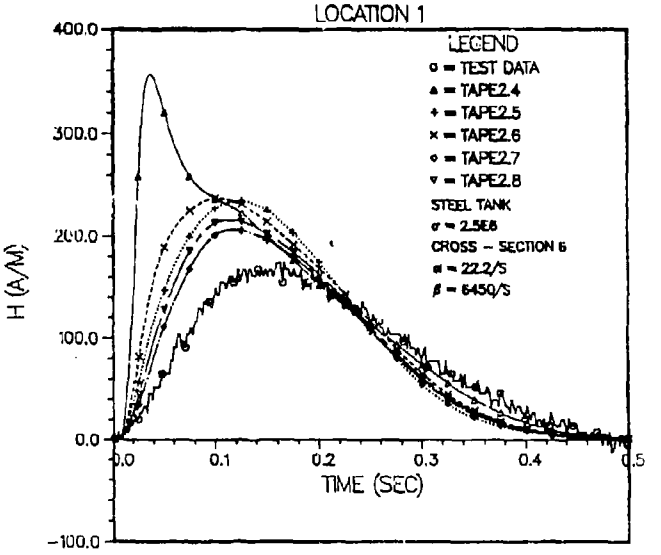

Figure 5. Overlay of Point 1, Plane 6 experimental H_x and the H_x predicted by the runs summarized in Table 1. The overshoot for Tape 2.4 occurs because part of the enclosure floor goes into saturation. In general, calculations on the enclosure floor overestimate H_x.

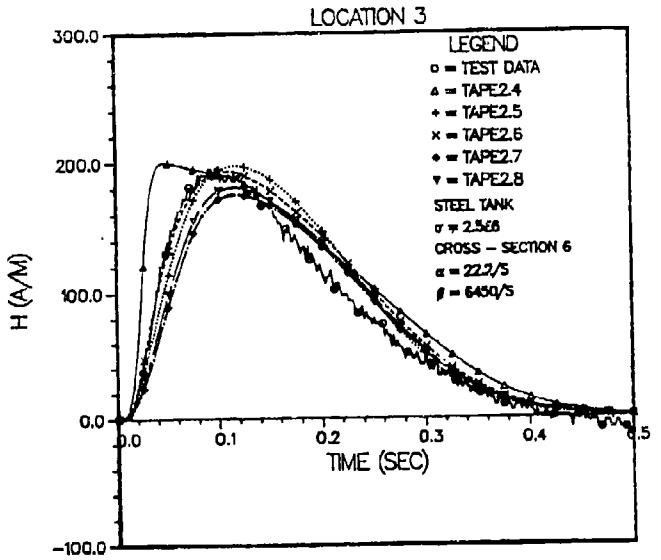

Figure 6. Overlay of Point 3, Plane 6 experimental H_x and the H_x predicted by the runs summarized in Table 1. There is again some saturation evident for Tape 2.4.

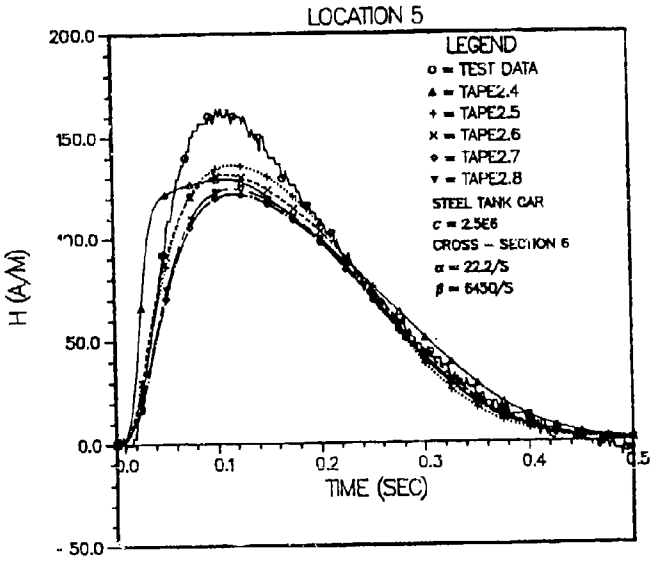

Figure 7. Overlay of Point 5, Plane 6 experimental H_x and the H_x predicted by the runs summarized in Table 1. In general, calculations at the enclosure ceiling underestimate H_x.

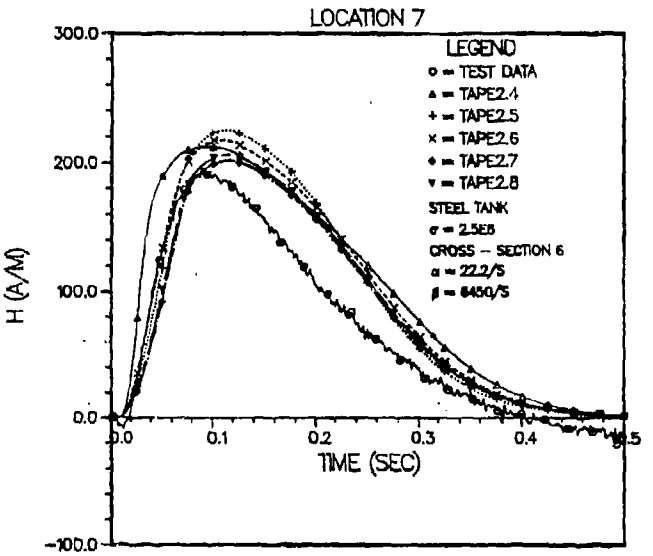

Figure 8. Overlay of Point 7, Plane 6 experimental H_x and the H_x predicted by the runs summarized in Table 1.

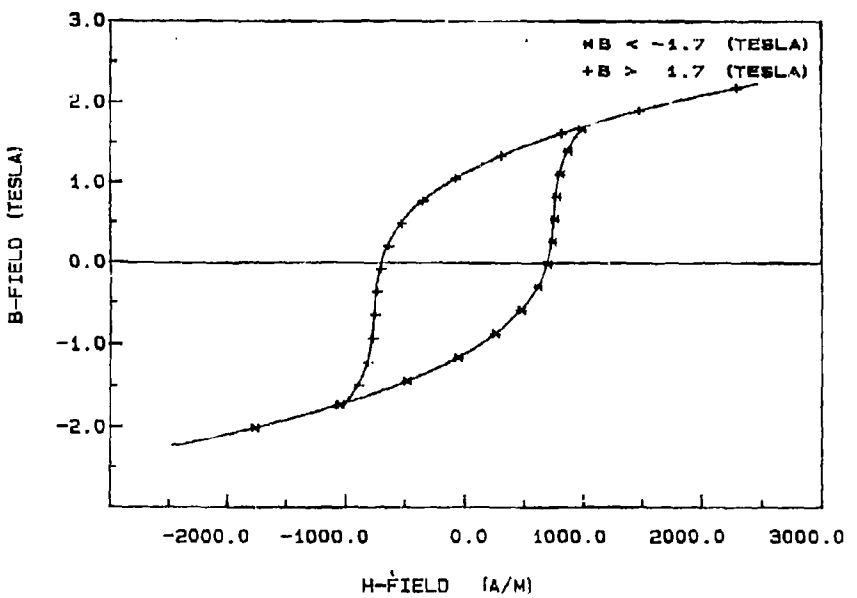

Figure 9. Bounding B vs. H hysteresis defined by the cubic fit of Eqs. (4) - (6).

Performance Prediction for Three-Dimensional Anechoic Chambers using FDTD

Vaughn Cable*
Lockheed Advanced Development Company
D/25-50 B/311
1011 Lockheed Way
Palmdale, CA 93599

Raymond Luebbers, Christopher Penney,
Scott Langdon, and Joseph Schuster
Department of Electrical Engineering
The Pennsylvania State University
University Park, PA 16802

INTRODUCTION

With the increased availability of more powerful computers for both visualization and calculation, the Finite Difference Time Domain (FDTD) method is being applied to problems of greater geometric complexity and larger electrical size. One such problem is the prediction of low frequency electromagnetic performance of microwave anechoic chambers.

Anechoic chamber performance at low frequency suffers from resonance or reverberation. Measurements and high frequency analysis cannot solve these problems. FDTD, on the other hand, can model these "cavity" problems.

APPROACH

In order to provide this prediction capability to users who are not necessarily experts in the FDTD method, a suite of computer codes has been developed which makes this analysis capability available in a user-friendly environment. Nevertheless, great generality in chamber design, calculation, and display has been preserved.

There are three separate computer codes involved. One generates the wall, ceiling, and floor geometries of absorber covering. The user can define various primitive shapes, such as pyramids and wedges, and specify the electrical parameters. The user can then assemble them to cover the walls, floor and ceiling. Sub-areas can also be covered, so that walls can include different absorber shapes. The areas covered need not be constrained to the wall planes, so that a chamber with a pit or with slanted walls can be modeled. This program then produces a cubical mesh from this geometry information.

Another code performs the actual FDTD calculations. It reads files containing geometry and calculation parameters, and produces various output files of calculated field quantities.

The interface between these two programs is an X-Windows Graphical User Interface (GUI) program. It reads the absorber geometry file produced by the first program. It can modify this mesh, and add feed antennas, reflector, and target. It also produces, under menu control, the run parameters for the FDTD calculations. After the FDTD calculations are complete, this same program reads the resulting field files and displays the calculated results. Individual components of the fields, as well as the electrical conduction currents or the instantaneous Poynting vectors, can be visualized, and the values of these components can be determined anywhere in the chamber.

DEMONSTRATION

Results derived from this suite of codes will be presented and discussed at the conference. This includes a video tape which illustrates the setup procedure and an FDTD visualization of the fields inside a sample chamber.

Application of the Finite-Difference Time-Domain Method in the Simulation of Delta-I Noise in Electronics Packaging

Jiayuan Fang, Zhonghua Wu, Yuzhe Chen and Yaowu Liu
Department of Electrical Engineering
State University of New York at Binghamton, Binghamton NY 13902

Abstract

This paper presents the application of the finite difference time domain method in the simulation of Delta-I noise in electronics packaging. The FDTD program is used to compute the electromagnetic fields between the power and ground planes, and is executed simultaneously and linked together with circuit simulators for lumped and transmission line components. Numerical tests show that the FDTD approach is far more efficient than other techniques presently used to model the effects of power and ground planes, and can provide much more accurate results than the widely used effective inductor model.

I. Introduction

As integrated circuits are operated in higher speed and built in more condensed packaging, the voltage fluctuation, which is often called the Delta-I noise, in the power supply system of integrated circuits has become a more significant limiting fact for the reliable operation of high-speed integrated circuits [1]. Power and ground planes are widely used in chip modules. However, present methods to model the effects of power and ground planes can hardly be considered accurate or efficient. The most widely used method of modeling power and ground planes has been the effective inductor model. This static field approximation does not take into account the field propagation and resonance in power and ground planes, and is inaccurate for high-speed circuits. The Method of Moment has also been used for the modeling of power and ground planes [2]. With the Method of Moment, the conducting planes are approximated by conducting wire grids. Then the current distribution on the conducting wires is solved for. This frequency domain approach is not easy to be directly incorporated with transient circuit simulators. In some circuit simulators, such as in ASTAP of IBM, the power and ground planes are represented by distributed capacitors and inductors. The main drawback of these circuit simulators is the requirement of excessive computer resources.

This paper presents the application of FDTD method to compute the fields between power and ground planes. The power and ground planes and lumped circuit elements are modeled altogether by linking the FDTD program with circuit simulators. It is found that substantial numerical error can be introduced if the FDTD program is directly linked with circuit simulators. However, it will be shown that such numerical error can be eliminated by adding an impedance transformer at the FDTD grid point where the linkage between the FDTD program and circuit simulators are made. The combined FDTD/circuit-simulator approach is found to be efficient and highly accurate.

II. FDTD Computations

Consider the configuration of a power and a ground plane connected to a number of pairs of vias, as shown in figure 1. As currents flow through vias onto the power and ground planes, they generate

transient fields which attribute to voltage fluctuations between power and ground planes. In typical packaging structures, the size of the power and ground planes is much larger than the separation between them. The electromagnetic fields between the power and ground planes, except near the via junctions, can be considered invariant in the z direction which is perpendicular to the power and ground planes. The two dimensional field between power and ground planes satisfies the following differential equations:

$$\nabla V(x,y,t) = -L_s \frac{\partial J_s(x,y,t)}{\partial t} \tag{1}$$

$$\nabla \cdot J_s(x,y,t) = -C_s \frac{\partial V(x,y,t)}{\partial t} \tag{2}$$

where V(x,y,t) represents the voltage between power and ground planes, $J_s(x,y,t)$ is the current density on the power plane, L_s is the inductance per square, and C_s is the capacitance per unit area. At the edges of power and ground planes, the current component normal to the edges are set to zero. By using central difference approximations of spatial and time derivatives, and assuming equal FDTD grid size in the x and the y directions ($\Delta x = \Delta y = dh$), the difference equations of equation (1) and (2) are:

$$\begin{aligned} V^{n+1}(k,l) = V^n(k,l) - \frac{\Delta t}{C_s (dh)^2} [& I_x^{n+1/2}(k+1/2,l) - I_x^{n+1/2}(k-1/2,l) \\ & + I_y^{n+1/2}(k,l+1/2) - I_y^{n+1/2}(k,l-1/2)] + \frac{\Delta t}{C_s (dh)^2} I_s^{n+1/2}(k,l) \end{aligned} \tag{3}$$

$$I_x^{n+1/2}(k+1/2,l) = I_x^{n-1/2}(k+1/2,l) - \frac{\Delta t}{L_s} [V^n(k+1,l) - V^n(k,l)] \tag{4}$$

$$I_y^{n+1/2}(k,l+1/2) = I_y^{n-1/2}(k,l+1/2) - \frac{\Delta t}{L_s} [V^n(k,l+1) - V^n(k,l)] \tag{5}$$

where the current $I_x = J_{sx} \cdot dh$ and $I_y = J_{sy} \cdot dh$. Difference equations (3) to (5) are applied alternatively until a pre-specified time step for termination.

III. Input Impedance of FDTD Grids and Linkage between FDTD Code and Circuit Simulators

In electronics packaging structures, power and ground planes are connected to lumped circuit elements or strip/microstrip lines through vias. At the FDTD grid points where vias are located, the FDTD program is linked with circuit solvers for lumped components. It is found that the direct linkage between FDTD code and a circuit analysis program at one single FDTD grid point can result in significant numerical error. This error is originated from the mismatch between the input impedance of a FDTD grid and that of the physical structure. The via and power/ground planes constitute a radial transmission line. The input impedance of the infinitely long radial transmission line, when the separation between the power and ground plane is d and the radius of the via is a, can be found as [3]:

$$Z_0(a) = \frac{j\eta d}{2\pi a} \frac{H_0^{(2)}(ka)}{H_1^{(2)}(ka)} \tag{6}$$

where $H_0^{(2)}(ka)$ and $H_1^{(2)}(ka)$ are Hankel functions. The input impedance of an infinitely large FDTD grid

$Z_{0FDTD}(dh)$ can also be found analytically [4]. As can be seen from equation (6), the input impedance of the radial transmission line depends on the radius of the via, whereas the input impedance of the FDTD grid depends on the grid size dh. These two impedances are generally not equal to each other. By adding an impedance transformer, defined as $Z_t = Z_0(a)$-$Z_{0\,FDTD}(dh)$, between the FDTD program and the circuit analysis program as shown in figure 2, the input impedance $Z_{0\,FDTD}(dh)$ of the infinitely large FDTD grid is transformed to the input impedance $Z_0(a)$ of the infinitely long radial transmission line. In figure 2, the voltage source W(t) represents the fields reflected from edges of finite size power/ground planes and/or fields generated from currents in other vias between the power/ground planes.

To examine the effects of the impedance transformer, consider the following example. Suppose the power and ground planes are of 6 cm × 6 cm in size, separated by a distance d = 150 μm, and filled by a dielectric material of ϵ_r=4. A current source with a sine-square waveform, as shown in figure 3, is applied across a pair of vias of radius a = 75 μm. Figure 4 shows voltage waveforms at the junction of the via and power/ground planes. The dashed curves in figure 4 are computed without impedance transformers and with grid size dh = 0.25, 0.5, 1.0 and 2.0 mm respectively. These curves reveal that numerical results obtained without using impedance transformers depend strongly on the mesh density. The solid curve in figure 4 is the voltage waveform computed with the impedance transformer. It is found that, by adding the impedance transformer, numerically computed voltage waveforms are virtually independent of the grid size dh.

Multiple power and ground planes are often used in packaging structures. Figure 5 shows the configuration of a packaging structure of two power planes and two ground planes. Suppose a pair of vias are connected to a power and a ground plane at point A. The two power planes are connected by a via at point B, and the two ground planes are connected by a via at point C. Define the voltage in each pair of conducting planes as shown in figure 5. The schematic program structure for solving this problem is shown in figure 6. Electromagnetic fields between each pair of planes are computed by one FDTD field solver. Impedance transformers Z_{t1}, Z_{t1} and Z_{t3} transform input impedances of FDTD grids to input impedances of corresponding radial transmission lines, and are placed at via junctions as shown in figure 6.

IV. Numerical Examples

IV.1. On the efficiency of the method

This example compares the efficiency of IBM's ASTAP using the capacitor/inductor mesh model and that of our method using the combined FDTD/circuit-simulator. Still consider the power and ground planes of 6cm × 6cm in size. A 60×60 mesh is used in FDTD method, and a 60×60 capacitor/inductor mesh is used in ASTAP. It is found that computed results by ASTAP also depend on mesh density, and they are numerically almost undistinguishable from those obtained by our method without using the impedance transformer [5]. It is apparent that the solution from ASTAP has the same kind of error as our method when no impedance transformers are used. On the issue of computation efficiency, there is a huge difference between the computer times spent by these two methods as can be seen from Table 1 below.

IV.2. On the validity of the effective inductance model

Consider the configuration shown in figure 7, where the power and ground pins connected to the d.c. voltage power are at a distance D from the pair of vias connected to IC circuits. The effect of power

and ground planes in electronics packaging has been most widely modeled as an effective inductor. This means that the input impedance Z_{in}, looked into the power and ground planes as indicated in figure 7, is approximated by the impedance of an inductor. With the FDTD method described above, the frequency dependent input impedance Z_{in} can easily be found by taking Fourier transforms of the transient current and voltage across the vias. Figure 8 displays the imaginary part of Z_{in} for different distance D, where the power and ground planes are 6cm × 6cm in size and separated by d = 150μm. Figure 9 shows the imaginary part of Z_{in} for a smaller size (1cm × 1cm) of power and ground planes. As can be clearly seen from figure 8 and 9, input impedance Z_{in} is strongly influenced by the resonance in the power and ground planes, which is not represented by the effective inductor model. The effective inductor model is generally not accurate to model the effects of power and ground planes, except for small conductor planes and in positions very close to Vcc/ground pins in the low frequency range, as in the case shown by curve 3 in figure 9.

V. Conclusions

This paper shows that the FDTD method can be effectively used to model electronics packaging structures containing power and ground planes. The modeling of the connection between via and conducting planes needs to be treated properly to avoid numerical errors. With the combination of FDTD and circuit simulators, the simulation of Delta-I noise distributions in complex electronics packaging of multiple power and ground planes can be accomplished accurately with high efficiency.

Acknowledgement

This work is supported by the National Science Foundation under contract MIP-9357561, and the Integrated Electronics Engineering Research Center (IEEC) at the State University of New York at Binghamton.

Reference

[1] R. Senthinathan and J. L. Prince, *Simultaneous Switching Noise of CMOS Devices and Systems*, Kluwer Academic Publishers, 1994.

[2] A. R. Djordjevic and T. K. Sarkar, "An Investigation of Delta-I Noise on Integrated Circuits," IEEE Trans. Electromagn. Compat., vol. 35, pp. 134-147, May 1993.

[3] S. Ramo, J. R. Whinnery, and T. Van Duzer, *Fields and Waves in Communication Electronics*, Wiley, 1965.

[4] Zhonghua Wu, Jiayuan Fang and Yaowu Liu, "A Closed Form Solution of the Input Impedance of Two-Dimensional FDTD Grids," accepted for presentation at the Tenth Annual Review of Progress in Applied Computational Electromagnetics, Monterey, CA, March 21-26, 1994.

[5] Yuzhe Chen, Zhonghua Wu, Amit Agrawal, Yaowu Liu and Jiayuan Fang, "Modeling of Delta-I Noise in Digital Electronics Packaging", accepted for presentation at the 1994 MCM Conference, Santa Cruz, CA, March 15-17, 1994.

Mesh Density	ASTAP on IBM 3090/021 Mainframe	Method of this paper on IBM R/6000-350 workstation	Ratio of CPU time
60 × 60	19 m 30.88 s	0.74 s	1582

Table 1. **Comparison of CPU times of ASTAP and the method of this paper.** (For both methods, 250 time steps are computed, with 4 ps time-step)

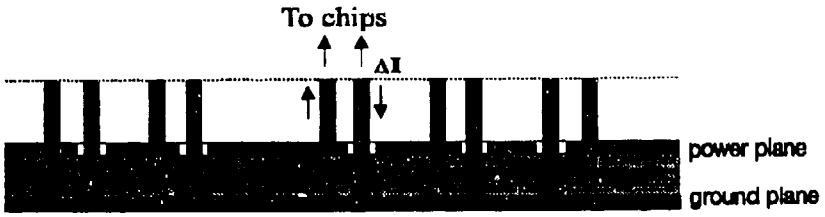

Fig. 1. A cross-sectional view of power and ground planes with vias connected to chips.

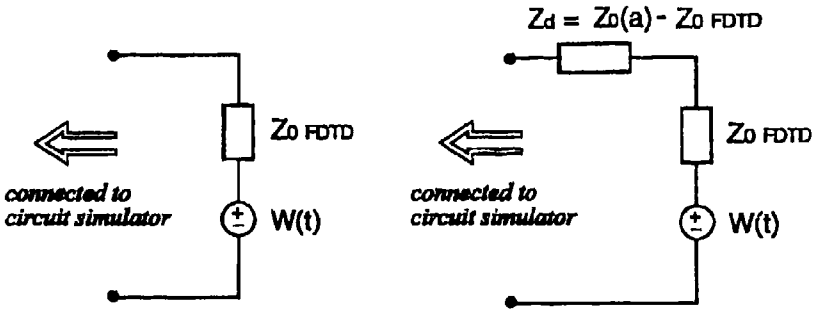

Fig. 2. Equivalent circuit model looking into the FDTD grid.
(a) without an impedance transformer. (b) with an impedance transformer.

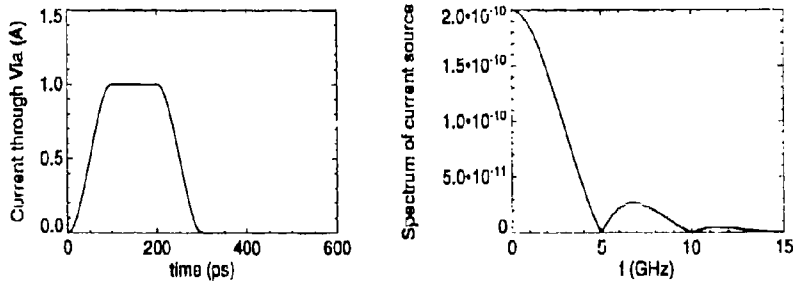

Fig. 3. Waveform and spectrum of the current source.

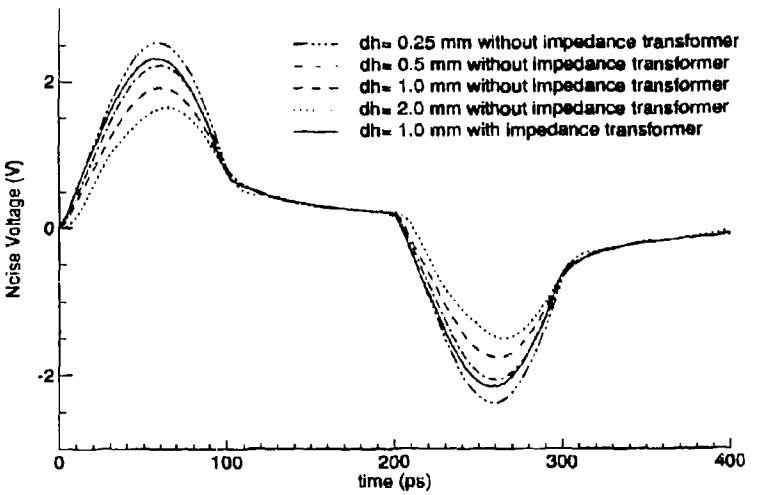

Fig. 4. Noise voltages without and with the impedance transformer.

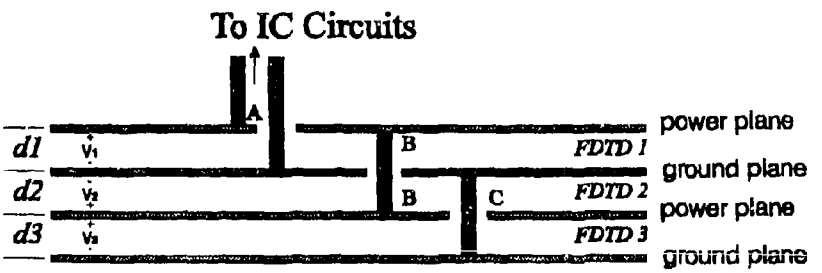

Fig. 5. Configuration of multiple power and ground planes.

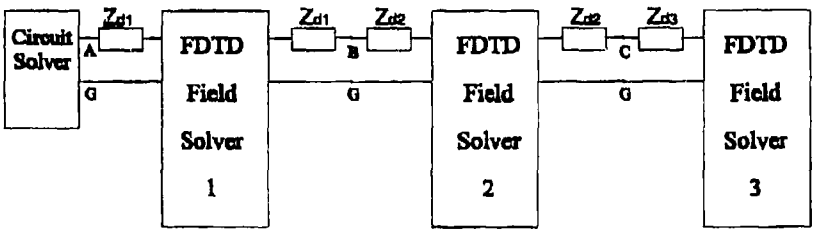

Fig. 6. Schematic diagram of linkage between field and circuit solvers for the configuration of multiple power and ground planes in figure 5.

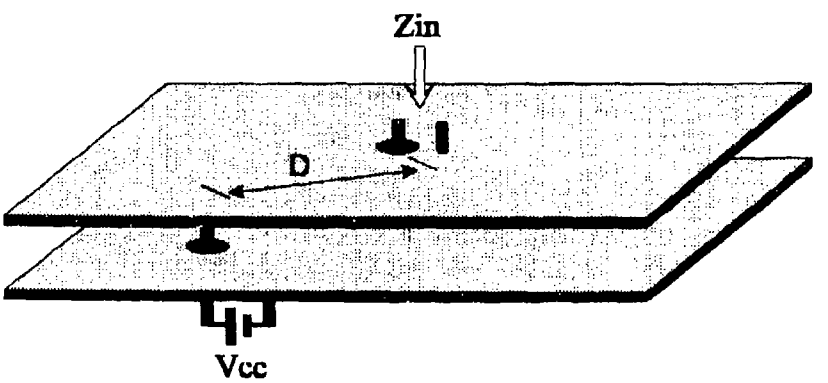

Fig. 7. The configuration of an electronics packaging structure for numerical tests.

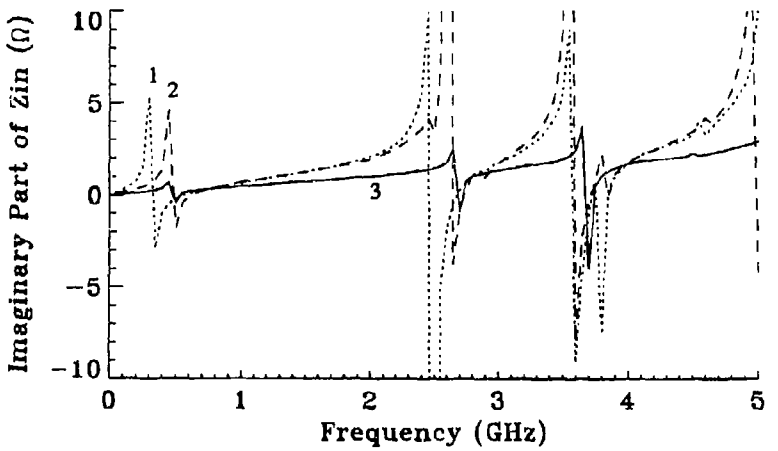

Figure 8. The imaginary part of the input impedance for the structure shown in figure 7, when the size of the power and ground planes is 6cm × 6cm. The separation D between Vcc/ground pins and the via at the center is 3.0cm (curve 1), 1.0cm (curve 2) and 0.1cm (curve 3) respectively.

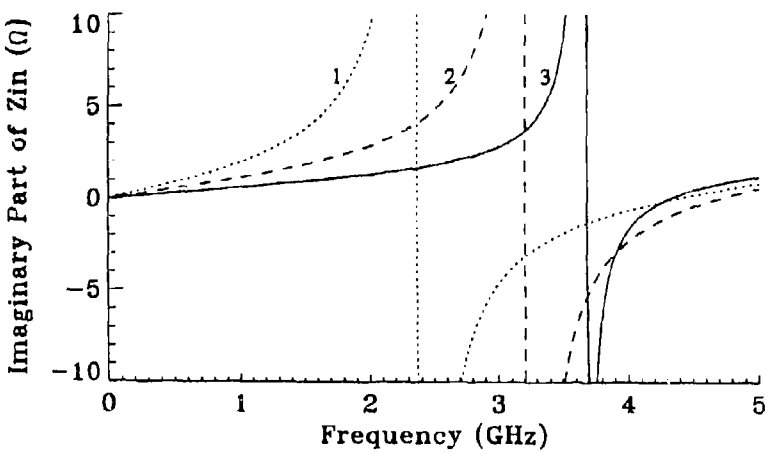

Figure 9. The imaginary part of the input impedance for the structure shown in figure 7, when the size of the power and ground planes is 1cm × 1cm. The separation D between Vcc/ground pins and the via at the center is 0.5cm (curve 1), 0.3cm (curve 2) and 0.1cm (curve 3) respectively.

A Closed Form Solution of the Input Impedance of Two-Dimensional FDTD Grids

Zhonghua Wu, Jiayuan Fang and Yaowu Liu
Department of Electrical Engineering
State University of New York at Binghamton, Binghamton NY 13902

Abstract

Finite Difference Time Domain (FDTD) method has been widely used in the modeling of interconnects and packaging structures of integrated circuits. It is found that in the modeling of the connection of a via/pin to a conducting plane at one FDTD grid point, substantial numerical error can be introduced. However, this numerical error can be eliminated if the input impedance of the FDTD grid is known. This paper presents the derivation of a closed form solution of the two-dimensional FDTD grids. The theoretical closed form solution of FDTD grids is verified by numerical tests.

I. Introduction

Electromagnetic modeling of many packaging structures of integrated circuits can be realized by using the finite-difference time-domain method. One such example is the simulation of voltage fluctuations, which is often called the simultaneous switching noise or Delta-I noise, in the power supply network of chip modules [1-2]. In typical packaging structures, power and ground planes are connected to lumped circuit elements or strip/microstrip lines through vias. Electromagnetic fields between power and ground planes can often be approximated by two-dimensional fields, and computed by two-dimensional FDTD analysis [2]. At the FDTD grid points where vias are located, the FDTD field solver for fields in power and ground planes is linked with circuit solvers for lumped and transmission line components. Although it is of great simplicity by modeling the connection of a via to the power/ground planes at a single FDTD grid point, substantial numerical error can be introduced if the FDTD field solver is directly linked with circuit solvers. This numerical error can be removed by adding an impedance transformer between each circuit solver and the FDTD field solver to transform the input impedance of the FDTD grid to the input impedance of the physical structure [2].

The question of the input impedance of a 2-D FDTD grid is equivalent to the following one: if a current is injected to one grid point of an infinite 2-D FDTD grid, what is the resultant electric field at the source point? The answer to this question can be found through direct FDTD computations, which results in an infinite data series (although it may be truncated within finite time steps). However, the numerical form of the input impedance is cumbersome to apply, because its values depend on FDTD grid size and it requires large computer memory to store the whole numerical solution. It is of advantage to have analytic expressions of the input impedance of FDTD grids. Unfortunately, such analytic expressions are not available in present literatures.

This paper presents the derivation of the closed form solution of the input impedance of 2-D FDTD grids through Fourier analysis. The analytically derived closed form solution of FDTD grids is verified by numerical results from direct FDTD computations.

II. Derivation of the Input Impedance of 2-D FDTD Grids

Consider the two dimensional field which is invariant in the z direction and satisfies the following Maxwell's equations:

$$\frac{\partial E_z}{\partial t} = \frac{1}{\epsilon}\left(\frac{\partial H_y}{\partial x} - \frac{\partial H_x}{\partial y}\right) - \frac{1}{\epsilon} J_z \tag{1}$$

$$\frac{\partial H_x}{\partial t} = -\frac{1}{\mu}\frac{\partial E_z}{\partial y} \tag{2}$$

$$\frac{\partial H_y}{\partial t} = \frac{1}{\mu}\frac{\partial E_z}{\partial x} \tag{3}$$

For a length d in the z direction, define the voltage as $V = -E_z d$, and the current density as $\mathbf{J}_s = -\mathbf{a}_z \times \mathbf{H}$. A physical example of this model in electronics packaging is the case of a power plane located above a ground plane by a distance d, then V represents the voltage between the power and ground planes, and $\mathbf{J}_s$ is the current density on the power plane. By using Yee's central difference schemes, and assuming the FDTD grid size in the x and the y directions are equal ($\Delta x = \Delta y = dh$), the difference equations of equation (1) to (3) in terms of the voltage V and currents $I_x = J_{sx} \cdot dh$, $I_y = J_{sy} \cdot dh$ are as follows:

$$V^{n+1}(k,l) = V^n(k,l) - \frac{\Delta t}{C}\left[I_x^{n+1/2}(k+1/2,l) - I_x^{n+1/2}(k-1/2,l) + I_y^{n+1/2}(k,l+1/2) - I_y^{n+1/2}(k,l-1/2)\right] + \frac{\Delta t}{C} I_s^{n+1/2}(k,l) \tag{4}$$

$$I_x^{n+1/2}(k+1/2,l) = I_x^{n-1/2}(k+1/2,l) - \frac{\Delta t}{L}\left[V^n(k+1,l) - V^n(k,l)\right] \tag{5}$$

$$I_y^{n+1/2}(k,l+1/2) = I_y^{n-1/2}(k,l+1/2) - \frac{\Delta t}{L}\left[V^n(k,l+1) - V^n(k,l)\right] \tag{6}$$

where the superscripts represent the time step, $C = \epsilon\, dh^2/d$, $L = \mu d$, and $I_s = dh^2 J_z$.

Suppose the source current $I_s(k,l)$ only exists at one grid point where $k=l=0$, and denote $I_s(0,0)$ as I_0. Assume

$$\begin{aligned} V^n(k,l) &= V(k,l)e^{jn\omega\Delta t} \\ I_x^n(k,l) &= I_x(k,l)e^{jn\omega\Delta t} \\ I_y^n(k,l) &= I_y(k,l)e^{jn\omega\Delta t} \\ I_0^n &= I_0 e^{jn\omega\Delta t} \end{aligned} \tag{7}$$

Substituting (7) into equations (4) to (6), and cancelling the term $e^{j(n+1/2)\omega\Delta t}$ on both sides of the equations, we get

$$V(k,l)2j\sin\frac{\omega\Delta t}{2} + \frac{\Delta t}{C}\left[I_x(k+1/2,l) - I_x(k-1/2,l) + I_y(k,l+1/2) - I_y(k,l-1/2)\right] = \begin{cases} \frac{\Delta t}{C} I_0 & k=l=0 \\ 0 & k,l\neq 0 \end{cases} \tag{8}$$

$$I_x(k+1/2,l) = -\frac{\Delta t}{2jL\sin\frac{\omega\Delta t}{2}}[V(k+1,l)-V(k,l)] \tag{9}$$

$$I_y(k,l+1/2) = -\frac{\Delta t}{2jL\sin\frac{\omega\Delta t}{2}}[V(k,l+1)-V(k,l)] \tag{10}$$

Substituting equations (9) and (10) into equation (8), equation (8) becomes

$$V(k+1,l)+V(k-1,l)+V(k,l+1)+V(k,l-1)-4(1-p^2)V(k,l) = \begin{cases} K_0 & k=l=0 \\ 0 & k,l\neq 0 \end{cases} \tag{11}$$

where

$$\begin{aligned} p &= \sqrt{LC}\frac{\sin(\frac{\omega\Delta t}{2})}{\Delta t} \\ K_0 &= -j\frac{2L\sin(\frac{\omega\Delta t}{2})}{\Delta t}I_0 \end{aligned} \tag{12}$$

Define the two dimensional discrete Fourier transform pair as:

$$\begin{aligned} \bar{V}(u,v) &= \sum_{k=-\infty}^{\infty}\sum_{l=-\infty}^{\infty} V(k,l)e^{-juk}e^{-jvl} \\ V(k,l) &= \frac{1}{4\pi^2}\int_{-\pi}^{\pi}\int_{-\pi}^{\pi}\bar{V}(u,v)e^{juk}e^{jvl}dudv \end{aligned} \tag{13}$$

After taking the 2-D discrete Fourier transform on both sides of (11), we get

$$\bar{V}(u,v) = \frac{K_0}{2\cos u+2\cos v-4(1-p^2)} \tag{14}$$

then take the 2-D inverse discrete Fourier transform of $\bar{V}(u,v)$,

$$V(k,l) = \frac{1}{4\pi^2}\int_{-\pi}^{\pi}\int_{-\pi}^{\pi}\frac{K_0e^{juk}e^{jvl}}{2\cos u+2\cos v-4(1-p^2)}dudv \tag{15}$$

Therefore, the input impedance of the 2-D FDTD grid is :

$$Z_{0FDTD} = \frac{V(0,0)}{I_0} = -\frac{j L \sin\left(\frac{\omega\Delta t}{2}\right)}{4\pi^2\Delta t} \int_{-\pi}^{\pi}\int_{-\pi}^{\pi} \frac{du\,dv}{\cos u + \cos v - 2(1-p^2)} \tag{16}$$

Let

$$\begin{aligned} z &= e^{ju} \\ a &= \cos v - 2(1-p^2) \\ G &= \frac{L \sin(\omega\Delta t/2)}{\pi\Delta t} \end{aligned} \tag{17}$$

Then

$$Z_{0FDTD} = -\frac{G}{\pi}\int_0^{\pi}\oint_{c_1} \frac{dz}{(z-z_1)(z-z_2)}dv \tag{18}$$

where the integration path c_1 is an unit circle centered at the origin of the complex z plane, and

$$z_{1,2} = -a \pm \sqrt{a^2-1} \tag{19}$$

According to Cauchy's integration formula, equation (18) becomes

$$Z_{0FDTD} = \begin{cases} jG\int_0^{\pi} \frac{dv}{\sqrt{a^2-1}} & a<-1 \\ G\int_0^{\pi} \frac{dv}{\sqrt{1-a^2}} & -1<a<1 \\ -jG\int_0^{\pi} \frac{dv}{\sqrt{a^2-1}} & a>1 \end{cases} \tag{20}$$

III. Numerical Tests

The input impedance of a 2-D FDTD grid can readily be calculated from equation (20) above once the FDTD grid size *dh* and the length in the z direction *d* are known. Figure 1 and 2 are the real and the imaginary parts of the input impedance for different grid size *dh* when d = 1mm and the relative dielectric constant of the medium ϵ_r = 4.0. Curve 1 to 7 in figure 1 and 2 correspond to the grid size *dh* of 25, 50, 100, 200, 400, 800 and 1600μm respectively. The time step Δt is chosen to be $0.7dh/v$, where v is the speed of light in the medium. From figure 1 and 2, we can see that both the real and the imaginary parts of the input impedance increase with frequency in the low frequency range (e.g. 0 - 30 GHz). The real part of the input impedance is almost independent of the grid size *dh* at low frequencies, whereas the imaginary part of the input impedance decreases with the increase of the grid size *dh*.

Figure 3 and 4 compare the input impedances computed from the closed form solution and from

direct FDTD computations. The parameters chosen for the results in figure 3 and 4 are: dh = 1000μm, d = 150μm, ϵ_r = 4.0, and $\Delta t = 0.7dh/v$. The input impedance of the FDTD grid from direct FDTD computations is obtained through the following procedure. Let a current source of Gaussian waveform injected into one grid point of the FDTD mesh; compute the transient solution of voltage at the source point; the input impedance is then the ratio of the Fourier transformed voltage and current. The FDTD mesh is chosen to be sufficiently large so that no reflection reaches the source point before the source current and the voltage at the source point vanish to virtually zero values. The expression in equation (20) for the input impedance of FDTD grids is verified by the excellent agreement between the closed form solution and the direct FDTD computations, as can be observed from figure 3 and 4.

The input impedance of the FDTD grid has some "abnormal" behaviors at high frequencies, which do not appear in the input impedance of the physical structure for which the FDTD grid represents. This can be observed from figure 5 and 6 which compare the input impedance of the FDTD grid and that of a radial transmission line representing a pair of infinitely large conducting planes separated by a distance d. The parameters selected for the results in figure 5 and 6 are the same as those in figure 3 and 4. As can be seen from figure 5 and 6, in the low frequency range, the real part of $Z_{\phi\,FDTD}$ converges to that of the radial transmission line, and the imaginary part of $Z_{\phi FDTD}$ is close to that of the radial transmission line at the radius of about one fifth of the grid size dh. A resonant behavior can be observed from $Z_{\phi\,FDTD}$ at around 52.85GHz, which corresponds to a wavelength of about 2.84mm = 2.84dh. Considering the numerical dispersion of FDTD method, it can be found that for a wave propagating along a grid axis and of frequency 52.85GHz, the numerical wavelength λ_n is actually twice of dh (note the numerical wavelength λ_n is anisotropic) [3]. Figure 5 and 6 also reveal that the smallest wavelength of fields modeled by FDTD method needs to be sufficiently large compared to the grid size dh to avoid significant numerical dispersion error.

IV. Conclusion

The closed form solution of the input impedance of 2-D FDTD grids has been presented in this paper. This closed form solution identically matches the direct numerical solution of FDTD method. The availability of a closed form solution of the input impedance of FDTD grid would greatly facilitate some numerical computations where the knowledge of the input impedance of FDTD grid is desirable [1-2].

Acknowledgement

This work is supported by the National Science Foundation under contract MIP-9357561, and the Integrated Electronics Engineering Research Center (IEEC) at the State University of New York at Binghamton.

Reference

[1] Yuzhe Chen, Zhonghua Wu, Amit Agrawal, Yaowu Liu and Jiayuan Fang, "Modeling of Delta-i Noise in Digital Electronics Packaging", accepted for presentation at the 1994 MCM Conference, Santa Cruz, CA, March 15-17, 1994.

[2] Jiayuan Fang, Zhonghua Wu, Yuzhe Chen and Yaowu Liu, "Application of the Finite-Difference Time-Domain Method in the Simulation of Delta-I Noise in Electronics Packaging," accepted for presentation at the Tenth Annual Review of Progress in Applied Computational Electromagnetics, Monterey, CA, March 21-26, 1994.

[3] Jiayuan Fang, *Time Domain Finite Difference Computations of Maxwell's Equations*, Ph.D. Dissertation, University of California at Berkeley, Dec. 1989.

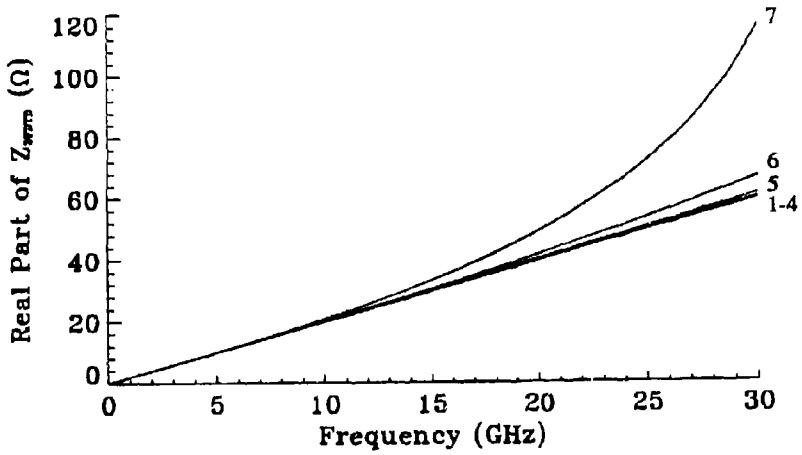

Figure 1. Real part of the input impedance of 2-D FDTD grid for d = 1mm, ϵ_r = 4.0, and Δt = 0.7dh/v. Curve 1 to 7 correspond to grid size dh of 25, 50, 100, 200, 400, 800 and 1600μm respectively.

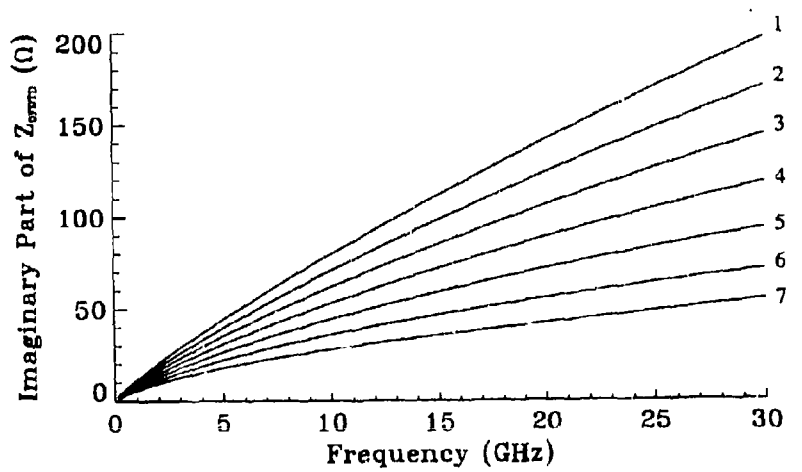

Figure 2. Imaginary part of the input impedance of 2-D FDTD grid for d = 1mm, ϵ_r = 4.0, and Δt = 0.7dh/v. Curve 1 to 7 correspond to grid size dh of 25, 50, 100, 200, 400, 800 and 1600μm respectively.

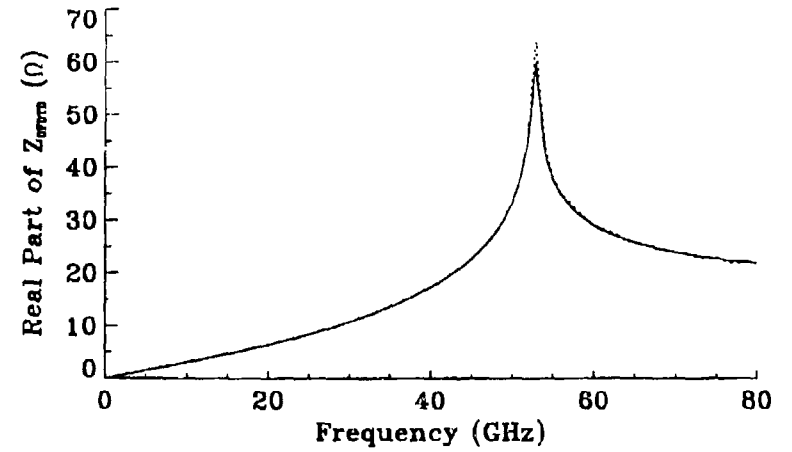

Figure 3. Real part of the input impedance of 2-D FDTD grid for d = 150μm, ϵ_r = 4.0, Δt = 0.7dh/v, and dh = 1000μm. The solid curve is from the closed form expression, and the dashed curve is from FDTD computation.

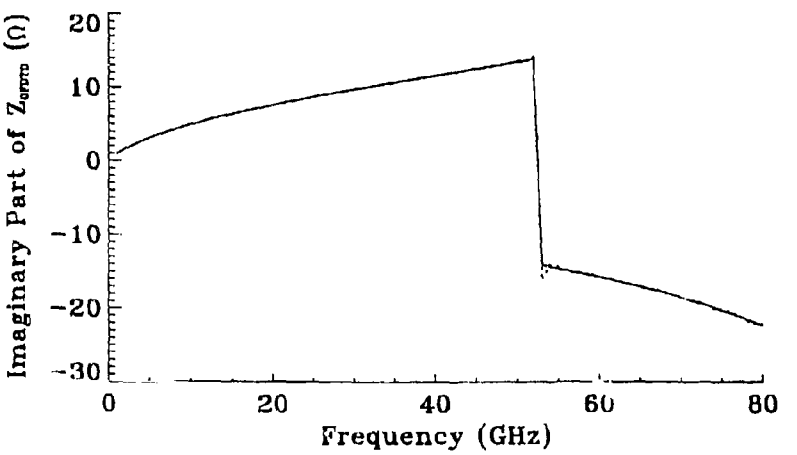

Figure 4. Imaginary part of the input impedance of 2-D FDTD grid for d = 150μm, ϵ_r = 4.0, Δt = 0.7dh/v, and dh = 1000μm. The solid curve is from the closed form expression, and the dashed curve is from FDTD computation.

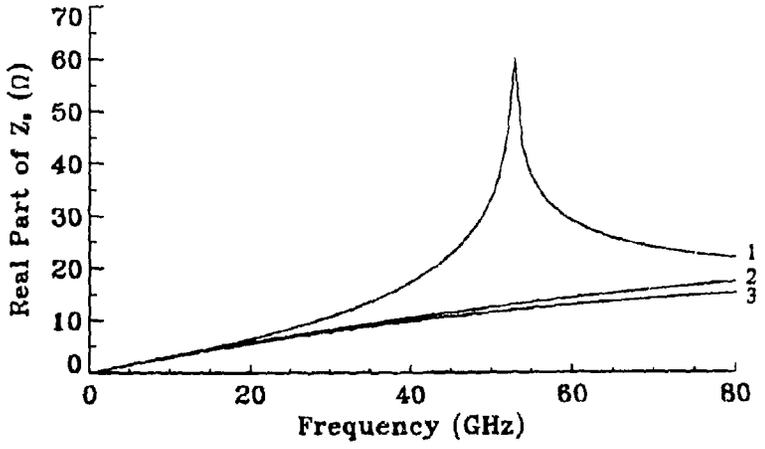

Figure 5. Comparison of the real part of the input impedance of 2-D FDTD grid for $d = 150\mu m$, $\epsilon_r = 4.0$, $\Delta t = 0.7dh/v$, and $dh = 1000\mu m$ (curve 1) and the real part of the input impedance of a radial transmission line at radius $150\mu m$ (curve 2) and $200\mu m$ (curve 3).

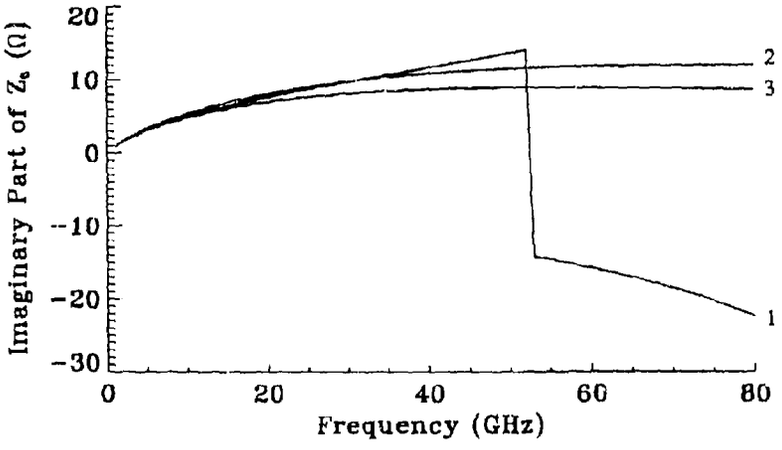

Figure 6. Comparison of the imaginary part of the input impedance of 2-D FDTD grid for $d = 150\mu m$, $\epsilon_r = 4.0$, $\Delta t = 0.7dh/v$, and $dh = 1000\mu m$ (curve 1) and the imaginary part of the input impedance of a radial transmission line at radius $150\mu m$ (curve 2) and $200\mu m$ (curve 3).

Deriving a Synthetic Conductivity To Enable Accurate Prediction Of Losses In Good Conductors Using FDTD

Kent Chamberlin and Lauchlan Gordon
University of New Hampshire

Abstract

FDTD is based upon the assumption that field behavior between sample points (*i.e.*, cell nodes) is linear; for propagation in lossless or low-loss materials, the assumption of linearity will be valid as long as the number of cells per wavelength is kept above some minimum value. For good conductors, where the wavelength decreases many orders of magnitude from its free-space size, and the fields are decaying exponentially, it becomes impractical to shrink the cell size so as to maintain linearity between cells. A consequence of using practical cell sizes when modeling good conductors is that the modeled conductor impedance will typically differ greatly from its actual impedance, causing significant errors in modeled reflection and transmission. By appropriately adjusting the modeled conductivity, which is the approach detailed here, the modeled impedance will equal the actual impedance, resulting in accurate estimates of conductor losses. This paper describes the mathematical development of synthetic conductivity, and validates its accuracy against theoretical data. The approach does not require modifications to the FDTD algorithms, and does not affect program execution time. Achieving accurate loss estimates will be of particular interest to those modeling resonant structures using FDTD.

Introduction

The impetus for the work reported here is to better model radiation from computer enclosures, which exhibit resonant characteristics. When modeling enclosures as PECs, the estimated resonant peaks were considerably higher than had been measured, which prompted this study into the FDTD modeling of good conductors. Past work with good conductors using FDTD[1] demonstrated that realistic loss values can be achieved by modeling good conductors as PEC's lined with a lossy material; the approach that is presented here is to calculate a new value of conductivity, which will typically differ from the actual conductivity, that will afford accurate model estimates of reflection from good conductors.

Modeling Good Conductors Using Synthetic Conductivity

As is generally recognized, FDTD does not correctly estimate losses at good-conductor

boundaries when using actual conductivity values. However, if appropriate conductivity values are used in FDTD modeling, accurate estimates of transmission and reflection at good conductor boundaries will be calculated. The purpose of this section is to develop the mathematics used to describe a synthetic conductivity that is used in place of the actual conductivity value in FDTD modeling. For simplicity, the development here is performed in one dimension, although the results are readily applicable to two and three-dimensional modeling as well. Reducing one of Maxwell's equations in Cartesian coordinates to one dimension, and orientating the coordinate system so that the Poyning vector and electric and magnetic fields align with one of the axes yields:

$$\nabla \times \bar{H} = \epsilon \frac{\partial \bar{E}}{\partial t} + \sigma \bar{E} \quad \rightarrow \quad \frac{\partial H_z}{\partial x} = \epsilon \frac{\partial E_y}{\partial t} + \sigma E_y \tag{1}$$

To put this equation of an x-traveling wave into finite-difference form, the electric and magnetic are generally staggered in space as indicated in the figure below (the y and z subscripts on the fields have been dropped to simplify the notation):

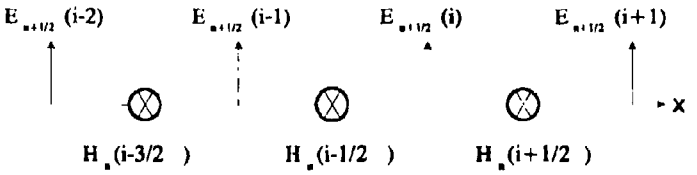

Figure 1 Field Locations in 1-D FDTD Formulation.

The increment in time is given by n (*i.e.*, $t = n\Delta t$) and the increment in the direction of propagation is given by i (*i.e.*, $x = i\Delta x$). Using this notation, Equation (1) can be put into finite-difference form. While the finite-difference approximations to the derivatives are determined by the coordinate system and time sampling scheme, there is some latitude in the calculation of the conduction term. Although Yee did not explicitly address the calculation of conduction current in his original formulation [2], a number of authors have proposed different strategies for making that calculation; the difference in those strategies relates to which time increment(s) the electric field used to calculate the conduction current is sampled. For example, one approach is to use the average of the present and next electric fields to calculate conduction current[3]; using this approach, the finite difference equation becomes:

$$\frac{H_n(i+\tfrac{1}{2}) - H_n(i-\tfrac{1}{2})}{\Delta x} = \epsilon \frac{E_{n+\frac{1}{2}}(i) - E_{n-\frac{1}{2}}(i)}{\Delta t} + \frac{\sigma}{2}\left(E_{n+\frac{1}{2}}(i) + E_{n-\frac{1}{2}}(i)\right) \tag{2}$$

Solving for the updated electric field yields:

$$E_{n+\frac{1}{2}}(i) = \left[\frac{2\epsilon - \sigma\Delta t}{2\epsilon + \sigma\Delta t}\right] E_{n-\frac{1}{2}}(i) + \frac{1}{\Delta x\left[\frac{\epsilon}{\Delta t} + \frac{\sigma}{2}\right]} \cdot \left(H_n(i+\tfrac{1}{2}) - H_n(i-\tfrac{1}{2})\right) \qquad (3)$$

In this form, the coefficient of the present value of the electric field has a zero for relatively low values of conductivity. For example, for a one-centimeter cell, and applying the Courant condition, a zero will occur for $\sigma = 0.92$ S/m. For greater conductivity values, the coefficient will become negative, causing the solution to become unstable. To overcome this difficulty, Luebbers, *et. al.*[4][5] suggested using the most recent value of electric field in computing conduction current (i.e., $\sigma E = \sigma E_{n-\frac{1}{2}}$). This enabled a solution for a new electric field value that would be stable for highly-conducting materials, as given by:

$$E_{n+\frac{1}{2}}(i) = a E_{n-\frac{1}{2}}(i) + b\left[\frac{H_n(i+\tfrac{1}{2}) - H_n(i-\tfrac{1}{2})}{\Delta x}\right] \qquad (4)$$

$$\textit{where} \qquad a = \frac{\epsilon}{\epsilon + \sigma\Delta t} \qquad \textit{and} \qquad b = \frac{\Delta t}{\epsilon + \sigma\Delta t} \qquad (5)$$

Referring to Equation (4), the electric field at any time can be derived in terms of the electric and magnetic fields at the previous time interval. This equation, and a corresponding equation defining an update for the magnetic field, make up the foundation for many FDTD codes, such as the one developed at The Pennsylvania State University[6] which was used for the work presented here. Consequently, the synthetic conductivity developed here is applicable only to FDTD algorithms in the form of Equation (4) above, although synthetic conductivities for any FDTD implementation can be found using the development described here.

In a good conductor, $\sigma\Delta t >> \varepsilon$, which will cause the variable "a" in Equation (5) to be negligible, and hence Equation (4) will be dominated by the adjacent magnetic field terms ($b/\Delta x >> a$ in a good conductor). Further, if a good conductor boundary is located at (i), with (i-½) inside the conductor and (i + ½) outside of the conductor, then $H^n(i-\frac{1}{2})$ will have a magnitude approaching zero. Using the above assumptions, the next value of electric field on the surface of a good conductor can be written:

$$E_{n+\frac{1}{2}}(i) = b\left[\frac{H_n(i+\frac{1}{2})}{\Delta x}\right] \tag{6}$$

In this form, we can determine explicitly a wave impedance (or more accurately a wave resistance, since FDTD deals only with real numbers) which relates the magnitudes of the electric and magnetic fields:

$$\eta_{FDTD} = \frac{b}{\Delta z} = \frac{\Delta t}{(\epsilon+\sigma\Delta t)\Delta z} \tag{7}$$

The rightmost equality is obtained by substituting for "b" using Equation (5) and by imposing the Courant condition for the ratio between time and distance step size. While impedance is defined by the relationship between quantities at a particular point, Equation (7) represents a relationship between fields offset spatially by one-half cell. This offset is negligible when calculating impedance in this application, as is shown at the end of this section.

The modeled intrinsic impedance (η_{FDTD}) will not in general equal the actual intrinsic impedance for practical values of Δz because of errors in the finite-difference approximation to derivatives of the fields near highly-conducting boundaries. Further, because there is no time history used

$$\eta_{FDTD} = \frac{1}{\sigma_{FDTD}\Delta z} \tag{8}$$

in deriving the modeled intrinsic impedance for practical cell sizes, FDTD solutions to wave interactions with good conductors will not exhibit frequency dependence (*i.e.*, dispersion). For good conductors such as metals, $\sigma\Delta t$ will be much greater than ϵ, and Equation (7) becomes:
As stated above, the objective here is to better model reflection and transmission at good conductor boundaries. Because the reflection and transmission coefficients are functions of the impedances at boundaries, the modeled impedances must agree with the actual impedances at a boundary. In the synthetic conductivity approach presented here, the modeled impedance at the conductor surface is set equal to the actual conductor impedance so as to derive a conductivity value to be used in modeling. For a good conductor:

$$\eta_{True} = \sqrt{\frac{j\omega\mu}{\sigma_{True}+j\omega\epsilon}} \approx \sqrt{\frac{\omega\mu}{2\sigma_{True}}}(1+j) \tag{9}$$

Setting the real parts of $\eta_{FDTD} = \eta_{True}$ and solving for σ_{FDTD} yields:

$$\sigma_{FDTD} = \frac{1}{\Delta z}\sqrt{\frac{\sigma_{True}}{\omega\mu}} \tag{10}$$

As is shown in the subsequent section, using the above value for conductivity in FDTD produces results that agree well with closed-form solutions for transmission and resonance characteristics.

As stated above, there is a spatial offset between the electric and magnetic fields in the impedance calculation of Equation (7); the electric field sample is on the boundary, and the magnetic field is sampled one-half cell from the boundary. While the exact solution for impedance would have both sample points collocated, the offset in magnetic field has only a negligible effect because its change with position is so small in the immediate vicinity of a good conductor. Specifically, the worst-case, spatial variation for this normal-component of magnetic field is defined by $H(d) = 2H^{i}\cos(\beta d)$, where H^{i} is the incident magnetic field, and d is the distance to the conductor boundary. The greatest electrical distance from the magnetic field sample point to the conductor boundary will be one-twentieth wavelength when observing conventional FDTD cell size. This offset will cause the impedance calculation in Equation (7) to be in error by a factor of $\cos(\pi/10)$ at the highest frequency of interest, and will decrease for lower frequencies. The effect of this offset can be seen by a comparison of the reflection coefficient both with and without compensating for the spatial offset:

$$\frac{\Gamma_U}{\Gamma_C} = \frac{\eta_0^2 + \eta_0\eta\,(1-\cos(\beta d)) - \eta^2\cos(\beta d)}{\eta_0^2 + \eta_0\eta\,(\cos(\beta d)-1) - \eta^2\cos(\beta d)} \tag{11}$$

where Γ_U is the reflection coefficient uncompensated for the spatial offset (*i.e.*, based upon the impedance of Equation (7)), Γ_C is the reflection coefficient compensated for the offset, η_0 is the impedance of free space, and η is the actual impedance of the conductor. A study of reflection coefficient error using Equation (11) for a worst-case situation (a lead conductor and a spatial offset of $\lambda/20$) shows accuracy to five significant digits without compensating for the offset. Because of the low error asssociated with the offset, the effect of the offset was not included in the calculation of synthetic conductivity presented here.

Validation

To verify that the approach for modeling good conductors presented here is valid, FDTD modeled results were compared against both closed-form solutions and measurements. The approach was applied to the difficult task of calculating the Q of a closed cavity, and was compared against known closed-form solutions. This test was considered to be the most crucial in validating the technique, since the estimated Q's contain the cumulative errors from tens of thousands of

reflections within the modeled cavity, and any error in the modeled reflection coefficient would be multiplied by the number of reflections.

The interior dimensions of the cavity used for this facet of the validation was 31 x 21 x 11 cm, and one cm^3 cells were used in the FDTD model. The modeled cavity was excited with a Gaussian pulse having a temporal half width of 32 time steps at a single, perpendicular, E-field sample point one cell from a corner on a 31 x 21 cm side; the source was comprised of an infinitesimally-thin, one-cell long, PEC. The E-field monitor point, used to estimate resonant behavior, was at the center of the side opposite the excitation source. The excitation point was selected so as to excite all the cavity modes within the usable frequency range of the model, while introducing only minimal shift in the resonant frequencies. The monitor point did not constitute a physical object within the modeled cavity, and its placement was arbitrary. Comparisons of modeled and theoretical resonances were made for the TE_{101} mode, and hence the TE_{101} frequency was used to calculate the model parameters for the approaches presented here.

The FDTD model was run until significant transients had died out, taking slightly over a million time steps for the lowest conductivity investigated, and over two million time steps for the highest conductivity. After the FDTD model was run, an FFT was performed on the time-domain data to obtain the resonance frequency spectrum, where the resonant frequencies and their associated Q's were calculated using cubic-spline interpolation.

The theoretical values of resonant frequency and Q for a lossy rectangular cavity are given in Harrington[7] or Balanis [8]. It should be noted that the closed-form solutions themselves are approximations, since they were developed using the assumption that the field distribution for finitely-conducting walls would be the same as for perfectly-conducting walls.

A comparison of theoretical data and modeled data obtained using the synthetic conductivity approach is given in Table 1 for a range of conductivity values.

σ_{True}	σ_{FDTD}	Modeled Freq.	Theory Freq.	Freq. Error (%)	Q_{Theory}	Q_{FDTD}	Q Error (%)
2.88×10^7	9200	861.8785	862.1631	-.0330	17744	16771	-5.5
2.43×10^7	8463	861.8713		-.0338	16321	11639	-28.7
9×10^6	5142	861.8748		-.0334	9917	8785	-11.42
4.5×10^6	3637	861.8772		-.3316	7014	6795	-3.13

Table 1 Theoretical and FDTD-Modeled TE_{101} Data For A Rectangular Cavity Using The Synthetic Conductivity Approach For A Range of Conductivity Values.

Acknowledgements

The work presented in this paper was funded jointly by the Digital Equipment Corporation and the Industrial Research Center at the University of New Hampshire.

The authors would like to thank Dr. Raymond Luebbers of The Pennsylvania State University for providing the FDTD code used in this study, as well as for his helpful comments and suggestions. The authors would also like to thank Messrs. Bruce Archambeault and Rich Mellitz of Digital Equipment Corporation, who aided in all phases of the effort.

References

[1] Kent Chamberlin, "FDTD Modeling of the Resonance Characteristics o[illegible]c Enclosures," Proceedings of the 9th Annual Review of Progress in Applied Comput[illegible]onal Electromagnetics Symposium, March, 1993.

[2] Yee, K.S.,"Numerical Solution of Initial Boundary Value Problems Involving Maxwell's Equations in Isotropic Media," IEEE Trans. Antennas Propagat., vol. AP-14, pp. 302-309, May, 1966.

[3] D.M. Sullivan, D.T. Borup, and O.P. Gandhi,"Use of the Finite-Difference, Time-Domain Method in Calculating EM Absorption in Human Tissues," IEEE Trans. Biomed. Engr., vol. BME-34, pp. 148-157, Feb. 1987.

[4] R. Luebbers, F. Hunsberger, K. Kunz," Transient Response of Highly Conductive Materials Using a New FDTD Formulation," presented at the Fifth Annual Review of Progress In Applied Computational Electromagnetics, Monterey, CA, March, 1989.

[5] R. Luebbers, F. Hunsberger, K. Kunz, "Application of a New FDTD Formulation to Highly Conductive Materials," URSI National Radio Science Meeting, San Jose, CA, June, 1989.

[6] John Beggs, *et. al.*,"User's Manual for Three Dimensional FDTD Version C Code for Scattering from Frequency-Independent Dielectric and Magnetic Materials," PSU Report, Dec 1992.

[7] R.F. Harrington, *Time-Harmonic Electromagnetic Fields*, McGraw-Hill, New York, 1961, pp. 190, problem 4-10.

[8] C.A. Balanis, *Advanced Engineering Electromagnetics*, Wiley, New York, 1989, pp. 391.

Creating FDTD Models of Aircraft with GWTOFDTD

C.W. Trueman, S.J. Kubina, and B. Messier,
Electromagnetic Compatibility Laboratory,
Concordia University,
7141 Sherbrooke Street West,
Montreal, Quebec, Canada H4B 1R6.

Abstract-GWTOFDTD is an interactive graphics program which allows the user to convert a wire-grid model of a complex object such as an aircraft to a cell model suitable for input to a finite-difference time-domain program. The user selects a cell size, and GWTOFDTD displays a cross-section of the aircraft superimposed on the cell space in a plane through the centers of the cells. The user fills cells interactively with the mouse. The program displays cross-sections in sequence from tail to nose of the aircraft for a systematic derivation of a complete cell model. This paper describes the GWTOFDTD program and its use in developing a model of a small aircraft. The radar cross-section for the aircraft computed with FDTD is compared with results obtained by wire-grid modelling.

Introduction

Yee's Finite-Difference Time-Domain(FDTD) method[1,2] subdivides a finite volume of space into N_x by N_y by N_z "cells", each of size Δx by Δy by Δz. To calculate the radar cross-section(RCS) of a perfectly-conducting scattering object such as the "Navajo" aircraft of Fig. 1, each cell in the cell space must be designated to be either a "free-space" cell or a "perfectly-conducting" cell; the result is a "building block" model or "cell" model of the object, such as that in Fig. 2. Curved surfaces are represented by a "staircase" approximation. In recent years FDTD has been used to compute the RCS of "canonical" objects such as spheres[3,4], strips, rods and cylinders[5] with excellent agreement with both wire-grid computations and with the measured RCS.

To construct an FDTD model of a complex object such as the small aircraft, we must decide whether each cell should be "filled", that is, designated perfectly-conducting, or should be free-space. This is done by examining the portion of the cell which lies inside the volume of the aircraft. The cell is filled if enough of its volume lies inside the perfectly-conducting surface. Rules of thumb exist for deciding whether to fill a cell. In modelling a sphere, Luebbers maintains the surfaces of the filled cells inside the surface of the sphere[6]. In modelling rods of square cross-section, it was found that the effective position of the surface of the cell model of the rod is 1/4 cell outside the surfaces of the filled cells[7,8]; hence the cells appear to be larger than Δx by Δy by Δz.

The radar cross-section(RCS) of complex objects such as the small aircraft is often computed by the "moment method"[9]. A reliable technique represents the aircraft with a wire-grid model[10] such as that shown in Fig. 1, and then calculates the currents flowing on the wires with the Numerical Electromagnetics Code(NEC)[11]. Indeed, wire-grid representations for many types of aircraft are available.

This paper presents a program called GWTOFDTD which takes advantage of the availability of wire-grid models of aircraft to derive FDTD "cell" models. The GWTOFDTD program draws the aircraft cross-section superimposed on the cell space through the cell centers, as shown in Fig. 3. The aircraft cross-section is derived from the coordinates of wire endpoints in the wire-grid model input file. The user generates a staircased approximation to the cross-section by "filling" cells interactively with the mouse. Note that the program does not attempt to automatically "translate" the wire-grid into an FDTD cell model. For each cross-section the program generates an initial guess at which cells to fill; then the user is required to interact with the program by modifying cells on the boundary of the cross-section, as discussed below.

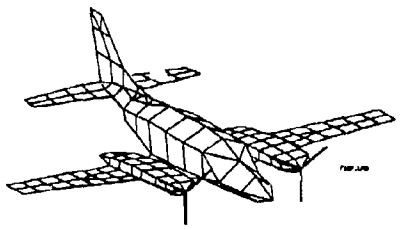

Fig. 1 A wire-grid model of the Navajo aircraft.

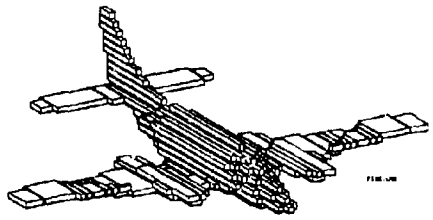

Fig. 2 A "cell model" of the Navajo for input to the FDTD program

This paper briefly describes the operation of GWTOFDTD program and how it is used to derive a "cell model". To explore the accuracy of FDTD computations, the RCS of a "generic aircraft" computed with FDTD is compared with wire-grid computations and measurements, and the RCS of the Navajo aircraft is compared with wire-grid computations.

The GWTOFDTD Program

The GWTOFDTD program assists the user in deriving a "cell" model of an aircraft, such as that in Fig. 2, from a wire-grid model like that shown in Fig. 1. The starting point is an input file for the NEC program describing the wire-grid model wire-by-wire with "GW cards"[11]. The radius of each wire in the grid is derived by running the program called MESHE3 to obtain a "meshes" file from the GW card file[12]. The "meshes" file describes the surface of the aircraft in terms of "mesh cells" bounded by wires of the grid, and is used by program FNDRAD to obtain a radius for each wire according to the "equal-area rule"[12]. The corners of a mesh cell are wire endpoints in the wire-grid model. The GW card file plus the "meshes" file form the input to GWTOFDTD.

Developing a cell model begins by selecting the cell size for the FDTD grid. The maximum permissible cell size is one-tenth of the wavelength at the highest frequency at which the RCS must be computed. Often, a much smaller cell size is chosen to obtain greater fidelity in the geometrical representation. The cell model is derived by subdividing the aircraft into slices one cell thick in vertical planes perpendicular to the fuselage axis. The GWTOFDTD program aids the user in determining which cells in each cross-sectional slice must be filled to best represent the aircraft shape.

GWTOFDTD's main menu shows the overall length of the aircraft in metres, the total number of cross-sections, the number of the cross-section currently being created and its position axially along the aircraft. Deriving the cell model proceeds by displaying the aircraft cross-sectional slices one-by-one, from tail to nose, and filling cells to represent the aircraft shape in each cross-section. The principal choices offered are: create the cell model for a given cross-section; edit a cross-section previously created; go on to the next cross-section in sequence; or exit, saving the partially-completed model so that the session can be resumed later. When the full aircraft has been modelled, the user tells the program to create a "build file" which forms the input for the FDTD program itself.

Modelling Each Cross-Section

For each cross-sectional slice through the aircraft, the GWTOFDTD program draws the cells and superimposes on them the cross-section of the aircraft itself, as shown in Fig. 3. The program approximates the aircraft cross-section by considering each "mesh" in the wire grid to be a solid plate. The intersection of these "mesh plates" with the cross-sectional plane is drawn on the screen to represent the cross-section of the aircraft. This provides interpolation between the specific wire endpoints that are present in the wire-grid model, which are usually much farther apart than one cell thickness. To generate the cell model, the user interacts via the mouse to select which cells should be filled with perfectly-conducting material.

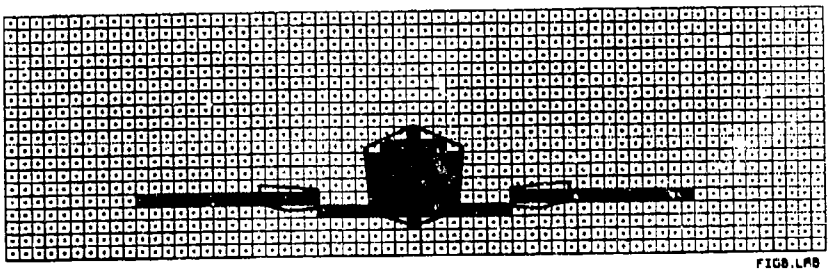

Fig. 3 A cross-section of the wire-grid model superimposed on a cross-section of the FDTD cell space.

The program starts the process with a "gross fill" in which any cell which is touched by the metallic skin of the aircraft is filled. The mouse is used to refine the representation. The left mouse button(LM) always returns to the main menu. The centre mouse button(CM) is used to fill-in regions which are inside the fuselage, hence completely surrounded with filled cells by the "gross fill" step. Position the mouse on an empty cell that lies within the aircraft fuselage and press CM; the program fills in cells in all directions until a previously-filled cell is found. If CM is accidentally pressed on a cell outside the aircraft, the program fills all the cells! Pressing CM again "undoes" the fill operation so it is easy to recover from this common error. The right-mouse button(RM) is used to toggle individual cells to be filled or empty.

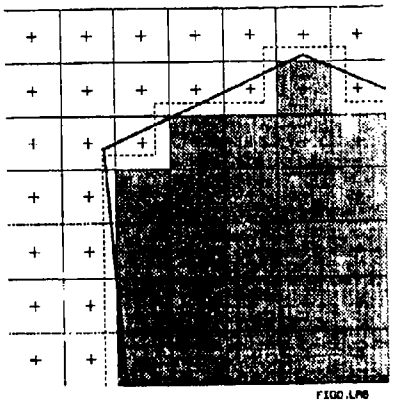

Fig. 4 An enlargement of part of the cross-section of Fig. 3 showing the quarter-cell margin as a dashed line.

To refine a given cross-section, it is useful to see the "effective" position of the surface, considered to be one-quarter of a cell outside the surface of the filled cells[8]. This is not easily seen on a full cross-section such as Fig. 3. The blowup option on the main menu permits zooming on parts of the cross-section. The mouse is used to outline a small region of the cross-section with a rectangular "cursor box", then to "zoom in" to make that region fill the entire screen, as in Fig. 4. A dashed line is drawn 1/4 cell away from the surfaces of the "filled" cells to aid the user in visualizing the effective position of the surface of the FDTD cell model relative to the actual surface of the aircraft. The RM button is used to fill or empty individual cells so that the dashed line is a reasonable approximation to the actual aircraft cross-section, represented by the heavy solid line.

Drawing the Aircraft in Three Dimensions

Once the user is satisfied that each cross-section of the cell model is the best fit to the actual aircraft shape, the program is used to create a "build file", which is the input file to the FDTD code itself. Drawings of the three-dimensional cell model with hidden-line removal, such as Fig. 2, are obtained by running the program "BLDMVI" to convert the "build file" format to one that can be understood by program "HIDNMOD". HIDNMOD produces drawings such as that in Fig. 2, showing groups of filled cells as solid boxes. The model can be viewed from any angle, and paper hard-copies of the pictures can be made.

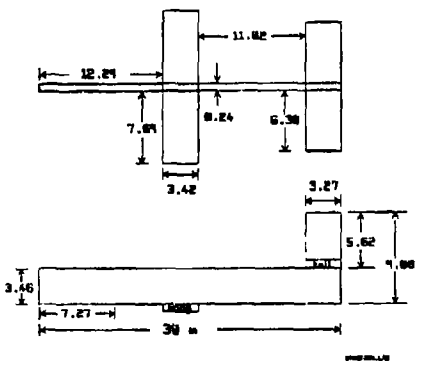

Fig. 5 The dimensions of the generic aircraft.

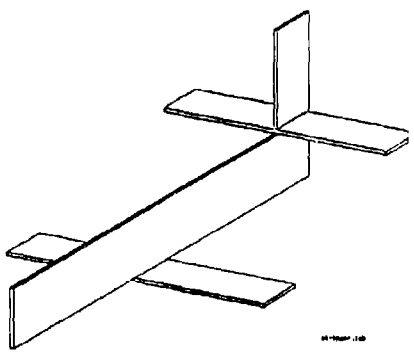

Fig. 6 The "cell model" of the generic aircraft.

The Generic Aircraft

Fig. 5 gives the dimensions of a simple aircraft-like structure called the "generic aircraft", which is shown in Fig. 6. To model the generic aircraft with FDTD, the cell size was set to 0.24 m, so that the thickness of the strips from which the structure is made equal to one cell width. The fuselage length of 30 m is 125 cells. The wingspan of 15.62 m is very close to 65 cells. The height of the strip representing the fuselage is 3.46 m, or 14.4 cells, and was modelled with 14 cells. The height from the bottom of the fuselage to the top of the dorsal was represented with 38 cells making the overall height 9.12 m compared to the actual value of 9.08 m in Fig. 5. Note that these choices ignore the result[8] that the effective location of the surface is about 1/4 of the cell size away from the surfaces of the cells.

To obtain the RCS, the generic aircraft was illuminated with a plane wave incident nose-on, with the electric field vector oriented vertically, parallel to the dorsal fin. The incident waveshape was a Gaussian pulse of width chosen to limit the energy content to frequencies below that which makes the cell size $\lambda/10$[2,5], which is 125 MHz for 0.24 m cells. The aircraft was separated from the Liao second-order absorbing boundary[13,14] by 19 cells of free-space on all sides. The time step was set equal to the Courant limit[2,5], and the FDTD computation was run for 4096 time steps. The backscattered field in Fig. 7 shows that this number of time steps is sufficient to trace the response to zero. The Fourier transform of the backscattered field and of the incident Gaussian pulse were found to determine the radar cross-section, which is shown by the solid curve in Fig. 8, in comparison to the wire-grid computation and to the measured RCS[15].

Fig. 8 shows quite good agreement between the three curves up to about 20 MHz. The low frequency behavior of the RCS is strongly influenced by the resonances of the aircraft geometry. A useful estimate of the airframe resonance frequencies was obtained in Ref. [15] by setting the length of a resonant path equal to 0.4 of the free-space wavelength. With this estimate, a path including the length of the fuselage and the height of the dorsal fin is expected to be resonant at about 3.4 MHz, and a path including one wing, the fuselage from wing to tail, and the dorsal fin is resonant at about 4.9 MHz. Fig. 8 shows that the FDTD computation has a maximum in the RCS at about 3.3 MHz, and a sharp minimum at 4.1 MHz, which is less deep in the FDTD computation at -39.6 dB than it is in the wire-grid computation, where it is -41.4 dB. The aircraft RCS rises rapidly to a maximum of 0.89 dB in the FDTD computation at 11.0 MHz, compared to 0.39 dB at 10.9 MHz in the wire-grid computation. This frequency roughly corresponds to the lowest resonant frequency of a "dorsal strip" of width 3.27 m and height 9.08 m[15]. At higher frequencies, above 20 MHz, the agreement between the wire-grid model and the measurement is fair, whereas the agreement with the FDTD computation is good. The RCS above 20 MHz has a series of

maxima and minima which are associated with the interference of the scattered field from the nose of the aircraft and from the tail[15].

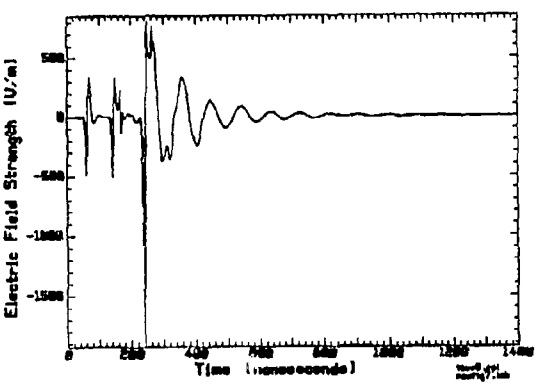

Fig. 7 The backscattered field from the generic aircraft.

Modelling the Navajo Aircraft

The Navajo is a smaller aircraft that the "generic aircraft" discussed above. Its length is 10.55 m from the nose to the tip of the tail, and its wingspan is 12.40 m. The height from the bottom of the fuselage to the top of the dorsal fin is 3.12 m. The wire-grid model of the Navajo was designed to obtain useful information to a frequency of about 55 MHz. The Navajo is a much more complex shape than the generic aircraft. The GWTOFDTD program was used to convert the wire-grid to an FDTD cell model, one cross-section at a time from tail to nose as discussed above. The "quarter-cell margin" rule was respected in generating the model. The cell size was set to 0.2 m, so tha. the cells are smaller than one-tenth wavelength to 150 MHz. Fig. 9 compares the top view and side view of the cell model to the wire-grid model, showing that reasonable fidelity was obtained. The leading edge of the wing of the cell model is further forward than it should be; this would be corrected in a revision of the model. The propellors were omitted from the cell model.

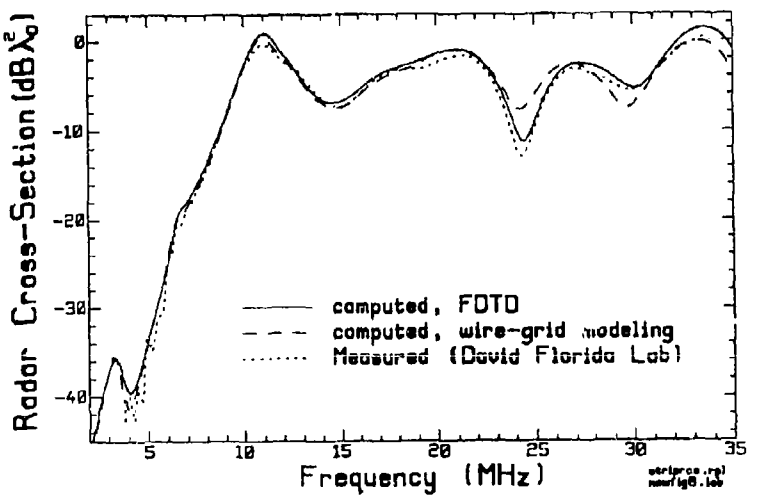

Fig. 8 Comparison of the RCS of the generic aircraft computed with FDTD with that computed with wire-grid modeling, and with the measured RCS.

The RCS of the Navajo was computed by using a Gaussian pulse plane wave to illuminate the aircraft nose-on, with the electric field vertically-oriented as before. Fig. 10 shows the time response, which was computed to 4096 time steps, is zero beyond about 2000 time steps. Fig. 11 compares the RCS obtained from the FDTD computation with that obtained by wire-grid modelling. In the wire-grid computation, the RCS rises rapidly to a peak at about 9.3 MHz, then has a sharp minimum at 11.8 MHz at -66.8 dB. The FDTD computation has a modest minimum at about 11.6 MHz at -45.8 dB, then rises following the wire-grid response quite well to the broad maximum at about 29.4 MHz. The deep notch in the RCS at 11.8 MHz is associated with a long resonant path on the aircraft. The longest path on the Navajo includes a wing, the fuselage from wing to dorsal, plus the dorsal fin, its length of 13.16 m is half a wavelength at about 11.4 MHz. The wingspan of 12.4 m is resonant at about 12.1 MHz, but the wing is almost perpendicular to the orientation of the electric field and so is weakly excited. A path including the whole fuselage and the dorsal is of length 11.5 m, and is estimated to be resonant at 13.0 MHz. Thus the notch at 11.8 MHz is likely to be associated with a wing-fuselage-dorsal path.

Above 20 MHz, the Navajo RCS rises to a "corner frequency" of about 30 MHz. Above this frequency the FDTD computation has a modest minimum at 39 MHz and a broad maximum at 53 MHz, whereas the wire-grid computation has a minimum at 37 MHz, a maximum at 41 MHz, a deeper minimum at 46 MHz, and a broad maximum at 56 MHz. To verify that the propellors do not have a signficant effect in this frequency range, the wire-grid computation was repeated with no propellors, and little change was seen. FDTD obtains the RCS to 150 MHz but the data has not been shown because there is no curve available for comparison.

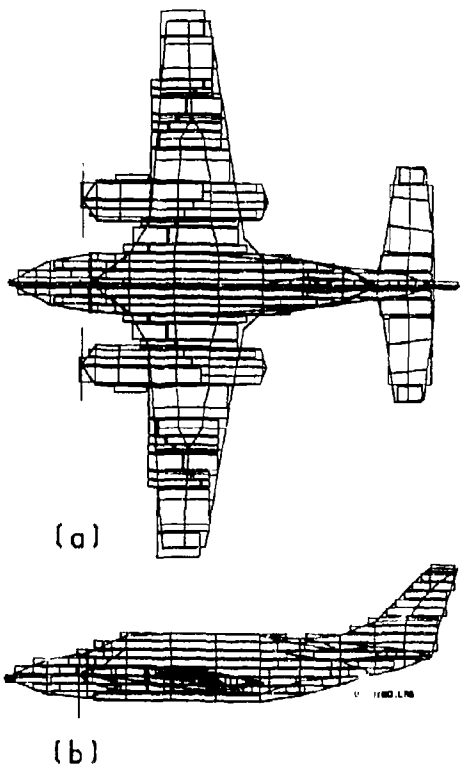

Fig. 9 Comparison of the "cell model" of the Navajo with the wire-grid model.

Conclusions

The GWTOFDTD program is an interactive graphical aid for the conversion of a wire-grid model of an aircraft into an FDTD "cell model". The user chooses a cell size, and then the program draws a cross-section of the cell space with the cross-section of the wire-grid superimposed; the user points with the mouse to "fill" cells to best represent each cross-section. The cell model is only as accurate geometrically as the underlying wire-grid. Better geometrical fidelity could be obtained by modifying the

program to accept an industry-standard description of the aircraft shape using many, many points on the surface. This has not been done here because such comprehensive geometrical descriptions are simply not generally available.

This paper has compared the RCS computed with FDTD with reference data for two cases. The simple "generic aircraft" geometry can be represented accurately with an FDTD cell model. But the RCS does not agree as well as might be expected with the measured RCS, nor with that computed by wire-grid modelling. The more complex geometry of the Navajo aircraft requires the power of the GWTOFDTD program to obtain a reasonable cell representation. The RCS shows disagreement with the wire-grid computation in the frequency range where the fundamental resonances of the airframe are expected, as well as at higher frequencies. These differences will be explored in the oral presentation.

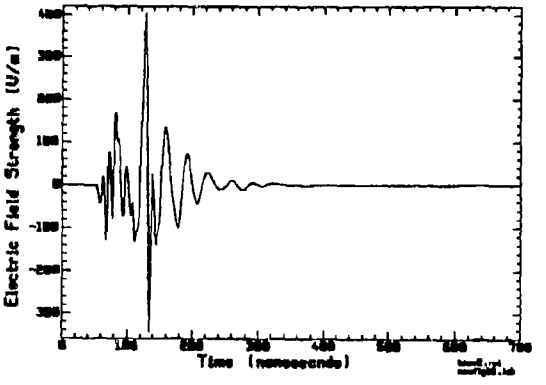

Fig. 10 The backscattered field from the Navajo aircraft.

References

1. K.S. Yee, "Numerical Solution of Initial Value Problems Involving Maxwell's Equations in Isotropic Media", IEEE Trans. on Antennas and Propagation, Vol. AP-14, No. 3, May, 1966.
2. K.S. Kunz and R.J. Luebbers, "The Finite-Difference Time-Domain Method for Electromagnetics", CRC Press, 1993.

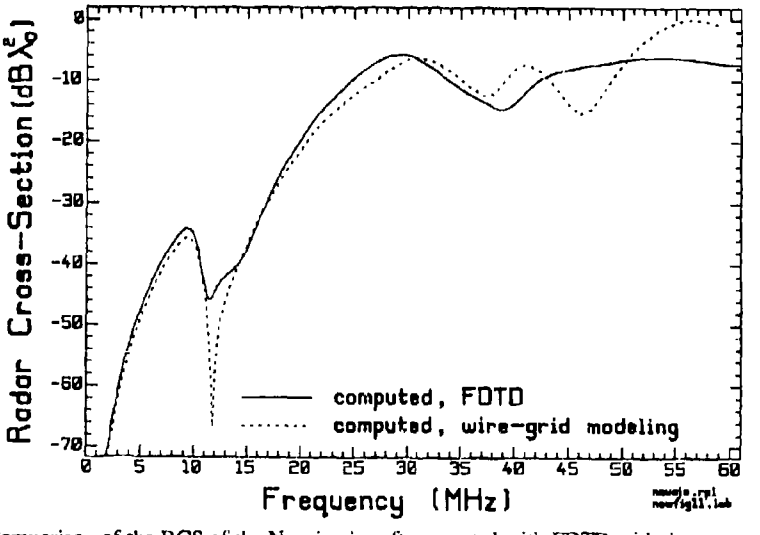

Fig. 11 Comparison of the RCS of the Navajo aircraft computed with FDTD with that computed with wire-grid modeling.

3. R. Luebbers, D. Steich, K. Kunz and F. Hunsberger, "RCS Calculation for Smooth Bodies of Revolution using FDTD", 7th Annual Review of Progress in Applied Computational Electromagnetics Conference Proceedings, pp. 682-690, Monterey, California, March 18-22, 1991.
4. R.J. Luebbers, K.S. Kunz, M. Schneider and F. Hunsberger, "A Finite-Difference Time-Domain Near Zone to Far Zone Transformation", IEEE Trans. on Antennas and Propagation, Vol. AP-39, No. 4, April, 1991.
5. C.W. Trueman, S.J. Kubina, R.J. Luebbers, K. Kunz, S.R. Mishra and C. Larose, "RCS of Cubes, Strips, Rods and Cylinders by FDTD", 8th Annual Review of Progress in Applied Computational Electromagnetics Conference Proceedings, pp. 487-494, Monterey, California, March 16-20, 1992.
6. R.J. Luebbers, private communication.
7. S.R. Mishra, C.L. Larose and C.W. Trueman, "Precision Radar Cross-Section Measurements for Computer Code Validation", IEEE Trans. on Instrumentation and Measurement, Vol. 42, No. 2, pp. 179-185, April, 1993.
8. C.W. Trueman, S.J. Kubina, R.J. Luebbers, S.R. Mishra and C. Larose, "Quarter-Cell Surface Adjustment for PEC FDTD Targets", manuscript in preparation.
9. C.A. Balanis, "Advanced Engineering Electromagnetics", Wiley, 1989.
10. C.W. Trueman and S.J. Kubina, "Fields of Complex Surfaces Using Wire-Grid Modelling", IEEE Trans. on Magnetics, Vol. 27, No. 5, pp. 4262-4267, Sept. 1991.
11. G.J. Burke and A.J. Poggio, "Numerical Electromagnetics Code - Method of Moments", Technical Document 116, Naval Electronic Systems Command(ELEX 3041), July, 1977.
12. C.W. Trueman and S.J. Kubina, "Automated Radius Calculation for Wire-Grid Models", 7th Annual Review of Progress in Applied Computational Electromagnetics Conference Proceedings, pp. 380-388, Monterey, California, March 18-22, 1991.
13. Z. Liao, H.L. Wong, B. Yang and Y. Yuan, "A Transmitting Boundary for Transient Wave Analyses," Scientia Sinica(Series A), Vol. XXVII, No. 10, pp. 1062-1076, Oct. 1984.
14. D. Steich, F. Luebbers, and K.S. Kunz, "Absorbing Boundary Condition Convergence Comparisons", 199[illegible] IEEE Antennas and Propagation Society International Symposium Digest, pp. 6-9, Ann Arbor, Michigan, June 28-July 2, 1993.
15. C.W. Trueman, S.J. Kubina, S.R. Mishra and C. Larose, "Radar Cross-Section of a Generic Aircraft at HF Frequencies", Canadian Journal of Electrical and Computer Engineering, Vol. 18, No. 2, pp. 59-64, April, 1993.

High Order F.D.T.D. Algorithm to Reduce Numerical Dispersion and Staircasing

Thierry DEVEZE
DASSAULT ELECTRONIQUE, Département Hyperfréquences
55, Quai Marcel DASSAULT, 92214 St Cloud
FRANCE

Developped by YEE[1] in 1966, the FDTD algorithm has been widely used in a large variety of electromagnetic applications. The YEE's scheme is based on the approximation of differential operators by second order centered Taylor's expansion, both in time and space (the so called 2x2. scheme).
Simplicity is the main advantage of the method and it enables to handle computations on large complex structures. This powerful tool has nevertheless some drawbacks. The second order central approximation leads to numerical dispersion that affects the accuracy of the solution. The stair case modeling may not fit properly the geometry of the structure. Some authors have found different solutions to conform the mesh to the geometry of the structure under study. HOLLAND[2], among others, has proposed a curvilinear version of the cartesian YEE's algorithm. Recently, TAFLOVE[3] and al. have exposed a contour path approach. These methods largely reduce the staircase modeling but increase the numerical dispersion. To reduce this drawback, a higher order FDTD scheme is proposed. After deriving the general formulation at the order N, it appears that the fourth order schemes give the best choice for the ratio : complexity over dispersion performance. The purpose of this paper is to build a fourth order scheme that can reduce the numerical dispersion and take into account the curved shape of the structure under study.

The free space case

The Maxwell's equations system in free space is hyperbolic and is based on first degree differential operators over time and space. The centered Taylor's expansion gives directly the second order discretisation.

Order 2 in space

$$\partial_r E^n(r) = \frac{E^n(r+\frac{\Delta r}{2}) - E^n(r-\frac{\Delta r}{2})}{\Delta r} + O(\Delta r^2) \qquad (1)$$

Order 4 in space

$$\partial_r E^n(r) = \frac{9}{8}\frac{E^n(r+\frac{\Delta r}{2}) - E^n(r-\frac{\Delta r}{2})}{\Delta r} - \frac{1}{24}\frac{E^n(r+\frac{3\Delta r}{2}) - E^n(r-\frac{3\Delta r}{2})}{\Delta r} + O(\Delta r^4) \qquad (2)$$

Equation (2) is obtained by a linear combination of two central differentiations around r , one with a step Δr and the other with $2\Delta r$. This procedure eradicates the third degree derivation term of the TAYLOR's expansion.

Order 2 in time

$$\partial_t E^{n+\frac{1}{2}}(r) = \frac{E^{n+1}(r) - E^n(r)}{\Delta t} + O(\Delta t^2) \qquad (3)$$

Order 4 in time

The method used for the fourth order discretisation in space cannot be applied to the time derivatives because it leads to a 5 time steps scheme which is not stable. By employing the so called "Modified Equation Method" proposed by JOLY and COHEN[4] for the acoustic wave equation, it is possible to convert the third degree time derivation by a combination of spatial operators. This conversion is done by replacing the MAXWELL's equations in the third degree derivation term [5] As an illustration of this, the TAYLOR's expansion of the Ex component is given by :

$$\partial_t E_x^{n+\frac{1}{2}}(r) = \frac{E_x^{n+1}(r) - E_x^{n}(r)}{\Delta t} - \frac{\Delta t^2}{24}\partial_t^3 E_x^{n+\frac{1}{2}}(r) + O(\Delta t^4) \tag{4}$$

With the constant constitutives of free space : (the permittivity, $\varepsilon=\varepsilon 0$, the permeability, $\mu=\mu 0$, and the velocity of light C), the third degree term has the following form :

$$\begin{aligned}
&\partial_t^3 E_x^{n+\frac{1}{2}}\left(i+\tfrac{1}{2},j,k\right) = \\
&+\frac{c^2}{\varepsilon\Delta y}\left[\begin{array}{l}
-\left(\frac{2}{\Delta x^2}+\frac{3}{\Delta y^2}+\frac{2}{\Delta z^2}\right)\left[H_z^{n+\frac{1}{2}}\left(i+\tfrac{1}{2},j+\tfrac{1}{2},k\right)-H_z^{n+\frac{1}{2}}\left(i+\tfrac{1}{2},j-\tfrac{1}{2},k\right)\right] \\
+\frac{1}{\Delta x^2}\left[\begin{array}{l}H_z^{n+\frac{1}{2}}\left(i+\frac{3}{2},j+\frac{1}{2},k\right)-H_z^{n+\frac{1}{2}}\left(i+\frac{3}{2},j-\frac{1}{2},k\right) \\ +H_z^{n+\frac{1}{2}}\left(i-\frac{1}{2},j+\frac{1}{2},k\right)-H_z^{n+\frac{1}{2}}\left(i-\frac{1}{2},j-\frac{1}{2},k\right)\end{array}\right] \\
+\frac{1}{\Delta y^2}\left[H_z^{n+\frac{1}{2}}\left(i+\tfrac{1}{2},j+\tfrac{3}{2},k\right)-H_z^{n+\frac{1}{2}}\left(i+\tfrac{1}{2},j-\tfrac{3}{2},k\right)\right] \\
+\frac{1}{\Delta z^2}\left[\begin{array}{l}H_z^{n+\frac{1}{2}}\left(i+\frac{1}{2},j+\frac{1}{2},k+1\right)-H_z^{n+\frac{1}{2}}\left(i+\frac{1}{2},j-\frac{1}{2},k+1\right) \\ +H_z^{n+\frac{1}{2}}\left(i+\frac{1}{2},j+\frac{1}{2},k-1\right)-H_z^{n+\frac{1}{2}}\left(i+\frac{1}{2},j-\frac{1}{2},k-1\right)\end{array}\right]
\end{array}\right] \\
&+\frac{c^2}{\varepsilon\Delta z}\left[\begin{array}{l}
+\left(\frac{2}{\Delta x^2}+\frac{2}{\Delta y^2}+\frac{3}{\Delta z^2}\right)\left[H_y^{n+\frac{1}{2}}\left(i+\tfrac{1}{2},j,k+\tfrac{1}{2}\right)-H_y^{n+\frac{1}{2}}\left(i+\tfrac{1}{2},j,k-\tfrac{1}{2}\right)\right] \\
-\frac{1}{\Delta x^2}\left[\begin{array}{l}H_y^{n+\frac{1}{2}}\left(i+\frac{3}{2},j,k+\frac{1}{2}\right)-H_y^{n+\frac{1}{2}}\left(i+\frac{3}{2},j,k-\frac{1}{2}\right) \\ +H_y^{n+\frac{1}{2}}\left(i-\frac{1}{2},j,k+\frac{1}{2}\right)-H_y^{n+\frac{1}{2}}\left(i-\frac{1}{2},j,k-\frac{1}{2}\right)\end{array}\right] \\
-\frac{1}{\Delta z^2}\left[H_y^{n+\frac{1}{2}}\left(i+\tfrac{1}{2},j,k+\tfrac{3}{2}\right)-H_y^{n+\frac{1}{2}}\left(i+\tfrac{1}{2},j,k-\tfrac{3}{2}\right)\right] \\
-\frac{1}{\Delta y^2}\left[\begin{array}{l}H_y^{n+\frac{1}{2}}\left(i+\frac{1}{2},j+1,k+\frac{1}{2}\right)-H_y^{n+\frac{1}{2}}\left(i+\frac{1}{2},j+1,k-\frac{1}{2}\right) \\ +H_y^{n+\frac{1}{2}}\left(i+\frac{1}{2},j-1,k+\frac{1}{2}\right)-H_y^{n+\frac{1}{2}}\left(i+\frac{1}{2},j-1,k-\frac{1}{2}\right)\end{array}\right]
\end{array}\right]
\end{aligned} \tag{5}$$

This gives a 3 time steps scheme with 25 spatial nodes.instead of 5 for the 2x2. The difference of spatial extension is shown in figure 1 a) for the 2x2 scheme and in figure 1.b) for the 4x4. In equation (5), the

discretisation of the spatial differentiations are written only at the second order which is sufficient to ensure the fourth order in (4) because (5) is multiplied by Δt^2. All the nodes involved in the formulation of the Ex node already exist in the regular 2x2 FDTD mesh. No extra memory storage is required. The number of computing operations is increased by 4, but the dispersion analysis shows that, for the same degree of accuracy, the spatial step is at least twice larger for the 4x4 scheme than the 2x2. This results in a factor 8 (in 3D) of computer memory saving and a factor 4 in computational speed because the time step is also twice larger.

The Stability

The stability criteria of the 2x2 and the 4x4 (free space) schemes are the same. The Von NEUMANN method has been used to derive the criteria of the fourth order heterogeneous space schemes.

The Numerical Dispersion

The dispersion of the numerical solution over the frequency variable strongly depends on the precision over the time differentiations. The anisotropy of the numerical mesh lays mainly on the accuracy over the the spatial derivatives. The figures 2.a) and 2.b) illustrate the anisotropic behavior of the 2x2 and 4x4 schemes. A line source,located at ($25\Delta x$,$25\Delta y$), in a 2D computational domain , generates a sinusoïdal wave. The zero isovalue curves give the wave front aspect which should be cylindrical. The darkened areas indicate the differences between the computed wave front and the exact circular one. A coarse space discretisation of $\Delta=\lambda/3.3$ emphasizes the phenomena. The derivation of the dispersion for each scheme allows a comparison of their capabilities in the case of a cubic cell meshing ($\Delta x=\Delta y=\Delta z=2.C.\Delta t$). The numerical dispersion is null, in free space, when vgroup/C=1 (Vgroup : Group velocity in the mesh). This rate is plotted in figure 3) for the two directions of propagation which correspond to the extrema of isotropy. For a discretisation rate of $\lambda/8$, the worst angle with the 4x4 scheme gives better results than the best angle of propagation in the 2x2 scheme. The 2x4 scheme generates a non physical value of the group speed (Vgroup>C).

The stair case problem and the heterogeneous formulation

The free space formulation using (2) and (4) is non longer applicable to the computation of a node in the vicinity of an interface for 3 reasons. 1.The spatial extension of the computational molecule (figure 1.b) may imply the use of nodes located behind interfaces.2. If the electric conductivity σ and the magnetic resistivity ρ are taken into account then "the modified equation method" results in an implicit scheme. The method used to derive the 4x4 scheme does not reduce the stair case modeling problem.

The solution proposed here is based on the idea that the electromagnetic field is numerically differentiated in a constant steps computational mesh and the constitutive functions ($\varepsilon,\mu,\sigma,\rho$) analytically derived. The AMPERE's and the FARADAY's laws are the starting points of this approach. The projection of the AMPERE's law on a plane z=constant (6) is used as an illustration.

(6) $$\iint_{\Omega_z} a_z.dx.dy = \oint_{\partial\Omega_z} \vec{H}.d\vec{l}$$, where Ω_z is a the square surface $\Delta x.\Delta y$ and $\partial\Omega_z$ its closed contour.

(7) $$a_z = \varepsilon\partial_t E_z + \sigma E_z$$

Taking the 3D TAYLOR's expansion of $\bar{H}$ and a_z in (6), a representation of the MAXWELL-AMPERE equation is obtained at the **Order N**

$$(8)\qquad \sum_{p=0}^{N}\sum_{q=0}^{N}\frac{\left(\frac{\Delta x}{2}\right)^{2p}\left(\frac{\Delta y}{2}\right)^{2q}}{(2p+1)!(2q+1)!}\partial_x^{2p}\partial_y^{2q}a_z = \sum_{p=0}^{N}\sum_{q=0}^{N}\frac{\left(\frac{\Delta x}{2}\right)^{2p}\left(\frac{\Delta y}{2}\right)^{2q}}{(2p+1)!(2q+1)!}\left[\partial_x^{2p+1}\partial_y^{2q}H_y - \partial_x^{2p}\partial_y^{2q+1}H_x\right]$$

Order 2 (N=0)

$$(9)\qquad a_z = \partial_x H_y - \partial_y H_x + O(\Delta x^2, \Delta y^2) = \delta_x H_y - \delta_y H_x$$

This is the classical form given by the limit $\Delta_x, \Delta_y \to 0$, where δ stands for the numerical second order differenciation operator as for the following example :

$$(10)\qquad \delta_x H_y(x_0, y_0, z_0 + \frac{\Delta z}{2}) = \frac{1}{\Delta x}\left[H_y(x_0 + \frac{\Delta x}{2}, y_0, z_0 + \frac{\Delta z}{2}) - H_y(x_0 - \frac{\Delta x}{2}, y_0, z_0 + \frac{\Delta z}{2})\right]$$

Order 4 (N=1)

$$(11)\qquad \begin{aligned} &a_z + \frac{\Delta x^2}{24}\partial_x{}^2 a_z + \frac{\Delta y^2}{24}\partial_y{}^2 a_z = \delta_x H_y - \delta_y H_x \\ &= \partial_x H_y - \partial_y H_x + \frac{\Delta x^2}{24}\left[\partial_x{}^3 H_y - \partial_x{}^2\partial_y H_x\right] + \frac{\Delta y^2}{24}\left[\partial_x\partial_y{}^2 H_y - \partial_y{}^3 H_x\right] + O(\Delta x^4, \Delta y^4) \end{aligned}$$

A second order discretisation is sufficient for the partial derivatives in (11), because they are multiplied by Δ^2. Equation (11) shows some spatial derivatives over the Ez field component and over the electric constitutives ε and σ. This feature enables the introduction of the local rates and curvatures of variation of ε and σ. These local variations do not have a step profile but a smooth cubic one. By a proper choice of the coefficients of the cubic polynomial, it possible to impose the real location of an interface intersecting the computational molecule. The larger the order N is, the better the geometrical approximation is, but the heavier the formulation becomes.

The heterogeneous media formulation

The second order case is given by the classical following form of (9)

$$(12)\qquad \bar{E}^{n+1} = \frac{\beta}{\alpha}\bar{E}^{n} + \frac{1}{\alpha}\bar{\nabla}_b \times \bar{H},$$

$$(13)\qquad \bar{H}^{n+1/2} = \frac{\beta'}{\alpha'}\bar{H}^{n-1/2} - \frac{1}{\alpha'}\bar{\nabla}_b \times \bar{E},$$

$$(14)\qquad \alpha = \frac{\varepsilon}{\Delta t}\left[1 + \frac{\sigma\,\Delta t}{2}\right] = \beta + \sigma,$$

$$(15)\qquad \alpha' = \frac{\mu}{\Delta t}\left[1 + \frac{\rho\,\Delta t}{2}\right] = \beta' + \rho$$

The fourth order spatial discretisation

The Spatial Correction Term is given in (11) and can be re-written as follow :

(16) $SCT = (\Delta x^2 \partial_x{}^2 + \Delta y^2 \partial_y{}^2)\left[\alpha\ E_z^{n+1} - \beta\ E_z^n\right]$

The partial derivatives are evaluated numerically for the Ez nodes and analytically for α and β.

(17) $\partial_x{}^2(\alpha\ E_z^{n+1}) = \partial_x{}^2\alpha\ .E_z^{n+1} + 2\partial_x\alpha\ .\delta_{2x}E_z^{n+1} + \alpha\ .\delta_{2x}{}^2E_z^{n+1}$

If the central node Ez is located at $(x_0, y_0, z_0 + \Delta z/2) = (i.\Delta x, j.\Delta y, (k+1/2).\Delta z)$, the SCT is :

(18) $SCT = \left[\Delta x^2.\partial_x{}^2\alpha \quad v^2.\partial_y{}^2\alpha\ -4.\alpha\ \right].E_z^{n+1} - \left[\Delta x^2.\partial_x{}^2\beta\ +\Delta y^2.\partial_y{}^2\beta\ -4.\beta\ \right].E_z^n$

$+\left[\Delta y\ .\partial_y\alpha\ +\alpha\ \right].E_z^{n+1}(j+1) - \left[\Delta y\ .\partial_y\beta\ +\beta\ \right].E_z^n(j+1)$

$-\left[\Delta x\ .\partial_x\alpha\ -\alpha\ \right].E_z^{n+1}(i-1) + \left[\Delta x\ .\partial_x\beta\ -\beta\ \right].E_z^n(i-1)$

$+\left[\Delta y\ .\partial_y\alpha\ +\alpha\ \right].E_z^{n+1}(j+1) - \left[\Delta y\ .\partial_y\beta\ +\beta\ \right].E_z^n(j+1)$

$-\left[\Delta y\ .\partial_y\alpha\ -\alpha\ \right].E_z^{n+1}(j-1) + \left[\Delta y\ .\partial_y\beta\ -\beta\ \right].E_z^n(j-1)$

Only the index that are differents from $(i,j,k+1/2)$ are noted in (18). This expression results in an implicit scheme because some other Ez nodes are requested, at time $t=(n+1).\Delta t$, in the computation of the central node.

The fourth order time discretisation

The Time Correction Term is given by the TAYLOR's expansion. The relation (4) is modified to take into account the loss term :

(19) $a_z = \varepsilon\ \delta_t\ E_z^{n+1/2} + \sigma\ \xi_t\ E_z^{n+1/2} - \frac{\Delta t^2}{24}\partial_t{}^2\left[\varepsilon\ \partial_t\ +3.\sigma\ \right].E_z^{n+1/2} + O(\Delta t^4\ )$

with the average operator

(20) $\xi_t\ E_z^{n+1/2} = \frac{1}{2}\left[E_z^{n+1} + E_z^n\right]$

Assumptions :

The magnetic constitutives μ and ρ are assumed to be constants in the electric formulation (respectively with ε and σ in the magnetic formulation).

The constitutives are assumed to be constants in the direction of the field component to compute. These assumptions are related to the planeness of the integration surface (Ωz in (6)).

(21) $TCT = \partial_t{}^2(\varepsilon\ \partial_t\ \vec{E} + 3.\sigma\ \vec{E}) =$

$$\frac{1}{\mu}\left[\frac{\rho}{\mu} - \frac{2.\sigma}{\varepsilon}\right].\vec{\nabla}\times\vec{\nabla}\times\left(\xi_t\ \vec{E}\right) - \frac{1}{\mu}\vec{\nabla}\times\vec{\nabla}\times\left(\delta_t\ \vec{E}\right) +$$

$$\frac{1}{\mu}\left[\frac{\rho}{\mu} - \frac{2.\sigma}{\varepsilon}\right].\vec{\nabla}\times\vec{\nabla}\times\left(\xi_t\ \vec{E}\right) - \frac{1}{\mu}\vec{\nabla}\times\vec{\nabla}\times\left(\delta_t\ \vec{E}\right) +$$

$$\left[\frac{\varepsilon\ \rho}{\mu}\left[\frac{\rho}{\mu} - \frac{2.\sigma}{\varepsilon}\right] - \frac{2\sigma^2}{\varepsilon}\right].\delta_t\ \vec{E} + \frac{\sigma\ \rho}{\mu}\left[\frac{\rho}{\mu} - \frac{2.\sigma}{\varepsilon}\right].\xi_t\ \vec{E} + O(\Delta t^2)$$

The TCT of (19) is obtained by projection on the 0z axis. By replacing (21) in (19) and (18) in (11), the heterogeneous media formulation is obtained for a Ez component.

$$(22)\quad \left\{\begin{array}{l}\frac{5}{6}\alpha + \frac{1}{24}\left[\Delta x^2\partial_x{}^2\alpha + \Delta y^2\partial_y{}^2\alpha\right] \\ -\frac{\Delta t^2}{24}\left[\frac{\alpha\rho}{\mu}\left[\frac{\rho}{\mu}-\frac{2\sigma}{\varepsilon}\right]-\frac{2\sigma^2}{\varepsilon\,\Delta t}-\frac{2}{\mu}\left[\frac{1}{\Delta x^2}+\frac{1}{\Delta y^2}\right]\left[\frac{1}{\Delta t}-\frac{1}{2}\left[\frac{\rho}{\mu}-\frac{2\sigma}{\varepsilon}\right]\right]\right]\end{array}\right\}.E_z^{n+1} =$$

$$\left\{\begin{array}{l}\frac{5}{6}\beta + \frac{1}{24}\left[\Delta x^2\partial_x{}^2\beta + \Delta y^2\partial_y{}^2\beta\right] \\ -\frac{\Delta t^2}{24}\left[\frac{\beta\rho}{\mu}\left[\frac{\rho}{\mu}-\frac{2\sigma}{\varepsilon}\right]-\frac{2\sigma^2}{\varepsilon\,\Delta t}-\frac{2}{\mu}\left[\frac{1}{\Delta x^2}+\frac{1}{\Delta y^2}\right]\left[\frac{1}{\Delta t}-\frac{1}{2}\left[\frac{\rho}{\mu}-\frac{2\sigma}{\varepsilon}\right]\right]\right]\end{array}\right\}.E_z^{n}$$

$$-\frac{1}{24}\left[\left\{\Delta x\,\partial_x\alpha + \alpha - \frac{\Delta t^2}{\mu\,\Delta x^2}\left[\frac{1}{\Delta t}-\frac{\rho}{2\mu}+\frac{\sigma}{\varepsilon}\right]\right\}.E_z^{n+1}(i+1)-\left\{\Delta x\,\partial_x\alpha - \alpha + \frac{\Delta t^2}{\mu\,\Delta x^2}\left[\frac{1}{\Delta t}-\frac{\rho}{2\mu}+\frac{\sigma}{\varepsilon}\right]\right\}.E_z^{n+1}(i-1)\right]$$

$$-\frac{1}{24}\left[\left\{\Delta y\,\partial_y\alpha + \alpha - \frac{\Delta t^2}{\mu\,\Delta y^2}\left[\frac{1}{\Delta t}-\frac{\rho}{2\mu}+\frac{\sigma}{\varepsilon}\right]\right\}.E_z^{n+1}(j+1)-\left\{\Delta y\,\partial_y\alpha - \alpha + \frac{\Delta t^2}{\mu\,\Delta y^2}\left[\frac{1}{\Delta t}-\frac{\rho}{2\mu}+\frac{\sigma}{\varepsilon}\right]\right\}.E_z^{n+1}(j-1)\right]$$

$$+\frac{1}{24}\left[\left\{\Delta x\,\partial_x\beta + \beta - \frac{\Delta t^2}{\mu\,\Delta x^2}\left[\frac{1}{\Delta t}+\frac{\rho}{2\mu}-\frac{\sigma}{\varepsilon}\right]\right\}.E_z^{n}(i+1)-\left\{\Delta x\,\partial_x\beta - \beta + \frac{\Delta t^2}{\mu\,\Delta x^2}\left[\frac{1}{\Delta t}+\frac{\rho}{2\mu}-\frac{\sigma}{\varepsilon}\right]\right\}.E_z^{n}(i-1)\right]$$

$$+\frac{1}{24}\left[\left\{\Delta y\,\partial_y\beta + \beta - \frac{\Delta t^2}{\mu\,\Delta y^2}\left[\frac{1}{\Delta t}+\frac{\rho}{2\mu}-\frac{\sigma}{\varepsilon}\right]\right\}.E_z^{n}(j+1)-\left\{\Delta y\,\partial_y\beta - \beta + \frac{\Delta t^2}{\mu\,\Delta y^2}\left[\frac{1}{\Delta t}+\frac{\rho}{2\mu}-\frac{\sigma}{\varepsilon}\right]\right\}.E_z^{n}(j-1)\right]$$

$$-\frac{\Delta t^2}{24\mu\,\Delta x\,\Delta z}\left[\frac{1}{\Delta t}-\frac{1}{2}\left[\frac{\rho}{\mu}-\frac{2\sigma}{\varepsilon}\right]\right]\left\{E_x^{n+1}(i+\tfrac{1}{2},k+1)-E_x^{n+1}(i-\tfrac{1}{2},k+1)-E_x^{n+1}(i+\tfrac{1}{2},k)+E_x^{n+1}(i-\tfrac{1}{2},k)\right\}$$

$$-\frac{\Delta t^2}{24\mu\,\Delta y\,\Delta z}\left[\frac{1}{\Delta t}-\frac{1}{2}\left[\frac{\rho}{\mu}-\frac{2\sigma}{\varepsilon}\right]\right]\left\{E_y^{n+1}(j+\tfrac{1}{2},k+1)-E_y^{n+1}(j-\tfrac{1}{2},k+1)-E_y^{n+1}(j+\tfrac{1}{2},k)+E_y^{n+1}(j-\tfrac{1}{2},k)\right\}$$

$$+\frac{\Delta t^2}{24\mu\,\Delta x\,\Delta z}\left[\frac{1}{\Delta t}+\frac{1}{2}\left[\frac{\rho}{\mu}-\frac{2\sigma}{\varepsilon}\right]\right]\left\{E_x^{n}(i+\tfrac{1}{2},k+1)-E_x^{n}(i-\tfrac{1}{2},k+1)-E_x^{n}(i+\tfrac{1}{2},k)+E_x^{n}(i-\tfrac{1}{2},k)\right\}$$

$$+\frac{\Delta t^2}{24\mu\,\Delta y\,\Delta z}\left[\frac{1}{\Delta t}+\frac{1}{2}\left[\frac{\rho}{\mu}-\frac{2\sigma}{\varepsilon}\right]\right]\left\{E_y^{n}(j+\tfrac{1}{2},k+1)-E_y^{n}(j-\tfrac{1}{2},k+1)-E_y^{n}(j+\tfrac{1}{2},k)+E_y^{n}(j-\tfrac{1}{2},k)\right\}$$

$$+\delta_z H_y - \delta_y Hx$$

All the derivations are operated at $(i,j,k+1/2)$ in (22). The explicit expression of Ez at $t=(n+1)\Delta t$ is obtained by replacing the projections of (12) in (22). The computation of a E node involves 24 H nodes and 12 E nodes when $\sigma \neq 0$. Respectively, the computation of a H node involves 24 E nodes and 12 H nodes when $\rho \neq 0$.

Absorbing Boundary Condition

The spatial extension of the fourth order scheme raises the problem of the field computation over the mesh boundary. Several approaches are available in [6]. It seems, from now that a good absorption performance is obtained by using a fourth order HIGDON condition on the boundary. The derivation operators are discretized at the second order in time and space. The plane of nodes located between the exterior absorbing boundary and the 4x4 interior scheme are computed with the regular 2x2 scheme.

Figure 2 : comparison on the anisotropy of the 2x2 and the 4x4 schemes, illustrated by the difference between the computed wave front and the ideal circular one. Discretisation $\Delta x=\Delta y=\lambda/3.3=2C\Delta t$

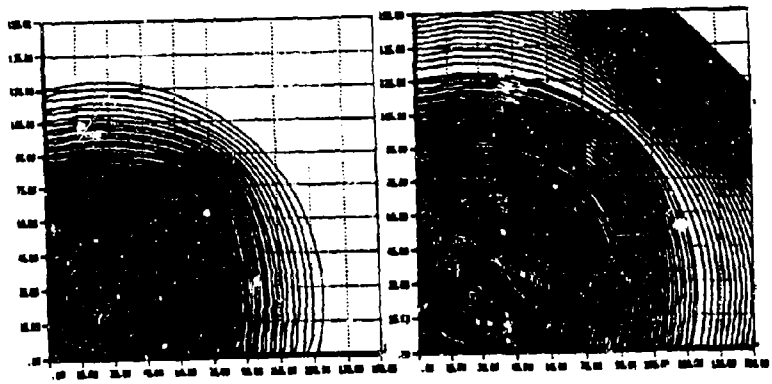

2.a) : 2x2 2.b) : 4x4

Figure 3 : dispersion error on the group velocity in the 2x2, 2x4 and the 4x4 schemes measured on the rate Vgroup/C

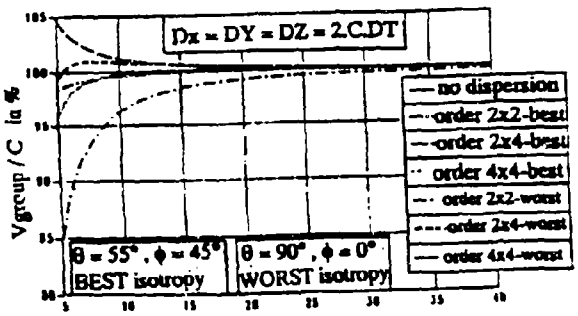

Conclusion

The 4x4 scheme has a heavier formulation than the 2x2, but shows better performance. The method exposed above may be applied to build higher order schemes. The main idea is to use the lower order formulations to build the higher one. The spatial extension over an interface is taken into account by a combination of 2x2 heterogenous formulations applied on both sides of the interface. The second degree derivatives over the constitutives enables to approximate the change of media index by a cubic polynomial. This gives a better geometrical modelisation of the structure to study.

[1] YEE K.S. "Numerical solution of initial boundary value problem involving MAXWELL's equations in isotropic media". IEEE Antenna and Propagation. MAY 19C . AP-14 N°3

[2] HOLLAND "Finite difference solution of MAXWELL's equations in generalized non orthogonal coordinates". IEEE Nuclear Science.DECEMBER 1983, Vol 30 N°6

[3] TAFLOVE A., UMASHANKAR K.R. "Review of FDTD numerical modeling of electromagnetic wave and radar cross section". Proceeding of IEEE. MAY 1989, Vol 77, N°5

[4] JOLY P., COHEN G. "Fourth order schemes in time and space for the heterogeous wave equations". Computational Math. in Apply Mech. and Eng.

[5] DEVEZE T."Contribution à l'analyse par différences finies des équations de MAXWELL dans le domaine temps". PhD report. Université PARIS6-Pierre et Marie CURIE. MAY 1992

[6] DEVEZE T."An absorbing boundary condition for the fourth order FDTD scheme".IEEE AP/S 92 .CHICAGO

Figure 1 Spatial dispositions of the electromagnetic nodes involved in the computation of the Ex(i+1/2,j,k) component in free space

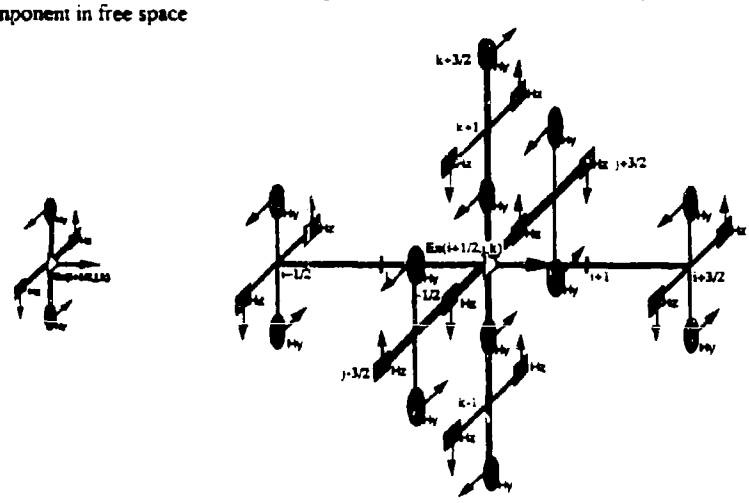

1.a) 2x2 scheme

1.b) 4x4 scheme

SESSION 13:

GEMACS

Chair: Ken Siarkiewicz
Co-Chair: Buddy Coffey

Recent Enhancements to GEMACS 5.3

Edgar L. Coffey, III
Advanced Electromagnetics
4516 Stockbridge Avenue NW
Albuquerque, New Mexico 87120

A number of new features, specifically requested by GEMACS users, has been added to the GEMACS (General Electromagnetic Model for the Analysis of Complex Systems) computer program [1] since the release of version 5.2 in early 1993. The purpose of this paper is to summarize the modifications made to the program and how these changes benefit the GEMACS user.

MOM Low Frequency Accuracy Enhanced

The low frequency accuracy of GEMACS' method of moments (MOM) module has been improved by addressing some of the numerical deficiencies of the original code. The wire segment basis function has been changed from its original

$$I(s) = A + B \sin(ks) + C \cos(ks)$$

to the one used in NEC3VLF [2],

$$I(s) = A + B \sin(ks) + C [1 - \cos(ks)]$$

where k is the wave number and s is the distance along a wire segment. This does not change any physics within the code. It merely rearranges terms so that the "C" function is a perturbation about zero instead of a perturbation about unity. Hence, the numerical difficulty of allocating current between to "A" and "C" terms is alleviated. At the same time the near and far zone field equations were rewritten for better numerical stability and to take advantage of numerical methods that have speeded up computations (matrix fill) by an average of 30% for large numbers. In addition, the evaluation of the exp(-jkR)/R has been changed per the technique in NEC3VLF.

The key to increased accuracy, however, was not so much the work described above as the total rewrite of the current basic function interpolation numerics for {A, B, C}. GEMACS, unlike NEC or NEC3VLF, makes more use of interpolation numerics. When segment lengths become electrically short, the numerical implementation of the interpolation breaks down. A significant rewrite of the code

This work was sponsored by the U. S. Air Force Rome Laboratory under contract F30602-92-C-0072.

has extended the numerical accuracy of this portion of GEMACS to nearly the dynamic range of the computer (typically 1E-38). These enhancements have allowed us to use GEMACS to model very small (electrical) features such as 0.1" pins on printed circuit boards without the numerical instabilities that occurred using earlier versions of the code.

The "small loop" numerical problem, also discussed in [2], still remains to a small extent in GEMACS 5.3. We plan on investigating fixes for it over the next twelve months.

GTD Ray Path Dump

It is now possible to dump GTD ray path coordinates and field magnitudes to an ASCII file using the new RAYPTH command. The path is traced from bounce to bounce and can be displayed using the GAUGE and WinGAUGE graphics packages.

HFIELD Command

At long last GEMACS has an HFIELD() command as a companion to EFIELD(). HFIELD computes magnetic fields for MOM, GTD, and MOM/GTD hybrid problems. Its syntax is identical to that of EFIELD(). It is of particular value in finding surface currents on GTD structures since J = n x H. HFIELD has not yet been implemented for finite difference (FD) problems since the structure of GEMACS for FD is quite different from its MOM and GTD structure.

CAD Geometry Data

Finally, in response to requests from GEMACS users which develop geometry models with commercial CAD packages, GEMACS 5.3 includes a feature to allow direct input of geometry data, bypassing the normal geometry input processor. The data are for the most part descriptions of polygons (with a wire segment defined as a two-vertex polygon). Data sets in this form are generally much easier to generate with CAD packages than data using the traditional GEMACS grammar and syntax.

The CAD geometry data input is activated by adding the CAD field to the GMDATA command. This causes GEMACS to interpret the ASCII data in the geometry file as point/polygon data instead of standard GEMACS geometry commands.

References

1. E. L. Coffey, D. L. Kadlec, and N. W. Coffey, "General Electromagnetic Model for the Analysis of Complex Systems (GEMACS), Version 5, User, Engineering, and Code Documentation Manuals, Rome Laboratory Technical Report RADC-TR-90-360, June 1990.

2. G. J. Burke, "Enhancements and Limitations of the Code NEC for Modeling Electrically Small Antennas," Lawrence Livermore National Laboratory, Report UCID-20970, January 1987.

Estimation of GEMACS Computer Resource Requirements

Robert Fisher
Science & Engineering Associates
6100 Uptown Blvd. NE
Albuquerque, NM 87110

Edgar L. Coffey
Advanced Electromagnetics
4516 Stockbridge Ave. NW
Albuquerque, NM 87120

James D. Letterio
Phillips Laboratory (PL/WSR)
3550 Aberdeen Ave. SE
Kirtland AFB, NM 87117-5776

Abstract

A computer resource requirements analysis was recently completed for the GEMACS program. The purpose of this analysis was to develop estimation techniques for several key resources associated with the execution of this code. Three mutually supportive tools were completed during this analysis. First, graphical results and estimation charts were prepared. Second, an interactive resource estimation program (GEMSIZ) was created to let the user enter proposed problem information to obtain requirements. Finally, a program was completed that will allow the user to read a GEMACS input file to obtain the estimates of resource requirements.

1. Introduction

GEMACS, like any large analysis program, can be difficult to use and apply. One of the application problems is the determination of the best computer platform for running various classes of models. This determination is usually dependent on such factors as the amount of available disk storage, memory and the speed of the computer. In the past, it has been difficult to estimate the actual number of required files for execution, the total disk size requirement or the expected execution time for a given model. Lack of knowledge of some of these parameters can be both frustrating and, in some cases, disastrous. For instance, there have been several cases where a problem is started on a specific system and run for many days only to have the system crash because of a lack of sufficient disk storage space. This can also occur if the problem is not started with sufficient file handles to accommodate the run. An estimate of the execution time can also be important for cases where a commitment of a computer for a particular problem would be unacceptable if the expected time is excessive. The resource requirements estimation tools described in this paper are intended to assist the user in making optimum use of available computer resources and to minimize the risk of program failure due to resource limitations.

This work was supported by the Air Force Phillips Laboratory under contract F29601-92-C-0109.

2. Objectives

The main objectives for the work summarized in this paper include the following:

- Analyze the basic computer resource requirements for GEMACS
- Create graphic/nomograph documentation of results
- Create an interactive resource estimation tool
- Create a resource estimation tool for evaluation of GEMACS input files

3. Approach

The approach throughout the work performed in support of this development was focused on providing useful and informative tools for the users of GEMACS in the area of resource specification and allocation. There were four principle resources focused on for this analysis, namely, the maximum number of files, maximum disk storage prior to and after checkpoint and the execution time. The general approach for the development of estimation tools for each of these factors will be discussed here briefly.

Test Cases. A number of general test cases were devised and executed to exercise GEMACS in as many ways as possible. The test cases included simple problems with only method-of-moments (MOM), general theory of diffraction (GTD) or frequency domain finite differences (FDFD). Other cases that exercised the code with hybrid combinations of MOM, GTD and FDFD were also executed. Finally, several test models were executed from a collection of benchmarks for GEMACS. The results of these computer runs were used to prepare graphical and tabular summaries of the various resource requirements associated with GEMACS under many conditions. Table 1 summarizes the benchmark test cases that were used in the characterization of the resource requirements.

Files. The GEMACS source code was modified to write diagnostic information concerning the opening and closing of all files during a model run. This allowed the capture of the information required to determine the maximum number of files that were open at any given time.

Disk storage requirements. The maximum disk storage requirement for GEMACS prior to and after checkpoint was documented in a similar fashion to the number of files. GEMACS source code was modified to write diagnostic information concerning the writing and reading of information to and from disk. This allowed the evaluation of the size of disk storage files being worked on as a function of time/operation as the GEMACS run progressed. From this information, the maximum size of the disk storage requirement was determined both before and after checkpoint. The same test cases were used for this analysis as for the characterization of the maximum number of files.

Execution time. Another key factor in the application of GEMACS to a given computer platform is the expected execution time or relative speed of the computer. Other test cases were devised to help characterize the various contributions of GEMACS solution techniques and operations on the

required execution time. Such factors as the number of unknowns (wires, patches and apertures), number of GTD elements (plates and cylinders) and number of FDFD grid cells were considered. Also, the contributions from varying numbers of output field requests and total number of output field points requested were analyzed.

GEMSIZ program. An interactive computer program was created to provide a tool for estimation of the computer resource requirements for GEMACS under most cases. The basis of this program were the results from the large number of computer runs that were made to generate the tabular and graphical summaries previously mentioned. This program requires the user to enter pertinent information on the GEMACS problem proposed in order to make an estimate of the required resources.

GEMCRC program. Another program was also developed that makes use of the user's GEMACS input file to directly evaluate the resource requirements for a specific problem. This program is not user interactive and obtains all required information from the input file. The estimates for computer resource requirements is performed by the GEMSIZ program after the appropriate information has been extracted from the input file.

4. Results

One of the goals of this work was to devise general nomographs and equations that would allow for the computation of the execution time requirements for GEMACS problems. At the inception of this work, it was envisioned that this would consist of perhaps just a single set of governing equations, or, at worst, a set for each type of computer platform (i.e., PC, Workstation, Mini or Mainframe). The complexity of interaction of the GEMACS program with different computers, operation systems and compilers has since become very evident. The result is that there appears to be no simple set of governing equations that will allow for the generic development of nomographs or programming equations. This section will review some of the performance comparison data from the analyses performed.

Figure 1 illustrates graphical data for the number of files required as a function of the number of output field requests. Figures 2 and 3 show, respectively, the typical results obtained for the maximum disk storage requirements prior to and after checkpoint for a hybrid case involving GTD and MOM elements. Typical results for predictions of execution times for MOM, GTD and FDFD cases are illustrated in Figures 4 through 6, respectively. Table 1 summarizes some of the typical disk requirements and execution time predictions as compared to the actual values generated as part of the validation process. Excellent predictions are achieved for maximum disk storage requirements. Predictions of the execution time that are generally within about ten percent of the actual values are also achieved.

The characterization of the execution time for a GEMACS problem from one computer to another exhibited unanticipated complexities. The computers from which timing information was obtained in support of this analysis are summarized in Table 1. Considerable variation in performance was noted from computer to computer as a function of the type of problem being solved (i.e. MOM, GTD, FDFD or hybrid). Also, variations were noted even from one computer to another in the same class (i.e. two PC's or two SUN Sparc workstations). This makes the generalization of timing

estimates difficult, at best. Reasonable characterizations were achieved for PC's, a SUN Sparc/10 and a Motorola/RISC system. More coarse estimates are provided for SGI's, DEC/Alpha and the Cray super computer. It is probable that a user of the tools provided in this analysis will want to perform their own benchmarks for timing characterization if their computer platform is not one cited in Table 1.

An effort was made to characterize the timing performance of a number of computer systems. All systems were compared to the performance of a 486 class, 50 MHz PC. There is considerable variation in the measured performance for each computer as a function of the number of unknowns in the problem as well as the type of GEMACS problem being worked, i.e. GTD, MOM, FDFD or a hybrid combination of these techniques. The estimates that are provided here and in the support programs are limited in their scope of both range of numbers of unknowns as well as problem types. Many different problem types were used in the development of the estimates, but a comprehensive compilation of all possible or probable cases was not feasible for this effort. Consequently, there is some uncertainty in the timing resources predicted for computers other than the 486 base system. In addition, there are uncertainties for all cases that exceed the maximum number of unknowns used in this analysis (this was typically 600 to 1000). The algorithms included in the support programs will provide projections of the estimates for the timing requirements based on the curve fit to the measured data for the class of cases in question, however, as one exceeds that maximum measured data by a larger and larger margin, the accuracy of the prediction can be expected to drop off.

5. Summary/Conclusions

The importance of creating this suite of tools for estimation of the resource requirements for GEMACS lies in the difficulty in determining before a run exactly how much disk storage and time will be required to complete the problem. This information is very important to the GEMACS user because without such estimates a problem may be committed to a particular computer that is either incapable of supporting the complete solution (i.e. too small a hard disk, etc.) or that is too slow for reasonable turnaround of results. The former problem has significant consequences since the user may start a problem with GEMACS that can run for many days before it exceeds the disk storage available on the computer and crashes. This is not uncommon for large problems.

A major effort was undertaken to develop a resource requirement analysis capability for the GEMACS program. Such a tool set becomes more and more important as the size of problem being worked with GEMACS increases. A set of sample problems was developed and exercised on a number of different computers to develop scaling relations for the relative performance of the computers. Unexpectedly complex behavior in the execution time for sample problems on different computers added greatly to the difficulty of developing a consistent and accurate set of predictive tools. The basic scaling relations for the number of files required to run a problem and the disk storage requirements was completed and validated for a variety of problem examples. The results from this study have been incorporated into a FORTRAN program called GEMSIZ. Timing scaling relations were also characterized and built into this program. In addition, a FORTRAN program was developed at PL (GEMSRC) that is able to take the users input file for GEMACS and use it directly to make all determinations concerning the resource requirements for a run.

Additional work may be required to improve the accuracy of the predictions for timing associated with large numbers of unknowns as well as the development of better scaling functions for computers other than the baseline 486/50, SUN Sparc/10 and Motorola/RISC. The source code for GEMSIZ and GEMSRC are distributed with the documentation to make this process relatively straightforward for the users.

Table 1. Typical benchmark models and results

Name	DESCRIPTION	kW-calc.	kW-actual	sec-calc.	sec-actual
DIPOLE	Simple 1 -gment dipole with 1 far-field request of 90 points	83	83	3.2	4.2
THIELE	Thiele monopole (6 segs) over a ground (1 GTD plate) with 1 far-field request of 36 points	83	83	15.4	14.4
SPHERE	Patch model of a sphere (224 patches) with 1 far-field request of 361 points	1484	1484	21.6	28.0
CAVITY	FDFD cavity model with 100 cells and 1 near-field request of 21 points	102	103	52.1	58.9
SPIRAL	MOM Archimedean spiral antenna model (302 wires) with 1 far-field request of 73 points	626	626	66.6	62.3
WAVGTD	Hybrid waveguide model (MOM-6 aperture elements, GTD-6 plates, FDFD-70 cells) with 2 far-field requests totaling 363 points	164	164	1784.	1687.
NATO-16	NATO cyl. benchmark (1056 patches) with 1 near-field request of 50 points and using 16-fold rotational symmetry	3604	3604	462.	410.
NATO-8	NATO cyl. benchmark (1056 patches) with 1 near-field request of 50 points and using 8-fold rotational symmetry	3604	3604	793.	820.
NATO-4	NATO cyl. benchmark (1056 patches) with 1 near-field request of 50 points and using 4-fold rotational symmetry	3604	3604	1606.	1684.

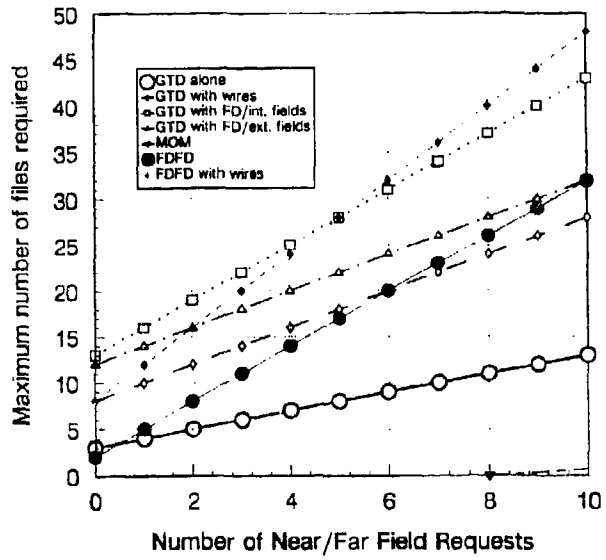

Figure 1. Maximum number of files required as a function of field requests

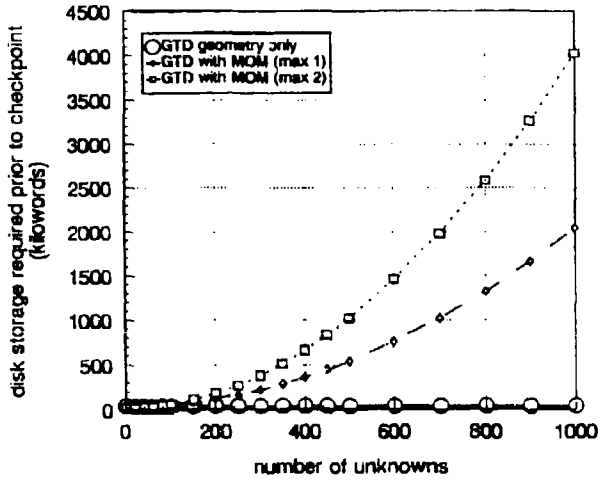

Figure 2. Maximum disk requirement prior to checkpoint for MOM/GTD cases.

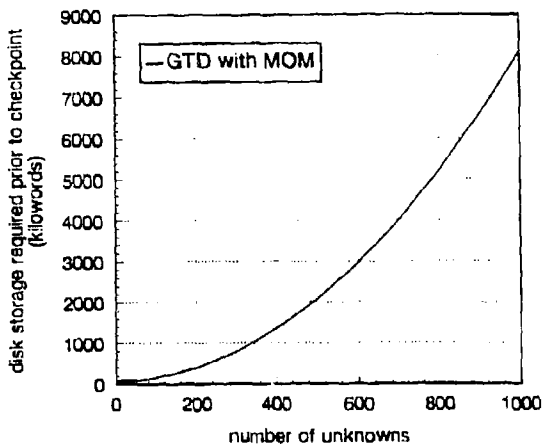

Figure 3. Maximum disk requirement at checkpoint for MOM/GTD cases.

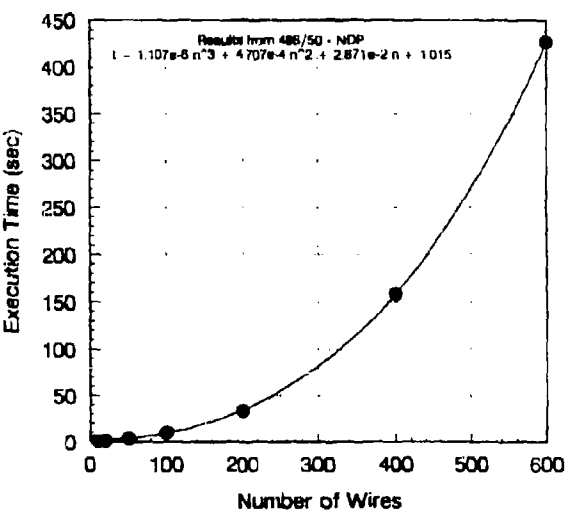

Figure 4. Execution time as a function of number of wires.

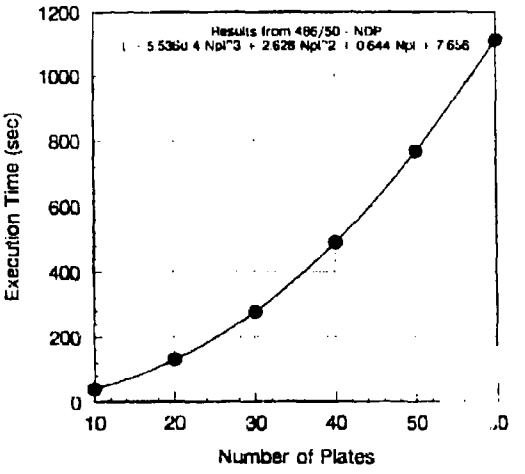

Figure 5. Execution time as a function of number of GTD plates.

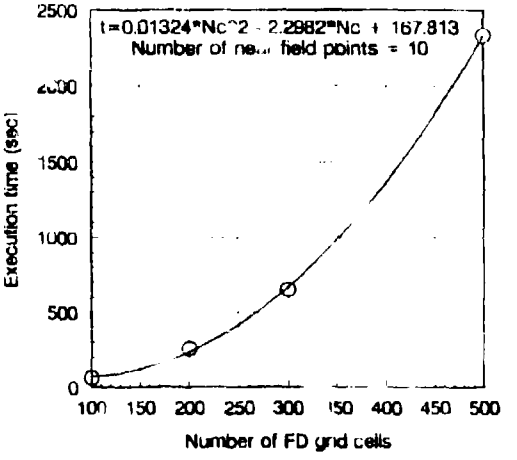

Figure 6. Execution time as a function of number of FDFD cells.

Modeling Cavity Problems with GEMACS 5.3

Edgar L. Coffey, III
Advanced Electromagnetics
4516 Stockbridge Avenue NW
Albuquerque, New Mexico 87120

The large number of modeling options with GEMACS (General Electromagnetic Model for the Analysis of Complex Systems) [1] may appear at times overwhelming to the new GEMACS user. For example, there are three (at least) methods for modeling cavity problems: finite differences (FD), method of moments (MOM) MFIE patches, and method of moments EFIE patches. A combined field integral equation (CFIE) approach is also possible, as well as an approximate ray tracing method using some of the features of the GTD/UTD module.

Within GEMACS FD methods are the only way to include cavity dielectrics or conducting cavity walls. FD is a volumetric model and is thus very computer intensive. It should be used only for small problems or problems requiring dielectrics.

The MOM approaches (MFIE, EFIE, or CFIE) are to be used with great care as interior and/or exterior resonances may completely swamp out the true solution. When they work, however, they work well. MOM allows high resolution modeling of geometrical detail and tends to be faster than FD for most problems.

The GTD/UTD approach relies on ray tracing and thus is applicable only to very large cavities. GTD is not normally useful in concave or cavity regions. GEMACS, however, has the ability to trace rays with up to ten bounces each. Convergence is obtained by relying on 1/R attenuation and the much longer path lengths (R) of multiple bounce rays.

The purpose of this paper is to explore the advantages and disadvantages of these different approaches in modeling a simple rectangular cavity. The applicability of each method to special cases (e.g., dielectric interior, imperfectly conducting walls, etc.) will be shown. Results will be compared with each other and with analytical data.

Perhaps more importantly the presentation will give the GEMACS user guidance in selecting commands and geometries for his or her particular cavity application.

F-16 Structure Modeling Using GEMACS 5.3

R. Fisher
Science and Engineering Associates, Inc.
6100 Uptown Blvd, NE, Suite 700
Albuquerque, New Mexico 87110

Edgar L. Coffey, III
Advanced Electromagnetics
4516 Stockbridge Avenue NW
Albuquerque, New Mexico 87120

An extensive, detailed model of the F-16 aircraft was developed by SEA and AE for use in computing surface currents and near-zone scattered fields from plane wave sources. The purpose of this paper and accompanying presentation is to describe the details of the modeling process, compromises made, and lessons learned. Comparisons will be made to near-zone laboratory data.

GEMACS 5.3 was used to predict surface currents and near-zone fields scattered from an F-16 aircraft. An MFIE surface patch model was made of the aircraft surface, as shown in figure 1. The size of the model that is required to adequately resolve the F-16 using MOM is quite large. (2,640 surface patch elements, or 5,280 matrix unknowns). Consequently, computer resources in storage space as well as execution time can be concomitantly large.

The first simulations were performed on a state-of-the-art, four-processor RISC work station. These did not take into account symmetry nor was banded matrix iteration (BMI) used. After 15 days, the run failed because all hard disk space had been taken by the MOM matrix, its LU factorization, observable data sets, etc. It was this lesson learned that led to the development of the GEMACS Resource Monitor reported on elsewhere in these proceedings, "Results of a GEMACS Resource Calculation Study."

Later runs (without symmetry) were performed on a Cray computer at USAF Phillips Laboratory. Subsequently, symmetry was used and array sizes increased sufficiently that the work station run completed (in about eight hours). The results of the work station were identical (five digits) to those from the Cray.

The primary observables computed were current densities over the F-16 surface. These are shown in gray-scale rendering in figure 2. Near-zone fields were computed from the currents using the GEMACS EFIELD() command and a grid spacing of 0.5 m. Figure 3 shows the results. The aircraft

This work was sponsored by the U. S. Air Force Phillips Laboratory under contract F29601-92-C-0109, subtask 05-01.

model has been overlaid on top of the field results to orient the viewer as well as to mask out interior fields erroneously computed by MOM. Since there are no field values associated with the model being superimposed, the area occupied by the model appears as black.

The zone at the rear of the aircraft in and behind the tail is anomalous. It is not known at this time the exact reason for the predicted high field levels in this region. It is believed that some approximations that were made in developing a functional model for the F-16, which violate to some degree standard modeling guidelines, may have generated or at least contributed to this anomaly.

Figure 4 shows a black and white rendition of IR results for the same configuration. A plastic model was coated with silver paint and embedded in conducting paper. This setup was illuminated by a plane wave excitation, which heated the conducting areas in some relationship to the field strength. An IR photograph was taken of the setup.

It is significant that with even a MOM model that violates a number of standard guidelines, the agreement qualitatively is rather good. The peaks and nulls along the fuselage and wing leading edge match node for node. The interference pattern generated between incident and scattered fields agrees fairly well, too. (It is difficult to make too strong a statement because of not having a reference for the IR work and the differences in color coding between IR and GEMACS displays.)

In summary, an F-16 model was generated that clearly reproduces the gross features of the IR measurements taken by Phillips Laboratory. This model, if all modeling guidelines had been followed, would have required 10,000+ patches to produce. Compromises were made in the model's geometrical and electromagnetic integrity to reduce the number of patches to 2,640. However, even this crude a model produced useful results. The 10,000+ patch model would have produced no results because we would not have been able to run it!

References:

1. E. L. Coffey, D. L. Kadlec, and N. W. Coffey, "General Electromagnetic Model for the Analysis of Complex Systems (GEMACS), Version 5, User, Engineering, and Code Documentation Manuals, Rome Laboratory, Technical Report RADC-TR-90-360, June 1990.

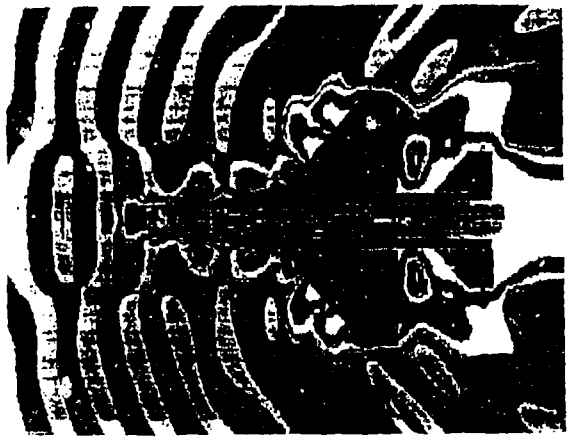

Figure 3. F-16 Local Electric Field Distribution Predicted by GEMACS.

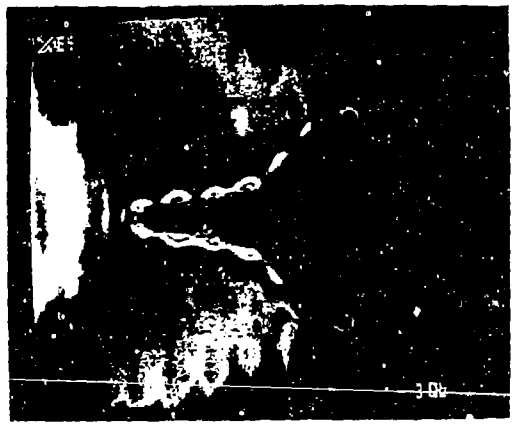

Figure 4. Black and White Rendition of Field Distribution for fR Model.

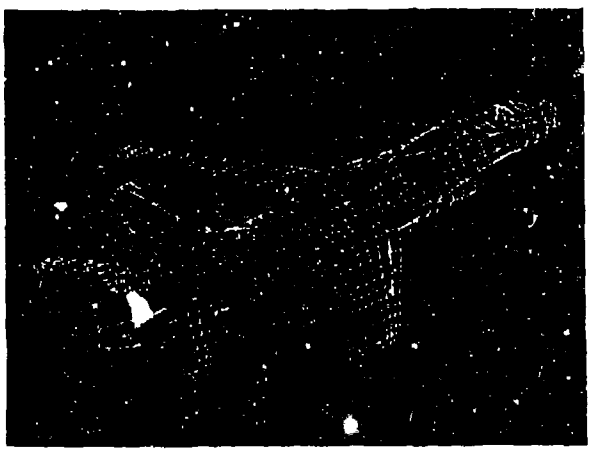

Figure 1. GEMACS MFIE Patch Model for the F-16.

Figure 2. F-16 Current Distribution Predicted by GEMACS.

THE MICROWAVE AND MILLIMETER-WAVE ADVANCED COMPUTATIONAL ENVIRONMENT PROGRAM

- A Computer Based Design Environment for High Frequency Electronics -

ROBERT H. JACKSON

VACUUM ELECTRONICS, CODE 6840
NAVAL RESEARCH LABORATORY
WASHINGTON, D.C. 20375-5347
Phone: (202) 767-6656
FAX: (202) 767-1280

Microwave and millimeter-wave power tubes are essential components of today's advanced military systems. Power tube design is a complex process which must simultaneously account for mechanical, magnetic, electrostatic, electron optic, electromagnetic, thermal, and other factors in order to meet performance requirements for existing and next generation systems. Existing design methods are time and labor intensive usually requiring the costly construction and testing of several prototypes by highly skilled and expensive technical labor. The creation of an advanced computer-based design capability for power tubes will significantly reduce the risk, cost, and development time associated with state-of-the-art tube development while improving performance and reliability.

The Microwave & Millimeter-wave Advanced Computational Environment (MMACE) Program is directed at the development of just such a comprehensive computational design environment for microwave power tubes. The MMACE program is a tri-Service effort with ARPA, NIST, NSF, and NASA participation which will operate over a three year period to define, develop, and validate this advanced design system. Many of the problems being addressed by the MMACE program are shared in varying degrees by a broad spectrum of technical disciplines and MMACE is addressing these common problems in a generic fashion.

This presentation will discuss both the unique and generic aspects of power tube design which have dictated the present programmatic and technical structure. The focus will be on tube design computational requirements, the key technical objectives which must be achieved to impact the design process, and the specific technical and programmatic approach adopted by MMACE. Mechanisms for cooperation and joint development on common design problems with other programs and technical communities have been given a high priority and initial cooperative efforts will be highlighted. A prototype design environment was developed in Phase I of the MMACE program and was released for testing in the US tube industry in the Fall of 1993. The structure and capabilities of the prototype will be discussed and demonstrated and the present status of the follow-on Phase II design system framework and tool development will be presented.

FURTHER CONSIDERATIONS REGARDING THE ELECTROMAGNETIC MODELING AND SIMULATION ENVIRONMENT FOR SYSTEMS (EMSES)

Kenneth R. Siarkiewicz
Rome Laboratory/ERPT
525 Brooks Road
Griffiss AFB NY 13441-4505
siarkiewiczk@lonex.rl.af.mil

ABSTRACT

This paper refines the concepts presented at the 9th Annual Applied Computational Electromagnetics Society Symposium [1]. At that symposium several papers were presented which outlined in broad terms the need for a more intelligent and efficient approach to computational electromagnetics (CEM) modeling, simulation, and code development.

This paper presents the results of further investigations and dialog in this critical arena. It focuses on the work being performed at Rome Laboratory to refine the concepts and specify the characteristics of several elements which are significant at this stage of the overall design of the EMSES. It should be noted that the refinements made are the result of collaboration and numerous conversations with individuals in DOD, DOE, industry, and academia. However, the conclusions presented are those of the author and do not necessarily reflect the positions of those who have contributed their time and talent.

In particular, this paper endorses the use of the Microwave and Millimeter-Wave Advanced Computational Environment (MMACE) for the overall framework within which the EMSES resides and operates. MMACE is a Tri-Service Program. The Naval Research Laboratory is the technical lead for its development. Although it is directed to the high power vacuum electronics community, the shell and its basic elements incorporate many of the tools and considerations which are necessary to the EMSES. The prototype has been demonstrated and it is now entering phase II. The electromagnetics community has a fortuitous opportunity to impact the overall design of MMACE to accommodate CEM codes.

This paper presents one view of how EMSES and MMACE can be synergistically designed to exploit the advantages of each for the benefit of both, while at the same time providing a system with an architecture sufficiently open to the incorporation of the modeling and simulation tools of other engineering and manufacturing disciplines (e.g., computational fluid dynamics, thermal transfer, computer-aided design).

INTRODUCTION

At the Ninth Annual Review of Progress in Applied Computational Electromagnetics several papers were presented [1-3] which focussed on issues which need to be considered in future development of computational electromagnetics (CEM) technology and computer-aided tools. The paper by Siarkiewicz [1] treated several generic issues related to the development of an integrated computational environment in which an electromagnetic engineer or systems integrator designs a system or analyzes the performance

of a proposed system design. *System* is defined as an electromagnetic radiating or scattering platform (e.g., airplane, tank, ship, spacecraft) on which are mounted deliberate (i.e., antennas) or accidental (e.g., doors, access panels, power cables) radiators or receptors of electromagnetic energy.

The referenced paper presents a very preliminary overview of the three major divisions of a next-generation electromagnetic modeling and simulation environment for systems (EMSES). These are the input processing function, which accesses the appropriate system and component databases and develops the electromagnetic model for the system under analysis. The second component is the computational engine, a computer-aided CEM tool to perform the required analysis on the electromagnetic model and compute the necessary output data to derive the requested system performance data. The third element is the output processing function which performs the tasks of data reduction and presentation, and database generation and modification.

This paper is a follow-on to the paper presented last year. It represents the results of further reflection on this complex area. The author gratefully acknowledges stimulating discussions with several other engineers and scientists who have given the concept of a next generation CEM environment much serious thought. These include, among others, Dr. Ed Miller, formerly of Los Alamos National Laboratory, Dr. Lou Medgyesi-Mitschang, McDonnell-Douglas, Dr. Bob McGahan, Rome Laboratory, Maj. Dennis Andersh, Wright Laboratory, and Capt. Tom Timmerman, Phillips Laboratory. However, the thoughts and reflections presented in this paper are solely those of the author and do not necessarily represent either implicitly or explicitly the ideas and opinions of these or other engineers working in the area of CEM.

THE CONCEPT

Figure 1 is a pictorial representation of the fundamental elements which comprise the initial development of EMSES. The rectangular boxes represent elements which are common to all versions of the framework. Each version is differentiated from others by the insertion of a computational engine which is specific to the application and type of analysis. For example, for the analysis of the integration of an antenna on a platform in order to characterize and minimize the pattern distortion one would use the GEMACS (General Electromagnetic Model for the Analysis of Complex Systems) computer program. For automatic target recognition applications one would use the XPATCH code being developed for the Air Force Materiel Command Wright Laboratory. Of course the necessary translators to prepare the data input for the code and the data output from the code would also be included in the oval area shown in figure 1.

The cylinders shown in figure 1 represent the database associated with the article under analysis (AUA). This includes a description of the physical geometry and the material properties of all defining surfaces. The database would also contain any measured and computed data that may be generated to define the operational performance of the AUA. This latter data may or may not be employed in a particular follow-on analysis. However, the results of any analysis would be added to augment the performance database for the system.

The database interface and visualization tools would access the database and generate a computer model of the geometry. Thus, this rectangle includes an appropriate database program and query system, as well as a graphics-based engine to display the geometry for viewing and editing as appropriate. Initially this is envisioned as a computer-aided design (CAD) package, for example, AutoCAD or the ACAD program being supported by the Electromagnetic Code Consortium (EMCC). The operations of the tools in this rectangle provide the analyst with a pictorial image from which an electromagnetic model appropriate for the computational engine will be generated.

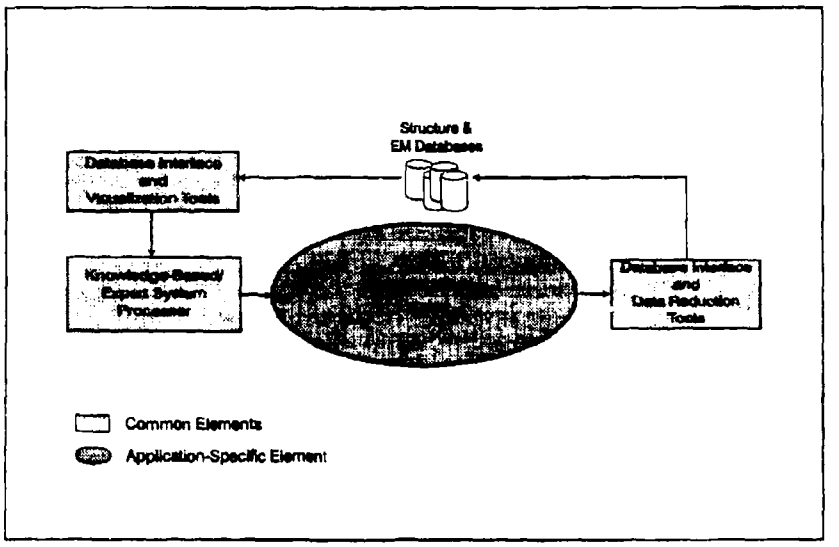

Figure 1. EMSES Conceptual Diagram

The concept includes a knowledge-based/expert system (KB/ES) processor which aids the analyst in the development of the electromagnetic model. While much of this element of the concept may be independent of the computational engine, there may be portions which are application-specific. An optional design possibility is to attach a translator to the computational engine which converts the output of a standard expert system into the syntax of the input language of the engine. In this way an identical KB/ES processor can be employed for any computational engine, thereby simplifying the long-term maintenance and enhancement of the processor.

As noted previously, the computational engine can be any CEM program which provides the data required by the analyst. Several possibilities and considerations were presented in last year's paper [1]. However, a rather radical and innovative alternative is presented later in this paper.

The output of the computational engine is the input to the element labeled "database interface and data reduction tools" in figure 1. This element performs two manipulative functions on the engine's output data. A full complement of graphing and charting functions would be available, such as polar and rectangular graphs, Smith chart templates, writing to file for transfer to plotters and laser printers, and other such utilities.

The second major function of this element is that of writing the data to a mass storage medium for future reference and use by other analysts. Thus, the output of any analysis augments the electromagnetic database for the AUA. A full complement of subfunctions would be available for database maintenance, such as renaming files, deleting obsolete files (e.g., those which are based on an earlier version of the

geometry), and combining files. Such file maintenance utilities are of benefit as the AUA undergoes the iterative design and analysis process. Working files would be transferred to various workstations as necessary, while the configuration control file would remain safely archived, at least until it is superseded through a well-established documentation update process.

AN INNOVATIVE CONCEPT FOR THE COMPUTATIONAL ENGINE

In the design thus far proposed it is assumed that the computational engine is a stand-alone CEM code, such as GEMACS or the Numerical Electromagnetic Code (NEC). A number of advantages accrue if the engine is dynamically composed to suit the geometry and analysis at hand. That is, instead of incorporating a number of large codes within the framework and having the analyst specify which one is to be inserted for a particular execution series, the environment would incorporate the electromagnetic analysis capability as a library of subroutines or modules, each of which would describe a single process of electromagnetic interaction. Thus, there would be separate modules to characterize diffraction from an edge of a surface, reflection from a surface, creeping waves around a cylinder, etc. Furthermore, if object-oriented programming were employed, then the edge-of-a-surface module would be generic in the sense that the edge would be the edge of a flat plate or the interface of two dissimilar materials (e.g., aluminum and fiberglass).

As a demonstration of this concept, assume that GEMACS is a computer code that has been inserted into the environment. Originally it would act as a stand-alone code for the computational engine, providing information about the degradation of the far-field beam pattern caused by the presence of the aircraft on which the antenna is mounted. This is depicted as phase 1 in figure 2.

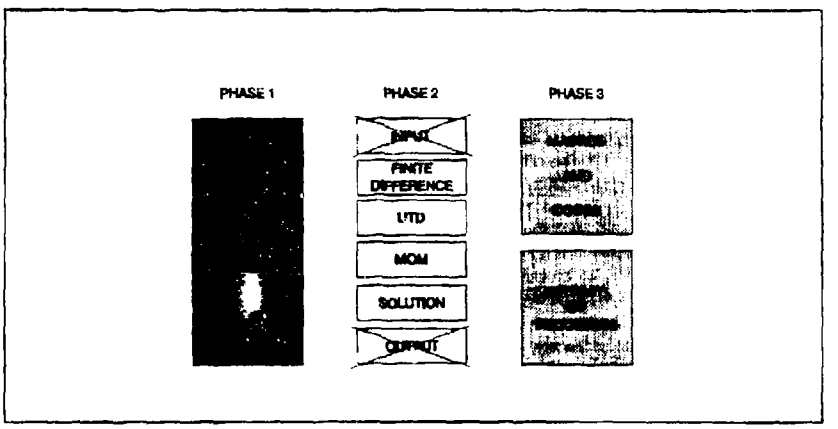

Figure 2. Development of an Electromagnetic Library

In a second phase of the integration process, GEMACS is broken up into its six individual modules,

as shown in the middle column of figure 2. The file handling capabilities of the environment are used to transfer data among the modules, rather than the built-in functions within GEMACS itself. As a further step in the process, the input and output modules of GEMACS are eliminated. The database interface tools, visualization tools, and data reduction tools of the environment provide the user interface with the remaining four modules of the GEMACS code.

In the third and final phase of the integration process, the individual electromagnetic phenomena processes within GEMACS are identified, separated from the various modules, and stored into an electromagnetic analysis library. Here would reside routines to calculate diffraction from the edge of a plate, diffraction from the rim of a cylinder, reflection from the surface of the plate bounded by edges, and many other similar functions. It is interesting to note that the first two phenomena identified above, diffraction from the edge of a plate and diffraction from the rim of a cylinder, may be identical except for the inclusion of a factor to represent radius of curvature. A single routine could replace two existing routines. The resulting routine could possibly be further generalized by including material properties for either side of the edge, and thus the function could be used to calculate the diffraction from an interface between dissimilar materials.

The process of integration (or disintegration into processes and libraries of functions) would be applied to many other codes. The library would eventually include formulations for finite element and finite difference calculations for volumes, a host of routines for various emerging asymptotic techniques such as shooting and bouncing rays, and routines for method of moments computations involving differing basis and testing functions each of which is appropriate for varying geometries and observables of interest.

In addition to storing the individual functions or processes, the library would also include entire codes if they are regularly needed to characterize a particular class of problems, as well as a set of macros which would be invoked to bring together the various individual processes to form an analysis tool to be applied to a particular problem at hand. In this way only the minimum amount of computer resources necessary to accomplish a particular analysis would be demanded by the dynamically generated CEM tool.

To be sure, such a scheme places an additional burden on the analyst. Not only must the electromagnetic model of the system be developed, but quite often a code for the analysis may need to be developed. However, if designed and implemented properly the KB/ES can be used to not only develop a prototype electromagnetic model but also to "develop" the computational engine "on the fly" through a dialogic process with the analyst. When implemented, such a scheme would give new meaning to the term *user friendly*.

Although challenging in its design and development, this radically innovative concept has many advantages. As has already been mentioned, the dynamically generated computational engine would be optimum in the sense of demanding a minimum amount of computer memory and storage resources. It may also have the benefit of decreased execution time since many unnecessary checks and computations would not need to be performed, as they are frequently executed in the current state-of-the-art general-purpose codes.

In addition, the maintenance and enhancement of CEM tools would be greatly facilitated. Working with the routines for individual processes is much easier than modifying a large code such as GEMACS or NEC. The modularity of the processes reduces the risk of coding error and greatly reduces the time required for the validation of the code segment. Furthermore, the change to the algorithm or the CEM capability needs to be accomplished in only one central location instead of in each individual stand-alone code.

Other advantages include the ability to more easily experiment with slightly different implementations of a formulation. How the algorithm is developed can affect the accuracy of the results

or the amount of time required for its execution. Thus, trade-off studies among competing code designs can be more easily accomplished, and sensitive elements of the theory and algorithm can be identified and quantified. Also, advances in the state-of-knowledge in electromagnetics, computer hardware and software technology, computational mathematics, and other CEM-related disciplines can more easily and quickly be incorporated into the environment and transitioned for use by the community.

The task is indeed monumental, but the rewards for accomplishing the development of an electromagnetic library of routines are even greater when viewed from the perspective of short-term gains in the ability to characterize a system and the long-term gains in ease of maintenance and enhancement.

ONE POSSIBLE APPROACH

There are many considerations which must be addressed in the development of the EMSES, whether or not the innovative concept for the computational engine is included in the design of the environment. Some of these focus on the component factors of input processing, the computational engine, and output processing; and some are directed toward the many system-level factors involved. Some of the many considerations are shown in figure 3.

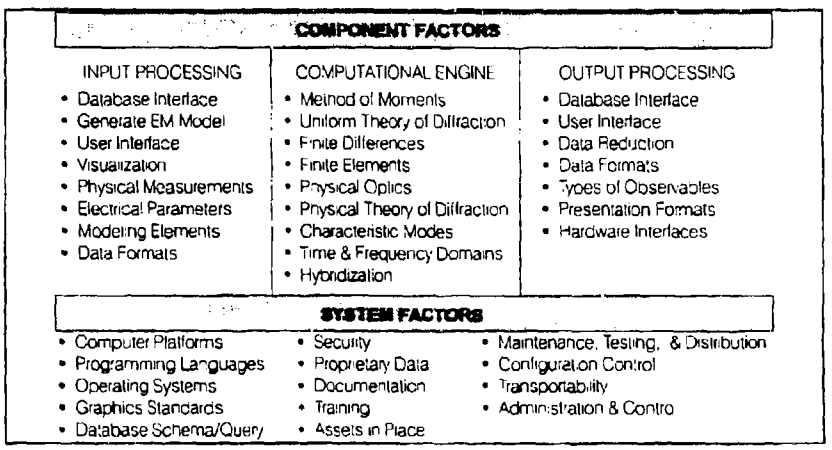

Figure 3. Some Design Considerations for EMSES

This is an intimidating list. However, much of the groundwork has been laid by the Microwave and Millimeter-Wave Advanced Computational Environment (MMACE) being developed under the sponsorship of the Naval Research Laboratory (NRL) [4]. This framework is conceptually depicted in figure 4.

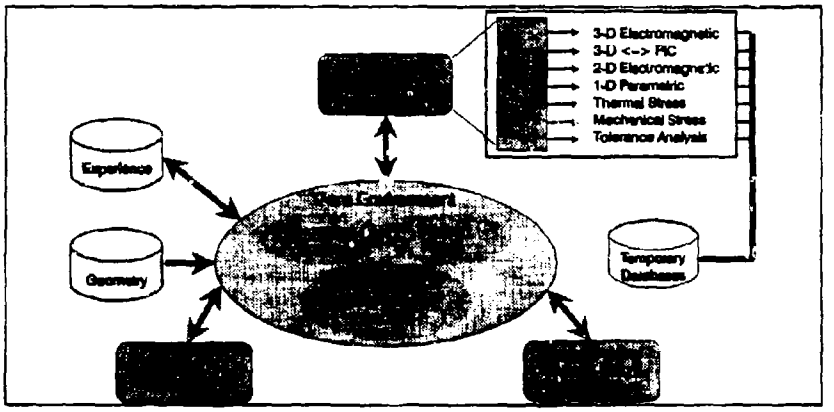

Figure 4. Microwave and Millimeter-Wave Advanced Computational Environment (MMACE)

An overview of the MMACE framework is described in the referenced paper. It is significant that this program has resulted in a prototype which demonstrates that it is possible to design and develop a computational shell which can support several diverse analysis disciplines and provide a somewhat seamless interface among them.

It is beyond the scope of this paper to provide any detail regarding the MMACE framework. The interested CEM scientist is encouraged to read the referenced paper and contact NRL for more details.

There are several comments which should be explicitly stated. First, the CEM community can replace the existing design and analysis tools (shown in the clear box in figure 4) with one or more of the tools for electromagnetic analysis. This would be either stand-alone codes or the suggested library of macros and functions shown in figure 2. It is true that initially the tools would need to be wrappered in specially developed pre- and post-processors. However, as new tools are developed their input and output elements would be tailored during the design process to meet the standards being established by the MMACE developers. The integration of CEM tools and capabilities would be an orderly and logically incremental progression.

Furthermore, and quite important, is the fact that the MMACE framework is currently being defined, designed, and developed. Standards are in the process of being refined and extended. They are currently prototypes developed specifically to match the needs of the vacuum electronics design community. They are open-ended and unconstrained. CEM community requirements have an opportunity to impact the direction and content of the standards.

The MMACE framework is totally government-owned, and the "buy-in" cost has been kept to a minimum. The analysis tools may eventually include company-proprietary products, but the advantage of the system is that this can be easily accommodated. The significance is that an analyst can use a tool with which he or she is familiar and has on hand. If any factor regarding EMSES is significant, this one is surely at the top of the list.

CONCLUSION

There can really be no conclusion at this point. There must be further thought and discussion given to this topic. New codes and specialized codes continue to be sponsored and developed. Existing codes, such as GEMACS, continue to be enhanced. In both instances a costly and time-consuming process is being carried out.

It is time for the CEM community to review how it does business. The Applied Computational Electromagnetics Society (ACES) is an excellent and logical forum in which this review can be pursued. This author is leaning heavily towards the use of the MMACE framework as a starting point, since there is no gain in doing again what has already been done. If there are other ideas and approaches, then it is an obligation of those who have them to bring them forward.

REFERENCES

1. Siarkiewicz, K. "The Electromagnetic Modeling and Simulation Environment for Systems (EMSES)." *9th Annual Review of Progress in Applied Computational Electromagnetics Conference Proceedings*, March 1993, pages 114-121.

2. Miller, E. K., R. P. Kruger, and S. Moraites, "A Proposed Approach for Developing Next-Generation Computational Electromagnetics Software." *9th Annual Review of Progress in Applied Computational Electromagnetics Conference Proceedings*, March 1993, pages 122-138.

3. Medgyesi-Mitschang, L. N., J. M. Putnam, and D. Wang, "Hybrid Approach for Large 3-D Platforms." *9th Annual Review of Progress in Applied Computational Electromagnetics Conference Proceedings*, March 1993, presentation only.

4. Jackson, R. "The Microwave and Millimeter-Wave Advanced Computational Environment Program——A Computer Based Design Environment for High Frequency Electronics." *10th Annual Review of Progress in Applied Computational Electromagnetics Conference Proceedings*, March 1994.

SESSION 14:

MOMENT METHODS

Chair: Paul Goggins

RESULTS USING IML WITH A NEW CFIE

Francis X. Canning
Rockwell Science Center
1049 Camino Dos Rios
Thousand Oaks, CA 91360

The impedance matrix localization method (IML) uses a somewhat unusual choice of basis and testing functions in the method of moments (MoM). These basis functions radiate very narrow beams resulting in a sparse matrix with distinct and highly localized peaks. A synergistic combination of IML and the combined field integral equation is presented here. This combination makes the impedance matrix banded. That is, all matrix elements greater than some distance from the diagonal (this distance will be called the bandwidth) are approximately equal to zero. Furthermore, within this bandwidth the great majority of the matrix elements are also equal to zero.

This formulation has been discussed previously (Radio Science, December 1993). In this paper, some of its computational consequences will be explored. For example, for a convex body the excitation is non zero only on the lit side of the body. This is notably similar to high frequency approximations such as the geometrical theory of diffraction (GTD). The banded nature of the impedance matrix also may be thought of as being similar to GTD. The excitation on the lit side propagates in a local manner to the shadow side. The word local is interpreted as meaning local within a region of size coresponding to the bandwidth of the matrix. Because of this locality the factorization of the impedance matrix is also a local operation. Examples are given illustrating the resulting computational efficiency.

In the past, the primary advantage to the combined field integral equation (CFIE) over the electric field integral equation (EFIE) and the magnetic field integral equation (MFIE) has been regarding the interior resonance problem. That is, for closed perfecting conducting bodies there are discrete frequencies at which resonant interior modes occur.

The MFIE and EFIE may have zero eigenvalues at such frequencies leading to stability problems near such frequencies. The CFIE has been proven to have no zero eigenvalues. However, in general there are no bounds about how far from zero the eigenvalue must be. Many papers have been written on choosing the combination parameter to improve the seperation of the eigenvalue from zero. Intuitively, the C works by decreasing the interaction of the incident field h the interior of the body. This decrease is very small; generally the interaction strength is not even halved. The new CFIE used here decreases the interaction by several orders of magnitude. Numerical results are presented showing how the condition number of the resulting matrix has been improved due to the much weaker interaction.

A NEW METHOD FOR EVALUATING THE GENERALIZED EXPONENTIAL INTEGRALS ASSOCIATED WITH THIN STRAIGHT-WIRE ANTENNAS

P. L. Werner*
The Pennsylvania State University
College of Engineering
DuBois, PA 15801

D. H. Werner
The Pennsylvania State University
Applied Research Laboratory
P.O. Box 30
State College, PA 16804

I. Introduction

The generalized exponential integral is one of the most fundamental integrals in antenna theory and for many years exact solutions to this integral have been sought. This paper considers an exact solution to this integral which is completely general and independent of the usual restrictions involving the wavelength, field point distance, and dipole (segment) length. The generalized exponential integral has traditionally been evaluated numerically or by making certain convenient but restrictive assumptions. The exact series representation presented in this paper converges rapidly in the induction and near-field regions of the antenna and therefore provides an alternative to numerical integration. It is demonstrated that, for very thin straight-wire antennas, an asymptotic expansion can be used to obtain a numerically convenient form of the generalized exponential integral. One of the major advantages of this expansion is that it eliminates the need to directly evaluate Bessel functions of the first kind in the computation of the series representation for generalized exponential integrals.

II. Theory

In this section an exact solution to the generalized exponential integral associated with a uniform current thin-wire vector potential will be introduced which is useful for computational purposes. Suppose we have a cylindrical antenna which has a length of $2h$ and a diameter of $2a$. The geometry for such an antenna is illustrated in Fig. 1 of [1]. The vector potential corresponding to this antenna may be expressed in the form [1,2]

$$A_z(\rho,z) = \frac{\mu}{4\pi}\int_{-h}^{h} I(z')\,K(z-z')\,dz' \tag{1}$$

where

$$K(z-z') = \frac{1}{2\pi}\int_0^{2\pi} \frac{e^{-jkR'}}{R'}\, d(\phi-\phi') \tag{2}$$

represents the cylindrical wire kernel, and

$$R' = \sqrt{(z-z')^2 + \rho^2 + a^2 - 2\rho a\cos(\phi-\phi')} \tag{3}$$

$$k = \beta - j\alpha \tag{4}$$

$$j = \sqrt{-1} \tag{5}$$

The cylindrical coordinates of the source point and the field point are (a,ϕ',z') and (ρ,ϕ,z), respectively.

An exact expression for the cylindrical wire kernel (2) has recently been found [1,3]. For thin-wire antennas, however, the kernel in (2) may be approximated by [2]

$$K(z-z') = \frac{e^{-jkR}}{R} \quad \text{for } \rho \geq a \tag{6}$$

where

$$R = \sqrt{(z-z')^2 + \rho^2} \tag{7}$$

If a uniform current distribution of $I(z') = I_0$ is assumed in conjunction with the thin-wire approximation of the kernel, then the vector potential (1) becomes

$$A_z(\rho,z) = \frac{\mu I_0}{4\pi} E_0^0(\rho,z,h)\ ,\ \rho \geq a \tag{8}$$

where

$$E_0^0(\rho,z,h) = \int_{-h}^{h} \frac{e^{-jkR}}{R}\, dz' \tag{9}$$

is a generalized exponential integral [4,5,6].

By applying the techniques developed in [1] and [7], an exact solution to (9) may be found. This exact solution is represented in compact form by

$$E_0^0(\rho,z,h) = J_0(k\rho)\left[a_0(\rho,z,h)\Pi(z) \pm b_0(\rho,z,h)\right] + \sum_{r=1}^{\infty} \frac{(-j)^r}{r} J_r(k\rho)\left[a_r(\rho,z,h)\Pi(z) \pm b_r(\rho,z,h)\right] \quad (10)$$

where the minus sign is used when $z \geq 0$ and the plus sign is used when $z \leq 0$. The quantities found in (10) are given by

$$\Pi(z) = \begin{cases} 0, & z \leq -h \\ 1, & -h < z < h \\ 0, & z \geq h \end{cases} \quad (11)$$

$$a_0(\rho,z,h) = 2\, ln(\sigma) \quad (12)$$

$$a_r(\rho,z,h) = 2\left[\sigma^r - \sigma^{-r}\right] \quad (13)$$

$$b_0(\rho,z,h) = ln\left(\gamma_-/\gamma_+\right) \quad (14)$$

$$b_r(\rho,z,h) = \left[\gamma_-^r - \gamma_+^r - \gamma_-^{-r} + \gamma_+^{-r}\right] \quad (15)$$

$$\sigma = \frac{\sqrt{(h-|z|)^2 + \rho^2} + h - |z|}{\rho} \quad (16)$$

$$\gamma_\pm = \frac{\sqrt{(z \pm h)^2 + \rho^2} + |z \pm h|}{\rho} \quad (17)$$

If the propagation constant k is complex, then the Bessel functions which are present in (10) have complex arguments. This situation may arise when an antenna is immersed in a dissipative medium. If the antenna is in free space, however, the propagation constant is real and the Bessel functions in (10) are real valued.

Suppose that the propagation constant k is real, then the generalized exponential integral (9) may be separated into its real and imaginary parts. This leads to

$$E_0^0(\rho,z,h) = C_0^0(\rho,z,h) - j\, S_0^0(\rho,z,h) \quad (18)$$

where

$$C_0^3(\rho,z,h) = \int_{-h}^{h} \frac{\cos(kR)}{R}\, dz' \tag{19}$$

is a generalized cosine integral and

$$S_0^0(\rho,z,h) = \int_{-h}^{h} \frac{\sin(kR)}{R}\, dz' \tag{20}$$

is a generalized sine integral. Exact solutions to these integrals may be readily obtained by equating the real and imaginary parts of (18), namely (19) and (20), to the real and imaginary parts of (10). Following this procedure results in

$$C_0^0(\rho,z,h) = J_0(k\rho)\left[a_0(\rho,z,h)\Pi(z) \pm b_0(\rho,z,h)\right] + \\ + \sum_{r=1}^{\infty} \frac{(-1)^r}{2r} J_{2r}(k\rho)\left[a_{2r}(\rho,z,h)\Pi(z) \pm b_{2r}(\rho,z,h)\right] \tag{21}$$

and

$$S_0^0(\rho,z,h) = \sum_{r=1}^{\infty} \frac{(-1)^{r-1}}{(2r-1)} J_{2r-1}(k\rho)\left[a_{2r-1}(\rho,z,h)\Pi(z) \pm b_{2r-1}(\rho,z,h)\right] \tag{22}$$

where the plus and minus signs are used when $z \le 0$ and $z \ge 0$, respectively.

A useful asymptotic expansion of (9) results when the small argument approximation for Bessel functions

$$J_r(k\rho) \sim \frac{(k\rho/2)^r}{r!} \quad \text{as } k\rho \to 0 \tag{23}$$

is substituted into (10). This yields an expression which is accurate for small values of $k\rho$, given by [1]

$$E_0^0(\rho,z,h) \sim \left[a_0(\rho,z,h)\Pi(z) \pm b_0(\rho,z,h)\right] + \\ + \sum_{r=1}^{\infty} \frac{(-j)^r}{(r)(r!)}\left[c_r(k\rho,z,h)\Pi(z) \pm d_r(k\rho,z,h)\right] \quad \text{as } k\rho \to 0 \tag{24}$$

where

$$c_r(k\rho,z,h) = 2\left[\left(\frac{k\rho}{2}\sigma\right)^r - \left(\frac{k\rho}{2}\frac{1}{\sigma}\right)^r\right] \tag{25}$$

$$d_r(k\rho,z,h) = \left[\left(\frac{k\rho}{2}\gamma_-\right)^r - \left(\frac{k\rho}{2}\gamma_+\right)^r - \left(\frac{k\rho}{2}\frac{1}{\gamma_-}\right)^r + \left(\frac{k\rho}{2}\frac{1}{\gamma_+}\right)^r\right] \tag{26}$$

Note that when $h - |z| >> \rho$ (25) may be approximated by

$$c_r(k\rho,z,h) = 2\left(\frac{k\rho}{2}\ \sigma\right)^r \tag{27}$$

and when $|z| - h >> \rho$ (26) reduces to

$$d_r(k\rho,z,h) = \left(\frac{k\rho}{2}\ \gamma_-\right)^r - \left(\frac{k\rho}{2}\ \gamma_+\right)^r \tag{28}$$

For the important special case when $z=0$, (24) reduces to the convenient form given by

$$E_0^0(\rho,0,h) \sim a_0(\rho,0,h) + \sum_{r=1}^{\infty} \frac{(-j)^r}{(r)(r!)}\, c_r(k\rho,0,h) \quad \text{as} \quad k\rho \to 0 \tag{29}$$

where

$$a_0(\rho,0,h) = 2\ tn(\sigma_0) \tag{30}$$

$$c_r(k\rho,0,h) = 2\left[\left(\frac{k\rho}{2}\ \sigma_0\right)^r - \left(\frac{k\rho}{2}\ \frac{1}{\sigma_0}\right)^r\right] \tag{31}$$

$$\sigma_0 = \frac{\sqrt{h^2+\rho^2}+h}{\rho} \tag{32}$$

The series expansion of $E_0^0(\rho,z,h)$ given in (24) may be expressed in terms of exponential integrals. That is, for the case in which $|z| \geq h$

$$E_0^0(\rho,z,h) \sim \pm \left\{ ln\left(\frac{\gamma_+}{\gamma_-}\right) + E_1\left(j\frac{k\rho}{2}\gamma_+\right) - E_1\left(j\frac{k\rho}{2}\gamma_-\right) - E_1\left(j\frac{k\rho}{2}\frac{1}{\gamma_+}\right) + E_1\left(j\frac{k\rho}{2}\frac{1}{\gamma_-}\right)\right\} \quad \text{as} \quad k\rho \to 0 \tag{33}$$

and for $|z| \le h$, we have

$$E_0^0(\rho,z,h) \sim 2\left[ln\left(\frac{1}{\sigma}\right) + E_1\left(j\frac{k\rho}{2}\frac{1}{\sigma}\right) - E_1\left(j\frac{k\rho}{2}\sigma\right)\right] \pm \left\{ln\left(\frac{\gamma_+}{\gamma_-}\right) + E_1\left(j\frac{k\rho}{2}\gamma_+\right) - E_1\left(j\frac{k\rho}{2}\gamma_-\right) - E_1\left(j\frac{k\rho}{2}\frac{1}{\gamma_+}\right) + E_1\left(j\frac{k\rho}{2}\frac{1}{\gamma_-}\right)\right\} \quad \text{as} \quad k\rho \to 0 \tag{34}$$

For the special case when $z=0$, (34) reduces to

$$E_0^0(\rho,0,h) \sim 2\left[ln\left(\frac{1}{\sigma_0}\right) + E_1\left(j\frac{k\rho}{2}\frac{1}{\sigma_0}\right) - E_1\left(j\frac{k\rho}{2}\sigma_0\right)\right] \tag{35}$$

where

$$E_1(jx) = \int_x^\infty \frac{e^{-jt}}{t}\,dt = -Ci(x) + j\,Si(x) - j\frac{\pi}{2} \tag{36}$$

$$Si(x) = \int_0^x \frac{\sin t}{t}\,dt \tag{37}$$

$$Ci(x) = \gamma + ln\,x + \int_0^x \frac{\cos t - 1}{t}\,dt \tag{38}$$

and $\gamma=0.57721\ldots$ is Euler's constant.

III. Results

The convergence properties of (24) have been investigated in [1]. It was found that this series expansion is extremely accurate for values of $\rho \leq 1 \times 10^{-4}\lambda$. This suggests that (24) would be useful for modeling very thin straight-wire antennas, especially since many of the conventional methods for evaluating the generalized exponential integral suffer from loss of precision when the wire radius becomes too small. The number of terms in (24), including the zero-order term, required to achieve five place accuracy in the magnitude of the generalized exponential integral as a function of z/λ are indicated in Figure 1. The X's and the O's represent numbers which correspond to values of $h/\lambda = 2.5 \times 10^{-3}$ and 2.5×10^{-2}, respectively. The results contained in Figure 1 are valid for the range $0 < \rho/\lambda \leq 1 \times 10^{-4}$.

Acknowledgement

This work was supported by CDR Gus K. Lott of the Naval Security Group Command.

References

[1] D. H. Werner, "An exact formulation for the vector potential of a cylindrical antenna with uniformly distributed current and arbitrary radius," *IEEE Trans. Antennas Propagat.*, Vol. 41, No. 8, pp. 1009-1018, August 1993.

[2] R. W. P. King, "The linear antenna - Eighty years of progress," *Proc. IEEE*, Vol. 55, pp. 2-26, Jan. 1967.

[3] W. Wang, "The exact kernel for cylindrical antenna," *IEEE Trans. Antennas Propagat.*, Vol. AP-39, pp. 434-435, April 1991.

[4] R. W. P. King, *The Theory of Linear Antennas*. Cambridge, MA: Harvard University Press, 1956, pp. 94-97.

[5] R. W. P. King, "Electric fields and vector potentials of thin cylindrical antennas," *IEEE Trans. Antennas Propagat.*, Vol. AP-38, pp. 1456-1461, Sept. 1990.

[6] R. F. Harrington, "Matrix methods for field problems," *Proc. IEEE*, Vol. 55, pp. 136-149, Feb. 1967.

[7] P. L. Overfelt, "An exact method of integration for vector potentials of thin dipole antennas," *IEEE Trans. Antennas Propagat.*, Vol. AP-35, pp. 442-444, April 1987.

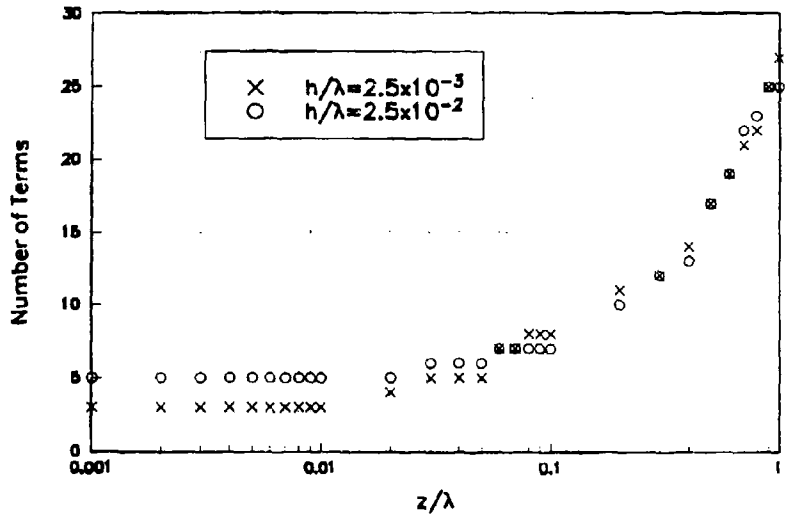

Figure 1. Minimum number of terms in (24), including the zero-order term, required to achieve five place accuracy in the magnitude as a function of z/λ.

TECHNIQUES FOR EVALUATING THE UNIFORM CURRENT VECTOR POTENTIAL AT THE ISOLATED SINGULARITY OF THE CYLINDRICAL WIRE KERNEL

D. H. Werner
Penn State University
Applied Research Laboratory
P.O. Box 30
State College, PA 16804

J. A. Huffman*
Penn State University
Department of Electrical Engineering
224 Electrical Engineering East
University Park, PA 16802

P. L. Werner
Penn State University
College of Engineering
DuBois, PA 15801

I. Introduction

The cylindrical wire kernel possesses a singularity which must be properly treated in order to evaluate the uniform current vector potential. Traditionally, the singular part of the kernel is extracted resulting in a slowly varying function which is convenient for numerical integration. This paper provides some new accurate and computationally efficient methods for evaluating the remaining singular integral. It is shown that this double integral may be converted to a single integral which no longer possesses a singular integrand and consequently may be efficiently evaluated numerically. This form of the integral is independent of the restrictions involving wire length and radius which are inherent in various approximations. Also presented is a highly convergent exact series representation of the integral which is valid except in the immediate vicinity of the singularity. Finally, a new intermediate wire approximation is introduced which is found to be an improvement over the classical thin wire approximation. It is demonstrated that each of these methods provides extremely accurate as well as efficient results for a wide range of wire radii and field point locations.

II. Theory

The vector potential associated with a cylindrical wire (segment) of length Δ and radius a is given by [1]

$$A_z = \int_{-\frac{\Delta}{2}}^{\frac{\Delta}{2}} I_z(z') K(z-z') dz' \tag{1}$$

where

$$K(z-z') = \frac{1}{2\pi} \int_{-\pi}^{\pi} \frac{e^{-j\beta R(z-z',\phi')}}{R(z-z',\phi')} d\phi' \tag{2}$$

represents the cylindrical wire kernel, in which

$$R(z-z',\phi') = \sqrt{(z-z')^2 + \rho^2 + a^2 - 2\rho a\cos\phi'} \tag{3}$$

The integrand in (2) contains a singularity which may be extracted by expressing the cylindrical wire kernel in the form [2]

$$K(z-z') = \frac{1}{2\pi}\int_{-\pi}^{\pi}\frac{d\phi'}{R(z-z',\phi')} + \frac{1}{2\pi}\int_{-\pi}^{\pi}\frac{e^{-j\beta R(z-z',\phi')} - 1}{R(z-z',\phi')}\,d\phi' \tag{4}$$

For the situation in which the current is assumed to be uniformly distributed over the surface of the wire, i.e. $I_s(z') = I_0$, the expression for the vector potential (1) reduces to

$$A_z = \frac{\mu I_0}{4\pi}\left\{\frac{1}{2\pi}\int_{-\frac{\Delta}{2}}^{\frac{\Delta}{2}}\int_{-\pi}^{\pi}\frac{d\phi'dz'}{R(z-z',\phi')} + \frac{1}{2\pi}\int_{-\frac{\Delta}{2}}^{\frac{\Delta}{2}}\int_{-\pi}^{\pi}\frac{e^{-j\beta R(z-z',\phi')} - 1}{R(z-z',\phi')}\,d\phi'dz'\right\} \tag{5}$$

The second integral has a very slowly varying integrand and may be readily evaluated numerically. The first integral, however, possesses a singular integrand when $\rho=a$, $z=z'$ and $\phi'=0$. For this reason, methods for evaluating integrals of the form

$$I(\rho,z,\Delta) = \frac{1}{2\pi}\int_{-\frac{\Delta}{2}}^{\frac{\Delta}{2}}\int_{-\pi}^{\pi}\frac{d\phi'dz'}{R(z-z',\phi')} \tag{6}$$

are of considerable interest from the computational standpoint. This paper will introduce and compare several new techniques developed for evaluating integrals of the type given in (6).

If the change of variables $\xi = z - z'$ and $\theta = \phi'/2$ is applied to the integral (6) when $\rho=a$, then it follows that

$$I(a,z,\Delta) = \frac{2}{\pi}\int_{\xi_1}^{\xi_2}\int_{0}^{\frac{\pi}{2}}\frac{d\theta\,d\xi}{R(\xi,\theta)} \tag{7}$$

where

$$R(\xi,\theta) = \sqrt{\xi^2 + 4a^2\sin^2\theta} \tag{8}$$

with $\xi_1 = z - \Delta/2$ and $\xi_2 = z + \Delta/2$.

Interchanging the order of integration, evaluating the inner integral, and introducing the change of variables $v=(4/\pi)\theta - 1$ leads to

$$I(a,z,\Delta) = \ln\left(\frac{\alpha_1}{\alpha_2}\right) + \frac{1}{2}\int_{-1}^{1} \ln\left[\frac{1+\sqrt{1+\alpha_2^2\sin^2(v+1)\frac{\pi}{4}}}{1+\sqrt{1+\alpha_1^2\sin^2(v+1)\frac{\pi}{4}}}\right] dv\ , \quad z > \Delta/2 \tag{9}$$

where $\alpha_1=2a/\xi_1$ and $\alpha_2=2a/\xi_2$. The restriction on the range of validity of (9) to positive values of z only, i.e. $z>\Delta/2$, can be easily removed to include negative values of z as well by making use of the identity $I(a,z,\Delta)=I(a,|z|,\Delta)$, which is valid for $|z|>\Delta/2$. A similar procedure can be followed for the special case where $z = 0$. The result for this case is found to be

$$I(a,0,\Delta) = 2\ln\left(\frac{1}{2\alpha}\right) + \int_{-1}^{1} \ln\left[1+\sqrt{1+\alpha^2\sin^2(v+1)\frac{\pi}{4}}\right] dv \tag{10}$$

where $\alpha = a/\Delta$. Equations (9) and (10) are in a convenient form for application of numerical integration techniques because their integrands are relatively smooth and do not contain singularities. The form of these integrals are particularly well-suited for numerical integration using a Gaussian quadrature technique. One significant advantage offered by (9) and (10), when compared with the conventional form of I [3], is that they do not require the evaluation of elliptic integrals.

A useful approximation to I has been derived in [4]. This approximation was found to be

$$I(a,z,\Delta) = \ln\left(\xi_1/\xi_2\right) + 2\,I_{thin}(a,z,\Delta)\ , \quad z > \Delta/2 \tag{11}$$

where I_{thin} is the well-known classical thin wire approximation given by [5]

$$I_{thin}(a,z,\Delta) = \ln\left[\frac{\xi_2+\sqrt{\xi_2^2+a^2}}{\xi_1+\sqrt{\xi_1^2+a^2}}\right] \tag{12}$$

Hence, (11) may be thought of as an extended thin wire or intermediate wire approximation. Similarly, it was shown that for the important case when $z = 0$, the intermediate wire approximation takes the form

$$I(a,0,\Delta) = 2\ln(a/\Delta) + 2\,I_{thin}(a,0,\Delta) \tag{13}$$

where

$$I_{thin}(a,0,\Delta) = 2\ln\left[\frac{\Delta+\sqrt{\Delta^2+(2a)^2}}{2a}\right] \tag{14}$$

is the corresponding thin wire approximation.

A power series expansion of I was derived by Butler [6] for the $z = 0$ case, which converges provided $\Delta/a > 4$. This expansion is given by

$$I(a,0,\Delta) = 2\ ln\left(\frac{\Delta}{a}\right) + 2\sum_{n=1}^{\infty}\binom{1/2}{n}(2n-1)\frac{(2n-1)!}{(n!)^2}\left[\frac{2a}{\Delta}\right]^{2n} \quad , \quad \Delta/a > 4 \tag{15}$$

A useful approximation may be obtained from (15) by retaining the logarithmic term and the first two terms of the series expansion. This leads to

$$I(a,0,\Delta) = 2\ ln\left(\frac{\Delta}{a}\right) + 4\left[\frac{a}{\Delta}\right]^2 - 18\left[\frac{a}{\Delta}\right]^4 \tag{16}$$

An exact expression for the integral I was found in [4] which is valid for $\rho \neq a$ or when $\rho = a$ and $|z| > \Delta/2$. This exact representation is

$$I(\rho,z,\Delta) = ln\left[\frac{x_2 + u_2}{x_1 + u_1}\right] + \sum_{n=1}^{\infty}\binom{-1/2}{n}^2\left[\frac{2\sqrt{\rho a}}{\rho + a}\right]^{2n} F_n(\rho,z,\Delta) \quad , \quad \rho \neq a \tag{17}$$

where

$$F_n(\rho,z,\Delta) = \int_{x_1}^{x_2}\frac{dx}{u^{2n+1}} \tag{18}$$

$$u = \sqrt{1+x^2} \tag{19}$$

with $x_1 = \xi_1/(\rho+a)$, $x_2 = \xi_2/(\rho+a)$, $u_1 = \sqrt{1+x_1^2}$ and $u_2 = \sqrt{1+x_2^2}$. A recurrence relation exists which provides a computationally efficient method for calculating the integrals F_n defined in (18). The form of this recurrence relation was found to be

$$F_n = \frac{1}{(2n-1)}\left[x_2(1/u_2)^{2n-1} - x_1(1/u_1)^{2n-1} + 2(n-1)F_{n-1}\right] \quad , \quad n \geq 2 \tag{20}$$

where

$$F_1 = (x_2/u_2) - (x_1/u_1) \tag{21}$$

An approximation of I may be obtained by retaining the logarithmic term and the first two terms in the series expansion (17). The resulting expression is

$$I(\rho,z,\Delta) = ln\left[\frac{x_2 + u_2}{x_1 + u_1}\right]$$
$$+ \frac{(\rho a)}{(\rho+a)^2}\left\{1 + \frac{3}{2}\frac{(\rho a)}{(\rho+a)^2}\right\}\left[\frac{x_2}{u_2} - \frac{x_1}{u_1}\right] + \frac{3}{4}\frac{(\rho a)^2}{(\rho+a)^4}\left[\frac{x_2}{u_2^3} - \frac{x_1}{u_1^3}\right] \tag{22}$$

When $\rho=a$ (17) reduces to

$$I(a,z,\Delta) = ln\left[\frac{x_2+u_2}{x_1+u_1}\right] + \sum_{n=1}^{\infty}\binom{-1/2}{n}^2 F_n(a,z,\Delta) \quad , \quad |z| > \Delta/2 \tag{23}$$

where $x_1 = \xi_1/2a$ and $x_2 = \xi_2/2a$. The corresponding expression for (22) when $\rho=a$ is given by

$$I(a,z,\Delta) = ln\left[\frac{x_2+u_2}{x_1+u_1}\right] + \frac{11}{32}\left[\frac{x_2}{u_2} - \frac{x_1}{u_1}\right] + \frac{3}{64}\left[\frac{x_2}{u_2^3} - \frac{x_1}{u_1^3}\right] \tag{24}$$

which is primarily useful when $\Delta/a \geq 4$ and $z/\Delta \geq 1$.

III. Results

At the point $z=0$, four methods were used to evaluate the uniform current vector potential integral of the isolated singularity associated with the cylindrical wire kernel. Equation (10) was computed using a three point Gaussian quadrature numerical integration technique, while (13), (14) and (16) give the intermediate approximation, the thin wire approximation and the three term approximation of the power series expansion derived by Butler [6], respectively. Plots of the relative percent error for the various methods versus the segment length-to-radius ratio, Δ/a, are shown in Figure 1. As a basis of comparison (10) was numerically integrated to a sufficiently high degree of accuracy. Clearly, the intermediate approximation and the three term Butler series have lower percent errors than the thin wire approximation across the entire range of Δ/a. This becomes significant as Δ/a approaches 4 (thicker wires) where the error associated with the thin wire approximation exceeds 1%. The three term Butler series proves to be extremely accurate and has the lowest error of the four methods for very thin wires ($\Delta/a \gtrsim 30$). However, the three point Gaussian quadrature and the intermediate approximation also give acceptable errors in this range. For thicker wires, the three point Gaussian quadrature is superior and, because no assumptions were made in modifying the integral to the form given in (10), Δ/a can be extended below the ratio of 4 and still achieve very accurate results.

When z is not in the immediate vicinity of the singularity, the Butler series expansion (15) is no longer valid, but can be replaced by the three term approximation (24) of the exact series representation defined in (23). A contour plot of the relative percent error as a function of Δ/a and z/Δ for the three term approximation (24) is shown in Figure 2. Also, a three point Gaussian quadrature numerical integration of (9) is valid as well as the intermediate and thin wire approximations of (11) and (12), respectively. Figure 3 shows a contour plot of the relative percent error associated with the three point Gaussian quadrature approximation of (9).

Acknowledgement

This work was supported by CDR Gus K. Lott of the Naval Security Group Command.

References

[1] R. W. P. King, "The linear antenna - Eighty years of progress," *Proc. IEEE*, Vol. 55, pp. 2-26, Jan. 1967.

[2] S. A. Schelkunoff, *Advanced Antenna Theory*. New York: Wiley, 1952, pp. 140-142.

[3] D. R. Wilton and C. M. Butler, "Effective methods for solving integral and integro-differential equations," in *Moment Methods in Antennas and Scattering*, R. C. Hansen, Ed., Boston: Artech, 1990, pp. 58-77.

[4] D. H. Werner, J. A. Huffman, P. L. Werner and J. K. Breakall, "Techniques for Evaluating the Uniform Current Vector Potential at the Isolated Singularity of the Cylindrical Wire Kernel," Submitted for Publication in *IEEE Trans. Antennas Propagat.*, July 1993.

[5] R. F. Harrington, "Matrix methods for field problems," *Proc. IEEE*, Vol. 55, pp. 136-149, Feb. 1967.

[6] C. M. Butler, "Evaluation of potential integral at singularity of exact kernel in thin wire calculations," *IEEE Trans. Antennas Propagat.*, pp. 293-295, March 1975.

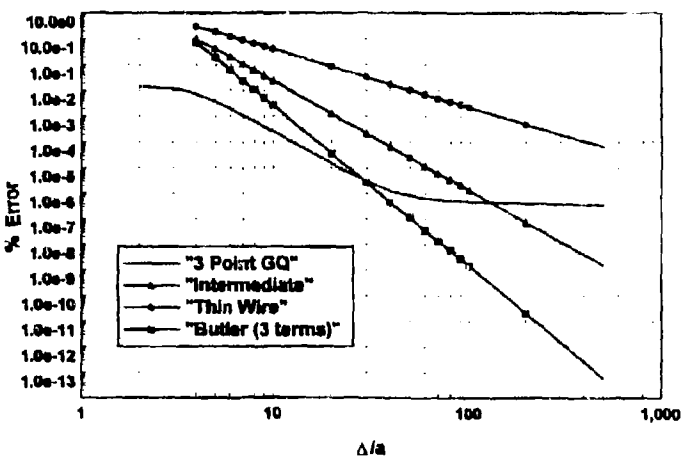

Figure 1. Relative Percent Error Versus Δ/a Associated With Various Techniques for Evaluating the Integral (6) When $\rho = a$ and $z = 0$.

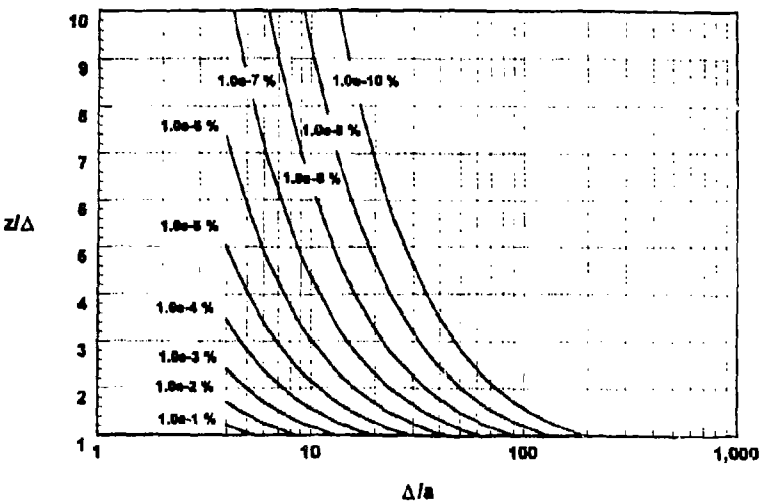

Figure 2. Contour Plot of the Relative Percent Error Associated With the Three Term Approximation (24).

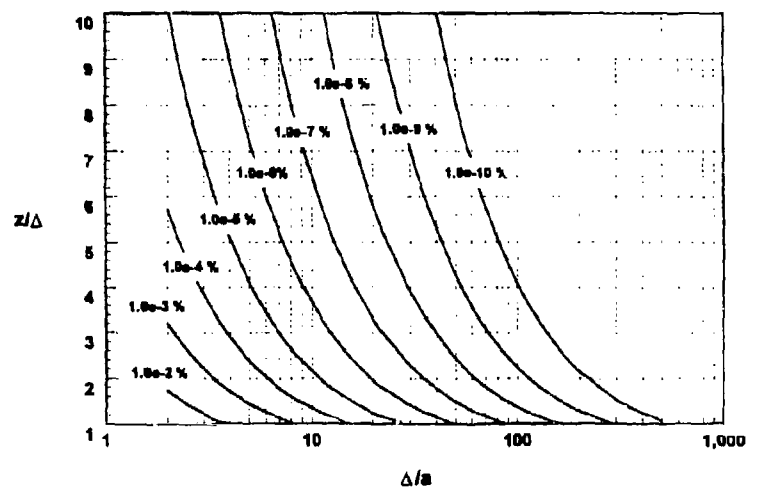

Figure 3. Contour Plot of the Relative Percent Error Associated With the Three Point Gaussian Quadrature Approximation of (9).

A Parallel Implementation of a Thin Wire EFIE Code

A. Tinniswood, AM. Tyrrell, SX. Cloude[1]
University of York
England

Abstract - A key problem with all CEM techniques is the increasing computer time required for evaluation of electrically large structures. In frequency domain techniques (such as the NEC code) computer time can be proportional to the sixth power of frequency (for the time domain there is a fourth order dependency). This provides a serious limitation, which can be alleviated by using problem symmetry, hybrid methods (such as MoM and GTD) or distributed processing. This paper investigates the latter as a means of solving time domain integral equation (TDIE). In particular it will look at the implementation of a thin wire EFIE on a transputer network, providing results to demonstrate the processing gain power available from such a system.

Introduction

Computational Electromagnetics (CEM) now offers a viable alternative to measurements and mathematical analysis for solving antenna, scattering and coupling problems [1].

Typical applications include:

- Self and mutual impedance for antennas.
- Antenna radiation patterns.
- Shielding effectiveness calculations for resonant cavities with apertures.
- Cross talk evaluation on multi-conductor transmission lines.
- Near and far electric and magnetic field calculations for immunity and susceptibility studies.
- Scattering from solid conducting and dielectric bodies.

There are two main disciplines in CEM, finite techniques such as finite element, finite difference[1] and the TLM method[2], and integral equation techniques formulated from the method of moments (MoM). A complementary approach to the formulation of EM problems arises from each of these techniques. Maxwell's equations when expressed as integrals can be manipulated to form the electric and magnetic field integral equations (EFIE and MFIE). IEs are solved to find the current response on the surface of the body as a result on an excitation field. As they represent the solution to a surface integral (as opposed to a volume integral in finite techniques) the dimensionality of the problem is reduced by one. The radiated field from the body can be calculated from a knowledge of currents on all segments on that body. An antenna response problem can be modelled by driving one or more of the segments on the surface. An incident field can be simulated by inducing currents on all segments of the body. Radar cross section (RCS) and scattering problems can therefore be evaluated. An additional advantage of IE solutions is that radiation boundary conditions are implicit (a problem often encountered in finite difference methods).

Although the dimensionality of the problem has been reduced by one the computer time and memory requirements restrict the size of the problem which can be modelled. In frequency domain techniques (such as the NEC code) computer time can be proportional to the sixth power of frequency (for the time domain there is a fourth order dependency)[1]. This limits the use of IE techniques for evaluation of electrically large structures. Whilst this limitation can be alleviated by using problem symmetry or hybrid methods (such as MoM or GTD) performance increases can be achieved by the application of parallel processing. This paper uses the Pocklington IE [4] to demonstrate how the application of parallel processing can provide faster solution times.

---

[1]Now at IRESTE, University of Nantes, France

The fine grain structure of finite techniques (with only local communications), make them highly suitable for implementation on parallel processing networks. A great deal of work has been carried out on the implementation of FDTD and TLM on multiple processors[5,6].

The EFIE and the MFIE can be solved in both the frequency or time domain. Frequency domain methods result in a dense matrix equation, expressing the interaction between all segments. Each solution provides information at one specific frequency. Solution in the time domain however can yield a broad band frequency response using a marching-in-time method, removing the need to solve a dense matrix equation. Some attention has given to fast parallel solvers for use with frequency domain techniques[5,7]. Relatively little attention has been paid to the parallel implementation of time domain integral equations. In the time domain the interaction between all the segments is expressed as retarded currents. The finite time interval between the cause and effect of these currents can be exploited to aid the implementation of TDIEs on parallel processors.

TDIE Techniques

This section demonstrates how the EFIE can be used to model a simple wire grid structure. Each of the four elements (radius r, length l) in the multiple array antenna (Fig. 1) is modelled using 25 segments and was driven on the centre segment with a Gaussian pulse of magnitude 1V. Figure 2 shows the drive point current of one antenna in the array. This agrees with the results obtained by Martin et al[6] when modelling the same problem.

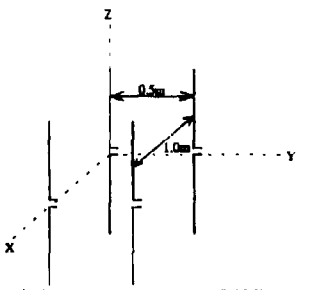

Figure 1 : Problem geometry. r = 0.00674, l = 1.0m

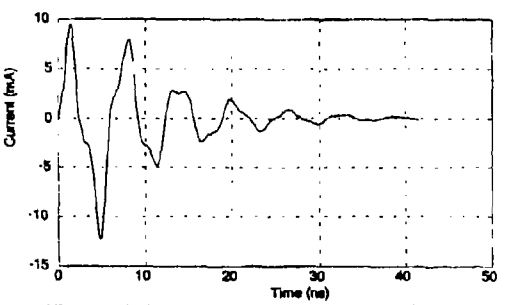

Figure 2 : Drive point current for one element of the array

The TDIE produces a space time history of the currents on each segment of the wire structure. The drive point current (Fig 2) represents a slice of this at the drive point. Using a Fourier transform on both the current waveform and the drive voltage the input impedance (Fig. 3) of the structure can be found by complex division.

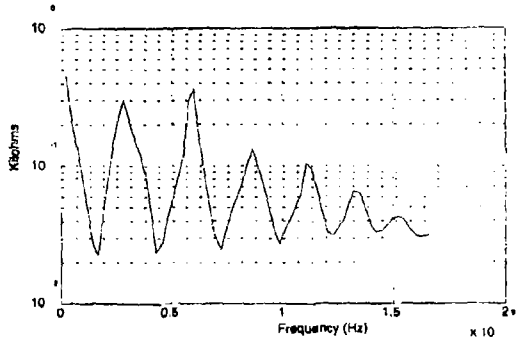

Figure 3 : Input impedance of the structure

The Pocklington IE

The Pocklington IE code is a three dimensional code which can be used to model an arbitrary structure of wires. The physical structure is described by the positioning of nodes and the description of the wires connecting them. This obviously allows the description of complex targets on which the current structure is evaluated as a result of either an incident field or one or more of the elements in the problem being excited. The interaction between individual elements in the problem is evaluated before commencing the time marching algorithm, thus the physical structure is independent of the functionality in the time marching algorithm.

The current in space and time can be approximated by

$$I(s',t') = \sum_{i=1}^{N_s} \sum_{j=1}^{\infty} I_{ij}(s'-s_i, t'-t_j) U(s'-s_i) V(t'-t_j)$$

where $I_{ij}(0,0) = I_{ij}$ is the current at the centre of the i-th space segment (from a total of N_s) and where

$$U(s'-s_i) = \begin{cases} 1, |s'-s_i| \le \Delta_i/2 \\ 0, \text{otherwise} \end{cases}$$

$$V(t'-t_j) = \begin{cases} 1, |t'-t_j| \le \delta_j/2 \\ 0, \text{otherwise} \end{cases}$$

where Δ_i and δ_j are the lengths of the space segment i and time step j respectively centred at s_i and t_j. The operation of the time marching algorithm can be explained with reference to figure 4. This shows the time history for a single straight wire, and the retarded currents necessary for evaluation of one space segment. At the onset of the algorithm all the currents in this array are zero and the array is filled with retarded currents as the algorithm progresses.

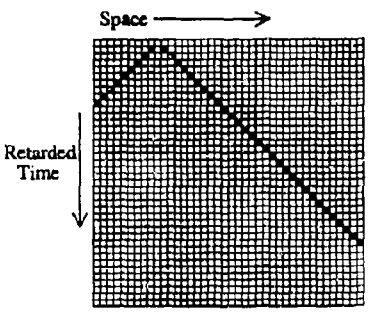

Figure 4 : Evaluation of the Current for a single space step

This demonstrates the way in which all segments in the problem are required for the evaluation of a single current element. In the case of multiple wires or curved wire structures the same method is used to calculate the current, however the indexing into the array (Fig. 4) is more complex. This indexing represents the time delay between the element under evaluation and the retarded element, and care must be taken to ensure that the array is large enough to cope with the maximum time delay.

Parallel Processing and the Transputer

The computational demands of many numerical methods are often close to the limits of computer power available from traditional serial machines [9, 10]. This demand together with a demand for increased problem size requiring more memory, has prompted the use of more novel processing techniques. Commercial, VLSI, digital signal processing devices provide dedicated signal processing capabilities thorough on chip shift registers, multipliers and accumulators. In general these devices only support sequential programming, have awkward instruction sets (not lending themselves to high level languages) and require assembly language programming to achieve good performance. An alternative is the use of descrete components which can be used to construct bit sliced systems. These can be used to provide primitive functions, such as inner product, step or more sophisticated algorithm specific functions (e.g. transversal filter). They do however required the designer to resort to micro coding.

Despite the advent of these devices, in many applications an adequate, often real-time, response can only be achieved by exploiting the parallelism inherent in these algorithms. Any algorithm using a sequence of processing steps in a regular, repeated manner is a prime candidate for parallel implementation. It is therefore increasingly common to use networks of processing cells configured into array or vector processors, pipelines, or more complex forms such as systolic arrays or wavefront arrays. The principle feature of these structures is the replication of processing cells to reflect the internal structure of the underlying algorithm. Each cell communicates with its neighbour(s) and it is these communications which synchronise and co-ordinate the operation of the structure. Communications are ideally kept local for high efficiency.

Transputers

The T414 and T800 transputers[11] are powerful pin-compatible 32-bit processors, specifically designed for use when implementing parallel architecture's. They have four high speed serial links supported by internal DMA channels, two on-chip timers and 2 or 4Kbytes of internal fast (50nS) static RAM, as shown in figure 5. The T800, in addition to the CPU has a floating-point unit that can handle 32 and 64-bit floating-point arithmetic. The total memory space is 4 Gigabytes on the T414/T800. The design philosophy is not, however, to have a lot of memory around a transputer, but a lot of transputers communicating through their four dedicated serial links at speeds up to 20 MBits/S. No external hardware is required when connecting transputers together.

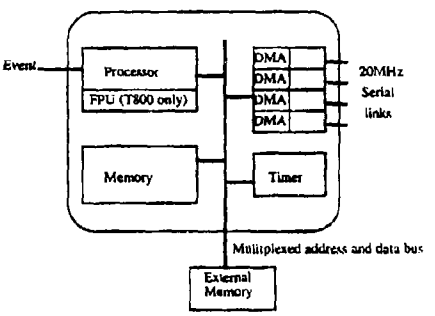

Figure 5 : The T400/T800 Transputer

Many of the traditional high level languages are available to assist the programming of the transputer together the dedicated transputer language occam[12]. Occam is designed for use with a parallel system including in its definition constructs which provide a method by which to describe a parallel algorithm. Although the parallel algorithm discussed in this paper was written using this language, there are alternatives to occam in the form of existing high level serial languages with functions to enable the interaction between concurrent processes. Although these languages (such as C, C++ and FORTRAN) are not specifically designed to program a parallel system they can be used to write more portable code (occam code can only be used on the Transputer).

A key measure of the performance of a parallel algorithm is its efficiency which is defined as follows

$$\eta = \frac{T_1}{T_n \times n} \times 100\%$$

where T_1 and T_n are the execution time on 1 and n processors respectively

This measure is affected by the ratio of computation to communication and stresses to point made above that communication must be minimised.

Implementation

This section shows how the TDIE can be distributed across a number of transputers and gives results demonstrating the efficiency of this algorithm. The transputers are configured as a doubly linked pipeline (Fig 6), providing an expandable and flexible network of processors. The calculation is divided across the network by assigning each processor a section of the wire structure. This processor must then calculate and store the currents on this section of the problem.

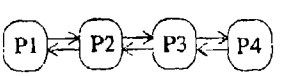

Figure 6 : The doubly linked pipeline.

To carry out its calculation each processor requires retarded currents in the form of previously calculated values from all segments in the problem. Most of these values will be stored on other processors and it would appear necessary to communicate these values across the processor network. However with careful algorithm design it is possible for each processor in the network to carry out a calculation based upon the values stored on that processor for each of the other processors. The result of this calculation is then passed along the pipeline to the relevant processor. This minimises the

communication as now only the result of a calculation is passed a opposed to a series of values required for that calculation. This is best expressed graphically with reference to a single straight wire.

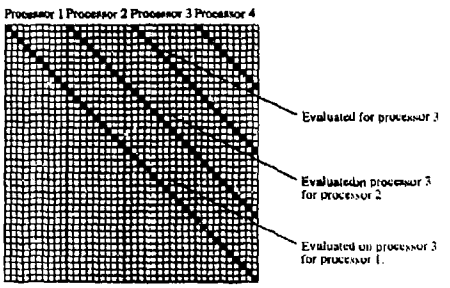

Figure 7 : The distributed calculation

Figure 7 shows half of the calculation of the current for one space step, demonstrating how processor 3 carries out calculations from processors 1 and 2. A similar calculation is carried out for currents to be passed in the other direction but is omitted from the diagram for clarity. Notice that during this step each processor will evaluate the current on one segment, hence of four processors are used.

This algorithm running on the transputer system allow a scalable number of processors to be added to the system. As more processors are added this increases the total amount of memory and computational power available thus allowing larger problems to be solved. Obviously there is a penalty incurred by implementing this algorithm as information must still be passed across the pipeline. The effect of this is to reduce the efficiency of the algorithm, and will increase as more processors are added to the network. This can be minimised by exploiting the fact that with careful algorithm design the transputer can perform communication and computation in parallel.

The effect of adding processors to the system upon speed-up and efficiency is illustrated in figure 8.

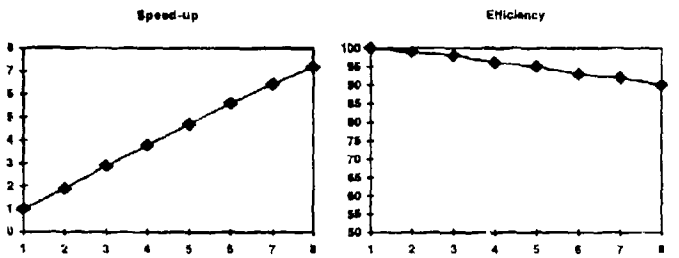

Figure 8 : Speedup and efficiency of the Pocklington IE code

Conclusions

This work discussed in this paper has shown that parallel processing can be used to provide a significant improvement in the run time of TDIE codes. Although the Pocklington IE is a thin wire code the same principles can be applied to surface patch IE codes. An ideal of the speed improvements involved with this implementation is given in Table 1. These results are the execution times for the evaluation of the problem described in figure 1 using the Pocklington IE

[10] A. Fernadez, J.M. Llaberia, J.J. Nanapro, M. Valero-Garcia, "Performance Evaluation of Transputer Systems with Linear Algebra Problems", Microprocessing and Microprogramming, Vol. 32 1991 pp 825-832.

[11] Inmos Tranputer Manual, Prentice Hall 1989

[12] Inmos occam 2 Reference Manual, Prentice Hall 1988

MORE IMPROVEMENT IN THE METHOD OF METHOD OF MOMENTS IN THE SOLUTION OF POCKLINGTON'S AND HALLEN'S INTEGRAL EQUATIONS

DR. F.M.EL-HEFNAWI
ELECTRONICS RESEARCH INSTITUTE
DOKKI / CAIRO / EGYPT

ABSTRACT

A novel numerical method is presented to solve Pocklington's and Halleln's integral equations using the method of moments applying extended boundary condition and kernel expansion.

The kernel expansion used is the well known finite Fourier cosine series with period of 2L where L is the ante na length. Current expansion is chosen as entire domain bases. The selection of the weighting functions and inner product domain are such that more simplification is reached. Hence the numerical computation of the impedance matrix is fairly fast and simple. Results obtained by this method agree with experimental and previous published ones.

INTRODUCTION

In order to handle complicated problems using the method of moments, it is necessary to optimize the numerical solution procedure from the point of view of speed, convergence and accuracy. This leads to the careful study of properties of the various integral equation formulations and the choice of the basis and testing functions in the solution methods and in the exciting fields so as to improve the numerical efficiency of a given computation. Also desirable are techniques which are conceptually simple to apply (so as to minimize the programming time) and which have a wide band of applicability.

Difficulties which frequently arise in the numerical solution of an integral equation are :

1) The first difficulty is the appearance of the derivatives outside the vector potential integrals on the induced currents. For thin wires problem, this appears when employing Pocklington's equation which is handled simply by expanding the kernel, current and employing the testing function such the orthogonalities are achieved so as to end up with no derivative.

2) The second difficulty is the calculation of integrations appearing in the integral equations which are either calculated numerically or analytically if one uses subdomain basis and point matching [1,2]. This is overcome by using appropriate kernel expansion functions, current expansion basis and proper weighting functions.

3) The third difficulty is type of exciting field where delta function generator is avoided since it is not in the range of the operator of either Hallen's or Pocklington integral equation [3,4] . Also the type of feeding suggested by Harrington and others [5,6] where one or more than one segment represents the incident field resulting in a solution which depends on the structure segmentation. To overcome this a frill of magnetic current is used which represents the field in the aperture of a coaxial fed monopole over a ground plane.

Finally the method is demonstrated in the following sections.

FORMULATION OF THE PROBLEM

The integral equation governing the current I(z') on an axially symmetric thin antenna or scatterer under axially symmetric incident field has the following form :

$$\int_{-h}^{h} K(z,z',R)\, I(z')dz' = f(z) \qquad (1)$$

where using Pocklington's integral equation the kernel and f(z) have the forms

$$K(z,z',R) = (k^2 + \frac{\partial^2}{\partial z^2}) \frac{e^{-jkR}}{R} \qquad (2)$$

and

$$\frac{-4\pi jk}{Z_o} E_{inc}(z) = f(z) \qquad (3)$$

and using Hallen's integral equation the kernel and f(z) are given as :

$$K(z,z',R) = \frac{e^{-jkR}}{R} \qquad (4)$$

and

$$f(z) = C_1 \cos(kz) - \frac{4\pi jk}{Z_o} E_{inc}(z) \int_{z'=0}^{z'=z} \sin(k|z-z'|)dz' \qquad (5)$$

with

$$R = \sqrt{a^2 + \rho^2 - 2\rho a \cos\phi + (z-z')^2} \qquad (6)$$

which is the distance between the source point and observation point having the cylindrical coordinates (a,ϕ,z') and (ρ,ϕ,z) respectively.

This integral equation suffers from singularity when both observation point and source point concide. To overcome this , extended line type boundary condition is employed making use of the fact that the electric field vanishes on the axis of the the dipole and within the dipole surface. Thus one may take the observation point to be on the axis of the antenna while the source point to be on the surface of the antenna. Hence R will have the following form :

$$R = \sqrt{a^2 + (z-z')^2} \qquad (7)$$

TYPE OF FEEDING

Since Hallen's and Pocklington's integral equations have Einc on the right hand side (where Einc represent the field of the exciting source) a knowledge of the source term must be available. The source Einc may be a delta function generator ($E_{inc}=V\delta(z)$) which is useful tool, but it is a rather poor model of the actual physical situation when compared with finite models and presents difficulties when calculating the imaginary part of the input impedance. This arises from the fact that the delta function generator corresponds physically to two circular knife edges that are separated by zero distance. Since such adjacent edges clearly corresponds to infinite capacitance, the current at these edges must be infinite. Fortunately, as has

been shown by Wu and King [10], the singularity in I(z') near z=0 is logarithmic and of very short rang. Since it actually contributes to the current in an exceedingly small and physically meaningless distance of the order of magnitude of exp(-1/ka), it may be, in principal, be subtracted out. The remaining current may then be related to the current in the actual antenna driven in physically realizable manner. Harrington [5] introduces a finite gap when solving by the method of moments. Such source segment or segments make the calculation extremely sensitive to structure segmentation. A particular appropriate source is to use a frill of magnetic current which represents the electric field distribution in the aperture of a coaxial fed monopole over a ground plane. The z-component of the electric field on the axis of the monopole resulting from such model is given by [10] :

$$E_{inc}(z) = \frac{V}{2n(b/a)} [\, K(a,z) - K(b,z)] \qquad (8)$$

where

$$K(a,z) = \frac{e^{-jkR_a}}{R_a} , \qquad (9)$$

$$K(b,z) = \frac{e^{-jkR_b}}{R_b} , \qquad (10)$$

$$R_a = \sqrt{a^2 + z^2} , \qquad (11)$$

$$R_b = \sqrt{b^2 + z^2} . \qquad (12)$$

KERNEL EXPANSION

The kernel of equation (1) is expanded in a finite Fourier series making use of the fact that z and z' enter only as square term of their difference. Since $h \geq z \geq -h$ and $h \geq z' \geq -h$ then let $\xi = z - z'$ yields $+2h \geq \xi \geq -2h$, hence a cosine series over the range $\xi = -2h$ to $\xi = 2h$ is sufficient and the expansion for the 2Q base points may be written as :

$$K(z,z',R) = K(\xi_r)$$

$$= \sum_{q=0}^{N1} (D_q/\varepsilon_q) \cos\left(\frac{q\pi r}{Q}\right),$$

$$r = -(Q-1), -(Q-2), \ldots, 0, \ldots, Q \qquad (13)$$

where

$$\xi_r = \frac{2h}{Q} r \qquad (14)$$

and

$$\varepsilon_q = 2 \qquad q/Q = 0,1,2,\ldots$$

$$= 1 \qquad \text{otherwise} \qquad (15)$$

$$D_q=\frac{1}{Q}\{K(\xi_0)+2\sum_{r=1}^{Q-1}K(\xi_r)\cos(\frac{q\pi r}{Q})+K(\xi_q)\cos(q\pi)\}$$

$$q = 0,1,2,\ldots,Q \qquad (16)$$

In equation (13) at the base points highest accuracy is reached if N1 is chosen to satisfy, [7]

$$N1=Q \qquad (17)$$

Thus the coefficients in equation (13) are calculates using least squares method.

COMPUTATIONAL ALGORITHM USING THE METHOD OF MOMENTS

The solution of equation (1) starts by expanding the current in entire domain basis employing truncated odd cosine infinite Fourier series giving :

$$I(z') = \sum_{m=1,3}^{M} A_m \cos(\frac{m\pi z'}{2h}) \qquad (18)$$

Substituting the kernel of equation (13) and (18) in equation (1) gives :

$$\sum_{m=1,3}^{M} A_m \sum_{q=0}^{Q} (D_q/\varepsilon_q) \int_{-h}^{h} \cos(\frac{q\pi\xi_r}{2h})\cos(\frac{m\pi z'}{2h})dz' = f(z) \qquad (19)$$

where f(z) is formally defined in equations (3),(5) and (8)-(12). Since $\xi_r=z-z'$ equation (19) reduces to

$$f(z)=\sum_{m=1,3}^{M} A_m \sum_{q=0}^{Q} (D_q/\varepsilon_q)\{\cos(\frac{q\pi z}{2h})\int_{-h}^{h}\cos(\frac{q\pi z'}{2h})\cos(\frac{m\pi z'}{2h})dz' + \sin(\frac{q\pi z}{2h})\int_{-h}^{h}\sin(\frac{q\pi z'}{2h})\cos(\frac{m\pi z'}{2h})dz'\} \qquad (20)$$

for sypsetrical feeding the second term of equation (20) containing $\sin(q\pi z'/2h)\sin(m\pi z'/2h)$ equal to zero thus equation (20) simplifies to :

$$f(z) = \sum_{m=1,3}^{M} A_m \sum_{q=0}^{Q} (D_q/\varepsilon_q)\cos(\frac{q\pi z}{2h})\ I_{mq} \qquad (21)$$

where

$$I_{mq} = \int_{-h}^{h} \cos(\frac{m\pi z'}{2h})\ \cos(\frac{q\pi z'}{2h})dz' \qquad (22)$$

Choosing the weighting functions as $\cos(q\pi z/2h)$ where p is taken as even numbers and performing the necessary inner product gives

$$\int_{-2h}^{2h} f(z)\cos\left(\frac{p\pi z}{2h}\right)dz = \sum_{m=1,3}^{M} A_m \sum_{q=0}^{Q} D_q\, I'_{pq}\, I_{mq} \qquad (23)$$

where

$$I'_{pq} = \frac{1}{\varepsilon_q}\int_{-2h}^{2h} \cos\left(\frac{p\pi z}{2h}\right)\cos\left(\frac{q\pi z}{2h}\right)dz \qquad (24)$$

Equation (24) is calculated yielding

$$I'_{pq} = 2h \qquad p = q$$

$$= 0 \qquad \text{otherwise} \qquad (25)$$

hence equation (21) is simplified in the following form

$$\int_{-2h}^{2h} f(z)\cos\left(\frac{p\pi z}{2h}\right)dz = 2h\, D_p \sum_{m=1,3}^{M} A_m\, I_{mp} \qquad (26)$$

where

$$I_{mp} = \frac{4hm}{\pi(m^2-p^2)}\sin\left(\frac{m\pi}{2}\right)\cos\left(\frac{p\pi}{2}\right)$$

$$p = 0,2,4,\ldots,M-1$$

$$m = 1,3,5,\ldots M \qquad (27)$$

Equation (27) is substituted in equation (26) giving ,

$$S(p) = \sum_{m=1,3}^{M} A_m \frac{m\sin\left(\frac{m\pi}{2}\right)}{(m^2-p^2)} \qquad p=0,2,4,\ldots,M-1 \quad (28)$$

$$S(p) = \frac{\pi}{8h^2 D_p \cos\left(\frac{p\pi}{2}\right)}\int_{-2h}^{2h} f(z)\cos\left(\frac{p\pi z}{2h}\right)dz$$

$$p = 0,2,4,\ldots,M-1 \qquad (29)$$

CALCULATION OF THE SOURCE TERM

To calculate the integration in equation (24) it is necessary to specify the type of exciting field. This is considered the resulting field in the aperture of a coaxial fed monopole over a ground plane. Referring to equation (29)

$$\int_{-2h}^{2h} f(z)\cos\left(\frac{p\pi z}{2h}\right)dz$$

will have two forms regarding equations (3) and (5) which represent the left hand side of equation (1) where the z-component of the incident electric field on the axis of the antenna is given by :

$$E_{inc}(\rho=0,\phi=0,z)=\frac{V}{2\ln(b/a)}\left[\frac{e^{-jkR_a}}{R_a}-\frac{e^{-jkR_b}}{R_b}\right] \quad (30)$$

where

$$R_a=\sqrt{a^2+z^2} \quad (31)$$

and

$$R_b=\sqrt{b^2+z^2} \quad (32)$$

Substitution of equation (30) in the left hand side of equations (3) and (5) and employing in equation (2) using Pocklington's integral equation gives:

$$S(p)=\frac{-j\pi^2 k}{2Z_o D_p\cos\left(\frac{p\pi}{2}\right)h^2}\int_{-2h}^{2h} E_{inc}(z)\cos\left(\frac{p\pi z}{2h}\right)dz \quad (33)$$

and using Hallen's integral equation gives

$$S(p)=\frac{\pi}{8h^2 D_p\cos\left(\frac{p\pi}{2}\right)}\left\{C_1\int_{-2h}^{2h}\cos(kz)\cos\left(\frac{p\pi z}{2h}\right)dz - \frac{4\pi jk}{Z_o}\int_{-2h}^{2h}\left[E_{inc}(z)\int_{0}^{z}\sin(k|z-z'|)dz'\right]\cos\left(\frac{p\pi}{2h}z\right)dz\right\}$$

$$p = 0,2,4,\ldots,M-1 \quad (34)$$

The first integration term in equation (34) after few manipulations reduces to :

$$W_{kp}=\int_{-2h}^{2h}\cos(kz)\cos\left(\frac{p\pi z}{2h}\right)dz = 4h \ , \quad k=\frac{p\pi}{2h}=0$$

$$= 2h \ , \quad k=\frac{p\pi}{2h}=0$$

$$=\frac{k}{(k^2-(\frac{p\pi}{2h})^2}\sin(2kh),$$

$$k\neq\frac{p}{2h} \quad (35)$$

The second term in equation (34) using Appendix reduces to

$$\frac{4-jk}{Z_o}\int_{-2h}^{2h} E_{inc}(z)\int_{o}^{z}\sin(k'z-z')dz'\cos(\frac{p\pi z}{2h})dz =$$

$$\frac{4-j}{Z_o}\int_{-2h}^{2h} E_{inc}(z)\cos(\frac{p\pi}{2h}z)dz - \int_{-2h}^{2h} E_{inc}(z)\cos[(2k+\frac{p\pi}{2h})z]dz$$

$$-\int_{-2h}^{2h} E_{inc}(z)\cos[(2k-\frac{p\pi}{2h})z)]dz) \qquad (36)$$

Equations (33) and (36) for

$$a_1 = \frac{p\pi}{2h} \qquad (37)$$

$$a_2 = (k + \frac{p\pi}{2h}) \qquad (38)$$

$$a_3 = (k - \frac{p\pi}{2h}) \qquad (39)$$

have integration in the form,

$$F(\gamma,z) = \int_{-2h}^{2h} E_{inc}(z)\cos(\gamma z)dz \qquad (40)$$

which using equation (30) may be written as :

$$\int_{-2h}^{2h} E_{inc}(z)\cos(\gamma z)dz = \frac{V}{j\ln(b/a)}\int_{-2h}^{2h}[\frac{e^{-jkR_b}}{R_a} - \frac{e^{-jkR_b}}{R_b}]\cdot$$

$$\cdot\cos(\gamma z)dz \qquad (41)$$

The integration in equation (39) has been carried out in [9] to be :

$$\int_{-2h}^{2h} E_{inc}(z)\cos(\gamma z)dz = \frac{-j\pi V}{\ln(b/a)}[H_o^{(2)}(\beta a) -$$

$$H_o^{(2)}(\beta b)] \qquad (42)$$

where β satisfies

$$\beta^2 = k^2 - \gamma^2 \qquad (43)$$

and

$$H_o^{(2)}(\beta a) - H_o^{(2)}(\beta b) = Y_o(\beta a) - Y_o(\beta b)$$

$$-j\,(J_o(\beta a) - J_o(\beta b) \quad k > \gamma$$

$$= \frac{2j}{\eta} \ln(b/a) \qquad K = \gamma$$

$$= \frac{2j}{\eta} [K_o(\gamma a) - K_o(\gamma b)] \quad K < \gamma \qquad (44)$$

MATRIX EQUATIONS

Using Pocklington's integral equation, equation (28) utilizing equation (33) is written in the compact matrix form

$$[S(p)] = [Z_{pm}][A_m] \qquad m = 1,3,5,\ldots,M$$

$$p = 0,2,4,\ldots,M-1 \qquad (45)$$

where

$$Z_{pm} = \frac{m \sin(\frac{m\pi}{2})}{m^2-p^2} \qquad (46)$$

using Hallen's integral equation let S'(p) in equation (34) be defined as

$$S'(p) = \frac{-j\eta^2}{2Z_o h^2 D_p \cos(\frac{p\pi}{2})} \int_{-2h}^{2h} E_{inc}(z)\cos(\alpha_1 z)dz -$$

$$\int_{-2h}^{2h} E_{inc}(z)\cos(\alpha_2 z)dz - \int_{-2h}^{2h} E_{inc}(z)\cos(\alpha_3 z)dz) \qquad (47)$$

Then equation (34) is written in the following form

$$S(p) = \frac{-\pi C_1}{8h^2 D_p \cos(\frac{p\pi}{2})} \int_{-2h}^{2h} \cos(kz)\cos(\frac{p\pi z}{2h})dz$$

$$+ S'(p) \qquad p = 0,2,4,\ldots,M-1 \qquad (48)$$

Making use of equation (28) from equation (48) one has

$$S'(p) = \left(\sum_{m=1,3}^{M} A_m \right) \frac{m \sin(\frac{m\pi}{2})}{(m^2-p^2)}$$

$$+ C_1 \frac{\pi}{8h^2 D_p \cos(\frac{p\pi}{2})} W_{kp}$$

$$p = 0,2,4,\ldots,M-1 \qquad (49)$$

Hence equation (49) is converted to the following compact matrix form

$$[S'(p)] = [Z_{pm}][A_m] \qquad p = 0,2,4,\ldots,M+1$$

$$m = 1,3,5,\ldots,M+2 \qquad (50)$$

where s"(p) is given in equation (39),

$$Z_{pm} = \frac{\pi}{8h^2 D_p \cos(\frac{p\pi}{2})} W_{kp} \qquad m = M+2$$

$$= \frac{m \sin(\frac{m\pi}{2})}{(m^2-p^2)} \qquad \text{otherwise} \qquad (51)$$

and

$$A_{M+2} = C_1 \qquad (52)$$

Solving equations (45) and (50) give [Am]. Thus the current distribution and input admittance may be calculated using equation (18)

$$Y_{in} = \sum_{m=1,3,}^{M} A_m \qquad (53)$$

NUMERICAL EXAMPLE AND RESULTS

A new method is presented to calculate the input admittance using Pocklington's integral equation and Hallen's integral equation. Specific example is concerned to Pocklington's integral equation as demonstration using equation (45),(46),(33),(42) and (44). Obtained results are tabulated in tables 1 and 2 and shown in figures 1-4.

CONCLUSION

It is concluded that the particular choice of weighting functions, basis functions and the type of kernel expansion helps the integrations to be performed completely analytic in addition that the coefficients of kernel expansion are calculated using the series summation.

Also the employed inner product is to be defined over the extended domain which reveals more orthogonalities to be achieved resulting in real matrix elements.

Hence this method is more simple, takes less C.P.U. time , storage, the results are fairly convergent and agree with experimental and other published results.

APPENDIX
CALCULATION OF INTEGRATION

$$\int_{-2h}^{2h} [E_{inc}(z) \int_{\bullet}^{z} \sin(k|z-z'|)dz'] \cos(\frac{p\pi z}{2h}) \, dz$$

Let U denotes the integration under consideration which is written

$$U = \int_{-2h}^{2h} [E_{inc}(z) \int_{\bullet}^{z} \sin(k|z-z'|)dz'] \cos(\frac{p\pi z}{2h})dz \tag{54}$$

with respect to the absolute value equation (54) is written as

$$U = \int_{-2h}^{2h} [E_{inc}(z) \int_{\bullet}^{z} \sin[k(z-z')]dz'] \cos(\frac{p\pi z}{2h})dz \tag{55}$$

carrying out the integration with respect to z' one has

$$U = \frac{1}{k} \int_{-2h}^{2h} [E_{inc}(z)(1-\cos(2kz)] \cos(\frac{p\pi z}{2h})dz \tag{56}$$

$$= \frac{1}{k} \int_{-2h}^{2h} E_{inc}(z) \cos(\frac{p\pi z}{2h})dz - \int_{-2h}^{2h} E_{inc}(z)$$

$$\cos(2kz) \cos(\frac{p\pi z}{2h})dz \tag{57}$$

for

$$\alpha_1 = \frac{p\pi}{2h} \tag{58}$$

equation (57) may be written as

$$U = \frac{1}{k} \{ \int_{-2h}^{2h} E_{inc}(z) \cos(\alpha_1 z)dz$$

$$- \int_{-2h}^{2h} E_{inc}(z) \cos(\alpha_2 z)dz$$

$$\int_{-2h}^{2h} E_{in}(z) \cos(\alpha_3 z)dz\} \tag{59}$$

$$\alpha_2 = (k + \alpha_1) \tag{60}$$

and

$$\alpha_3 = (k - \alpha_1) \tag{61}$$

Table 1 INPUT ADMITTANCE

h = 0.25 λ a = 0.007022 λ

Method	I.F.C.S Q=108 M=41	F.F.C.S Q=25 M=9	Measured by R.B.Mack.	Calculated by King	Calculated by Popovic
Y_{in} m℧	8.89-j3.94	8.80-j4.215	8.90-j3.46	9.825-j3.452	8.81-j3.31

Table 2 INPUT ADMITTANCE

h = 0.25 λ a = 0.03368974 λ

Method	F.F.C.S Q=263 M=37	I.F.C.S Q=25 M=9	Calculated by Mie	Calculated by King
Y_{in} m℧	10.07-j4.6	10.24-j4.03	9-j4	9.652-j4.392

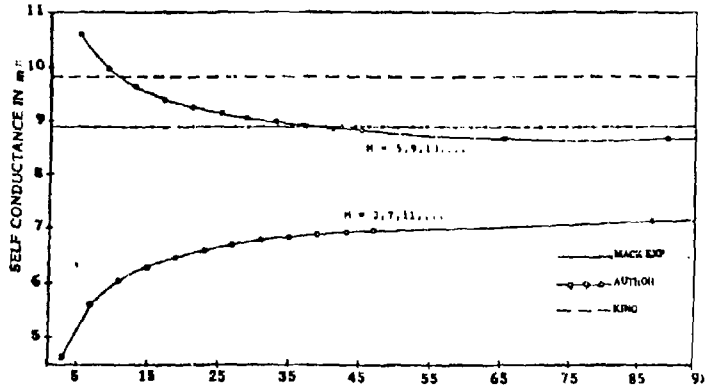

Fig. 1 SELF CONDUCTANCE AGINAST HIGHEST TRUNCATED ORDER OF CURRENT EXPANSION , a=0.007022λ ω=108

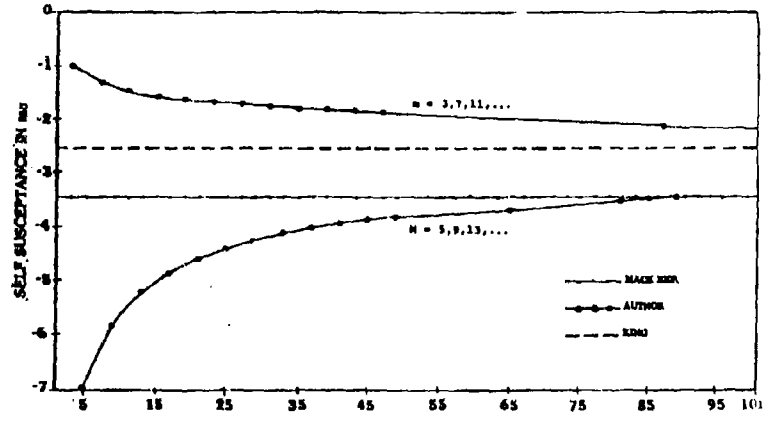

Fig. 2 SELF SUSCEPTANCE AGINAST HIGHEST TRUNCATED ORDER OF CURRENT EXPANSION, a 0.007022λ ω=108

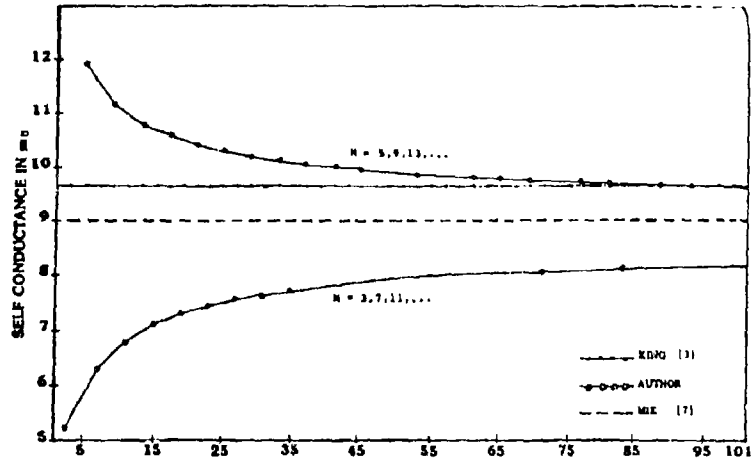

FIG. 3 SELF CONDUCTANCE AGAINST HIGHEST TRUNCATED ORDER OF CURRENT EXPANSION $a=0.003368979\lambda_0=.263$

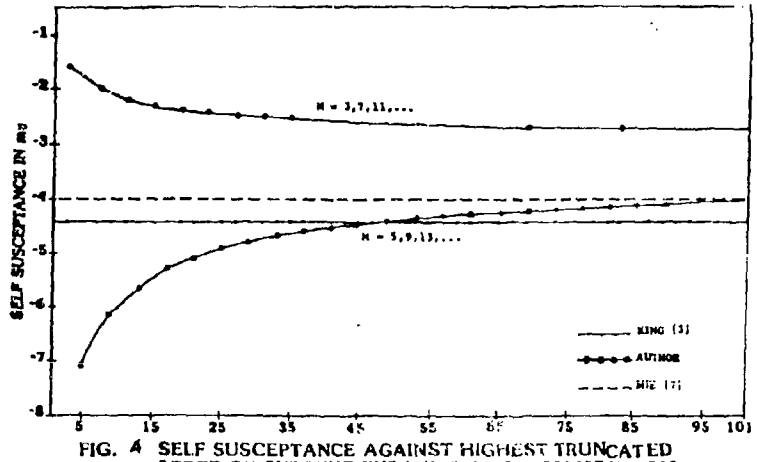

FIG. 4 SELF SUSCEPTANCE AGAINST HIGHEST TRUNCATED ORDER OF CURRENT EXPANSION $a=0.003368974\lambda_0=.263$

REFERENCES

[1] E.K.Miller ,"A selective survey of computational electromagnetics ," IEEE AP-36 , No 9 ,pp 1281-1305 , Sept 1988 .

[2] J.A.Cummins "Analysis of circular array of antennas by matrix method", PhD dissertation ,Electrical Engineering Dept. Syracuse Univ. New York 1969.

[3] D.H.Sinnot ,"Analysis and design of circular array by matrix method". Ph.D. dissertation , electrical engineering department . Syracuse University , N.Y. , Jan. 1972.

[4] T.K.Sarkar ,"A study of the various methods for computing electromagnetic field utilizing thin wire integral equation ," Radio Science , Vol. 18 . pp 28-38 , 1983 .

[5] R.F.Harington ,Field computation by moment methods ,N.Y., Macmillan,1968.

[6] R.J.Mitra (editor) , "Numerical and asymptotic techniques in electromagnetics ," Topics in applied physics Vol. 3 Springer Verlag , Berlin 1974.

[7] R.W.Hanning ,Numerical methods for scientists and engineers , N.Y. 1962

[8] K.A.Al-Badwaihy and J.L.Yen ," Extended boundary condition integral equation for perfectly conducting and dielectric bodies : formulation and uniqueness ", IEEE AP-23 , No 4 , pp 546-551, July 1975.

[9] R.H.Duncan and F.A.Hinchey ,"Cylindrical antenna theory ", J.Res. NBS, Sec.D (Radio Propagation) , Vol. 64 ,pp 569-584 , Sept./Oct. 1960.

[10] D.C.Chang ,"On the electrically thick monopole : Part I theoretical solution ," IEEE AP-16 , No 1 , pp 58-64 , Jan. 1968.

[11] R.W.P.King ,The theory of linear antennas ,Cambridge , Mass. : Harvard University Press, 1956.

[12] R.B.Mack,"A study of circular arrays ," Cruft Lab. Tech. report 383 , May 1963 .

[13] B.D.Popovic,"On the polynomial approximation of current along a thin symmetric dipole ," Proc. IEEE Vol. 117 , No 5 pp 873-878 ,May 1970.

Upgrading Common Wire-Grid MoM Programs

Aharon Blank

Tel-Aviv University, P.O.B 193 Kiryat Ono, 55228, ISRAEL.

Shmuel Averbuch

Department 2464, Israel Aircraft Industries, Ben Gurion Airport, ISRAEL.

Abstract- A method of moments using Bi-linear surface patches for modeling and solving the electromagnetic scattering at low frequencies, is presented. The Bi-linear method of modeling a body is discussed, and it is shown how a sub-domain surface current modes are constructed on a body described by a the Bi-linear surface patch method. A brief description of the computer code and the method of upgrading common wire-grid programs to handle the Bi-linear patches is given and finally some numerical results for some canonical bodies are provided.

1. INTRODUCTION

MANY COMPUTER CODES, based on the MoM (Method of Moments) for determining the electromagnetic scattering from bodies in the resonance region have been presented in the past two decades [1-4]. Wire grids [1], polygonal plates [2,3], or triangular plates [4], have been used to model the body. For these models, it is a great effort to define the sub-domain current modes for complex bodies. Moreover, the geometry of compucer aided designed (CAD) bodies are not usually modeled and stored in computers using wire grids or triangulars.

This paper presents a new and efficient approach to modeling a realistic complex structure using Bi-linear surface patches. The electromagnetic scattering problem can be modeled more easily and can provide more accurate results in less computer time. Also, the new method can be easily combined with computer aided design (CAD) programs to perform automatic calculations for realistic bodies. Another important feature of this method, is that it can use common wire-grid programs, after a minor upgrading process.

2. BI-LINEAR PATCH THEORY

The most common way of approximating the geometry of a complex body in the computer is the use of the Bi-linear patch geometry [7].

The surface of the scattering body is divided into an assembly of Bi-linear patches.

The geometry of each patch is shown in Fig 1. The coordinates of a point $\bar{P}$ on the patch is given by:

$$\bar{P} = \bar{P}_{12} + v(\bar{P}_{34} - \bar{P}_{12}) \qquad (1\text{-a})$$

where

$$\bar{P}_{12} = \bar{P}_1 + u(\bar{P}_2 - \bar{P}_1) \qquad (1\text{ b})$$

$$\bar{P}_{34} = \bar{P}_3 + u(\bar{P}_4 - \bar{P}_3) \qquad (1\text{-c})$$

From eqs. 1-a,b and c it follows that:

$$\bar{P} = [\bar{P}_1 + u(\bar{P}_2 - \bar{P}_1)](1-v) + v[\bar{P}_3 + u(\bar{P}_4 - \bar{P}_3)] \qquad (1\text{-d})$$

Mathematically speaking, the Bi-linear patch is a finite portion of the hyperboloidal surface.

It is sufficient to store the coordinates of the four corners $\bar{P}_1, \bar{P}_2, \bar{P}_3$ and $\bar{P}_4$ only in order to fully describe the patch.

Any quadrangle can be considered as a special case of the Bi-linear patch. However, in cases where the four corners of the patch do not lie in a plane, the Bi-linear patch fits the surface of the scattering body more accurately than quadrangles. For this reason, and for the reason of using sinusoidal sub-domain current modes, relatively large patches (up to a leading dimension of more than a quarter of a wavelength) can be chosen when Bi-linear patches are used.
The current modes on each patch are defined following the natural way in which the patch is described, considering Fig. 1 the Bi-linear patch is approximated by two sets of wires, one set is in the direction of the lines of constant v, and the other in the direction of the lines of constant u. On the wires of constant v the current is given by:

$$I(z) = \hat{z}\frac{Sin(kz)}{Sin(kl)} \qquad (2\text{-a})$$

where

$$k = \frac{2\pi}{\lambda} \qquad (2\text{-b})$$

l - is the wire length
λ - is the wavelength

and $\hat{z}$, z are the unit vector and the coordinate along the wire.

The current on the wires of constant u are written similarly.
Having defined the current elements, the mutual impedance of each pair of wire current elements can be computed efficiently [5].
In order to demonstrate how the surface of the scattering body is divided into Bi-linear patches and how the sub domain current modes are defined, consider the surface in Fig 2-a which is a portion of a cylinder.
First the surface is cut from the top to the bottom into slices which can have a leading dimension of up to 0.25λ.
Then each slice is divided into segments which again, can be up to 0.25λ long as shown.
The corners of the patches thus obtained form the matrix of Fig 2-b which describes the surface accurately.
The appropriate sub-domain current modes which describe the currents in the two major directions are consequently defined on the surface patches. An example of the first current mode in the axial direction is shown in Fig. 2-c. The surface current mode of Fig 2-c is approximated by a finite number of dipoles with the current distribution of the form described by Eq.2. These current modes can be considered as the generalization of the modes used by Newman in the case of polygonal patches [6].
The other current modes in both major directions (axial and circumfrencial) are summarized in Table 1 which identifies the current modes by their 3 creating lines (one for the maximum of the sine and two zero lines as shown in Fig. 2-c), every line segment is identified by the two points which it connects.

second null line	maximum line	first null line	mode number
9 - 10	5 - 6	1 - 2	1
10 - 11	6 - 7	2 - 3	2
11 - 12	7 - 8	3 - 4	3
3 - 7	2 - 6	1 - 5	4
4 - 8	3 - 7	2 - 6	5
7 - 11	6 - 10	5 - 9	6
8 - 12	7 - 11	6 - 10	7

Table 1. Current modes on the cylindrical surface of Fig.2.

Any complex surface can be divided into Bi-linear patches similarly.
For intersecting surfaces such as those of Fig. 3, the current modes are constructed separately for each surface (matrix) and an appropriate overlapping current modes must be added in both major directions.
In Fig. 3 it is shown how the overlapping current modes for one current direction are defined between the surfaces, in addition to the regular current modes. These current modes are summarized in Table 2.

second null line	maximum line	first null line	mode number
7 - 8	5 - 6	1 - 2	1
8 - 9	4 - 5	2 - 3	2
10 - 11	5 - 6	1 - 2	3
11 - 12	4 - 5	2 - 3	4

Table 2. Overlapping current modes for one current direction.

This procedure can be manual, for few intersecting parts, or automatic for larger numbers of intersecting parts.

3. THE COMPUTER CODE

This section gives a short description of the computer code and the upgrading process.
The upgrading process is made as follows:
The computer code receives the matrix of the geometrical coordinates of the body, the user has to assure that the points are not too far apart (maximum distance of 0.25λ between the points). This is easily performed by the computer codes dealing with the planning of the body as mentioned earlier.
Consequently, the current modes are defined as described above.
The impedance matrix of surface/surface dipoles is computed by numerical integration using the regular impedance elements subroutine which computes the wire/wire mutual impedance, Every single matrix element is calculated as the sum of about 64 small matrix elements of wire/wire type. The wire/wire type impedance

elements are easily computed [5,10].
The excitation vector is computed also by numerical integration using the regular wire excitation subroutine. Afterwards, the usual matrix solution and RCS computation can be calculated by the regular program.
At present, the program can deal with perfectly conducting bodies or bodies that have some surfaces which are perfectly conducting and some surfaces which are thin dielectric layers, (kt<0.01 k-wave vector, t-patch thickness).
In the case of dielectric patches the impedance matrix has the added contribution of [8]:

$$\Delta Z_{mn} = \frac{\eta}{\gamma t} * \iint J_m \bullet J_n ds \qquad (3\text{-a})$$

$$\eta = \sqrt{\frac{\mu}{\varepsilon}} \qquad (3\text{-b})$$

$$\gamma = j\omega\sqrt{\mu\varepsilon} \qquad (3\text{-c})$$

Where t - the thickness of the dielectric material.
J_m, J_n - are the sub domain basis current modes.
The integration is on the overlapping area between the two modes (if it exists).
A more general code is now under final stages of development which deals with dielectic materials with width of up to 0.1λ , and coated bodies, using the method described in [12].
The code provides a useful engineering tool for computing the RCS of the body very accurately and easily, using a standard geometrical description of the body.

4. NUMERICAL RESULTS

In this section some numerical results are presented, which show how the Bi-linear patch segmentation can be easily applied to complex bodies.
Fig. 4. shows a sphere whose radius is 0.46λ. The geometry of the sphere is represented by the Bi-linear patch method.
The bistatic RCS of this sphere was calculated for two cases. In the first case, the illumination was from the direction of the positive z axis which is normal to the small opening caused by the modeling. In the second case, the illumination was from the positive x axis direction. The polarity was as shown in Fig.4 . The computed results are compared to analytical results of Ruck [9] and appear in Fig. 5. It can be seen that the computed results are accurate, but depend slightly upon the method by which the body is approximated.
Fig. 6-b shows a Bi-linear surface patch.
The surface was made by twisting an original flat plate of 2.19*1.25 wavelengths in dimension, which lied in the y=x plane (Fig 6-a). The line segment between points 1-2 was twisted to lie along the x axis, and the line segment between points 3-4 was twisted to lie along the y axis.
Both surfaces (the flat plate and twisted plate) were computed and were measured in the IAI radar range. The flat plate was used as a reference. The measured results (VV polarization) appear in Fig. 7. The computed results appear in Fig. 8. It can be seen, that the agreement between calculated results and measurements is very good.

ACKNOWLEDGMENT

The authors wish to express thanks to Saeid Shammas and Shmuel Goldberg for their help in the various stages of the work.

REFERENCES

[1] J.H. Richmond, "A wire-grid model for scattering by conducting bodies," *IEEE Trans. Antenn. Prop.*, vol. AP-14, pp 782-786, Nov. 1966.
[2] G.J. Burke and A.J. Poggio, "Numerical electromagnetic code-Method of moments," Naval Ocean Systems Center tech. document 116, AFWL-TR-76-320, July 1977.
[3] E.H. Newman, P. Alexandropoulous, and E. K. Walloon, "Polygonal Plate Modeling of Realistic Structures," *IEEE Trans. Antenn. Prop.*, vol. AP-32, No. 7, July 1984, pp. 742-747.
[4] S.M. Rao, D.R. Wilson, A.W. Glisson, "Electromagnetic scattering by Surfaces of Arbitrary Shape," *IEEE Trans. Antenn. Prop.*, Vol. AP-30, No 3, May 1982.
[5] J.H. Richmond and N.H. Geary, "Mutual impedance of non-planar-skew sinusoidal dipoles," *IEEE Trans. Antenn. Prop.*, vol. AP-23, May 1975.
[6] E.H. Newman and P. Tulyathan, "A Surface Patch Model for Polygonal Plates," *IEEE Trans. Antenn. Prop.* vol. AP-30, No.4, July 1982, pp. 588-593.
[7] S. Averbuch, "Computational Geometry," IAI Training Center, publication No. 7597, Dec. 1985.
[8] E. H. Newman, M.R. Schrote, "An Open Surface Integral Formulation for Electromagnetic Scattering by Material Plates,"
IEEE Trans. Antenn. Prop. Vol. AP-32, No. 7, July 1984.
[9] G.T. Ruck, C.K. Krichbaum, D.E. Barrick, W.D. Stuart, "Radar Cross Section Handbook," Volume 1, P.152.
[10] E.H. Newman, D.M. Pozar , "Considerations for Efficient Wire/Surface Modeling," *IEEE Trans. Antenn. prop.* Vol. AP-28, no.1, Jan 1980.

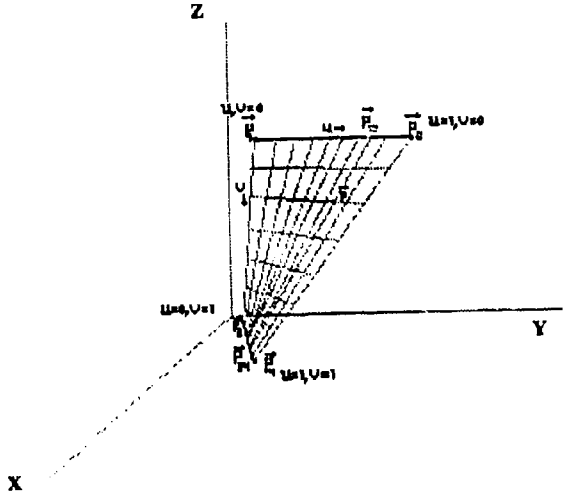

Fig. 1: A Bi-linear patch

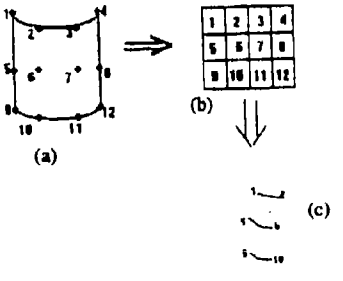

Fig. 2: (a) Points on the body which describes it's geometry.
(b) 2-D map of the body's surface in the memory.
(c) A single surface current dipole.

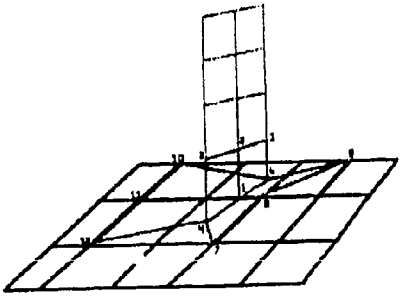

Fig. 3: Overlapping modes for two intersecting bodies (see text).

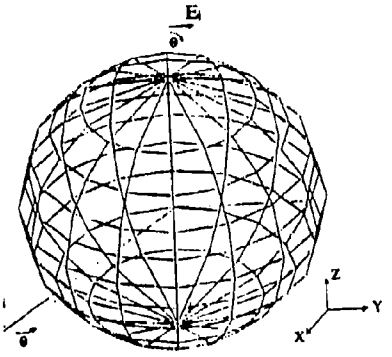

Fig. 4: A sphere geometry.

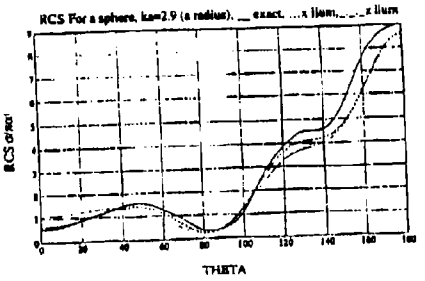

Fig. 5: Bistatic RCS of a sphere, Analytical results appear in solid line.

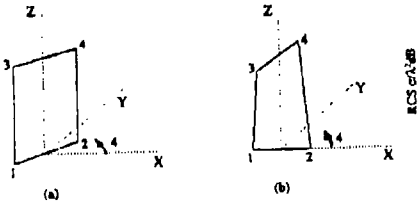

Fig. 6: Plate and twisted plate geometry.

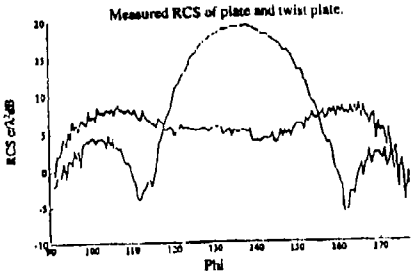

Fig. 7: Measured RCS results for the plate and twisted plate

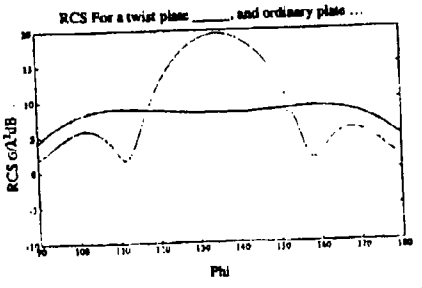

Fig. 8: Computed RCS results for the plate and twisted plate.

UTILIZING STRUCTURE SYMMETRY IN REDUCING THE CPU TIME FOR COMPUTING THE MOMENT METHOD [Z] MATRIX ELEMENTS

Zeyad O. Al-Hekail
Electrical Engineering Department, King Saud University
PO Box 800, Riyadh 11421, Saudi Arabia

1. Introduction

Method of moments (MM) is often used to accurately compute the radiated or scattered fields from simple or complex structures. However, huge computer memory is required when utilizing it to solve electrically large structures. Even if the memory requirements are satisfied by the available computers, the needed CPU time is often very long and in many cases unjustified.

In some problems, such as scattering from plate structures, it was noted that the main portion of the CPU time is consumed in the process of computing the *[Z]* matrix elements. The rest of the CPU time is for inverting the matrix and computing the fields. The matrix inversion share of the total CPU time increases with the increase of the number of matrix elements, and can become the main share for relatively large problems. That depends on the nature of the moment method code and the way it computes the matrix elements as well as on the computer vectorization capabilities.

The CPU time required for computing the *[Z]* matrix can be dramatically reduced by utilizing the possible symmetry in the problem. Such symmetry may not be very obvious, but it is not always difficult to observe. In this paper, a technique which is used to reduce the required CPU time for computing the *[Z]* matrix elements is explained. This technique utilizes the possible symmetry in the problem. An example involving MM computation of the scattered fields from a large triangular dihedral using the ESP4 code [1] is worked out in detail with CPU time reduction of about 75%. Some notes are also given on the use of this code for solving plate modeled structures.

2. Triangular dihedral

Figure 1 shows a triangular dihedral consisting of two triangular plates. The plates are such that $L_1=2m$, $L_2=1m$ and $\psi=90^\circ$. The back or bistatic scattering from such a structure is an interesting problem that involves different scattering mechanisms and has been investigated in several studies [2,3,4,5,6]. The need for accurately analyzing the scattered fields from dihedral structures arises in several situations; for example, when using the dihedral as a calibration target in scattering measurements or when a reference solution is needed for checking another method's result.

For reasons to be clarified later, let us use a 4-plate model for the dihedral, such as shown in Figure 2(a). Also, let us use the ESP4 code, which is a MM code, to solve for the scattered fields from the dihedral. The code solves for the currents induced on the dihedral surface by an incident

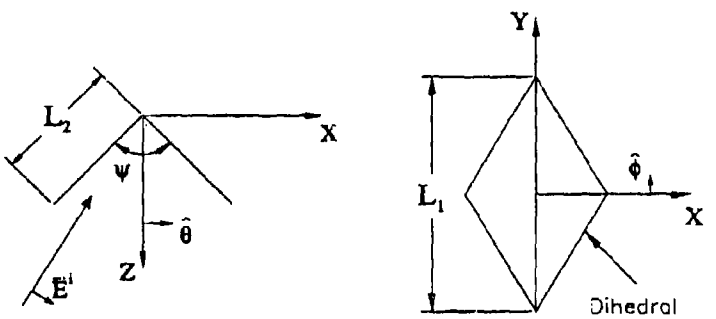

Figure 1: Triangular dihedral.

electromagnetic field, say a plane wave. The scattered fields are then computed using radiation integrals. This code uses the Electric Field Integral Equation to relate the unknown induced currents to the incident fields. The unknown currents are expanded in terms of N surface patch modes that cover each plate such as shown in Figure 2(b). In Figure 2(b), the plate is divided (segmented) into a set of quadrilateral surface patches. The current modes have a piecewise sinusoidal function that covers two patches. That is indicated in the figure by placing arrows (which represent modes) such that every arrow covers two patches, i.e., the patches covered by that mode. Overlapping modes that cover the junction between any two plates are also included in the expansion of the unknown currents such as shown in Figure 2(c). That leaves us with the following unknown current vectors $[I_1],[I_2],[I_3],[I_4],[I_{1,1}],[I_{1,2}],[I_{1,3}]$ and $[I_{1,4}]$ that corresponds to the currents on the plates in the way shown in Figure 2(d). Then, by enforcing the Electric Field Integral Equation for N linearly independent test modes, one obtains an NXN simultaneous linear equations, which can be written as

$$[Z]\, I = V$$

where $[Z]$ is the NXN impedance matrix, V is the voltage vector with length N, I is the unknown current vector with length N. These linear equations can then be solved for the unknown currents.

The impedance matrix is the main concern of this paper and can be written as shown in Figure 3. The element Z_{mn} of $[Z]$ is called the mutual impedance between the current modes m and n. Computing the elements of such a matrix involves many computations and can consume a long CPU time. This, however, can be reduced by utilizing the symmetry of the structure under consideration. For example, one can say that $Z_{mn} = \pm Z_{kl}$ if mode m is identical to mode k and mode n is identical to mode l and the relative position of mode k to mode l is the same as that of mode m to mode n. The $\pm$ sign is to accommodate for differences in the directions of the assumed reference currents.

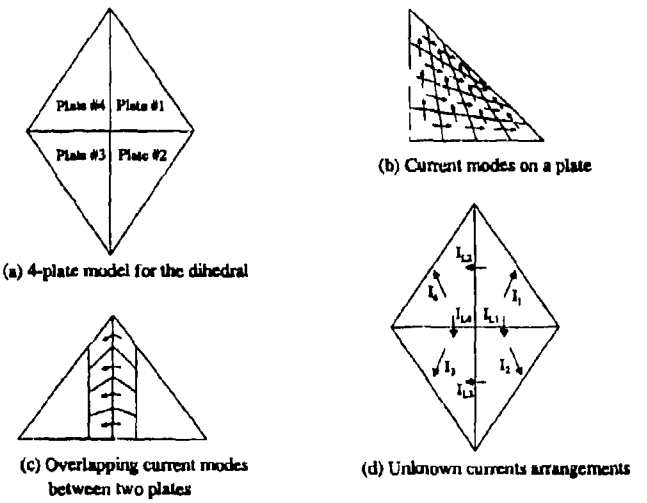

(a) 4-plate model for the dihedral

(b) Current modes on a plate

(c) Overlapping current modes between two plates

(d) Unknown currents arrangements

Figure 2: 4-plate model and current arrangements for the triangular dihedral

The *[Z]* matrix of the triangular dihedral problem can be defined by blocks such as those shown in Figure 3. Block (1/1) (the upper left) contains the mutual impedances between the current modes of the first plate. Block (1/2) contains the mutual impedances between the current modes of plate #1 and the current modes of plate #2. Likewise, block (L_1/L_1) contains the mutual impedances between the first overlapping current modes. Block (L_1/1) contains the mutual impedances between the first overlapping current modes and the first plate current modes. Every block is labeled with a capital letter (A,B,C,....). Only blocks labeled with an underlined bold letter need to be computed. The other blocks can then be filled according to the labels. For example, block (2/1) is labeled with "B" that means that the elements of block (2/1) are identical to block (1/2) elements. Also, the elements of block (L_3/4) are equal to (-) the elements of block (L_2/1). The relations of Figure 3 are evident from the symmetry of the problem. For example, blocks (1/1), (2/2), (3/3) and (4/4) are the same because plates 1,2,3 and 4 are identical and have identical segmentation. Also, block (2/3) is the same as block (1/4) because plate 2 current modes are identical to plate 1 current modes, plate 3 current modes are identical to plate 4 current modes, and the locations of plate 2 modes relative to plate 3 modes are the same as the locations of plate 1 modes relative to plate 4 modes. Likewise, block (L_4/4) elements equal to the negative of (L_1/1) elements. That is because L_4 modes are identical to L_1 modes, plate 4 modes are identical to plate 1 modes and the locations of L_4 modes

1/1 **A**	1/2 **B**	1/3 **C**	1/4 **D**	$1/L_1$ **E**	$1/L_2$ **F**	$1/L_3$ **G**	$1/L_4$ **H**
2/1 B	2/2 A	2/3 D	2/4 C	$2/L_1$ -E	$2/L_2$ G	$2/L_3$ F	$2/L_4$ -H
3/1 C	3/2 D	3/3 A	3/4 B	$3/L_1$ H	$3/L_2$ -F	$3/L_3$ -G	$3/L_4$ E
4/1 D	4/2 C	4/3 B	4/4 A	$4/L_1$ -H	$4/L_2$ -G	$4/L_3$ -F	$4/L_4$ -E
$L_1/1$ **I**	$L_1/2$ -I	$L_1/3$ **L**	$L_1/4$ -L	L_1/L_1 **M**	L_1/L_2 **N**	L_1/L_3 -N	L_1/L_4 **O**
$L_2/1$ J	$L_2/2$ K	$L_2/3$ -J	$L_2/4$ -K	L_2/L_1 **P**	L_2/L_2 **Q**	L_2/L_3 **R**	L_2/L_4 -P
$L_3/1$ K	$L_3/2$ J	$L_3/3$ -K	$L_3/4$ -J	L_3/L_1 -P	L_3/L_2 R	L_3/L_3 Q	L_3/L_4 P
$L_4/1$ L	$L_4/2$ -L	$L_4/3$ I	$L_4/4$ -I	L_4/L_1 O	L_4/L_2 -N	L_4/L_3 N	L_4/L_4 M

Figure 3: The impedance matrix *[Z]*.

relative to plate 4 modes are the same as the locations of L_1 modes relative to plate 1 modes. The only difference between the two cases is the reference current direction. L_1 modes reference current is flowing out of plate 1 while L_4 modes reference current is flowing into plate 4, leading to the (-) sign in the above relation. Note that, in general, the above *[Z]* matrix is not symmetric. It is symmetric if the test modes used in enforcing the integral equation are the same as the expansion modes [1]. So, the relation $Z_{mn}=Z_{nm}$ only holds when modes m and n are identical.

One can see that this technique can save about 75% of the CPU time required for computing the *[Z]* matrix elements. Figure 4 shows the CPU time required to compute the *[Z]* matrix elements versus frequency, with and without using symmetry. The figure should be viewed as if it shows only a relative time, since it greatly depends on the machine and its compiler and vectorization capabilities. But, for the sake of an example, on a CRAY YMP computer, the CPU time needed to compute a 264X264 matrix was 68 seconds. The use of the symmetry mentioned above reduced that time to 17.1 seconds. A 1680X1680 matrix computation consumed about 650 seconds on the same

computer, using symmetry. Without using symmetry that time would have been about 2600 seconds. For reference, the CPU time to invert this matrix and to compute the radiated fields was about 100 seconds. Note that this latter time is relatively short because of the available vectorization on the CRAY computer. On a non vector computer, the matrix inversion time would be more than the computation time for such a large matrix. For the interested reader, Figure 5 shows the X-Z plane, θ-Polarized back scattered field from the dihedral at 1GHz.

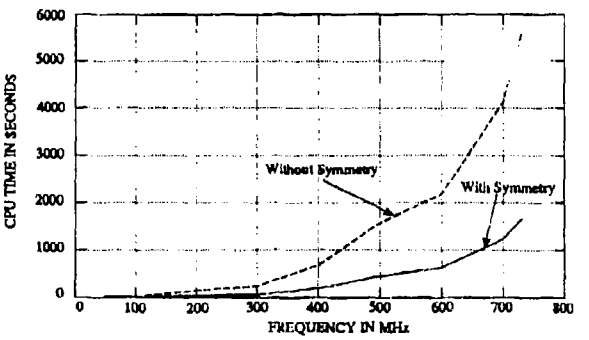

Figure 4: The CPU time required to compute the *[Z]* matrix elements versus frequency with and without using symmetry. The dihedral dimensions are $L_1=2m$, $L_2=1m$ and $\psi = 90^{\circ}$.

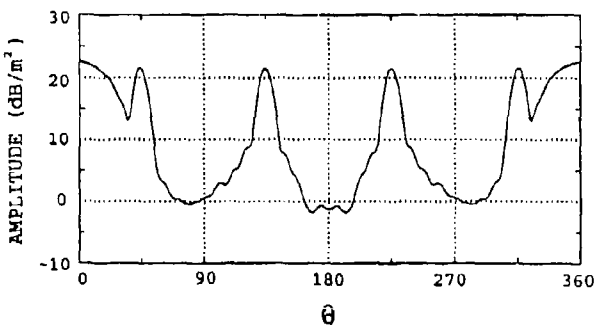

Figure 5: θ-Polarized backscattered field from the dihedral at 1GHz, X-Z plane.

Modeling and segmentation issues

The ESP4 code utilizes one method for plate segmentation, such as shown in Figure 2(b). Such a method is general and does not take advantage of the nature of the plate that needs to be segmented. That results in an inefficient segmentation of the plates, i.e., more unknown current modes, and hence requires more computer memory, when compared to other possible segmentation methods. In fact, the above 4-plate model for the triangular dihedral results in fewer modes than a 2-plate model, using the default ESP4 segmentation method (routine) in both cases. This is because of the general nature of the segmentation routine. Using a 10-plate model for the dihedral, such as the one shown in Figure 6(a), results in an even fewer unknown current modes. A better approach is to "custom make" a segmentation routine for the problem under consideration. For example, one can segment the dihedral plates as shown in Figure 6(b). Such a segmentation approach results in about a minimum number of unknown current modes. But, one needs to make sure that such segmentation methods produce convergent results before the resulting solution can be trusted.

Figure 7 shows the number of unknown dihedral current modes versus frequency for the above mentioned four segmentation methods. In all cases the maximum segment width is .2 wavelength. One can see that the 4-plate model results in a smaller number of modes when compared with the 2-plate model. Note that unlike the 2-plate model, the 4-plate model permits an efficient use of the structure symmetry, which is the reason behind choosing the 4-plate model at the beginning of this section. The 10-plate model requires less computer memory and CPU time when compared to the 4-plate model. However, utilizing the structure symmetry in the 10-plate model is more complicated. The custom made segmentation with the 4-plate model results in the smallest number of unknown current modes, compared to the other 3 models, and hence the minimum required computer memory and CPU time.

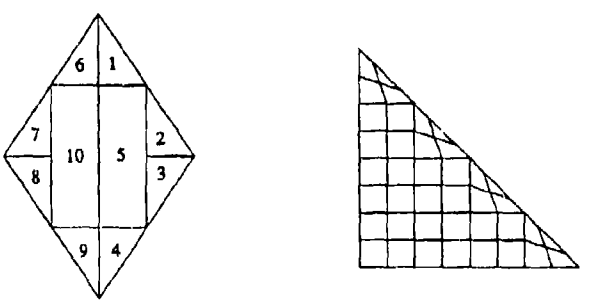

Figure 6: a) 10-plate model for the triangular dihedral. b) Custom segmentation for the triangular plate.

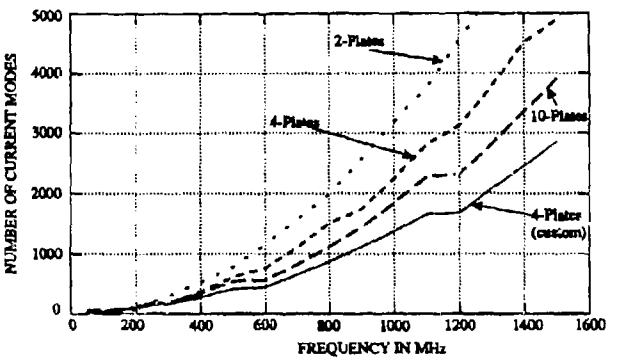

Figure 7: Number of current modes versus frequency for 2-plate, 4-plate and 10-plate models for the triangular dihedral with the ESP4 code segmentation, as shown in Figure 2(b). Also shown in the figure is the number of current modes for the 4-plate model with custom segmentation, as shown in Figure 6(b). In all cases the maximum segment width is .2 wavelength.

3. Conclusions

A technique that can save about 75% of the CPU time required for computing the MM *[Z]* matrix elements is described. This technique utilizes the structure symmetry that exists in the problem. It requires extra work and specific treatment for every new problem. However, accurate solutions to some problems are always desired, especially in the absence of measurement results. Lack of measurement's facility or the unacceptable cost or time required for building measurement's model(s) can make this technique's extra work justifiable for several interesting problems. Also, the process of utilizing the symmetry in the problem can be simplified or built in the moment method codes, leaving the user with minimum work to do.

It was noted that the *[Z]* matrix size depends on the method used for segmenting the plates making the structure under consideration. Designing a specific segmentation routine may result in a reduced number of unknowns and hence less memory and CPU time requirements. The structure symmetry may be further utilized to reduce the number of unknowns. This can be achieved by realizing that several symmetrical unknown current mode amplitudes are equal. One can use this information in solving the linear equations, to reduce CPU time, or in reducing the number of unknowns in the problem, to reduce memory requirements.

4. References

[1] Newman, "A user manual for the Electromagnetic Surface Patch Code: ESP version IV, " Technical Report 716199-11, The Ohio State University, ElectroScince Laboratory, Department of Electrical Engineering, August 1988.

[2] Eugene F. Knott,"RCS Reduction of Dihedral Corners," *IEEE Trans. Antennas Propagat.*, vol. AP 25, pp. 406-409, May 1977.

[3] Akhter and R.J. Marhefka, "Far Zone Scattering from Rectangular and triangular Dihedrals in the Principal Plane," Technical Report 721198-1, The Ohio State University, ElectroScince Laboratory, Department of Electrical Engineering, June 1988.

[4] Timothy Griesser and Constantine Balanis, "Dihedral Corner Reflector Backscatter Using Higher Order Reflection and Diffraction," *IEEE Trans. Antennas Propagat.*, vol. AP-35, pp. 1235-1247, Nov. 1987.

[5] Timothy Griesser and Constantine Balanis. "Backscatter Analysis of Dihedral Corner Reflectors Using Physical Optics and Physical Theory of Diffraction," *IEEE Trans. Antennas Propagat.*, vol. AP-35, pp. 1137-1147, Oct. 1987.

[6] Zeyad O. Al-hekail, *A Hybrid Method for Computing the Scattered Fields from Complex Structures*, Ph.D. thesis, Ohio State University, Department of Electrical Engineering 1992.

NUMERICAL-ANALYTICAL ALGORITHMS BASED ON DUAL SERIES EQUATIONS TECHNIQUE

Yury TUCHKIN, Vladimir VEREMEY, Yury SVISCHOV and Valentin DUDKA
Institute for Radiophysics & Electronics Ukrainian Academy of Sciences,
12 ac Proskura st. Kharkov, 310085 Ukraine

ABSTRACT. The Dual Series Equation Technique (DSET) is applied to analyzing cylindrical and spherical reflector antennae and to calculation of the radar cross-sections of cavity-backed aperture structures. It was proved that the method is a rigorous one and may serve as effective tool in reflector antenna design and in the analysis of near and far fields scattered from the canonical cavity-backed apertures formed by slotted circular cylinders or by spheres with a circular hole.

It is shown that the obtained numerical DSET codes can be used both in a resonance wave band and in a shortwave band (more than 100 wavelengths in the aperture). A considerable advantage of the suggested approach is that the method allows to obtain results with any prespecified accuracy and that is why DSET codes can be used as a criterion of the correctness of the results obtained by the approximate methods (Such as Method of Moments, Finite Differences Method, Finite Elements Method and others). Characteristics of the antennae formed by one or two circular cylindrical reflectors or by the spherical ones with an additional axial reflector have been calculated and numerical results are presented. The cases of a line magnetic or electrical current excitation of cylindrical antennae and of a monopole source excitation of the spherical antennae are considered. A numerical analysis of radar cross-section of structures formed by a finite number of circular cylinders with longitudinal axial slots is proposed. The influence of the "interaction" between cavity-backed apertures on the scattering characteristics of the structures is discussed.

1. Well known approximate methods for solving the diffraction wave problem on a conductive reflector is effective and rather simple but it is impossible to estimate the accuracy of solutions thus obtained by means of these methods.

The widely used direct numerical methods (MM,FD,FE) results in systems of linear equations of the first kind with ill-conditioned matrices; the application of these methods leads to incorrect results when scatterers wavedimensions are considerable.

A method of investigating cylindrical (two-dimensional) antennae with the reflectors of circular or arbitrary cross-sections or spherical antennae (the scalar case) was proposed in [1-9]. The main peculiarity of the suggested method is the reduction of the problem to a linear algebraic equations system of the second kind, i.e. to an equation in l_2 which has a form $(I + H)x = b$,where I is an identical matrix operator and $H = \{h_{nm}\}$ is a compact matrix operator in l_2 , x and b are vectors in l_2 . As a matter of fact, in all considered cases the stronger feature of H is valid:

$$\sum_{n=-\infty}^{\infty} \sum_{m=-\infty}^{\infty} (1 + |n|)(1 + |m|)|h_{mn}|^2 < \infty \qquad (1)$$

The procedure of singling out the operator part and then the analytical inversion of this part for obtaining the system of the second kind is rather complicated. This complexity requires from the investigator a higher qualification in numerical methods for using the

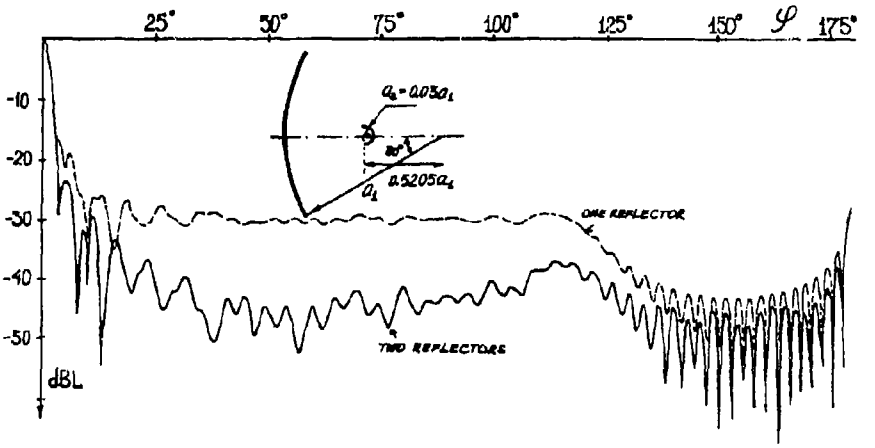

Fig 2. Far field patterns of the spherical two-reflectors antennae

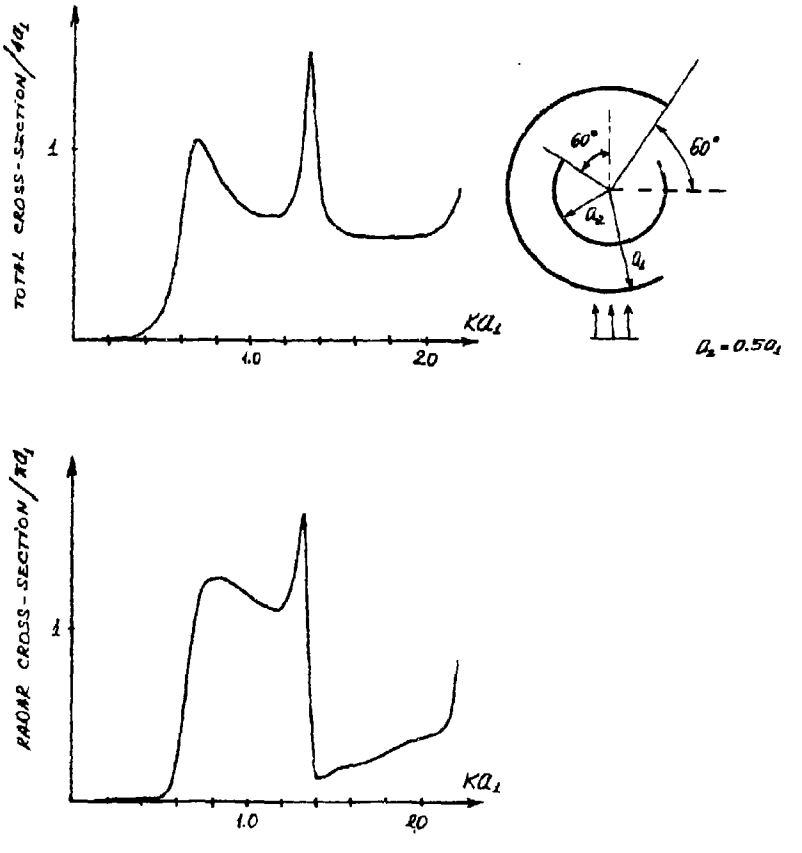

Fig 3. The Total and Radar Cross- Sections of two slotted cylinders versus frequency parameter $ka_1 = 2\pi a_1/\lambda$

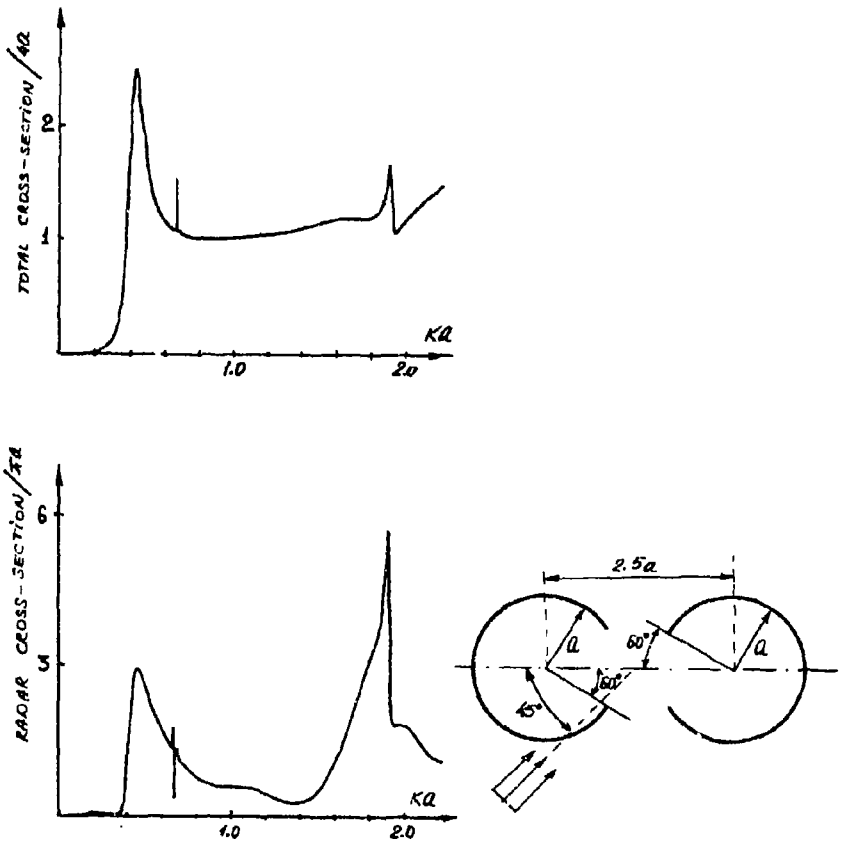

Fig 4. The Total and Radar Cross- Sections of two slotted cylinders versus frequency paremeter $ka_1 = 2\pi a_1/\lambda$

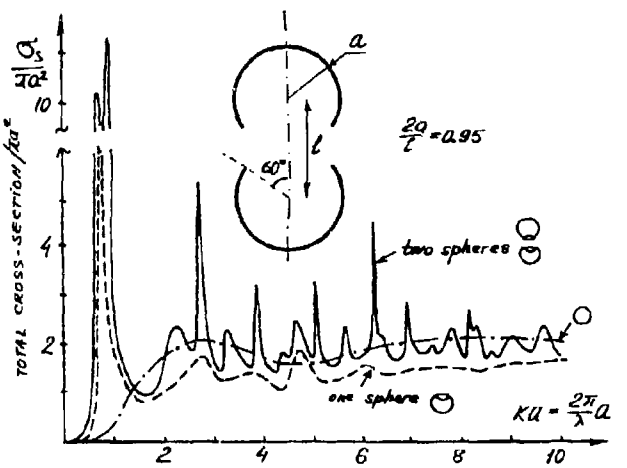

Fig 5. The Total Cross- Sections of two spherical screens with a hole versus frequency paremeter $ka = 2\pi a/\lambda$

MOMENT METHOD ANALYSIS OF NON-ORTHOGONAL WAVEGUIDE TO WAVEGUIDE COUPLING THROUGH SLOT

S.CHRISTOPHER, A.K.SINGH AND K.U.LIMAYE
Electronics and Radar Development Establishment
Bangalore-560 093, India

Abstract- A detailed analysis of finite wall thickness non-orthogonal rectangular waveguide to waveguide coupling through centered inclined slot is carried out. Pertinent integral equations for slot electric field are solved using the method of moments. Slot scattering parameters are then deduced; including slot resonant length and equivalent series impedance. A special case of numerical results for resonant length and scattering parameters are compared with results available in the literature. The analysis presented in this paper has significant application in the design of feeder network for planar slotted array of complex geometries.

I. INTRODUCTION

In the design of high performance slotted arrays, two structures are commonly used to feed the power [1]. In the first case, each waveguide with radiating slots in one of its broad walls is short-circuited at one end, at an appropriate point beyond its last slot, and fed from the other end. In second method, the branch-line waveguides (containing radiating slots) are short-circuited at both the ends and an additional waveguide (called mainline waveguide) underneath the branchline waveguide is used to feed the radiating slots via coupling slots situated in the common wall at the junction of mainline and branchline waveguides. Since most of the slotted array designers use a center fed design as a broad banding technique [2], the second configuration is a preferable choice. Also, depending on the array geometry and space constraints, the mainline may or may not be perpendicular to the branchline. Although, there has been a significant theoretical and experimental attack on crossed orthogonal waveguide slot coupler [3-7], no literature is available, to the best of our knowledge, for the case where branchline and mainline waveguides are not perpendicular. In this paper, an attempt has been made to analyse non-orthogonal waveguide to waveguide slot coupler. The procedure begins with the development of fundamental integral equations using Schelkunoff's equivalence principle, dyadic Green's function formulations in mainline, branchline and cavity regions, and appropriate boundary conditions. Since the feeding waveguide generally adopts resonant slot to couple power to branchline waveguides, effort has been made to calculate the resonant length accurately. The computer code developed employs integral equation formulation of the problem that is solved by the method of moments. In the present case, contrary

to earlier resonance conditions, a more appropriate resonance condition has been adopted to calculate resonant length and other scattering parameters.

The moment method code developed, computes various coupling slot characteristics; which include, slot resonant length, backscattered and forward scattered wave amplitude and phase variation, and coupling ov a range of values of mainline and branchline 'a' and 'b' dimensions, wall thickness, slot tilt angle, angle between mainline and branchline waveguides, slot width and frequency. The validity of the code developed is established by comparing it for a special case where mainline becomes perpendicular to branchline against published results in the literature.

II. FORMULATION OF THE PROBLEM

The geometry of the nonorthogonal waveguide coupler under investigation is depicted in Fig 1.1. It consists of two air filled rectangular waveguides namely mainline and branchline waveguides crossing each other at angle Θ_{mb} of cross-sections ($a_m x b_m$) and ($a_b x b_b$) respectively. The branchline waveguide is coupled to mainline waveguide by a centered inclined rectangular slot of dimensions (2lxwxt) cut in the common wall between mainline and branchline.

Upon invocation of Scheiknuoff's equivalence principle the do of the problem of interest is divided into three regions : maina veguide interior; the branchline waveguide interior and a rectangular cavity of dimension (2lxwxt) designated as regions I, III, II respectively as shown in Fig(1.2). In this problem, only the transverse component of slot field exists across slot and this is equivalent to a longitudinal magnetic current. For the purpose of solving the problem, the slot end facing the mainline waveguide side y=b and y=b+T are covered with perfectly conducting sheets placed over gap and magnetic current sheets (Km_ζ^1, $-Km_\zeta^1$) and ($-Km_\zeta^2$, Km_ζ^2).

III. FORMULATION OF THE INTEGRAL EQUATIONS

In derivation of the integral equations, we impose the continuity of tangential component magnetic fields across each aperture namely y=b and y=b+T. These equations are

$$H_\zeta(P_1^-) = H_\zeta(P_1^+) \qquad (1.a)$$

$$H_\zeta(P_2^-) = H_\zeta(P_2^+) \qquad (1.b)$$

Here P_1^- and P_1^+ have the same co-ordinates in the lower slot aperture. The subscript (-) refers to "just inside" the cavity. Similarly P_2^- and P_2^+ are points "just inside" the cavity and "just inside" the branch waveguide interior respectively. Above equations can be rewritten as

$$H_{\zeta_1}^c - H_{\zeta_1}^{scat} = H_{\zeta_1}^{inc} \qquad (2.a)$$

$$H_{\zeta_2}^{scat} - H_{\zeta_2}^{c} = 0 \qquad (2.b)$$

Here

(i) $H_{\zeta_1}^{inc}$ is the longitudinal magnetic field in the lower slot aperture due to a TE_{10} mode source incident at port #1 of mainline waveguide and is given by

$$H_{\zeta}^{inc} = A_{10} e^{-j\beta_{10}x}\left[j \cos\left(\frac{\pi x}{a_m}\right) \cos\theta_{ms} - \frac{\beta_{10}}{(\pi/a_m)} \sin\left(\frac{\pi x}{a_m}\right) \sin\theta_{ms} \right] \qquad (3.a)$$

where A_{10} represents amplitude of incident dominant mode.

(ii) $H_{\zeta_1}^{scat}$ is the longitudinal magnetic field in the aperture region of main waveguide interior scattered by slot due to magnetic current $K_{m\zeta}^{1}$ and it can be expressed in terms of integral involving $K_{m\zeta}^{1}$ and corresponding Stevenson's Green function as

$$H_{\zeta_1}^{scat} = \iint_{S_1} \left[\sin\theta_{ms} \;\; \cos\theta_{ms}\right] \left[G_w^{scat} \right] \begin{bmatrix} \sin\theta_{ms} \\ \cos\theta_{ms} \end{bmatrix} K_{m\zeta}^{1} \, ds' \qquad (3.b)$$

where θ_{ms} is the slot tilt with the z-axis of the mainline waveguide and G_v^{scat} is the dyadic Green's functions [8]

(iii) $H_{\zeta_1}^{c}$ is the lower aperture field in the cavity due to the magnetic current sheets $-K_{m\zeta}^{1}$ and $-K_{m\zeta}^{2}$ i.e

$$H_{\zeta_1}^{c} = \iint_{S_1} G_{e_{\zeta\zeta}}^{c} \left(-K_{m\zeta}^{1}\right) ds' + \iint_{S_2} G_{e_{\zeta\zeta}}^{c} \left(-K_{m\zeta}^{2}\right) ds' \qquad (3.c)$$

where S_2 is the exterior slot aperture area $G_{s_{\zeta\zeta}}^{c}$ and $G_{e_{\zeta\zeta}}^{c}$ are cavity region Green's functions [3].

(iv) H_{ζ}^{c} is the upper aperture cavity magnetic field in the cavity due to the magnetic currents $-K_{m\zeta}^{1}$ and $-K_{m\zeta}^{2}$ i.e

$$H_{\zeta_2}^{c} = -\iint_{S_1} G_{c_{\zeta\zeta}}^{c} K_{m\zeta}^{1} \, ds' - \iint_{S_2} G_{s_{\zeta\zeta}}^{c} K_{m\zeta}^{2} \, ds' \qquad (3.d)$$

(v) $H_{\zeta_2}^{scat}$ is the field in the aperture region of branch waveguide interior scattered by slot due to magnetic current $+K_{m\zeta}^{2}$, i.e.,

$$H^{scat}_{\zeta_2} = \iint_{s_2} \left[\cos\theta_{bs} \;\; \sin\theta_{bs}\right] \left[G_w^{scat}\right] \begin{bmatrix}\cos\theta_{bs}\\ \sin\theta_{bs}\end{bmatrix} K^2_{m\zeta}\, ds' \quad (3.e)$$

where θ_{bs} is the slot tilt with the Z-axis of branchline waveguide.

IV. METHOD OF MOMENT SOLUTION OF INTEGRAL EQUATIONS

The set of integral equations (2.a&b) have been solved by th method of moments using Galerkin's method of testing [9]. In thi method basis functions are used for testing integral equations. Her $K^1_{m\zeta}$ and $K^2_{m\zeta}$ are expressed in terms of entire domain basis function and unknown weighting coefficients. The basis function shoul satisfy the same boundary conditions as satisfied by the magneti current sources; in order to converge magnetic current expansion-series. Thus it has been assumed that

$$K^1_{m\zeta}(\xi,\zeta) = \sum_{q=1}^{N} A_q \sin[q\pi((\zeta+1)/(21))] \quad (4.a)$$

$$K^2_{m\zeta}(\xi,\zeta) = \sum_{q=1}^{N} B_q \sin[q\pi((\zeta+1)/(21))] \quad (4.b)$$

The distribution of $K^1_{m\zeta}$ and $K^2_{m\zeta}$ across the slot is assumed to be constant (that is taken as unity for convenience in analysis) Substitution of these expansions of $K^1_{m\zeta}$ and $K^2_{m\zeta}$ into integra equations (2) results in equations with 2N unknown coefficient: $[A_q, B_q, q = 1,2,3,\ldots,N]$. The continuity equations (2) should b satisfied at each and every point on corresponding apertures. If on attempts to do so there will be infinite number of equations fo only 2N unknowns. Therefore these continuity equations are teste in average sense over the slot aperture by using basis functions a testing functions. We obtain 2N simultaneous equations by choosin different values of p from 1 through N. These equations can b collectively written in the following matrix form.

$$\begin{bmatrix}[Y_{11pq}] & [Y_{12pq}]\\ [Y_{21pq}] & [Y_{22pq}]\end{bmatrix}\begin{bmatrix}[A_q]\\ [B_q]\end{bmatrix} = \begin{bmatrix}[I]\\ [0]\end{bmatrix} \quad (5)$$

Where all block matrices Y_{11} ,Y_{12} ,Y_{21} ,Y_{22} are NxN square matrices and A, B are column vectors containing the N coefficients of magnetic currents $K^1_{m\zeta}$ and $K^2_{m\zeta}$ respectively. I is also a column vector resulting from TE_{10} mode source term in (3.a).

A typical element in $[Y_{ii}]$ is,

$$Y_{ii\,pq} = Y_{ii\,pq}^{main} - Y_{ii\,pq}^{cavity} \tag{6.a}$$

$$Y_{ii\,pq}^{main} = Y_{ii\,pqx}^{main} + Y_{ii\,pqz}^{main} \tag{6.b}$$

$$Y_{ii\,pqx}^{main} = \int_{\zeta=-L}^{+L} \sin\frac{p\pi}{2L}(\zeta + L) \iint_{s_i} \left[\sin^2\theta_{ms}\, G_{xx}^{scat} + \sin\theta_{ms}\cos\theta_{ms} G_{xz}^{scat}\right] \sin\frac{q\pi}{2L}(\zeta' + L)\, d\xi'\, d\zeta'\, d\zeta \tag{7.a}$$

$$Y_{ii\,pqz}^{main} = \int_{\zeta=-L}^{+L} \sin\frac{p\pi}{2L}(\zeta + L) \iint_{s_i} \left[\sin\theta_{ms}\cos\theta_{ms}\, G_{zx}^{scat} + \cos^2\theta_{ms}\, G_{zz}^{scat}\right] \sin\frac{q\pi}{2L}(\zeta' + L)\, d\xi'\, d\zeta'\, d\zeta \tag{7.b}$$

$$Y_{ii\,pq}^{cavity} = \int_{\zeta=-L}^{+L} \sin\frac{p\pi}{2L}(\zeta + L) \iint_{s_i} G_{s_{\zeta\zeta}}^{c} \sin\frac{q\pi}{2L}(\zeta' + L)\, d\xi'\, d\zeta'\, d\zeta \tag{8.a}$$

A typical element in Y_{iz} matrix is,

$$Y_{iz\,pq}^{cavity} = \int_{\zeta=-L}^{L} \sin\frac{p\pi}{2L}(\zeta + L) \iint_{s_z} G_{c_{\zeta\zeta}}^{c} \sin\frac{q\pi}{2L}(\zeta' + L)\, d\zeta'\, d\zeta'\, d\zeta \tag{8.b}$$

A typical element in Y_{zi} matrix is,

$$Y^{cavity}_{21\ pq} = -Y^{cavity}_{12\ pq} \tag{9}$$

A typical element in Y_{22} matrix is,

$$Y_{22\ pq} = Y^{branch}_{22\ pq} + Y^{cavity}_{22\ pq} \tag{10.a}$$

here,

$$Y^{branch}_{22\ pq} = -Y^{main}_{11\ pq} \Big|_{\substack{b_b \rightarrow b_b \\ a_m \rightarrow a_b \\ \theta_{ms} \rightarrow \theta_{bs}}} \tag{10.b}$$

$$Y^{cavity}_{22\ pq} = -Y^{cavity}_{11\ pq} \tag{10.c}$$

A typical element of source matrix in source matrix [I] is,

$$I_p = I^1_p + I^2_p \tag{11.a}$$

$$I^1_p = \cos\theta \int_{\zeta=-L}^{+L} \sin\left[\frac{p\pi}{2L}(\zeta + L)\right] j \cos\left(\frac{\pi x}{a}\right) e^{-j\beta_{10}z}\, d\zeta \tag{11.b}$$

$$I^2_p = \sin\theta \int_{\zeta=-L}^{+L} \sin\left[\frac{p\pi}{2L}(\zeta + L)\right] \left(\frac{-\beta_{10}}{\pi/2}\right) \sin\left(\frac{\pi x}{a}\right) e^{-j\beta z} d\zeta \tag{11.c}$$

Once the [Y] and [I] matrices are known, [A] and [B] can be obtained by solving matrix equation (5).

V. NUMERICAL RESULTS AND DISCUSSIONS

The slot length at which the power coupled from main waveguide to branch waveguide is maximum can be called as a resonant length. For compound radiating and coupling slots, resonance has been defined by the condition wherein the scattered wave (C_{10}) is out of phase with incident TE_{10} wave [3]. A second definition of resonance is based on the condition wherein the back scattered wave (B_{10}) is out of phase with incident TE_{10} wave. But the resonant length based on the above two definitions differs significantly and maximum coupling occurs for a slot length between the two resonant lengths [3]. This leads to an ambiguity in getting the exact resonant length for maximum coupling. Hence there is a need to calculate this parameter to a great accuracy because of its sensitivity in moment method solution . To avoid the ambiguity, a new method based on the condition that slot magnetic current is purely real, has been adopted to calculate the resonant length and subsequently other scattering parameters. The resonant length, aperture electric field magnitude, and forward and backscattered wave amplitudes are dependent on the magnitude of θ_{mb}, θ_{bs} and θ_{ms}.

Since no result has been reported for the non-orthogonal waveguide slot coupler in the open literature, the validity of moment method code developed has been checked for a special case when θ_{mb} becomes 90^{o}. Computed values of resonant length ($2l_{res}$) and $|S_{11}|$ are in good agreement with previously reported values [4]. The results are shown in table-I.

TABLE-I

θ	$2l_{res}$ [ref 4]	$2l_{res}$	$\|S_{11}\|$ [ref 4]	$\|S_{11}\|$
15^{o}	0.655"	0.6555"	0.099	0.099
20^{o}	0.657"	0.6579"	0.161	0.161
30^{o}	0.662"	0.6616"	0.299	0.299
35^{o}	0.665"	0.6649"	0.367	0.367

(a=0.9", b=0.2", w=0.0625", t=0.01", $\theta_{bm}=90^{o}$, f=9.17 GHz)

VI. CONCLUSION

For a planar non-resonant slot arrays with complex geometry such as ellipse, a new type of feeding arrangement has been investigated. Integral equations have been developed for non-ortogonal waveguide slot coupler, including the effect of waveguide wall thickness, and they have been solved by the method of moments. Numerical results for a special case has been validated with the available results in the literature.

REFERENCES

[1] J.J.Gulick,"The Design of Linear and Planar Arrays of waveguide-Fed Longitudinal Slots," Ph.D. Dissertation, UCLA, Jun 1987.

[2] M. Hamadallah," Frequency Limitations on Broad-Band Performance of Shunt Slot Arrays," *IEEE-AP*, vol. 37, pp. 817-823, July 1989

[3] S.R. Rengarajan," Characteristics of a Longitudinal/Transverse Coupling Slot in Crossed Rectangular Waveguides", *IEEE Trans on MTT*, vol. 37, no. 8, pp. 1171-1177, Aug 1989.

[4] S.R. Rengarajan, "Analysis of Centered-Inclined Waveguide Slot Coupler". *IEEE Trans. on MTT*, Vol. *MTT*-37, pp. 884-889, May 1989

[5] T. Vu Khac and C.T. Carson,"Coupling by Slots in Rectangular Waveguides," *Electron. Lett.*, vol.8, pp. 456-458, Sept. 1972.

[6] Park *et al.*," Shunt/Series Coupling Slot in Rectangular waveguides," *IEEE Int. Antennas Prop. Symp. Dig.*, pp. 62-65, 1984.

[7] W. Hanyang and W. Wei,"Moment Method Analysis of a Feeding System in a Slotted Waveguide Antenna," *IEE Proc.*, vol. 135, Pt. H, No. 5, pp. 313-318, Oct. 1988.

[8] A.F. Stevenson,"Theory of Slots in Rectangular Waveguides," *J. Appl. Phys.*, vol. 19, pp. 24-38, Jan. 1948.

[9] R.F. Harrington, *Field computations by Moment Method*, New York: McGraw Hill, 1968.

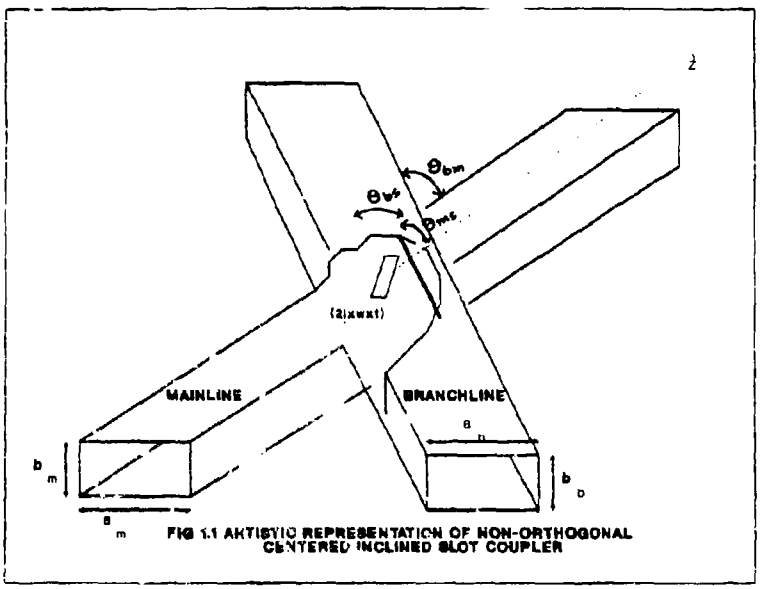

FIG 1.1 ARTISTIC REPRESENTATION OF NON-ORTHOGONAL CENTERED INCLINED SLOT COUPLER

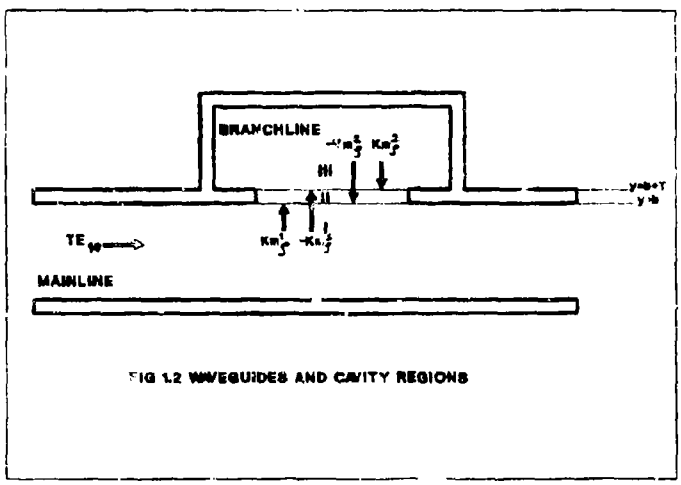

FIG 1.2 WAVEGUIDES AND CAVITY REGIONS

An $O(n \log^2 n)$ Iterative Method for Solving Dense Linear Systems.

Serge Kharchenko, Paul Kolensnikov,
Eugene Tyrtyshnikov, Alex Yeremin
Russian Academy of Sciences
Elegant Mathematics, Inc.
Michael A. Heroux, Qasim Sheikh*
Cray Research, Inc.

Abstract

It is well-known that the computational bottleneck in using boundary integral methods is typically the solution, via LU decomposition, of dense linear systems $Ax = b$. This is especially true as the problem dimension grows large since the the arithmetic complexity of LU decomposition is $O(n^3)$, which is an order of magnitude greater than any other phase of the computation. In previous papers we have presented iterative methods with $O(n^2)$ computational complexity for solving linear systems of equations arising from application of boundary integral techniques to industrial class problems. These methods construct a block diagonally perturbed sparse preconditioner from the given matrix and use a stablized version of block GMRES method to solve the linear system. However, these methods still require $O(n^2)$ memory locations to store the dense matrix. For dense linear systems of sizes close to 100000 and more the disk space needed to store such matrices becomes unrealistic for todays storage technologies.

In this paper we present results from a class of iterative method for solving dense linear systems that have $O(n \log^2 n)$ computational

*Corresponding Author: 655 Lone Oak Drive, Eagan, MN 55121 USA, email: qasim.sheikh@cray.com, Phone: (612) 683-3634, Fax: (612) 683-3599

and I/O complexity and need $O(n)$ memory locations. We use singular value decompositions of subblocks of A to create a block low rank approximation $\tilde{A}$. The memory requirements to store $\tilde{A}$ and the computational complexity of computing $\tilde{A}x$ are significantly less than the storage and computational requirements for A. These low rank approximations are computed after a certain gangster projector is applied to the matrix. This process ensures that the approximation is nonsingular whenever the original matrix is nonsingular.

We show the efficiency of these methods by solving dense complex and real linear systems of sizes 74K and 72K with single as well as multiple right hand sides on CRAY Y-MP vector/parallel computers. These problems are extracted from NASA Almond benchmark for computational electromagnetics and a commercial computational fluids dynamic package. Our experiments show an order of magnitude reduction in the memory requirement and an all most two orders of magnitude reduction in computation time as compared to a fully optimized direct solver.

DEVELOPING OPTIMAL AND AUTOMATIC FREQUENCY SAMPLING IN MOMENT-METHOD SOLUTIONS

G. J. Burke, L-156, Lawrence Livermore National Laboratory, Livermore, CA 94550
E. K. Miller, EKMiller Associates, 3225 Calle Celestial, Santa Fe, NM 87501

ABSTRACT

The need often arises in electromagnetics (EM) to obtain a wideband response from frequency sampling. The usual approach of running a model at many equally spaced frequencies and using linear interpolation may result in substantial over sampling, especially when the response involves sharp resonances. Sampling finely only near resonances might be useful, assuming the resonance locations are known, but much more can be done by taking advantage of the problem physics. EM frequency responses can be quite accurately approximated as a sum of poles, a procedure of curve fitting known more generally as model-based parameter estimation (MBPE). By fitting rational functions (as generalized pole series) to frequency-sampled data, resonant behavior can be well represented, and the number of samples can be reduced to as few as two per resonance. In addition, varying the model parameters can show where additional samples are needed to identify an unsuspected resonance. The program ZPLOT, currently distributed with the NEC program to plot admittance data, includes an MBPE capability to manually implement simple adaptive sampling of frequency responses. Examples of using MBPE are shown to illustrate this process for resonant wire antennas.

INTRODUCTION

Obscured by the mathematical detail and descriptive complexity associated with most electromagnetic analysis is the possibility of representing physical observables in simpler ways using reduced-order models. Knowledge of such models can be helpful in ways ranging from reducing the computer cost of achieving desired solutions to developing more compact representations of observables. The basic approach is to estimate unknown parameters of the models from sampled data, a process called "model-based parameter estimation" (MBPE) [Miller and Burke (1991)]. The idea behind MBPE is intuitively straightforward and conceptually simple: data or complex analytical formulations are replaced by simpler mathematical representations--the "fitting model," (FM) which ideally is physically based--whose parameters are obtained from fitting it to the original description (a first-principles or generating model [GM]) in the "parameter-estimation" step. Parameter estimation often must be accomplished in the presence of noise, incomplete data and/or uncertainty, thus introducing some "art" into the MBPE process.

A FM can provide a more efficient Computational ElectroMagnetics (CEM) numerical approach by reducing the complexity and cost of GM computations and/or by making more efficient use of the results that are computed, either separately or in combination. Both applications might be described as "smart" curve fitting, because the FM originates from basic physics.

MBPE can reduce the cost of a sample based on a first-principles model in various ways, one of which is simplifying evaluation of an integral-equation (IE) kernel by approximating the kernel with (ideally) a physically motivated model that provides a reduced-order mathematical description to decrease computational complexity while retaining acceptable accuracy. Possible applications of kernel modeling include the Sommerfeld integrals of interface problems [speedups of 100 or more are possible, Burke and Miller (1984)] and the Green's functions for periodic boundaries such as rectangular and spherical cavities [Demarest et al. (1989)]. In such applications, sampled values of the kernel are replaced by a simplified model to reduce the operation count (OC) of numerically evaluating the interaction coefficients that appear in a moment-method matrix.

MBPE can also be used to reduce the number of samples needed for certain applications, e.g., to obtain a wideband frequency response or to obtain angle scattering or radiation patterns, again via exploiting physical simplicity and a reduced-order mathematical model to represent the response of interest. In such applications, model parameters derive from fitting the model to appropriate samples of the desired response, e.g., as a function of time, frequency, angle or space, where the samples can come from the actual response or derivatives thereof (with respect to the independent variable).

Succinctly summarized, MBPE involves three basic operations:

1. a process or data providing observables to be modeled,
2. a suitable model to represent that process/data,
3. parameters to be estimated by fitting the model to that process/data

with the goal of reducing the overall OC of obtaining the desired information. Subsequent discussion here focuses on the particular application where the data comes from a frequency-domain (FD) transfer function with the goal of minimizing the number of GM evaluations required to determine a transfer function over a specified band to a desired accuracy.

WAVEFORM- AND SPECTRAL-DOMAIN MODELS

Since electromagnetic phenomena satisfy Maxwell's equations and the wave equation, they can exhibit both exponential- (for example, transient fields in the time domain) or pole-like (spectra in the FD) behavior. Thus, one of the basic MBPE models begins either as an exponential series (in what we refer to as the waveform domain since the variable "x" is often time)

$$f(x) = f_p(x) + f_{np}(x) = \sum_{\alpha=1}^{W} R_\alpha e^{s_\alpha x} + f_{np}(x) \tag{1}$$

or as a pole series (in what we refer to as the spectral domain because the variable "X" is then a frequency if x is time)

$$F(X) = F_p(X) + F_{np}(X) = \sum_{\alpha=1}^{W} \frac{R_\alpha}{(X - s_\alpha)} + F_{np}(X) \tag{2}$$

i.e., the models, where the subscript "p" refers to the pole part of the response and the "np" to the non-pole part. The 2W model parameters are the modal amplitudes (residues), R_α, and the complex resonances (poles), s_α, to be estimated from waveform samples $f_n = f(x_n)$ (or derivative samples $f_n = d^n f/dx^n$) or spectral samples $F_n = F(X_n)$ (or derivative samples $F_n = d^n F/dX^n$). Whatever combination of domain and data are used, the process of using the sampled data with Eqs. (1) or (2) leads to a linear system whose solution provides the FM parameters [Miller and Burke (1991)].

OBTAINING BROADBAND EM RESULTS

MBPE can expedite the development of broadband EM results, being applied in what we call the "formulation" domain and "solution" domain. By formulation domain, we mean the original problem description as developed from Maxwell's equations, an IE for example, whereas solution domain refers to the observable solutions developed from the original description. More specifically, the impedance matrix, $Z_{m,n}$, that results from a moment-method discretization of the IE is a formulation-domain entity whereas the admittance matrix, $Y_{m,n}$, that results from inverting (or otherwise solving) $Z_{m,n}$ is a solution-domain entity. In either case, having analytical knowledge of the frequency variation of $Z_{m,n}$ or $Y_{m,n}$ between the discrete frequencies at which a CEM computation has been performed can substan-

tially reduce the overall OC of determining a broadband frequency response.

Whether modeling the impedance or admittance matrix in IE applications will yield the greater reduction in overall OC in a frequency range of interest depends on the relative OC required for each part of the solution, i.e., in computing $Z_{m,n}$ or solving for $Y_{m,n}$, as illustrated conceptually in Fig. 2. For three-dimensional IE models of conducting objects, the overall OC is almost wholly due to these two computation steps, which vary in proportion to $a_{fill}f^4$ and $b_{solve}f^6$, respectively, with f the frequency, and where a_{fill} and b_{solve} are algorithm- and computer-dependent coefficients. At lower frequencies, $a_{fill}f^4 > b_{solve}f^6$ because $a_{fill} > b_{solve}$ for essentially all models, so that the matrix-fill OC is larger, but with increasing frequency, eventually $a_{fill}f^4 < b_{solve}f^6$ and the solution OC dominates. This suggests that the greatest efficiency improvement would result from using MBPE to minimize the number of $Z_{m,n}$ computations at lower frequencies, and the number of $Y_{m,n}$ computations at higher frequencies. Both matrices might be modeled across the same bandwidth, of course, because among the other benefits of using MBPE other than decreased OC alone is that of replacing matrices of numbers by analytical formulas.

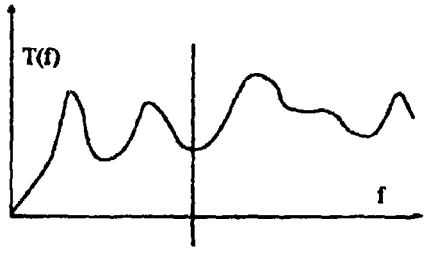

$a_{fill}f^4 > b_{solve}f^6$ $\qquad$ $a_{fill}f^4 < b_{solve}f^6$

Figure 1. Representative transfer function T(f) obtained from a CEM FDIE model. At lower frequencies, matrix fill dominates the total OC whereas at higher frequencies, the solution OC is the dominate factor.

Modeling $Z_{m,n}$

In order to use MBPE for estimating the coefficients of $Z_{m,n}$ between frequencies at which the interactions are computed from their defining equations, a suitable FM is needed. The exponential-series model of Eq. (1) is appropriate (without the non-pole terms) for this purpose, since the FD Green's function from which $Z_{m,n}$ is derived exhibits a complex-exponential behavior. For example, a generic FDIE interaction coefficient using subdomain bases and and delta-function testing has the form

$$Z_{m,n}(\omega) = \int_{\Delta_n} S_n(\omega) K_{R,m,n}(\omega) K_{\Delta,m,n}(\omega) d\Delta_n \qquad (3)$$

where m and n denote observation and source "patches," S_n is the source strength on patch Δ_n, $K_{R,m,n}$ is the "patch-to-patch" (P-P) part of the IE kernel and $K_{\Delta,m,n}$ is the "in-patch" (I-P) part of the kernel. The P-P term describes a "fast" frequency variation of the form $\exp(jkr_{m,n})$, where $r_{m,n}$ is the distance between the centers of patches m and n and for which $kr_{m,n} \gg 1$ is generally true. Similarly, the I-P term describes a "slow" variation whose exponential variation is of order $\exp(jk\Delta r_{m,n})$, while $\Delta r_{m,n}$ is

the distance variation caused by integration over a patch and for which $k\Delta r_{m,n} \ll 1$, because the patch size is small in wavelengths. The P-P term can be factored from the integral to obtain

$$Z_{m,n}(\omega) = e^{jkR_{m,n}} \int_{\Delta_n} S_n(\omega) K'_{\Delta,m,n}(\omega) d\Delta_n \tag{4}$$

where $R_{m,n} + \Delta r_{m,n} = r_{m,n}$ and $K'_{\Delta,m,n}$ is a modified slow-frequency kernel.

Eq. (4) indicates that if $Z_{m,n}(\omega_1)$ has been computed from the defining equations at ω_1, then $Z_{m,n}(\omega_2)$ can be estimated as (assuming ω_2 is not "too far" from ω_1)

$$Z_{m,n}(\omega_2) = Z_{m,n}(\omega_1) e^{jk(\omega_2-\omega_1)R_{m,n}} M_{m,n}(\omega_2-\omega_1) \tag{5}$$

where $M_{m,n}(\omega_2-\omega_1)$ is an interpolation model that accounts for the slow variation of the integral in (4).

For the thin-wire electric-field IE (EFIE), Newman (1988) has used

$$M_{m,n}(\omega_2-\omega_1)|_{imag} = A + B\omega + C\omega, \tag{6a}$$

$$M_{m,n}(\omega_2-\omega_1)|_{real} = A + B\omega + C\omega^2. \tag{6b}$$

for modeling $Z_{m,n}$ variations. Benthien and Schenck (1991) followed a similar approach for elastodynamic scattering. An interesting aspect of modeling the frequency variation of $Z_{m,n}$ is that the sampled frequencies can be spaced many resonances apart while retaining an accurate representation of the solution-domain resonance behavior as a function of frequency. This is because the resonances come from interactions between object extremities, whose convolutional relationship is developed through the solution process which itself requires only that the phase and amplitude frequency dependencies of $Z_{m,n}$ be maintained with accuracy sufficient to yield adequate accuracy in $Y_{m,n}$.

Modeling $Y_{m,n}$

While the $Z_{m,n}$ coefficients exhibit a phase-driven exponential behavior modulated by distant-dependent terms, the coefficients of $Y_{m,n}$ exhibit a pole-like behavior, as can be surmised from observing the resonance structure of a typical EM transfer function. Thus, an appropriate model for the latter is given by the pole series of Eq. (2). In this case however, the non-pole terms might be anticipated to play a significant role [Miller and Burke (1991)]. Such terms might be reasonably approximated by adding a frequency-dependent polynomial to the pole series. This polynomial might also help to approximate the contribution of poles that lie outside the frequency range to be covered by the FM. The result is to generalize the rational-function form of the pole series from one where the numerator polynomial has an order one less than the denominator polynomial to one of equal order, or exceeding it by the order, P, of the highest term in the added polynomial.

Thus, the pole-series model can be expanded in rational-function form as

$$\sum_{\alpha=1}^{W} \frac{R_\alpha}{X - s_\alpha} = F_p(x) = \frac{N_0 + N_1X + N_2X^2 + \cdots + N_{W-1}X^{W-1}}{1 + D_1X + D_2X^2 + \cdots + D_{W-1}X^W} = \frac{N(X,W-1)}{D(X,W)} \tag{7a}$$

where D_0 has been set to unity. Adding a constant for the non-pole term then yields

$$F_{np}(X) = \text{CONSTANT} \Rightarrow F(X) = \frac{N(X,W)}{D(X,W)}. \tag{7b}$$

Adding an additional term linear in frequency then leads to

$$F_{ap}(X) = C_1 + C_2X \Rightarrow F(X) = \frac{N(X,W+1)}{D(X,W)} \qquad (7c)$$

so that in general, the numerator polynomial will be of order N = W + P, requiring a total of at least D = W + P + 1 GM samples to evaluate the FM coefficients. Note however, that the FM remains simply a rational function, retaining a natural fit to a pole-based resonance response.

DEVELOPING A SAMPLING STRATEGY

Fitting a model, even one that is mathematically compatible with the physical process from which the sampled data has been derived, is only one aspect of using MBPE to represent a FD transfer function. Knowledge of the fitting error, i.e., the difference between the FM and GM, is necessary if the goal of achieving a desired error in the estimated transfer function across the bandwidth of interest is to be realized. Errors produced by a FM are of three basic types: 1) non-physical results, e.g., negative conductance; 2) baseline shifts between the FM and GM; 3) resonance shifts between the FM and GM. Each of these errors might suggest a different kind of adaptive sampling strategy to be used. For non-physical results, the most appropriate approach would be to sample where the negative peak in conductance (or resistance) occurs in the FM. For baseline shifts, we might instead sample at the maximum difference between the FM and GM if it exceeds a specified error criterion. Similarly, for resonance shifts, it might be most appropriate to sample midway between the model peaks if the shift between them exceeds some error criterion.

Note that it is a distinct disadvantage if the fitting error could only be estimated by requiring additional GM data, since a goal of using MBPE is to minimize the number of GM evaluations. Therefore, if at all possible, a different approach to obtaining the fitting error is needed. Of the three errors listed, only the first can be directly realized using FM results. However, it is feasible to estimate the other two errors using only FM results as well. It should be emphasized at this point that the number of GM data points, D, the frequency range spanned by a FM, and the orders of the numerator and denominator polynomials, N and W, are relatively ambiguous. On the one hand, this "ambiguity" can be considered a detriment because in introduces unavoidable uncertainty into the MBPE process. On the other hand, it can be productive because different FMs can use some of the same GM data. Thus, an estimate of the fitting error can be obtained by comparing results from two (or more) FMs over a frequency range where they

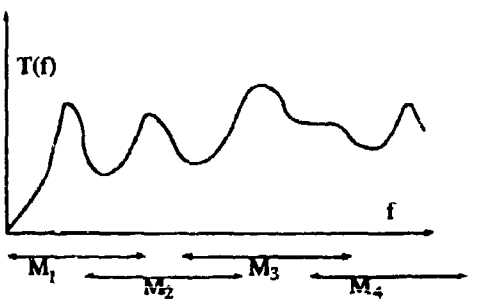

Figure 2. Developing a broadband transfer function using a series of overlapping, cascaded, reduced-order FMs, M_i. The FMs use common GM data samples in the overlap regions. These different FMs provide a measure of the fitting error in terms of their separate estimates for T(f) as a function of frequency where the FMs overlap.

share common data, or overlap. Although the FM differences, or estimated errors, can not be guaranteed to be an upper bound on the actual fitting error, they do show the relative consistency of the FMs in the overlapping regions. Where these differences exceed acceptable limits, an additional GM sample would be suggested, thus providing a rationale for adaptive sampling, ensuring that GM computations are being done at frequencies where the new information they yield is nearly maximized. Using over-

lapping "windows" of reduced-order FMs to estimate errors and to determine where new GM samples are needed leads logically to the idea of developing a broadband transfer function from a cascaded series of FMs, as illustrated conceptually in Fig. 2. This is basically the approach used to develop the transfer functions presented below.

SAMPLE APPLICATIONS

A simple example of using a series of FMs to estimate a broadband transfer function is shown in Fig. 3 for a center-fed dipole antenna. In this case, 20 GM samples spaced 0.15 L/λ apart were developed over an L/λ range from 0.15 to 3 using NEC. A series of FMs, each shifting upward in frequency by 0.15 L/λ, was used to obtain the estimated transfer function, and each was used to plot the estimated transfer function over the center 0.15 L/λ interval of its 0.9 L/λ window, except for the ends of the frequency range where the FMs extended to 0 and 3 L/λ respectively. The FM curves are ensured to pass through the GM samples because the number of samples equals the number of FM coefficients.

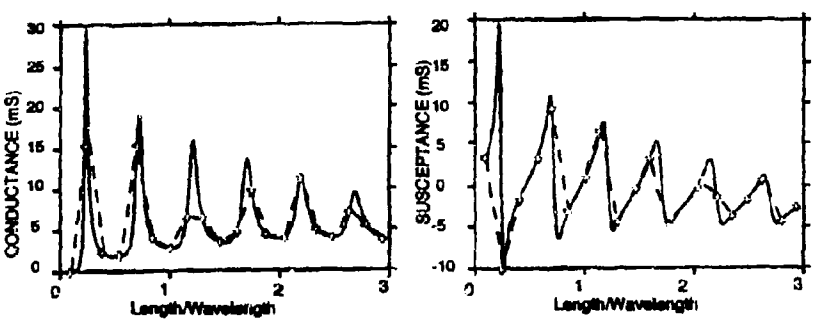

Figure 3. Input conductance and susceptance of monopole antenna versus length in wavelengths as obtained from a series of rational-function fitting models using D = 7 (W = N = 3) (the solid line) based on 20 samples spaced 0.15 apart in L/λ). The GM samples are indicated by the open crosses and are joined by a dashed line for clarity.

An example of varying the FM parameters in the vicinity of a sharp resonance is shown in Fig. 4 for the admittance of a "forked-monopole" antenna [a short, straight dipole with V ends where one arm is slightly shorter than the other, Burke et al. (1989)]. The two fitting models, one using D = 7 (W = N = 3) and the other using D = 5 (W = N = 2) are based on GM samples at 0.5 MHz intervals. On this expanded scale, the 7-sample FM model coincides graphically with 21 additional GM samples spaced 10^{-4} MHz apart starting at 0.717 MHz, indicating that the higher-order FM is highly accurate and that the fitting error is probably comparable with the accuracy provided by the NEC model.

A further example of modeling a sharply resonant antenna is demonstrated in Fig. 5 for the admittance of a fan antenna (a bottom-fed monopole consisting of a three unequal-length wires spreading outward from the feed). Two sets of FM curves are plotted here as obtained from two different sets of GM samples, one set of 15 beginning at 2 MHz and spaced at 0.5 MHz intervals. The other set consists of 51 samples also beginning at 2 MHz but spaced at 0.14 MHz intervals. In plotting these results, each new FM is shifted upwards in frequency by their respective GM sampling intervals.

These two examples demonstrate the relative insensitivity of the estimated transfer function to variations

in both the GM data used and the FM parameters. They also indicate how differences in the resulting FMs can show where, and if, additional sampling might be needed. In cases where the FM curves are slightly different, one approach for combining them would be by averaging their FM coefficients.

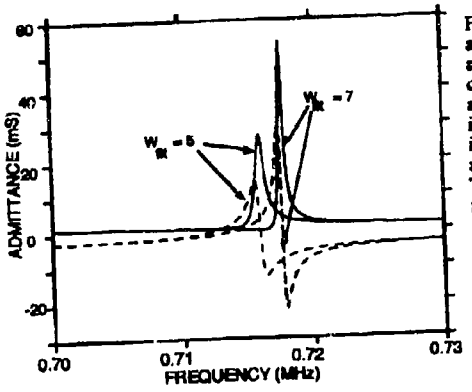

Figure 4. Results for the input admittance of a forked-monopole antenna in the vicinity of a sharp resonance, where a differential-mode current can exit on the two unequal-length arms of the dipole. Although the resonance is quite accurately located (to within 1% or so in frequency), there is some variation in the admittance values provided by the two FMs. The 7-sample model is the more accurate, as it is found to agree with 21 additional GM samples spaced 10^{-4} L/λ apart beginning at 0.717 MHz.

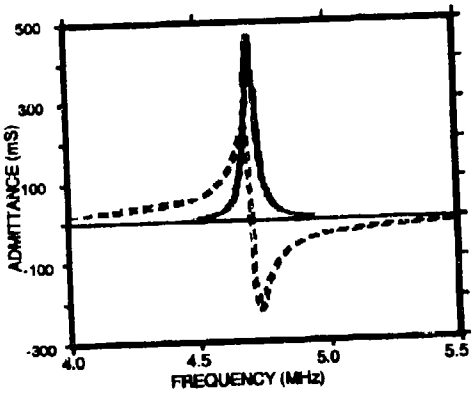

Figure 5. Results for the input admittance of a fan antenna using different sets of GM data and various FMs (solid, conductance; dashed, susceptance). Two FMs, one using D = 7 (with W = N = 3) and the other having D = 11 (W = N = 5), both using GM samples at 0.5 MHz intervals, yield the curves having the rightmost resonances. The other model, having D = 9 (W = N = 4) and using GM samples at 0.14 MHz intervals, yields the curves having the leftmost resonances. As before, these curves are obtained by plotting each FM over the its center sample interval, with each new FM shifted upward one interval. The agreement of the 9-sample FM with the 51-sample GM indicates it is the more accurate of the FMs.

A broader view of applying MBPE to the fan antenna is illustrated in Fig. 6 where its input impedance (referred to 50 ohms) is plotted on a Smith chart for two different FMs. One FM uses D = 7 (W = N = 3) and the other D = 8 (W = 3, N = 4), both based on GM data sampled at 1-MHz intervals from 2 to 9 MHz. The curve labeled "truth" is based on 51 GM samples beginning at 2 MHz and spaced at 0.14 MHz intervals. The 7-point FM produces a negative resistance in the vicinity of the resonance "loop," a problem that is corrected by increasing the order of the FM by one, but <u>without</u> computing any more additional GM samples. Over most of the frequency range covered here, the 8-point FM is in close agreement with the GM data, indicating the good accuracy of the MBPE representation.

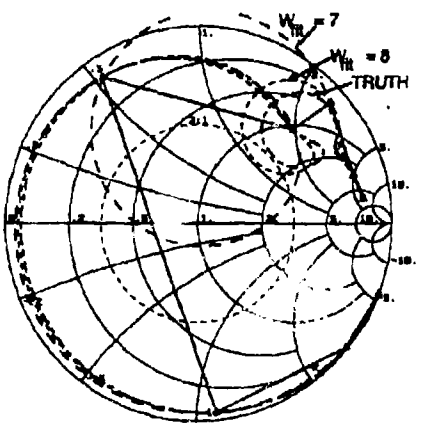

Figure 6. Smith-chart representation of the input impedance of the fan antenna over the frequency range 2 to 9 MHz. The GM samples are shown by the triangles and are connected by a straight, solid line. The 7-sample FM produces a non-physical input resistance near the resonance "loop." Simply increasing the FM order by one brings it into to close agreement with the GM samples labeled "truth" which are computed at 0.14 MHz intervals and connected by straight lines.

CONCLUDING COMMENTS

A capability for conveniently incorporating NEC (or any other FD model results or measurements) data with MBPE as illustrated above is provided by ZPLOT. The program includes capabilities for displaying multiple curves, combining data files and interpolating data using MBPE FMs. Data points from new files can be added to existing curves, and the combined data will be sorted in order of increasing frequency and plotted. Data read from NEC output files or combinations of files or data generated by FMs can be written to new files in a format including frequency and admittance or impedance. These files written from ZPLOT will be much smaller than the NEC output files which include a large amount of additional information. The impedance or admittance files written by ZPLOT can also be read by ZPLOT and plotted. Although ZPLOT, as presently implemented, accommodates adaptive sampling only through user intervention, a future extension would be to extend the procedure to locate GM samples and determine FM parameters automatically while limiting the fitting error to a specified value.

REFERENCES

Bentbien, G. W. and H. A. Schenck (1991), "Structural-acoustic coupling," in *Boundary Element Methods in Acoustics*, ed. R. D. Ciskowski and C. A. Brebbia, Computational Mechanics Publications.

Burke, G.J. and E.K. Miller (1984), "Modeling Antennas Near to and Penetrating a Lossy Interface", *IEEE Transactions on Antennas and Propagation*, AP-32, pp. 1040-1049.

Burke, G. J., E. K. Miller, S. Chakraborti, and K. R. Demarest (1989), "Using Model-Based Parameter Estimation to Increase the Efficiency of Computing Electromagnetic Transfer Functions", *IEEE Transactions on Magnetics*, 25(4), pp. 2807-2809.

Demarest, K. R., E. K. Miller, K. Kalbasi, and L-K Wu (1989), "A Computationally Efficient Method of Evaluating Green's Functions for 1-, 2-, and 3D Enclosures", *IEEE Transactions on Magnetics*, 25(4), pp. 2878-2880.

Miller, E. K. and G. J. Burke (1991), "Using Model-Based Parameter Estimation to Increase the Physical Interpretability and Numerical Efficiency of Computational Electromagnetics," *Computer Physics Communications*, 68, 43-75.

Newman, E. H. (1988), "Generation of wideband data from the method of moments by interpolating the impedance matrix," *IEEE Trans. Antennas Propagat.*, Vol. 36, No. 12, pp. 1820-1824, Dec. 1988.

REFLECTIONS ON SOME OF THE FOLKLORE OF THE MOMENT METHOD

Richard C. Booton, Jr.
Center for Microwave/Millimeter-wave Computer-Aided Design
University of Colorado at Boulder
Boulder CO 80309-0425

ABSTRACT

Several "facts" that many people believe to be true and can be considered to be part of the folklore of the moment method are examined. The simple example of a thin cylinder, either as a plane-wave scatterer or as part of a center-fed dipole antenna, is analyzed numerically and results obtained that shed light on the folklore. Several more general points are made regarding numerical analysis.

BACKGROUND

The pioneering work of Galerkin and Harrington established the moment method as a major tool in the numerical analysis of electromagnetic problems, and the work of many others has resulted in the moment method becoming a well understood and widely used method for the solution of integral equations in electromagnetics. There are several "well-known facts" that may be said to constitute the folklore of this method, but do not seem to be universally true. Some of these will be stated and discussed in light of a simple problem, the thin cylinder, either as a scatter or as a center-fed dipole, described by the appropriate form of Hallen's integral function.

QUESTIONABLE BELIEFS

(A) Galerkin weighting is much superior to colocation.

Statements frequently are made that Galerkin weighting (using as the set of weighting functions the set of basis functions) is better than using other weighting functions and in particular much better than delta function weighting for colocation (point matching.) Proofs have been offered to show the optimality of the Galerkin method. Usually such arguments depend upon variational considerations and do not consider the fact that Galerkin weighting requires additional integrations, compared to colocation. When the moment integrals are evaluated by numerical integration, the additional integration results in additional run time.

A simple example is given by plane-wave scattering off a thin cylinder, as analyzed by Hallen's equation. For such one-dimensional equations the Galerkin method requires numerical double integration rather than the single integration required by point matching. Fig.1 shows the RCS of a cylinder using triangle basis functions, both for colocation and for Galerkin weighting, as a function of the number of basis functions. For the same number of basis functions Galerkin weighting is somewhat better. The Galerkin weighting program, however, has a longer run time

on the computer. Fig. 2 shows the same results as a function of computer run time, and on this basis colocation is better. Figs. 3 and 4 repeat this comparison but for pulse basis functions. The Galerkin solutions are much better than the colocation results for the same number of basis functions, but again colocation is superior for the same computer run time.

(B) Basis functions that correspond to discontinuous current are much inferior to those that correspond to continuous current. Specifically, in one dimension triangular basis functions are much better than pulse basis functions.

From the point of view of integration theory, this would seem to be questionable. Basic numerical analysis texts show that stairstep (pulse) integration comparable to (and in fact is more accurate than) trapezoidal (triangle) integration. This fact would lead one to expect that results from the use of pulse basis functions might be comparable to those resulting from use of triangle basis functions. Figs. 5 and 6 use the same numerical results computed for Figs. 1-4 and compare results for triangle and pulse basis functions, first for Galerkin and then for colocation. For Galerkin weighting the triangle results are slightly better. The colocation comparison shows a larger difference, but clearly both curves are similar and converge well to an accurate answer.

(C) Results from different methods can be meaningfully compared even though the computations have not converged.

This is a general error not confined to the moment method, but is well illustrated by several well-known results obtained with the moment method. As an example, the input current for the infinitesimal-gap-fed dipole has been solved numerically a number of times and some attempts have been made to compare the results. It is known theoretically that the imaginary part of the input current is infinite and hence numerically can never converge to a definite value. This has apparently not been noticed because most of these analyses have used a relatively small number of basis functions.

[D] Singularities in the Green's function are bad and the reduced Green function is a good approximation.

Although the presence of singularities in the Green's function require careful handling, their presence makes the integral equation well posed. Although a useful approximation in some circumstances, the reduced Green's function does not have a singularity and hence the corresponding integral equation is ill-posed. If the number of basis functions is steadily increased, eventually the solution becomes totally unstable.

(E) The Green's function is integrated numerically, except where analytic expressions are available.

The spectral method usually leads to expressions for the Green's function as a Fourier series or a Fourier integral. In the case of Fourier series, the moment integration usually can be applied term-by-term, and one never computes the Green's function. In this case, the Galerkin

method results in much faster convergence.

(F) The matrix of coefficients is inverted to find the solution.

This usually is probably just a matter of semantics, but some people takes the statement literally. Solution of a set of linear algebraic equations by inversion of the matrix is terribly inefficient and should never be done.

CONCLUSIONS

The examples presented here suggest that care be taken in interpreting "well-known truths." A realistic look at the results of numerical computations should be taken in the comparisons of various methods. One should be careful about believing all of the established truth (folklore.) The author has some concern that others may have concentrated on other problems and drawn different conclusions than expressed here. These topics should be more fully discussed.

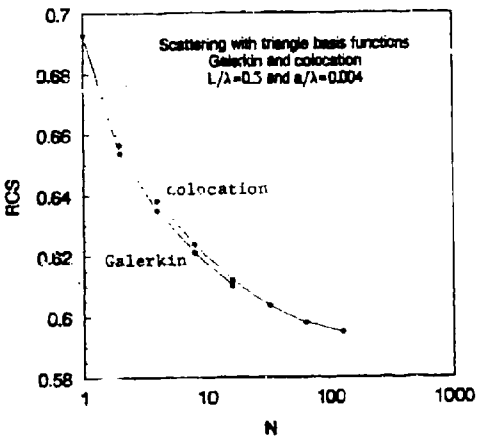

Figure 1. Galerkin and colocation solutions with triangle basis functions.

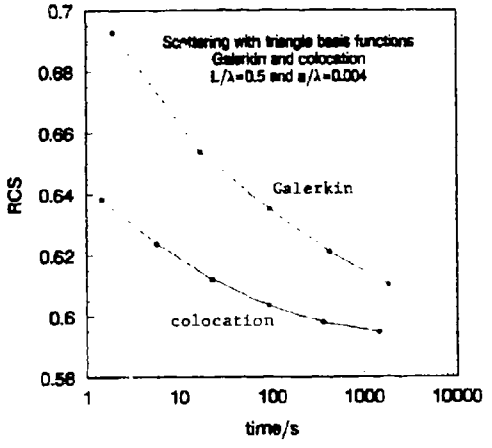

Figure 2. Galerkin and colocation solutions with triangle basis functions.

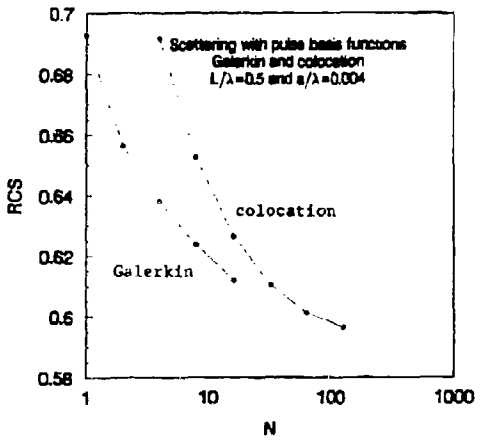

Figure 3. Galerkin and colocation solutions with pulse basis functions.

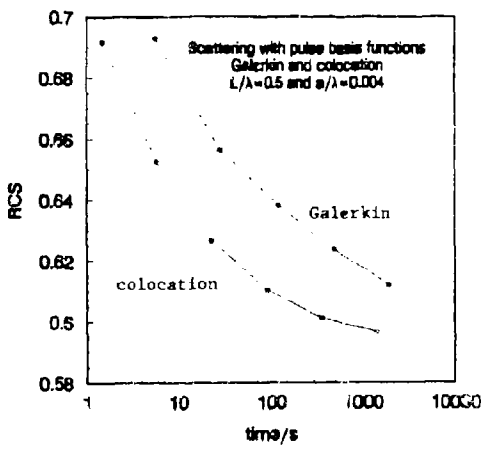

Figure 4. Galerkin and colocation solutions with pulse basis functions.

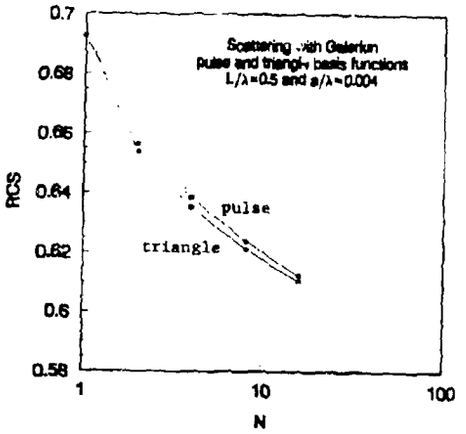

Figure 5. Galerkin solutions with triangle and pulse basis functions.

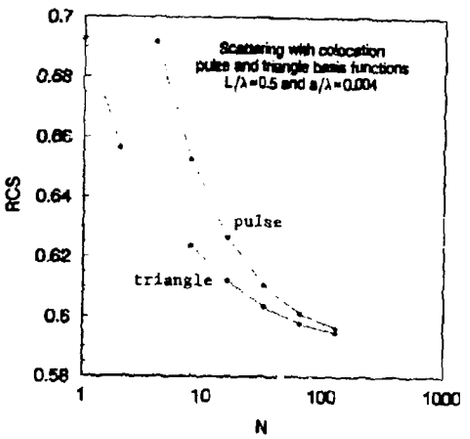

Figure 6. Colocation solutions with triangle and pulse basis functions.

SESSION 15:

EMI/EMP/EMC

Chair: Frank Walker
Co-Chair: Renaldo Perez

Validation of a Numerical Finite Integration Code to Solve Transient Electromagnetic, Acoustic and Elastic Wave Scattering in 2D

Karl J. Langenberg
René Marklein
Dept. Electrical Engineering
University of Kassel
D-34109 Kassel, Germany

Introduction

Recently, a unified numerical scheme to solve transient acoustic, electromagnetic and elastic wave scattering has been developed, which utilizes the Finite Integration Technique (FIT) originally applied to Maxwell's equations [1,2], whence the acronyms AFIT for acoustics, EMFIT for electromagnetics, and EFIT for elastodynamics. The concise and broad evaluation of EMFIT has resulted in the well-established MAFIA computer code [3], whereas EFIT is relatively new [4], and AFIT resulted as a byproduct during the development of EFIT [5]. In [4], stability, convergence and consistency of the EFIT code in 2D and 3D is addressed. As a matter of fact, in two spatial dimensions, Maxwell's equations can be completely decoupled into two scalar problems — the TE- and TM-case — and, therefore, it seems appropriate to validate the essentially scalar AFIT code — specialized to 2D — against canonical 2D scattering and diffraction problems, which could be analytically solved. The possibly most famous one among those is Sommerfeld's half-plane diffraction problem [6]. Recently, Shirai and Felsen [7] published a hybrid ray-mode technique to solve the coupling of a plane wave into a twodimensional waveguide at least approximately for high frequencies. The present paper compares the numerical results of AFIT with Sommerfeld's, Shirai's and Felsen's results and states excellent agreement; it even answers the question when the Shirai-Felsen high frequency approximation is no longer good enough.

Basic Equations

FIT is based on the integral formulation of the basic field equations, i.e. Maxwell's equations in integral form in the case of EMFIT. These read:

$$\iint_{\Gamma_{em}} \mu(\underline{\mathbf{R}})\,\dot{\underline{\mathbf{H}}}(\underline{\mathbf{R}},t)\cdot\underline{\mathbf{n}}\,\mathrm{d}S \;=\; -\oint_{\Lambda_{em}} \underline{\mathbf{E}}(\underline{\mathbf{R}},t)\cdot\underline{\mathbf{s}}\,\mathrm{d}R - \iint_{\Gamma_{em}} \underline{\mathbf{J}}_m(\underline{\mathbf{R}},t)\cdot\underline{\mathbf{n}}\,\mathrm{d}S \qquad (1)$$

$$\iint_{\Gamma_{em}} \varepsilon(\underline{\mathbf{R}})\dot{\underline{\mathbf{E}}}(\underline{\mathbf{R}},t)\cdot\underline{\mathbf{n}}\,\mathrm{d}S \;=\; \oint_{\Lambda_{em}} \underline{\mathbf{H}}(\underline{\mathbf{R}},t)\cdot\underline{\mathbf{s}}\,\mathrm{d}R - \iint_{\Gamma_{em}} \underline{\mathbf{J}}_e(\underline{\mathbf{R}},t)\cdot\underline{\mathbf{n}}\,\mathrm{d}S\ , \tag{2}$$

where $\underline{\mathbf{H}}(\underline{\mathbf{R}},t)$ and $\underline{\mathbf{E}}(\underline{\mathbf{R}},t)$ denote magnetic and electric field strengths, respectively, as function of position $\underline{\mathbf{R}}$ and time t; $\varepsilon(\underline{\mathbf{R}})$ and $\mu(\underline{\mathbf{R}})$ characterize an inhomogeneous medium in terms of permittivity and permeability. The field sources are given by electric and magnetic current densities $\underline{\mathbf{J}}_e(\underline{\mathbf{R}},t)$ and $\underline{\mathbf{J}}_m(\underline{\mathbf{R}},t)$. The double integrals extend over open surfaces Γ_{em} with unit normal $\underline{\mathbf{n}}$, whereas the line integrals extend over the closed boundary contour Λ_{em} of Γ_{em} with unit tangential vector $\underline{\mathbf{s}}$. The top dots indicate time derivatives.

In scalar acoustics, the material parameters are mass density $\varrho_{a0}(\underline{\mathbf{R}})$ and compressibility $\kappa(\underline{\mathbf{R}})$, the field quantities are pressure $p(\underline{\mathbf{R}},t)$ and particle velocity $\underline{\mathbf{v}}(\underline{\mathbf{R}},t)$, and the sources are forces $\underline{\mathbf{f}}(\underline{\mathbf{R}},t)$ as well as deformation rates $h_a(\underline{\mathbf{R}},t)$. Hence, the following equations

$$\iiint_{\Omega_a} \varrho_{a0}(\underline{\mathbf{R}})\,\dot{\underline{\mathbf{v}}}(\underline{\mathbf{R}},t)\,\mathrm{d}V \;=\; -\oiint_{\Gamma_a} \underline{\mathbf{n}}\,p(\underline{\mathbf{R}},t)\,\mathrm{d}S + \iiint_{\Omega_a} \underline{\mathbf{f}}_a(\underline{\mathbf{R}},t)\,\mathrm{d}V \tag{3}$$

$$\iiint_{\Omega_a} \kappa(\underline{\mathbf{R}})\dot{p}(\underline{\mathbf{R}},t)\,\mathrm{d}V \;=\; \oiint_{\Gamma_a} \underline{\mathbf{n}}\cdot\underline{\mathbf{v}}(\underline{\mathbf{R}},t)\,\mathrm{d}S + \iiint_{\Omega_a} h_a(\underline{\mathbf{R}},t)\,\mathrm{d}V \tag{4}$$

hold, which relate acceleration forces, volume forces and forces of inertia — equation (3) — and deformation rates (equation (4)). The triple integrals extend over volumes Ω_a, whereas the double surface integrals are to be taken over the closed surfaces Γ_a of Ω_a with outward normal $\underline{\mathbf{n}}$.

In elastodynamics, the physics of equ.'s (3) and (4) has to be generalized to solids being characterized by a mass density $\varrho_{e0}(\underline{\mathbf{R}})$ and a forth rank compliance tensor $\underline{\underline{\underline{\underline{\mathbf{s}}}}}(\underline{\mathbf{R}})$; the symmetric part of the second rank tensor $\underline{\mathbf{n}}\,\underline{\mathbf{v}}(\underline{\mathbf{R}},t)$ defines the time derivative of the strain tensor after integration over the volume Ω_e and transformation into a surface integral with surface Γ_e applying Gauss' theorem. In linear elastodynamics the strain tensor is related to the stress tensor $\underline{\underline{\mathbf{T}}}(\underline{\mathbf{R}},t)$ through Hooke's law via the double contraction with the compliance tensor. These remarks illustrate the basic equations of elastodynamics:

$$\iiint_{\Omega_e} \varrho_{e0}(\underline{\mathbf{R}})\,\dot{\underline{\mathbf{v}}}(\underline{\mathbf{R}},t)\,\mathrm{d}V \;=\; \oiint_{\Gamma_e} \underline{\mathbf{n}}\cdot\underline{\underline{\mathbf{T}}}(\underline{\mathbf{R}},t)\,\mathrm{d}S + \iiint_{\Omega_e} \underline{\mathbf{f}}_e(\underline{\mathbf{R}},t)\,\mathrm{d}V \tag{5}$$

$$\iiint_{\Omega_e} \underline{\underline{\underline{\underline{\mathbf{s}}}}}(\underline{\mathbf{R}}) : \dot{\underline{\underline{\mathbf{T}}}}(\underline{\mathbf{R}},t)\,dV \;=\; \oiint_{\Gamma_e} \mathrm{sym}\,\{\underline{\mathbf{n}}\,\underline{\mathbf{v}}(\underline{\mathbf{R}},t)\}\,\mathrm{d}S + \iiint_{\Omega_e} \underline{\underline{\mathbf{h}}}_e(\underline{\mathbf{R}},t)\,\mathrm{d}V\ . \tag{6}$$

Discretization

FIT chooses two cubic staggered grids to solve the basic equations numerically. For the 2D-TE EMFIT, as well as for the 2D AFIT code these grids are displayed in Fig. 1. As usual, TE indicates an electromagnetic field having no electric field component in *that* direction from which all field components are independent; here, this is the z-direction. The discrete equations resulting from an approximate integration of the field equations are given as follows:

$$\mathrm{E}_x^{\left(i_x,i_y+\frac{1}{2},z+1\right)} \;=\; \mathrm{E}_x^{\left(i_x,i_y+\frac{1}{2},z\right)} + \frac{\Delta t}{\varepsilon}\left\{\frac{1}{\Delta y}\left[\mathrm{H}_z^{\left(i_x,i_y,z+\frac{1}{2}\right)} - \mathrm{H}_z^{\left(i_x,i_y+1,z+\frac{1}{2}\right)}\right] -\right.$$

$$- J_{ex}^{(i_x, i_y+\frac{1}{2}, z+\frac{1}{2})} \Big\} \tag{7}$$

$$E_y^{(i_x+\frac{1}{2}, i_y, z+1)} = E_y^{(i_x+\frac{1}{2}, i_y, z)} + \frac{\Delta t}{\varepsilon} \left\{ \frac{1}{\Delta x} \left[H_z^{(i_x+1, i_y, z+\frac{1}{2})} - H_z^{(i_x, i_y, z+\frac{1}{2})} \right] - \right.$$
$$\left. - J_{ey}^{(i_x+\frac{1}{2}, i_y, z+\frac{1}{2})} \right\} \tag{8}$$

$$H_z^{(i_x, i_y, z+\frac{1}{2})} = H_z^{(i_x, i_y, z-\frac{1}{2})} + \frac{\Delta t}{\mu} \left\{ \frac{1}{\Delta y} \left[E_x^{(i_x, i_y-\frac{1}{2}, z)} - E_x^{(i_x, i_y+\frac{1}{2}, z)} \right] + \right.$$
$$\left. + \frac{1}{\Delta x} \left[E_y^{(i_x+\frac{1}{2}, i_y, z)} - E_y^{(i_x-\frac{1}{2}, i_y, z)} \right] - J_{mz}^{(i_x, i_y, z)} \right\} . \tag{9}$$

The grid widths are given by Δx and Δy, and time — counted by discrete values of z — is discretized in Δt-increments in terms of a central difference formula; the details can be found in [2], [4] and [5]. It should be pointed out, that — at least for EMFIT — it has been proven, that the discrete equations have the same physical properties as the continuous system of Maxwell's equations [2].

Sommerfeld's Half-Plane Proolem

Fig. 2 illustrates Sommerfeld's half-plane problem: A plane TE-polarized time harmonic wave of wavenumber $k = 2\pi/\lambda$ is incident upon an infinitely thin perfectly conducting half-plane. This electromagnetic problem is equivalent to the acoustic problem with a Neumann boundary condition of vanishing normal derivative of the pressure on the half-plane. Fig. 3 compares results obtained with Sommerfeld's analytical solution and with the EMFIT/AFIT code, respectively; since FIT, in this presentation, is a transient scheme, the EMFIT code is run for a switched-on sinusoidal wave until the stationary state is reached. Absorbing boundary conditions prevent reflections from the finite grid boundaries. Fig. 3 displays the magnitude of the H_z-component as grey scale plots, together with amplitude variations along two particularly chosen lines. Obviously, EMFIT/AFIT is perfectly validated against the analytical solution.

Shirai's and Felsen's Open-Ended Waveguide Problem

Fig. 4 illustrates the problem attacked by Shirai and Felsen; a plane TE-polarized time harmonic plane wave couples into an open-ended waveguide composed of two infinitely thin perfectly conducting plates. Their method of solution, which involves an intricate evaluation and decomposition of spectral integrals into rays and modes, is approximately valid for high frequencies. Fig. 5 gives EMFIT/AFIT results for the field in the waveguide in terms of a grey scale plot, and, additionally, for a distance of $kx = 204$ from the waveguide aperture, the cross-sectional $|H_z|$-field amplitude is displayed; Fig. 6 shows the results of Shirai and Felsen copied from their paper to the same scale. Obviously, the agreement is striking.

References

[1] K.S. Yee: Numerical Solution of Initial Boundary Value Problems Involving Maxwell's Equations in Isotropic Media. 14 (1966) 302

[2] M. Bartsch et al : Solution of Maxwells' Equations. Computer Physics Communications **72** (1992) 22

[3] The MAFIA Collaboration (Ed.: T. Weiland): MAFIA, Release 3.1. Darmstadt 1991

[4] P. Fellinger, R. Marklein, K.J. Langenberg, S. Klaholz: Numerical Modeling of Elastic Wave Propagation and Scattering with EFIT. Wave Motion (1994) (to be published)

[5] R. Marklein: Die Akustische Finite Integrationstechnik (AFIT) — Ein numerisches Verfahren zur Lösung von Problemen der Abstrahlung, Ausbreitung und Streuung von akustischen Wellen im Zeitbereich. Master Thesis, University of Kassel, Dept. El. Eng., Kassel 1992

[6] A. Sommerfeld: Mathematische Theorie der Diffraktion. Mathematische Annalen **47** (1896) 317

[7] H. Shirai, L.B. Felsen: Rays, Modes and Beams for Plane Wave Coupling into a Wide Open-Ended Parallel-Plane Waveguide. Wave Motion **9** (1987) 301

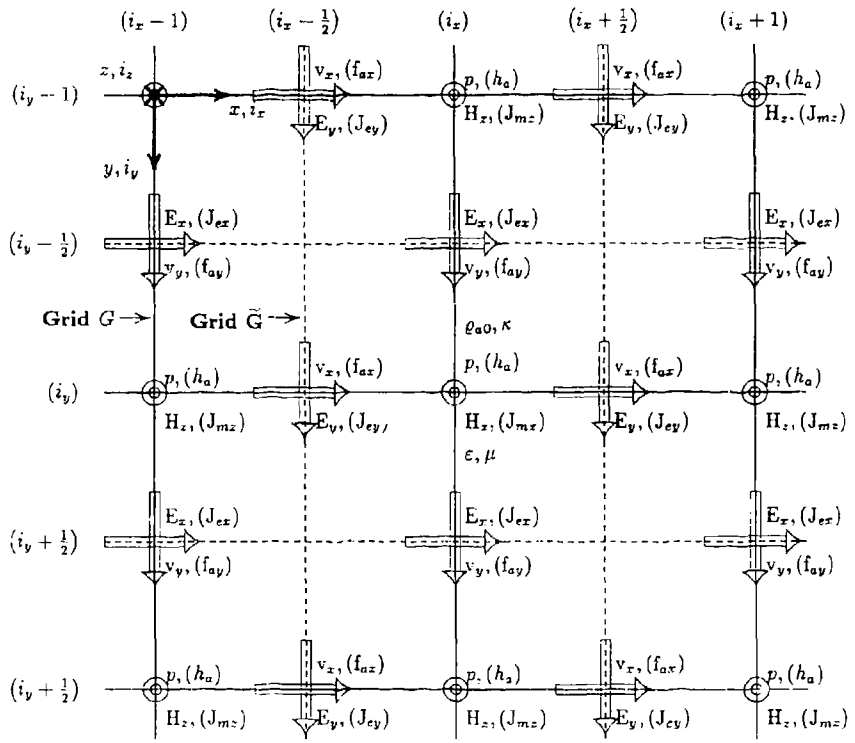

Figure 1: 2D-TE EMFIT and 2D AFIT staggered grids

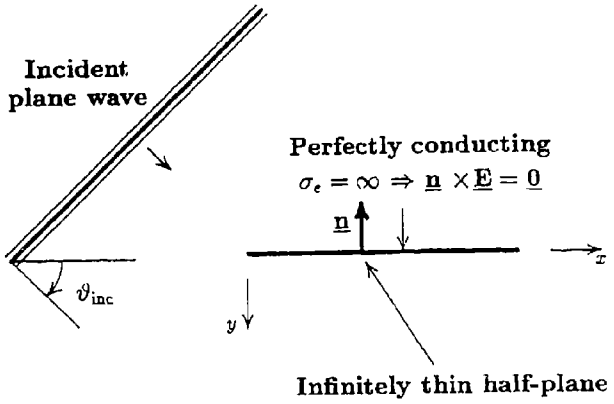

Figure 2: Sommerfeld's half-plane problem

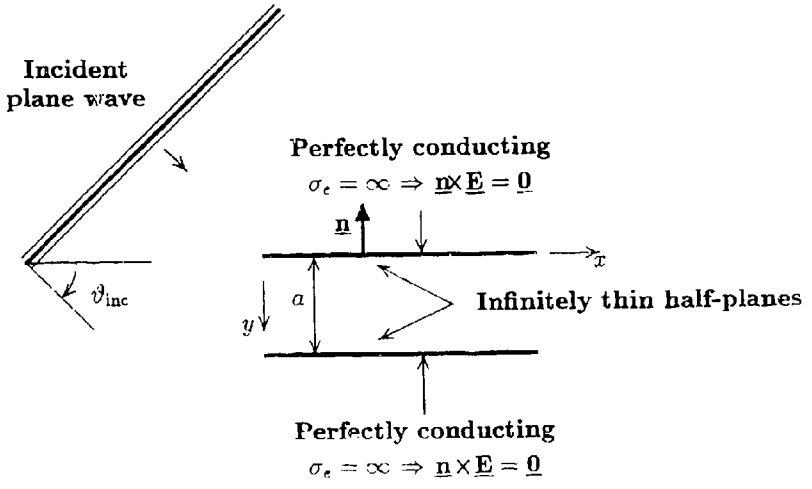

Figure 4: Shirai's and Felsen's open-ended waveguide problem

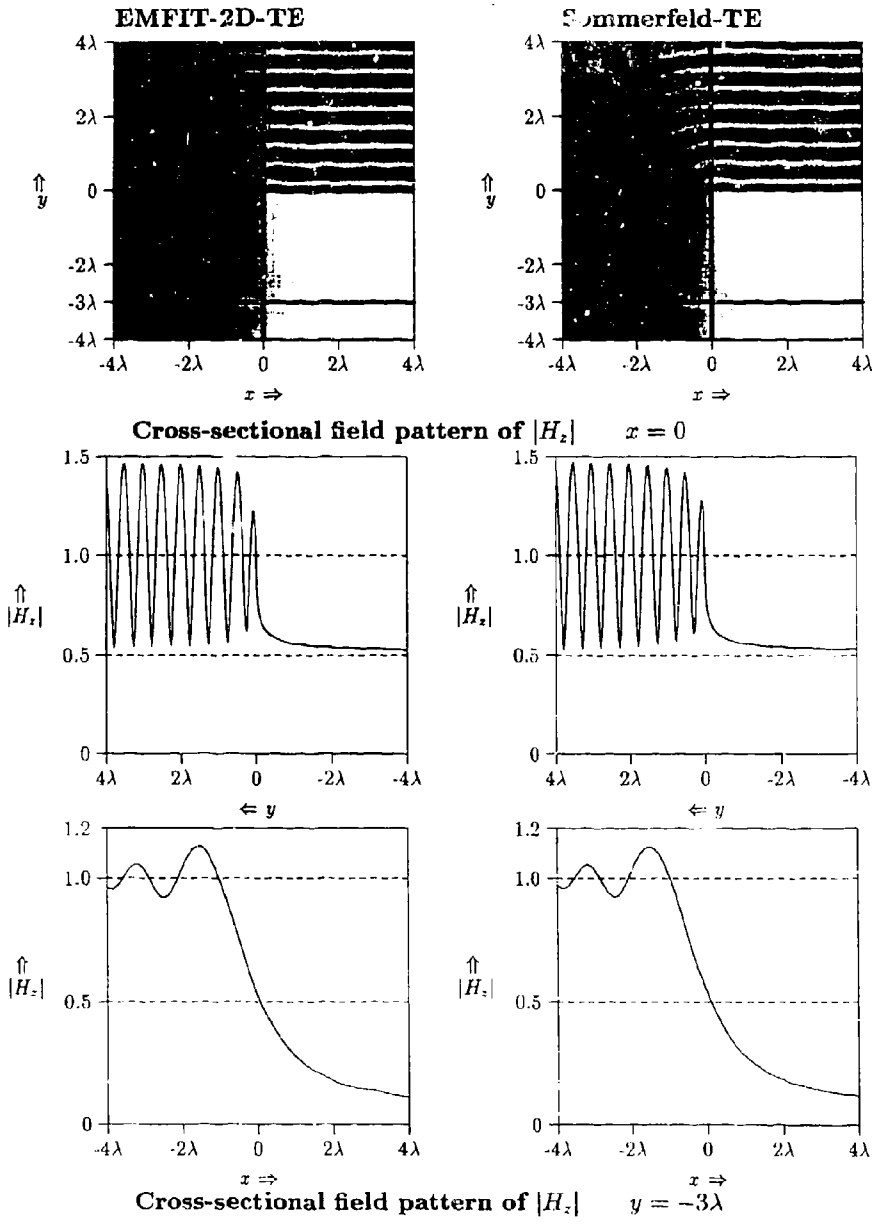

Figure 3: Sommerfeld's half-plane problem: Results

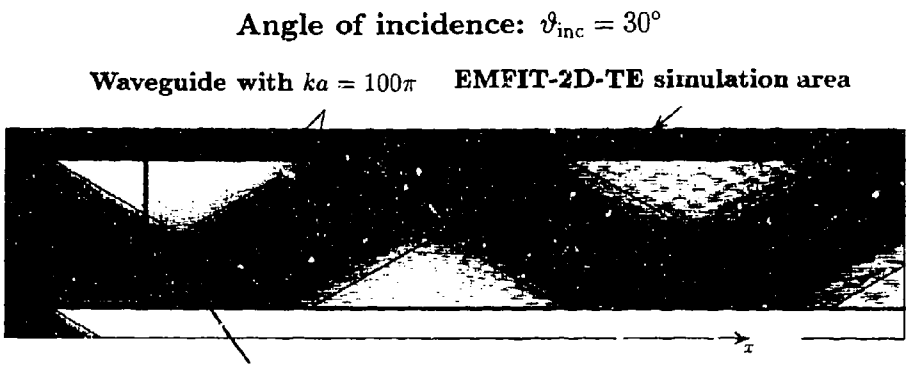

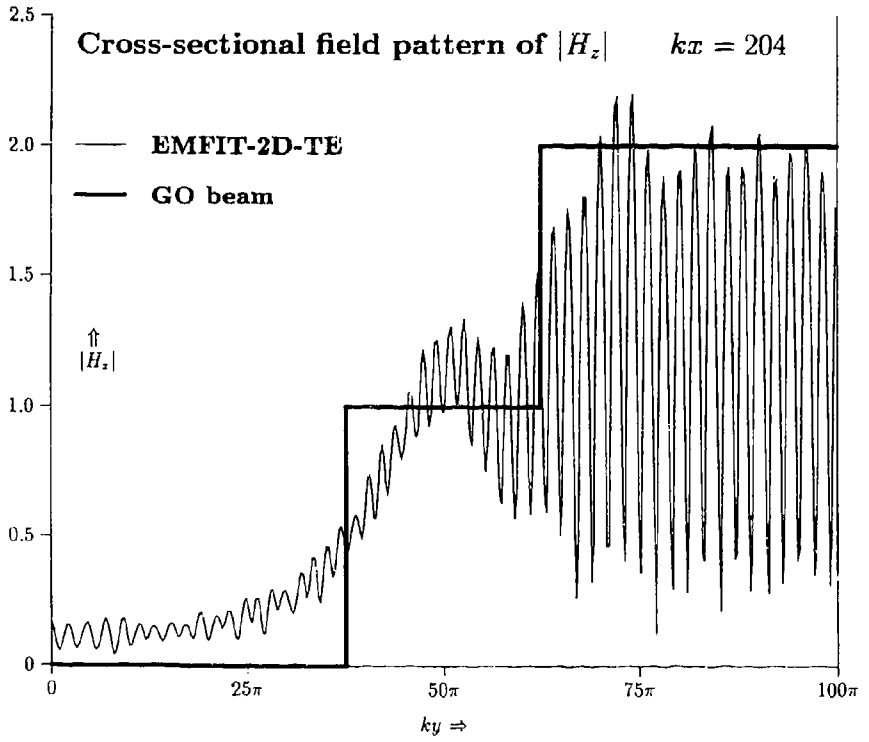

Figure 5: Shirai's and Felsen's open-ended waveguide problem: EMFIT/AFIT-Results

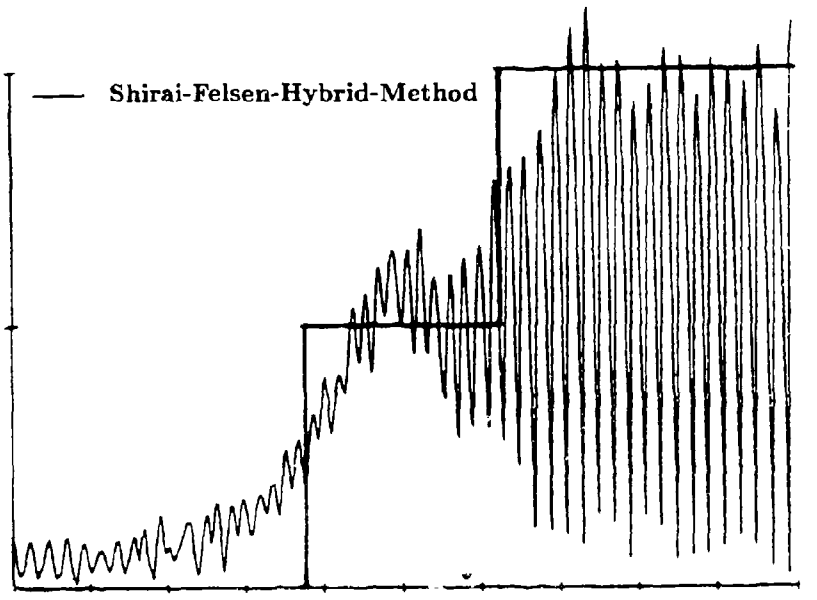

Figure 6: Shirai's and Felsen's open-ended waveguide problem: Results

Karl J. Langenberg is professor of electromagnetic theory at the University of Kassel in Germany. His main research interests are numerical methods for wave propagation problems as well as computational methods for inverse scattering problems with special emphasis on elastic waves as applied to nondestructive testing. Professor Langenberg is vice-president of the International Union of Radio Science in Germany (U.R.S.I), and he serves as a member of the Editorial Board of the ACES Journal and Wave Motion.

Comparison Between LEMP & NEMP Induced Overvoltages in 33 kV Overhead Distribution Lines

R. Moini, B. Kordi, B. Vahidi, AND M. Abedi
AmirKabir University of Technology
Electrical Engineering Department
No 424, Hafez Ave., TEHRAN, I.R.IRAN
Phone:(+98)216139480,FAX:(+98)216406469

Abstract :

In this paper an attempt has been made to introduce a method for evaluation of induced overvoltages caused by nuclear electromagnetic pulse (NEMP) in overhead lines. NEMP occurs in space in high altitude, due to nuclear explosion in space. The paper also compares the induced overvoltage caused by NEMP, with overvoltage produced by lightning electromagnetic pulse (LEMP). In LEMP analysis, lightning is a local phenomena, therefore the performance of transmission lin can be examined conveniently, using suitable model for lightning stroke channel, and applying transmission line theory. However NEMP covers large area simultaneously, and has specific characteristics. So it is impossible to utilize transmission line theory similar to LEMP analysis. In this paper direct solution of Maxwell's equations has been used in time domain, using electric field integral equation (EFIE) for evaluation of induced voltage and current in any point of overhead line, due to NEMP. The results presented in this article belong to 33 kV overhead distribution line. With comparing the LEMP and NEMP results, it is found out that the overvoltage protective devices (arresters), installed at the receiving or sending ends of transmission line may protect the line against LEMP, however it may fail to respond against NEMP.

1) Introduction:

In most publications the performance of OHL due to applied electromagnetic waves ha been evaluated in frequency domain, using transmission line theory. Then the voltage-time and current-tin characteristics of OHL can be obtained by using Fourier transformation [1,2]. It is clear that above technique can not be used for narrow pulses, such as NEMP. In this paper time-space integral equation is used for evaluation of voltage-time and current-time characteristics along OHL, in order to be able to asses the performance of OHL against NEMP [3]. The following items have considerable effects on induced voltage and current caused by NEMP :

- Geometry of OHL such as length, conductor diameter, height of conductor.
- System configuration such as both ends conditions.
- Periphery conditions such as earth conductivity and permitivity.
- Location of OHL for considering the direction of incident wave caused by nucl r explosion.
- Polarization of incident wave in respect to line location on earth surface.

Keywords :
Nuclear Electromangnetic Pulse (NEMP) , Lightning Electromagnetic Pulse (LEMP) , Lightning Induced Voltage (LIV) , Nuclear Induced Voltage (NIV) , Over Head Line (OHL)

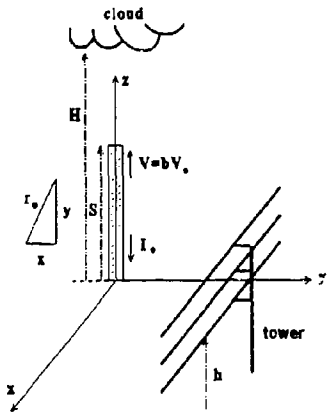

Fig.1 : Three dimensional XYZ coordinate with return stroke channel and 3-phase power conductors [6].

Fig.2 : 33 Kv OHL nearby lightning channel.

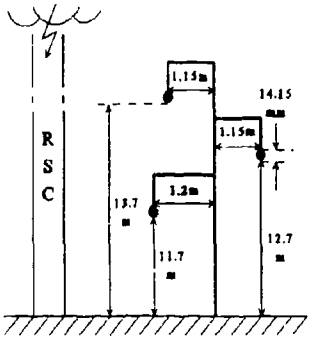

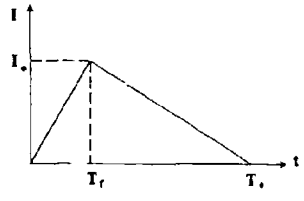

Fig.3 : Conventional lightning current wave shape [4].

In this paper with comparing the results belonging to LEMP and NEMP for sample 33 kV line, one can find out considerable differences in line performance, due to these two distinct pulses. The accurate evaluation of above items provides outstanding idea for designing new devices for OHL protection against nuclear explosions .

2) Lightning Induced Voltage (LIV) :

Fig.1 shows the geometry of OHL line along with lightning stroke channel. The results presented in this section are related to tower of 33 kV line shown in Fig.2. The lightning current wave shape is depicted in Fig.3. The method for LIV evaluation is mentioned exclusively in [4,5]. Fig.4 shows LIV for following parameters :

T_f = 1.2 μsec T_e = 100 msec
h = 13.7 m I_0 = 100 KA
H = 2 Km X=0 ,Y=100 m
1: b=0.3 2: b=0.1

Fig.5 shows LIV for I_0 = 200 kA and Y = 200 m, however other parameters are similar to Fig.4. Fig.6 illustrates normalized LIV for :

I_0 = 1kA , h = 1m ,Y = 200m

3) NEMP Effects

3-1) Characteristics of the Electromagnetic pulse due to high altitude nuclear explosion :

In the case of nuclear explosion in high altitude above the earth shown in Figs.7-a, 7-b, many Gamma photons would be released. These photons deliver energy to the electrons which are released from the orbits of space molecules. Such electrons are called Compton electrons. These electrons have low inertia, therefore move faster than produced positive ions. Thus some sort of static electric field can be established. In addition, due to earth magnetic field, deviation will be occured in initial path of Compton electrons. Thus the time-variant electric current causing time-variant electromagnetic wave would be established above the atmosphere.

Different measurements show that the radiowave caused by nuclear explosion can be shown by electromagnetic pulse [6]:

$$E(t) = A\ [\ exp(-\alpha t) - exp(-\beta t)\ ]$$

Fig.8 illustrates time variation of such pulse. t_0 , t_1 and A are related to explosion parameters, such as air density, intensity, altitude, etc. In some cases t_0 is less than few nanoseconds, and the maximum amplitude of electric field is about 50 kV/m .

3-2) Theoretical Method :

Fig.2 shows 33 kV distribution overhead line considered in this paper which is illuminated by NEMP with following parameters. These parameters are issued by North Atlantic Treaty Organization (NATO) [7,8], therefore:

A = 50 kV/m t_0 = 5 ns t_1 = 200 ns

Now, we analyse the scattering of the perfect conductor wires illuminated by the transient electromagne

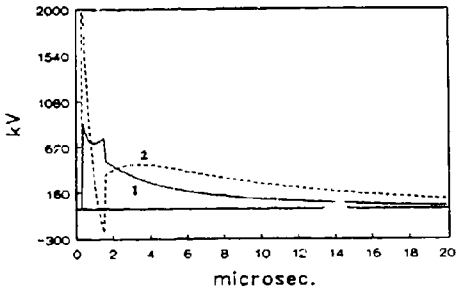

Fig.4 : LIV for I_0 = 100 KA
1:b = 0.3 , 2:b = 0.1

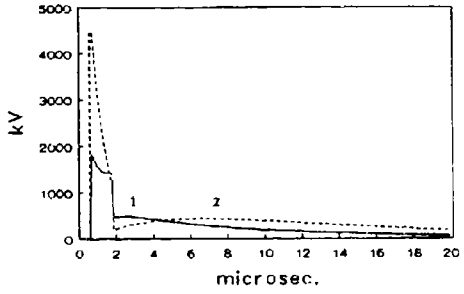

Fig.5 : LIV for I_0 = 200 KA
1:b = 0.3 , 2:b = 0.1

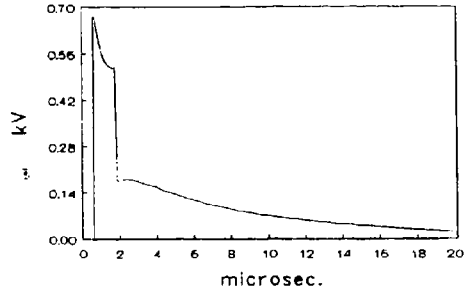

Fig.6 : Normalized LIV

In this paper with comparing the results belonging to LEMP and NEMP for sample 33 kV line, one can find out considerable differences in line performance, due to these two distinct pulses. The accurate evaluation of above items provides outstanding idea for designing new devices for OHL protection against nuclear explosions .

2) Lightning Induced Voltage (LIV) :

Fig.1 shows the geometry of OHL line along with lightning stroke channel. The results presented in this section are related to tower o V line shown in Fig.2. The lightning current wave shape is depicted in Fig.3. The method for LIV c tion is mentioned exclusively in [4,5]. Fig.4 shows LIV for following parameters :

T_f = 1.2 μsec T_e = 100 msec
h = 13.7 m I_0 = 100 KA
H = 2 Km X=0 ,Y=100 m
1: b=0.3 2: b=0.1

Fig.5 shows LIV for I_0 = 200 kA and Y = 200 m, however other parameters are similar to Fig.4. Fig.6 illustrates normalized LIV for :

I_0 = 1kA , h = 1m ,Y = 200m

3) NEMP Effects

3-1) Characteristics of the Electromagnetic pulse due to high altitude nuclear explosion :

In the case of nuclear explosion in high altitude above the earth shown in Figs.7-a, 7-b, many Gamma photons would be released. These photons deliver energy to the electrons which are released from the orbits of space molecules. Such electrons are called Compton electrons. These electrons have low inertia, therefore move faster than produced positive ions. Thus some sort of static electric field can be established. In addition, due to earth magnetic field, deviation will be occured in initial path of Compton electrons. Thus the time-variant electric current causing time-variant electromagnetic wave would be established above the atmosphere.

Different measurements show that the radiowave caused by nuclear explosion can be shown by electromagnetic pulse [6]:

$$E(t) = A\ [\ exp(-\alpha t) - exp(-\beta t)\ ]$$

Fig.8 illustrates time variation of such pulse. t_0 , t_1 and A are related to explosion parameters, such as air density, intensity, altitude, etc. In some cases t_0 is less than few nanoseconds, and the maximum amplitude of electric field is about 50 kV/m .

3-2) Theoretical Method :

Fig.2 shows 33 kV distribution overhead line considered in this paper which is illuminated by NEMP with following parameters. These parameters are issued by North Atlantic Treaty Organization (NATO) [7,8], therefore:

A = 50 kV/m t_0 = 5 ns t_1 = 200 ns

Now, we analyse the scattering of the perfect conductor wires illuminated by the transient electromagnetic

waves [3,9]. Reffering to Fig.9, the incident wave ($\bar{e}_i$, $\bar{h}_i$) is reflected ($\bar{e}_r$, $\bar{h}_r$) by the ground, as a result the total field is $\bar{e}_a = \bar{e}_i + \bar{e}_r$.

The total field will induce a current I(M,t) on the perfect conductor wire and the induced current will generate the scattered field ($\bar{e}_d$, $\bar{h}_d$). Therefore, the total field in the space is

$$\bar{e}(P,t) = \bar{e}_a(P,t) + \bar{e}_d(P,t)$$

Now by the continuity of the electric field on the antenna OHL, we have

$$\bar{s} \cdot \bar{e}(M,t) = 0$$

$$\bar{s} \cdot [\, \bar{e}_a(M,t) + \bar{e}_d(M,t) \,] = 0$$

Considering that $\bar{e}_d(M,t)$ is the result of the induced current on the power line, we get

$$\bar{e}_d(M,t) = L(I(M,t))$$

where L is the integro-differential operator derived from Maxwell's equations. Therefore, the integral equation for the induced current on the power line is [3]

$$\bar{s} \cdot \bar{e}^{\,a}(s,t) = \frac{\mu_0}{4\pi} \int_{Co} \left\{ \frac{\bar{s} \cdot \bar{s}_0}{R} \frac{\partial I}{\partial t_0}(s_0, t_0) + \right.$$

$$v \frac{\bar{s} \cdot \bar{R}}{R^2} \frac{\partial I}{\partial s_0}(s_0, t_0) + v^2 \frac{\bar{s} \cdot \bar{R}}{R^3} \int_0^{t_0} \frac{\partial I}{\partial s_0}(s_0, \tau)\, d\tau -$$

$$\frac{\bar{s} \cdot \bar{s}_0^{\,*}}{R^*} \frac{\partial I}{\partial t_0^*}(s_0, t_0^*) - v \frac{\bar{s} \cdot \bar{R}^*}{R^{*2}} \frac{\partial I}{\partial s_0}(s_0, t_0^*) -$$

$$\left. v^2 \frac{\bar{s} \cdot \bar{R}^*}{R^{*3}} \int_0^{t_0^*} \frac{\partial I}{\partial s_0}(s_0, \tau)\, d\tau \right\} dCo$$

$$R = \left[(s - s_0)^2 + a^2 \right]^{1/2} \quad , \quad R^* = \left[(s - s_0^*)^2 + a^2 \right]^{1/2}$$

$$v = \frac{c}{\sqrt{\varepsilon_r}} \quad , \quad t_0 = t - R/v \quad , \quad t_0^* = t - R^*/v$$

Note that $\bar{e}_a$ represents the plane wave due to NEMP and its reflection by the ground (perfect conductor)

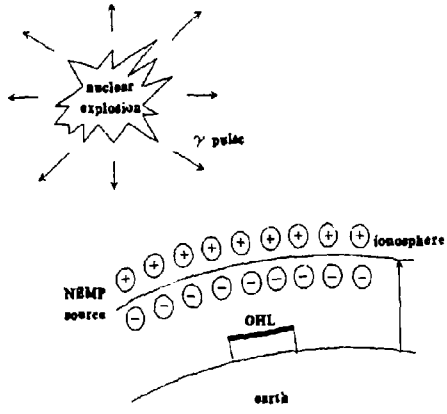

Fig.7-a : Schematic illustration showing nuclear explosion in space in respect to OHL.

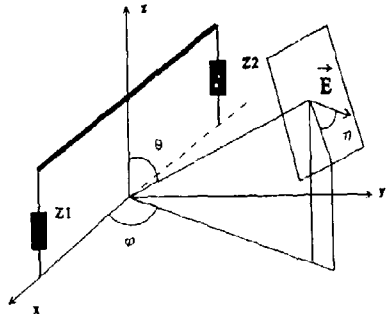

Fig.7-b : Polarization of incident wave in respect to single conductor line.

and the integrations are performed on the wires that model the transmission line. Now the resultant equation is solved by the method of moment in the time domain and the induced currents and voltages on the wires are calculated [9].

4) Simulation Results :

In this section some simulation results will be presented for illustrating the effects of NEMP on induced overvoltage in 33 kV OHL. In any simulation procedure, the main goal is to reduce the storage, and computing time. Thus, firstly the authors have decided to test the effect of line length. For this purpose three distinct single conductor lines with earth return and the length of 50 , 100 and 200 m have been examined (single phase electromagnetic line).

For these lines two cases are observed :

- case 1 : both ends are terminated to characteristic impedance (Fig.10).
- case 2 : both ends are open (Fig.11).

Fig.10 shows the overvoltages of above three single phase lines at sending or receiving ends caused by NEMP. For deducing these plot it is assumed thet all points along the line are illuminated simultaneously and electric field integral equation (EFIE) technique has been used for solving Maxwell's equations. It can be seen that in all three single phase lines (Fig.10), all overvoltages will be eventually damped. It is also clear that the voltage rises sharply at one end, reaching the first positive peak. For 50 m line, after the other end received wave travells 50 m with light velocity, the voltage drops sharply towards first negative peak, which will be eventually damped. For 100 and 200 m single phase lines, sharp voltage drop towards associated negative peak occurs at 100 and 200 m respectively. Therefore if the line length is assumed to be infinity, first positive peak will be seen, however first negative peak will not be appeared.

Fig.11 illustrates the transient overvoltages caused by NEMP for above single phase lines, while both ends are open. It can be seen that the first positive peak with sharp rise time is similar for all lines with different length.

Since for selection of protection schemes first peak value, and associated rise time is necessary and sufficient quantities, therefore for saving computing time 50 m line is selected for digital simulations. Now suppose 50 m three phase 33 kV distribution line shown in Fig.2. It is assumed that one end is open circuited and other end is terminated to characteristic impedance. Figs.12 to 15 show the induced overvoltages caused by NEMP for different location of OHL, in respect to point of nuclear explosion. Note that in Fig.15 voltage wave appears at the point under consideration with time delay, exactly equal to time corresponding to passing 50 m with light velocity. The results shows that protective schemes such as arresters, which is capable to protect the system against lightning stroke, is not sufficient protective device for protection the system against nuclear explosion.

Conclusions :

By comparing the LIV and NIV, presented in this article, it is concluded that :

- In calculating LIV, the probability of lightning current magnitude in order of 100 to 200 kA is 3.77% [10]. In this article the above two cases have been examined For b = 0.3, the voltage amplitude would be 850 to 1800 kV respectively.

However it is shown that for b = 0.1 voltage peak would be much higher. The probability of lightning current magnitude in order of 50 kA and higher is 22.3%. If b = 0.3 the voltage amplitude for 50 kA, will be 430 kV [5]. Therefore for current higher that 50 kA, the induced voltage will be more than 430 kV which is harmful for distribution lines. The rise time of LIV is about few microsecond.

- In calculating NIV, it is found out that the peak voltage would be more than 1000 kV and induced overvoltage rise time is about few nanoseconds. Although the voltage magnitude of NIV ($\geq$1000 kV) is less than voltage magnitude of LIV (1800 kV in case of 250 kA lightning current), but the rise time in NIV is

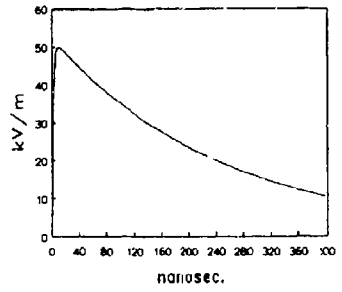

Fig.8 : NEMP pulse.

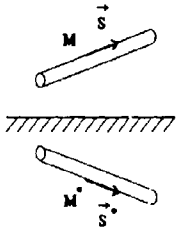

Fig.9 : Incremental section of conductor and its image.

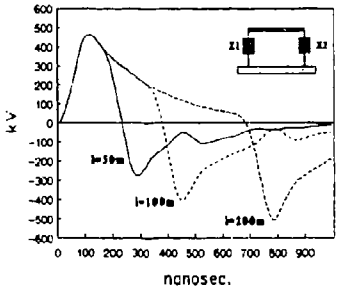

Fig.10 : Overvoltage in single phase line with different length (sending end) .Z1=Z2=Zc

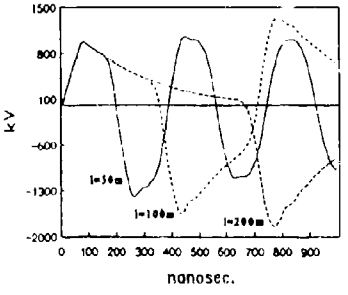

Fig.11 Overvoltage in single phase line with different length (sending end) Z1=Z2=∞

more highly less than rise time of LIV.

- By comparing the results of LIV and NIV it is clear that both phenomenas such as LEMP and NEMP will have harmful effects on OHL particulary for distribution and subtransmission systems.

- By installing lightning arresters the OHL can be protected against LIV, caused by LEMP. However these arresters can not protect the system against NIV, caused by NEMP. The main reason is that the risetime in LIV is about few microseconds, while the risetime in NIV is around nanoseconds.

- Due to large pro developing and third world countries, as well as developed and western nations in nuclear technology ggest that intensive efforts should be made into research of designing new equipments to respond . . NIV as well as LIV.

References :

[1] : M.Ianoz, P.Blech, C.A occi
Analyse de sensibilite des imetres du couplage entre une IEM et une ligne aerienne.
4eme Colloque sur la compatibilite electromagnetique, Limoges 1987, 23-25 Juin.

[2] : M.Aguet,C.C.Lin
Transient electromagnetic field coupling to long shielded cables, IEEE Trans. on EMC, Vol 22, N°4, Nov.1980.

[3] : J.Herault, R.Moini, A.Reineix, B.Jecko
A new approach of microstrip antennas using a mixed analysis : Transient-Frequency, IEEE Trans. on Antennas and Propagation, Vol 38, N°8, Aug. 1990.

[4] : B.Vahidi, M.Abedi
Induced voltage evaluation using simple integration procedure, Power High Tech'91, Taiwan, March 4-7, 1991.

[5] : B.Vahidi
A new approach to evaluation of lightning induced voltages and its comparison with present methods. ICEE'93, May 18-21 1993, Tehran-Iran.

[6] : C.Longmire
On the electromagnetic pulse produced by nuclear explosion, IEEE Trans. on EMC, Vol.20, Feb.1978.

[7] : J.L.Press
EMP response of a generic ground based facility, IEEE EMC Symposium, August 21-23, 1990, Washington DC.

[8] : High voltage laboratory planning
Nils Hylten.Cavallius, Heaffely, 1986.

[9] : R.Moini, G.Z.Rafi, A.Tavakoli
Radar cross section of microstrip patch antennas, a single element and array, ICEE'93, May 18-21, 1993, Tehran-Iran.

[10] : IEEE lightning group
A simplified method for estimating lightning performance of transmission lines, IEEE Vol.PAS-104, N°4, April 1985.

[11] : S.Rusck
Induced lightning overvoltages on power transmission lines with special preferences to the overvoltage protection of low voltage protection of low voltage network, Trans. Royal Inst. of Tech., Stockholm, Sweden.

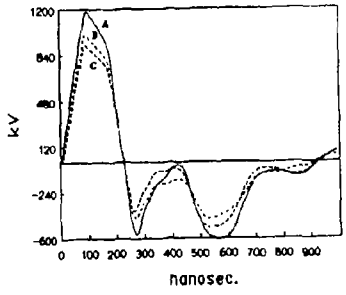

Fig.12 : Induced voltage of 3 phase line at sending end.
$\theta = 0$, $\phi = 0$, $\eta = 0$

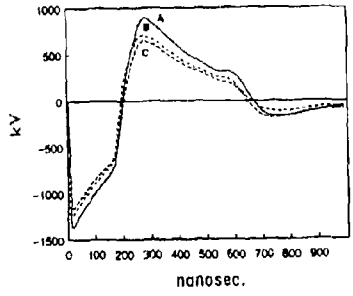

Fig.13 : Same as Fig.12 , $\theta = 90$, $\phi = 90$, $\eta = 180$

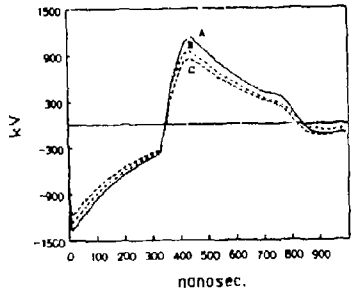

Fig.14 : Same as Fig.12 , $\theta = 90$, $\phi = 0$, $\eta = 180$

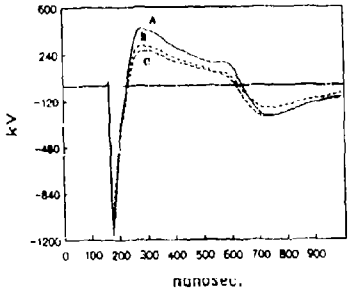

Fig.15 : Same as Fig.12 , $\theta = 90$, $\phi = 180$, $\eta = 180$

Monopole Near-Field Coupling Analysis -- Comparison of Experimental and NEC Results

M. L. Wheeler and R. J. Levin
Georgia Tech Research Institute
Georgia Institute of Technology
Atlanta, Georgia 30332

ABSTRACT

This paper examines the capability of the Numerical Electromagnetic Code (NEC) to predict near-field coupling between monopoles located on a common ground plane (co-site location). NEC-computed coupling data are compared to measured data that were collected in two separate experimental investigations. The initial investigation focuses on coupling between two monopoles mounted on a flat ground plane at antenna-to-antenna spacings varying between 3 wavelengths and 0.05 wavelengths (λ). NEC data generated using an infinite ground plane (IGP) model are presented for this comparison. The second investigation examines coupling between monopoles mounted on an equipment shelter of an Army Command and Control, Communications, and Intelligence (C^3I) vehicle. Aluminum scale models of the equipment shelters were constructed and measured coupling data were collected for typical antenna locations on the models (a total of six coupling paths). All antenna spacings on the scale models were less than one wavelength. NEC wire mesh models of the top surface (antenna mounting surface) of the equipment shelter were used to generate NEC coupling values for this comparison. The measured scale model data was compared to NEC-computed data using both the mesh models and the IGP model. Coupling data computed using the IGP model compared well with the measured data for both the flat ground plane and equipment shelter investigations. The mesh models performed well for five of the six coupling paths in the equipment shelter investigation.

INTRODUCTION

Near-field coupling predictions are an important part of electromagnetic compatibility (EMC) analyses in which two or more low frequency, low gain monopole antennas are mounted on a single ground vehicle or aircraft. Also, in these types of analyses, there is often an uncertainty as to how the limited ground plane area affects the impedance and the coupling characteristics of the monopoles. This paper examines the capabilities and usefulness of NEC when used as a tool for calculating the near-field coupling of monopoles located in these limited ground plane situations.

The usefulness of a computer code is judged by how accurately it can predict real (measured) quantities. In this paper, the accuracy

of the NEC coupling predictions were evaluated by comparing calculated coupling values with measured data that were collected in two separate experimental investigations. The initial investigation was carried out using two tuned quarter-wave monopoles mounted on a thin flat aluminum ground plane. Coupling was measured for monopole spacings of three wavelengths down to one-twentieth of a wavelength (λ). Also, impedance effects induced by locating a monopole close to the edge of the ground plane were investigated. NEC coupling data generated using an infinite ground plane (IGP) model are compared with the measured ground plane data.

The second investigation involved modeling the equipment shelter of a C^{3}I vehicle. These vehicles often have two or more VHF whip antennas mounted on the top of the equipment shelter in the rear cargo bay. The spacing between the antennas is typically only a few tenths of a wavelength at the low end of the VHF band. Scaled box shaped models of the equipment shelter were constructed and coupling measurements were made fo scaled quarter-wave monopoles mounted at various locations on these oxes. NEC wire mesh models representing the top plate surface (antenna mounting surface) were created and the coupling data generated with the mesh models were compared with measured data. In addition, coupling values obtained with the IGP model were also compared to the scale model measured data.

NEC COUPLING CALCULATION METHOD

The NEC code uses network admittance parameters to calculate coupling between antenna feed ports. The code can calculate coupling between as many as five antennas; however, in this investigation only the coupling between two antennas was considered. Any two antennas can be treated as a two port network and analyzed using network admittance or Y-parameters (See Figure 1). In Figure 1, Port 1 is the feed port of the first antenna and Port 2 is the feed port of the second antenna. The four variables of interest are the voltage and current at the feed port of the first antenna (V_1, I_1) and the voltage and current at the feed port of the second antenna (V_2, I_2). Only two of the four variables are independent and their linear relationship can be expressed as

$$I_1 = Y_{11}V_1 + Y_{12}V_2 \tag{1a}$$

$$I_2 = Y_{21}V_1 + Y_{22}V_2 \tag{1b}$$

Y_{11} and Y_{21} are determined by setting V_2 to zero and are defined as

$$Y_{11} = \frac{I_1}{V_1}\Big|_{V_2=0} \tag{2}$$

$$Y_{21} = \frac{I_2}{V_1}\Big|_{V_2=0} \tag{3}$$

Y_{12} and Y_{22} are determined by setting V_1 to zero and are defined as

$$Y_{12}=\frac{I_1}{V_2}\Big|_{V_1=0} \tag{4}$$

$$Y_{22}=\frac{I_2}{V_2}\Big|_{V_1=0} \tag{5}$$

NEC determines the Y-parameters sequentially as shown above. First, the user-defined excitation is applied to the feed port of antenna 1 and the feed port of antenna 2 is short-circuited. I_1 and I_2 are derived from the method of moments calculation and thus Y_{11} and Y_{21} are determined. Next, the user-defined excitation is applied to the feed port of antenna 2 and the feed port of antenna 1 is short-circuited. Again, I_1 and I_2 are calculated and thus Y_{12} and Y_{22} can be determined.

Once the Y-parameters have been determined, the coupling between the two antennas is calculated by finding the ratio of the network's output power to it's input power. This ratio can be expressed as

$$G=\frac{P_o}{P_i}=\frac{Re[Y_L]}{Re[Y_{in}]}\left|\frac{V_2}{V_1}\right|^2 \tag{6}$$

V_2 is the output voltage at Port 2 and Re Y_L is the real part of the load admittance. V_1 is the input voltage at Port 1 and Re Y_{in} is the real part of the admittance looking into Port 1. Equation (6) can be solved in terms of the Y-parameters and the load admittance Y_L. By using equation (1) and solving $Y_{in} = I_1/V_1$ with $I_2 = -V_2Y_L$, Y_{in} can be expressed as

$$Y_{in}=Y_{11}-\left[\frac{Y_{12}Y_{21}}{Y_L+Y_{22}}\right] \tag{7}$$

Equation (1) can also be used to express the output to input voltage ratio as

$$\left|\frac{V_2}{V_1}\right|=\left|\frac{Y_{21}}{Y_L+Y_{22}}\right| \tag{8}$$

Thus, the power gain or coupling can be expressed as

$$G=\frac{Re[Y_L]\,|Y_{21}|^2}{Re[Y_{in}]\,|Y_L+Y_{22}|^2} \tag{9}$$

NEC calculates only the maximum possible coupling by using a Y_L that maximizes Equation (9). This perfectly matched Y_L is found using the Linville Analysis approach [1],[2]. Additional loss due to the

mismatch between the output antenna port and an actual load can be calculated by hand. There are versions of MININEC that allow a user-defined load impedance to be used [3].

GROUND PLANE COUPLING ANALYSIS

GROUND PLANE TEST CONFIGURATION

All coupling experiments were conducted in a 20'X 16' anechoic chamber. The ground plane used was a 4'X 8', 1/16th inch thick aluminum sheet. The monopoles used in the ground plane tests and the subsequent scale model equipment shelter tests were constructed from N-type panel-mount connectors and brass rods (0.072" in diameter). A brass rod was soldered to the solder cup of each panel-mount connector as shown in Figure 2.

The monopoles were mounted in the center of the ground plane for tuning. The length of the brass rod was then trimmed until the antenna was resonant at 500 MHz. The monopole used as the transmit antenna was tuned to an impedance of 55.0 + j7.3 (Return Loss = -21.6 dB) and the receive monopole was tuned to a similar impedance of 56.1 + j7.4 (Return Loss = -20.9). The measured impedances were determined using a HP 8752A Network Analyzer. In order to determine ground plane edge effects on the impedance of the antennas, one of the tuned monopoles was sequentially mounted at locations 0.5λ and 0.1λ from the ground plane's edge. When mounted 0.5λ from the edge, the magnitude of the impedance changed only 0.5% and the phase changed only 2.0 degrees. At the 0.1λ location, the magnitude changed by 9.8% and the phase by 7.9 degrees. This result indicates that effects on the antenna's impedance, and thus it's coupling characteristics, due to the finite ground plane is negligible for antenna locations greater than 0.5 lambda from an edge. Also, this result supports previous studies that showed that the location of two antennas mounted on a finite ground plane had little effect on the coupling between the antennas [4],[5].

The ground plane test was conducted with both antennas located along the center line of the ground plane as shown in Figure 3. At the test frequency of 500 MHz the ground plane is approximately two wavelengths wide and four wavelengths long. The transmit and receive antennas were initially located 0.5λ from each edge of the ground plane. The receive antenna was then stepped in toward the transmit antenna at either four-inch or two-inch increments. At each location, the coupling between the antennas was measured using the HP 8752A Network Analyzer. The various antenna spacings ranged from three wavelengths to 1/20th of a wavelength. This test insured that the antennas were never closer than 0.5λ to the edge of the ground plane. Thus, edge effects on the antennas were negligible and all impedance changes could be attributed to mutual coupling between the monopoles.

COMPARISON OF MEASURED AND CALCULATED DATA

In Figure 4 the measured ground plane data is compared with

calculated values using the Friis far-field coupling equation and NEC. The Friis equation is defined as

$$Coupling = G_t + G_r - 20\log(4\pi d/\lambda) \qquad (10)$$

where,
G_t = Transmit antenna gain, dBi
G_r = Receive antenna gain, dBi
d = antenna spacing
λ = wavelength

For monopoles mounted on a common ground plane there is an uncertainty as to what gain values should be used in the Friis equation. The far-field gain patterns of monopoles vary significantly as a function of ground plane size. However, for line of sight coupling, it was reasoned that two monopoles on a common ground plane would be equivalent to two dipoles in free space. Thus, an ideal dipole gain of 2.15 dBi was used for both the transmit and receive antennas. At some point, as the antenna-to-antenna spacing is decreased, the measured data should diverge below the Friis calculated values. This is because the Friis equation has no mechanism for taking into account mutual coupling effects. From Figure 4, it can be seen that the measured coupling does start to diverge below the calculated Friis values at a spacing of approximately 1.2 wavelengths. Also, it should be noted that for spacings between 1.2 wavelengths and 3 wavelengths the measured coupling was somewhat higher (as much as 2.2 dB) than that predicted by the Friis equation.

The NEC values were obtained by modeling two quarter-wave monopoles mounted on an infinite ground plane (IGP). It was hoped that the IGP model would be valid since it had already been determined that antenna impedance effects due to antenna proximity to the ground plane's edge were negligible. The NEC calculated data tracks the measured data very well for spacings between 1.2 wavelengths and 0.1 wavelengths and is only 1.4 dB lower than the measured value at the 0.05 wavelength spacing. The NEC calculated coupling for monopoles is identical to dipole coupling for any given spacing. This is because the impedance at the monopole's feed segment is halved relative to a dipole and therefore the current is doubled relative to a dipole. However, the coupled current onto the second monopole is also doubled and the relative coupling is identical to the values calculated between two dipoles. It can be seen that the NEC data merges with the Friis curve for spacings above 1.2 wavelengths.

SCALE MODEL COUPLING ANALYSIS

SCALE MODEL TEST CONFIGURATION

The purpose of the scale model testing was to simulate the coupling between VHF whip antennas located on the top of a S-250 C^{3}I equipment shelter. The VHF communications systems in the shelter

operate over a band of 30.0 - 88.0 MHz and scale models that represented the low and high end of this band were built. The models are box shaped and were constructed from flat aluminum plates. The first model was built to a 1/4.4 scale so that testing at 390 MHz would be representative of testing the actual equipment shelter at 88 MHz. The second model was built to a scale of 1/11.67 and was tested at 350 MHz to represent testing of the actual shelter at 30 MHz. Holes for mounting the monopole antennas were cut in three of the four corners of the top plate of each box. The mounting holes are centered approximately 5/8" from both edges of a corner. The corner locations were chosen because they are representative of typical antenna locations on an equipment shelter. The S-250 box model is illustrated in Figure 5.

The antenna locations (on the top surface of the models) are labeled A, B, and C (See Figure 6). The electrical lengths of the coupling paths are also shown in Figure 6. The "LB" indicates the large box dimensions (1/4.4 scale model) and "SB" indicates the small box dimensions (1/11.67 scale model). Antenna-to-antenna coupling from locations A to B, A to C, and B to C were measured for each box.

NEC MESH MODELING

For the scale model coupling analysis, NEC wire mesh models were created. Only the top plate surface (antenna mounting surface) of the equipment shelter scale models were simulated with the wire mesh. The purpose of the wire mesh modeling was to determine if mesh models would predict the measured coupling more accurately than the infinite ground plane model. It was felt that possibly the IGP model would not be appropriate since the antennas were mounted only 0.02λ from the corner edges of the equipment shelter box models.

A common general guideline for mesh modeling is that the total surface area of the wire segments comprising the mesh should at least be equal to twice the actual surface area to be modeled [6]. The total wire mesh surface area can be calculated as follows,

$$A=\sum_{i=0}^{N} 2\pi r_i L_i \qquad (11)$$

where

A = Total surface area of the wire mesh
r_i = radius of the ith wire segment
L_i = length of the ith wire segment

In addition, it is generally recommended that wire segment lengths be 0.1λ and the ratio of segment length to segment radius be approximately eight [7]. However, it also has been suggested in the literature that the 0.1λ segment length can be relaxed to 0.25λ when modeling areas in which the currents do not change rapidly; and that a segment length to radius ratio of five gives good results [8],[9].

For this study, six separate mesh models were created: three to

represent the top plate surface of the large box scale model and three to represent the top plate surface of the small box scale model. The segment length to radius ratio was at least five for all cases. The maximum length of the wire segments used was varied to determine if this parameter had any effect on the calculated coupling. It can be seen from Figure 7 that the top plate surface is slightly longer in the y-dimension than in the x-dimension. The segments located in the square portion of the surface (bordered by a bold solid line in Figure X) all had equal lengths which were the maximum segment lengths for any given case. The additional column of segments outside the square had a length of 0.05λ for the large box and 0.02λ for the small box. It should be noted that when segment length increases, the number of segments needed to represent the surface decreases. Also, the total surface area of the wires comprising the mesh increases as the segment lengths increase because the segment radius can be increased and still maintain an acceptable length-to-radius ratio of five. Two times the actual surface area for these models is 0.78λ for the large box and 0.088λ for the small box. All the mesh models have total wire surface areas that are at least 88% of this recommended guideline. The run times (in minutes) are for the NEC-2 code running on a WIN 386SX 16 MHz computer. Using each of the six mesh models, coupling values for the three antenna-to-antenna coupling paths (A-B, A-C, and B-C) shown in Figure 6 were compiled. A summary of mesh parameters and calculated coupling results is presented below in Table 1.

Table 1. Summary of NEC Coupling Results Using Mesh Models

Box Model	No. of Mesh Segs.	Max. Seg. Len. (λ)	Mesh Area (λ^2)	Run Time (Min)	NEC-2 Coupling (dB)		
					A-B	A-C	B-C
Large	31	0.200	0.856	0.69	-9.5	-17.8	-9.5
Large	97	0.100	0.729	4.22	-9.3	-17.1	-9.2
Large	161	0.075	0.691	12.57	-9.2	-16.5	-9.0
Small	4	0.220	0.132	0.23	-10.1	-5.5	-10.1
Small	17	0.100	0.110	0.44	-8.1	-5.4	-8.7
Small	49	0.500	0.089	1.14	-7.3	-5.1	-7.9

COMPARISON OF MEASURED AND CALCULATED DATA

Figure 8 presents a comparison of computed and measured data for the S-250 scale model analysis. The NEC wire mesh modeling results are represented as diamond symbols connected by vertical lines. The vertical lines show the range of coupling values obtained using NEC wire mesh models for the six (three for the large box and three for the small box) coupling paths investigated in the scale model analysis.

The coupling path spacings for the large box are 0.83λ (Path A-C), 0.61λ (Path A-B), and 0.55λ (Path B-C). The computed coupling for

large box paths A-B and B-C varied no more than 0.5 dB for the three large box mesh models. Coupling values obtained for path A-C varied 1.3 dB. The best case computed coupling values were within 1.0 dB, 3.0 dB, and 2.7 dB for coupling paths A-C, A-B, and B-C respectively.

The coupling path spacings for the small box are 0.25λ (Path A-C), 0.18λ (Path A-B), and 0.17λ (Path B-C). The computed coupling for path A-C varied only 0.4 dB. The computed coupling for paths A-B and B-C varied 2.8 dB and 2.2 dB respectively. For small box coupling paths A-B and B-C the computed range encompassed the measured values. However the best case computed value for path A-C was 4.9 dB higher than the measured value. It also should be noted that the small box four segment case (maximum segment length 0.22λ) constitutes only the rim of the modeled surface.

Also, in Figure 8, the measured coupling values from the scale model analysis are compared to computed coupling values using the infinite ground plane model. The infinite ground plane model performs surprisingly well, giving computed values that are within 2.8 dB of the measured data for all six cases.

CONCLUSIONS

The capabilities of NEC for predicting near-field coupling between monopoles mounted on a common ground plane has been examined. The accuracy of the NEC code has been evaluated by comparing computed coupling data to measured data collected in two separate investigations. The first investigation was for two monopoles mounted on a flat ground plane. The monopoles were never closer than 0.5λ to an edge of the ground plane. The infinite ground plane (IGP) model predicted the measured data to within tenths of a dB for antenna spacings between 1.2λ and 0.1λ and was within 1.4 dB for the closest measured spacing of 0.05λ. For spacings of 1.2λ to 3.0λ the predicted coupling was within 2.2 dB of the measured data. For EMC analyses, predictions tracking measured results this well is generally considered adequate.

The second investigation involved the modeling of an C³I equipment shelter. Mesh models having varying parameters were created to represent the top (antenna ground plane) surface of the shelter. The mesh models gave computed results that were within 3 dB of the measured coupling for five of the six coupling paths examined. However, for three of the six coupling paths, the IGP model produced values that were closer to the measured data than were the mesh model values. Also, the IGP coupling predictions were within 2.8 dB of the measured data for all six coupling paths. This was surprising since the antennas on the equipment shelter scale models were mounted only 0.02λ from both edges of the corners. This result would suggest that for line of sight coupling (even for antennas mounted close to an edge of a ground plane) the IGP model will produce good coupling predictions. The mesh models do not provide an overall increase in coupling prediction accuracy for these line of sight situations.

REFERENCES

[1] G. Johnson, "High Frequency Amplifier Using Admittance Parameters," Electro Technology, December, 1963.

[2] G. Johnson, "High Frequency Amplifier Using Admittance Parameters, Part 2," Electro Technology, December, 1963.

[3] Li, S. T., Logan, J. C., Rockway, J. W., and Tam, D. W. S., "The MININEC System: Microcomputer Analysis of Wire Antennas," Artech House.

[4] Harris, J. M. and Levin, R. J., "Far-Field Techniques for Predicting Aircraft Antenna Coupling," Record of the 1992 IEEE International EMC Symposium, pg 112.

[5] Levin, R. J. and Wheeler, M. L., "Examination of Near-Field Vehicular Antenna Coupling," Record of the 1993 IEEE International EMC Symposium, pg 73

[6] Lugwig, L. C., "Wire Grid Modeling of Surfaces," IEEE Transactions on Antennas and Propagation, Vol. AP-35, No. 9, September, 1987, pg 1045.

[7] Burke, G. J. and Poggio, A. J., "Numerical Electromagnetics Code (NEC) - Method of Moments, Part III: User's Guide," January, 1981.

[8] Lin, Y. T. and Richmond, J. H., "EM Modeling of Aircraft at Low Frequencies," IEEE Transactions on Antennas and Propagation, Vol. AP-23, No. 1, January 1975, pg 53

[9] Coffey, E. L., Kadlec, D. L., and Coffey, N. W., "General Electromagnetic Model for the Analysis of Complex Systems (GEMACS) Version 5, Engineering Manual," June 1990.

Figure 1 Two Port Network Definition.

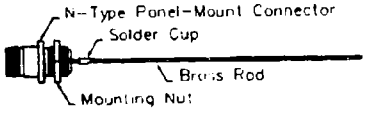

Figure 2 Test Antenna (Side View)

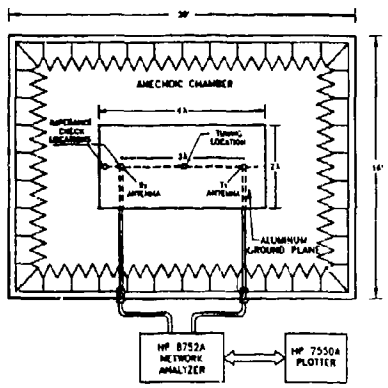

Figure 3 Ground Plane Test Setup (Top View).

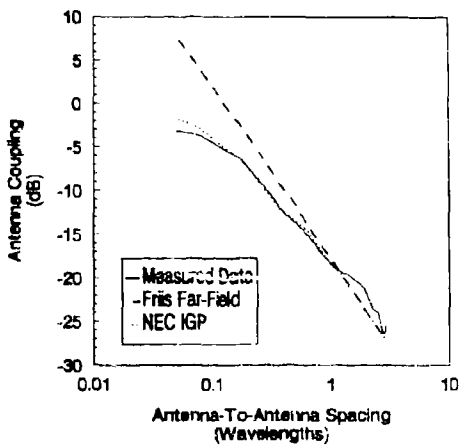

Figure 4 Comparison of Calculated and Measured Coupling for the Ground Plane Analysis.

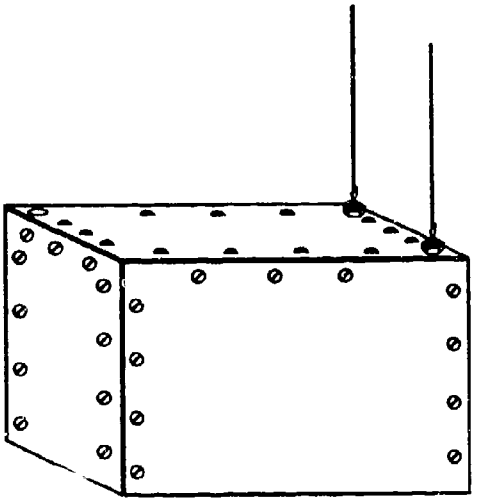

Figure 5 S-250 Scale Model.

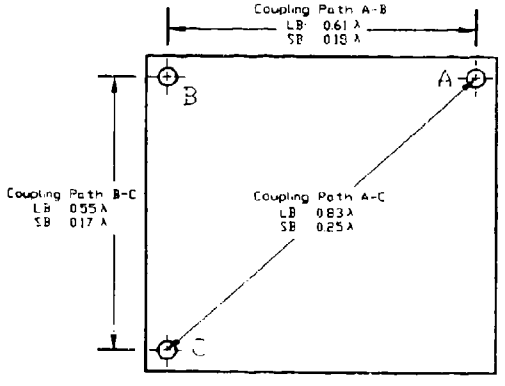

Figure 6 Antenna Locations on the S-250 Scale Models (Top View).

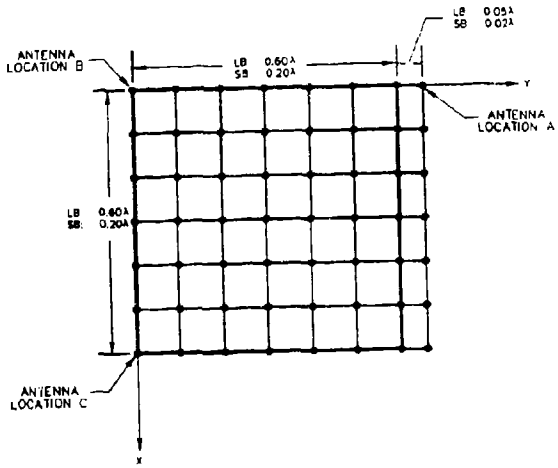

Figure 7 NEC Wire Mesh Model of the Top Surface of the S-250 Scale Models.

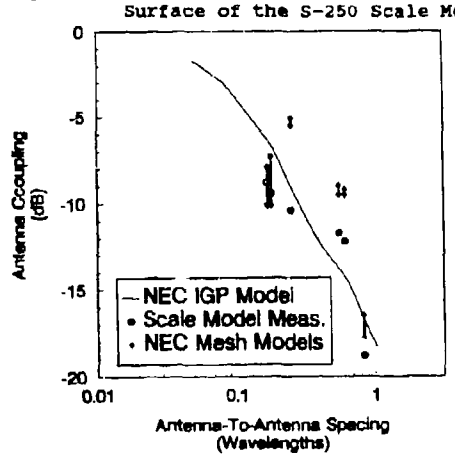

Figure 8 Comparison of Calculated and Measured Coupling for the Scale Model Analysis.

"Development of a High Power Microwave Susceptibility Simulation Capability at Phillips Laboratory's Satellite Assessment Center"

Captain Michael L. Zywien, PL/WSH, Kirtland AFB, NM

ABSTRACT: A comprehensive modeling and simulation capability currently exists with Phillips Laboratory's Satellite Assessment Center to assess satellite susceptibility to laser and nuclear threats. A corresponding capability to understand space system susceptibility to radio frequency (RF) electromagnetic effects is not available at the present time. This deficiency in numerical simulation capability mandates almost total reliance on experimental measurements, which can be extremely costly. Though experiments will always be necessary, a modeling capability can help with the identification and design of efficient experiments. This paper presents a plan to provide the Satellite Assessment Center with a methodology applicable to a wide variety of space system electromagnetic effect problems. The long term goal is to simulate an entire threat engagement scenario in an integrated computer code that will run on a SUN workstation.

BACKGROUND: Technology advances in the materials used to construct aerospace vehicles are of extreme interest to the defense sector in that we now build stronger yet lighter systems. Coincidentally, we are advancing electronics at a tremendous rate. Electronic components are now smaller, faster, more complex, more efficient, and more capable. More processing of signals is done at the satellite to enhance communications, command and data transfer link performance. Unfortunately, these advances sometimes increase the electromagnetic susceptibility of the electronics packages, and understanding this susceptibility is critical to hardening components and subsystems.

Determining the susceptibility of a satellite to electromagnetic energy involves a quantitative understanding of three processes: the environment in the immediate vicinity of the satellite, coupling of energy to the internal circuitry, and the functional response of the system to the incident radiation. Military space systems must function in high-intensity ambient electromagnetic environments and in any potential foreign EM threat environment. Taking advantage of Phillips Laboratory's work in the areas of high power microwave (HPM) source, antenna and component technology, we can estimate an upper bound on EM space environments that satellites may face (from a ground threat) over the next two decades. Coupling, which determines how much energy gets to interior electronic circuit nodes, depends strongly on system geometry. If sufficient energy is present, local heating can damage electronic components. The component functional responses determine how the system responds to the radiation and if the system can continue to perform its mission with damaged components.

Candidate program objectives are as follows: to quantitatively predict the RF environment on space systems for given sources, to support test programs by quantifying stresses on subsystems, to estimate requirements needed to make a system survivable, and to quantify responses and effects for space subsystems and systems exposed to specified RF environments. The environment prediction models will need to treat the source, including antenna radiation pattern, and the propagation, including attenuation, nonlinear, and dispersive effects. For most test support, upper limit bounds are adequate for purposes of determining simulator requirements, designing or selecting instrumentation, and for initial scope settings, etc. To evaluate the risk of unacceptable damage by test drives, however, component test data is needed to support high confidence analysis. For hardening support, bounds on the stresses at given points and on the susceptibility of components and subsystems are usually acceptable. Survivability analysis will present the greatest challenge to the models. To show that a system will survive, bounding analyses can be used. For cases when it appears that the system will not survive in the bounding sense, the largest uncertainties need to be identified to determine if additional tests or analysis will provide results which are meaningful.

APPROACH: To provide simulations of EM effects, several important issues are considered: tradeoffs between calculations and testing, stochastic variations among engagement scenarios, incomplete system specification, physically realistic statistical models, and tradeoffs between effort expended and accuracy obtained.

In the tradeoff between calculation and test, one would always prefer a full-up system test. Unfortunately, cost and sensitivity of satellite systems limit the amount of full system testing that is normally done. Therefore, system response must be evaluated using calculations and limited component and subsystem testing. Confidence levels increase as the amount and fidelity of test data increases.

All engagement scenarios involve uncertainties. Some factors are uncertain because of lack of knowledge of system design or design implementation. We may be uncertain of our ability to model certain factors with high confidence. There are also factors which can vary for a given engagement (e.g. orbit location, angle of incidence, threat source pointing and tracking, polarizations, etc.). Each factor must be treated, sometimes in different ways.

The level of effort required to estimate a system response should be consistent with the expected accuracy of the answer. For example, because finite difference codes produce specific solutions, proponents believe they can improve accuracy by using extensive computer calculations for specific subsystems. However, repositioning a single component or common manufacturing variations can change susceptibility predictions by several orders of magnitude. The uncertainty in these detailed models tends to increase as one goes farther into the system to the component level. This is partially due to the difficulty of knowing all of the relevant details that should be modeled, and partially due to the accuracy of the models we use to solve the identified problem.

Assessment of RF effects on electronic systems, then, is inherently a statistical process. Given that adequate data is obtained, device upset can be characterized with a family of stress distributions (using goodness of fit testing) and statistically quantified parameter estimates can be made. RF damage characterization based on device fragility distributions might be impractical given most practical testing limitations (distribution fitting requires extensive data to yield adequate results). Thus, it should be accepted that only statements about probability of upset or damage for tested parameters (power levels, frequencies, pulse widths, etc.) can be given. Any other statements, postulation or interpolation would have basis only in the judgment of the modeler.

In selecting our approach to RF modeling, the needs, projected threats, goals and objectives are all carefully considered such that the resulting methodology is flexible enough to handle a wide range of simulation scenarios. Threat source, propagation, coupling and effects calculation are all required aspects of the overall simulation problem. The final tool must handle any potential RF threat waveform, propagate this waveform to the target, define the target geometry at the level of detail required, couple the energy to the target vehicle, and determine the probability of effect on components, subsystems and the mission functions of the system. Statistical variation of each aspect of the engagement must be addressed.

The basic methodology chosen for this effort is called the Predictive Radio Frequency Effects and Coupling Tool (PRFECT). The capabilities of PRFECT are addressed later in this paper, and the dependence of PRFECT on a comprehensive effects data base is highlighted. PRFECT uses mission, threat and system design inputs with effects data to help predict susceptibilities and bound uncertainties.

For a wide range of cases, PRFECT handles the entire RF assessment problem. Source characteristics are defined as inputs, and energy is propagated using atmospheric models and target orbital mechanics modules. Coupling to front door paths (antennas) is handled by defining the coupling characteristics of the antenna or sensor, and then the RF energy is propagated to internal components in the RF path. Fault or event tree logic is included to the subsystem level only.

For other problems of interest, additional simulation elements are required. For these problems, other codes are used and a satellite modeling tool must be integrated with the codes. For full system impact analysis, additional fault tree logic must be added to supplement what is currently available in PRFECT. The specific codes and models chosen to supplement PRFECT are described in the next section. Each of these codes has been validated for use in stand-alone applications. However, when these codes are integrated, there will be a need to validate the singular integrity and the integrated methodology.

MODELING TOOLS

PREDICTIVE RF EFFECTS COUPLING TOOL (PRFECT): The Satellite Assessment Center will use PRFECT to support RF component and subsystem analysis. Version 1.0 of this code was delivered to the Phillips Lab in February of this year. The basis for PRFECT is that assessment of RF effects on electronic systems is inherently a statistical process. A statistical analysis of a particular system-threat interaction seeks to characterize the response by a probability of effect (PE) and associated confidence intervals. Given that the user may or may not be aware of statistical assumptions underlying the software, the statistical predictions should possess a rigorous foundation even if that requires limiting the scope of the prediction.

Rigorous, physics-based algorithms are used in each step of a PRFECT assessment. For example, the well-known far field diffraction pattern for RF antennas is used for the RF intensity profile. However, the pointing accuracy determines the actual intensity relative to the maximum on-axis intensity that the satellite receives. This pointing angle will vary due to tracking errors and servo control uncertainties. Thus, the pointing angle error, and hence the reduction in intensity, is best accounted for by using a random variable for the error. Other parameters that may vary statistically during an engagement are also modeled using random variables. If all variables are fixed for the particular engagement, the user may fix these parameters and the model will provide a deterministic solution.

A detailed discussion of the degree of rigor of some statistical methods commonly applied to RF effects and the methods believed appropriate is presented in Reference 2. This discussion defines the concept of probability of effect, reviews the features of basic statistical modeling of physical phenomena, provides example results which indicate the number of test data points required to support various types of conclusions, discusses data samples and distributions, and reviews binomial testing and possible conclusions which may be drawn. A brief summary of these discussions is presented here.

Electronic devices will sustain upset or damage when exposed to an RF signal of some power level. The variation of the device fragility between different samples of the device type defines a fragility (strength) random variable. The many scenarios under which the device may experience RF irradiation also define a stressing power random variable. Symbolically,

$$PE = P(\text{Strength} \leq \text{Stress}),$$

and the density of the effect random variable is found as a convolution of the stress and strength, which may be interpreted statistically as the expectation of the cumulative fragility against the stress. Instead of fixing specific distributions for strength and stress, one could assume that the distributions are drawn from specified families of distributions (Bayesian approach) with the defining parameters themselves being random variables distributed in some manner. However, this expanded interpretation requires increasingly complex statistical models, and without substantial justification for the Bayesian priors, the analysis reduces to "expert opinion" and is no longer a rigorous statistical inference drawn from measured data.

A statistical methodology aimed at characterizing a data set begins with the selection of a distribution function on the grounds that it satisfactorily summarizes the data in question. Goodness-of-fit tests provide probabilistic grounds to justify a particular selection. Because of the uncertainty of available data, a number of distributions may adequately represent the data. Of course, general physical principles can also guide the distribution selection process. Density functions chosen to represent failure processes must be unimodal, and must be defined for power levels between zero and infinity.

As an example, assume that the failure processes are lognormally distributed, and that (given a random sample of data) specific values for μ and σ must be determined. If values are hypothesized, we now must determine the number of tests that must be performed to reach a desired level of confidence. This process exhibits increasing accuracy as the number of tests is increased, and also indicates that statistical statements based on data samples of less than a few tens of points cannot have high confidence.

The PRFECT algorithm, much like the ARES algorithm developed by Kaman Sciences, allows the PE as a random variable to be determined in essentially closed form. To calculate PE, the algorithm convolves the stressing power random variable distribution with the mean cumulative distribution function (CDF) chosen to fit experimental effects data. Non-linear least squares fitting routines can

provide fitting parameters for the CDF and also provide uncertainties on the fitting parameters. PRFECT is general in nature and can combine numerous arbitrary distributions to generate the power distribution. In many cases, the power distribution can be represented as a beta distribution.

In PRFECT, there are two options to evaluate the convolution of the power density and the failure effects CDF. In the Monte Carlo method, the stressing power density is sampled repeatedly, and the mean CDF is evaluated at each corresponding point, summed, and then divided by the number of sample points, yielding a PE with respect to the mean. In the second method, analytic expressions or numerical representations for the power density and mean CDF are numerically integrated to yield PE. In both cases, the power density is also convolved with the 95% confidence CDFs to yield error bounds on PE.

This approach is sensitive to the form of the distribution selected to describe the device failure characteristics. Without known, quantifiable confidence statements concerning these distributions and without a rigorous means of evaluating sample-based estimates of required parameters, the attendant uncertainties introduce unstated confidence levels which may limit the conclusions drawn from the analysis. These notions explain why many tests are required to select a distribution with high confidence.

The PRFECT code is being developed with integral ties to an extensive susceptibility testing program and a susceptibility data base effort. The major goal in tying these efforts together is to minimize reliance on first principles models. This development approach makes it important that supporting data provide the right information, at the right level of detail, in an efficient manner. The level of detail needed depends on the solutions needed and the quality and level of verification of the analysis codes. For example, suppose a PRFECT model for the coupling to an antenna or for the response of a certain semiconductor component exists. Suppose, further, that this model has been verified by test data for frequency and amplitude ranges of interest. This submodel can probably, then, be used for select cases to determine values for intermediate parameters (or for limited extrapolation) where data is not available, without seriously impacting confidence in predicted results. In other cases, more direct use of test data may be required.

Three basic types of data are required for the data base: coupling data, transfer function data, and "effects" data, including upset, degradation and damage characteristics. Coupling data includes all required descriptions of the interaction of the incident RF signal, propagating in space, with the spacecraft to produce surface currents and charge densities on all parts of the vehicle exterior, on antennas, and inside of deliberate apertures such as receiver elements and sensor optical trains. Transfer function data includes everything needed to describe the transfer of RF signal energy from the external coupled responses to the component level where the effects on the system are usually produced. This could include propagation inside a signal cable, through an aperture, or through a diode or integrated circuit. Effects data should include information which describes the upset (temporary decrease in electronic performance to include transient effects), degradation (permanent decrease in performance) or damage (permanent cessation of electronic function) induced in components or subsystems as functions of the incident stress parameters.

Test data will usually be available for only a finite number of cases. PRFECT or another analysis module will often be required to take whatever data is available from the data base and perform appropriate interpolations or extrapolations to cases of interest. Results in such analyses must be used carefully, with proper caveats, and the uncertainty estimate associated with these results would be expected to increase.

In addition to degradation or damage effect calculations, PRFECT allows the user to investigate the probability of upset. An approach similar to the one described above is used to calculate the probability density function for carrier power and thus energy per bit (E_b). By determining a probability density function for the noise density (N_o), the ratio of both these random variables provides an estimate of the bit error rate (BER) for a particular modulation scheme. The capability to calculate a probability of effect for both degradation and upset provides a unique capability for assessing space system susceptibility.

CODE FOR ANALYSIS OF RADIATORS ON LOSSY SURFACES (CARLOS): A more rigorous EM code is needed to supplement the PRFECT code in some threat-target scenarios where the incident fields at the satellite cannot be calculated using the modules included in PRFECT. In these cases, surface current and charge densities on the vehicle exterior are calculated using CARLOS, converted to incident power densities, and passed as inputs to PRFECT.

CARLOS is a code developed by McDonnell-Douglas (partially funded by the Electromagnetic Code Consortium - EMCC). The code implements the method of moments solution for fully arbitrary three dimensional scatterers. These solutions are obtained for perfectly conducting bodies as well as fully or partially penetrable ones. The electromagnetic scattering formulation is based on surface integral equations spanning the entire external surface of the body and the internal boundaries between penetrable and perfectly conducting regions. The analysis capability is extended to boundaries (or surfaces) which may be characterized by resistive or magnetic sheets as well as impedance boundary conditions. This results in a rigorous theoretical formulation for all of the foregoing classes of problems, with the computational domain terminated at the outer surface of the scatterer. The development of the CARLOS software for the various boundary and interface conditions is carried out in terms of an operator-based integro-differential calculus, independent of geometry and expansion functions. Hence, the structure of the analysis and the architecture of the implementing software are general. In the present implementation, planar triangular patch and/or wire representations are required for all surfaces and boundaries of the system of interest. Implications of this requirement for the overall code integration task are discussed in the next section.

One use of CARLOS will be to find the threat power at the terminals of an antenna when the rule-of-thumb models built into PRFECT are inadequate to model the coupling of the threat to the antenna and satellite. Another use will be to find the threat power coupled into various systems through unintended ("[illegible]x") paths. CARLOS will also be used to estimate the cross-coupling between cables and RF paths. Another use will be to find responses for antennas or other sensors which are outside the normal operating frequency band, and thus not likely to be specified. A final use will be to find the coupling of threats to system elements not normally part of an RF system (for example solar arrays and power cables).

Because of the complexity of the algorithms which CARLOS uses to do its analyses, running it as part of an interactive PRFECT session is probably not feasible. It will more likely be run in a batch mode to supply the analyst with the desired input information for a PRFECT session. Because of the computational power limitations of the SUN workstations, there will be some upper limit to either the analysis frequency or the model complexity, and tradeoffs will be required. To extend the frequency range over which analyses can be performed, the satellite model complexity must be reduced or the analysis must be focused on some subset of the entire system. In some instances, only the antenna of interest needs to be modeled, and it is expected that the usable CARLOS frequency range would then include typical operating frequencies of the antenna.

SATELLITE ASSESSMENT CENTER MODELING TOOL (SMT): SMT, developed at Phillips Laboratory's Satellite Assessment Center, provides the capability for analysts to quickly develop a solid geometry model of a system. The graphics editing capabilities of SMT allow analysts to create and modify solid model representations of complex objects using Combinatorial Solid Geometry. Eleven solid shapes or "primitives" form the basis for building subsystem or system models, which can be used by analysis tools such as CARLOS. Hence, the SMT models facilitate an approach to modeling the susceptibility of a constructively defined system to a range of threats.

The solid geometric elements from which a model of a satellite is built in SMT are not compatible with the input formats for electromagnetic codes such as CARLOS. Therefore, part of the integration effort is to write a "translator" which puts SMT models into a format compatible with RF analysis.

Additional modifications and enhancements to SMT are also being planned as part of the overall RF tool integration effort. For example, links to the RF data base are necessary in order to associate the transfer function and coupling data stored there with a particular component in the SMT functional model. In addition, new capabilities will be needed in the display of the existing solid modeling

information. It will be necessary to edit the entire geometric model to eliminate some components which are not needed or to extract elements to form new models with decreased complexity. It would greatly simplify the generation of an RF model if the display could be constrained by certain physical parameters of each element. An important constraint for RF analyses is electrical conductivity. All elements of a certain material or with conductivity greater than a certain value could be displayed, and all other elements could be ignored, for example. An important issue for the use of SMT for RF problems is the need for additional information which has not been needed for laser and nuclear studies. This would include cable types and locations, descriptions of connector types, etc. In general, just more (or perhaps different) details. These will often be more important than the conductivity factors discussed.

SYSTEM FAULT TREE / EVENT TREE CODES: PRFECT outputs the probability of effect from a given RF threat on a critical component in a particular subsystem configuration. To understand how individual failures combine in terms of system level measures of degradation, a fault tree methodology is employed.

A fault tree is a graphical model which logically relates a failure top event (e.g. a satellite's inability to conduct its designated mission) to subordinate failure events (e.g. loss of attitude control, electrical power or communications). The subordinate events are further broken down into successive failure events until a set of basic events are obtained. Basic events are failure events that are subjectively deemed by the analyst as not requiring further breakdown. This usually occurs when the basic events match the level of measured or predicted failure information available to the analyst.

The procedure currently in place within the Satellite Assessment Center begins with the SMT system model. A utility program is used to process the geometric description and generate a "straw man" fault tree that parallels the geometric hierarchy. From this first cut, the analyst uses a text file editor to alter the logic sequence to reflect functional relationships with respect to the top event of interest. Once the logic is correctly assembled, it is input into a post-processor along with individual element failure information generated by an analysis code (such as PRFECT) to compute intermediate and top event failure levels.

The Integrated Reliability and Risk Analysis System (IRRAS) code grew out of the US Nuclear Regulatory Commission's need to analyze and quantify the safety of nuclear power plants. IRRAS is an interactive program designed to build, maintain, and analyze fault and event trees. The code is generic enough to handle a variety of problems associated with aggregating probabilities of failure in complex systems. Among the benefits of IRRAS are a good graphical interface for interactive manipulation of both fault and event trees, multiple techniques for analytical quantification, handling of uncertainties associated with basic failure events, detailed user manuals, and low cost to obtain updates from the Department of Energy's repository at Oak Ridge.

The application of IRRAS to situations involving exposure to RF radiation is a natural extension of its original use. First, a criteria (e.g. some level of device upset) must be established to determine whether or not an event occurred. The analyst must then generate a fault tree that considers all the basic events that could lead to the top level event. In the RF case, this would include all electrical components of interest in the system, including all redundancy and any safety features built into the system. PRFECT produces an output that is a probability function (PE) for each critical component. To analyze the system at higher levels, PE functions for each component are input as basic events to the IRRAS-generated fault tree via keyboard and the IRRAS data base menus.

DATABASE DEVELOPMENT: As discussed previously, directly relevant test data are required to support any high-confidence model predictions, particularly for cases where "predictive" results are required instead of "bounding" results. The objectives for the database development effort are:

- to store and organize both existing data and new data from experiments
- to allow users to easily query the database
- to permit manipulation of the selected data
- to display the selected data
- to output selected data that is in a format compatible with modeling programs such as PRFECT.

The database system is being developed for SUN workstations and for a PC environment. PC versions of the database are needed to provide an efficient means of transferring data to users outside the Satellite Assessment Center. In addition, security considerations dictate that the database handler must run on a stand-alone system (i.e. it cannot operate in a client-server mode on two systems). These requirements impact the overall design/development effort.

The database system is based upon three software components that work together: a database manager, a graphics system, and a special function environment. The basis for the system is a commercial environment, Ingres, that provides necessary data structures as well as a set of development tools such as form generators and report writers that are critical in reducing development time and enhancing the quality of the database. The database will store text, numeric data, images and arrays, and includes an extensive security facility that is important in view of the many types of data and the wide variety of users expected to employ the system. A commercial graphics package, GnuPlot, is used for the graphics component. Special functions (written in C++) are required to provide capabilities appropriate to the susceptibility database that cannot be implemented within the database or graphics components. These special functions permit capabilities such as calculation of statistics, Fourier transforms, and digital filters, interactive definition of curve fits to data, or selection of some portion of a displayed data set.

The database is being developed in phases. The first phase will address design and implementation of the basic code structure and functional capabilities. To parallel the PRFECT development, initial emphasis is given to in-band communications system data. The second phase of development will involve augmenting the software capabilities with additional graphics flexibility, and additional functions to represent data sets. During each phase, features will be checked out using database user interfaces as well as the analysis module interfaces. This helps assure that the database and the analysis module are properly compatible.

MODEL OPTIMIZATION CONSIDERATIONS: The form and detail of the required system model will be highly dependent on the particular application of the integrated RF analysis tool. For example, if a ground-based microwave source "front-door", in-band engagement with a satellite's command link is to be modeled, a functional model of the command link in PRFECT is all that is required. However, for a "back-door" analysis, necessary for survivability problems, a model that captures all the "significant" aspects of the system must be used. The "right" RF model, then, is highly dependent on the particular application for which the model is intended and on the computer resources available to run the model. In using the CARLOS code, for example, the fineness of the model grid has a direct impact on the simulation run time and memory requirements.

There are several rules-of-thumb for RF modeling which will need to be observed as geometries are created for CARLOS. First, as a lower bound, there should be approximately 10 segments of the model per wavelength for wires, and 100 segments per square wavelength for surfaces. For a given faceted model, this will limit the highest frequency at which analyses can be performed. Second, there should be enough segments to adequately represent the normal spatial variations of current. Third, segmentation should be finer on the parts of the model where the analysis is focused (though it is not always safe to grid finely only near the point of interest). Finally, while it is tempting to use increasingly finer segmentation to produce better results, this can impact the accuracy of the solution by, for example, violating some basic assumption of the analysis code (e.g. modeling a "thin" wire as a stack of poker chips). Therefore, the judgement of the modeler will be a critical factor in the setup of each problem.

One of the goals of this program is to use SUN workstations as the computational platform for all RF analyses. This may prohibit certain types of analyses (e.g. large satellite models at high frequencies). It may be necessary to gain access to mainframe or supercomputing platforms from time to time to perform all desired analyses. It is hoped that the general growth in capabilities of workstations will make the use of mainframes the exception rather than the rule. However, it is expected that access to a more capable computational platform will be needed in order to handle all kinds of problems likely to be encountered.

VALIDATION: Each of the codes presented in previous sections (with the notable exception of the developing PRFECT code) has been validated to some degree for use in stand-alone applications. CARLOS has been tested against benchmarks defined by the EMCC. SMT is being used now for various laser and nuclear susceptibility studies. IRRAS has been tested by the NRC. However, when these codes are combined into an integrated RF effects assessment capability, there will be a need to validate that each piece of code maintains its integrity singly and as part of the integrated package.

Analytic verification of the correct operation of PRFECT can be done on three levels. First, for chains of elements with a limited combination of probability density functions, a closed form solution can be obtained. Second, for a much more general combination of density functions, a numerical result can be obtained using another code such as Mathematica. Third, for very complex chains, a Monte-Carlo simulation can be run. The results from PRFECT can be compared with the results from any of these three methods to verify the correct operation of the planned mathematics. To verify the accuracy of PRFECT results for a given problem of interest, there is no substitute for test data. If proper test scenarios can be defined such that data is directly applicable to the level of detail appropriate to the model, a comparison of PRFECT output with relevant test results should be made. For example, a test with a plane wave source incident on an antenna connected to a receiver subsystem could be performed. Measured results could then be compared to PRFECT calculations. Such tests are planned for the validation effort.

Specific tests are also planned to support validation of the CARLOS software to the coupling application. The DMSP command antenna is currently being modeled, and computed patterns and coupling characteristics will be compared to measured near and far field pattern data.

Proposed changes to SMT are principally in the development and display of models. Verifying the correct operation of the code will consist of creating, displaying, storing, retrieving and editing several satellite models. Verifying the correct operation of the code used to translate SMT geometry into CARLOS input format can be accomplished by creating some simple geometric models in SMT. These models can then be converted to the CARLOS input format and manually checked for correctness. Finally, the models can be run through CARLOS to determine if the expected scattering properties are correctly resolved. These scattering properties are well known for simple shapes such as spheres, boxes and wedges. However, reliable indications of the accuracy or adequacy for real problems will require validation with realistic experiments. Test plans are currently being developed and several candidate facilities are under evaluation.

SCHEDULED AVAILABILITY OF INTEGRATED CODES

Integration planning, code acquisition and evaluation, and PRFECT code development were initiated during FY93. Version 1.0 of the PRFECT code, which concentrates on communications subsystem modeling, was delivered in February 94. Code integration work has begun, and the goal is to provide an initial on-line capability with User's Manuals by the end of CY94. It should be noted that the modeling tools described in this paper are designed for narrowband (CW) sources. The treatment of broadband effects will require significant modification (or substitution).

REFERENCES:

1. Alexander, A., et. al., "Probability of Effect Calculations For RF Effects on Satellite Receivers", Mission Research Corporation, Albuquerque, NM, June, 1993, Rev. 1 December 1993.

2. Jones, C.W., et. al., "Space System Data Base Requirements and Development Considerations", Report for Contract F29601-91-C-0072, Subtask 15, Metatech Corp., Albuquerque, NM, 30 December 1992.

3. Metzger, D., "Suggestions for the RF Assessment Integration Plan", Memo for Contract F29601-92-C-0024, Kaman Sciences Corporation, Albuquerque, NM. 15 June 1993.

4. Putnam, J.M., et. al., "CARLOS-3D Three Dimensional Method of Moments Code", Vol 1,2, McDonnell-Douglas Aerospace East, St. Louis, MO, 10 December 1992

Test Fidelity in Anechoic Chambers

Clifton Courtney and Donald Voss
Voss Scientific
416 Washington St. SE
Albuquerque, NM 87108

Abstract - Anechoic chamber susceptibility and vulnerability tests of electronic systems to high power microwave (HPM) must achieve radiated electromagnetic fields that mimic uniform plane-wave illumination to simulate battlefield conditions. Unfortunately, these conditions are hard to achieve for large targets with multiple points-of-entry, such as found on aircraft. RF measurements of the electromagnetic field in the chamber prior to a test are often impractical, and electromagnetic modeling tools and software are often incapable of integrating the many computational tasks required. In contrast, this paper describes a new, Windows-based computational tool designed to rapidly assess HPM test fidelity in anechoic chambers; the software described here performs all computations required to assess the fidelity of anechoic chamber tests.

I. Introduction

Susceptibility and vulnerability tests of electronic systems (assets) to intense electromagnetic environments are often conducted in an anechoic chamber. Although such tests are generally the most convenient way to determine system susceptibilities, one must ensure that the electromagnetic (EM) environment within the anechoic chamber is a realistic representation of the EM environment to which the asset will be exposed. Typically the scenario of interest is the exposure of systems to uniform, plane-wave illumination. Tests conducted with an incident field that is a poor approximation to a uniform plane-wave over the test volume, particularly at point-of-entry (PoE) locations, may generate misleading or useless data. Poor test fidelity can occur when any of a number of non-ideal effects become important. Non-ideal effects include: (1) reflections of the incident radiation from the walls, floor, and ceiling of the chamber (denoted "primary reflections"); (2) reflections of the incident field from the target, followed by further reflections from the interior of the chamber (denoted "secondary reflections"); (3) cross-sectional variation of the incident field (amplitude, direction, and phase) within the test volume due to the proximity of the antenna to PoE's; and (4) variation of the radiated power density with distance from the antenna.

Convenient and easy to use, the Windows-based Test Fidelity in Anechoic Chambers (TFAC) software provides test personnel with a capability to rapidly calculate a single figure-of-merit which indicates the degree to which wall reflections, antenna pattern, test asset placement, and antenna radiation characteristics affect overall test fidelity. Over a user defined volume of interest TFAC calculates a test T-factor; an indication of the departure from plane-wave conditions of the total field incident on PoE's. To determine the T-factor figure-of-merit TFAC rigorously calculates the incident near-zone radiated field of wire antennas (via a method of

moments solution method), and rectangular and conical horn antennas (using experimentally validated aperture integration techniques). Also, by incorporating extensive absorber reflectivity measurements and a low frequency scattering model, TFAC implements two absorber scattering models; a specular scattering model is most appropriate at low frequencies, while a non-specular scattering model better expresses the absorber scattering properties at high frequencies. In addition, TFAC utilizes the NEC-Basic Scattering Code to determine the secondary scattering from the test asset, to the absorber covered enclosure, back to the test asset.

This paper will present an overview of the Test Fidelity in Anechoic Chambers software. It will first describe some of the issues associated with anechoic chamber tests, next present a summary of the antenna modeling capability of the software, discuss the absorber scattering models implemented in the program, highlight the graphical user interface used for asset selection and positioning, and finally describe how the Numerical Electromagnetics Code - Basic Scattering Code (NEC-BSC) is used to determine secondary scattering. A definition for the T-factor, a scalar test fidelity figure of merit, and a discussion of its use are also given. Finally, the paper will conclude with a sample calculation of free-field radiated field and associated T-factor.

II. Overview of Anechoic Chamber Test Issues

Test fidelity in this context is the ability of a test, or simulation, to reproduce plane-wave conditions. One must consider a number of important issues when planning or conducting tests in an anechoic chamber. Unambiguous descriptions of these issues will help clarify the discussion that follows. Consider the situation depicted in Figure 1. Here the test asset (a missile in this case) is located in the main beam of the source antenna. Ideally, the asset test volume, the region of space occupied by the asset, would be subjected to an incident plane wave. However, non-ideal effects can prevent the realization of plane wave conditions in the test volume. Non-ideal conditions include:

1. Primary reflections - reflection of free-field radiation from the absorber covered surfaces of the anechoic chambers.
2. Secondary reflections - reflections of free-field radiation from the asset, followed by further reflections from the absorber covered surfaces of the anechoic chambers.
3. Cross-Sectional Phase and Amplitude Variations - due to the proximity of the asset to the source antenna, phase, amplitude and polarization variations of the radiated **E** and **H** free-field of the antenna will exist across cross-sectional planes perpendicular to the direction of propagation.
4. Power Density Variations - again, due to the proximity of the asset to the source antenna, inverse square law power density variations will exist along the length of the test asset.

The term *free-field* is used to mean the radiation from the antenna in free space, while *points-of-entry* will be used below to indicate areas where EM energy can gain access to the interior of the asset.

Items 3 and 4 above are usually the dominant factors in compromising test fidelity and are a consequence of the close proximity of the antenna and test asset. For well designed chambers items 1 and 2 are generally of less consequence, unless tests are conducted at low frequencies where the absorber can become highly reflective. Figure 2 presents a qualitative assessment of the relative impact on test fidelity of each mechanism as a function of frequency. It indicates

that absorber scattering is of most concern at lower frequencies, while cross-sectional plane wave departures are most dominant at higher frequencies. Power density dependence on distance from the antenna is shown to be of concern at all times, especially for assets with extended (axially long compared with wavelength) points-of-entry.

III. TFAC Field Computation Capability

To assess the impact upon test fidelity in anechoic chambers of items 3 and 4 above, the TFAC software must compute accurately the radiated near-field of the source antenna, primary scattering from the absorber covered walls, and secondary scattering from the test asset to the absorber covered walls and back. This section reviews the TFAC computation capabilities for each of the above.

Antenna Radiated Field Computations

Since the antenna used in a test depends on the type of test being conducted, and the source being used, TFAC computes antenna near-fields from rectangular and conical aperture antennas, and a number of common wire antennas. User selections and antenna parameter inputs are accomplished through dialog boxes accessible to the user under the *Antenna* field of the program's main dialog box; Figure 3a depicts the dialog box for a rectangular antenna. Further specification of frequency, mode and power are accomplished under the *Drive* field; Figure 3b illustrates how the program depicts the field structure of a conical horn antenna when driven in the TE_{11} mode.

Computations for aperture antennas are prefaced by a description of the physical geometry of the antenna and feed waveguide, specification of the dominant mode, frequency of operation, and total radiated power. Calculation of the radiated fields are then made using a technique similar to the Stratton-Chu technique [Ref. 1]. These calculations have been experimentally shown to be accurate to within fractions of a dB for values of **E** and **H**, both magnitude and phase of all components, in the radiating nearfield. If a wire antenna is used, test personnel specify the general type of wire antenna (log periodic, yagi, dipole array, and dipole antennas are currently supported), the physical dimensions, operating frequency, radiated power, and for some types, the gain. TFAC then constructs a thin model of the antenna, formulates an impedance matrix description via the method of moments [Ref. 2], and solves for the corresponding antenna current distribution. Radiated fields are then calculated from the current distribution in the usual manner.

Primary Scattering Computations

To compute primary scattering from absorber covered surfaces, TFAC first determines the reflection coefficient of the metal backed pyramidal absorber as a function of frequency, angle of incidence, and polarization. The low frequency reflection coefficient, where the pyramids are less than $\lambda/2$ in height, is determined from an analytical model [Ref. 3], while the high frequency reflection coefficient is primarily found from experimental measurements. Then TFAC computes the magnitude of the radiated field incident on the wall. Two absorber scattering models are used: The first assumes a specular scattering mechanism and is most accurate in the low frequency regime. For this model only the field incident on the specular point of the wall (determined by the chamber geometry and the specification of the points-of-entry) need be determined. The second model assumes the energy is scattered back isotropically (applicable

for high frequencies) and requires the computation of the incident field at many locations on the walls of the chamber. The magnitude of the field due to primary scattering that arrives in the test volume is then compared with the direct incident field and a determination of the impact on test fidelity made.

Secondary Scattering Computations

Due to the size of the scattering surfaces of the asset and the path lengths involved, the significance or impact on test fidelity of secondary scattering will, in most cases, be minor. However, since the asset is typically located in the main lobe of the source antenna, the secondary scattering can be comparable to the primary scattering when asset scattering centers and points-of-entry are located close to chamber walls. The NEC-BSC [Ref. 4] code is used to help TFAC accounts for secondary scattering mechanisms. NEC-BSC computes the near and far zone field of antennas in the presence of scattering structures. It exists as an element of a dynamic link library (DLL) and called as a C function from TFAC. Asset selection and positioning, via a Windows dialog box, enables TFAC to construct a NEC-BSC input data file that describes the experimental arrangement. NEC-BSC computations then yield the scattered field incident on the chamber walls. Since directional information is not available, TFAC uses the isotropic scattering model and propagates it toward the points-of-entry (properly accounting for distance dependence of field strength) to determine the level of secondary scattering relative to the direct incident field.

III. T-Factor and Determination of Test Fidelity

The primary test fidelity figure-of-merit is the $T - factor$ [Ref. 5]. This scalar quantity is easy to calculate, and expresses amplitude, phase and polarization deviations from a plane wave. It is defined as

$$T(\mathbf{r}) = \frac{|\mathbf{E}_{err}(\mathbf{r})|^2 + \eta^2 |\mathbf{H}_{err}(\mathbf{r})|^2}{|\mathbf{E}_{pl}(\mathbf{r})|^2 + \eta^2 |\mathbf{H}_{pl}(\mathbf{r})|^2} \tag{1}$$

where the error field (for the electric field) is $\mathbf{E}_{err} = \mathbf{E} - \mathbf{E}_{pl}$. The terms $\mathbf{E}$ and $\mathbf{E}_{pl}$ are the true field (rigorously calculated as described earlier) and the plane wave construction at the observation point. The plane wave field, $\mathbf{E}_{pl}$, is a *best fit* field formed from the Poynting vector (to avoid bias toward the electric or magnetic field) which is calculated at a user specified reference position and propagation direction. For example, at a reference position $\mathbf{r}_0$ and direction $\hat{\mathbf{z}}$, the plane wave E-field is:

$$\mathbf{E}_{pl} = E_{mag}\, e^{j\phi} \left(\hat{\mathbf{x}}|E_{plx}| + \hat{\mathbf{y}}|E_{ply}|\right)/|\mathbf{E}| \tag{2}$$

where the components used above are

$$E_{plx} = \frac{1}{2}\left(E_x(\mathbf{r}_0) + \eta H_y(\mathbf{r}_0)\right) \tag{3a}$$

$$E_{ply} = \frac{1}{2}\left(E_y(\mathbf{r}_0) - \eta H_x(\mathbf{r}_0)\right) \tag{3b}$$

and the magnitude of the electric field is $E_{mag} = (\eta |Re(\mathbf{E} \times \bar{\mathbf{H}})|)^{1/2}$. The phase ϕ is given by

$$\phi = \left[|E_{plx}|\ ph(E_{plx}) + |E_{ply}|\ ph(E_{ply})\right] / \left[|E_{plx}| + |E_{ply}|\right]. \tag{4}$$

The function $ph(\cdot)$ takes the phase of its complex argument, similar definitions apply for the magnetic fields. The $T - factor$ is the average energy density of the error field to that of an ideal plane wave; for perfect plane wave simulation conditions $T = 0$. TFAC will calculate and plot the value of T at any user defined point, line, or cross section.

IV. Example

In this section we demonstrate the use of the test fidelity software by a brief, and simple example of the computation of the $T - factor$. Consider a standard gain rectangular horn ($G \approx 16.2\ dB$, $A = 0.208\ m^2$) operated at 1.41 GHz. At 6 m directly in front of the horn, the $T - factor$ in a 0.25 m^2 cross-sectional plane is calculated and displayed as shown in Figure 4a. Making the somewhat obtuse assumption that the E and H fields are related simply as in the far-field (to enable us to unfold the $T - factor$, we can show

$$(1 - \sqrt{T})^2 \leq |E|^2 \leq (1 + \sqrt{T})^2. \tag{5}$$

Study of Figure 4a shows that $T \leq 0.1$ across the 0.5 $m \times 0.5$ m area. Then, use of Eq. (5) reveals that the power density can vary instantaneously by more than 5 dB over the area. Figure 4b presents the computation of T at 12 m (approximately the antenna far-field) directly in front of the horn across a 0.25 m^2 cross-sectional square plane. For this case, $T \leq 0.02$, which indicates that the power density can vary instantaneously by 2.5 dB over the area. A general rule of thumb is that if $T \leq 0.02$ across cross-sectional areas that cover points-of-entries, then instantaneous power density variation across points-of-entries will be less than 3 dB. In addition, numerical experiments will show that at distances close (in terms of wavelengths) to the source antenna, test fidelity can be maintained over small cross-sectional areas.

V. Summary

Many times, tests conducted in anechoic chambers strive to achieve plane-wave conditions over extended spatial areas. The *Test Fidelity in Anechoic Chambers* software program provides test personnel an ability to rapidly and accurately determine the electromagnetic environment in which a test asset is placed. The impact on test fidelity (the degree to which the simulation approximates a plane wave) of test asset proximity to the antenna, and scattering from absorber surfaces is expressed as a simple scalar number. Prior assurance of good test fidelity reduces test setup efforts, and ultimately lends confidence in the experimental results.

Acknowledgement The authors would like to acknowledge the contributions made by Robert A. Koslover to this program; and thank Lt. C. Heron, the program project officer, for her support. This work is funded by the Air Force Small Business Innovation for Research program, Contract No. F29601-91-C-0077.

References

1. T. Li and R. H. Turrin, "Near zone field of the conical horn," IEEE Trans. Ant. and Prop., vol. AP-12, no. 6, pp. 800 - 803; November 1964.

2. D. R. Wilton and C. M. Butler, "Effective methods for solving integral and integro-differential equations," Electromagnetics, vol. 1, pp. 289 - 308; 1981.

3. C. L. Holloway, *Low-Frequency Analysis of Anechoic Chambers*, Master's Thesis, University of Colorado, Boulder, 1988.

4. R. J. Marhefka and J. W. Silvestro *Near Zone - Basic Scattering Code User's Manual with Space Station Applications*, The Ohio State University Electroscience Laboratory, Columbus Ohio, Technical Report 716199-13, March 1989.

5. J. E. Hansen, Ed., *Spherical Nearfield Antenna Measurements*, Peter Peregrinus Ltd., London, IEE Electromagnetic Wave Series No. 26, 1988.

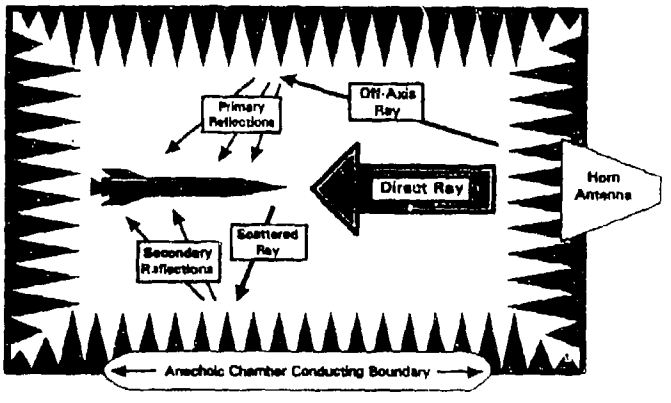

Figure 1. Direct, primary, and secondary illumination of test asset. The test asset is exposed to direct illumination from the source, (primary) reflections from the absorber covered walls of direct illumination, and (secondary) reflections of direct field incident on the asset, scattered to the walls and reflected back to the text zone.

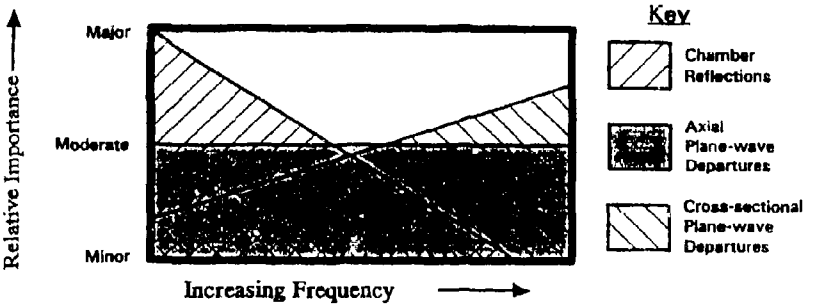

Figure 2. Relative importance of perturbations to test fidelity caused by anechoic chamber reflections and radiating near-field effects versus frequency.

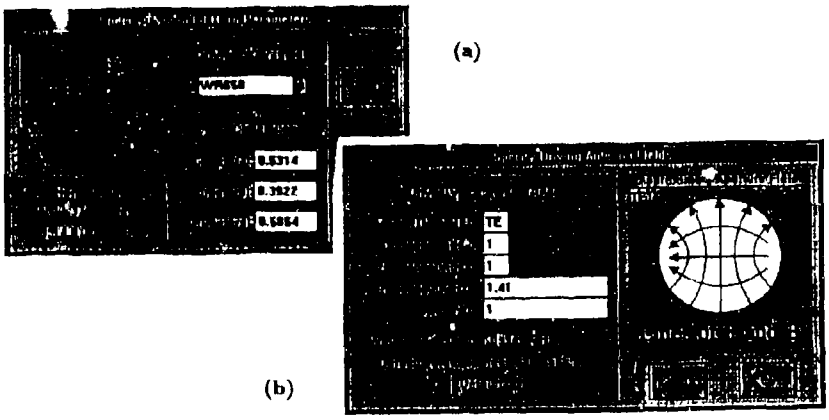

Figure 3. Dialog boxes for descriptions of aperture antennas: (a) rectangular aperture physical dimensions and driving waveguide; and (b) conical antenna mode specifications, frequency, and output power.

(a)

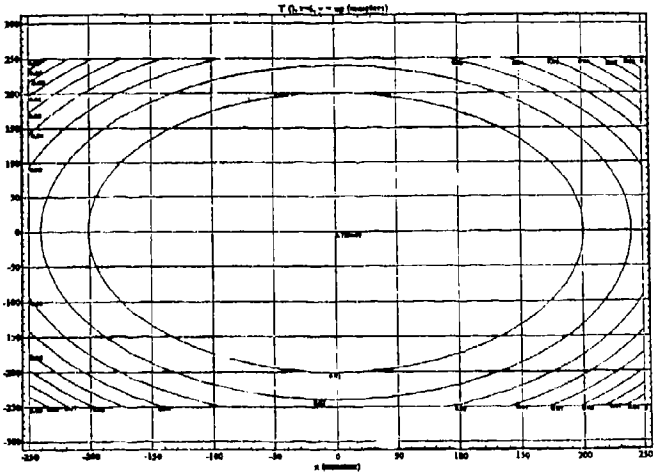

(b)

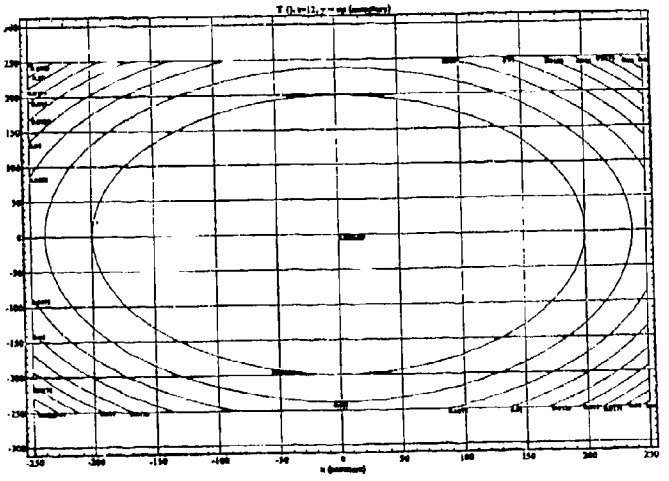

Figure 4. Contour graph of $T - factor$ for a standard gain horn operated at $f = 1.41\ GHz$: (a) T over a cross-sectional area 6 m in front of the horn on boresight; and (b) T over a cross-sectional area 12 m in front of the horn.

An Investigation into Alternative Construction Techniques to Reduce Shielded Room Resonance Effects

Bruce Archambeault
Digital Equipment Corporation

Kent Chamberlin
University of New Hampshire

Introduction

The need to measure electromagnetic fields accurately is greater than ever before in industry. As computers and their associated devices increase in speed they tend to increase the pollution of the electromagnetic spectrum, while the reliance on communication devices requiring a quiet spectrum is increasing. It is no surprise that manufacturers spend enormous amounts of money to build shielded rooms with sufficient absorber material so they can meet the test facility requirements of the Federal Communications Commission (FCC) while eliminating the ambient signals that could cause measurement inaccuracies.

This paper discusses a new construction technique that, when combined with a reduced amount of absorber material, can greatly reduce the cost and size requirements of such anechoic shielded rooms. Modeling is used to verify the room's performance.

Background

Typically, EMI test laboratories have little choice in the test site type. They can either build an open area test site (OATS) or a shielded anechoic room. An OATS is much less expensive to build than the shielded anechoic room, but requires the user to deal with poor weather conditions and an intrusive electromagnetic ambient. If a wood or plastic enclosure is placed around the test site, then extra care (meaning extra expense) must be used to insure the materials do not allow small amounts of reflections which could render the site unacceptable to the FCC. (The FCC requires a measurement uncertainty of less than 4 dB.)

Shielded rooms offer protection from the weather environment as well as the electromagnetic environment. However, the metal walls allow reflections which result in resonances. These resonance frequencies are determined by the construction dimensions and can result in typical measurement uncertainties of at least 40 dB. [1] Placing anechoic absorber material on the walls reduces the Q of the room, and can greatly reduce the measurement uncertainty.

Since measurements for the FCC (and other commercial standards) are typically at distances of at least 3 meters the construction costs associated with the shielded anechoic room is normally in the area of $1 Million. The shielded room must be large enough to include 6-8 feet thickness of the absorber material on all the walls and ceiling making the shielded room much larger then would normally be required to provide the same working space (hence part of the extra cost). The absorber material is quite expensive and can often be at least half of the total room costs.

Approach

Since the room resonances are due to the physical parameters of the shielded room, this work changed the most basic assumption, that is, the room must be rectangular. The walls were made to be non-parallel (by varying degrees) and the effect upon the room resonance frequencies was observed. Small amounts of absorber material were added to observe the effect upon the measurement uncertainty.

The Finite-Difference Time-Domain (FDTD) modeling technique was used to model the shielded room with non-parallel walls (with and without the absorber material). A two-dimensional model was used to reduce the run time and memory requirements. The FDTD results were compared to the closed form solution for the rectangular case.

Rectangular Room Resonances

A rectangular cavity has resonant frequencies which depend upon the the three linear dimensions between the parallel walls. Equation (1) is given in [2] to determine these resonant frequencies. Since the analysis was to be performed in only two dimensions, equation (1) was reduced to equation (2).

$$FREQ_R = \frac{1}{(2\pi\sqrt{\mu\varepsilon})}\sqrt{\left(\frac{m\pi}{a}\right)^2 + \left(\frac{n\pi}{b}\right)^2 + \left(\frac{p\pi}{c}\right)^2} \qquad (1)$$

$$FREQ_R^{2d} = \frac{1}{(2\pi\sqrt{\mu\varepsilon})}\sqrt{\left(\frac{m\pi}{a}\right)^2 + \left(\frac{n\pi}{b}\right)^2} \qquad (2)$$

The resonant frequencies of a 2-D cavity with dimensions 3.024 meters by 1.89 meters were found using both equation (2) and FDTD. The results are shown in Table 1. There was good agreement between the two approaches.

One of the disadvantages of using FDTD to determine resonant room characteristics is its tendency to report infinite Q's (since the walls are perfect electrical conductors). Naturally, before an infinite Q can be found, the model must run for an infinite amount of time as well. The model must also run long enough for all the resonant frequencies to be found. The question of the best trade-off between accuracy of the Q and the long run times needed to be settled.

The run time needed for the FDTD model was determined by using different run times and observing the response over an area. Figure 1 shows the basic model geometry. The FDTD model was run for 10,000, 30,000, 50,000, and 100,000 time steps. The maximum received spectral signal strength over all the monitor points is shown in Figure 2 for the various run times.

From the response in Figure 2 it was determined that 30,000 time steps was sufficient to allow the resonance to develop. Although the Q may not be absolutely correct for the non-coated walls, the measurement uncertainty was at least 20 dB, which is much more than allowed. As the absorber material is added to the walls the Q of the room will be lowered significantly and

the run time need not be as long. This is verified later in this report.

Table 1
Resonant Frequency Comparison between Techniques

Mode	FDTD	Balanis
1	95.5 MHz	93.5 MHz
2	131.4 MHz	12[illegible].9 MHz
3	172.5 MHz	168.5 MHz
4	192 MHz	187 MHz
5	219.7 MHz	217.4 MHz
6	246.4 MHz	242.9 MHz
7	260.2 MHz	257.7 MHz

Anechoic Absorber Material

The anechoic absorber material used in most shielded rooms is a carbon loaded foam. It is most often pyramidal shaped. The bulk conductivity has been determined at the National Institute of Standards and Technology (NIST) empirically [7] and verified by others [8]. The conductivity was found to vary as a function of frequency less than an order of magnitude. Since FDTD is a time domain technique and a wide bandwidth Gaussian shaped pulse was used, the model for the absorber material conductivity required a single value. The average absorber conductivity across the frequency range was used (5×10^{-2} Siemens).

The thickness of the absorber material was varied (as described in the next section) and a stairstep approximation for the triangular cones was used in the FDTD model.

Evaluated Models

It was desired to create a shielded room with enough usable space to allow testing at a distance of 3 meters, including the space needed for an internal turntable with a large equipment-under-test (EUT). Figure 3 shows a graphical representation of the desired room and the various spaces allowed. The result was a room overall dimension of 18 x 33 feet. Note if the 8 foot thick absorber cones were used, the overall dimension would be 34 x 49 feet.

The room was then scaled down by a factor of 4 to allow sufficient resolution of the FDTD model without creating a huge computational domain. The final room dimension was 1.89 x 3.024 meters.

A series of room shapes were then analyzed. These shapes are shown in Figure 4. Note that only in one case were there any parallel walls.

Anechoic absorber was added to each of the rooms in thicknesses of 1, 2, 3, and 4 feet.

The goal was to reduce or eliminate the measurement uncertainty across the measurement area. That is, if the EUT (as a source) was moved slightly within the measurement area, while keeping the total distance between the EUT and the receive antenna constant, then the measured signal strength should remain constant. Since the FDTD model contained a number (50) of monitor points and one source (the reciprocal problem), then the difference between the maximum and minimum signal strength across the frequency range should be the same as for an OAFS.

Model Results

A number of different cases were modeled. Table 2 shows the reference name for each case, and their associated parameters. As mentioned earlier, the minimum and maximum spectral response for each case was determined. An example of the large variation between a rectangular room with no absorber (Case RC10a) and the maximum non-rectangular room with the 4 foot thick absorber material (Case RC14e) is shown in Figure 5a and 5b, respectively. Both the monitor maximum and the monitor minimum is shown for both cases. Note the large resonant effects at the resonant frequencies throughout the frequency range in Figure 5a and the nearly flat response in Figure 5b.

Once the post-processing was completed, only the difference between the monitor maximum and the monitor minimum was considered. Figures 6 through 10 show the same parameter for the various non-parallel wall rooms.

As can be seen from Figures 6 through 10, the absorber material has a much greater effect when the walls of the room are not parallel. In fact, the greater the angle of the walls, the greater the effect of the absorber material.

Conclusions

The use of non-parallel walled shielded rooms can reduce the amount of RF absorber material required to reduce measurement uncertainty. A relatively modest amount of absorber material can be used (on the order of 4 feet rather than the typical 8 feet thick), thus reducing the overall construction cost through reduction on the amount of absorber material purchased, the size of the basic shielded room (needed to maintain a usable internal space), and the area required to house the facility. The room response is very slowly varying with frequency with this modest amount of absorber thickness in a non-parallel room, and so further reduction in measurement uncertainty can be realized by using a calibrated 'room correction factor' in all measurements. This correction factor could eliminate any further variations in measured response as a function of frequency, since the response is slowly varying.

Summary

This paper has used the FDTD modeling technique to model the effect of non-parallel walls in a shielded enclosure on the room's resonances and therefore on its measurement uncertainty. Small amounts of anechoic absorber material can be used to great advantage compared to the normal requirements for rectangular shielded rooms. This result allows a great reduction in cost to create commercial EMI test facilities using shielded rooms.

Acknowledgments

The authors wish to acknowledge the contribution of Professor Ray Lubbers of Penn State University for his providing the FDTD core programs.

Table 2
Description of Modeled Cases

Room #	Absorber Thickness	Case
1	none	Case RC10A
1	1'	Case RC10B
1	2'	Case RC10C
1	3'	Case RC10D
1	4'	Case RC10E
2	none	Case RC11A
2	1'	Case RC11B
2	2'	Case RC11C
2	3'	Case RC11D
2	4'	Case RC11E
3	none	Case RC12A
3	1'	Case RC12B
3	2'	Case RC12C
3	3'	Case RC12D
3	4'	Case RC12E
4	none	Case RC14A
4	1'	Case RC14B
4	2'	Case RC14C
4	3'	Case RC14D
4	4'	Case RC14E

References

[1] M. L. Crawford, "Evaluation of Shielded Enclosure for EMI/EMC Measurements with and without RF Anechoic Material," IEEE International Symposium on EMC, Zurich, March 1983.

[2] C. A. Balanis, "Advanced Engineering Electromagnetics," Wiley, 1989

[3] C. M. Harris, "Application of Wave Theory of Room Acoustics to the Design of Auditoriums," Annals of Physics, #159, 1989, pp 59-65.

[4] D. E. Baxa, A. Seireg, "A Strategy for the Optimum Design of Acoustic Space," Journal of Mechanical Design, Vol. 100, July 1978, pp. 411-416.

[5] T. J. Schultz, "Concert Hall Acoustics," SAAI 1980 International Symposium on Sound, Buildings, and People, October 1980, pp. 35-47.

[6] G. Berry, G. L. Cruise, "Assisted Resonance," Journal of the Audio Engineering Society, Vol. 24, Number 3, April 1976, pp. 171-177.

[7] Santi Tofani, A. Ondrejka, and M. Kanda, "Time-Domain method for characterizing the reflectivity of absorbing materials from 30 to 1000 MHz," IEEE Trans. Electromagn. Compat., vol. 33, pp. 234-240, 1991.

[8] Santi Tofani, A. Ondrejka, M. Kanda and David Hill, "Bistatic Scattering of Absorbing Materials from 30 to 1000 MHz," IEEE Trans. Electromagn. Compat., vol. 34, Number 3, August 1992.

Figure 1
Basic Model Geometry

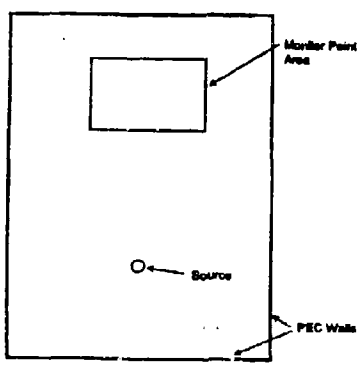

Figure 3
Desired Room Geometry

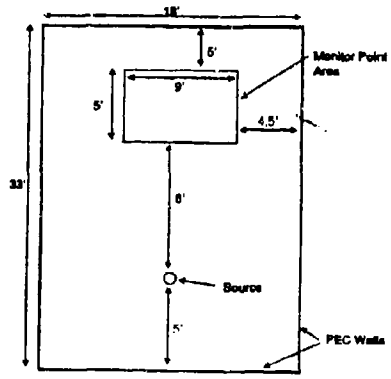

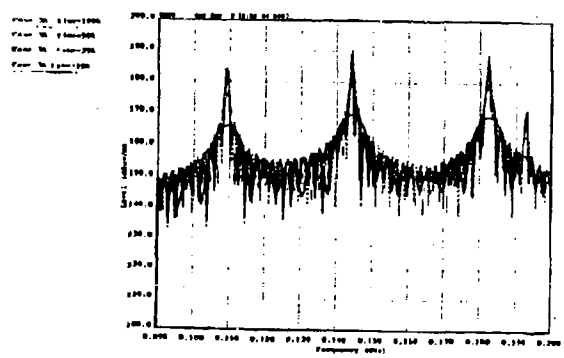

Figure 2
FDTD Resonance Q-Factor vs Run Time

Figure 4
Modeled Room Shapes

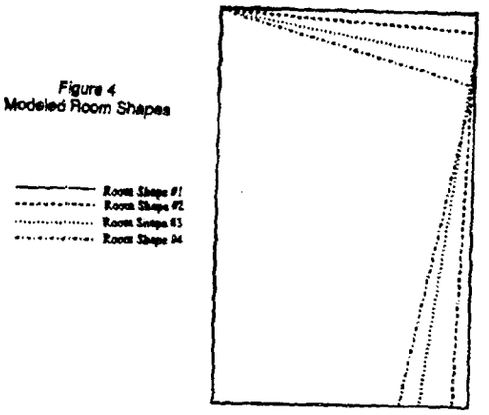

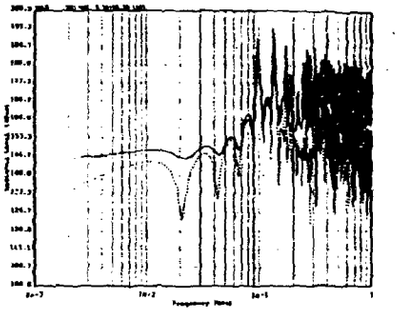

Figure 5a
Example Maximum-to-Minimum Monitor Point
Variation for No Absorber (Rectangular Room)

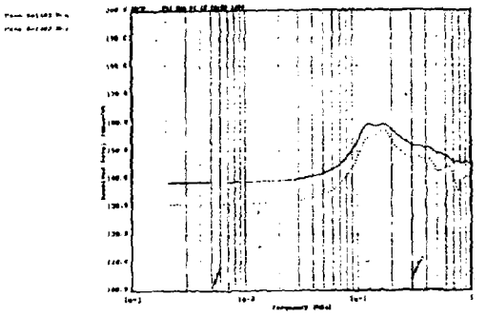

Figure 5b
Example Maximum-to-Minimum Monitor Point
Variation for 4" Thick Absorber (Non-Rectangular Room)

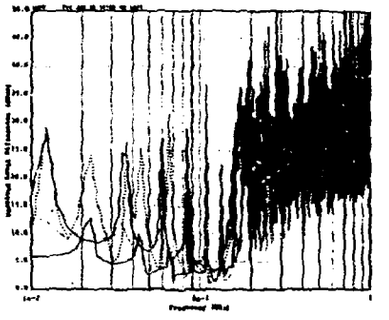

Figure 6
Maximum Monitor Point Variation
No Absorber Material

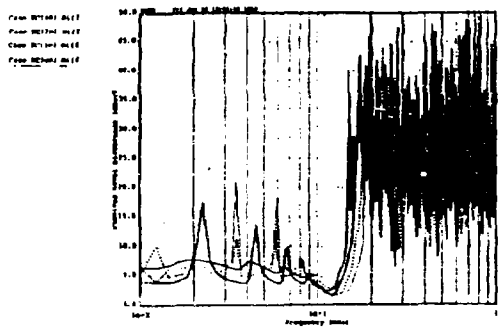

Figure 7
Maximum Monitor Point Variation
Absorber Material 1" Thick

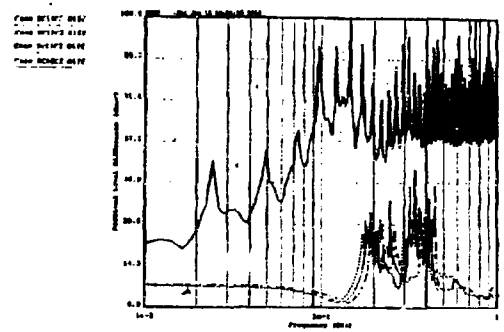

Figure 8
Maximum Monitor Point Variation
Absorber Material 2" Thick

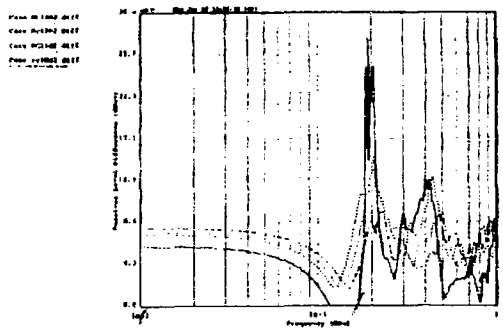

Figure 9
Maximum Monitor Point Variation
Absorber Material 3" Thick

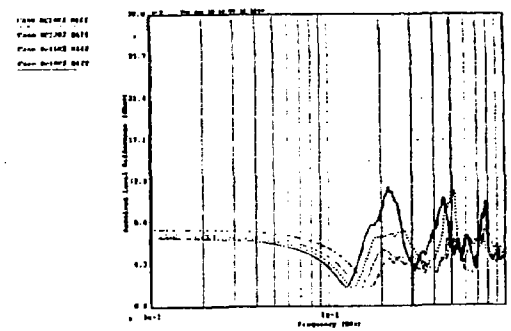

Figure 10
Maximum Monitor Point Variation
Absorber Material 4" Thick

Electromagnetic Interference (EMI) Susceptibility Analysis of an Airborne Phased Array Antenna System

Frank E. Walker and Scott L. Badger
Boeing Defense & Space Group; Seattle, WA

Abstract

This paper describes the results of two approaches to approximating the susceptibility of an airborne phased array system to electromagnetic interference (EMI). Simple models were used in an attempt to develop a "quick-look" capability to determine the gross coupling of threat-level electromagnetic (EM) environments into the antenna system. In the first case, NEC-3 was used to approximate external field coupling into the system by modeling the antenna as a half-wave dipole into a 50-ohm load. In the second case, external-to-internal field, internal field-to-wire, and internal field-to-antenna coupling approximations were made with IEMCAP.[1]

These modeling approaches could provide the program engineer with a tool to approximate EMI effects. However, their application is limited because of the detailed modeling requirements necessary in order to avoid errors induced by approximations and simplifying assumptions. Accurate external-to-internal field coupling was not calculated in this analysis due to detailed modeling requirements that were beyond the scope of this effort. A WIRANT model was sufficient to calculate airframe surface currents but requires further refinements of fuselage apertures to predict internal field strengths. External-to-internal field coupling data are needed to improve the internal field estimate in the IEMCAP model. Again, this will require more detailed modeling of the aircraft airframe or EM environmental test measurements, which is time consuming and costly. Such detailed modeling and testing are often beyond the available resources of the program engineer for estimating purposes.

Introduction

Preliminary EM coupling estimates are necessary to determine EMI effects on an airborne antenna system. The system design engineer can determine EMI effects on system elements from known system susceptibility parameters using approximations of coupling from external EM environments. Recent studies have been conducted to learn more about the susceptibility of antenna elements to RF interference.[2,3,4,5] From the system engineering point of view, it is desirable to be able to quickly and easily approximate the effects of new EM environments as they are identified. Extensive EMI analysis may be required to guarantee the integrity of a complex system in a hostile EM environment.[6]

In this effort, the computation of EM environments coupling into a typical phased array antenna element and into internal system ports was modeled to demonstrate the analysis approach. The modeling was not based upon actual system parameters but rather general approximations were used to allow reasonable simulation of a system. For a real array system configuration, the transfer function of the specific antenna elements, both in-band and out-of-band, can be calculated from actual system parameters. The approach to modeling EMI coupling depends on the type of element into which the RF energy will be coupled.

NEC-3 Modeling of External Field-to-Port Coupling

We have chosen, for this simple analysis, a half-wave dipole to model the antenna element. The dipole is 5-cm long, making the fundamental frequency 3 GHz. It is modeled as a 50-ohm center segment loaded thin-wire dipole with varying numbers of segments in a NEC-3 model file, as shown in figure 1, for a method of moments analysis.

Figure 1 50 ohm Half-Wave Dipole Antenna Element Model.

The number of segments varies with frequency because NEC-3 has numerical difficulties with segments that are extremely short in terms of a wavelength, and NEC-3 is not as accurate with segments that are much more than a tenth of a wavelength. This posed problems because the environments covered a range of 1 kHz to 100 GHz. Even with varying numbers of segments, the lowest frequency at which NEC can handle a 5-cm-long wire is approximately 1 MHz. The computed transfer function seems to converge to a straight line on a log-log scale and is sufficiently small, at 1 MHz and lower, that extrapolation seems appropriate. The transfer function as calculated by NEC-3 is shown in figure 2 and is shown transposed onto environmental levels and in the same units in figure 3. The transfer function can be applied to EM environment levels to find the signal strengths dumped into a 50-ohm load by the antenna. These signal levels are shown in figure 4 and can be used to model the combined worst case threat to the phased array receiver.

Method of moments codes, such as GEMACS, NEC-3, or WIRANT, can be used to calculate vehicle surface currents such as those on the fuselage of an aircraft. Currents around apertures can be calculated to determine field strengths entering the fuselage. Interior field strengths are then analytically coupled into cabling on the interior of the fuselage to determine the energy in the cables and at the system port circuits. A WIRANT model of a 707-320B is shown in figure 5. This model would be sufficient for determining surface currents on the wings and fuselage, but requires further refinement around the cockpit to be useful to determine internal field strengths.

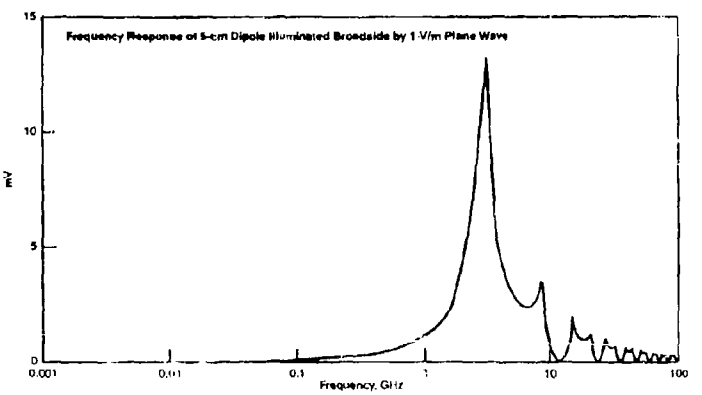

Figure 2 Dipole Antenna Transfer Function

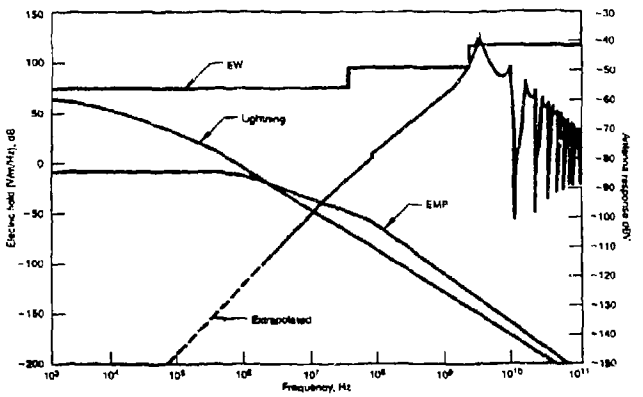

Figure 3 Antenna Response and Environmental Spectra.

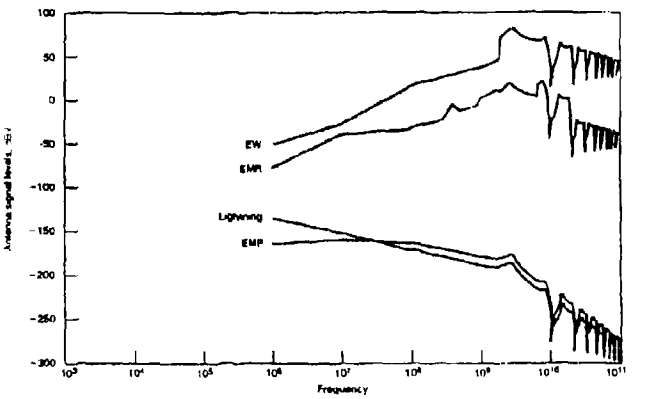

Figure 4 EM Environments Coupled Into RF Ports.

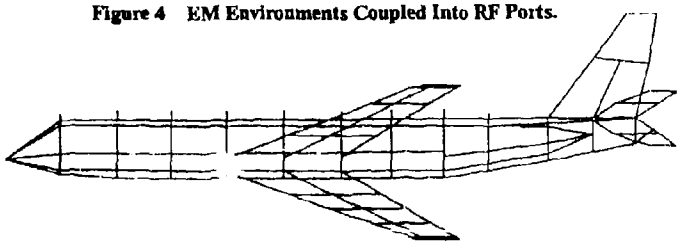

Figure 5 Wire Model Used to Compute Fuselage Surface Currents.

IEMCAP Modeling of System Field-to-Port Coupling

In this study, IEMCAP was used to determine internal port circuit energy coupled from external EM fields. IEMCAP was used to perform the field strength, field-to-wire, and field-to-antenna calculations. A Boeing 707-320B was used as a representative platform, and some typical equipment cases for a phased array radar were assumed and located in arbitrary locations on the aircraft. A diagram of the locations of these cases is shown in a side view in figure 6 and in a plan view in figure 7. The cargo door of the 707-320B was assumed to be a practical location for a conformal phased array antenna. An equipment case for the radar was placed just aft of the door, which would derive its power from cables coming from one of the engine nacelle generators into a junction box at the wingroot. An equipment case for a display or some other piece of auxiliary equipment was located just aft of the forward personnel door. The actual model of the aircraft used by the IEMCAP code is rather a simplistic one. The fuselage is represented by a truncated cone for the nose of the aircraft, which is attached to either a round-bottomed or a flat-bottomed cylinder that extends backward to infinity from the nose. The wings are represented by flat plates specified by the wingroot and wingtip locations. An illustration of this basic model is shown in figure 8.

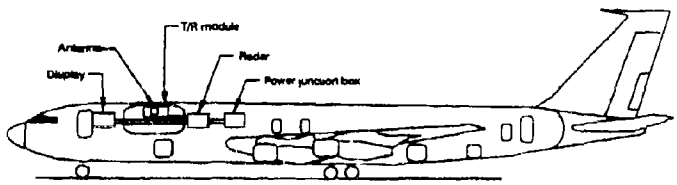

Figure 6 Equipment Locations on 707-320B Model.

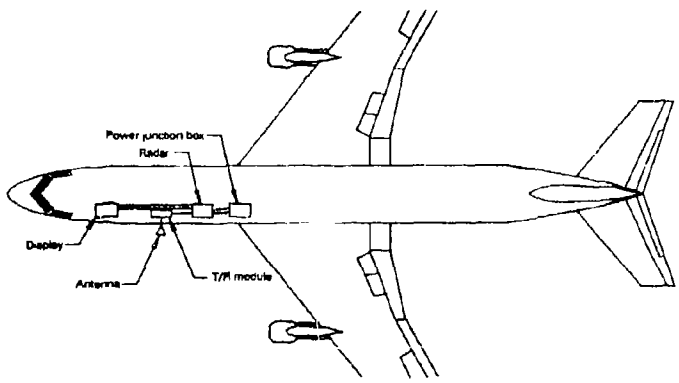

Figure 7 Plan View of Equipment Location on 707-320B Aircraft.

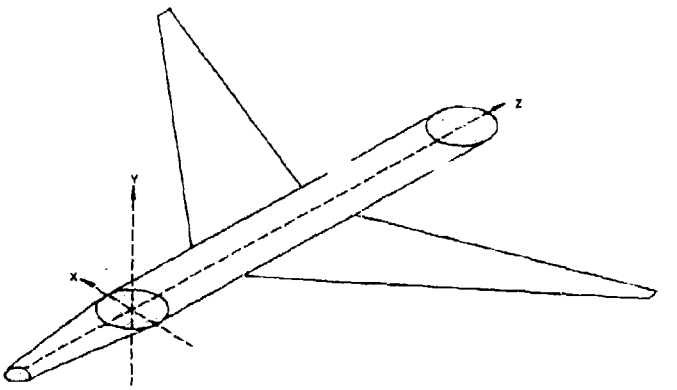

Figure 8 IEMCAP Model of 707-320B Aircraft.

The equipment in the IEMCAP model is specified by locating cases by their water lines, butt lines, and stations. Ports are assigned to each case and can be filtered. The cabling is assigned locations by bundles whose end points are given by the ports to which they are connected. The characteristics of the cable are taken from a wire table, which specifies all the particulars of cable type and dimensions. Antennas are specified by location, in water line, butt line, and station units, using some basic simple types, such as dipoles and horns. The 3-dB beam-width of the antenna can be specified, but it is a fixed pattern and does not vary with frequency. Figure 9 illustrates the equipment modeled for the IEMCAP analysis.

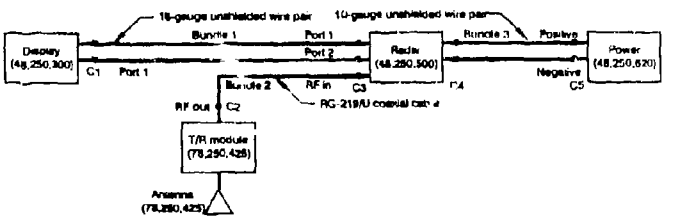

Figure 9 Model of Equipment Used for IEMCAP Analysis.

Worst case environmental field levels, which were those for electronic warfare sources, were fed into the IEMCAP model as external field levels. Because the internal fuselage field levels were not specified, IEMCAP defaulted these to 40 dB below those of the external field levels. Equipment cases are treated as simple dipoles exposed to plane waves at the internal field strength. The signal levels for the cases, as calculated by IEMCAP, are shown in figure 10. The field-to-wire coupling calculations are solved using transmission line theory for low frequencies and moment methods for high frequencies. The signal levels for the ports as calculated by IEMCAP are shown in figure 11. These levels are very much higher than were expected and can be reduced by further refinements of the IEMCAP model.

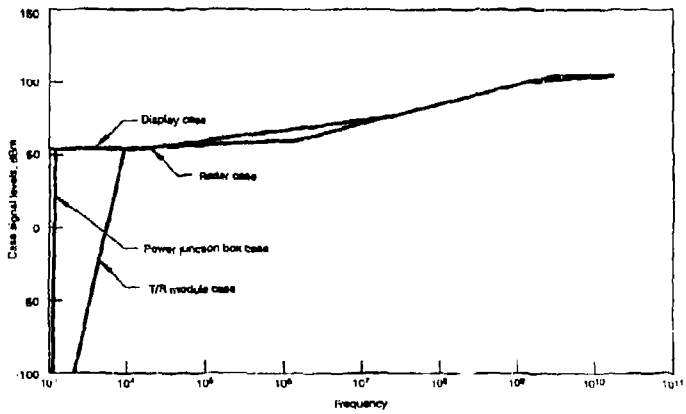

Figure 10 IEMCAP Predicted Equipment Case Coupling.

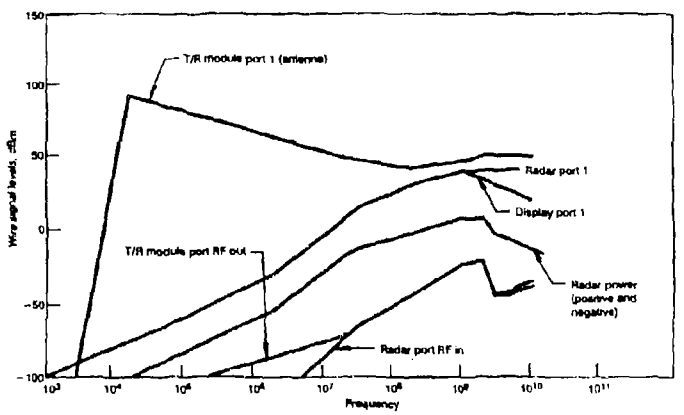

Figure 11 IEMCAP Predicted Equipment Port Coupling.

Findings and Recommendations

Our initial NEC antenna model is sufficient for approximations of gross antenna response to EMI environments. The IEMCAP analysis provides upper bounds on the EMI coupled to the system ports but is excessively conservative for design evaluation based upon interference predictions. It is difficult to avoid the eventual necessity of detailed system modeling to achieve

reasonably accurate EM coupling estimates. We would hope that as computational codes like NEC and IEMCAP become refined and easier to use that they will be relied upon more often to perform cursory computations on which system designs can be based. Unfortunately today this is only true in cases where the EMI threat is sufficient to warrant a detailed modeling effort.

The IEMCAP code provides substantial computational capability, but requires a considerable investment of time to achieve the necessary familiarity with the code to avoid excessively conservative or pessimistic coupling and interference predictions. This code would be of considerably greater value to the system EMC design effort if it were modernized to include improved coupling analysis and approximating techniques. The IEMCAP code would also profit from the kind of interface improvements such as modeling graphics and a WINDOWS interface that have been developed for some of the other EM analysis codes.

Acknowledgments

The results reported in this paper were demonstrated to the U.S. Air Force at Rome Laboratory under contract Contract F30602-89-C-0004, Electrom Effects Mitigation Techniques for Advanced Arrays.[7] The contract technical m Mr. Michael Seifert, provided valuable assistance in the publication of this paper.

References

1. J. Bogdanor, R. Pearlman, and M. Siegel, Intrasystem Electromagnetic Compatibility Analysis Program: Vol. 1 and 2 - User's Manual Usage Section, Final Technical Report RADC-TR-74-342, Rome Air Development Center, December 1974.

2. F. Walker and S. Badger, RF Device Modeling for Electromagnetic Effects Analysis, Government Microcircuit Applications Conference (GOMAC) Digest of Papers, p. 329, November 1993.

3. F. Walker and S. Goodman, Non-Linear Effects Errors Encountered in Performing Interference Analysis Using an RF Circuit Analysis Code, 9th Annual Review of Progress in Applied Computational Electromagnetics, p. 777, 1993.

4. J. Rohrbaugh and R. Pursley, X-Band T/R Module Conducted Interference Simulation and Measurement, Final Technical Report RL-TR-92-319, Rome Laboratory, December 1992.

5. McDonald Douglas, Integrated Circuit Electromagnetic Susceptibility Handbook, MDG-E1929, September 1978.

6. G. Lee and S. Ellersick, Methodology for Determination of Circuit Safety Margins for MIL-E-6051 EMC System Test, IEEE Transactions on Electromagnetic Compatibility, p. 502, 1985.

7. F. Walker et al, Electromagnetic Effects Mitigation Techniques for Advanced Arrays, Final Technical Report RL-TR-93-205, Rome Laboratory, February 1993.

SESSION 16:

HYBRID

Chair: Bob Burkholder

A Hybrid Approach for Computing the EM Scattering from Complex Terminations Inside Large Open Cavities*

Robert J. Burkholder, Paul R. Rousseau, and Prabhakar H. Pathak
The Ohio State University ElectroScience Laboratory
1320 Kinnear Road, Columbus, Ohio 43212

Abstract—The electromagnetic (EM) scattering from complex terminations within open-ended cavities, such as engine terminations inside jet inlets, is computed using a hybrid combination of high frequency asymptotic and numerical methods. High frequency methods are used to find the coupling into the cavity via the open end and the propagation down the smoothly varying duct, and numerical methods are used to find the reflection from the complex termination. The duct and the termination sections are decoupled at a cross-section S_T near the termination using a discrete plane wave expansion (PWE), so that the analyses of the two sections may be performed separately. The external field scattered by the termination is found using a reciprocity integral over the incident and reflected fields at S_T. Numerical results are presented which demonstrate the accuracy of this approach by comparison with reference solutions.

1 Introduction

The EM scattering from complex terminations within electrically large open-ended cavities may contribute very significantly to the radar cross-section (RCS) of the body containing the cavity. Typical geometries of interest are the complex fan-blade or engine face terminations of aerodynamic inlet/exhaust ducts present in modern jet aircraft. Generally, these geometries are very large in terms of wavelength so numerical methods are not suitable for doing the entire problem. In the hybrid approach presented here, the geometry is bisected at a cross-section S_T near the termination as shown in Figure 1. The electrically large duct section is smooth and slowly varying so high frequency asymptotic methods may be used to find the coupling of the external fields into the duct via the open end, and the propagation down the duct to S_T. Numerical methods may then used to find the reflection from the more detailed but smaller engine termination section. The scattered field in the external region due to the engine termination is found using a reciprocity integral over the fields incident at S_T reacted with the fields reflected by the termination [1].

The main advantage of this approach is that realistically large and complex cavities may be analysed efficiently by combining high and low frequency methods. A high frequency method alone would not be able to handle the complex termination with accuracy, and a numerical method alone could not efficiently handle the entire cavity geometry because of its large electrical

*Sponsored by General Electric Aircraft Engines, Evandale, OH, McDonnell Douglas Aerospace, St. Louis, MO, and the Air Force Wright Laboratory Target Recognition Technology Branch, Wright-Patterson AFB, OH.

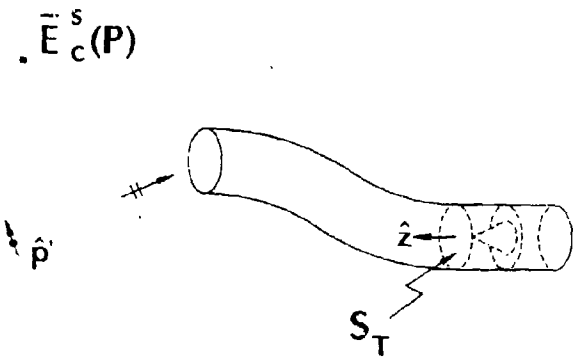

Figure 1: Geometry of an open-ended cavity with a complex termination illuminated externally by a dipole source $\hat{p}'$.

size. Another advantage is that the duct and termination sections are analyzed separately, allowing changes to be made to one of the sections without having to repeat the analysis of the other.

The high frequency asymptotic methods used here to analyze the duct section are the hybrid asymptotic modal method [2], the shooting and bouncing ray (SBR) method [3], and the generalized ray expansion (GRE) method [4]. The hybrid modal method uses high frequency asymptotic methods to find the coupling of the externally incident fields into the waveguide modes of the duct at the open end, which then propagate to S_T. It is very accurate for large ducts, but is limited to canonical waveguide configurations so it is used mainly as a reference solution. The SBR and GRE methods launch and track geometrical optics (GO) ray tubes into the duct from the open end. They are not as accurate as the hybrid modal method, but can be applied to much more arbitrarily shaped cavities. The only difference between the SBR and GRE methods is in the way the ray tubes are initially launched. SBR only tracks the GO field in the cavity, while the GRE method includes fields diffracted into the cavity by the aperture at the open end.

To couple the solutions for the two separate regions, the fields at S_T are expanded into an orthogonal plane wave basis set [5]. Plane waves are chosen over waveguide modes because they may be used with arbitrarily shaped duct cross-sections (although most ducts of interest are circular near the engine face), but more importantly they allow the termination section to be characterized by a plane wave scattering matrix which is obtained using a conventional plane wave scattering analysis of the isolated termination section. The method of moments is used in the results presented here to obtain the termination scattering matrix.

The duct analysis methods and the method of moments solution for the termination section will not be described in any more detail here. The theory section will focus on the reciprocity integral and the discrete plane wave expansion of the fields at S_T. The associated plane wave scattering matrix which characterizes the termination will also be discussed. An $e^{j\omega t}$ time

convention is assumed and suppressed throughout the following. Z_o is the free space impedance and $k = 2\pi/\lambda$ is the free space wave number.

2 Theory

In this section the reciprocity integral is presented first, followed by the discrete plane wave expansion (PWE) of the fields over S_T. Then the termination plane wave scattering matrix will be expressed in terms of the bistatic scattering pattern of the isolated termination section.

2.1 The Generalized Reciprocity Integral

Referring again to Figure 1, the generalized reciprocity integral [1] for obtaining the fields at point P scattered by the engine termination inside a cavity illuminated by the dipole source $\hat{p}^i$ is given by

$$\vec{E}_t^s(P) \cdot \hat{p}_t \;=\; \int_{S_T} \left(\vec{E}^s \times \vec{H}_t^i - \vec{E}_t^i \times \vec{H}^s \right) \cdot \hat{z} dS \tag{1}$$

where $\hat{p}_t$ is a test dipole source located at P. $(\vec{E}_t^i, \vec{H}_t^i)$ are the fields excited by $\hat{p}_t$ which are incident at S_T from the duct section, and $(\vec{E}^s, \vec{H}^s)$ are the fields at S_T scattered by the termination excited by $\hat{p}^i$. For simplicity, multiple interactions between the termination and the aperture at the open end are ignored when using this equation because these effects are generally insignificant for electrically large cavities.

2.2 The Discrete Plane Wave Expansion

The incident and scattered fields at S_T are expanded into a discrete set of $-\hat{z}$ and $+\hat{z}$ propagating plane waves, respectively. The plane waves are orthogonal over a square cross-section of width $2a$ which completely encloses the cross-section S_T and is generally chosen to be as small as possible for efficiency. This expansion is only valid for the fields in the plane of S_T. The $\pm\hat{z}$ propagating fields at S_T may be expanded as

$$\left\{ \begin{array}{c} \vec{E}^{\pm} \\ \vec{H}^{\pm} \end{array} \right\} \;=\; \sum_{mn} A_{mn}^{\pm} \left\{ \begin{array}{c} \vec{E}_{mn}^{\pm} \\ \vec{H}_{mn}^{\pm} \end{array} \right\} \tag{2}$$

with the plane waves categorized into TE and TM polarizations as

$$\left\{ \begin{array}{c} \vec{E}_{mn}^{\pm} \\ \vec{H}_{mn}^{\pm} \end{array} \right\}_{TE} \;=\; \left\{ \begin{array}{c} \hat{\phi}_{mn} e^{\mp j \vec{k}_{mn} \cdot \vec{r}} \\ \mp \hat{\theta}_{mn} e^{\mp j \vec{k}_{mn} \cdot \vec{r}} / Z_o \end{array} \right\} ; \left\{ \begin{array}{c} \vec{E}_{mn}^{\pm} \\ \vec{H}_{mn}^{\pm} \end{array} \right\}_{TM} \;=\; \left\{ \begin{array}{c} \hat{\theta}_{mn} e^{\mp j \vec{k}_{mn} \cdot \vec{r}} \\ \pm \hat{\phi}_{mn} e^{\mp j \vec{k}_{mn} \cdot \vec{r}} / Z_o \end{array} \right\} \tag{3}$$

The propagation vector $\vec{k}_{mn} = \hat{x}k_x + \hat{y}k_y + \hat{z}k_z$ of each plane wave is defined by

$$k_x \;=\; \frac{m\pi}{a} \; ; \; k_y \;=\; \frac{n\pi}{a} \; ; \; k_z \;=\; \sqrt{k^2 - k_x^2 - k_y^2} \tag{4}$$

for all m and n which satisfy

$$m^2 + n^2 \;<\; \left(\frac{ka}{\pi} \sin\theta_{max} \right)^2 \tag{5}$$

where θ_{max} is the maximum angle the propagation vector may make with the z-axis. This truncates the expansion to include propagating plane waves with no evanescent terms.

In a spherical coordinate system centered at S_T with $\hat{z}$ oriented as in Figure 1, the incident plane waves propagate to the right and the scattered plane waves propagate to the left along radial paths defined by $\pm\bar{k}_{mn}$. The polarization vectors $\hat{\phi}_{mn}$ and $\hat{\theta}_{mn}$ are orthogonal to $\bar{k}_{mn}$ and are defined in the conventional sense by

$$\hat{\theta}_{mn} = \hat{x}\cos\theta_{mn}\cos\phi_{mn} + \hat{y}\cos\theta_{mn}\sin\phi_{mn} - \hat{z}\sin\theta_{mn} \quad (6)$$

$$\hat{\phi}_{mn} = -\hat{x}\sin\phi_{mn} + \hat{y}\cos\phi_{mn} \quad (7)$$

where

$$\theta_{mn} = \cos^{-1}(k_z/k) \; : \; 0 \leq \theta_{mn} < \theta_{max} \quad (8)$$

$$\phi_{mn} = \tan^{-1}(k_y/k_x) \; : \; -\pi < \phi_{mn} \leq \pi. \quad (9)$$

The plane waves are assumed to exist in free space so the expansion of (2) is approximate because it can not perfectly account for the truncation of the fields at the duct walls. However, the approximation is very accurate for electrically large cross-sections as will be seen in the numerical results.

2.3 The Termination Plane Wave Scattering Matrix

The plane wave scattering matrix which characterizes the termination section is obtained approximately by finding the bistatic scattered field pattern when the isolated termination section is illuminated by each of the incident plane waves in turn. It may be shown that the element of this matrix which relates the coefficient of the mn^{th} reflected plane wave to the coefficient of the pq^{th} incident plane wave is given by [5]

$$\Gamma_{mn,pq} \approx \frac{\pi}{j2a^2k_{zmn}} \lim_{r\to\infty} \frac{r}{e^{-jkr}} \hat{\beta}_{mn} \cdot \bar{E}^s_{pq}(\theta_{mn}, \phi_{mn}) \quad (10)$$

where $\bar{E}^s_{pq}(\theta_{mn}, \phi_{mn})$ is the scattered field in the direction of the mn^{th} reflected plane wave ($+\hat{z}$ propagating) due to illumination by the pq^{th} incident plane wave ($-\hat{z}$ propagating). $\hat{\beta}_{mn}$ is the polarization of the mn^{th} reflected plane wave, and is equal to $\hat{\phi}_{mn}$ or $\hat{\theta}_{mn}$ if the mn^{th} (reflected) plane wave is TE or TM polarized, respectively.

In the numerical results presented here, the scattering matrix is obtained using CICERO which is a method of moments code developed at McDonnell Douglas Research Laboratories, St. Louis, MO, for body-of-revolution (BOR) geometries [6].

3 Results and Conclusions

The results are in the form of co-polarized monostatic RCS vs. aspect angle for both vertically (ϕ-ϕ) and horizontally (θ-θ) polarized plane wave illuminations. For this case, $\bar{p}^r$ and $\bar{p}_t$ are located at the same point and have the same orientation. The units of RCS are in decibels relative to a square wavelength (DBSW), and the dimensions of the geometries are in wavelengths. The cavities are all perfectly conducting.

Figure 2 shows the RCS patterns of a long cylindrical cavity with a flat termination. The 45λ duct section is analyzed using the hybrid modal method, and the plane wave scattering matrix for the 8λ termination section is also found using the hybrid modal method for this simple termination. The results are compared with the hybrid modal solution for the entire geometry. The small differences in the solutions are due entirely to the approximations associated with the truncated PWE.

Figure 3 shows the RCS patterns of a smaller cylindrical cavity with a hemispherical hub on a flat termination. The duct section is analyzed using the hybrid modal method and the termination matrix is found using the method of moments (MM). The results are compared with a MM solution for the entire geometry. The differences are due mainly due to unwanted external scattering effects which are present in the MM solutions.

Figure 4 shows the RCS patterns of a cylindrical cavity with a hemispherical hub termination found using the hybrid modal, GRE, and SBR methods for the duct section and the method of moments for the termination. The GRE results are expected to agree better with the hybrid modal solution because the GRE method includes the effects of fields diffracted into the cavity by the aperture at the open end, whereas the SBR method only includes the geometrical optics field.

References

[1] P. H. Pathak and R. J. Burkholder, "A Reciprocity Formulation for the EM Scattering by an Obstacle within a Large Open Cavity," *IEEE Trans. Microwave Theory and Techniques*, vol. 41, pp. 702–707, April 1993.

[2] P. H. Pathak and R. J. Burkholder, "Modal, Ray and Beam Techniques for Analyzing the EM Scattering by Open-ended Waveguide Cavities," *IEEE Trans. Antennas Propagat.*, vol. AP-37, pp. 635–647, May 1989.

[3] H. Ling, R.-C. Chou and S. W. Lee, "Shooting and Bouncing Rays: Calculating RCS of an Arbitrary Cavity," *IEEE Trans. Antennas Propagat.*, vol. AP-37, pp. 194–205, February 1989.

[4] P. H. Pathak and R. J. Burkholder, "High-frequency Electromagnetic Scattering by Open-ended Waveguide Cavities," *Radio Science*, vol. 26, pp. 211–218, Jan-Feb 1991.

[5] P. R. Rousseau, "A Study of Electromagnetic Scattering by Obstacles Placed within Open Cavities," M.S. Thesis, Dept. Elec. Eng., Ohio State Univ., Columbus, Ohio, 1992.

[6] J. M. Putnam and L. N. Medgyesi-Mitschang, "Combined Field Integral Equation Formulation for Axially Inhomogeneous Bodies of Revolution," MDC Report No. QA003, McDonnell Douglas Research Laboratories, Dec. 1987.

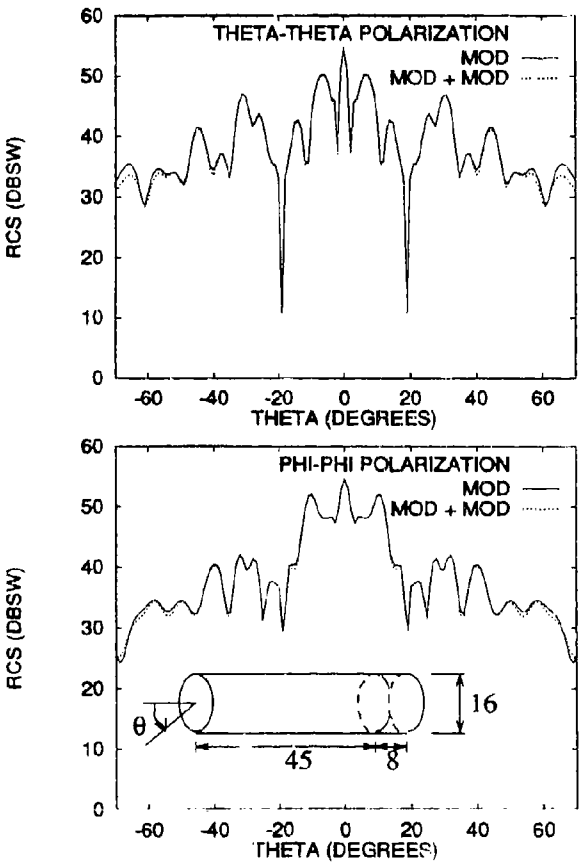

Figure 2: RCS patterns of a cylindrical cavity with a flat termination found using the hybrid modal method for both the duct and termination sections (MOD + MOD), and compared with a modal reference solution (MOD). Dimensions are in wavelengths.

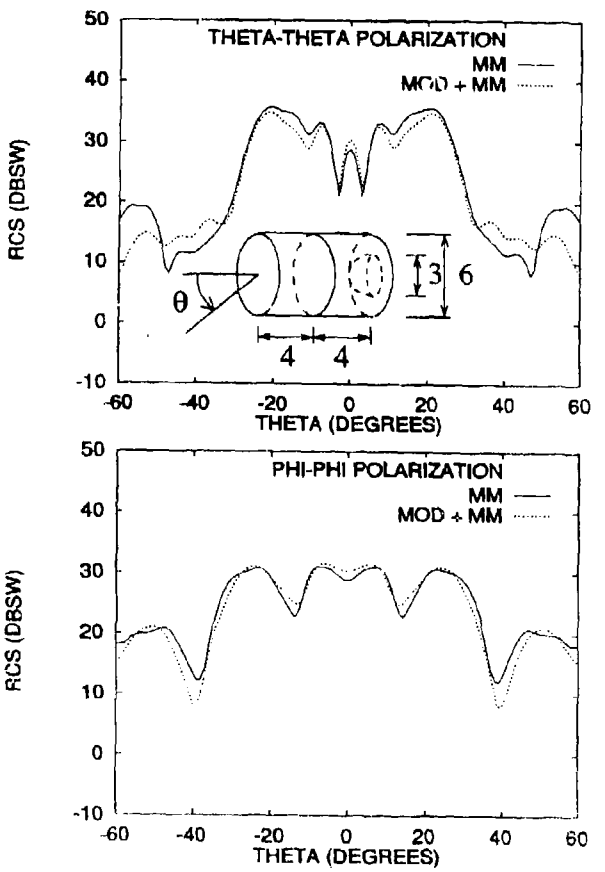

Figure 3: RCS patterns of a cylindrical cavity with a hemispherical hub termination found using the hybrid modal method for the duct section and the moment method for the termination section (MOD + MM), and compared with a moment method reference solution (MM). Dimensions are in wavelengths.

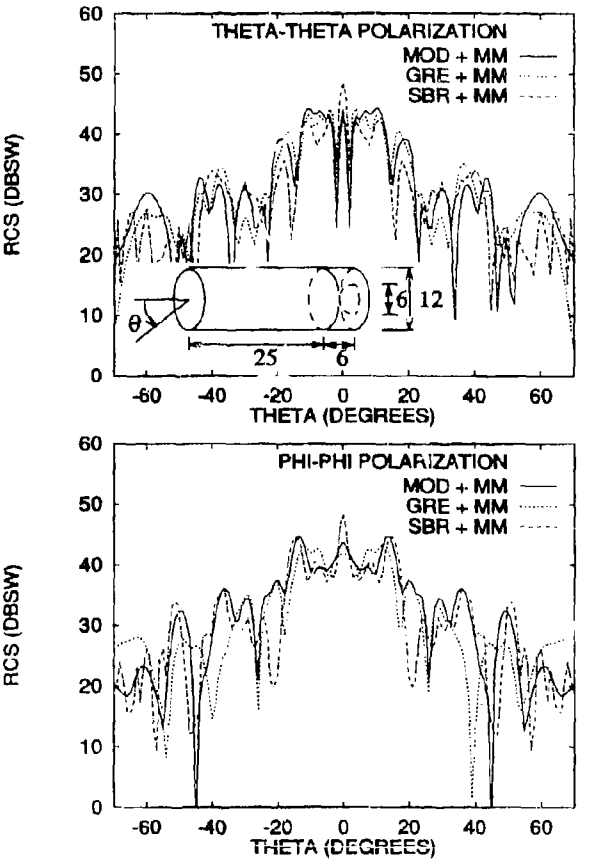

Figure 4: RCS patterns of a cylindrical cavity with a hemispherical hub termination found using the hybrid modal (MOD + MM), the GRE (GRE + MM), and the SBR (SBR + MM) methods for the duct section and the moment method for the termination section. Dimensions are in wavelengths.

Electromagnetic Modeling of Jet Engine Cavities with the CAVERN Code

by

Janice L. Karty
and
Scott D. Alspach

McDonnell Douglas Aerospace
P. O. Box 516
St. Louis, MO 63166

Abstract

CAVERN (Cavity Electromagnetic Analysis) is a computer code developed at McDonnell Douglas, used to analyze scattering from arbitrary inlet shapes which can include effects of an engine face. It incorporates standard ray optic approaches, the generalized ray expansion, and modal solutions. Upgrades to the engine face modeling capability are underway.

Standard approaches to predicting scattering from electrically large cavities consist of tracing ray bundles in and out of a cavity while keeping track of trajectory and polarization of the electric field vector [1]. The calculations in CAVERN use a parametric bi-cubic (PBC) ray trace. Ray patch information, including the divergence factor at each bounce is combined with a geometrical optics/aperture integration technique.

Another option in CAVERN for the initialization of the ray trace is the generalized ray expansion [2]. At the aperture, the incoming plane wave is converted into starbursts, and all the rays are traced only once for all the excitation angles. This method better approximates the effects of the edges of the inlet opening, and thus provides a better solution for certain cavities. For large analysis matrices where the scattering for a very large number of incidence angles is needed, this method holds much promise.

CAVERN uses ray/modal analysis to calculate radar cross section (RCS). Rays are initiated in the aperture plane and traced to an area near the back of the cavity where the geometrical cross section becomes uniform. The ray representation of the electric field is expanded in terms of the known modal field. An application of the reciprocity theorem of electromagnetics requires the rays to be traced to the back of the cavity for the RCS computation [3]. Since rays do not have to be traced back out of the cavity, the combined ray/modal analysis can be more efficient for long ducts. This capability in CAVERN will work for ducts up to 40 wavelengths in diameter, which is the equivalent of a fighter sized aircraft at X-band. In order to speed the conversion of rays to modes, a Fast Fourier Bessel Transform is being investigated.

Upgrades to the engine face termination capability of CAVERN are being pursued through cooperatives with Ohio State University, the University of Michigan, GE Aircraft Engine Division, and the Air Force. Some of the approaches being investigated for the termination are physical optics/physical theory of diffraction, coupled with a plane wave expansion of the ray optic field, or a finite element analysis, coupled with a modal expansion of the ray optic field.

I. Introduction

Identification of scattering mechanisms associated with cavities is of prime importance in the specification of RCS for aircraft. The cavity return dominates the signature for certain angular sectors of interest. CAVERN can be used to guide designers in the specification of inlets and nozzles.

Figure 1 divides the cavity into three areas. First, initialization of the rays is necessary in the aperture plane. This can be done with either the Shooting and Bouncing Rays (SBR) or Generalized Ray Expansion (GRE) approach. Propagation into the duct proceeds according to the laws of geometric optics. Then, the termination aperture decomposition can be accomplished with either modes or plane waves. Finally, modes or plane waves are reflected from the termination obstacle. The ray/modal approach used in conjunction with an advanced ray trace for curved parametric surfaces is unique to CAVERN, and the Fast Fourier Bessel Transform (FFBT) approach applied to this problem is also novel, so these techniques will be covered in more detail.

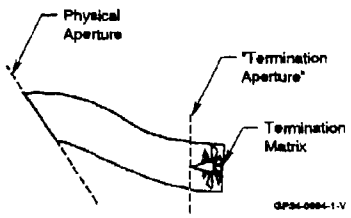

Figure 1. Areas of Major Focus

The purpose of this paper is to provide an overview of the capabilities available in CAVERN and to detail the treatment of the hybrid ray/modal methods. Recent advances in computation times for the modal algorithms have been made possible with the FFBT. Section II outlines the initialization of rays with SBR and GRE. The next two sections provide the required calculations for the use of the reciprocity integral with ray tracing and modal decomposition, and modifications necessary to use the FFBT.

II. Initialization of Rays with SBR and GRE

For SBR, rays are tracked with attention paid to phase changes due to path length, divergence and caustics. Aperture integration is performed at the exit to calculate RCS. Fresnel reflections are taken into account for both metal and treated surfaces. In this case, as shown in Figure 2, rays are tracked into and out of the cavity one at a time and the RCS is summed over all rays. Then the cavity is illuminated at another incidence angle, and the ray trace information must be recalculated. With the GRE, ray tubes are initiated for each subaperture. Rays are sent out at the center of each subaperture in the manner shown. Rays are tracked into and out of the cavity and the information is stored. For each angle, the expansion coefficients are calculated, and summed over all ray tubes to calculate RCS.

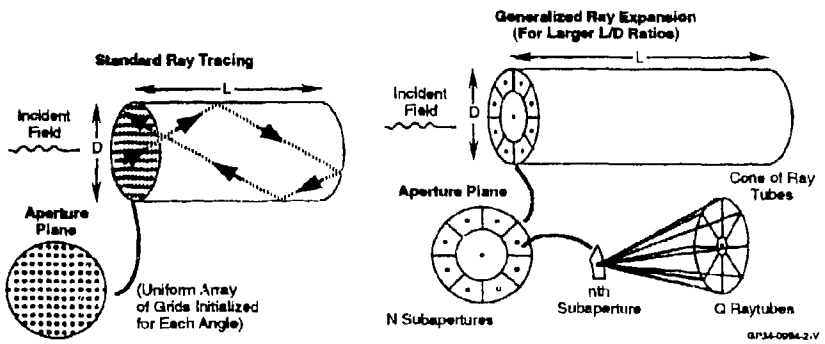

Figure 2. Incorporation of Generalized Ray Expansion With Aperture Integration

The consequences of accuracy for small ducts are seen in Figure 3 where the exact modal solution is compared with GRE and SBR solutions. For SBR, the solution is very choppy and oscillates about the true solution, with deviations in RCS as large as 10 dB. The ray solution tends to discretize the electric field within the cavity, instead of allowing a smooth distribution and this discretization leads to these oscillations. One of the major causes of the discretized nature of the ray traced electric field is the fact that the incident radiation just inside the aperture is modeled as a plane wave, thus ignoring the effect of the edges at the aperture opening. Any diffraction effects are not included in the calculation and for small apertures, this can be significant. By sending rays out in starburst fashion, some effects

from the walls resulting in a non-planar wavefront can be modeled. Rays emanate from the phase center of each subaperture correctly weighted with the far field amplitude and phase. For large cavity openings, the inaccuracies present for SBR near the aperture will be less prevalent. However, for treated cavities, where the scattering may be decreased, it may become more important to include diffraction effects. It has also been found that the ratio of the length (L) to the diameter (D) of the cavity is important in assessing the accuracy of the different techniques. Figure 4 shows this effect. The SBR solution is actually performing quite well for this case where the opening of the cavity is six wavelengths in diameter and the L/D ratio is 1. For the L/D ratio of 2 to 1 the SBR solution is exhibiting a narrower peak than the exact solution. For larger L/D ratios, the problem is even more apparent.

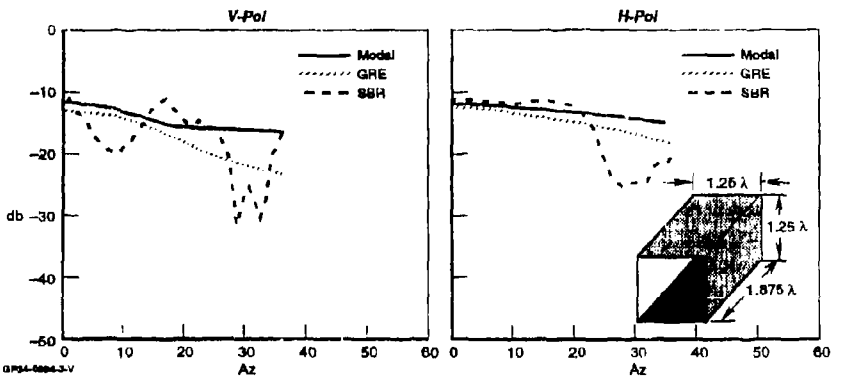

Figure 3. Comparison of Modal, GRE and SBR Methods for a Small Rectangular Duct at 5.9 GHz

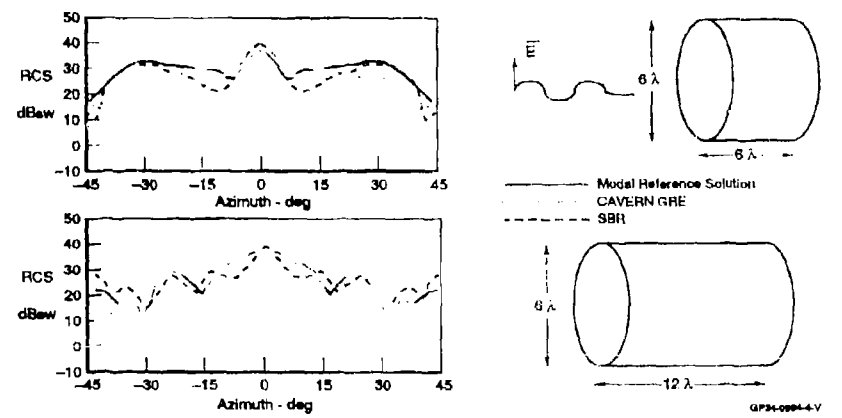

Figure 4. GRE Calculation for a 6λ Diameter Cylinder, Vertical Polarization

Figure 5 shows the results for a 1m diameter by 3 m length cavity at 10 GHz. This is a diameter of almost 35 wavelengths. For an opening this large, the agreement of pure SBR with the exact modal solution is improved as shown. However, run times possible with GRE are faster than with SBR. For this case, a 50 degree sweep in azimuth takes approximately 6 hours for SBR on an SG4D35 versus 0.66 hours for 9 subapertures with GRE or 1.66 hours for 25 subapertures, which is almost four times faster than the SBR. Approximately 10 rays per wavelength used in this SBR run. For 25 subapertures, the GRE solution is in very good agreement with the SBR solution.

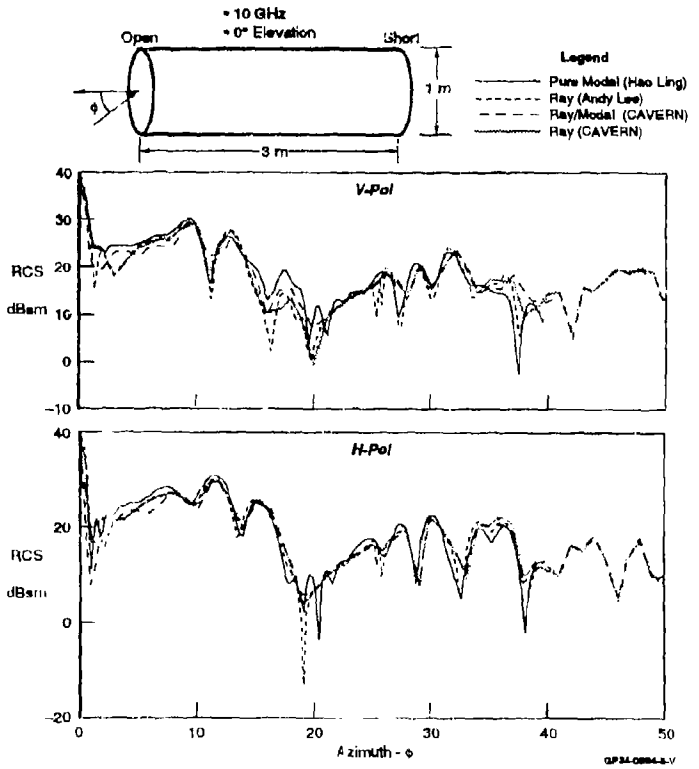

Figure 5. Circular Waveguide RCS Comparisons

III. Reciprocity Integral with Ray Tracing and Modal Decomposition

The uniqueness of CAVERN is found in its combination of the ray and modal solutions and the calculation of RCS with this combination in conjunction with the reaction integral based on the reciprocity theorem. Rays are traced to a uniformly circular section of the waveguide, and equivalent modes are found. The termination reflection coefficients matrix can be found with finite element methods under development [4]. Here, we will focus on the modal decomposition. Note that in the ray/modal reciprocity integral, the rays do not have to be traced back out of the cavity. This can make the method more efficient for long thin ducts. Plane wave decomposition and physical optics/physical theory of diffraction (PO/PTD) termination matrices are being pursued cooperatively with Ohio State University [5].

Figure 6 shows the geometry definitions necessary for an application of the reciprocity theorem [3]. This theorem leads to the reaction integral:

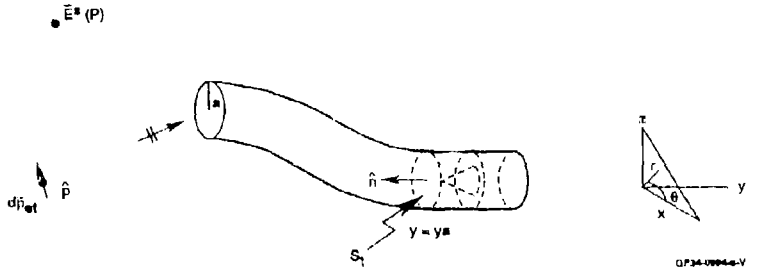

Figure 6. Geometry of the Inlet Scattering Problem

$$\bar{E}^s(p)\cdot d\bar{p}_{et} = \iint_{S_t}\left(\bar{E}_R \times \sum_q b_q^- \bar{h}_q^- - \sum_q b_q^- \bar{e}_q^- \times \bar{H}_R\right)\cdot\hat{n}\, ds$$

where $\bar{E}^s(p)$ is the backscattered field at point p due to fields incident from dipole dp_{et},

$\bar{E}_R$, $\bar{H}_R$ are the incident fields at S_t (found using ray tracing),

b_q^- are the modal coefficients for the fields reflected from the termination,

with $q = nm$, where n is the order of the Bessel function and m is the root index

and $\bar{e}_q^-$, $\bar{h}_q^-$ are the modal basis functions for the uniform section of the cavity.

(1)

We express the ray traced fields as a sum of waveguide modes near the termination aperture as follows, letting

$$\left(\bar{E}_R, \bar{H}_R\right) = \sum_q a_q^+\left(\bar{e}_q^+, \bar{h}_q^+\right) \tag{2}$$

where + refers to modes propagating in the +y direction and – refers to modes propagating in the -y direction, and

$$\bar{e}_q^+ = \left[\bar{e}_{qt} \pm \hat{y}\, e_{qy}\right] e^{\mp j\beta_q (y - y_a)}$$

$$\bar{h}_q^+ = \left[\pm \bar{h}_{qt} + \hat{y}\, h_{qy}\right] e^{+j\beta_q (y - y_a)} \tag{3}$$

Here, β_q is the propagation constant for the qth mode and t refers to the transverse modes (in the x, z plane). Using the orthonormal properties of the modes, the integral in equation 1 reduces to

$$\vec{E}^s(p) \cdot d\vec{p}_{et} = 2 \sum_q a_q^+ b_q^- \tag{4}$$

Application of the waveguide excitation integral given in [6] yields:

$$a_q^+ = \frac{1}{2} \iint_{S_t} \left(h_{qr} \hat{r} - h_{q\theta} \hat{\theta} \right) \cdot \left(2\vec{E}_H \times \hat{y} \right) \tag{5}$$

Expanding, this becomes

$$a_q^{+\,V}_{\;\;H} = \frac{1}{2} \sum_A \left(-h_{qr} E_{R_x}^{\;\;V}_{\;\;H} \sin\theta - h_{q\theta} E_{R_x}^{\;\;V}_{\;\;H} \cos\theta + h_{qr} E_{R_z}^{\;\;V}_{\;\;H} \cos\theta - h_{q\theta} L_{H_z}^{\;\;V}_{\;\;H} \sin\theta \right) \Delta S_A \tag{6}$$

where ΔS_A is the area of the Ath ray tube in the plane of S_t. The V and H represent vertical and horizontal polarizations.

Both TM and TE modes are given in [6]. We assume that the ray traced fields are constant across a ray tube and then sum over all ray tubes. However, this can be very time consuming. For Figure 5, it took approximately an hour an angle on an SG4D35 for the ray/modal calculations in CAVERN. The major reason is that the Bessel function has to be recalculated for each ray/mode pair. For cavities with thousands of rays and hundreds of excited modes, this can be cumbersome. When the Bessel functions are precaloulated and accessed with a table look up, the run time can decrease by a factor of five. Furthermore, if we convert the ray traced field across the face of the aperture to an appropriately spaced grid, then we can take advantage of FFBT techniques discussed in Section IV. The gridding approach is outlined in [7].

IV. Modal Decomposition with the FFBT

Here we note that equation 6 is a sum of terms which are always of the form

$$a_q^+ = \int_0^{2\pi} \int_0^a f(r,\theta)\, g_n\left(p_q\, r/a\right) g(\theta) \begin{Bmatrix} \cos n\theta \\ \sin n\theta \end{Bmatrix} r\, dr\, d\theta$$

$$\text{where} \quad g_n(x) = J_n(x) \text{ or } J_n'(x)$$

$$\text{and}$$

$$g(\theta) = \cos\theta \text{ or } \sin\theta \tag{7}$$

The derivative of the Bessel function $J_n'(x)$ can be written as a sum of Bessel functions $J_n(x)$ so that the r integration can be written as linear combinations of

$$F(\theta) = \rho g(\rho,\theta) = 2\pi\rho \int_0^\infty r f(r,0) J_n(2\pi\rho r)\, dr$$

$$\text{where} \quad \rho = p_q / 2\pi a \tag{8}$$

Then the integral in equation 7 becomes

$$a_q^{\pm} = \int_0^{2\pi} F(\theta)\, g(\theta) \begin{Bmatrix} \cos n\theta \\ \sin n\theta \end{Bmatrix} d\theta \tag{9}$$

which in turn can be written as linear combinations of

$$a_q^{\pm} = \int_0^{2\pi} G(\theta)\, e^{\pm jn\theta}\, d\theta \tag{10}$$

Applying the FFBT to the integral of equation 8, we employ the technique of [8] where a Gardner transform with $r = r_0 e^{\alpha x}$ and $\rho = \rho_0 e^{\alpha y}$ is used. Here x and y are the dummy transformed variables. The parameters r_0, ρ_0 and α depend on the size of the inlet and the frequency of the incident radiation.

An exponential grid is used for the radial component. The method in [8] translates the problem to three simple FFT's. The theta integral can be performed as a straightforward numerical integration or with additional FFT's. Comparing results to the previous non-FFBT modal version, the RCS plot is virtually identical, although there has been more than an order of magnitude improvement in runtime for the case of Figure 5. Performing the theta integral first with an FFT provides all the modal information for all at once, and may be a more efficient way to evaluate the integral of equation 7. This modification is being pursued.

V. Summary Discussion

In CAVERN, we have included options for the SBR and GRE ray initialization, as well as options for modal decomposition. With the use of the FFBT, runtimes for the ray/modal approach are very competitive with conventional SBR. Combining the more accurate modal decomposition methods with the termination matrix reflection coefficients calculated from finite element or FD/PTD methods should improve on the accuracy of RCS results for cavities with complex terminations.

VI. Acknowledgments

The authors are very grateful to Drs. Pathak and Burkholder of Ohio State University for many discussions and personal communications which made this work possible. We are also very grateful to Jim Roedder of MDA in providing valuable, insightful discussions, efficient programming, and quoted runtimes.

References:

[1] H. Ling, R.-C. Chou, and S. W. Lee, "Shooting and bouncing rays: Calculating the RCS of an arbitrary cavity," IEEE Trans. Antennas and Prop., Vol. 37, No. 2, pp. 194-205, Feb. 1989.

[2] P. H. Pathak and R. J. Burkholder, "High-frequency electromagnetic scattering by open-ended waveguide cavities," Radio Science, Vol. 26, No. 1, pp. 211-218, Jan.-Feb. 1991.

[3] P. H. Pathak and R. J. Burkholder, "A Reciprocity Formulation for Calculating the EM Scattering by an Obstacle within an Open-Ended Waveguide Cavity," IEEE Trans. Microwave Theory and Techniques, Vol. 41, No. 4, April 1993.

[4] P. Ross, J. L. Volakis and T. Ozdemir, "A new finite element formulation for modeling circular inlets with irregular termination," University of Michigan Radiation Laboratory Report, May 1993.

[5] P. R. Rousseau, R. J. Burkholder, C. W. Chuang, R. C. Chou, and P. H. Pathak, "Computing the EM scattering from a Bifurcated Flat Inlet Cavity with a Body-of-Revolution Termination," Ohio State University, ElectroScience Lab Report, March 1993.

[6] P. H. Pathak, C. W. Chuang, M. C. Liang, "Inlet Modeling Studies," Ohio State University, ElectroScience Lab Report, October 1986.

[7] R. J. Burkholder, "Converting Ray-Tubes into Modes via a Numerical Gridding Scheme," Personal Communication, May 1993.

[8] A. E. Siegman, "Quasi Fast Hankel Transform," Optics Letters," Vol. 1, No. 1, pp.13-15, July 1977.

AN ITERATIVE METHOD FOR COMPUTING THE SCATTERED ELECTRIC FIELDS AT THE APERTURES OF LARGE PERFECTLY CONDUCTING CAVITIES

Daniel D Reuster* and Gary A Thiele
Department of Electrical Engineering
University of Dayton
300 College Park
Dayton, OH 45469-0227

Abstract

An iterative method is developed for computing the scattered electric fields at the apertures of large perfectly conducting cavities. The technique uses Kirchhoff's approximation to initiate a two stage iterative process, involving both the magnetic field integral equation (MFIE) and the electric field integral equation (EFIE), to calculate the electric currents on the internal cavity walls and the electric fields across the aperture of the cavity. The technique combines the flexibility of the boundary-integral method with the speed necessary to efficiently analyze large scale cavity problems. The following paper presents the general theory, and applies the technique to the problem of TE scattering from 2-dimensional perfectly conducting cavities.

1. Introduction

The problem of electromagnetic scattering from large open-ended cavities (see figure 1) has received much attention in research areas such as automatic target recognition and low-observable vehicle design. The cavity problem presents many interesting challenges from the standpoint of computational electromagnetics. The cavity's large electrical size makes it a prime candidate for ray based or asymptotic techniques, while the cavity's geometrical complexities require more exact techniques such as the method of moments or the boundary integral approach. As a result of these diverse requirements, many hybrid techniques have been developed, in an effort to meet these computational challenges. Techniques, such as shooting and bouncing rays (SBR) [1] and the generalized ray expansion (GRE) [2], were created in an effort to enhance asymptotic based methods in order to analyze the complex geometries associated with the cavity problem. Likewise, approaches such as the hybrid boundary-integral/modal method [3] were developed in hopes of increasing the electrical size limitations of moment method based techniques. While both of these approaches to the cavity problem show promise in the small to mid-size cavity range, their ability to effectively analyze large scale cavity problems is still a matter of debate, and the need for new approaches is evident.

The cavity problem, such as the electromagnetic scattering from a jet engine, may be visualized as consisting of three unique phenomenon: 1) an aperture field is established from the external region sources; 2) the electric and magnetic fields propagate down the cavity, "guided" by the cavity walls; 3) a reflection occurs at the termination. After reflection, the fields propagate back towards the aperture where they may be integrated to give the scattered field (i.e., the RCS). The purpose of this paper is to propose an efficient and accurate way of propagating the field from the aperture to the termination (i.e., item 2 above) and back to the aperture. In the examples that follow, the termination will be approximated as a short circuit. In an actual engine, the termination is very complex and must be accounted for by other methods such as the finite element method. In this paper we bypass the termination problem by employing the simplest of all possible terminations, the short circuit, since our objective here is to focus on the duct propagation problem.

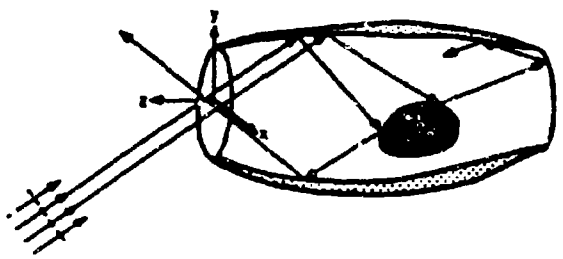

Figure 1 Common Cavity Scattering Problem

2. Methodology

The two stage iterative process developed in this paper is an extension of previous work [4-8] performed on iterative solutions to the MFIE with regards to the external scattering problem. In their previous work [6] Kaye, Murthy and Thiele showed that iterative solutions to the MFIE (Eq. 1) would always yield convergence, provided the PEC scattering body of interest satisfied the following three constraints:

1) the body of interest can be expressed as a simple closed surface,
2) the body is configured such that no internal resonances are present,
3) the body can be divided into at least two self consistent, magnetically coupled, sub-surfaces.

Thus, iterative solutions to the MFIE are limited to a class of problems meeting these constraints, and it is necessary to pose the scattering problem appropriately. Once the scattering problem has been properly posed, knowledge of the incident field on one of the two self consistent sub-surfaces is sufficient to initiate the iteration procedure.

Formulation of the Cavity Scattering Problem

The arbitrary cavity geometry (figure 2a) may be transformed into a simple closed surface by sealing the aperture of the cavity with a perfectly conducting flat plate and an impressed magnetic current equivalent to the total electric field at the aperture of the cavity (figure 2b) [9]. The resulting simply closed surface, obtained from the sealed cavity geometry, may now be used to pose the MFIE describing the internal cavity scattering problem (Eq. 1)

$$\bar{H}_{total}(r) = \frac{1}{4\pi}\oint_s \bar{J}(r') \times \nabla' G(r,r')\, ds' \tag{1}$$

$$-\frac{j\omega\epsilon}{4\pi}\oint_s \bar{M}(r')\, G(r,r')\, ds' - \frac{j}{4\pi\omega\mu}\nabla\nabla\cdot\oint_s \bar{M}(r')\, G(r,r')\, ds'$$

where $\bar{J} = \hat{n}\times\bar{H}_{total}$

and $\bar{M} = (\bar{E}_{inc}+\bar{E}_{scat})\times\hat{n} = \bar{E}_{total}\times\hat{n}$ along the closed cavity surface $S = S_1 + S_2$.

Replacing the sealed cavity walls by their equivalent electric and magnetic currents, and enforcing the electric field boundary condition along the perfectly conducting walls of the cavity (figure 2c) allows Eq. 1 to be rewritten as:

$$\bar{H}_{total}(r) = \frac{1}{4\pi}\int_{s_2+s_1} \bar{J}(r') \times \nabla' G(r,r')\, ds' \tag{2}$$

$$-\frac{j\omega\epsilon}{4\pi}\int_{s_2} \bar{M}(r')\, G(r,r')\, ds' - \frac{j}{4\pi\omega\mu}\nabla\nabla\cdot\int_{s_2} \bar{M}(r')\, G(r,r')\, ds' .$$

Applying image theory to the aperture wall of the cavity (figure 2d) allows Eq. 2 to be further simplified to its final working form (Eq. 3).

$$\bar{H}_{total}(r) = \frac{2}{4\pi}\int_{s_2} \bar{J}(r') \times G(r,r')\, ds' \tag{3}$$

$$-\frac{j\omega\epsilon}{4\pi}\int_{s_1} 2\bar{M}(r')\, G(r,r')\, ds' - \frac{j}{4\pi\omega\mu}\nabla\nabla\cdot\int_{s_1} 2\bar{M}(r')\, G(r,r')\, ds'$$

Eq. 3 completely describes the cavity scattering problem with the exception of the knowledge of the scattered electric field at the aperture of the cavity. However, this field may be calculated directly from the currents on the cavity walls by using the EFIE (Eq.4).

$$\bar{E}_{scat}(r) = -j\frac{\eta}{4\pi\beta}\left[\beta^2\int_{s_2} \bar{J}(r')\, G(r,r')\, ds' + \nabla\int_{s_2} \nabla'\cdot\bar{J}(r')\, G(r,r')\, ds'\right] \tag{4}$$

Eq 3. and Eq. 4, along with the knowledge of the incident electric field at the aperture of the cavity, now provide a complete description of the cavity scattering problem and satisfies the constraints necessary to produce an iterative solution.

3b. The Iteration Procedure

The iteration process is initiated by assuming that the total electric field at the aperture is equal to the electric field incident upon the aperture. Substituting this approximation into Eq. 5 provides the initial magnetic field along the cavity walls, S_2. The initial magnetic field along S_2 is then substituted into Eq. 6 to obtain the scattered electric field at the aperture of the cavity, S_1. Next, the scattered electric field is added to the incident electric field to obtain an updated version of the total electric field along S_2. The updated version of the total electric field is then substituted back into Eq. 5 and the above process is repeated to produce a further updated version of total electric field along S_1. This process is repeated until the mean square difference in the field quantities between each iteration reaches an acceptable level. The iteration procedure is found to converge quite rapidly (10 to 20 iterations) for the cavities tested. Furthermore, since the iterative procedure consists solely of vector inner products, the iterative solution process is directly applicable to high speed vector processing computer systems.

3c. Computer Implementation

Eq. 3 and Eq. 4 may be implemented numerically on a digital computer by approximating the integral operators by matrix operators. Using a pulse-basis, point-matching approximation technique, Eq. 3 and Eq. 4 may be approximated by the following matrix equations:

$$\begin{bmatrix} H_2 \end{bmatrix} = \begin{bmatrix} U \end{bmatrix} \begin{bmatrix} H_2 \end{bmatrix} + \begin{bmatrix} V \end{bmatrix} \begin{bmatrix} E_2 \end{bmatrix} \tag{5}$$

$$\begin{bmatrix} E_s \end{bmatrix} = \begin{bmatrix} W \end{bmatrix} \begin{bmatrix} H_2 \end{bmatrix} \tag{6}$$

$$\begin{bmatrix} E_2 \end{bmatrix} = \begin{bmatrix} E_i \end{bmatrix} + \begin{bmatrix} E_s \end{bmatrix} \tag{7}$$

where the matrices U, V and W represent the corresponding integral operators and the lengths of the vectors E_{aper} and H_{aper} depend on the electrical size of the surfaces S_1 and S_2 respectively. None of these matrices are inverted since Eqs. (5) and (6) are solved by iteration.

Due to the basis functions selected, the elements of each matrix may be calculated in closed form. For the 2-dimensional TE case, the matrix elements are as follows, a similar set of equations may be developed for the TM case.

$$U_{m,n} = \frac{-j\beta\Delta_n}{4} H_1^{(2)}(\beta r) \frac{(x_m - x_n)\,Nx_n + (y_m - y_n)\,Ny_n}{r} \tag{8}$$

$$V_{m,n} = \frac{-\beta\Delta_n}{2\eta} H_0^{(2)}(\beta r) \tag{9}$$

$$w_{m,n} = \frac{-\beta\eta\Delta_n}{8}\left[Nx_n H_0^{(2)}(\beta r) + H_2^{(2)}(\beta r)\left(\frac{2(y_m-y_n)^2}{r_{m,n}^2}-1\right)\right.$$

$$\left.-Ny_n H_2^{(2)}(\beta r)\frac{2(x_m-x_n)(y_m-y_n)}{r_{m,n}^2}\right] \qquad (10)$$

where Δ_n is the length of the nth facet

$$r_{m,n} = \sqrt{(x_m-x_n)^2+(y_m-y_n)^2}$$

and Nx_n, Ny_n are the components of the inward pointing normal of the nth facet.

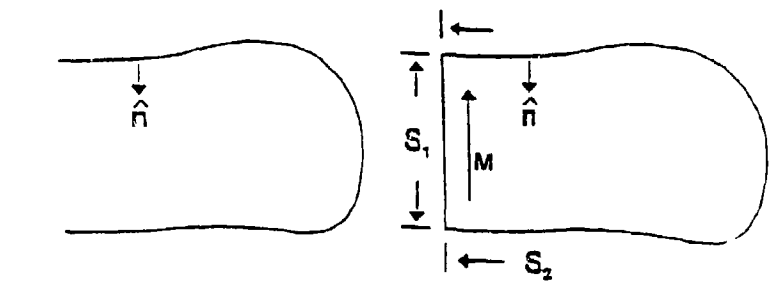

(a) Cavity Contour (b) Internal Cavity Problem

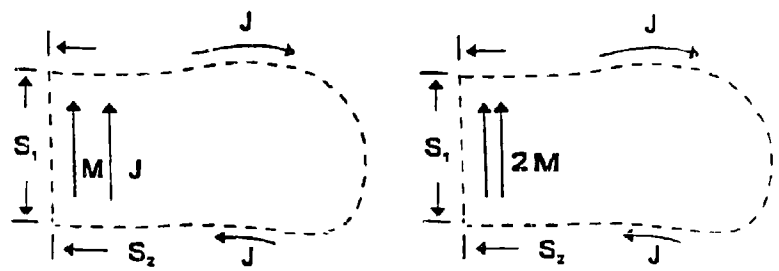

(c) Equivalent Current Model (d) Image Theory Model

Figure 2 Cavity Models

4. Results

The iterative technique was used to calculate the scattered electric fields at the apertures of various rectangular cavities, and the aperture fields were integrated to produces RCS predictions for the cavities. These RCS predictions were compared with those produced by other techniques (see figures 3a and 3b). Since the external scattering from the cavities were not included in the iterative RCS predictions, the predictions obtained were expected to give good agreement in only those regions where the internal scattering problem is dominant, these regions being the main beam and the first few side lobes of the aperture's radiation pattern. As can be seen from figures 3a and 3b, the RCS levels predicted by the iterative technique are in very good agreement with the RCS levels predicted by other methods.

5. Conclusions

Based upon the presented accurate performance of the iterative prediction code, the iterative technique shows promise as a fast and accurate method for analyzing the RCS behavior of large PEC cavities. However, before any substantial claims can be made regarding the method, the technique needs to be implemented on various massively parallel computers, and the resulting RCS predictions need to be compared to those measured from actual cavities of interest.

References

[1] H. Ling, R. Chou, and S. W. Lee, "Shooting and Bouncing Rays: Calculating RCS of an Arbitrary Cavity," *IEEE Trans. on Antennas and Propagation*, Vol. AP-37, No. 2, pp. 194-205, Feb. 1989.

[2] R. J. Burkholder and P. H. Pathak, "High-Frequency Electromagnetic Scattering by Open-Ended Waveguide Cavities," *Radio Science*, Vol. 26, pp. 211-218, Jan.-Feb. 1991.

[3] H. Ling, "RCS of Waveguide Cavities: A Hybrid Boundary-Integral/Modal Approach," *IEEE Trans. on Antennas and Propagation*, Vol. AP-38, No. 9, pp. 1413-1419, Sept. 1990.

[4] T. J. Kim and G. A. Thiele, "A Hybrid Diffraction Technique - General Theory and Applications," *IEEE Trans. on Antennas and Propagation*, Vol. AP-30, Sept. 1982.

[5] Li Zhi-Hi and G. A. Thiele, "A Hybrid Theory of Diffraction for the RCS Calculation of Ogive-Like Bodies," *Radio Science*, Vol. 19, Nov.-Dec. 1984.

[6] M. Kaye, P. K. Murthy, and G. A. Thiele, " An Iterative Method for Solving Scattering Problems," *IEEE Trans. on Antennas and Propagation*, Vol AP-33, Nov. 1985.

[7] P. K. Murthy, K. C. Hill and G. A. Thiele, "A Hybrid-Iterative Method for Scattering Problems," *IEEE Trans. on Antennas and Propagation*, Vol. AP-34, Oct. 1986.

[8] R. P. Penno, G. A. Thiele and P. K. Murthy, "Scattering from a perfectly Conducting Cube Using HIM," Special Issue of *IEEE Proceeding*, on Radar Cross-Section, Vol. 77,May 1989.

[9] R. F. Harrington, Time-Harmonic Electromagnetic Fields, McGraw-Hill Book Company, New York, 1961.

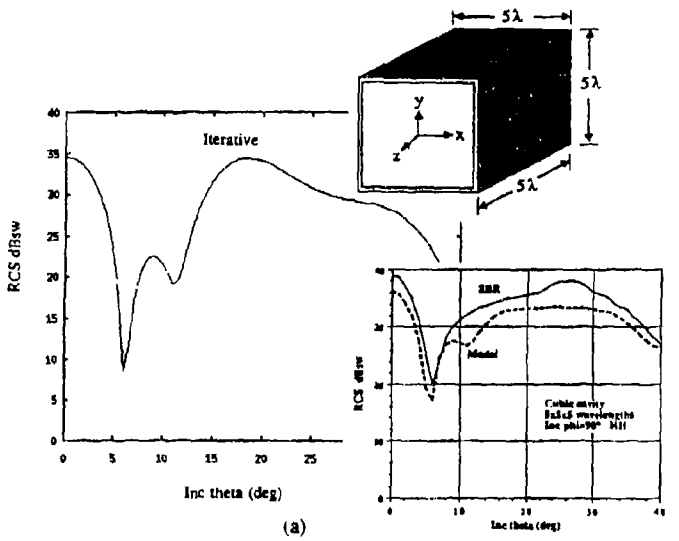

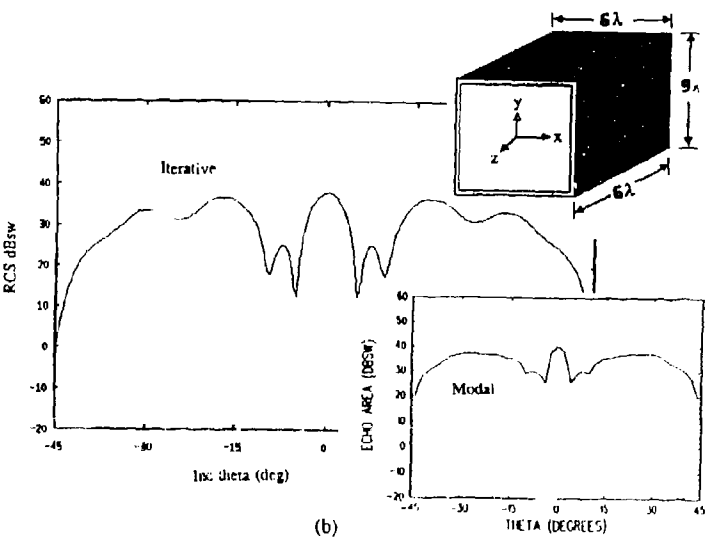

Figure 3 Comparison of Cavity RCS Predictions

Hybrid Formulation for Arbitrary 3-D Bodies

L. N. Medgyesi-Mitschang and John M. Putnam
McDonnell Douglas Corporation
P.O. Box 516
St. Louis Missouri 63166

Abstract
The hybrid formulation presented here builds on recent advances in applying the Galerkin form of the method of moments (MM) theory to arbitrary 3-D objects. The formulation is a current-based one. The optic-derived current Ansatz in the present hybrid formulation is physical optics, although the formulation is easily generalizable to higher order asymptotics as well. The numerical algorithm implementing this formulation is based on a derivative of the *CARLOS-3D™* code developed at McDonnell Douglas . This code is based on the MM technique using flat triangularly facetized surfaces. The Galerkin expansion uses Rao-Wilton-Glisson roof-top functions. For maximum generality all the principal features of the original *CARLOS-3D™* code are retained in this hybrid formulation. Thus objects with perfect electrically conducting or partially penetrable surfaces can be treated with this formulation. In addition, special cases such as the Leontovich condition and electrically resistive or magnetically conducting boundary conditions are also addressed. The formulation is demonstrated for electrically large as well as small scattering objects. The latter form the lower limit where the efficacy of the physical optics Ansatz becomes problematic.

1. Introduction

Extensive prior investigations have been carried out using hybrid methods that couple the method of moments (MM) technique with the optic-derived methods such as physical optics (PO) and the physical theory of diffraction (PTD). The bulk of these investigations dealt with bodies of revolution (BOR) and bodies of translation (BOT). This restriction in earlier studies was primarily due to the limitation of the geometries that could be handled by the then-existing MM based computer codes. Since there were many MM/BOR and MM/BOT codes available, hybrid methods were applied to these geometries. The investigations in Refs. (1), (2), (3) and (4) are representative. From these investigations there emerged a detailed understanding of the power and limitation of hybrid methods. In general, it was shown that "current-based" hybrid formulations were easier to implement and provided more robust numerical solutions than "field-based" methods. A detailed discussion of the relative merits of the current based versus the field-based hybrid methods is given in Ref. (5). The present investigation builds on an earlier current-based hybrid formulation for arbitrary 3-D perfectly conducting bodies, Ref. (6) This formulation generalizes to imperfectly conducting bodies (or coated surfaces) with application of the Leontovich impedance boundary condition (IBC).

2. Basic Concepts

The formulation begins with the Stratton-Chu surface integral representation of Maxwell's equations. For clarity of exposition and space limitations, we confine the theoretical discussion to the perfect electrically conducting case only. However, the formulation can be extended to penetrable cases as illustrated in the numerical results. Using the notation in Ref. (6) for the generic geometry depicted in Fig. 1, the integral equation for a perfectly conducting body written in the usual operator form is

$$\bar{E}^s\Big|_{tan} = -\bar{E}^i\Big|_{tan} = -L\,\bar{J} \tag{1}$$

where the integro-differential operator L is given as

$$L\,\bar{J} = jk\eta \int_S \left(\bar{J} + \frac{1}{k^2} \nabla\nabla' \bullet \bar{J} \right) \Phi \, ds' \tag{2}$$

and where the free space Green's function is

$$\Phi = \frac{e^{-jkR}}{4\pi R} \tag{3}$$

with R being the distance from the source to the field point, ∇ the surface gradient on the body with respect to the unprimed variables, $k = 2\pi/\lambda$ and $\eta = \sqrt{\mu/\varepsilon}$. In a scattering problem, the incident electric field $\bar{E}^i$ is the known quantity with the induced current $\bar{J}$ being the unknown. Equation (1) is termed the electric field integral equation (EFIE) formulation. Note we could have started with the dual magnetic formulation, given by the magnetic field integral equation (MFIE). As is well known, the EFIE is more general since it applies to closed bodies as well as open surfaces.

Next, we partition the domain of the integral operator into two regions, namely that spanning the MM represented region and that associated with the Ansatz part. Formally, this can be stated as:

$$L\,\bar{J}_{MM} = \bar{E}^i\big|_{tan} - L\,\bar{J}_{PO} \tag{4}$$

where the currents subscripted with *MM* and *PO* are associated with the MM and the Ansatz representations, respectively. The MM representation is used on that part of surfaces of a body for which no optic-derived asymptotic forms are available. These include surface and/or material discontinuities, most edges, apertures, and generally all penetrable regions of a body. The asymptotic Ansatz regions cover the remainder of the body.

The partitioning may involve more than two regions for the MM and Ansatz parts. For clarity of exposition, we assume here that the scatterer is partitioned into only two regions. Note that Fig. 1 has been shown generically to include an MM piece of the geometry embedded in the illuminated (Ansatz) region. Another generalization is that the partitioning may be over several unconnected surfaces. Many antenna and scattering problems can be formulated in this way. Ref. (8) discusses these cases.

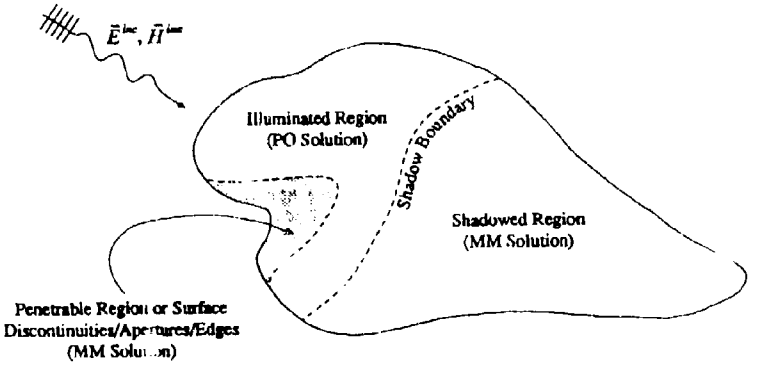

Figure 1: Generic Partitioning of a Body for Hybrid Analysis.

3. Specialization to 3-D Geometries

Next, we solve the partitioned EFIE using the Galerkin MM technique. We expand the unknown current functional in terms of a finite set of basis functions. Since in the present case we represent the 3-D body as a triangularly-faceted surface, we choose the conventional roof-top functions as the basis set for the expansion of the unknown currents and the testing of the integral equation (see Fig. 2). (Ref. 8)

Expansion of MM Currents: Specifically, the currents in the MM region S_{MM} are expanded as

$$\vec{J}_{MM}(\vec{r}) = \sum_{n=1}^{N_i+N_j} I_n^{MM}\, \vec{f}_n(\vec{r}) \tag{5}$$

where the roof-top functions $\vec{f}_n$ are given by (see Fig. 2)

$$\vec{f}_n(\vec{r}) = \begin{cases} \dfrac{l_n}{2A_n^+}\left(\vec{r}-\vec{v}_n^+\right) & , \vec{r} \in T_n^+ \\ \dfrac{-l_n}{2A_n^-}\left(\vec{r}-\vec{v}_n^-\right) & , \vec{r} \in T_n^- \\ 0 & , \text{otherwise} \end{cases} \tag{6}$$

and triangles $T_n^{\pm}$ share a common edge with length l_n and have areas $A_n^{\pm}$, respectively. In Eq. (5), N_i and N_j denote the number of interior edges and junction edges spanning S_{MM}, respectively, where the junction edges are included in order to enforce current continuity between the MM and PO regions on the body.

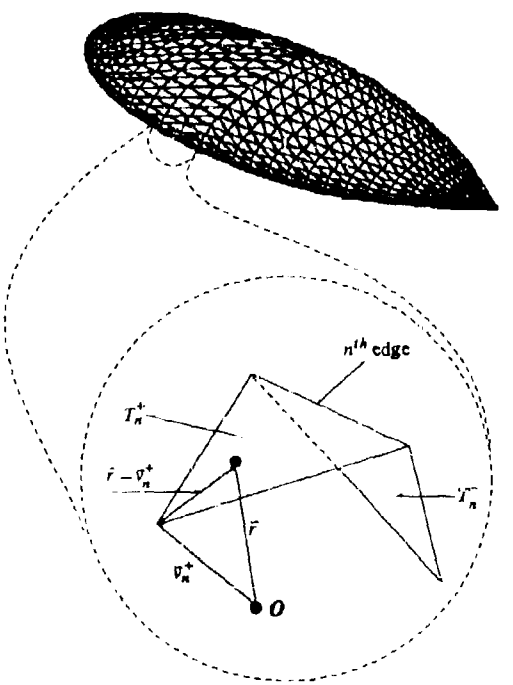

Figure 2: Faceted 3-D Scatterer with Details of Patch Coordinates Used in Roof-Top Surface Current Expansion Functions.

Expansion of PO Currents: To achieve efficient numerical implementation, one needs to expand the Ansatz PO currents in terms of the roof-top functions as well, i.e.,

$$\begin{aligned}\bar{J}_{PO}(\bar{r}) &= \sum_k I_k^{PO}\, \bar{f}_k(\bar{r}) \\ &= \sum_k I_k^{PO}\, \frac{\pm l_k}{2A_k^{\pm}}\left(\bar{r}-\bar{v}_k^{\pm}\right)\end{aligned} \tag{7}$$

We note that I_k represents the component of $\bar{J}$ normal to the k^{th} edge (see Fig. 3). If we denote $\hat{u}_k^{\pm}$ as the unit normal vector to the k^{th} edge and lying in the plane of $T_k^{\pm}$, then

$$\begin{aligned}\hat{u}_k^{+}\bullet\bar{J}_{PO}(\bar{r}) &= \hat{u}_k^{+}\bullet\left(\bar{r}-\bar{v}_k^{+}\right)\frac{I_k^{PO}\, l_k}{2A_k^{+}} \\ &= h^{+}\,\frac{I_k^{PO}\, l_k}{2A_k^{+}} \\ &= I_k^{PO}\end{aligned} \tag{8}$$

where $\bar{r}$ approaches the edge from the plus side and h^{+} denotes the triangle height associated with T^{+}. Similarly,

$$\hat{u}_k^{-}\bullet\bar{J}_{PO}(\bar{r}) = -I_k^{PO} \tag{9}$$

where $\bar{r}$ approaches the edge from the minus side. These relationships hold for any point $\bar{r}$ on the edge. Therefore the coefficients in Eq. (7) can be obtained from the plus side

$$\begin{aligned}I_{k^+}^{PO} &= \lim_{\bar{r}\to k^+}\hat{u}_k^{+}\bullet\bar{J}_{PO}(\bar{r}) \\ &= 2\,\hat{u}_k^{+}\bullet\hat{n}^{+}\times\bar{H}^{i}(\bar{r}) \\ &= -2\,\hat{p}_k^{+}\bullet\bar{H}^{i}(\bar{r})\end{aligned} \tag{10}$$

or the minus side

$$\begin{aligned}I_{k^-}^{PO} &= -\lim_{\bar{r}\to k^-}\hat{u}_k^{-}\bullet\bar{J}_{PO}(\bar{r}) \\ &= -2\,\hat{u}_k^{-}\bullet\hat{n}^{-}\times\bar{H}^{i}(\bar{r}) \\ &= 2\,\hat{p}_k^{-}\bullet\bar{H}^{i}(\bar{r})\end{aligned} \tag{11}$$

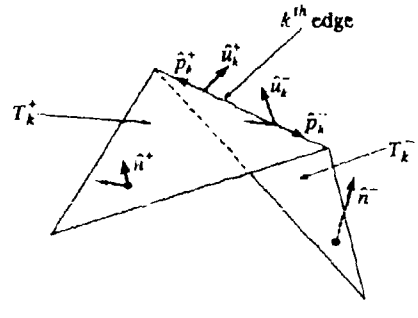

Figure 3: Detailed Geometry of Unit Normal Vectors on Triangular Facets.

Note $\hat{p}_k^+ = \hat{n}^+ \times \hat{u}_k^+$ is parallel to the edge with $\hat{p}_k^- = -\hat{p}_k^+$, yielding $I_{k^+}^{PO} = I_{k^-}^{PO}$. Thus, the PO coefficient for the k^{th} edge can be obtained from either side. Using the foregoing expansions, Eq. (4) is transformed into

$$\mathcal{L}^{MM,MM} I_{MM} = \mathcal{C}^{i} - \mathcal{L}^{MM,PO} I_{PO} \tag{12}$$

where $\mathcal{L}^{MM,MM}$ is the Galerkin (matrix) operator which results from testing the unknown MM currents. An element of the matrix is given by

$$\mathcal{L}_{kl}^{MM,MM} = \left\langle \hat{f}_k^{MM}, L\left(\hat{f}_l^{MM}\right) \right\rangle \tag{13}$$

where $\hat{f}_k^{MM}$ and $\hat{f}_l^{MM}$ are expansion functions on the MM part of the surface. Similarly, $\mathcal{L}^{MM,PO}$ is obtained from testing the known Ansatz PO currents, and an element is given by

$$\mathcal{L}_{kl}^{MM,PO} = \left\langle \hat{f}_k^{MM}, L\left(\hat{f}_l^{PO}\right) \right\rangle \tag{14}$$

where $\hat{f}_k^{MM}$ and $\hat{f}_l^{PO}$ are expansion functions on the MM and PO surfaces, respectively.

In this result the left side of Eq. (12) denotes the MM system matrix multiplied by the unknown current coefficient (column) vector I_{MM}. The right side denotes the Galerkin-transformed effective illuminating field, i.e., consisting of the incident electric plane wave $\bar{E}^i$ and the near field contributions from the Ansatz region. Note the effective illuminating field is no longer a plane wave. Furthermore, as the illumination angle around the body shifts, the relative contributions of these two field components also varies.

For an arbitrarily-shaped 3-D facetized surface as noted above, the Galerkin (matrix) operators $\mathcal{L}$ in Eq. (12) can be derived with its elements having the form

$$\begin{aligned} \mathcal{L}_{kl}(\;\cdot\;) = j \iint_{S_k} ds \iint_{S_l} ds' \Big\{ & \omega\mu\, \bar{f}_k(\bar{r}) \cdot \bar{f}_l(\bar{r}')\, \Phi(\bar{r}-\bar{r}') \\ & + \frac{1}{\omega\varepsilon} \left(\bar{f}_k(r) \cdot \nabla\Phi(\bar{r}-\bar{r}')\right) \nabla' \cdot \bar{f}_l(r') \Big\} \end{aligned} \tag{15}$$

where $S_k = T_k^+ \cup T_k^-$ and T_k^+ are the two triangular facets (Figure 2) which form the k^{th} edge. Similarly, $S_l = T_l^+ \cup T_l^-$. The form of the roof-top functions $\bar{f}_k$ allows one to transfer the differentiation from the Green's function F to the testing function $\bar{f}_k$. The $\mathcal{L}$ operator can now be re-written in a symmetric form as

$$\begin{aligned} \mathcal{L}_{kl}(\;\cdot\;) = j \iint_{S_k} ds \iint_{S_l} ds' \Big\{ & \omega\mu\, \bar{f}_k(r) \cdot \bar{f}_l(r') \\ & - \frac{1}{\omega\varepsilon} \left(\nabla \cdot \bar{f}_k(r)\right) \left(\nabla' \cdot \bar{f}_l(\bar{r}')\right) \Big\} \Phi(r-r') \end{aligned} \tag{16}$$

If the roof-top functions are used in Eq. (16), then the operator $\mathcal{L}$ becomes

$$\mathcal{L}_{kl}(\cdot)=\frac{j\,l_k l_l}{4}\sum_{p=\pm}\sum_{q=\pm}\frac{p\,q}{A_k^p A_l^q}\iint_{T_l^q} ds \iint_{T_l^q} ds'\left\{\omega\mu\left(\bar{r}-\bar{v}_k^p\right)\cdot\left(\bar{r}'-\bar{v}_l^q\right)-\frac{4}{\omega\varepsilon}\right\}\Phi(\bar{r}-\bar{r}') \qquad (17)$$

where we split each surface integral into an integral over T^+ and an integral over T^-, and further we used the fact that

$$\nabla\cdot\bar{f}_n(\bar{r})=\begin{cases}\dfrac{l_n}{A_n^+} & ,\ \bar{r}\in T_n^+\\ \dfrac{-l_n}{A_n^-} & ,\ \bar{r}\in T_n^-\\ 0 & ,\ \text{otherwise}\end{cases} \qquad (18)$$

The double surface integrals in Eq. (17) over a pairs of facets can be expressed as generic integrals that can be evaluated numerically. For a given pair of facets, these generic integrals can be used to compute the $\mathcal{L}$ operator contribution to nine pairs of edges forming the sides of the triangular facets.

Finally, there remains the evaluation of the incident field term on the right side of Eq. (12). Formally, elements of this column vector can be written explicitly as

$$\begin{aligned}\mathcal{E}_k^i(S;\bar{k},\alpha)&=\left\langle\bar{f}_k\,,\,\bar{E}_\alpha^i\right\rangle_S\\ &=\left\langle\bar{f}_k(\bar{r})\,,\,\hat{\alpha}\,e^{-j\bar{k}\cdot\bar{r}}\right\rangle_S\end{aligned} \qquad (19)$$

where the vector $\bar{k}$ is the incident plane-wave propagation vector, and α specifies the polarization of the incident E-field in spherical coordinate components (i.e., $\alpha=\theta$ or ϕ). Substituting the roof-top function into Eq. (19), we can write

$$\mathcal{E}_k^i(S;\bar{k},\alpha)=\frac{l_k}{2}\sum_{p=\pm}\frac{p}{A_k^p}\hat{\alpha}\cdot\left[\iint_{T_k^p} ds\left(\bar{r}-\bar{v}_k^p\right)e^{-j\bar{k}\cdot\bar{r}}\right], \qquad (20)$$

where p refers to the two facets forming the edge (See Figure 3). The polarization vector $\hat{\alpha}$ and propagation vector $\bar{k}$ can be written out in terms of the spherical angles (θ,ϕ) which specify the incident direction. The surface integral over a triangular facet in Equation (20) can be either be approximated using the centroid of the facet or evaluated analytically.

4. Some Representative Numerical Results

The hybrid formulation discussed in the foregoing sections was first applied to a number of canonic cases to test the efficacy of this approach for which the specular and nonspecular scattering phenomenology is well known. These included mono- and bistatic scattering from PEC right circular cylinders and hemisphere . The PO Ansatz was used with the MM representation spanning various portions of the scatterer. A representative result for a more complex scatterer (a 3D flat bottom kite) is depicted in Figure 4. The approximate kite dimensions are 5 wavelengths in length and 2.8 wavelegths in width. The edges and the bottom surface are represented with MM and the top portion with PO. For comparison these hybrid results are superimposed on calculations using an "exact" all

MM solution and one using only PO. As can be seen the PO results fail at nonspecular aspects, while the hybrid results are in good agreement with the exact results.

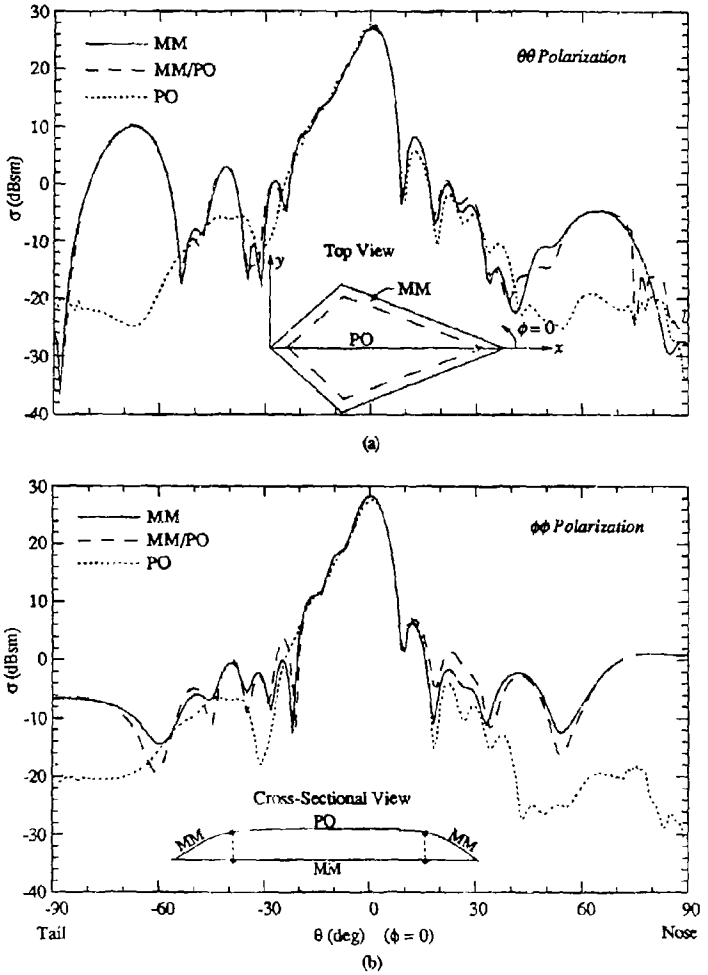

Figure 4: Monostatic Scattering of a 3-D Kite. The bottom of the kite lies in the xy plane. Nose and tail illuminations are at $\theta = \pm 90°$, as indicated in the figure. The angular cut is in the xz plane over the top of the body.
(a) $\theta\theta$ Polarization ; (b) $\phi\phi$ Polarization.

5. Conclusions

We showed that a current-based hybrid formulation can be extended to fully arbitrary 3-D configurations. This can be done within the framework of the *CARLOS-3D™* algorithm. A special feature of the current-based hybrid formulation is that Ansatz currents from a variety of high frequency asymptotic formulations can be used, i.e., the Fock theory, the Leontovich formulation, equivalent edge currents, and of course, physical optics which was explicated here. As was shown in earlier investigations (Refs. 1-4), these other formulations can yield a hybrid Ansatz that is more accurate and can address specialized scattering situations such as certain lossy surfaces (coatings) and edges for which the PO approximation is intractable.

Some of the cases to which we applied the present MM/PO hybrid formulation were electrically small. This meant that the PO Ansatz was actually a very poor approximation to the real currents induced by the incident illuminating fields. This was verified in the poor results obtained by the PO calculations themselves. However, even in these limiting cases when combined with the MM representation, the PO Ansatz yielded satisfactory answers at all mono- and bi-static angles. For electrically extended scatterers, the MM/PO hybrid formulation yields even better results. This conclusion is in consonance with earlier MM/PO hybrid formulations for BORs and BOTs.

References

[1] L. N. Medgyesi-Mitschang and D.-S. Wang, *Hybrid solutions for scattering from perfectly conducting bodies of revolution*, IEEE Trans. Antennas Propag., AP-31 (1983) 570.

[2] L. N. Medgyesi-Mitschang and D.-S. Wang, *Hybrid solutions for scattering from large bodies of revolution with material discontinuities and coatings*, IEEE Trans. Antennas Propag., AP-32 (1984) 717.

[3] E. H. Newman, *An overview of the hybrid MM/Green's function method in electromagnetics*, Proc. IEEE 76 (3) (1988) 270.

[4] D.-S. Wang, *A simple method of translation in hybrid analysis for large conducted scatterers* (Proc. of PIERS, Boston, MA, 1989).

[5] L. N. Medgyesi-Mitschang and D.-S. Wang, *Hybrid methods for analysis of complex scatterers*, Proc. IEEE 77 (5) (1989) 770.

[6] L.N.Medgyesi-Mitschang and J.M. Putnam, *Hybrid Formulation for 3-D Geometries*, Sandia National Laboratories Report, 15 August 1993.

[7] J. M. Putnam, L. N. Medgyesi-Mitschang, M. B. Gedera, *CARLOS-3D™: Three Dimensional Method of Moments Code*, MDA Report, Vol. I, 10 Dec 1992.

[8] L. N. Medgyesi-Mitschang and J. M. Putnam, *Review of hybrid methods on antenna theory*, ANN. Telecommun. 44, (9-10), pp. 445-455 (1989).

[9] S. M. Rao, D. R. Wilton, and A. W. Glisson, *Electromagnetic scattering by surfaces of arbitrary shape*, IEEE Trans. Antennas Propagat., AP-30(3), pp. 409-418, 1982.

HYBRID (MM–UTD) ANALYSIS OF EM SCATTERING BY LARGE CONVEX OBJECTS WITH APPENDAGES

M. Hsu, P.H. Pathak, and H. Tseng
The Electroscience Laboratory
Department of Electrical Engineering
The Ohio State University
Columbus, Ohio 43212

1 Introduction

Hybrid methods, the combination of two or more analytical or numerical methods, are used for analyzing problems more accurately or efficiently than is generally possible using a single method alone. A hybrid combination of the method of moments (MM) and the uniform theory of diffraction (UTD) has been developed to solve the electromagnetic (EM) scattering from electrically large, perfectly conducting, convex scatterers containing appendages which can be modeled by a set of perfectly conducting plates. This development can be employed to analyze the EM scattering by an aerospace vehicle; a simple model of such a configuration is shown in Figure 1 where the large convex scatterer would model the fuselage and the appendages would

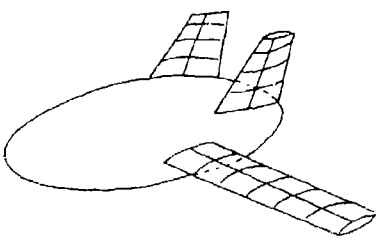

Figure 1: Complex Finned Structure

represent the control surfaces. The MM is a very accurate mathematical technique which is commonly used to solve the governing integral equation but usually involves the computation, storage, and inversion of an extremely large matrix when analyzing electrically large radiating objects. The UTD is an asymptotic high frequency ray method which describes through closed-form, physically insightful expressions the basic radiation mechanisms such as reflection from a surface, diffraction from discontinuities, and creeping waves, etc., provided the pertinent UTD solutions are available. However, there are only a limited number of ray mechanisms for which UTD expressions currently exist. Therefore, it would be advantageous to use the UTD whenever possible to account for the presence of objects (i.e. the reflection, diffraction, etc. from them) and thus not require the unknowns in the integral equation to exist on those surfaces. This would

drastically reduce the number of unknowns which need to be solved via the MM procedure. With regards to the present configuration of interest, the hybrid MM-UTD scheme restricts the unknown currents to the appendages by using a UTD-based Green's function to account for the presence of the rest of the body which here is an electrically large convex scatterer. Such a hybrid technique makes it possible to analyze the high frequency radiation/scattering from complex aerospace vehicles in a far more efficient and tractable fashion than is currently possible by either the MM or the UTD alone.

Past work on a hybrid combination of the MM and the GTD (or UTD) is divided into two categories: (1) an extension of the GTD (or UTD) using the MM ([1], [2], [3], [4], [5]) and (2) an extension of the MM using the GTD ([6], [7], [8]). One major difference between the two techniques is that the basis functions cover the entire body in the former method but only part of the geometry in the latter. The hybrid method developed here extends the latter method first introduced by Thiele and Newhouse [6]. An even more general hybrid procedure than the one described in this paper is possible if, in addition to using MM subsectional basis fuctions, UTD-based basis functions are used over the portions of the appendages not close to discontinuities or electrically small regions. This would further reduce the number of unknowns in the MM solution and will be attempted in the near future.

2 Hybrid Approach

2.1 Moment Method Matrix Equation

Given a complex object consisting of an electrically large, PEC, smooth convex surface with a set of PEC plates, the electric field scattered by this object is

$$\bar{E}^s = -j\omega\mu \int_{body+plates} \bar{J} \cdot \bar{\bar{G}}_{special}\, ds' \tag{1}$$

where the condition on the Green's function,

$$\hat{n} \times \bar{\bar{G}}_{special} = 0\,, \quad \text{on the convex PEC boundary} \tag{2}$$

reduces (1) to only an integration over the plates.

$$\bar{E}^s = -j\omega\mu \int_{plates} \bar{J} \cdot \bar{\bar{G}}_{special}\, ds' \tag{3}$$

One may express the special Green's function as

$$\bar{\bar{G}}_{special} = \bar{\bar{G}}_0 + \bar{\bar{G}}_{scat} \sim \bar{\bar{G}}^{UTD}_{special} \tag{4}$$

where $\bar{\bar{G}}_0$ is the free-space dyadic Green's function and $\bar{\bar{G}}_{scat}$ represents the effect of the convex body. Since the convex body is electrically large, $\bar{\bar{G}}_{special}$ may be approximated asymptotically by its UTD form denoted by $\bar{\bar{G}}^{UTD}_{special}$. Using (4) and applying the boundary condition to the PEC plates, the integral equation to be solved is

$$\hat{n} \times \bar{E}^i = j\omega\mu \int_{plates} \hat{n} \times (\bar{J} \cdot \bar{\bar{G}}_0)\, ds' + j\omega\mu \int_{plates} \hat{n} \times (\bar{J} \cdot \bar{\bar{G}}_{scat})\, ds' \tag{5}$$

where $\bar{\bar{G}}_{scat}$ in (5) is approximated by the UTD as $(\bar{\bar{G}}^{UTD}_{specular} - \bar{\bar{G}}_0)$. In using the MM to solve (5), the current on the plates is approximated in terms of a set of basis functions $\bar{J}_n$ with unknown coefficients I_n

$$\bar{J} = \sum_{i=1}^{N} I_n \bar{J}_n \quad , \tag{6}$$

and (5) is tested on the plates with a set of test functions, w_m where $m = 1, N$. The resulting matrix equation is

$$[V_m] = [Z_{0_{mn}}] [I_n] + [\Delta Z_{mn}] [I_n] \tag{7}$$

with

$$V_m = \bar{w}_m \cdot (\hat{n} \times \bar{E}^i) \tag{8}$$

$$Z_{0_{m,n}} = j\omega\mu \int_{n^{th}\ basis} \bar{w}_m \cdot [(\hat{n} \times \bar{J}_n) \cdot \bar{\bar{G}}_0]\, ds' \tag{9}$$

$$\Delta Z_{m,n} = j\omega\mu \int_{n^{th}\ basis} \bar{w}_m \cdot [(\hat{n} \times \bar{J}_n) \cdot \bar{\bar{G}}_{scat}]\, ds' \tag{10}$$

Recapitualating, V_m is the tangential component of $\bar{E}^i$, the field incident at the observation point in the presence of the convex body without the plates, evaluated at the test function. $Z_{0_{mn}}$ is the mutual impedance between the basis and test functions without the main convex body present and thus is dependent only on the geometry of the plates and not the main body. It describes the interaction between the current and fields of the N current basis elements making up the plates, typical of a standard MM impedance matrix. On the other hand, ΔZ_{mn} is the mutual impedance due to the presence of the main convex body, e.g. scattering or radiation from it, and thus is dependent not only on the geometry of the plates but also of the convex scatterer. It will be determined by the UTD. Finally, the current on the plates is

$$\bar{J} = [\bar{J}_1 \cdots \bar{J}_n] [I_1 \cdots I_n]^T \tag{11}$$

2.2 Basis and Test Functions

In the MM part of this hybrid method, overlapping piecewise sinusoids will be used as the $\bar{J}_n$ to approximate the current on the irregular parts of the object, i.e. the appendages. Piecewise sinusoids were found to be particularly well-suited for this hybrid method because they provided the most accurate results when used with the UTD. In addition, for reasons of simplicity and computational efficiency, Galerkin's method is chosen for testing, i.e. the test functions are identical to the basis functions.

2.3 UTD–based Green's function

The difference between the conventional MM procedure and the hybrid MM-UTD scheme lies in the type of Green's function in the kernel of the integral equation for the currents induced on the scatterer by an external source. The former procedure uses a free-space Green's function which results in the unknown currents lying on the entire complex structure. However, the hybrid scheme uses a special, UTD–based Green's function which accounts for the presence of

the electrically large convex scatterer, and as a result, the unknown surface currents are restricted to the region of the appendages. Therefore, when the MM is used in the hybrid scheme to solve the integral equation for these currents, the resulting MM impedance matrix is significantly smaller and more manageable than in the conventional MM procedure.

The aforementioned special Green's function, which accounts for an arbitrarily-located source and observer in the presence of the large convex scatterer, was a result of being able to extend the UTD to predict the scattering due to a near field source. Previous UTD expressions applicable to this problem existed only for the following limiting positions of a source and an observer:

1. Mutual coupling between source and observer on the surface of a PEC convex object [11]
2. Radiation from a source on a PEC convex object [10]
3. Scattering from a source in the far field of a PEC convex object [9]

However, in determining the Green's function, there will be sources and observers on the appendages which may be close to the convex scatterer. In anticipation of this, new UTD expressions have been developed to handle the following two cases:

4. Modified coupling: source and observer close to the surface of a PEC convex object
5. Modified radiation: source close to but observer far from the PEC convex object

With this extended UTD, we can treat the complex object described earlier.

3 Results

Since measurement results exist for the geometry shown in Figure 2a, preliminary verification of the hybrid procedure has concentrated on analyzing this particular PEC convex cylinder with a single fin from 2 Ghz to 8 Ghz. At present, we have analyzed this object by the following procedure:

1. Z, the MM impedance matrix, is calculated by approximating the electrically large cylinder by a ground plane.
2. V, the MM excitation vector, uses the hybrid procedure and accounts for the PEC cylinder by the special Green's function.
3. I, the currents on the single fin are calculated by the MM ($I = Z^{-1}V$)
4. The scattered field due to the currents on the fin radiating in the presence of the cylinder is determined using the hybrid procedure as in item 2.

Figure 3 shows the RCS as a function of frequency of the object in Figure 2a determined by this procedure versus measurements. In addition, results using the conventional MM to analyze the approximate planar model of Figure 2b are shown. The model shown in Figure 2b, which approximates the cylinder in the original configuration of Figure 2a by a planar surface, was used because even at the lowest frequency (2 Ghz) the radius and length of the cylinder in Figure 2a

are 2 λ and 6 λ, respectively; thus, computer time and storage restricted us from applying the conventional MM to the original geometry of Figure 2a. The improvement made by using the UTD to include the cylinder effect in the calculation of the V vector and the scattered fields is shown by the large difference in RCS predicted, especially at the lower frequencies, by the MM for Figure 2b and the MM–UTD for the original geometry of Figure 2a. This occurs because the observer is in the far field in the calculations in items 2 and 4 above; thus, the cylinder, though large, is not infinite in radius. By including the curvature in the Z matrix calculation, we expect only a small improvement in the RCS results since all sources and observers on the appendages are close to the cylinder, and thus the cylinder does look very much like a flat ground plane. However, more importantly, we expect a large savings in computer time since calculation of the impedance matrix is the most time consuming part of the MM calculation at these frequencies. Further refinements to the hybrid approach are in progress to handle more realistic aerospace vehicles and to integrate in a self-consistent fashion the effects of antennas and jet inlet cavities that may be present on such objects.

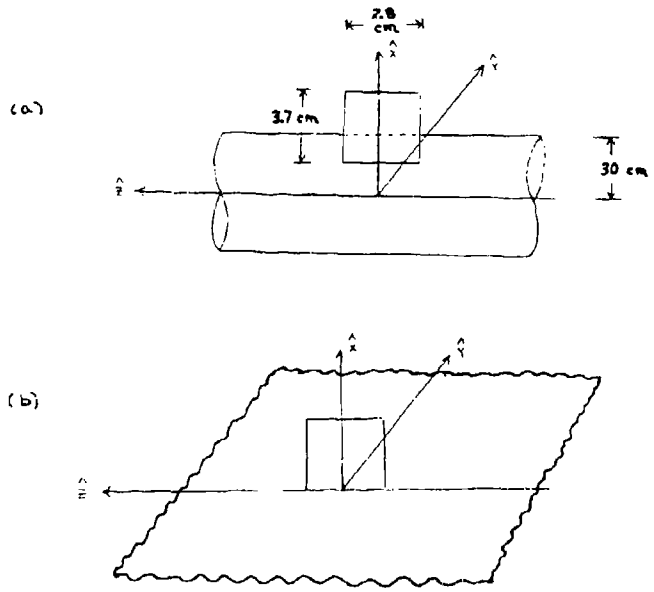

Figure 2: (a) Original geometry (b) Ground plane approximation to cylinder

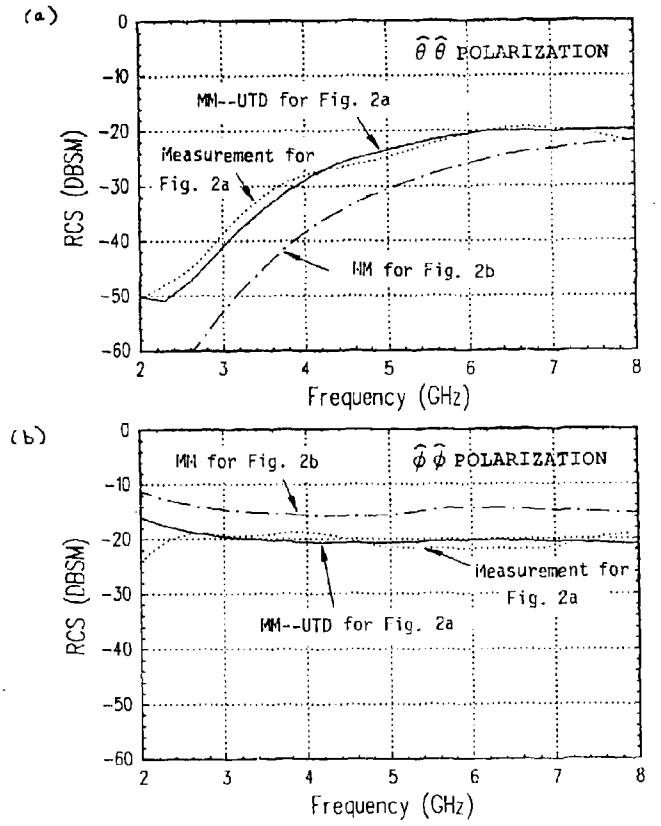

Figure 3: RCS vs. frequency for finned cylinder of Figure 2a. ($\theta' = 70°, \phi' = 80°$) (a) $\hat{\theta}\hat{\theta}$ and (b) $\hat{\phi}\hat{\phi}$ polarization

References

[1] W.D. Burnside, C.L. Yu, and R.J. Marhefka, "A Technique to Combine the Geometrical Theory of Diffraction and the Moment Method," IEEE Trans. on Antennas and Propagation, Vol. AP-23, July, 1975, p. 551-558.

[2] J.N. Sahalos and G.A. Thiele, "On the Application of the GTD-MM Technique and its Limitations," IEEE Trans. on Antennas and Propagation, Vol. AP-29, Sept. 1981, p. 780-786.

[3] L.N. Medgyesi-Mitschang and D.-S. Wang, "Hybrid Solutions for Scattering from Perfectly Conducting Bodies of Revolution," IEEE Trans. on Antennas and Propagation, Vol. AP-31, July, 1983, p. 570-583.

[4] S. Srikanth, P.H. Pathak, and C.W. Chuang, "Hybrid UTD-MM Analysis of the Scattering by a Perfectly-Conducting Semicircular Cylinder," IEEE Trans. on Antennas and Propagation, Vol. AP-34, Oct. 1986, p. 1250-1257.

[5] A.H. Chang and R. Mittra, "Using Half-Plane Solutions in the Context of MM for Analyzing Large Flat Structures with or without Resistive Loadings," IEEE Trans. on Antennas and Propagation, Vol. AP-38, July, 1990, p. 1001-1009.

[6] G.A. Thiele and T.H. Newhouse, "A Hybrid Technique for Combining Moment Mthods with the Geometrical Theory of Diffraction," IEEE Trans. on Antennas and Propagation, Vol. AP-23, Jan. 1975, p. 62-69.

[7] E.P. Ekelman and G.A. Thiele, "A Hybrid MM-GTD Technique for combining the moment method treatment of wire antennas with the GTD for curved surfaces," IEEE Trans. on Antennas and Propagation, Vol. AP-28, Nov. 1980, p.

[8] L.W. Henderson and G.A. Thiele, "A Hybrid HH-Geometrical Optics Technique for the Treatment of Wire Antennas Mounted on a Curved Surface," IEEE Trans. on Antennas and Propagation, Vol. AP-30, Nov. 1982, p. 1257-1261.

[9] P.H. Pathak, W.D. Burnside, and R.J. Marhefka, "A uniform GTD analysis of the scattering of electromagnetic waves by a smooth convex surface," IEEE Trans. on Antennas and Propagation, Vol. AP-28, Sept. 1980, p. 631-642.

[10] P.H. Pathak, N.N. Wang, W.D. Burnside, and R.G. Kouyoumjian, "A uniform GTD solution for the radiation from sources on a convex surface," IEEE Trans. on Antennas and Propagation, Vol. AP-29, July 1981, p. 609-622.

[11] P.H. Pathak and N.N. Wang, "Ray Analysis of Mutual coupling Between Antennas on a Convex Surface," IEEE Trans. on Antennas and Propagation, Vol. AP-29, Nov. 1981, p. 911-922.

REDUCING THE OPERATION COUNT IN COMPUTATIONAL ELECTROMAGNETICS USING HYBRID MODELS

E. K. Miller, 3225 Calle Celestial, Santa Fe, NM 87501

ABSTRACT

Proceeding on the assumption that no single technique is best suited to all problems that might be encountered in computational electromagnetics (CEM), it follows that a variety of formulations and models will continue to be needed. Furthermore, as problem complexity increases, it is also likely that no single technique will be equally well-suited to all the features that a given problem might possess. For these reasons, development of hybrid models, defined here to be those that integrate two or more distinct model types, offers one of the more profitable approaches for future CEM model research. The basic idea is to apply each kind of model to only those parts of a problem to which it is best suited, as measured by the operation count (OC) required to provide a desired accuracy, and to obtain the desired information. A paradigm for generalizing the development of hybrid models, which currently primarily involve producing specialized computer programs, is to exploit the commonality of the source/field (S/F) relationship (in the form of the field propagator that a given model uses) that is required of all models. This propagator is a Green's function for an integral-equation (IE) model, the Maxwell curl equations for a differential-equation (DE) model, analytical expansions for the generalized multipole technique (GMT), and ray tubes, refraction, and diffraction coefficients for an optical model. By applying that field propagator most appropriate to the separate parts of a complex problem and linking them through continuity and boundary conditions at adjoining surfaces or within common regions, a flexible hybrid modeling environment can be achieved.

INTRODUCTION

Whatever field propagator is employed in EM analysis, all CEM can be observed to involve a discretized, sampled, approximated representation of a physical problem, since the problem is:

--DISCRETIZED in time, space, angle, frequency, . . .;

--SAMPLED to quantify EM observables, i.e., sources/fields (S/F);

and

--APPROXIMATED due to use of a finite number of samples, or degrees of freedom.

All first-principles models (FPMs) require the same two kinds of sampling:

1) Of the S/Fs for which a solution is sought, using basis or expansion functions,

and

2) Of the equations that the S/Fs are to satisfy, using testing or weight functions,

whether the model is based on integral equations, differential equations, modal expansions, or optical descriptions (although not a first-principles approach, optical models might be viewed as such at high frequencies), and whether developed in the frequency domain (FD) or time domain (TD).

All such models thus share a method-of-moments (MoM) commonality and involve two essential computational steps:

1) Developing a set of interactions that usually, but not always (a TD model using explicit time-stepping produces a diagonal interaction matrix) leads to a linear system of equations (or coefficient matrix), that we call the "system" matrix;

and

2) Solving the system matrix for unknown S/Fs.

The total OC must grow at least as fast as the number of S/F samples since each sample requires at least one computation for its evaluation. The OC may grow much faster, however, because the S/F samples are usually related, where the nature of the interaction relationship determines how many operations per S/F sample will actually be required. A limiting-case exception for an integral description is physical optics (PO) where there are no interactions between sources, so that the initial operation count (to evaluate the current) is proportional to the number of source samples. Besides the number of sources, the total OC is determined by the additional observables that might also be subsequently obtained from the sources.

FPMs can also be characterized as to whether they are global, where equation sampling produces a dense, or full, matrix of interactions, or local, where equation sampling produces a sparse matrix, in terms of the interactions that occur between the S/F samples. A categorization based in the S/F relationship and the domain (frequency or time) in which the model is formulated leads to the following four major CEM FPMs and observations:

1) Frequency-domain integral-equation (**FDIE**) global models have been most widely developed since they were the first approach to receive detailed study, where it should be noted that some GMT models are basically equivalent.
2) Time-domain differential-equation (**TDDE**) local models are receiving substantially increasing attention as computer memory and speed have increased, and are especially suited to highly-parallel computers.
3) Frequency-domain differential-equation (**FDDE**) local models have been less used, in large part because the TDDE offers better OC efficiency.
4) Time-domain integral-equation (**TDIE**) global models have been least explored, probably because they are perceived to be most difficult to implement.

The basic difference between IE and DE models is the field propagator that they employ. As illustrated in Fig. 1:

--An IE-based model uses a Green's function	--A DE-based model used the Maxwell curl equations (or wave equation)
--The field at R_0 involves integration integration over enclosing surface S	--The field at R_0 involves adjacent field values in volume V
--The solution space has the dimensionality of enclosing surface S	--Solution space has dimensionality of volume V

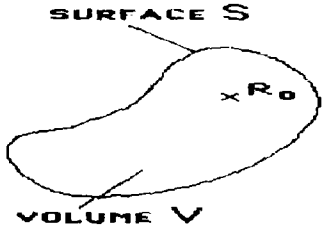

Figure 1. For a homogeneous, interior problem, finding the field at an interior point using an IE model requires sampling over only the enclosing surface while a DE model requires sampling over the enclosed volume.

It is generally true that DE propagators lead to more unknowns, but produce a sparser matrix having simpler interaction coefficients. DE models are also applicable to more general problems than are the corresponding IE models, including those having medium nonlinearity and inhomogeneity and time variation, because of the lack of a Green's function for most such problems. In TD modeling, the interaction matrices may be diagonal, using an explicit formulation, whereas FD matrices never are.

Clearly, an important, universal measure of CEM model complexity is the number of spatial unknowns.

For interior problems involving homogeneous media, IE models sample only on bounding surfaces while DE models sample throughout the volume enclosed by those surfaces. DE models, furthermore, require a "closure" condition for exterior problems to truncate spatial sampling that would otherwise extend to infinity. Optics models, by contrast, usually need only to sample edges and discontinuities of the problem space, although the ray tracing that is required can be a challenging requirement for geometrically (and electrically) complex problems. In all other CEM models, the number of unknowns is also driven by the wave nature of EM fields, since the spatial sampling density must usually be some number per wavelength in each space dimension.

REDUCING THE OPERATION COUNTS OF FIRST-PRINCIPLES MODELS

A major challenge in CEM is to increase the size and complexity of problems that can be affordably modeled. One way of doing so is hardware-based, by better matching CEM models to new computer architectures (e.g., those that are distributed, highly parallel, etc.). The other is by decreasing:

–the number of S/F samples required to achieve acceptable fidelity;
–the number of operations required per sample;

and

–the amount of redundant computation that is done,

all with respect to obtaining the needed information, for which a variety of approaches are being pursued.

Reducing the amount of redundant computation implies eliminating unneeded numerical steps in the modeling process. A simple, yet often-encountered, example is that of not fully utilizing all N^2 coefficients of the admittance matrix that comes from factoring or inverting an IE impedance matrix. When modeling antennas having a single (or only a few) feed point, only a single column (or a few columns) of the admittance matrix is needed, an application for which iterative solutions offer an attractive alternative. A similar observation holds if scattering results are needed for only one, or a few, incidence angles. Other examples are provided by over-sampling observables in space because there is no reliable way to estimate the solution accuracy *a priori* for a given spatial sampling density (or in frequency or angle), because known problem physics are not being fully exploited to estimate the behavior between samples. Model-based parameter estimation (MBPE) provides one approach for addressing this problem [Miller and Burke (1991)].

Ways of reducing the operation count of matrix-based CEM approaches are relatively few, but varied. They include:

–Decreasing the size of the system matrix (the matrix produced by a FPM);
–Simplifying computation of the system matrix;
–Developing a system matrix that is easier to solve;
–Minimizing the number of system-matrix solutions that are needed.

Some specific examples of OC reduction (OCR) along these lines are:

For a DE model, the system matrix can be decreased in size by moving the closure boundary nearer an object being modeled through using a more suitable local closure condition [e.g., the "on-surface radiation condition, Kriegsmann et al. (1987); using IE-closure, Cwik (1992)].

For an IE model, the OC required to compute the system matrix can be reduced by replacing rigorous field expressions with more easily computed approximations or representations [e.g., for the interface problem, where Sommerfeld integrals are replaced by reduced-order models Burke and Miller (1984); or where complex-image theory is used Lindell et al. (1986)].

Again, for an IE model, the system matrix might be made easier to solve by concentrating significant interactions into fewer coefficients (a near-neighbor-like approximation) [e.g., the "impedance-localization procedure, [Canning (1993)]; using "directive

basis functions, [Pogorzelski (1993)]; reducing the complexity of far interactions through the fast-multipole method, [Coifman et al. (1993)]; using "divide and conquer" techniques such as spatial decomposition, [Umashankar et al. (1992)], diakoptics [Swerling et al. (1987)], compartmentalization [Wang and Ling (1991)], and partitioning [Spring and Cangellaris (1992), Chupongstimun and Lee (1992)]}.

For any FD-based model, the number of system-matrix solutions that are need might be decreased by using reduced-order models for a sampled frequency response or angle radiation pattern [using model-based parameter estimation, Miller and Burke (1991)].

A RATIONALE FOR HYBRID MODELS

A means for achieving OCR that involves aspects of all the approaches just mentioned is that of developing and using hybrid models. The rationale for hybrid modeling is that of assigning the most appropriate S/F propagator to the different parts of a complex problem with the goal of substantially reducing the total OC required to obtain the desired information. A generic problem that illustrates the principle involved is shown in Fig.2, where the various field propagators that might be used to model different parts of a missile-like object are suggested. While it may be feasible to solve a problem having such different electrical and geometrical characterisiics using a one-propagator model, the computer resources required to do so, and the accuracy that might be achieved, can be far from optimal compared with instead using a multi-propagator, hybrid model. In the following discussion, we consider a sequence of simpler problems to demonstrate this point conceptually, first estimating their solution OCs when solved using each of the four FPMs discussed above, and then estimating the reduction in OC that can be realized using a hybrid model.

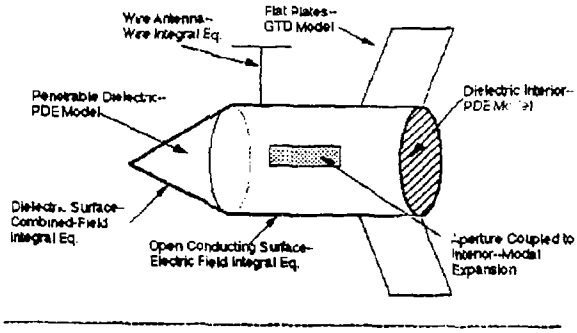

Figure 2. A generic problem to illustrate how different kinds of field propagators might be used for modeling a problem that is geometrically and electrically complex.

OPERATION COUNTS FOR SINGLE-PROPAGATOR MODELS OF SOME SIMPLE PROBLEMS

We consider four related problems, beginning with an isolated conducting body in free space, then separately adding an inhomogeneous dielectric sheath and a nearby conducting plate, and finally including both features together. We first express the total OC as a function of problem parameters for the four major FPM types as outlined above and indicate the most efficient single-propagator model in terms of OC, by denoting that model with a double underline. Then, we derive the total OC for three kinds of hybrid models applied to these separate problems to estimate the speedup, in terms of reduced OC, that these hybrid models offer over a single-propagator model of the same problem. In each example, we consider one of the problem parameters to be largest, for illustrative purposes, and designate this parameter as the controlling problem parameter (CPP). Those parameters that appear in a particular model's OC are similarly designated as controlling model parameters (CMP). We emphasize that choosing another parameter would affect the specific results, but not affect the general benefits of using a hybrid model. It should become apparent that, for even such a simple problem, the ramifications of varying the problem parameters can be non-trivial. For the four FPM types, the estimated OCs are those associated

with obtaining a solution at a single frequency. Note that if broadband results are needed, TD models are inherently more efficient, since results can be obtained across a wide frequency range from a single model run compared with FD models that require many frequency samples across that frequency range. Also, X_s and X_t denote, respectively, the number of spatial samples for all models and number of time samples needed for a TD model. Note that X_s for a DE or IE model is essentially independent of whether that model is implemented in the FD or TD.

Example 1: Isolated Conducting Body in Free Space

An isolated, conducting body of area "B" square wavelengths in free space is one of the simplest configurations to model, leading to the OCs shown in Fig. 3. Note that only the highest-order B-dependent terms are included in these OC estimates, and that algorithm-dependent multiplying coefficients can substantially affect the total OC for a given problem. The symbolic quantities "i" and "d" are the linear, spatial sampling densities required for IE and DE models, respectively, and I is the number of iterations required for convergence to a specified accuracy for an iterative solution.

MODEL	X_s	X_t	OC
FDIE	i^2B	--	i^4IB^2, Iteration i^6B^3, Factorization
FDDE	$d^3B^{3/2}$	--	$d^3IB^{3/2}$, Iteration $d^7B^{7/2}$, Banded Solution
TDIE	i^2B	$i\sqrt{B}$	$i^5B^{5/2}$, Explicit time-stepping
TDDE	$d^3B^{3/2}$	$d\sqrt{B}$	d^4B^2, Explicit time-stepping

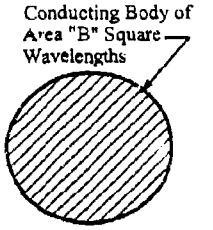

(a) (b)

Figure 3. OC dependence on object area for the four FPMs [part (a)] of an isolated body in free space of B in square wavelengths [part (b)], where B is the CPP, and, by definition for this case, the CMP as well. In this case, when solved using iteration, the FDDE provides the lowest-order dependence on B, assuming that convergence of the iterative solution occurs such that $I \propto X_s$.

Example 2: Isolated Conducting Body with Inhomogeneous Sheath

The same conducting body of surface area B square wavelengths covered by an inhomogeneous, dielectric sheath of electrical thickness "t" wavelengths in the radial direction, leads to the results shown in Fig. 4. For thin-enough sheaths (nominally assumed here to be of order one wavelength, with $t \ll \sqrt{B}$), we consider that B remains the CPP, resulting in its being the CMP for DE models, while B and t together are CMPs for IE models. The IE models become less OC-efficient because they require additional spatial samples in the inhomogeneous sheath while the DE models are relatively unaffected by the sheath since they sample volumetrically out to the closure boundary in any case.

Example 3: Conducting Body Located Near A Conducting Plate

When a conducting plate of area "P" square wavelengths is located a distance "s" away from the conducting body of example 1, assuming that s is the CPP, where $s \gg \sqrt{B}$ and $\sqrt{P}$, the OC results shown in Fig. 5 are obtained. Even though s is the CPP, we see that only B and P are CMPs for the FDIE model because the spatial sample count for an IE model does not depend on s. However, s also becomes a CMP for the TDIE model, because of needing to account for propagation time between the plate and body in the time-stepping solution. B, P and s all become CMPs for the DE models, because such models need to sample a volume determined by the plate area, the plate-body separation distance, and the body extent beyond that. The TDDE model includes an extra s factor over the FDDE because of the interaction time over that separation distance, in the same way as occurs for the FDIE models.

Example 4: Conducting Body with Inhomogeneous Sheath Located Near a Conducting Plate

Finally, a combination of the conducting body having both an inhomogeneous sheath and a nearby conducting plate leads to the results shown in Fig. 6, where it is assumed that the plate area P is the CPP. For this application, the IE models both exhibit higher-order P dependencies that either of the DE models, which is also the CMP for these models. The DE models also contains and √B as CMPs, and as for example 2, the FDDE model again exhibits the lowest-order P dependence.

MODEL	X_s	X_t	OC
FDIE	i^2B + i^3tB	--	$i^6t^2B^2$, Iteration $i^9t^3B^3$, Factorization
FDDE	$d^3B^{3/2}$	--	$d^3tB^{3/2}$, Iteration $d^7B^{7/2}$, Banded Solution
TDIE	i^2B + i^3tB	i√B	$i^{7.2}B^{5/2}$, Explicit time-stepping
TDDE	$d^3B^{3/2}$	d√B	d^4B^2, Explicit time-stepping

(a)

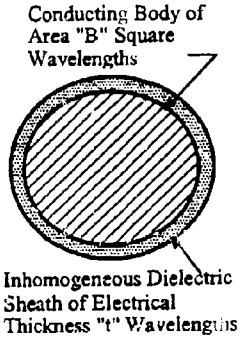

(b)

Figure 4. OC dependencies [part (a)] for conducting body covered by inhomogeneous sheath [part (b)]. While the sheath thickness, t, affects the IE OC, because additional volumetric samples are now needed, a thin sheath is not a factor for DE models because they need to sample between the body and the closure boundary in any case. The FDDE model again produces the lowest-order OC dependence on B.

MODEL	X_s	X_t	OC
FDIE	$i^2(B + P)$	--	$i^4(B+P)^2$, Iteration $i^6(B+P)^3$, Factorization
FDDE	$[d^3(P + B)s]$	--	$d^3I(B+P)s$, Iteration,
TDIE	$i^2(B+P)$	is	$i^5(B+P)^2s$, Explicit time-stepping
TDDE	$[d^3(P + B)s]$	ds	$d^4(B+P)s^2$, Explicit time-stepping

(a)

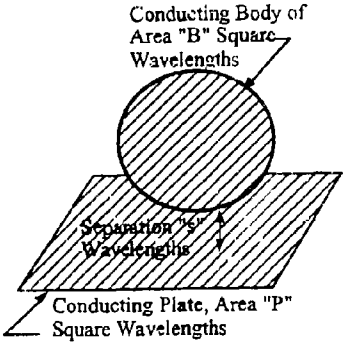

(b)

Figure 5. OC dependencies [part (a)] for conducting body of area B separated by a distance s from a conducting plate of area P [part (b)], all quantities measured in wavelengths.

MODEL	X_s	X_t	OC
FDIE	$i^2(B+P)$ + i^3tB	--	i^4iP^2, Iteration i^6p^3, Factorization
FDDE	$[d^3P(\sqrt{B}+s)]$	--	$d^3]P(\sqrt{B}+s)$, Iteration
TDIE	$i^2(B+P)$ + i^3tB	$i(\sqrt{P}+s)$	$i^5P^{5/2}$, Explicit time-stepping
TDDE	$[d^3P(\sqrt{B}+s)]$	$d\sqrt{P}$	$d^4P^{3/2}(\sqrt{B}+s)$, Explicit time-stepping

(a)

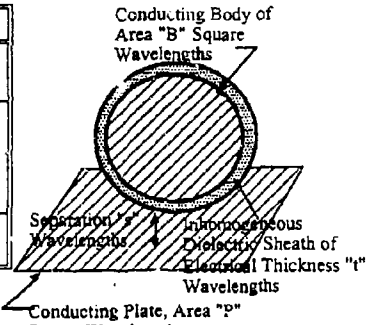

(b)

Figure 6. OC dependencies [part (a)] for conducting body of area B with inhomogeneous sheath of electrical thickness t separated by a distance s from a conducting plate of area P [part (b)], all quantities measured in wavelengths.

OPERATION-COUNT REDUCTION USING HYBRID MODELS

We consider three different hybrid models that might be applied to the generic problems just discussed.

Hybrid IE/GTD Model for Plate-Body Problem

As a first example of using a hybrid model, we consider the simplest of the examples considered above, the plate-body problem, modeled using a combination of an IE for the body and an optics [geometrical theory of diffraction (GTD)] model for the plate compared with an IE model for the entire problem. This hybrid IE/GTD model has the effect of reducing X_s from $\sim i^2(P+B)$ to instead $\sim i^2B$. The number of interaction coefficients is then $\sim i^4B^2$ rather than $i^4(P+B)^2$. The LU-decomposition OC for the hybrid IE/GTD model then is of order i^6B^3, producing a savings relative to the full IE model $\sim(1+P/B)^3$. The OC savings provided by this hybrid model over an IE model for the entire problem is seen to grow as the cube of the plate area. Were an iterative solution to be used instead, the OC savings would grow as the square of the plate area.

Hybrid DE/IE/GTD Model for Plate-Sheath-Body Problem

When the inhomogeneous sheath is added to the conducting body, an appropriate hybrid model would be one that again models the plate using GTD, the sheath using a DE model and an IE for the sheath surface. The number of IE unknowns for the hybrid model would be $\sim i^2B$ rather than the $i^2(B+P+Bit)$ that the full IE model would require. The total number of interaction coefficients (non-zeros in the problem system matrix) for the hybrid model would then be $\sim i^4B^2 + kd^3Bt$ rather than the $i^4(B+P+Bit)^2$ required for the full IE model with k a small integer depending on the DE numerical model. An iterative-solution OC for the hybrid model is thus of order Ii^4B^2, resulting in a savings relative to the full IE model, also solved using iteration, of order $(1+P/B+it)^2$. Thus, as the sheath becomes thicker, the savings provided by the hybrid model would eventually grow as the square of the sheath thickness, assuming that B remains » t, numerically.

Hybrid DE/Modal/GTD Model for Plate-Sheath-Body Problem

As a final example of a hybrid model applied to the plate-sheath-body problem, consider using a modal expansion for the surface fields while retaining the GTD propagator for the plate and a DE model for the inhomogeneous sheath. Furthermore, in the modal spectrum retain only modes in the range of

the resonance peak from 0.9 to 1.1 ka, where a is the effective sheath radius in wavelengths. Also, assume the modes on the dielectric surface can be approximated in product form as $F(\eta,\zeta) \approx f_1(\eta)f_2(\zeta)$, so that the number of mode-expansion unknowns would be $\approx 2a \approx \sqrt{B/4\pi}$. The number of interaction coefficients would then be $\sim B/\pi + Btd^3$ rather than $\sim i^4(B + P + Bit)^2$. The iteration OC for the hybrid model is then $\sim I(B/\pi + Btd^3) \approx IBtd^3$ FOR $td^3\pi \gg 1$. The savings relative to the full IE model solved using iteration is then $\sim \{iB(it + 1 + P/B)^2\}/t$, assuming $d \sim i$. The speedup that these three hybrid models might offer relative to a single-propagator IE model for the same problems are summarized in Fig. 7 as a function of plate area P as the CPP.

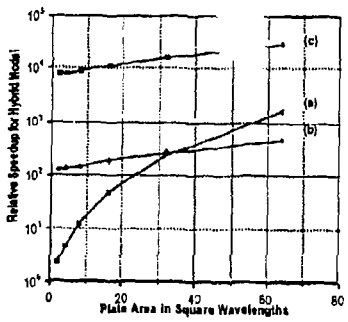

Figure 7. Relative speedups (OC reduction) achieved using the hybrid models discussed in the text over a full IE model, both solved using the same approach (see text for discussion). The result for curve (a) applies where t = 0 (i.e., there is no sheath), and for (b) and (c) where an inhomogeneous sheath one wavelength thick is present. Curve (a) is for a hybrid IE/GTD using LU decomposition. Curve (b) is for a hybrid DE/IE/GTD model using an iterative solution. In curve (c), the speedup is shown for a hybrid DE/Modal/GTD model, again solved using iteration. It is assumed that the sampling density is 10 per wavelength in linear dimension (i.e., 100 per square wavelength and 1000 per cubic wavelength), and that the object area is six square wavelengths.

CONCLUDING COMMENTS

The operation counts associated with applying the four major kinds of first-principles models to some simple generic problems have been shown. The potential benefits of instead using multi-propagator or hybrid models has been demonstrated by comparing the decreased operation count such models can produce relative to single-propagator models, showing possible orders-of-magnitude improvement.

REFERENCES

Burke, G.J. and E.K. Miller (1984), "Modeling Antennas Near to and Penetrating a Lossy Interface", *IEEE Trans. Antennas Propagat.*, AP-32, pp. 1040-1049.

Canning, F. X. (1993), "Improved Impedance Matrix Localization Method," *IEEE Trans. Antennas Propagat.*, AP-41, pp. 659-667.

Chupongstimun, V. and R. Lee (1992), "A Finite Element Technique for Solving an Electrically Large Electromagnetic Scattering Problem," in Digest of URSI Radio Science Meeting, p. 229.

Coifman, R., V. Rokhlin, and S. Wandzura (1993), "The Fast Multipole Method for the Wave Equation: A Pedestrian Prescription," *IEEE Trans. Antennas Propagat. Magazine*, 35, pp. 7-12.

Cwik, T. (1992), "Coupling Finite Element and Integral Equation Solutions Using Decoupled Boundary Meshes," *IEEE Trans. Antennas Propagat.*, AP-40, pp. 1496-1504.

Kriegsmann, G. A., A. Taflove, and K. R. Umashankar (1987), "A New Formulation of Electromagnetic Wave Scattering Using an On-Surface Radiation Condition," *IEEE Trans. Antennas Propagat.*, AP-35, pp. 153-161.

Lindell, I. V., E. Alanen, and H. von Bagh (1986), "Exact Image Theory for the Calculation of Fields Transmitted Through a Planar Interface of Two Media," *IEEE Trans. Antennas Propagat.*, AP-34, pp. 129-137.

Miller, E. K. and G. J. Burke (1991), "Using Model-Based Parameter Estimation to Increase the Physical Interpretability and Numerical Efficiency of Computational Electromagnetics," *Computer Physics Communications*, 68, 43-75.

Pogorzelski, R. J. (1993), "Improved Computational Efficiency via Near-Field Localization," *IEEE Trans. Antennas Propagat.*, AP-41, pp. 1081-1087.

Spring, C. T. and A. C. Cangellaris (1992), "A Partitioning Approach to the Electromagnetic Characterization of Large Two- and Three-Dimensional Structures," in Digest of URSI Radio Science Meeting, p. 230.

Swerling, P., N. N. Puri, and C. M. Butler (1986), "Modified Diakoptic Theory of Antennas," *IEEE Trans. Antennas Propagat.*, AP-34, pp. 1273-1281.

Umashankar, K. R., S. Nimmagadda, and A. Taflove (1992), "Numerical Analysis of Electromagnetic Scattering by Electrically Large Objects Using Spatial Decomposition Technique," *IEEE Trans. Antennas Propagat.*, AP-40, pp. 867-877.

Wang, T.-M. and H. Ling (1991), "Electromagnetic Scattering from Three-dimensional Cavities via a Connection Scheme, *IEEE Trans. Antennas Propagat.*, AP-39, pp. 1505-1513.

A Hybrid Technique For NEC (Numerical Electromagnetics Code)

S. R. Rousselle
and
W. F. Perger
Electrical Engineering Department
Michigan Technological University
Houghton, MI 49931-1295

Abstract A modification of the magnetic field integral equation (MFIE) in Numercial Electromagnetics Code (NEC) which permits faster execution without appreciable change in accuracy is described. For several antennas, results are presented which show a reduction in computation time as large as a factor of 135 y[illegible] maintain acceptable accuracy.

1. Introduction

Since the development of NEC [2], it has undergone numerous changes to improve accuracy or include specialized phenomena[1]. Few of these advancements, however, have focused on taking advantage of the way in which NEC solves problems. By assuming that the physical optics approximation is valid for surfaces, a hybrid code has been developed to reduce the solution time while maintaining accuracy.

NEC was developed to use a hybrid equation for the interaction of the electric field integral equation (EFIE) to model wires and the magnetic field integral equation (MFIE) to model closed surfaces. Because the MFIE is strictly valid only for closed surfaces and is therefore not as flexible as the EFIE for complex structures, wire-grid models and the EFIE are commonly used[5]. However, it has been found that, at least for some cases, NEC will accurately predict the far-field pattern of an antenna structure over an infinitesimally thin open surface which acts as a reflector. In principle, this should not give the correct result and is an incorrect modeling technique. In this paper, we will provide examples as to when we have found this to succeed.

One of our goals is to use this observation for improving upon the computation time associated with the matrix filling and subsequent solving for surface patch currents when they can simply be obtained using a physical optics current density upon completion of the EFIE solution.

2. Background

An interactive design package [6] was used to reveal that the current was approaching zero at the surface edges. From these observations and suggestions, [4], it became evident that a hybrid code could be developed to reduce the computation time associated with the matrix filling and solution. The MFIE solved in NEC is[2, Part 1]:

$$-\hat{n}(\vec{r}_o) \times H^i(\vec{r}_o) = -\frac{1}{2}\vec{J}_s(\vec{r}_o) + \frac{1}{4\pi}\int_{PV,S} \hat{n}(\vec{r}_o) \times \left[\vec{J}_s(\vec{r}') \times \nabla' g(\vec{r}_o, \vec{r}')\right] dA'. \qquad (1)$$

where $\vec{H}^I$ is the magnetic field incident on the surface, $\vec{J}_s$ is the surface current that it induces, $\hat{n}(\vec{r}_o)$ is the outward directed normal vector at $(\vec{r}_o)$, $g(\vec{r},\vec{r}')$ is the Green's function given by:

$$g(\vec{r},\vec{r}') = \frac{exp(-jk|\vec{r}-\vec{r}'|)}{|\vec{r}-\vec{r}'|}. \tag{2}$$

and the subscripts "P.V., S" indicate the principal value of the surface integral. In the Physical Optics (PO) approximation, the term in Eq.(1) is negligible for a smooth surface whose radius of curvature is large compared to a wavelength[3].

3. Results

Our first example, shown in Figure 1 is the far-field pattern of a monopole perpendicularly

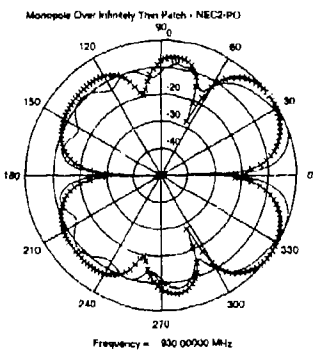

Figure 1: Comparison of far-field pattern for a monopole over thin patch for the hybrid NEC2-PO code (marked line) and experiment (solid line).

oriented over an infinitesimally thin conducting patch using the hybrid NEC2-PO code (the marked line) and a comparison with experimental data measured in an anechoic chamber. For comparison, Figure 2 shows the agreement between the far-field pattern of the same monopole antenna from NEC2 (unmodified, the marked line) and the same experimental data (solid line). As can be seen, there is relatively little difference between either of the two computed patterns compared with experiment. The strong agreement between the measured and NEC2 patterns suggests that infinitesimally thin patches can be used to model reflectors.

Our second example is the Example 4 of the NEC2 User's Guide, a T antenna on a box over a perfect ground. Figure 3 shows the close agreement between the NEC2-PO code (marked line) and the original NEC2 code (solid line).

The last example a model of a monopole antenna on a 1992 Cadillac Seville with 10 wire segments and 344 patches, as illustrated in Figure 4, and was created using our NEW_IDEAS

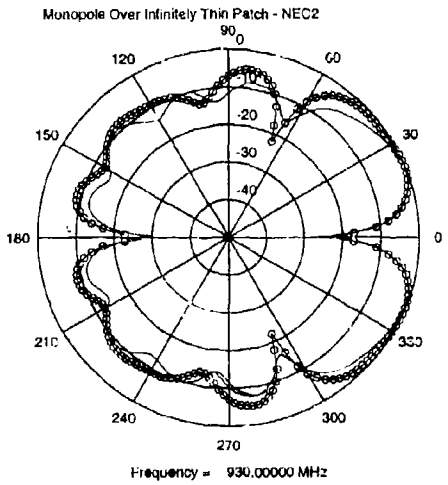

Figure 2: Comparison of far-field pattern for a monopole over thin patch for the original NEC2 code (marked line) and experiment (solid line).

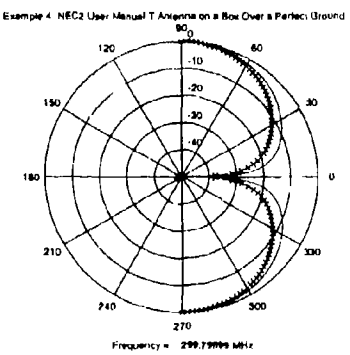

Figure 3: Comparison of far-field pattern for Example 4 of the NEC User's Guide for the hybrid NEC2-PO code (marked line) and the original NEC2 code (solid line).

software [6]. In Figure 5 we have plotted the far-field pattern for this structure using the hybrid NEC2-PO code (marked line) and the original NEC2 code (solid line). It is interesting to note that for this example, the hybrid NEC2-PO code ran in 3.8 seconds as compared with 401 seconds, on an RS6000 model 540. The particular frequency chosen in this example was 100 MHz, or nearly middle of the FM band.

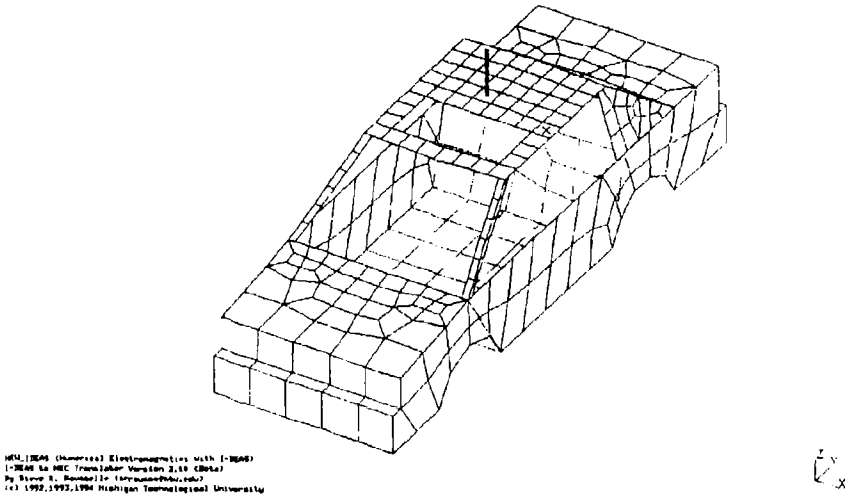

Figure 4: Illustration of the patches and wire segments used to model a 1992 Cadillac Seville

4. Conclusions

From the examples given, it appears that the use of a physical optics approximation within the NEC program can result in a considerable computational savings. Future work will necessarily include testing this hypothesis for its range of applicability.

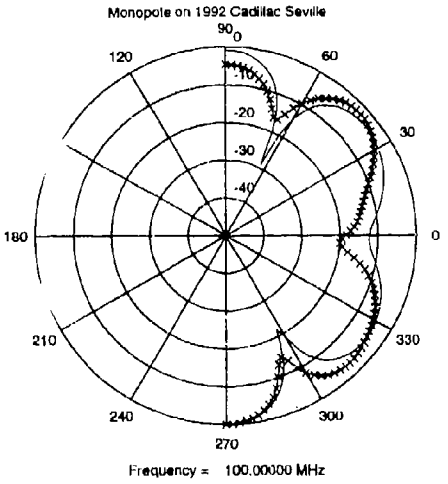

Figure 5: Comparison of far-field pattern for a monopole on a 1992 Cadillac Seville using the hybrid NEC2-PO code (marked line) and the original NEC2 code (solid line).

References

[1] G. J. Burke. Recent advances to NEC: Applications and validation. UCRL Preprint 100651, Lawrence Livermore National Laboratory, to be published at the Modern Antenna Design Using Computers and Measurement conference, Ankara, Turkey, Oct. 19-20, 1989, 1989.

[2] G. J. Burke and A. J. Poggio. Numerical electromagnetics code (NEC)- method of moments. Technical document 116, Naval Ocean Systems Center, San Diego, California, 1981.

[3] Akira Ishimaru. *Electromagnetic Wave Propagation, Radiation and Scattering.* Prentice-Hall, Englewood Cliffs, NJ 07632, 1991.

[4] E. K. Miller, private communication.

[5] Jian Peng, Constantine A. Balanis, Craig R. Birtcher, and George C. Barber. Improvement of the NEC code's upper limit and pattern prediction of a helicopter structure, volume 1, pages 56-59, Ann Arbor, Michigan, June 1993. IEEE, IEEE Antennas and Propagation Society International Symposium.

[6] Steve Rousselle, S. S. Marlor, and Warren F. Perger. An interactive antenna design technique using I-DEAS, pages 77-88, ICCON, ICCON User's Conference Proceedings, May 1993.

AN APPROACH FOR SOLVING SYSTEM-LEVEL ELECTROMAGNETIC COUPLING PROBLEMS

Everett G. Farr and Robert J. Antinone
Farr Research and BDM Federal, Inc.

I. INTRODUCTION

When a complex system is exposed to an external electromagnetic (EM) field, voltages are generated at the pin level of sensitive electronics that can upset or damage a system. The ability to predict the field levels required to generate such an event is of critical importance to the understanding of the survivability/vulnerability (S/V) of a system. However these predictions are quite difficult because of the complexity of the systems involved. We summarize here an approach for solving this problem by using a variety of codes that already exist, as well as some new technology in the area of interpolating sparsely sampled data.

The type of problem one encounters is shown in Figure 1. A plane wave is incident upon a system with apertures and slots in the exterior surface. The external fields leak into a cavity, which contains equipment boxes connected together by shielded cables or bare wires. Since there are multiple conductors in a bundle, multiconductor transmission line theory is required to solve the cable problem. There are one or more sensitive circuits at the end of the cables. The voltages at the inputs to the circuits cannot exceed some maximum. We propose here an approach for solving this problem using a combination of EM fields codes, a multiconductor transmission line code, a circuit code, and a scheme for interpolating sparsely sampled data.

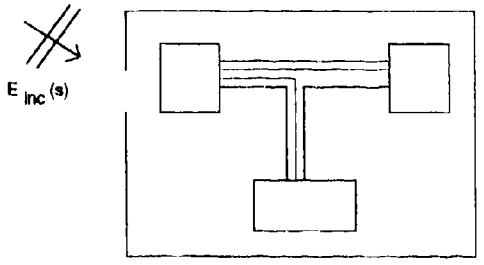

Figure 1. A typical system-level EM coupling problem.

II. THE CHALLENGES IN SOLVING THE SYSTEM-LEVEL COUPLING PROBLEM

The challenges in solving system-level EM coupling problems lie in four main areas. First, there is a natural separation of codes into distinct areas, EM fields, transmission lines, and circuits. In general, these problems are solved separately, with no clean method of passing the output of one problem to the input of the others. This problem can be overcome by adjusting the Input/Output (I/O) of the various codes to be in a

format that is compatible with the other codes. While this is simple in principle, in practice it may require considerable effort.

A variety of codes are required to solve this problem. Looking from the outside in, first one requires an electromagnetics fields code. Two codes are currently available that could serve such a purpose, GEMACS [1] and XPATCH. Inside the cavity, one would use GEMACS. At the transmission-line level, one might use QV7TA, which provides a solution to the "BLT" multiconductor transmission line equations, developed by Baum, Liu, and Tesche [2,3]. Finally, at the circuit level, one could either write one's own code, since we propose to linearize the problem, or use an existing code such as SPICE.

A second challenge to solving the system-level problem lies in the complex nonlinear circuits that must be analyzed in order to test their sensitivity. In many cases, one can assume a linearized model for the circuit, and still achieve reasonable accuracy. An example of where this is valid is the problem of back-door HPM coupling, where the frequency of the incident field is far above the intended operating frequency of the nonlinear solid-state devices. It has been shown that this problem can be linearized by measuring the input impedances of nonlinear circuits out of band [4]. This is discussed in more detail later in this article.

A third challenge lies in the very large amount of data required to demonstrate hardness of the asset. If one wishes to show that the voltage at a certain component never exceeds some maximum value, one would need to show this for many different angles of incidence, for two polarizations of the incident field, and for many different frequencies. The necessity of demonstrating hardness at many different frequencies is potentially the most troublesome, since one must anticipate the possibility of sharp resonances in the response data that could be missed if the data were sampled too sparsely. An approach for addressing this problem is to use a procedure called Model Based Parameter Estimation (MBPE) [5,6]. This procedure allows one to make calculations at sparsely sampled frequency points, and then interpolate intelligently between the samples. One uses known information about the system, such as its response at zero frequency, to fit a rational function to a sparse sampling of data points. We discuss this technique in more detail later in this article, and provide some examples.

A final challenge lies in the complicated geometry specifications of the external shell. Typically, the first step in the analysis is to calculate the skin currents on a complex object such as an aircraft, helicopter, or tank. It is tedious, however, to provide complete geometry data to an EM fields code in a format that it is useful. One way this can be done is to take advantage of Computer Aided Design (CAD) drawings of an asset, which are often available from the manufacturer. However, these drawings typically are not discretized in a form that is compatible with the EM field computation of skin currents. Fortunately, at least one CAD package, called ACAD, has developed the capability to discretize a surface model directly. This program provides either quadrilateral patches for Method of Moment (MoM) surface patch analysis, or triangular patches for Shooting and Bouncing Ray (SBR) analysis. Once discretized, the geometrical description of the asset can be output to an ASCII file, which could then be converted to a format compatible with the geometry file of the fields code.

III. CIRCUIT ANALYSIS

For back-door HPM coupling, the circuit problem consists of effects that occur at microwave frequencies, and effects that occurs at the lower frequencies, where the circuits were designed to operate. We consider here only the effects at microwave frequencies, and we end our analysis when we determine a device has either been upset or damaged. The system's response to that upset or damage can then be determined by a systems analyst.

The first consideration must be whether to carry out the analysis in the time or frequency domain. Time domain analysis can deal with nonlinearities, but it is more complex and costly to perform. Study of

HPM phenomena to date indicates that the problem can be considered linear and that frequency domain analysis is suitable.

Researchers noted during damage testing that the signal reflected from the device under test usually did not change when damage occurred. Researchers expected to see the reflected power change when the component failed, but in many cases it did not. The nonlinearity was masked. Researchers conceived a sensitive experiment to determine the linearity of circuits subjected to HPM signals. Figure 2 shows a measurement scheme that uses the wide dynamic range of a spectrum analyzer to determine the nonlinearity affecting the reflected signal. A 300-MHz signal was incident on the device under test, a 74LS00 NAND gate. A directional coupler was used to sample the signal reflected from the gate. The spectrum analyzer was connected to the directional coupler and was set to sweep the frequency range covering 300 MHz to 900 MHz. This allowed the spectrum analyzer to look at the fundamental, second harmonic, and third harmonic reflected from the gate under test. By using such arrangements, it has been observed that the second and third harmonics are down by more than 40 dB from the primary. This suggests that the nonlinear effects are not critical to model.

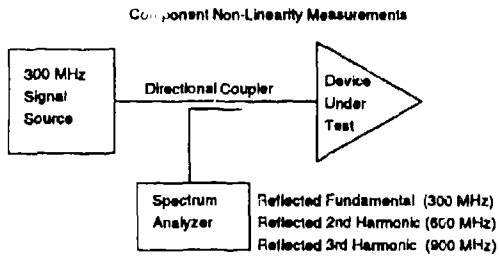

Figure 2. Nonlinearity measurement system.

These data raise the question of why components that are known to be nonlinear do not manifest that nonlinearity when subjected to HPM signals. The answer appears to be that parasitic capacitances and inductances associated with the device and its package dominate the device impedance at higher frequencies. Input impedance measurements have been made, for example on 741 operational amplifiers. The impedance is high at normal operating frequencies but rolls off at higher frequencies. In fact, at high frequencies the impedance looks like that of a capacitor up to about 1.3 GHz where a resonance occurs and it begins to look inductive. The parasitic inductance and capacitance that dominate the impedance are linear, and they mask the internal nonlinearity. Thus, for most back door coupling cases the affected circuitry can be treated as having a linear response to HPM signals. The parasitic capacitances and inductances isolate the internal nonlinearities. Thus, frequency domain circuit analysis is adequate for these problems.

Even if one chooses to use simple linear circuit theory, complications can arise. For example, Figure 3 shows the impedance of a common ceramic capacitor. At low frequencies it behaves as expected, but at higher frequencies it does not. It resonates with its own lead inductance and internal inductance at about 60 MHz and acts more like an inductor at higher frequencies. The analyst must take this behavior into account when applying the code to HPM frequencies. Note that simple elements adequately model this behavior, but more elements are required than just the capacitor.

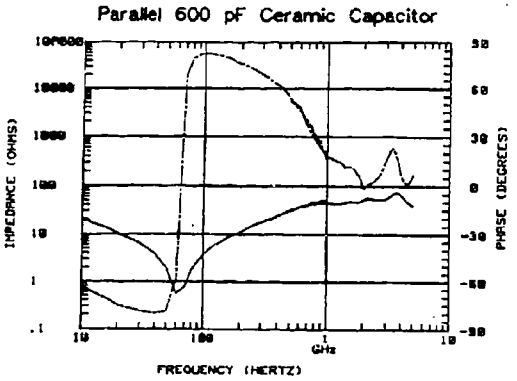

Figure 3. Impedance of a common capacitor. (The solid line is magnitude and the dashed line is phase.)

In the case of back door upset most analog components respond with square law response when the incident HPM signals are low. That is, the rectified voltage out of the component is proportional to the square of the incident HPM voltage. An order of magnitude increase in the HPM voltage results in a two order of magnitude increase in output signal. For digital components, there is a threshold HPM signal that causes a change of state at the output. Table 1 shows the typical incident HPM power required to cause a 10-mV response referred to the input for analog components and a change of state for digital components.

Table 1. Nominal response data for common components.

Device Family	0.1 GHz (dBW)	0.2 GHz (dBW)	0.5 GHz (dBW)	1 GHz (dBW)	2 GHz (dBW)	5 GHZ (dBW)	9 GHZ (dBW)
TTL	-17	-17	-17	-14	-11	-7	-3
CMOS	-10	-10	-10	-10			
Linear	-49	-47	-43	-40	-32	-27	-21
GP Si XSTRS	-49	-47	-43	-40	-32	-27	-21
Ge XSTRS	-20	-20	-15	-12	-10	-8	-5

For degradation or damage the effect can be considered to occur when a threshold power or energy is reached. Absorbed power can be calculated from the incident voltage and component impedance. Table 2 shows typical damage thresholds for common [illegible]aic components.

Table 2. Typical damage thresholds for common components.

Device Family	1 μs Pulse Failure Power (dBW)	100 ns Pulse Failure Power (dBW)
TTL	20	25
CMOS	23	28
Linear	24	29
General Purpose Transistors	24	29
Medium Power Transistors	30	35
RF Transistors	20	25
Microwave Mixer Diodes	6	6

IV. INTERPOLATION OF THE DATA USING MODEL BASED PARAMETER ESTIMATION

When one calculates a response parameter in the frequency domain, one typically calculates many more frequencies that are necessary to specify the curve. One does so because there might be a resonant spike in the response that could be easy to miss. The problem with this approach is that it is expensive to sample a large number of points. Furthermore, even after going through the effort of calculating the response at a large number of points, there is still the lingering question of whether it was enough.

The technique of MBPE attempts to address this issue from a physics-based point of view [5,6]. When using this technique one makes assumptions about what the response must look like, and then one fits the sparsely sampled data to a rational function model. In doing so, it is hoped that one will find the prominent features of a response curve with considerably fewer samples than would otherwise be necessary.

The MBPE technique arises from both experimental observation and from recent theoretical developments. Experimentally, it has been observed for some time that if an object is illuminated by an impulsive waveform, then the resulting currents and fields tend to be sums of damped sinusoids. Theoretically, the Singularity Expansion Method (SEM) arrives at much the same conclusion [7]. One must be cautious, however, because in some cases there can be an additional contribution to the response corresponding to the driven response, which cannot be represented by a damped sine, and must be accounted for in other ways.

The MBPE technique therefore assumes a observable of the form

$$f(t) = \sum_{n=1}^{N} R_n e^{s_n t} + f_{np}(t) \tag{1}$$

where s_n represents the N complex poles associated with the damped sines, and R_n represents their residues, or weightings. The subscript "np" indicates the non-pole portion of the response, and it often corresponds to the driven response. In most cases, this is assumed to be either very small or zero, however, some additional degrees of freedom may be included in the model in order to account for this possibility.

In the frequency domain one can express this model as

$$F(s) = \sum_{n=1}^{N} \frac{R_n}{s - s_n} + F_{np}(s) \tag{2}$$

Assuming the non-pole portion of the waveform is zero, this is expanded as

$$F(s) = \frac{N(s)}{D(s)} = \frac{N_o + N_1 s + N_2 s^2 + \cdots + N_{N-1} s^{N-1}}{D_o + D_1 s + D_2 s^2 + \cdots + D_{N-1} s^{N-1} + s^N} \tag{3}$$

If the function is now sampled at the pole locations s_i, one obtains in sampled form

$$F_i \hat{D}(s_i) = \hat{N}(s_i) \tag{4}$$

This is just a linear set of equations that can be solved for the N_n's and D_n's , provided that there are at least as many samples as there are unknowns.

If one wishes to include a non-pole portion to waveform, this is typically modeled as

$$F_{np}(s) = \sum_{m=-Q}^{R} C_m s^m \tag{5}$$

Using this, equation (3) is recast into a slightly different form, but one still solves a set of linear equations to obtain the coefficients. Including the non-pole part of a solution may be important if there is a forcing function (source) in the observable. The non-pole part of the model can also be used to model poles that are far outside the modeled frequency range. Poles where $s_n << s$ behave approximately as $1/s$, and poles where $s_n >> s$ behave as $1/s_n$.

Finally, note that one can often reduce the number of computations by calculating the derivative of a response with respect to frequency, in addition to the response at that frequency. Often the derivatives are available in closed form from the solutions, and this capability has already been included into a version of NEC. However, if one must couple the output of an EM fields code to a transmission line code, generating the frequency derivatives is somewhat more complicated. If the validity of MBPE can be demonstrated for system-level coupling without the frequency derivatives, then it may be useful to study the possibility of even better performance by including frequency derivatives at a later date.

Let us consider an example problem, in order to test the validity of MBPE for fields in a cavity. Consider the problem of a closed rectangular cavity with conducting walls of conductivity 5.7×10^7 mhos/m (Figure 4). The cavity is excited by a dipole near one end of the waveguide, located at (0.54747, 5.47, 2.735) cm.

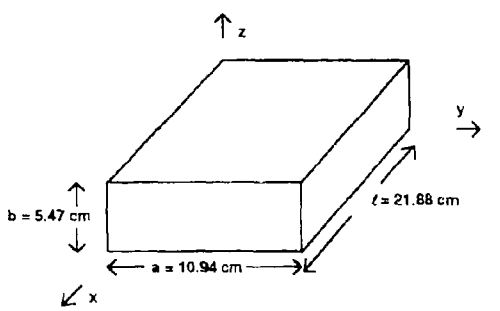

Figure 4. The resonant cavity to be analyzed.

The field at the center of the cavity (E_z) was calculated and plotted at six frequencies. A rational function model was then fitted to the data. The model had the form

$$E_z(s) = \frac{\sum_{n=0}^{2} N_n s^n}{\sum_{n=0}^{2} D_n s^n + s^3} \quad (6)$$

There are six complex unknowns in the above function (the N_n's and D_n's), so one has enough information if the function $E_z(s)$ is calculated at six frequencies.

The fields calculated at six frequencies are shown as triangles in Figure 5. These data were then used to generate the six unknown coefficients in Equation 6, and the resulting model function is shown as a solid line in Figure 5.

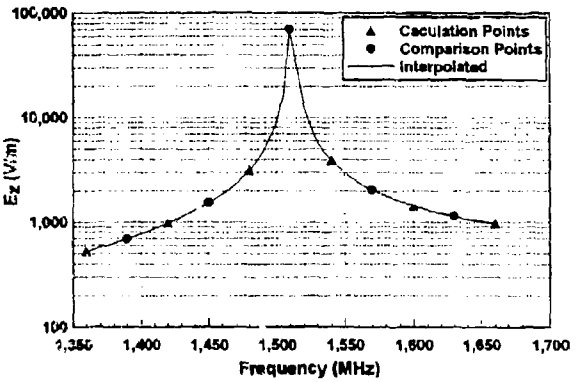

Figure 5. A comparison of a MBPE model to some frequency points calculated numerically. The data points represented by triangles were used to generate the model, which is represented as a solid line. The round dots were additional frequency points calculated numerically to check the validity of the model.

The final step in the analysis is to calculate some extra points using GEMACS, and verify that they fall on the calculated model. The additional points are round dots in Figure 6. There is excellent agreement between the model (solid line) and the additional calculated frequencies (round dots). Note that in the points used to create the model, there are no fields larger than 4 kV/m, and the model predicts a value of 67.1 kV/m at 1.51 GHz. At the same frequency, GEMACS predicts 70.2 kV/m, so the error in the model near a resonance is just 4%. This is excellent agreement, and it shows that the MBPE model performs as expected.

V CONCLUSIONS

A wide variety of techniques must be applied in order to address the system-level EM coupling problem. This article presents an approach for addressing this problem at lower frequencies. The approach involves a combination of EM fields codes, multiconductor transmission line codes, and circuit codes, all in the frequency domain. The response can be sampled sparsely in the frequency domain and then interpolated using MBPE.

A review of how to simplify the circuit analysis was provided. A review of model based parameter estimation was provided. Results were obtained for the case of fields in a rectangular cavity, and it was shown that MBPE interpolates the fields with quite good accuracy, even in the presence of sharp resonances.

REFERENCES

1. E. L. Coffey, et al, General Electromagnetic Model for the Analysis of Complex Systems (GEMACS), Version 5, Users and Engineering Manuals, RADC-TR-90-360, Rome Air Development Center, Griffiss AFB, NY, June 1990.

2. Baum, C. E., Liu, T. K., and Tesche, F. M., "On the Analysis of General Multiconductor Transmission - Line Networks," Interaction Note 350, Air Force Weapons Laboratory, November 1978.

3. Tesche, F. M., and Liu, T. K. "User Manual and Code Description for QV7TA: A General Multiconductor Transmission-Line Analysis Code," Interaction Application Memo 26, Air Force Weapons Laboratory, August 1978.

4. Antinone, R. J., *Proceedings of the High Power RF Effects Assessment Methodology Short Course*, DDV-92-0015, Directed Technologies Inc., Arlington, VA, p. 134, March 11-15, 1991.

5. Miller, E. K., "Model Based Parameter Estimation Application in Electromagnetics, in *Electromagnetic Modelling and Measurements for Analysis and Syntheses Problems*, B. de Neumann (ed.), pp. 205-256, Kluwer Academic Publishers, The Netherlands, 1991.

6. Miller, E. K. and Burke, G. J., "Using model-based parameter estimation to increase the physical interpretability and numerical efficiency of computational electromagnetics," *Computer Physics Comm.*, Vol. 68, pp. 43-75, 1991.

7. C. E. Baum, "On the Singularity Expansion Method for the Solution of Electromagnetic Interaction Problems," Interaction Note 88, Air Force Weapons Laboratory, December 11, 1971.

EFFICIENT MMP COMPUTATION OF PERIODIC STRUCTURES

Ch. Hafner, Swiss Federal Institute of Technology, Zurich
L. Bomholt, MIT, Cambridge

ABSTRACT

The original version of the 3D MMP code offers several features for EM scattering. Although periodic structures can be computed without any modification of the code, two new features are required in order to make such computations efficient and user-friendly. In this paper we discuss the problems of previous atempts to compute periodic structures with the unmodified 3D MMP code and the new features. A comparison with other techniques shows that the modified version of 3D MMP is useful for obtaining very accurate and reliable results.

INTRODUCTION

The 3D MMP code [1] is a powerful tool for numerical electromagnetics with a wide range of applications. It is based on the Generalized Multipole Technique (GMT) [2], i.e., it is closely related to both analytic techniques and to the MoM. Therefore, 3D MMP is well suited when high accuracy and reliability is desired. Moreover, the 3D MMP code allows to easily handle lossy dielectrics with arbitrary complex permeability and permittivity constants, which is important for gratings used in optics.

Recently, the method of fictitious sources [3] and similar methods [4] have successfully been applied to periodic structures. These methods are essentially based on the GMT but they work with a small subset of the basis functions available in the 3D MMP code. Thus, one would expect that excellent results can be obtained with 3D MMP. Since the published version of 3D MMP version was not designed for periodic structures, the brute-force method was used in [5]. In this method, a periodic structure with infinitely many cells is replaced by a similar structure with a finite, but large number of cells. Naturally, one obtains extremely large computation times even for simple examples. A more sophisticated approach works with Floquet and similar theories. This requires no modification of the code and allows one to imbed 3D MMP in a simple Floquet environment. Unfortunately, the convergence of these techniques is so bad that the computation still is completely inefficient.

PERIODIC BASIS FUNCTIONS

In the GMT, the EM field is approximated by a series expansion of the following form:

$$Field = \sum_{k=1}^{K} A_k \, field_k + Error \qquad (1)$$

The basis field functions $field_k$ fulfil the Maxwell equations inside a homogeneous domain. The parameters A_k are computed from the boundary conditions. 3D MMP offers many different types of basis (field) functions. Due to the numerical properties, multipole functions are favoured. Different types of basis functions are often mixed.

For periodic structures, one can use the same expansion with periodic basis functions. If all basis functions are appropriate periodic functions, the boundary conditions have to be matched in one single cell of the periodic structure and the boundary conditions in all other cells will be automatically matched. One easily can construct periodic multipole functions. Such functions consist in an array of multipoles at different locations. The amplitudes of the different multipoles are computed from the direction of the incident plane wave. The number of the multipoles of such an array is infinite. Thus, one either has to find an analytic solution for the infinite array or one has to truncate. An analytic solution is known for monopoles, i.e., zero-order multipoles, but it is missing for general multipoles and other basis functions implemented in 3D MMP.

A truncated series of Multipoles with different amplitudes can be introduced in 3D MMP by means of a special feature, called meta expansions. I.e., no modification of the code is required for testing periodic arrays of multipoles. Although this is encouraging, the result is disappointing - as one might have known in advance. The convergence of the series is so slow that a huge number of multipoles has to be computed for obtaining a reasonable accuracy. I.e., periodic multipole functions are inefficient.

From the solution of Maxwell's equations in Cartesian coordinates, one finds another set of periodic functions, the very well known Rayleigh expansions. These periodic basis functions are plane waves and evanescent plane waves. They can easily be computed and are available in the original version of 3D MMP. If many terms of the Rayleigh series have to be separately defined by these functions, the user has to perform time-consuming and tedious work. For this reason, Rayleigh expansions have been introduced as new basis functions in the code. These expansions are used to expand the reflected and transmitted EM field, but they are known to be incomplete for modelling the entire EM field of a general periodic structure.

Although one can model periodic structures with a mixture of Rayleigh expansions and periodic arrays of monopoles, this approach is not satisfactory for MMP users who like to take advantage of the entire palette of basis functions available for general EM scattering problems. Since the implementation of the corresponding basis function is cumbersome and inefficient, a different approach is proposed in the following

PERIODIC BOUNDARY CONDITIONS

The GMT is a pure boundary method. It is well known that domain methods such as finite elements usually work with simpler types of basis functions that cause less numerical problems. Thus, we might be tempted to entirely abandon the GMT in order to avoid the severe problems with the basis functions discussed in the previous section. But we can solve our problems by a small step into the direction of an entire discretization of the domains by subdividing a homogeneous domain into subdomains with different basis field functions inside each subdomain. This requires the matching of the EM field on the "fictitious" boundaries between the subdomains. In 3D MMP, fictitious boundaries can easily be introduced without any modification of the code. For periodic structures, such boundaries are useful for separating the space where reflected and transmitted EM waves are modelled with Rayleigh expansions from the rest of the structure. This is illustrated in Figure 1.

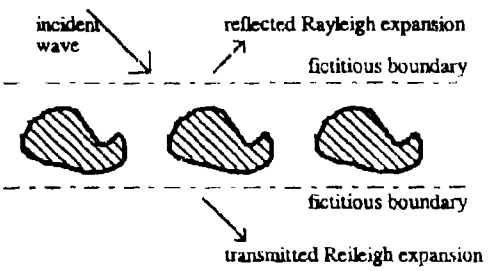

Figure 1: Fictitious boundaries are introduced for separating the periodic structure and the area of the reflected and transmitted Rayleigh expansions.

Obviously, one also can introduce fictitious boundaries for separating the different cells of the periodic structure. On these boundaries, the EM field has to fulfil the following periodic boundary conditions.

$$Field(\vec{r} + \vec{d}) = C \cdot Field(\vec{r}) \qquad (2)$$

where $\vec{d}$ is the vector that shifts a point in one cell to the corresponding point in the neighbour cell and C is a constant computed from the incident wave. Periodic boundary conditions have been implemented in 3D MMP as a new feature. This technique is illustrated in figure 2. In order to obtain high flexibility, one can introduce periodic boundary conditions with different vectors $\vec{d}$. Up to 3 different periodic boundary conditions can be defined in 3D MMP. The constant C can either be defined by the user or it can be computed automatically if the incident field is a plane wave.

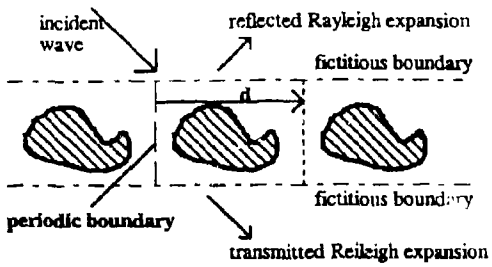

Figure 2: Periodic boundaries are introduced to isolate a cell of the periodic structures from its neighbours. The periodic boundary condition (2) must be fulfilled on the dashed boundary only. In the periodic boundary condition, the information of the field on the dotted neighbour boundary is also required. Only the field in one cell is explicitly modelled by multipoles and other expansions. After the solution of the problem, the field in all other cells is obtained by a simple transformation.

Fictitious boundary conditions and periodic boundary conditions allow to isolate a single cell of the periodic array. The EM field is approximated inside this cell according to (1). In the area of reflected and transmitted Rayleigh expansions, Rayleigh expansions are most reasonable and simple for modelling the EM field. It would be possible to apply other periodic basis functions in these domains but one usually is interested in the Rayleigh terms themselves. Furthermore, the convergence of these expansions is excellent if the fictitious boundaries are sufficiently far away from the periodic structure. Incidentally, neither the location nor the shape of the fictitious boundaries and of the periodic boundaries are unique. Straight lines (planes in 3D) are preferred because of their simplicity. The fictitious boundaries can be shifted in order to obtain more information on the stability and reliability of the results.

This technique is closely related to the technique that had successfully been applied to waveguide discontinuities [7]. Instead of the Rayleigh expansions one has waveguide modes for modelling the reflected and transmitted waves in waveguides. Fictitious boundaries are used to separate the discontinuity from the undisturbed waveguides. Periodic boundary conditions are not required although the field in rectangular waveguides is periodic (MMP is not restricted to rectangular waveguides). The geometry of waveguide discontinuities can be very complex. In the simplest case, the relation to the modelling of periodic structures is obvious (see Figures 2 and 3).

The introduction of the fictitious boundaries is somehow ambiguous. If the fictitious boundaries are very close to the structure, the length of the periodic boundaries is small and the number of basis functions for modelling the discontinuity is also small. But in this case, the number of orders of the reflected and transmitted waves can be large. If the fictitious boundary is moved away from the discontinuity, the number of orders can be reduced because the higher orders are exponentially damped in the direction perpendicular to the structure. So far, no essential problems for setting the fictitious boundaries have been encountered. In contrary, using different models with different fictitious boundaries is helpful for testing the stability and accuracy of the solution.

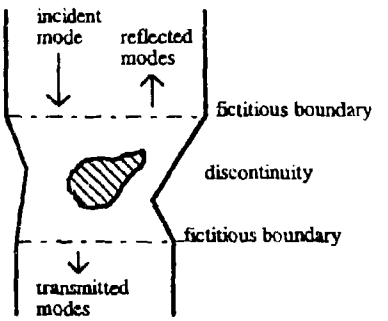

Figure 3: MMP model of a simple waveguide discontinuity.

No information of the EM field in the neighbour cells is required for the computation of the EM field in one cell with periodic boundary conditions. Once the EM field is known in one cell, one obtains the field in the neighbour cells by a simple transformation that is essentially the same as the one used for defining the periodic boundary conditions (2).

A SIMPLE TEST CASE

A simple grating consisting of wires with a rectangular cross section (see Figure 4) and a complex refraction index n=0.3+8i has been computed in [8,9] with very different numerical methods. If one compares the measured cross section of such gratings, one can recognize that the rectangular shape with ideal corners is a considerable simplification. This simplification is required by several methods, for example, modal expansions. On ideal conductors the sharp edges would cause a singularity of the field. For the lossy conductors in the model one still obtains very high electric fields. In codes that are able to accurately compute the EM field on the surface of any domain, this can cause numerical problems. In the MMP model, rounded edges were used in order to obtain more reliable results. Incidentally, such models are more realistic.

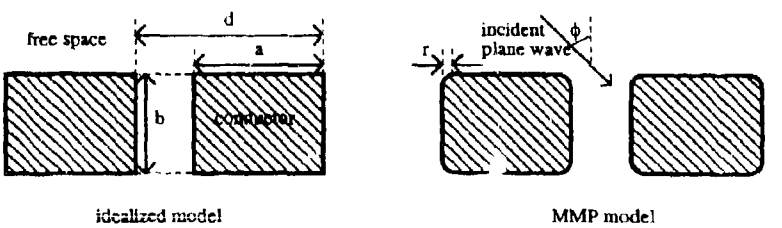

Figure 4: Idealized model used by several methods and MMP model with rounded edges for estimating the error made by the idealization. The following data were used in [8]: d=1μm, a=0.5μm, b=0.4μm, λ=1.5μm, n=0.3+8i, ϕ=0.

Among the methods compared in [8,9], the modal method [10] is considered to be most accurate. When the radius r of the curvature of the edges in the MMP model is very small, the results of the MMP computation are closer to the results of the modal method than the results of any of the other methods. For example, the transmitted 0-order efficiency for the s-polarization computed with the modal method, the modal-SIBC and Lochbihler's method is 0.76785, 0.76501, 0.764979 respectively. Two different MMP models with r/d=0.01 led to the values 0.76647 and 0.76684. The first of these models was relatively rough and inaccurate with a maximum mismatching of about 9%. Thus, one can conclude that very accurate results are obtained with 3D MMP.

It seems that MMP allows to achieve any desired accuracy if the radius is sufficiently small (r/d=0.01 is still too large for obtaining an accuracy of more than 3 digits!) and if the discretization is sufficiently fine, but for obtaining an accuracy of several digits for the efficiencies, the computation time can be quite long (several hours on a PC for one single run with a fixed frequency, fixed excitation, etc.). For realistic values of the radius r, one can obtain fast and accurate MMP results. If one compares the efficiencies in function of the radius r, one finds that the influence of this parameter is far from being negligible (see also Figure 5). For example, for r/d=0.02 the transmitted 0-order efficiency for the s-polarization is already 0.7425. From a comparison of several MMP models it is assumed that all 4 digits are exact.

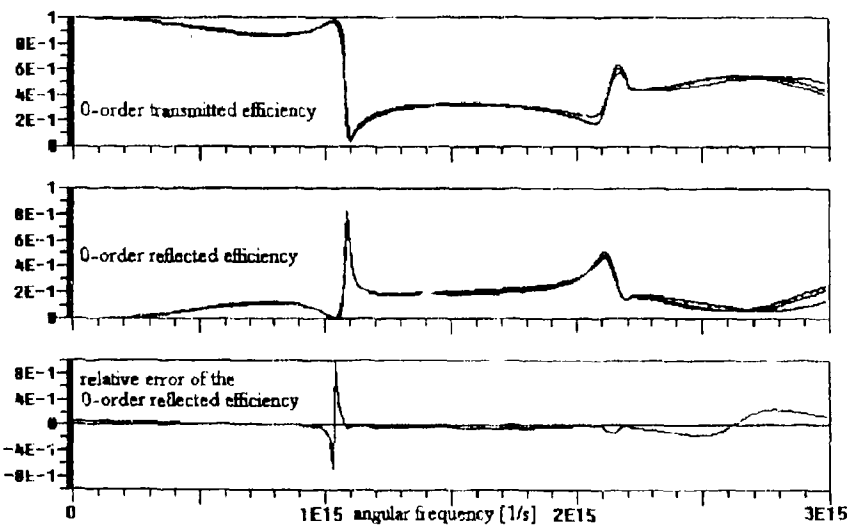

Figure 5: 0-order efficiencies (top and middle) versus angular frequency ω for the MMP models illustrated in figure 4 for r/d=0.025, 0.05, 0.1, ϕ=45°, complex refraction index n=0.3+8i. Relative error ε=2(e(0.05)-e(0.025))/(e(0.05)+e(0.025)) of the 0 order reflected efficiencies, where e(0.05) is the 0 order reflected efficiency for r/d=0.05.

SURFACE IMPEDANCE BOUNDARY CONDITIONS (SIBC)

Several numerical methods seem to have problems with the material properties of the conductors. For avoiding such problems, Surface Impedance Boundary Conditions (SIBC) are applied by some authors. The value and problems of SIBC shall not be discussed in this paper but it should be mentioned that such boundary conditions are available in the 3D MMP code upon request. Thus, one can easily compare MMP computations with and without SIBC. Introducing SIBC into a 3D MMP model has the following effect: the number of boundary conditions on the conductor is reduced and the field inside the conductor is not approximated by a series expansion anymore. Thus, the size of the matrix to be solved and the computation time can considerably be reduced. Some results are presented in Figure 6.

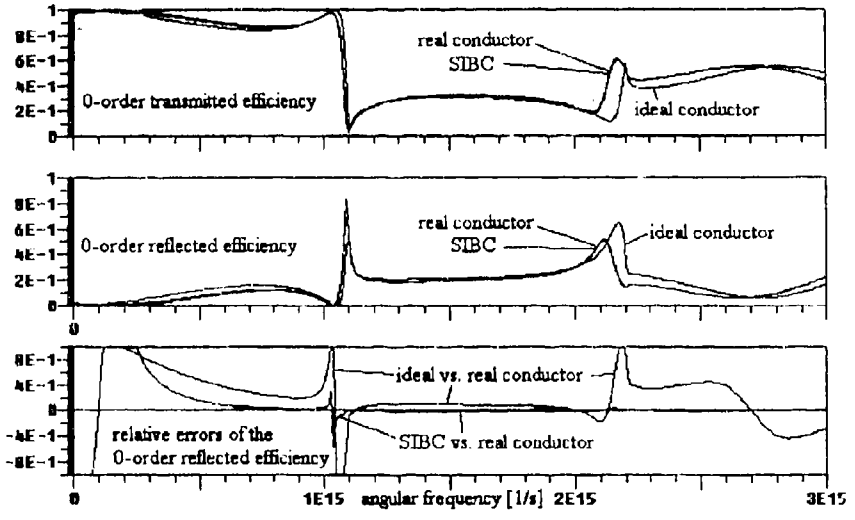

Figure 6: Efficiency versus angular frequency ω. 3D MMP computation of the grating illustrated in figure 4 for r/d=0.05, φ=45°, complex refraction index n=0.3+8i. Comparison of three models: 1) exact computation (real conductor), 2) simplified model with SIBC on the conductor, 3) idealized model with an ideal conductor.

The 3D MMP results obtained with the SIBC are much better than the results obtained with an ideal conductor. The accuracy obtained with SIBC obviuosly is high for frequencies above the first resonance. It is important to note that the complex refraction index is constant in these computations. This assumption is neither realistic nor necessary for the 3D MMP computation. It has been used because the frequency dependence of the refraction index was not available.

REMARKS ON THE EFFICIENCY OF THE NUMERICAL TECHNIQUE

The introduction of fictitious boundaries and of periodic boundaries is most important for obtaining high flexibility and user-friendliness. Obviously, these boundaries increase the total length of the boundaries to be discretized. Periodic basis field functions would allow to compute periodic structures without these additional boundaries. Thus, one is tempted to assume that this could be an even more efficient approach, provided that efficient algorithms for the evaluation of the periodic basis functions are found. This might be true for such cases where the fictitious boundaries are much longer than the real boundaries. But one should not forget that introducing fictitious boundaries often allows to increase the error on these boundaries and to reduce the error on the real boundaries at the same time. This means that one can obtain more balanced errors and that one can reduce not only the number of equations on the real boundaries but also the total number of equations. I.e., introducing appropriate, "unnecessary" fictitious boundaries can make MMP models more efficient. A longer total length of all boundaries does not always require a higher total number of equations and expansions. A typical example can easily be found in the simple model discussed above. If the fictitious boundary is very close to the surface of the rectangular wires, the field has (almost) singular points on the fictitious boundary. Consequently, the convergence of the Rayleigh expansion is very bad and many orders are required for obtaining useful results. To compute many unknown parameters in the Rayleigh expansion, a very fine discretization of the fictitious boundary is required. If the fictitious boundary is moved away, the total length of all boundaries is increased. At the same time, the field on the fictitious boundary becomes smoother, much fewer Rayleigh terms are required, and a much rougher discretization is sufficient for obtaining the same accuracy.

References

[1] Ch. Hafner and L. Bomholt, *The 3D Electrodynamic Wave Simulator*, John Wiley & Sons, 1993.

[2] Ch. Hafner, *The Generalized Multipole Technique for Computational Electromagnetics*, Artech House Books, Boston, 1990.

[3] R. Petit and F. Zolla, "The Method of fictitious sources....", *to be published*.

[4] A. Boag, Y. Leviatan and A. Boag, "Analysis of diffraction from doubly periodic arrays of perfectly conducting bodies by using a patch-current model", *J. Opt. Soc. Am. A*, 7, no. 9, 1990.

[5] J. Li and S. Kiener, "On the solution of periodical structures with GMT", *Proc. IEEE AP-S Int. Symposium*, Dallas, May 1990.

[6] J. Li, *GMT&MMP Applied to the Computation of General Periodic Structures*, Diss. ETH No. 10154, Zurich, 1993.

[7] Ch. Hafner, "Multiple Multipole (MMP) computations of guided waves and waveguide discontinuities", *Int. J. of Numerical Modelling*, vol. 3, 1990.

[8] J. Lochbihler, *Eine theoretische und experimentelle Untersuchung von hochleitenden Drahtgittern im Resonanzbereich*, Diss. TU München, ISSN 0178-0719, Munic, 1993. (MPE Report 246)

[9] H. Lochbihler, R.A. Depine, *Diffraction from highly conducting wire gratings of arbitrary cross section*, Journ. Mod. Opt., vol. 40, 1993.

[10] L.C.Botten, M.S. Craig, R.C. McPhedran, J.L. Adams, J.R. Andrewartha, *The finitely conducting lamellar diffraction grating*, Optica Acta, vol. 28, 1981.

SESSION 17:

PROPAGATION
AND
IMAGING

Chair: Dennis Andersh

A PHYSICAL OPTICS MODEL FOR SCATTERING OF HF RADIATION BY IRREGULAR TERRAIN *

G. J. Burke
Lawrence Livermore National Laboratory
P.O. Box 5504, L-156, Livermore, CA 94550

Abstract

Physical optics models were developed for scattering of HF radiation by irregular terrain when an antenna is located on or near the scattering surface. The primary interest was in skywave radiation patterns for communication links using the ionosphere. Second-order reflections were included in the solution through an image approximation, and the UTD result for an impedance half-plane was used to reduce reflections due to truncating the current distribution on the surface. Arbitrary 2-D or 3-D terrain profiles can be entered into the codes, and the source can be an antenna with currents generated by the NEC method-of-moments code or a point source. Results were validated by comparing with 2-D integral equation solutions for actual terrain contours.

1. INTRODUCTION

The scattering of HF radiation by irregular terrain is difficult to model due to the size of the region involved and the variety of conditions that may occur. Also, the terrain scattering depends on the radiation pattern of the antenna, which itself may present a difficult modeling problem. Several techniques for modeling terrain effects were considered in a previous study [1] and can be divided into solutions based on integrating induced sources over the ground surface, ray-based methods of geometrical optics or GTD/UTD and differential equation solutions. A 3D geometrical optics model for terrain scattering was described in [1], and related investigations have been conducted by Breakall et al. [2] of UTD models and by Janaswamy [3, 4] of integral and differential equation techniques.

This report describes the development and validation of physical optics (PO) models for scattering of HF radiation by two- and three-dimensional terrain surfaces. Results of some initial PO calculations for terrain scattering were included in [5]. It has since been found that in order to get accurate results when the antenna is located on the irregular terrain it is necessary to invoke reciprocity to put the source at the distant receiver location and evaluate the field at the original antenna location near ground. In addition, second-order reflections in the vicinity of the antenna and receiver were found to be important. Reflected and diffracted fields from the UTD solution for an impedance half-plane were added to the model to reduce ripple in the radiation patterns that would result from truncating the PO currents on the surface. This last extension saves computation time by reducing the range over which the PO currents must be integrated.

* Work performed under the auspices of the U. S. Department of Energy by the Lawrence Livermore National Laboratory under Contract W-7405-Eng-48.

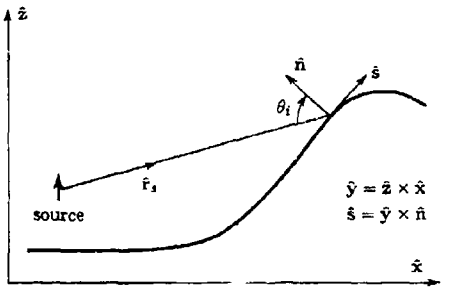

Fig. 1. Coordinates for the 2-D model of the terrain surface.

The PO codes will model a terrain with an arbitrary elevation profile by interpolating between input elevation values, and the transmitting antenna can be a point or line source or segment coordinates and current values from a modified version of the NEC-MoM code.

The development of the PO models for 2-D and 3-D terrain scattering is briefly described in Section 2 of this paper. Also, a code for solving the Fredholm integral equations (MFIE for vertical polarization and EFIE for horizontal polarization) was developed to validate the PO models, and this solution is described in Section 3. Section 4 contains some results generated to validate the codes. A more complete description of the PO and integral equation models and additional examples for validation are contained in [6].

2. THE PHYSICAL OPTICS MODEL

For the 2-D PO model the terrain surface will be assumed to vary in height in the x direction ($z = h(x)$) and be constant in the y direction, with surface normal $\hat{\mathbf{n}}$ and tangent vector $\hat{\mathbf{s}}$ as shown in Figure 1. The lossy ground is characterized by relative permittivity ϵ_r and conductivity σ, and these parameters may be functions of x. Also needed are the wavenumber in air $k_0 = \omega\sqrt{\mu_0\epsilon_0}$ and in the earth $k_g = k_0\sqrt{\tilde{\epsilon}_g}$ where $\tilde{\epsilon}_g = \epsilon_r - j\sigma/\omega\epsilon_0$. The wave impedances in air and earth are $\eta_0 = \sqrt{\mu_0/\epsilon_0}$ and $\eta_g = \eta_0/\sqrt{\epsilon_g}$, respectively, and the time dependence $e^{j\omega t}$ is assumed.

In PO the current at each point on the surface is determined by the direct, incident field from the source with the assumption that the field reflects as it would from an infinite plane tangent to the surface at that point. Hence PO is sometimes called the tangent-plane approximation. On a lossy surface an impedance boundary condition is enforced and reflected fields are determined by the Fresnel plane-wave reflection coefficients. At points shaded from direct illumination by the source the PO currents are assumed to be zero. An arbitrary incident field can be decomposed into TE and TM components, and in 2-D these components are not coupled by scattering. It is possible to solve two scalar scattering problems for the transverse field components, but the vector electric field will be computed since that is the field most often measured. While the measurement points will be in the far field of the antenna, they may not be in the far field of the

terrain scattering surface, so $E/H = \eta_0$ cannot always be assumed.

If the incident fields at point (x, z_s) on the surface, where $z_s = h_s(x)$, are $\mathbf{E}^i(x, z_s)$ and $\mathbf{H}^i(x, z_s)$ the equivalent surface currents given by the PO approximation are

$$\mathbf{K}_{\mathrm{TM}}(x) = -\hat{\mathbf{n}} \times \mathbf{E}^t_{\mathrm{TM}}(x, z_s) = -(1 - R_{\mathrm{TM}}) \left[\mathbf{E}^i(x, z_s) \cdot \hat{\mathbf{s}}\right] \hat{\mathbf{y}} \tag{1}$$

$$\mathbf{J}_{\mathrm{TM}}(x) = \hat{\mathbf{n}} \times \mathbf{H}^t_{\mathrm{TM}}(x, z_s) = -(1 + R_{\mathrm{TM}}) \left[\mathbf{H}^i(x, z_s) \cdot \hat{\mathbf{y}}\right] \hat{\mathbf{s}} \tag{2}$$

for TM polarization and

$$\mathbf{K}_{\mathrm{TE}}(x) = -\hat{\mathbf{n}} \times \mathbf{E}^t_{\mathrm{TE}}(x, z_s) = (1 + R_{\mathrm{TE}}) \left[\mathbf{E}^i(x, z_s) \cdot \hat{\mathbf{y}}\right] \hat{\mathbf{s}} \tag{3}$$

$$\mathbf{J}_{\mathrm{TE}}(x) = \hat{\mathbf{n}} \times \mathbf{H}^t_{\mathrm{TE}}(x, z_s) = (1 - R_{\mathrm{TE}}) \left[\mathbf{H}^i(x, z_s) \cdot \hat{\mathbf{s}}\right] \hat{\mathbf{y}} \tag{4}$$

for TE polarization, where $\mathbf{E}^t$ and $\mathbf{H}^t$ are the total surface fields. The reflection coefficients are given by [7]

$$R_{\mathrm{TE}} = E^r_y / E^i_y = \frac{k_0 \cos\theta_i - k_g \cos\theta_t}{k_0 \cos\theta_i + k_g \cos\theta_t} \tag{5}$$

and

$$R_{\mathrm{TM}} = H^r_y / H^i_y = \frac{k_g \cos\theta_i - k_0 \cos\theta_t}{k_g \cos\theta_i + k_0 \cos\theta_t} \tag{6}$$

where the angle θ_i is between the incident ray and the normal, so that $\cos\theta_i = -\hat{\mathbf{r}}_s \cdot \hat{\mathbf{n}}$, and θ_t is the complex angle of the ray transmitted into the ground

$$\cos\theta_t = \left[1 - (k_0/k_g)^2 \sin^2\theta_i\right]^{1/2}.$$

The total surface currents are then

$$\mathbf{K}(x) = \mathbf{K}_{\mathrm{TE}}(x) + \mathbf{K}_{\mathrm{TM}}(x)$$

$$\mathbf{J}(x) = \mathbf{J}_{\mathrm{TE}}(x) + \mathbf{J}_{\mathrm{TM}}(x)$$

over illuminated parts of the surface. The scattered field is obtained by integrating over the surface currents as

$$\mathbf{E}^s(x, z) = -j\omega\mu \int_{x_1}^{x_2} \bar{\Gamma}_c(\mathbf{r}, \mathbf{r}') \cdot \mathbf{J}(x')\, ds' + \int_{x_1}^{x_2} \nabla G_c(\mathbf{r}, \mathbf{r}') \times \mathbf{K}(x')\, ds' \tag{7}$$

where ds' is the element of length on the surface $ds' = \sqrt{1 + [h'_s(x')]^2}\, dx'$ and $\bar{\bar{\Gamma}}_c(\mathbf{r}, \mathbf{r}')$ is the dyadic Green's function. In two dimensions

$$\bar{\bar{\Gamma}}_c(\mathbf{r}, \mathbf{r}') = \left(\bar{\bar{\mathbf{I}}} + \frac{1}{k^2}\nabla\nabla\right) G_c(\mathbf{r}, \mathbf{r}')$$

$$G_c(\mathbf{r}, \mathbf{r}') = \frac{-j}{4} H_0^{(2)}(k|\mathbf{r} - \mathbf{r}'|)$$

where $\mathbf{r} = x\hat{\mathbf{x}} + z\hat{\mathbf{z}}$ is the vector to the field evaluation point, $\mathbf{r}' = x'\hat{\mathbf{x}} + h_s(x')\hat{\mathbf{z}}$ is the vector to the source point on the surface and $H_0^{(2)}$ is the Hankel function. The limits x_1 and x_2 should be positive and negative infinity, but in practice the integral is truncated at points beyond which the contributions are negligible.

In the direct application of PO the antenna on the ground produces fields over the terrain that determine the currents in equations (1) through (4). Significant scattering is expected from points over the irregular terrain and also from the ground near the antenna even if it is flat. Fields that reflect from the ground under the antenna and then are scattered by the terrain irregularities can also be important, and these represent second-order scattering terms. A second-order PO solution would require much more computation than first-order, or else difficult decisions about which terms to retain. However, when the antenna is located over flat ground the PO integral can be stopped over the flat region between the antenna and a mountain, where the contribution is small, and the direct and reflected rays from the antenna that illuminate the mountain can be obtained from geometric optics. This GO/PO model gave better accuracy than simple first-order PO. However, it cannot easily be extended to the case of an antenna located on the mountain. Also, PO is not accurate for an antenna near the surface of finitely conducting ground, even flat ground, unless the solution is modified to use the accurate near field over the ground, involving Sommerfeld integrals or approximations.

To avoid these difficulties reciprocity was invoked to make the distant receiver, sweeping an arc in the sky, the source of $\mathbf{E}^i$ and $\mathbf{H}^i$ in equations (1) through (4). The scattered field at a test dipole at the antenna location near ground is then evaluated using the near-field form of equation (7). To approximate the field that scatters from the terrain and then is reflected again from the ground near the antenna, the field is also evaluated at the image of the test dipole reflected in a plane tangent to the ground under the antenna. Since the equivalent currents in equations (1) through (4) were obtained with the assumption of zero field behind the surface, the evaluation at the image point should yield zero field if only first-order scattering occurs. The actual field evaluated at the image point will include fields that have scattered once from the terrain before passing through the surface and also errors due to truncation of the PO integrals and curvature of the surface. When the field at the test dipole and its image are combined these errors can be partially cancelled for horizontal polarization where they are often most significant.

The field evaluated at the image of the test dipole is assumed to actually reflect from the surface and reach the antenna location, and hence should be multiplied by the appropriate reflection coefficient before being added to the direct field. However, the angle of incidence needed in the reflection coefficient is not known since the field has an integral rather than a ray representation. To approximate the angle of incidence the terrain is initially searched to determine the average angle for all points on the terrain than can be seen from the location of the image test dipole. This angle is not allowed to be less than about 10 degrees to avoid negative angles when the antenna is on top of a mountain. In such a case the second-order reflection would actually take place on the side of the mountain with a positive angle, but an accurate configuration could not be determined without ray tracing. Despite these approximations, the inclusion of the image field was found to significantly improve the accuracy in the cases tested. The field due to the image of the distant source (original receiver) is also included in the incident fields in equations (1) through (4) when it illuminates the front of the scattering surface.

The final addition to the PO model was to include the fields reflected and diffracted from half-planes extending from the limits of the PO integral to negative and positive infinity. The UTD solution for an impedance half plane by Volakis [8] was used. UTD does not provide a seamless transition from the PO solution due to the different edge treatments. However, the inclusion of

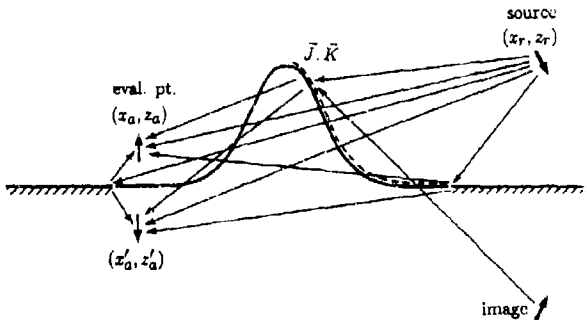

Fig. 2. Illustration of the components treated in the PO model, including reflection and diffraction from the UTD half-planes.

the UTD half-planes does provide a substantial reduction in the ripple in the radiation pattern due to truncation of the PO integral. The terms included in the final PO model are illustrated in Figure 2. The extension of the 2D PO model to 3D is straight forward, with the UTD half-planes replaced by a frame formed by four half-planes.

3. THE 2-D INTEGRAL EQUATION MODEL

Integral equation solutions for the current on the terrain surface were developed as a means to check the validity of the PO results and also were invaluable for determining which contributions were important in developing the PO model. The MFIE was solved for vertical polarization and the EFIE for horizontal polarization [9] with an impedance boundary condition over the surface. For TE polarization the equation for the magnetic surface current K_s is

$$E_y^i(\mathbf{r}) = \frac{1}{2}K_s(x) - \int_{x_m}^{x_p} K_s(x') \left(-j\omega\mu/\eta_g + \frac{\partial}{\partial n'}\right) G_c(\mathbf{r},\mathbf{r}') \, (\hat{\mathbf{z}} \cdot \hat{\mathbf{n}}')^{-1} \, dx' \qquad (8)$$

where $x_m \le x \le x_p$ and $\partial G_c/\partial n' = \hat{\mathbf{n}}' \cdot \nabla' G_c$. The equation for TM polarization is related to (8) through duality, so only one code is needed. The only difference in the solutions is that the source of E_y^i in (8) will be an electric line current in the y direction, while the source of H_y^i for TM polarization will be a strip of vertical electric current J_z extending over $-\infty < y < \infty$.

The integral equations were solved by the method of moments with pulse expansion of the current and point matching. To reduce reflections in the solution at the ends of the integration range the first and last pulse basis functions were extended to negative and positive infinity, respectively. The extensions used functions of the form $\exp[-jkR_s(x)]/R_s^n(x)$, where $R_s(x)$ is the distance from the source antenna to the point (x, z_s) on the surface, and the exponent n was taken as 1/2 for vertical polarization and 3/2 for horizontal polarization. The integration contours to infinity were deformed into the complex x plane to obtain rapid convergence. This extension of the basis functions essentially eliminated reflections in the solution for current. However, a simila

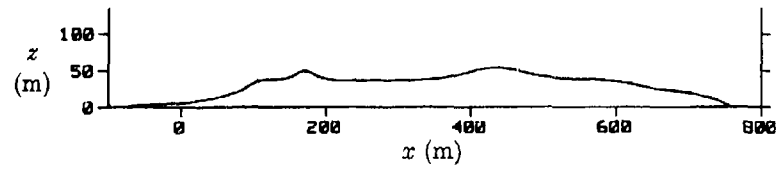

Fig. 3. Terrain profile for the Cedar Valley, Utah site.

extension of the current in computing the radiated field is more difficult since the integration in the complex x plane could encounter branch cuts. Hence the current was truncated at x_{v_0} and x_p in computing the radiated field, producing some ripple in the pattern unless the limits extended sufficiently far from the source.

4. RESULTS AND VALIDATION

To validate the PO model and the independent work reported in [2], [3] and [4], measurements have been made of the radiation from antennas in hilly terrain at a site in Utah [10]. The terrain shape along the helicopter flight path at Cedar Valley, read from a topographic map for input to the 2D PO code, is plotted in Figure 3. Vertical monopole and horizontal dipole antennas were located at the base of the hill ($x = 0$ m) and on top of the hill ($x = 170$ m) and also at a site in the valley behind the hill. A vertical dipole at height 2 m above the surface and a horizontal dipole at 4.57 m above the surface were used for validation. The patterns computed by the PO code for the actual monopole and dipole dimensions were very close to the patterns of these point sources.

The results of the PO model were first compared with the integral equation solution to postpone dealing with real-world uncertainties. Comparisons are shown in Figure 4 for vertical and horizontal sources at the base of the hill and at the top of the hill at 27.7415 MHz. Generally good agreement is seen between the PO and integral equation models in these cases. Similar agreement was obtained at 8.015 MHz. The codes were also compared for a simple Gaussian curve approximating the front side of the hill at Cedar Valley. This smooth hill produced a scattering pattern with much less fine detail, and the codes were again in good agreement. The PO model was also compared with radiation patterns measured at Cedar Valley and was in agreement on the main features of the pattern, with some differences apparently due to uncertainties in the ground profile or factors in the measurements that were not taken into account.

4. CONCLUSION

A model using physical optics was developed for scattering of HF radiation by irregular terrain. Both 2D and 3D models were developed, since the 2D model offers a faster solution and simpler definition of the terrain shape, while the 3D model is needed when scattering occurs from obstacles out of the vertical plane from transmitter to receiver. Reciprocity was invoked to place the source at the distant receiver location, and second order scattering was included through geometrical optics approximations. The UTD solution for an impedance half-plane was included

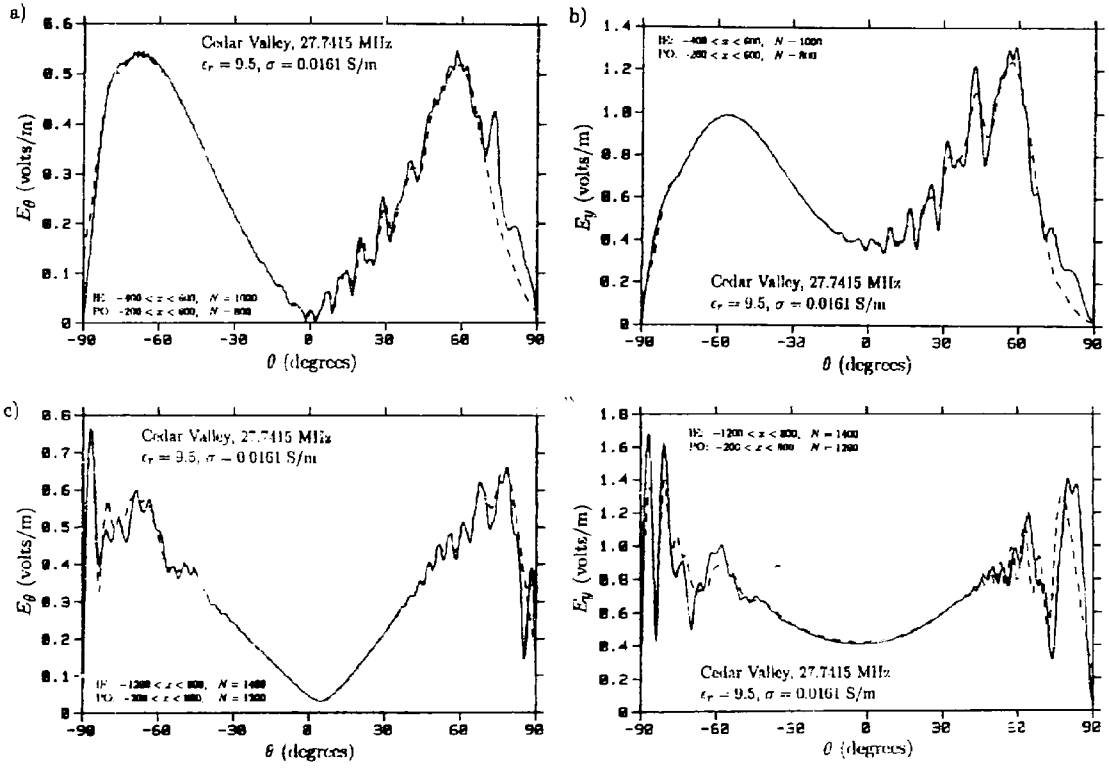

Fig. 4. Radiation patterns of antennas at 27.7415 MHz on the terrain of Figure 3: a) Vertical dipole at bottom of hill; b) Horizontal dipole at bottom of hill; c) Vertical dipole at top of hill; d) Horizontal dipole at top of hill. Results from the PO model (solid) and integral equation solution (dashed) are compared.

to reduce errors due to truncating the PO integral. Results from the PO codes for an actual terrain profile were in good agreement with an integral equation solution which is expected to be accurate.

The PO codes are set up to model terrain of arbitrary shape and to read antenna geometry and currents from a file written by a modified version of the NEC-MoM code. Alternately, point or line sources can be used. The terrain shape is described by generating a file containing elevations at a number of points read from a topographic map, and the code applies cubic-spline interpolation to the points entered to determine the surface for the PO solution.

This work was supported by the Naval Security Group Command through CDR Gus K. Lott.

References

[1] G. J. Burke, "Numerical Modeling of HF Skywave Radiation from Antennas in Irregular Terrain," Tech. Rept. UCRL-ID-105656, Lawrence Livermore Nat. Lab., Nov. 1990.

[2] J. K. Breakall, R. J. Lunnen, D. H. Werner, J. S. Young and T. A. Erdley, "Interim Report, High Frequency (HF) Antenna Siting Effects in Irregular Terrain," Penn State University Applied Research Laboratory, 15 Dec. 1991.

[3] R. Janaswamy, "A Fredholm Integral Equation Method for Propagation Predictions Over Small Terrain Irregularities," *IEEE Trans. Antennas and Propagation*, Vol. AP-40, pp. 1416-1422, Nov. 1992.

[4] R. Janaswamy, "Application of the Measured Equation of Invariance to Wave Propagation over Irregular, Inhomogeneous Terrain," Naval Postgraduate School Report NPS-EC-93-018, October 1993.

[5] R. H. Ott and G. J. Burke, "Comparison of Numerical Integration of RING Surface Fields and 1st Order Physical Optics for the Skywave Field of HF Antennas in the Vicinity of the Utah Test Site and an Electrically Large Gaussian Ridge," Conference Proceedings, 8th Annual Review of Progress in Applied Computational Electromagnetics, Monterey, CA, March 16-20, 1992.

[6] G. J. Burke, "Numerical Modeling of HF Skywave Radiation from Antennas in Irregular Terrain," To be published as a Lawrence Livermore Nat. Lab. Technical Report, 1994.

[7] J. A. Stratton, *Electromagnetic Theory*, New York: McGraw-Hill, 1941.

[8] J. L. Volakis, "A Uniform Geometrical Theory of Diffraction for an Imperfectly Conducting Half-Plane," *IEEE Trans. Antennas and Propagation*, Vol. AP-34, pp. 172-180, 1986.

[9] A. J. Poggio and E. K. Miller, "Integral Equation Solutions of Three-Dimensional Scattering Problems," Chapt. IV in *Computer Techniques for Electromagnetics*, edited by R. Mittra, Pergamon Press, NY, 1973.

[10] G. H. Hagn, D. L. Faust, "Cedar Valley Antenna Tests, Covering Period 10-24 May 1990," SRI International, Arlington VA, 28 May 1990.

Enhanced Facet Model for Terrain: Xpatch SAR Image Prediction for Ground Vehicles in Benign Clutter Environments

Patricia A. Ryan
Georgia Tech Research Institute, Atlanta Georgia

Richard. F. Schindel and Ron Dilsavor
Sverdrup, Dayton Ohio

Dennis J. Andersh and Edmund K. Zelnio
WL/AARA, WPAFB, Dayton Ohio

Abstract

As high frequency RCS prediction techniques have matured such that simulated data is useful for object algorithm development, there is interest in the development of prediction models for objects in natural terrain environments. Because the return from a given class of terrain is a complex function of geography and weather conditions, models for terrain reflectivity are based on measured data. The development of theoretical scattering models in combination with random process models is of interest for the application of ground scene imagery prediction. Xpatch is used to predict SAR imagery of a ground object in a sand terrain setting modeled by a faceted ground plane with a Gaussian height distribution. Statistical analysis indicates the predicted imagery is suitable for preliminary object algorithm development based on first order statistical differences in terrain and object pixel returns. The predicted image data is not suitable for object algorithm development based on polarimetric scene returns.

Introduction

Advances in digital signal and image processing capabilities and speed in on board radar hardware are allowing more sophisticated object detection and classification algorithms to be developed for future radar systems. High quality measured data taken from a simulated scenario of interest can be used to test new detection or classification algorithms. However, it is cost prohibitive to measure every scenario geometry and environment of interest. The development of an accurate computer model for predicting radar sensor images of ground objects in land clutter environments allows the radar image prediction of additional scenario geometries and environments. The modeled image data can then be used for more complete testing of object detection and classification algorithms.

In Radar Cross Section (RCS) signature analysis of discrete objects shows that multiple interactions dominate the scattering pattern at non cardinal aspects. It is likely that multiple bounce interactions between a ground object and its environment are also critical at non cardinal angles. Thus, any scene model that is used to predict data for algorithm development must include a multiple interaction capability to model the scattering interactions between elements in a scene.

Xpatch, based on the Shooting and Bouncing Ray (SBR) technique developed by S. W. Lee and colleagues at the University of Illinois[1], is providing the most accurate simulated RCS data for reflective objects. SBR models multiple bounce interactions and shadowed regions of the object that are important for an accurate prediction for any practical vehicle.

Theoretical models for terrain scattering have been investigated since the 1950's. Early theoretical terrain models postulated a facet model for rough terrain based on geometrical optics [2]. The facets that are oriented in the specular direction of the radar contribute to the terrain cross section, while facets that are not oriented towards the radar do not. In early facet models, multiple bounce between facets forming the terrain model were not computed.

Xpatch is used to predict Synthetic Aperture Radar (SAR) imagery of ground vehicles on a sandy road surface. A Gaussian distribution of height is used to generate a faceted terrain to simulate a rough unimproved road setting, and a flat ground plane is used to simulate flat ground. A dielectric constant for sand is assigned to both terrain models. Sample SAR imagery for the faceted ground plane case and flat ground plane case is presented, and the statistical distribution of terrain returns in a sample rough ground plane image is computed to asses the realism of the simulated imagery.

Since the SBR technique models the multiple bounce interactions between the object and terrain facets and interactions between terrain facets, the Xpatch model provides an enhanced facet model for terrain returns. This paper describes the development of the enhanced facet model and presents sample simulated SAR imagery. Statistical analysis of predicted X band imagery is discussed.

Development of Enhanced Facet Model for SAR Image Prediction

Figure 1 shows a flow chart of predicting a SAR image of an object on a terrain background using WL/AARA radar modeling tools. The ground objects used in this project were developed in ACAD by Viewpoint, and the files were saved in IGES format. The ground plane facet representation for a flat or rough faceted terrain model is created by the FACET_TERRAIN option in Cifer.

Measured SAR data is usually characterized by the center frequency and the range and cross range resolution capabilities of the imaging radar. SAR_PARAMS, computes the frequency bandwidth, step size, aperture width and azimuth step size for swept frequency and angle RCS predictions based on the input scene size and desired image resolution.

To simulate the SAR radar signal processing directly, Xpatch predicts the RCS of the object over a bandwidth of frequencies and a range of angles. The SBR technique is used to compute the RCS of the input object geometry for the input incident and scattered directions. A grid of incident rays is launched at an object from the radar direction. Geometrical Optics is used to compute the reflection of the ray from the object surface. A reflected ray from one point on the object surface can hit the object surface at a second point. GO reflections are computed up to the maximum number of "bounces" specified in the input file. The contribution of rays emerging from the object surface are summed to compute the scattered far field. Xpatch includes a ray divergence factor for curved surfaces, a capability to handle layered material transmission/reflection, and first order edge diffraction

To simulate a SAR image, the swept frequency and azimuth angle RCS data predicted by Xpatch is processed with a 2D Inverse Fast Fourier Transform (IFFT). KHOROS is a visual programming environment that includes data and image processing tools, and image display capabilities. A KHOROS workspace reads the Xpatch output RCS data file, performs the IFFT processing, and displays the resulting 2D SAR image.

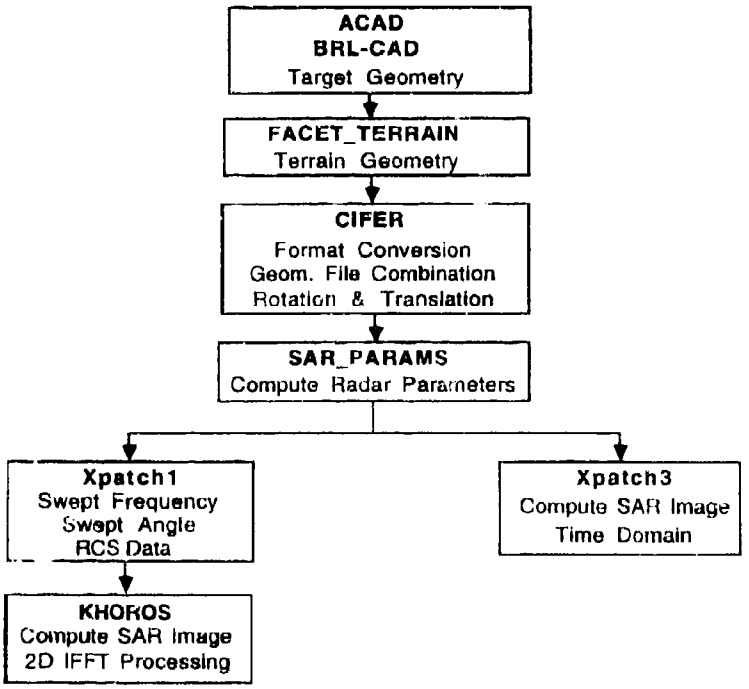

Figure 1: WL/AARA SAR image simulation process.

Computing the data for a SAR image of a complex target requires significant computing resources. Xpatch includes a SAR simulation capability that applies time domain mapping methods to form the SAR image from the object returns computed at the center of the aperture width at the center frequency. The main accuracy limitation of this method is that the image is formed at the center of the aperture width, such that the field is assumed constant over the aperture. Criteria for when this approximation is valid are not well defined.

Xpatch Simulated SAR Imagery of Ground Objects on Terrain

The Xpatch RCS model, is used to predict SAR imagery of ground objects on a sandy terrain surface. The terrain is modeled as 100 ft. by 100 ft. rough sand surface with a Gaussian distribution of height and as a flat sand surface also 100 ft by 100 ft. Triangular terrain facets are formed by a grid of points spaced 1 ft apart. The rms surface roughness of the rough sand surface is modeled as 3 inches The frequency dependent dielectric constant [3] and the rms surface roughness as a function of wavelength is shown in Table

1. As the surface roughness is greater than 0.1λ at all frequencies, the terrain is considered rough by the Rayleigh roughness criterion [4].

Scene images are predicted at 0.5 GHz, 1 GHz and 10 GHz. For 0.5 and 1 GHz the range and cross range resolution in the simulated imagery is 1 ft. At 10 GHz, the simulated imagery resolution is 3 inches. Table 2 summarizes the radar parameters for the SAR image simulation. 2 rays per wavelength are specified for the incident ray grid. The maximum number of bounces for the SBR computation of the object scattered field is 10, and the first bounce is computed by the hardware Z buffer as opposed to straight PO.

Figure 2 shows the ray behavior for the case of a tank on the smooth sand surface. The radar is at 30 degrees elevation for this monostatic scenario. This Xpatch Previewer visualization shows that only terrain/object interactions close to the tank contribute to the scene return. The rays that are incident on the terrain but do not bounce from the terrain to the tank reflect off the terrain away from the radar. There are no terrain/terrain interactions. Xpatch3, the time domain SAR simulation, is used to simulate a SAR image from the 30 degree elevation aspect picture at 1 GHz. The simulated image of the tank over the smooth terrain is shown in Figure 3. This image is consistent with the ray behavior shown in Figure 2. The only terrain contribution to the image occurs near the tank. The edge terms are an artifact from truncating the terrain model that can be removed in image processing. The terrain that is not involved in a terrain/object interaction does not contribute any significant return to the image.

The ray behavior for the case of a tank on the rough sand surface is shown in Figure 4. Again, the radar is at 30 degrees elevation. This visualization shows terrain/object interactions near the tank, terrain/object interactions between an outlying terrain region and the tank, and terrain/terrain interactions. The random orientation of the facets simulating a sandy terrain scatter the incident radiation in random directions. The random facet model in combination with the multiple bounce capability of Xpatch simulates the more omni-directional diffuse scatter expected from a rough surface. The corresponding simulated SAR image is shown in Figure 5. This image confirms the ray behavior shown by the Previewer. The rough terrain scatters the incident energy in a diffuse manner, thus a portion of the terrain scattered field is directed back towards the radar.

Figure 6 shows a predicted image of a fire truck over the rough sandy terrain. This image is predicted with Xpatch3 at an elevation angle of 10 degrees and azimuth angle broadside to the vehicle for HH polarization. The frequency is 10 GHz, and the image bin size is 3 inches by 3 inches. A density function computed from 10,000 terrain pixels in the image is shown in Figure 7. The mean pixel reflectivity, -20.0 dB, is proportional to the terrain reflectivity, and the standard deviation is 4.6 dB. The mean to median ratio is 0.98, and the density function is approximately Gaussian. Figure 8 shows the pixel reflectivity density function for the HV polarization. The mean HV pixel reflectivity is -46 dB, and the standard deviation is 7.1 dB. Although the mean to median ratio is 0.99, the density function appears weighted towards the lower pixel reflectivities.

A direct comparison to measured data for terrain clutter is difficult because published results from separate measurement programs for a given terrain type vary by as much as 10 dB. Long[5] gives a 8.6 dB range for the X band HH polarized σ^o, radar cross section per unit area, for disked field at a depression angle of 10 degrees. A spread of 17 dB is given for an asphalt road with gravel. The pixel reflectivity standard deviation indicates that 80% of the pixel reflectivities are within a 9.2 dB range. Thus, the pixel reflectivity density function width predicted by Xpatch3 is within the expected range in comparison with similar terrain types.

Table 1: Frequency dependent dielectric constant [4] and surface roughness.

Frequency	Sand Rel. Permittivity	RMS Rough (λ)
0.5 GHz	2.55 - j 0.0250	0.127λ
1.0 GHz	2.55 - j 0.0160	0.254λ
10.0 GHz	2.55 - j 0.0092	2.54λ

Table 2: Radar parameters for SAR simulation.

Frequency (GHz)	Bandwidth (GHz)	Number Freq. Steps	Synthetic Aper. (Deg.)	Number Az. Step	Total Iterations
0.5	0.492	101	37.8	953	95,300
1.0	0.492	101	72.6	1593	159,300
10.0	1.968	401	9.42	15,237	6,130,000

The HV pixel reflectivity is 26 dB below the HH pixel reflectivity. The difference between the HH and HV return is higher than expected for sand terrain. In general rough surfaces tend to depolarize the incident field, thus the difference in the cross-polarized and and co-polarized fields is not as high as the difference for smooth surfaces. The large difference between the HH and HV return is caused by modeling the terrain by smooth flat plates.

Conclusions

Xpatch3 has been used to simulate SAR imagery of ground objects over rough sandy terrain. The predicted image pixel reflectivity distribution in the HH polarization predicted is in agreement with published ranges for similar terrain types. The HH reflectivity pixel distribution predicted by Xpatch3 is similar to the distribution predicted by empirical models that rely on statistical distributions characterized by a mean and spread factor. Because Xpatch uses a Fresnel reflection model for dielectric surfaces, the statistical distribution of predicted returns is a function of the terrain geometry model. Thus, the accuracy of the terrain reflectivity distribution predicted by the enhanced facet model depends on how accurately the statistics of the ground plane model represent the terrain type.

Preliminary object detection algorithms that exploit first order statistical differences between object returns and ground returns should be applied to the simulated data set. The rough facet terrain does not model the depolarization caused by a rough terrain surface. Therefore, the difference in HH and HV terrain returns predicted by Xpatch are higher than expected for rough terrain. Xpatch predicted SAR data for faceted terrain models is not appropriate for polarimetric object algorithm development.

Further analysis of simulated image data from rough facet terrain generated by a wider variety of statistical and texture distributions will quantify the relationship between physical model roughness and the terrain reflectivity distribution in simulated imagery. This investigation should be pursued if preliminary object algorithm development for ground objects in benign clutter environments based on this data is promising.

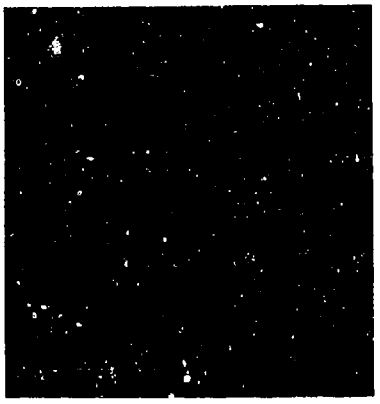

Figure 2: Xpatch Previewer ray diagram for tank on smooth ground plane: 0° Az. 30° El.

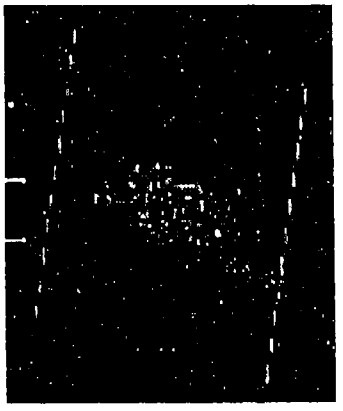

Figure 3: Xpatch3 predicted image of tank on smooth ground plane: 1 GHz, 0° Az. 30° El.

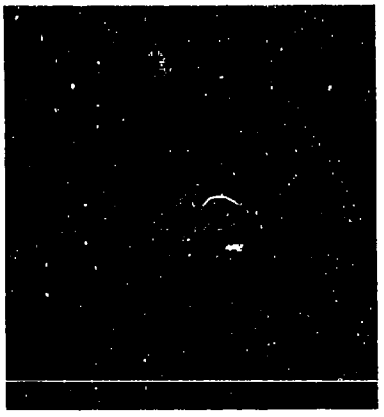

Figure 4: Xpatch Previewer ray diagram for tank on rough ground plane: 0° Az. 30° El.

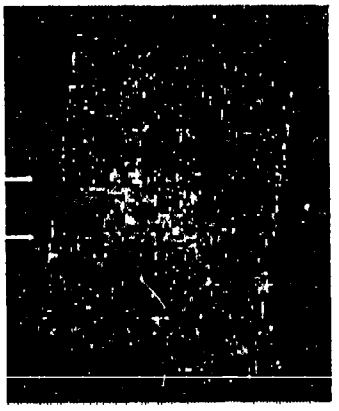

Figure 5: Xpatch3 predicted image of tank on rough ground plane: 1 GHz, 0° Az. 30° El.

Figure 6: Xpatch 3 simulated SAR image of fire truck over rough ground plane: 10 GHz, 90° Az. 10° El.

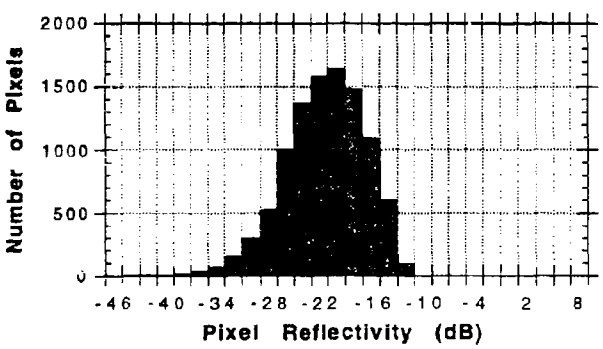

Figure 7: HH pixel reflectivity density.

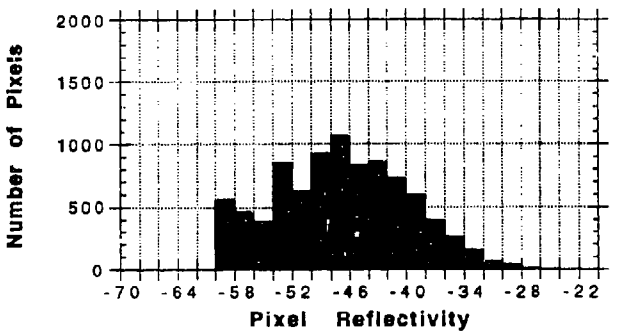

Figure 8: HV pixel reflectivity density.

Acknowledgments

This work was supported by the Air Force Office of Scientific Research (AFOSR) Summer Faculty Research Program.

References

[1] Lee S. W., "Xpatch1, A High Frequency RCS Computation Code for Facet Targets: Version 4.4", Defense Electromagnetic Analysis Company, Champaign, IL, 1992.

[2] Moore, R. K., "Ground Echo," in Radar Handbook, M. I Skolnik, Ed., McGraw Hill, New York, 1970, pp. 25-6 - 25-12.

[3] Harrington, R. F., Time Harmonic Electromagnetic Fields, McGraw Hill, New York, 1961, pp. 452-455.

[4] Beckmann, P. and A Spizzichino, The Scattering of Electromagnetic Waves from Rough Surfaces, Pergamon, New York, 1963.

[5] Long, M. W. Radar Reflectivity of Land and Sea, Lexington Books, Lexington Massachusetts, 1975, p. 235.

On The Use of Ray Tracing for Complex Targets[1]

Thomas Moore, Earl C. Burt, Forrest P. Hunsberger
Massachusetts Institute of Technology
Lincoln Laboratory
Lexington, MA 02173

1. Introduction

Modern high frequency codes are migrating towards the use of ray tracing as a means of computing the scattered field from complex objects. The current state of the art in ray tracing is codified in the Xpatch series of computer codes. There are a number of key issues that arise when developing ray tracing algorithms for complex scattering problems. This paper addresses three critical design issues: facetization effects, current element shadowing, and estimating the scattered fields that arise from multiple reflections of rays. These issues will be discussed in order in the following sections of this paper. The paper concludes with recommendations on these issues.

2. Facetization Effects

This section considers the effect of target model facetization. Complex models are typically modeled using flat triangular facets since tracing rays with flat surfaces is very efficient. The obvious effect of using facets is that many facets are required to accurately model a curved surface. There exists a point where the time required to trace rays with a very large faceted model exceeds the benefits of using facets in place of curved surfaces. Although the question of facet representation vs. curved surface representation is important, this section assumes that the model will be faceted. The question that is addressed in this section is what effect does facetization have on multiple reflections.

The effect of model facetization on multiple scattering from curved surfaces is best demonstrated by an example. Consider a electrically large cylinder in front of an electrically large plate. The cylinder is offset from the center of the plate in order to eliminate any effects due to symmetry. This geometry is depicted in Figure 1. In order to demonstrate the effect of the facetization of the cylinder, high resolution inverse synthetic aperture radar (ISAR) images are generated from predicted data using the Xpatch-1 code. The predicted data are generated over a frequency band from 9.5 GHz to 10.5 GHz. This yields a range resolution of approximately 25 cm.

Figure 2 contains an ISAR image of the cylinder-plate complex when the cylinder was facetized with 64 facets. An arc of responses appears down range from the plate. This arc is a consequence of the facetization of the cylinder. Figure 3a and 3b demonstrate the effect of increasing the facetization of the cylinder by factors of 2 and 4 respectively. It is clear from Figure 3 that the effect is not alleviated with moderate increases in the facetization of the cylinder. This is a non-intuitive result since it is generally believed that as the number of facets representing a surface is increased the accuracy also increases. This example indicates that increasing the facetization of geometries does not uniformly approach the curved surface representation.

The anomalous returns can be explained by examining the physics of the problem. The geometry configuration admits rays that reflect off of the cylinder, reflect off of the plate, and then reflect off of the cylinder back towards the receiver. Since the plate is the last body that the rays reflect from, the currents that

1. This work was sponsored by the Department of the Air Force under Contract F19628-90-C-0002 and Wright Laboratories AARA.

the rays set up on the plate are integrated back to the receiver. Figure 4 depicts a typical distribution of current patches that are set up by the reflected rays. Figure 4 indicates that the currents on this plate are discontinuous. It is these discontinuities that give rise to the anomalous returns. It is important to note that in the images higher ray densities do not mitigate this effect. A curved surface representation of the model would only mitigate this effect with a very large ray density.

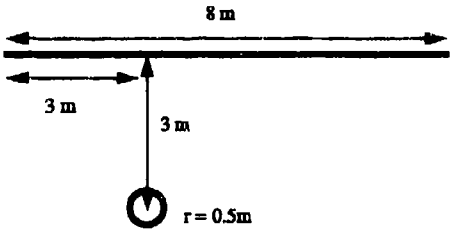

Figure 1. Geometry of the cylinder-plate example.

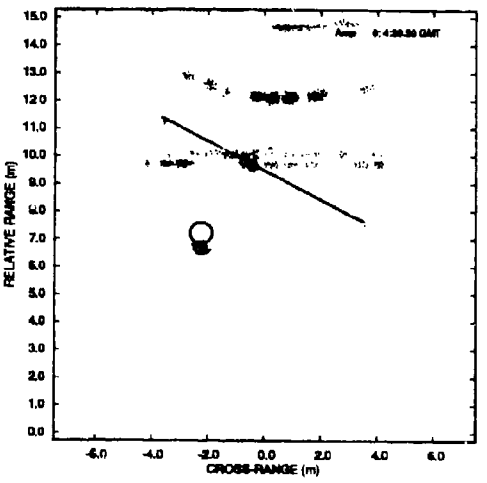

Figure 2. Xpatch image of the cylinder-plate geometry (64 facets), aspect angle = 27 deg.

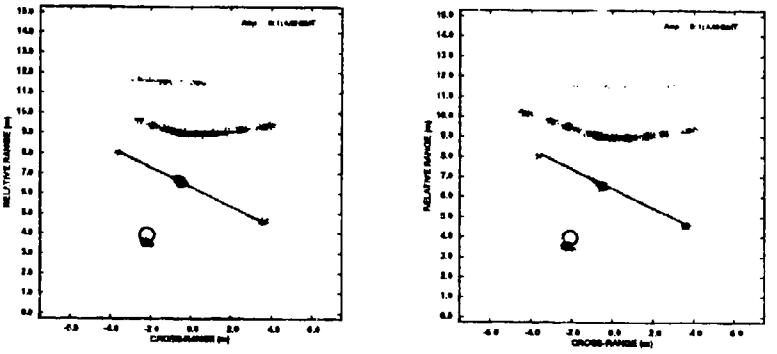

Figure 3. Xpatch image of the cylinder-plate geometry 128 and 256 facets.

Figure 4. Depiction of current patch distributions on the plate.

3. Current Shadowing

Another question that arises when using ray tracing is when to integrate the current induced by a ray reflecting off of a surface back towards the receiver. The Physical Optics principle states that a current is induced on a surface visible to the source, e.g. a ray hits a point on the target after several bounces, and then the target is removed and the induced currents are integrated to find the response at the receiver.

Errors arise when the current patch is not directly visible to the radar. A prototypical anomalous response can be demonstrated with the example shown in Fig. 5. The parallel plate example is representative of geometries found on modern aircraft, e.g. the plate geometry is a canonical example for wing pylons. Figure 6 shows the Xpatch ISAR image of the parallel plates at an aspect angle of 45 deg. along with a corresponding image formed using the Method of Moments. Figure 6 indicates an anomalous response exists down range from the parallel plates. This response is only present over a limited set of aspect angles as demonstrated by Figures 7a and 7b.

Careful examination of the ray paths indicate that around an aspect angle of 45 degrees there is a set of rays that exit out of the parallel plates after reflecting off of the top plate. The majority of the rays exit from the parallel plates after reflecting off of the bottom plate. The algorithm that Xpatch uses to find the PO response is a combined E and H formulation[1]. Under this formulation there is very little response in the forward scattered direction. This accounts for the anomalous response not being present when the rays exit after reflecting off of the bottom plate. This is depicted in Fig. 8.

The large response down range from the top plate in the images results from the multiple reflections that exit from the top plate. The response is smeared in the image plane since the rate-of-change of the path length is a strong function of the aspect angle. This is a non-physical response that is a consequence of the current integration scheme present in the Xpatch code. This type of response can be eliminated by sending a "test" ray from the current patch to the receiver to check for visibility. If Physical Optics is used to calculate the first bounce response, then information on the visibility of each patch is already available and can be used in place of the "test" ray for the monostatic case. In either approach, the current patch should only contribute to the scattered field if the patch is visible to the receiver.

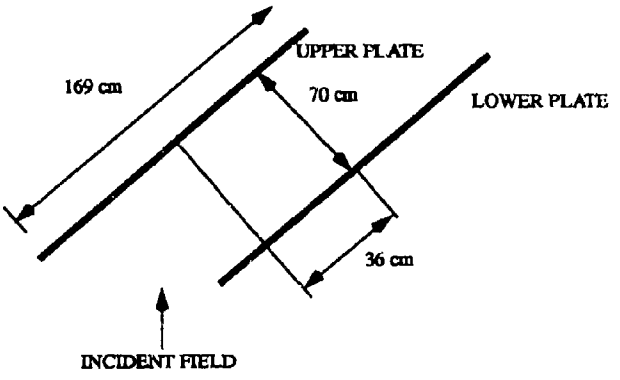

Figure 5. Parallel plate scatterer geometry.

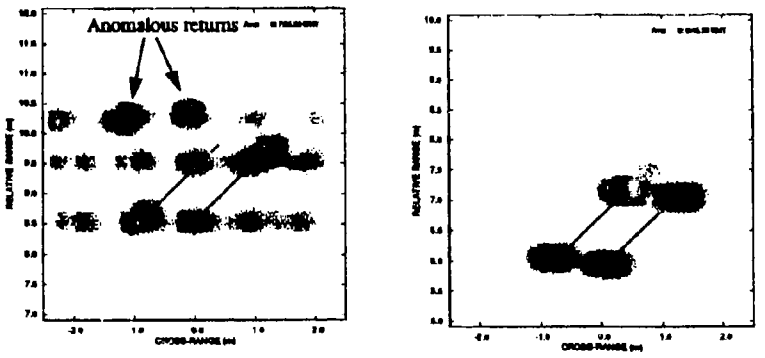

Figure 6. Comparison between Xpatch and MOM images of the parallel plate geometry.

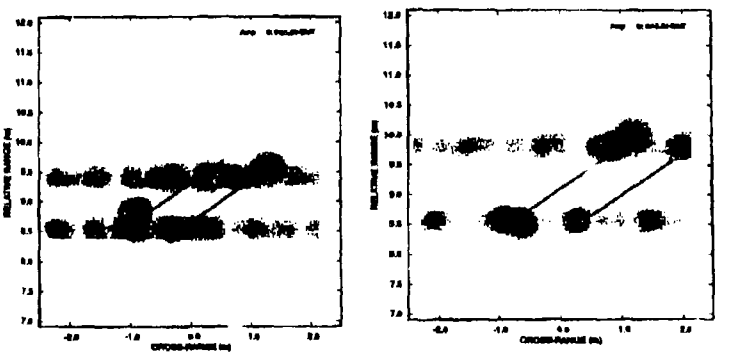

Figure 7. Xpatch images of the parallel plate geometry at aspect angles of 35 deg and 55 deg.

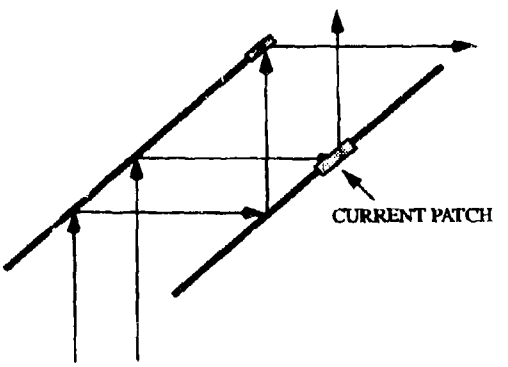

Figure 8. Ray trace of the parallel plate geometry.

4. Integration of current patches

A more subtle question that arises when tracing rays is at what point are the induced currents integrated back to the receiver. In the last section the problem of visibility was addressed. In this section the question of whether to only integrate the currents induced at the last reflection point (as in Xpatch), or to integrate the currents induced at each surface the ray reflects from. The previous example of the parallel plates demonstrates the effect of the different methods of integration. For the parallel plates the image changed dramatically depending on the last exit point. This is a non-physical effect.

In general, the amount that a current patch will contribute to the received scattered field is related to the angle between the average radar line of sight and the normal vector of the surface. The average radar line of sight is defined as the average of the unit vector from the transmitter to the current patch and the unit vector from the receiver to the current patch. The amount of energy that an individual reflection contributes to the scattered field is typically small since most of the energy is reflected in the direction of the ray.

Although the contribution to the scattered field from a ray reflecting from a surface is small, it is not negligible as was demonstrated in the previous example. It can be argued that the contribution from a section of the target surface illuminated by a ray should always contribute to the scattered field, since physically the currents induced on the surface from a ray reflection are not effected by what happens to the ray after the reflection.

5. Summary and Recommendations

This paper considered three critical issues that arise when using ray tracing to calculate the scattered field from complex targets. The examples presented indicate that the issues of facetization and current integration, have a real impact on the accuracy of the scattered field. Based upon our research it is recommended that the current induced by ray reflection should be integrated back to the receiver, if the receiver is visible from the reflection point, after every reflection.

6. References

[1] J. Baldauf, S.W. Lee, L. Lin, S.K. Jeng, and S.M. Scarborough, "High frequency scattering from trihedral corner reflectors and other benchmark targets: SBR versus experiment," *IEEE Trans. on Antennas and Propagation*, APS-39, 1991, pp. 1345-1351.

Technique to Calculate the Cross-Section of the Optoelectronic Radar with Impulse Source of Electromagnetic Radiation

V. Ovod, K. Bauckhage*, S.T. Koval,
A.V. Perekrest, A.E. Ivanisov **

* Universität Bremen, Verfahrenstechnik/FB 4, Badgasteinerstr. 3, 28359 Bremen, Germany.
** Kiev Polytechnical Institute, ave. Brest-Litovski, 37, 252055 Kiev, Ukraine.

Abstract

A technique to calculate the time-dependent cross-section of the optoelectronic radar with a narrow angle of the field of view, with a short duration of the laser pulse and for the relatively uniform meteorological situation is suggested. This technique is based on the use the "weighted" influence energetic coefficients of aerosol space elementary volumes taking into account spatial, energetic, temporary and other parameters of radiation source and receiver.

1 Introduction

Optoelectronic devices of active type (radars) constructed on the principle of recording the radiation scattered by aerosols are widely used for the investigation (remote [1] and laboratory [2]) of aerosol parameters for process testing, for solving various problems in meteorology, and for the navigation of moving objects.

As shown in the figure the pulse laser and the detector of the radar system can generaly be located on the different platforms of the illuminating and receiving system moving in the real time t_r. Let the coordinate system XYZ of the illuminating system be the main coordinate system. The propagation vector of the laser beam and the optical axis of the receiver system are located in the XOZ plane and intersect at the angle ψ. The contour *klmn* in the plane XOZ is formed by intersection of the laser beam with the field of view. The location $z_c(t)$ of the center of the illuminated zone depends on the current time of a single pulse measurement because the laser pulse propagates with light velocity c:

$$z_c(t) = \frac{(tc)^2 - z_d^2 - x_d^2}{2(tc - z_d)}, \qquad (1)$$

where $x_d(t_r)$ and $z_d(t_r)$ are the coordinates of the detector in the real time; c is the light velocity; t is the current time elapsed since the beginning of propagation of the single illuminating pulse. When $t = 0$ the value of radiation flux of this pulse reaches the maximum. Thus the scattering flux incident upon the detector is also time-dependent.

So-called timeindependence radar equations for single [2],[3] and multiple [4] scattering aerosol models are well known.

Our **aim** is to develop the technique to calculate the time-dependent cross-section of the optoelectronic radar with the narrow angle 2β of the field of view and the short duration $2\tau_l$ of the laser pulse. The purpose is to solve navigation problems of moving objects in the case when the meteorological situation is relatively uniform.

2 Formulation

The calculation of the intensity $I_s(\theta_i,\varphi_i,r_i)$ of the field scattered by the i-th elementary $S_i(X)$ scattering volume should be realized in the spherical $(XYZ)_{si}$ coordinate system of the mentioned volume. X is the position vector in the maine XYZ coordinate system. It is evident that the following relationships are valid for the far field scattering and for the narrow angle of the field of view

$$\theta_i = \theta\ , \qquad \varphi_i = \varphi\ , \qquad r_i = R\ , \tag{2}$$

where $\{\theta,\varphi,R\}$ are the spherical coordinates in the main scattering coordinate system $(XYZ)_{s0}$ the center of wich is located in the intersection point of the propagation vector of the laser beam and the optical axis of the receiver system.

Let $d\sigma_{vs}(\theta,\varphi,X)$ be the volume differential cross-section of the scattering by an elementary volume $S_i(X)$ [5]. The dimension of $d\sigma_{vs}(\theta,\varphi,X)$ is $[m^2m^{-3}sr^{-1}]$. Consequently the volume cross-section $\sigma_{vs}(\theta_0,\varphi_0,\Omega,X)$ of the scattering by this volume in solid angle Ω, restricted by the collection aperture is equal:

$$\sigma_{vs}(\theta_0,\varphi_0,\Omega,X) = \int_{\Omega} d\sigma_{vs}(\theta,\varphi,X)\ d\Omega\ , \qquad [m^2m^{-3}]\ , \tag{3}$$

where $d\Omega = \sin\theta\ d\varphi\ d\theta$ is the unit solid angle; $\{\theta_0,\varphi_0,R_0\}$ are the spherical coordinates of the receiver center in the $(XYZ)_{s0}$ coordinate system of the scattering space V_s; $\theta_0 = \pi - \psi$.

In general a powerful pulsed laser is used as radar radiation source. Owing to the pulsed nature of radiation the elementary scattering volumes of space V_s (which is common for the intersected laser beam and the field of view) differently influence upon the detected signal. This influence can be estimated by the function $f_1(t_i)$ ("weighted" coefficient) which describes the form of radiation pulse:

$$f_1(t_i) = \exp\left(-2\frac{t_i^2}{\tau_L^2}\right), \tag{4}$$

where τ_L is the half of full pulse duration at the exp(-2) level, t_i is the parameter which determines the part of influence of the elementary volume $S_i(X)$ on the receiving signal at the moment t;

$$t_i(X,t) = t - \frac{z_s(X) + R_s(X)}{c}\ . \tag{5}$$

Consequently the radiation flux density in any beam section at any instant t is calculated by:

$$\varphi(X,t) = P_L(z)\ f_1(t_i)\ f_2(X)\ , \qquad [Wm^{-2}]\ , \tag{6}$$

where $f_2(X)$ is the function taking into consideration the nonuniformity of the radiation distribution on the beam cross-section; $P_L(z)$ is the power of radiation on the axis Z. This function takes the following form for the most widespread Gaussian beam:

$$f_2(X) = \frac{2}{\pi\omega_L^2(z)}\exp\left\{-2\frac{x^2+y^2}{\omega_L^2(z)}\right\}\ , \qquad P_L(z) = \frac{2}{\sqrt{\pi}}\frac{Q_L(z=0)}{\tau_{L0}}\tau_L(z)\ , \tag{7}$$

where
$$\omega_L(z) = \sqrt{[\omega_L(z=0) + z\ tg\alpha_L]^2 + \omega_t^2(z)} \tag{8}$$

is the radius of the laser beam in the cross-section z; α_L is the beam divergence; $\omega_t(z)$ is the increase parameter of the laser beam because of atmospheric turbulence; $Q_L(z=0)$ is the energy of radiation in the cross-section $z = 0$;

$$\tau_t(z) = \exp[-\int_0^z \beta_{ext}(z')dz'] \tag{9}$$

is the coefficient of atmosphere transmittance along the optical path with the length z; $\beta_{ext}(z')$ is the volume extinction coefficient which is related to the meteorological distance of visibility $S_m(z')$ by an empirical formula, e.g.:

$$\beta_{ext}(z') = \frac{3,91}{S_m(z')}\left(\frac{0,55}{\lambda}\right)^{0,585\ S_m(z')^{1/2}}, \quad [m^2 m^{-1}], \tag{10}$$

where z' is the coordinate characterizing the elementary optical path.

All elementary scattering volumes located at the moment t in the region V_s determine the total detected radiation flux:

$$P(t) = \int_{V_s} \varphi(X,t)\,\sigma_w(\theta_0,\varphi_0,\Omega,X)\,\tau_t(R_0)\,dV, \quad [W], \tag{11}$$

where $dV = dx\,dy\,dz$. It is evident that without sufficient decrease of the accuracy of calculation the limits of the integration with respect to z can be narrowed down to the dimension commensurable with the duration of the incident pulse

$$z_c(t) - k\tau_L c \le z \le z_c(t) + k\tau_L c, \tag{12}$$

where $k = 1,2,3,4$ is the coefficient of the accuracy of calculation in this approximation.

3. Engineering technique to simulate the radar cross-section

Eq. (11) allows to carry out the rigorous calculations of the time-dependent signal for the short pulsed radar. To simplify above simulation the following assumptions can be made.

Let the laser pulse have a rectangular shape with duration $2\tau_L$ as described by

$$f_1(t_i) = \begin{cases} 1, & for \quad -\tau_L \le t_i \le \tau_L \\ 0, & otherwise \end{cases}, \quad P_{Lr}(z,t) = \begin{cases} P_{Lr}(z), & for \quad -\tau_L \le t_i \le \tau_L \\ 0, & otherwise \end{cases}, \tag{13}$$

where
$$P_{Lr}(z) = \frac{Q_L(z)}{2\tau_L} = \frac{\sqrt{2\pi}}{4}\,I_{t\max}(z) \tag{14}$$

is the radiation flux in the rectangular pulse, resulting from the following normalization condition:

$$Q_L(z) = \int_{-\infty}^{\infty} P_L(z,t)\,dt_i = P_{L\max}\frac{\sqrt{2\pi}}{2}\tau_L = P_{L'}2\tau_L \ . \tag{15}$$

Thus taking into account the above mentioned assumption, the distribution of the flux density in a cross-section z can be written by

$$\varphi_{a1}(X,t) = \begin{cases} P_{L'}(z)\, f_2(X) \ , & for \quad z_c(t) - \tau_L c \le z \le z_c(t) + \tau_L c \\ 0 \ , & otherwise \end{cases} \ . \tag{16}$$

Let the flux density in a cross-section be constant, satisfying the condition

$$\varphi_{a2}(z,t) = \begin{cases} \dfrac{P_{L'}(z)}{\pi\,\omega_L(z)^2} \ , & for \quad z_c(t) - \tau_L c \le \quad) + \tau_L c \\ 0 \ , & othewise \end{cases} \ . \tag{17}$$

For the far field scattering, the narrow field of view and for the small beam divergence the following relationships are valid for all elementary scattering volumes:

$$\sigma_{vs}(\theta_0,\varphi_0,\Omega,z) = d\sigma_{vs}(\theta_0,\varphi_0,z)\ \Omega \ , \quad [m^2m^{-3}] \quad and \quad \Omega = \frac{A_0}{R_0^2} \ , \ [sr] \ , \tag{18}$$

where A_0 is the area of the detector aperture.

Thus taking into account the above approximations the formula to determine the total scattering flux detected by the radar receiver can be written by

$$P(t) = \tau_i(R_0)\,\varphi_{a2}(z_c(t))\,\sigma_R(\theta_0,\varphi_0,\Omega,z_c(t)) \ , \tag{19}$$

where

$$\sigma_R(\theta_0,\varphi_0,\Omega,t) = d\sigma_{vs}(\theta_0,\varphi_0)\,\Omega\,V_{as}(t) \ , \quad [m^2] \tag{20}$$

is the time-dependent radar cross-section;

$$\varphi_{a2}(z_c) = \frac{Q_L(z=0)}{\pi\,\omega_L^2(z_c)2\tau_L}\tau_i(z_c) \ ; \tag{21}$$

$$V_{as}(t) = \int_{V_{as}} dV = V_{il}(t)\,k_c(t) \tag{22}$$

is the scattering volume in the case of the mentioned approximations;

$$V_{il}(t) = 2\pi\,\omega_L^2(z_c)\,\tau_L c \tag{23}$$

is the scattering volume of the illuminated zone;

$$k_c(t) = \frac{V_{as}(t)}{V_{ll}(t)} \approx \begin{cases} 0 & , \ for \quad z_c \le z_k \quad , \ or \quad z_c \ge z_m \ ; \\ 1 & , \ for \quad z_l \le z_c \le z_n \ ; \\ k_{c2}(z_c) & , \ for \quad z_k \le z_{\min} \quad , \ where \ z_{\min} = \min(z_l \ ; \ z_n); \\ k_{c3}(z_c) & , \ for \quad z_{\max} \le z_c \le z_m \ , \ where \ z_{\max} = \max(z_l \ ; \ z_n) \ ; \\ k_{c2}(z_c) - k_{c3}(z_c) & , \ for \quad z_n \le z_c \le z_l \ ; \end{cases} \tag{24}$$

is the cutting coefficient of the field of view for the far field scattering when the cross-section of the field of view in the plane z_{s0} is larger as the cross-section of the beam;

$$k_{c1}(z_c) = \begin{cases} 1 - \Delta k_{c1}(z_c) & , \ for \ \omega_{s1}(z_c) \ge \omega_L(z_c) \\ \Delta k_{c1}(z_c) & , \ otherwise \end{cases} \ ; \quad k_{c2}(z_c) = \begin{cases} \Delta k_{c2}(z_c) & , \ for \ \omega_{s2}(z_c) \ge \omega_L(z_c) \\ 1 - \Delta k_{c2}(z_c) & , \ otherwise \end{cases} \ ; \tag{25}$$

$$\Delta k_{cj}(z_c) = \frac{S_{cj}(z_c)}{\pi \omega_L^2(z_c)} \ ; \qquad S_{cj}(z_c) = \frac{\omega_L^2(z_c)}{2}\left(\frac{\pi \alpha_j(z_c)}{180} - \sin\alpha_j(z_c)\right) \tag{26}$$

is the square of the segment characterized by the angle $\alpha_j(z_c)$ in the cross-section z_c [6]; j = 1,2;

$$\alpha_j(z_c) = \begin{cases} 2\arccos\dfrac{\omega_{sj}(z_c) - \omega_L(z_c)}{\omega_L(z_c)} & , \ for \quad z_k \le z_c \le z_l \ ; \ or \ \ z_n \le z_c \le z_m \ ; \\ 0 & , \ otherwise \ ; \end{cases} \tag{27}$$

$$\begin{aligned} \omega_{s1}(z_c) &= \begin{cases} (z_c - z_k)[tg(\psi + \beta) + tg\alpha_L] \ , & for \ \ z_k \le z_c \le z_l \\ 0, & otherwise \end{cases} \ ; \\ \omega_{s2}(z_c) &= \begin{cases} (z_c - z_m)[tg(\psi - \beta_L) + tg\alpha_L] \ , & for z_n \le z_c \le z_m \\ 0 & , \quad otherwise \end{cases} \ , \end{aligned} \tag{28}$$

where $\omega_{sj}(z_c)$ is the part of the laser beam diameter $2\omega_L(z_c)$ in the cross-section z_c which is located under the surface of the cone of the field of view [6]. Ignoring atmospheric turbulence the coordinates of the contour *klmn* can be estimated by

$$z_k = \frac{x_d - \omega_{L0} + \mu_1}{\mu_1 + tg\alpha_L} \ , \quad z_l = \frac{x_d + \omega_{L0} + \mu_1}{\mu_1 - tg\alpha_L} \ , \quad z_n = \frac{x_d - \omega_{L0} + \mu_2}{\mu_2 + tg\alpha_L} \ , \quad z_m = \frac{x_d + \omega_{L0} + \mu_2}{\mu_2 - tg\alpha_L} \ , \tag{29}$$

where $$\mu_1 = z_d tg(\psi + \beta) \ , \qquad \mu_2 = z_d tg(\psi - \beta) \ , \qquad \omega_{L0} = \omega_L(z = 0) \ . \tag{30}$$

The calculation of the volume cross-section of multiple scattering $d\sigma_{vs}(\theta,\varphi,z)$ gives most complication in the above simulation [7]. However this simulation is simplified when single scattering by spherical aerosol particles is valid [5]:

$$d\sigma_{vs}(\theta,z) = \beta_{ext}(z)\frac{1}{4\pi}\left\{\frac{1}{2}[P_1(\theta,z) + P_2(\theta,z)]\right\} , \tag{31}$$

where

$$\beta_\xi(z) = \frac{\pi}{k^3}\int_0^\infty \rho^2 n(\rho,z) k_\xi(m,\rho)\, d\rho \ , \tag{32}$$

$$k_s = \frac{2}{\rho^2}\sum_{n=1}^{\infty}(2n+1)(|\alpha_n(m,\rho)|^2 + |\beta_n(m,\rho)|^2) \ , \quad k_{ext}(m,\rho) = \frac{2}{\rho^2}\sum_{n=1}^{\infty}(2n+1)Re(\alpha_n(m,\rho)+\beta_n(m,\rho)) \tag{33}$$

are the efficiency factors of scattering and extinction [8]; $\alpha_n(m,\rho)$, $\beta_n(m,\rho)$ are the complex coefficients which are calculated according to the known formulas of Mie theory [8]; $m=n-j\chi$ is the complex refractive index of the aerosol at the wavelength λ of incident radiation;
$n(\rho)$, $[m^{-3}m^{-1}]$ is the density of particle concentration distribution along the diffraction parameter $\rho = kr$; $k = 2\pi/\lambda$ is the wavenumber; r is the radius of the aerosol particle; $\xi = s$, ext is the subscript denoting the scattering volume coefficient β_s or the extinction volume coefficient β_{ext};

$$P_\zeta(\theta,z) = \frac{4\pi}{k^3\beta_s(z)}\int_0^\infty n(\rho,z)\ |S_\zeta(m,\rho,\theta)|^2\ d\rho \ , \tag{34}$$

where $S_\zeta(m,\rho,\theta)$ are the elements of the scattering matrix for a single particle [8]; $P_\zeta(\theta,z)$ are the normalized coefficients of the scattering matrix for a ensemble of polydispersion particles; $\zeta = 1,2,3,4$ ($\zeta = 1,2$ for a spherical particle).

Thus taking into account the above mentioned approximations the formula to determine the detected scattering flux can be written by

$$P_{a2}(t) = \frac{Q_t(z=0)\,\beta_{ext}(z_c)\,\omega_\alpha(z_c)\,c}{4\pi R_0^2}\ \frac{P_1(\theta)+P_2(\theta)}{2}\ \tau_t(z_c+R_0)\ k_c(t) \ , \tag{35}$$

where $\omega_\alpha(z) = \beta_s(z)/\beta_{ext}(z)$ is the albedo of a scattering aerosol [3]. It is well known that for backscatter ($\theta \approx 180°$) the following relationship is valid: $P_1(\theta) \approx P_2(\theta)$.

Conclusions

The technique to calculate the time-dependent radar signal (11) was derived with the aims to increase design efficiency of new high-precise radar with arbitrary configuration and to decrease expenditures of this work. This technique is based on the use of "weighted" influence energetic coefficients of aerosol space elementary volumes taking into account spatial, energetic, temporary and other parameters of radiation source and receiver. Taking into account a number of approximations the relatively simple formulas for the time-dependent radar cross-section (20) and the detected scattering flux (35) are obtained. This thechnique is scheduled to integrate in the early created program [9].

The detected radar signal can be simulated both for the single scattering model of aerosol particles and for the multiple scattering model. The formulas to calculate the volume scattering cross-section $d\sigma_{vs}$ are presented for the single scattering case. It is planned to modify the technique to simulate the volume cross-section of navigation and atmosphere sounding radas for the multiple scattering case and more complicated meteorological situations.

References

1. H. Jager and D. Hofmann, Midlatitude Lidar Backscatter to Mass, Area, and Extinction Conversion Model Based on in Situ Aerosol Measurement from 1980 to 1987, *Appl.Opt.*, vol. 30, pp. 127-138, 1991.
2. T.G. McRae and T.J. Kulp, Backscatter Absorption Gas Imaging: a New Technique for Gas Visualization. *Appl. Opt.*, vol 32, pp.4037-4050, 1993.
3. G.Hanel, Single Scattering Albedo, Asymmetry Parameter, Apparent Refrective Index, and Apparent Soot Content of Dry Atmospheric Particles, *Appl.Opt.*, vol. 27, pp. 2287-2291, 1988.
4. M. Wiegner and G.Echle, Lidar Multiple Scattering: Iimprovement of Bissonnette's Paraxial Approximation. *Appl. Opt.*, vol. 32, pp. 6789-6803, 1993.
5. D.Deirmendjian, *Electromagnetic Scattering on Spherical Polydispersions Particles*, American Elsevier publishing company. INC. New York, *1969.*
6. I.N.Bronstein and K.A.Semendjajew, *Taschenbuch der Mathematik*, Thun, Frankfurt/Maine, 1987.
7. A-K.M. Hamid, Electromagnetic Wave Scattering by Many-Sphere Systems with Application to Simulation of Three Dimensional Bodies, Ph.D. thesis, University of Manitoba, Canada, 1991.
8. H.C. van de Hulst, *Light Scattering by Small Particles*, Dover, New York, 1981.
9. V.I.Ovod, Calculation of Calibration Characteristics of Laser Microparticle Analyzers, *Sov. J. Opt. Technol.*, vol. 54, pp. 199-202, 1987. (In English).

These research results were attained with the assistance of the Alexander von Humboldt Foundation.

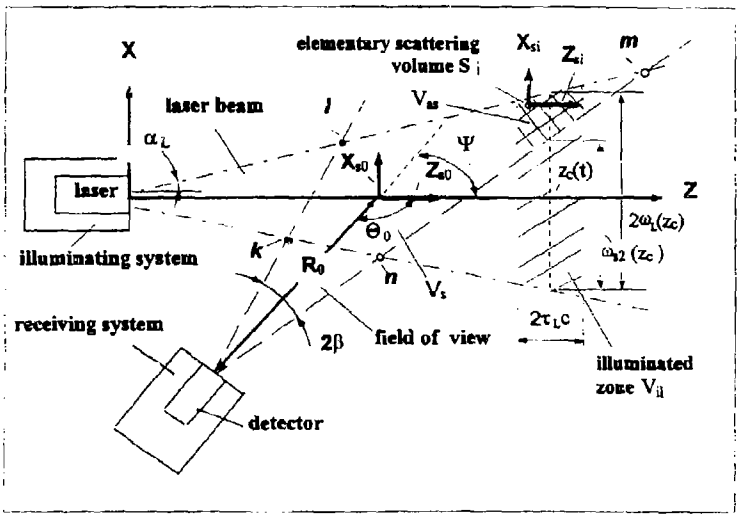

Figure. Radar system geometry

Technique to Increase the Computation Accuracy of the Scattered Electromagnetic Field in the Simulation of the Phase-Doppler Size Analyzer

V. Ovod, T. Wriedt, K. Bauckhage *, V.M. Zemljansky **

* Universität Bremen, Verfahrenstechnik/FB 4, Badgasteinerstr 3, 28359 Bremen, Germany.
** Kiev Civil Aviation Engineers Institute, ave. Komarova,1, 252058 Kiev, Ukraine.

Abstract

Phase-Doppler Anemometry (PDA) is one of the most advanced optical technique to measure the size and the velocity of moving particles in liquid atomization and spray systems. Increasing the measurement accuracy is significant to improve PDA systems. In this connection it is very important to simulate the influence of the incident beam profile and the position of the spherical particle in the measurement volume on the PDA signal. Angular plane wave spectrum (PWS) of the incident beam is one of the perspective method which allows to calculate mentioned effects. A fast-technique based on the PWS method to simulate the PDA signal is presented. To decrease calculation time it is suggested to simulate the unit polarization vector of the electric field scattered to an arbitrary observation point and its amplitude in the coordinate system of the i-th PWS plane wave and then to transform this vector in the coordinate system of the receiver polarizer.

1 Introduction

Recently a lot of attention has been paid to increase the precision of the Phase-Doppler Anemometry which has a wide range of application in control of different technological processes [1]. One of the most essential conditions for this improvement is an increase of the calculation accuracy of the PDA signal simulation by a light scattering theory. These calculations are based on the Mie theory which gives a rigorous solution the scattering of a plane wave by a sphere [2].

The problem to consider the influence of the intensity and phase profile of the incident non-plane beam has been solved using the so-called beam shape coefficients $q^m_{n,TM}$ and $q^m_{n,TE}$: at first -for a circular Gaussian beam [3]; then - for a Gaussin beam having elliptical cross-section [4]. The investigation of Morita et al.[5], Tsai and Pogarzelski [6], Tam and Corriveau [7], Kim and Lee [8] and Barton et al. [9] are also widely known. However, it seems reasonable to say that the high-speed algorithms to calculate the above mentioned scattering of the Gaussian beams are developed by using the so-called localized approximation [4].

The angular spectrum of plane waves is a subject of much current interest to simulate the PDA signal with arbitrary incident beams which can be expressed as a sum of homogeneous plane waves. The scattered field in this case is a superposition of the fields which are scattered by a sphere illuminated by each i-th PWS plane wave.

This technique makes it relatively simple to interpret the physical essence of the results obtained for the each i-th PWS plane wave. The PWS method is used to simulate the signal amplitude of the optical particle size laser analyzer [10], to investigate the electric and magnetic fields scattered by an arbitrary located sphere [11] or by an arbitrary shaped dielectric particle [12]. The last problem (scattering by non-spherical particles) is solved with the T-matrix technique.

Our **aim** has been to adopt the PWS method for the simulation PDA signals when a moving sphere interacts with two coherent elliptically polarized beams having an arbitrary intensity profile. A fast calculation technique is presented.

2 PDA System Geometry

As shown in the Fig. 1 the optical system of a PDA incorporates two incident beams: the approaching beam (corresponded by subscript "a") and the trailing beam (subscript "t"). A measurement volume is formed by crossing these two beams. Let the propagation direction of these beams in the main Cartesian coordinate system $(XYZ)_{(0)}$ of PDA be represented by vectors $\mathbf{k}_{a(0)} = k_a \mathbf{s}_{a(0)}$ and $\mathbf{k}_{t(0)} = k_t \mathbf{s}_{t(0)}$ (where $k_a = 2\pi/\lambda_a$ and $k_t = 2\pi/\lambda_t$ are the wavenumbers; λ_a and λ_t are the wavelenghts in the surrounding medium); $\mathbf{s}_{a(0)}$ and $\mathbf{s}_{t(0)}$ are the unit propagation vectors.

The subscripts enclosed in brackets indicate the corresponding coordinate system. Let the main coordinate systems for the two beams be represented by $(XYZ)_{(0a)}$ and $(XYZ)_{(0t)}$. The centers $O_{(0a)}$ and $O_{(0t)}$ of these coordinate system are located in the beam zones characterized by a high flux density. The same named axises of the $(XYZ)_{(0)}$, $(XYZ)_{(0a)}$ and $(XYZ)_{(0t)}$ coordinate systems are oriented parallel. For this reason $\mathbf{s}_{a(0a)} = \mathbf{s}_{a(0)}$, $\mathbf{s}_{t(0t)} = \mathbf{s}_{t(0)}$.

The vectors $\mathbf{X}_{\omega a(0)}$, $\mathbf{X}_{\omega t(0)}$ show the maladjustment of a PDA. The vectors $\mathbf{X}_{p(0)}(t)$, $\mathbf{X}_{v(0)}$, $\mathbf{X}_{v0(0)}$ are the position vectors of a p-sphere particle moving with velocity $\mathbf{V}_{p(0)}$, of a observation point and of the center of the receiving aperture.

Obviously the position or propagation unit vector (for example, position vector $\mathbf{s}_{v(\xi)} = s_{xv(\xi)}\mathbf{x}_{(\xi)} + s_{yv(\xi)}\mathbf{y}_{(\xi)} + s_{zv(\xi)}\mathbf{z}_{(\xi)}$ of the point V) in arbitrary ξ-th coordinate system $(XYZ)_{(\xi)}$ can be presented (as illustrated in Fig. 2) by two angle groups: $\{\theta_{v(\xi)}, \varphi_{v(\xi)}\}$ or $\{\psi_{v(\xi)}, \mu_{v(\xi)}\}$, where $\{\theta_{v(\xi)}, \varphi_{v(\xi)}, |\mathbf{X}_{v(0)}|\}$ are spherical coordinates; $\psi_{v(\xi)}$ is the elevation angle and $\mu_{v(\xi)}$ is the off-axis angle. From the standpoint of simulation of PDA signals the calculation of the polarization vectors $\mathbf{e}_{sav}$ and $\mathbf{e}_{stv}$ of the electric field scattered (subscript "s") by the p-sphere to an arbitrary observation point V is of particular interest. These vectors can be obtained in arbitrary $(XYZ)_{(\theta v\xi)}$ or $(XYZ)_{(\psi v\xi)}$ coordinate system or to be transformed from one to another. In other words, the components of the polarization vectors have orientations along the corresponding orthonormal basis vectors $\{\boldsymbol{\theta}_{(\theta v\xi)}, \boldsymbol{\varphi}_{(\theta v\xi)}, \mathbf{r}_{(\theta v\xi)}\}$ or $\{\boldsymbol{\psi}_{(\psi v\xi)}, \boldsymbol{\mu}_{(\psi v\xi)}, \mathbf{r}_{(\psi v\xi)}\}$ such that $\boldsymbol{\theta}_{(\theta v\xi)} \parallel \mathbf{X}_{(\theta v\xi)}$, $\boldsymbol{\varphi}_{(\theta v\xi)} \parallel \mathbf{Y}_{(\theta v\xi)}$, $\mathbf{r}_{(\theta v\xi)} \parallel \mathbf{Z}_{(\theta v\xi)}$ and $\boldsymbol{\psi}_{(\psi v\xi)} \parallel \mathbf{X}_{(\psi v\xi)}$, $\boldsymbol{\mu}_{(\psi v\xi)} \parallel \mathbf{Y}_{(\psi v\xi)}$, $\mathbf{r}_{(\psi v\xi)} \parallel \mathbf{Z}_{(\psi v\xi)}$ (see Fig.2). It is obvious that the $(XYZ)_{(\theta v\xi)}$ coordinate system is generated by the corresponding right-handed rotation of the initial $(XYZ)_{(\xi)}$ coordinate system through the angle $\varphi_{v(\xi)}$ (rotation matrix $\mathbf{R}_{\varphi}(\mathbf{s}_{v(\xi)})$) and then though the angle $\theta_{v(\xi)}$ (transformation matrix $\mathbf{R}_{\theta}(\mathbf{s}_{v(\xi)})$). Coordinate system $(XYZ)_{(\psi v\xi)}$ is formed by rotating $(XYZ)_{(\xi)}$ through the angle $\mu_{v(\xi)}$ (transformation matrix $\mathbf{R}_{\mu}(\mathbf{s}_{v(\xi)})$) and then through the angle $\psi_{v(\xi)}$ (transformation matrix $\mathbf{R}_{\psi}(\mathbf{s}_{v(\xi)})$). The above transformation matrixes and the relationship between elements of the generalized unit vector $\mathbf{s}_{v(\xi)}$, on the one hand, and the angles $\theta_{(\theta v\xi)}, \varphi_{(\theta v\xi)}, \psi_{(\psi v\xi)}, \mu_{(\psi v\xi)}$, and matrix rotation elements, on the other hand have a relatively simple form [13].

In the general case PDA receiver system incorporates a polarizer which coordinate system $(XYZ)_{(pol)}$ is given in the following manner: axis $\mathbf{Z}_{(pol)} \in \mathbf{Z}_{(\psi 0v)}$ and the angle $\varphi_{(pol)}$ defines the orientation of the parallel axis $\mathbf{X}_{(pol)}$ regarding receiver axis $\mathbf{X}_{(\psi 0v0)}$.

The above described coordinate systems are necessary to achieve the main aim of this work, namely: to elaborate a modified technique for calculation of the polarization vectors $\mathbf{e}_{sav(pol)}$ and $\mathbf{e}_{stv(pol)}$ of the scattered fields in the $(XYZ)_{(pol)}$ polarizer coordinate system by using the PWS method.

3. Formulation

As early shown [12] the field scattered by a sphere which is illuminated by the non-plane "a" (or "t") beam can be obtained by superposition of the fields scattered by this sphere being illuminated by PWS plane waves. The propagation direction of the i-th plane wave of the "a" beam spectrum is conveniently presented by the unit propagation vector $\mathbf{s}_{i(a)}$ in the $(XYZ)_{(a)}$ coordinate system of the "a" beam (or by vector $\mathbf{s}_{i(t)}$ for the "t" beam in the $(XYZ)_{i(t)}$ coordinate system): $\mathbf{s}_{i(ia)} = s_{xi(a)}\mathbf{x}_{(a)} +$

$s_{yi(a)}y_{(a)} + s_{zi(a)}z_{(a)}$, where the $(XYZ)_{(a)}$ coordinate system is formed by rotating the $(XYZ)_{(0a)}$ coordinate system through the angles $\mu_{a(0)}$ and $\psi_{a(0)}$. In the general case the illuminated beams have elliptical polarization. Thus polarization vector of the "a" beam in the center of its $(XYZ)_{(a)}$ coordinate system expressed by

$$e_{a(a)}(z_{(a)}=0) = e_{xa(a)}(z_{(a)}=0)x_{(a)} + e_{ya(a)}(z_{(a)}=0)y_{(a)} \quad . \tag{1}$$

The angular plane-wave spectrum of the electric field of this monochromatic beam (in other words the electric field vector $\mathbf{E}_{i(ia)}(s_{i(ia)},z_{(a)}=0,t)$ of the i-th plane wave of this spectrum in cross-section $z_{(a)} = 0$ of the "a" beam coordinate system $(XYZ)_{(a)}$ is well known [12]:

$$\begin{aligned} E_{i(a)}(s_{i(a)},z_{(a)}=0,t) = F\{E_{a(a)}(x_{(a)},y_{(a)},z_{(a)}=0)\}f_{ta}(\omega_a t) = \\ A_a(|X_{(a)}|=0)\cdot A^{(1)}_{i(a)}(s_{i(a)})\cdot e^{(1)}_{i(a)}(s_{i(a)})\, f_{ta}(\omega_a t) \quad , \end{aligned} \tag{2}$$

where $A_a(|\mathbf{X}_{(a)}|=0)$ is the amplitude of the electric field vector of the "a" incident beam in the center of its $(XYZ)_{(a)}$ coordinate system; $\mathbf{X}_{(a)}$ is the position vector of an arbitrary point in the above coordinate system; $A^{(1)}_{i(a)}(s_{i(a)}) = \mathbf{F}\{f_{na}(x_{(a)},y_{(a)},z_{(a)}=0)\}$ and

$$e^{(1)}_{i(a)}(s_{i(a)}) = \begin{bmatrix} e^{(1)}_{xi(a)} \\ e^{(1)}_{yi(a)} \\ e^{(1)}_{zi(a)} \end{bmatrix} = \begin{bmatrix} e_{xa(a)}(z_{(a)}=0) \\ e_{ya(a)}(z_{(a)}=0) \\ \dfrac{-[s_{xi(a)}e_{xa(a)}(z_{(a)}=0) + s_{yi(a)}e_{ya(a)}(z_{(a)}=0)]}{s_{zi(a)}} \end{bmatrix} \tag{3}$$

are amplitude and non-unit polarization vector of the i-th plane wave of the angular spectrum in the $(XYZ)_{(a)}$ coordinate system; $\mathbf{F}$ is the Fourier transform operator; $f_{na}(\mathbf{X}_{(a)}) = A_a(\mathbf{X}_{(a)})/A_a(z_{(a)},x_{(a)}=y_{(a)}=0)$ is the coefficient taking into consideration the non-uniformity of the amplitude distribution of the electric field in $z_{(a)}$ cross-section; $f_{ta}(\omega_a t) = \exp(-j\omega_a t)$ is the time-harmonic dependence of the "a" beam.

The polarization vector and the amplitude of the i-th plane wave of the angular plane-wave spectrum for "a" incident beam can be determine in the $(XYZ)_{(ia)}$ coordinate system of i-th wave by the following equipments taking into account the above mentioned transformation matrix:

$$e^{(1)}_{i(ia)}(s_{i(ia)}) = R_\varphi(s_{i(a)})R_\mu(s_{i(a)})e^{(1)}_{i(a)}(s_{i(a)}) \quad , \qquad A^{(1)}_{i(ia)}(s_{i(ia)}) = A^{(1)}_{i(a)}(s_{i(a)}) \quad . \tag{4}$$

The Eqs. (3) and (4) are the governing equations for simulation of the polarization vector of a scattered field. To simplify this calculation and the physical interpretation of the obtained results, the matrix of modified expansion coefficients $[\mathbf{P}^{\Delta}_{\varepsilon mn,c}(s_{i(\xi)})]_c$

$$[P^{\Delta}_{\varepsilon mn,c}(s_{i(\xi)})]_c = \frac{1}{k_p(s_{i(a)},X_{p(a)})}\,[P_{\varepsilon mn,c}(s_{i(\xi)})]_c \tag{5}$$

and the matrix of modified vector spherical wave functions $[[\mathbf{N}^{(1,3)\Delta}_{mn,r}(s_{pv(\xi)})]_r]_c$

$$[[N^{(1,3)\Delta}_{mn,r}(s_{pv(\xi)})]_r]_c = \frac{1}{k_N(s_{pv(\xi)},|X_{pv}|)}\,[[N^{(1,3)}_{mn,r}(s_{pv(\xi)})]_r]_c \qquad (6)$$

are suggested taking into account that $\exp(jk_a s_{i(a)} X_{p(a)}) = \exp(jk_a s_{i(ia)} X_{p(ia)})$. In Eqs. (5),(6) superscript Δ shows the modified vectors; m,n are the order and degree of the vector spherical wave functions $\mathbf{M}_{mn}$, $\mathbf{N}_{mn}$; superscripts 1 and 3 are the type number of the spherical vector wave functions; subscript $\xi = a,ia$ shows the coordinate system $(XYZ)_a$ or $(XYZ)_{ia}$ in which unit propagation vector $s_{i(\xi)}$ of the i-th plane wave or unit vector $s_{pv(\xi)}$ of the direction from particle center p to the observation point V are presented; subscript $\varepsilon = x,y,z$ indicates the x,y or z component of the corresponding vectors; subscripts d,c,r mean that a corresponding vector (matrix) is a diagonal, column or row vector (matrix).

Modification coefficients k_P and k_N are the phase and amplitude-phase factors appeared in the expression for $\mathbf{P}_{\varepsilon mn,c}(s_{i(\xi)})$ and $\mathbf{N}^{(1,3)}_{mn,r}(s_{pv(\xi)})$:

$$k_P(s_{i(a)},X_{p(a)}) = k_{Pe}(s_{i(a)},X_{p(a)})k_{Pn} \quad and \quad k_N(s_{pv(\xi)},|X_{pv}|) = k_{Nn}\,k_{Ne}(|X_{pv}|)\,\Phi_m(\varphi_{pv(\xi)}) \;; \qquad (7)$$

$k_{Pn} = (j^n)^\alpha$ and $k_{Nn} = (j^{-n})^\alpha$ are the coefficients with imaginary unit;

$$k_{Pe}(s_{i(a)},X_{p(a)}) = \exp(jk_a s_{i(a)} X_{p(a)}) \;,\quad k_{Ne}(|X_{pv}|) = \left[j\,\frac{\exp(jk_a|X_{pv}|)}{k_a\cdot|X_{pv}|}\right]^\alpha \;,\quad \Phi_m(\varphi_{pv(\xi)}) = \exp(jm\varphi_{pv(\xi)}) \qquad (8)$$

are the phase factors; $|X_{pv}|$ is the direction between particle center p and observation point V; $\alpha = 0$ for the incident field and for the near- and far scattered field; $\alpha = 1$ only for the far ($k_a\,|X_{pv}| \gg n^2$) scattered field.

It has been known [14],[15] that for the case when $s_{yi(\xi)} = 0$ the matrix of expansion coefficients of the incident field, having x- or y polarization, can be presented by the expressions

$$[P^{\Delta}_{xmn,c}(s_{i(\xi)})]_c = \begin{bmatrix} P^{\Delta}_{xmn,c}(s_{i(\xi)}) \\ Q^{\Delta}_{xmn,c}(s_{i(\xi)}) \end{bmatrix} = (j^n)^\beta \begin{bmatrix} j\tau^m_{n,c}(\theta_{i(\xi)})D_{mn,d} \\ j\pi^m_{n,c}(\theta_{i(\xi)})D_{mn,d} \end{bmatrix} \;, \qquad (9)$$

$$[P^{\Delta}_{ymn,c}(s_{i(\xi)})]_c = \begin{bmatrix} P^{\Delta}_{ymn,c}(s_{i(\xi)}) \\ Q^{\Delta}_{ymn,c}(s_{i(\xi)}) \end{bmatrix} = (j^n)^\beta \begin{bmatrix} \pi^m_{n,c}(\theta_{i(\xi)})D_{mn,d} \\ \tau^m_{n,c}(\theta_{i(\xi)})D_{mn,d} \end{bmatrix} \;, \qquad (10)$$

where $\beta = 1$ for the arbitrary field ; $\beta = 0$ only for the far scattered field;

$$\pi^m_{n,c}(\theta_{i(\xi)}) = \begin{bmatrix} \pi_{m1}(\theta_{i(\xi)}) \\ \vdots \\ \pi_{mn}(\theta_{i(\xi)}) \end{bmatrix} \;,\qquad \tau^m_{n,c}(\theta_{i(\xi)}) = \begin{bmatrix} \tau_{m1}(\theta_{i(\xi)}) \\ \vdots \\ \tau_{mn}(\theta_{i(\xi)}) \end{bmatrix} \;; \qquad (11)$$

$$\pi_n^m(\theta_{i(\xi)}) = \frac{m}{\sin(\theta_{i(\xi)})} P_n^m(\cos(\theta_{i(\xi)})) \quad , \quad \tau_n^m(\theta_{i(\xi)}) = \frac{\partial}{\partial\theta_{i(\xi)}} P_n^m(\cos(\theta_{i(\xi)})) \quad ; \tag{12}$$

$P_n^m(\cos(\theta_{i(\xi)})$ is the associated Legender function of the first kind; $\theta_{i(\xi)}$ is the angle between the unit propagation vector $\mathbf{s}_{i(\xi)}$ of the i-th plane wave and the axis $\mathbf{Z}_{(\xi)}$ of the $(\mathbf{XYZ})_{(\zeta)}$ coordinate system;

$$\boldsymbol{D}_{mn,d} = \begin{bmatrix} D_{m1} & 0 & \dots & 0 \\ \dots & \dots & \dots & \dots \\ 0 & 0 & \dots & D_{mn} \end{bmatrix}, \qquad D_{mn} = \frac{2n+1}{n(n+1)} \frac{(n-m)!}{(n+m)!} \tag{13}$$

are the diagonal matrix and the normalization factor D_{mn}.
The modified matrix of the vector spherical wave functions can be written

$$[[N_{mn,r}^{(1,3)\Delta}(s_{pv(\xi)})]_r]_c = \begin{bmatrix} [N_{\theta mn,r}^{(1,3)\Delta}(s_{pv(\xi)})]_r \\ [N_{\phi mn,r}^{(1,3)\Delta}(s_{pv(\xi)})]_r \\ [N_{rmn,r}^{(1,3)\Delta}(s_{pv(\xi)})]_r \end{bmatrix} = \begin{bmatrix} [z_{n,d}(\gamma)]_d [\tau_{mn,r}(\theta_{pv(\xi)}]_c & [\frac{\partial z_{n,d}(\gamma)}{\partial\gamma}]_d [\pi_{mn,r}(\theta_{pv(\xi)})]_c \end{bmatrix} , \tag{14}$$

$$\textit{where} \quad [N_{\zeta mn,r}^{(1,2)\Delta}(s_{pv(\xi)})]_r = \begin{bmatrix} N_{\zeta mn,r}^{(1,3)\Delta}(s_{pv(\xi)}) & \boldsymbol{M}_{\zeta mn,r}^{(1,3)\Delta}(s_{pv(\xi)}) \end{bmatrix} ; \tag{15}$$

$$N_{\zeta mn,r}^{(1,3)\Delta}(s_{pv(\xi)}) = \begin{bmatrix} N_{\zeta m1}^{(1,3)\Delta}(s_{pv(\xi)}) & N_{\zeta m2}^{(1,3)\Delta}(s_{pv(\xi)}) & \dots & N_{\zeta mn}^{(1,3)\Delta}(s_{pv(\xi)}) \end{bmatrix} ; \tag{16}$$

the subscript $\zeta = \theta,\varphi$ or r shows the corresponding component of the vector;

$$[z_{n,d}(\gamma)]_d = \begin{bmatrix} z_{n,d}(\gamma) & 0 & 0 \\ 0 & z_{n,d}(\gamma) & 0 \\ 0 & 0 & z_{n,d}(\gamma) \end{bmatrix}, \qquad \tau_{n,d}(\gamma) = \begin{bmatrix} z_1(\gamma) & \dots & 0 \\ \dots & \dots & \dots \\ 0 & \dots & z_n(\gamma) \end{bmatrix} , \tag{17}$$

where $\gamma = k_a |\mathbf{X}_{pv}|$; $z_n(\gamma) = j_n(\gamma)$ for the subscript (1); $z_n(\gamma) = h_n^{(1)}(\gamma)$ for the subscript (3); $j_n(\gamma)$ and $h_n^{(1)}(\gamma)$ are the spherical Bessel function and the spherical Hankel function [19]; the type of matrix $[\partial z_{n,d}(\gamma)/\partial\gamma]_d$ is similar to the matrix $[z_{n,d}(\gamma)]_d$; $\theta_{pv(\xi)}$ is the angle between the vector $\mathbf{X}_{pv}$ and axis $\mathbf{Z}_{(\xi)}$;

$$[\tau_{mn,r}(\theta_{pv(\xi)})]_c = \begin{bmatrix} \tau_{\theta mn,r}(\theta_{pv(\xi)}) \\ \tau_{\phi mn,r}(\theta_{pv(\xi)}) \\ \tau_{rmn,r}(\theta_{pv(\xi)}) \end{bmatrix}_{(\theta,\phi,r)_{pv(\xi)}} = \begin{bmatrix} \tau_{mn,r}^m(\theta_{pv(\xi)}) \\ j\pi_{n,r}^m(\theta_{pv(\xi)}) \\ \mu_{n,r}^m(\theta_{pv(\xi)}) \end{bmatrix} , \quad [\pi_{mn,r}(\theta_{pv(\xi)}]_c = \begin{bmatrix} j\pi_{n,r}^m(\theta_{pv(\xi)}) \\ -\tau_{n,r}^m(\theta_{pv(\xi)}) \\ 0 \end{bmatrix} , \tag{18}$$

where the matrixes $\tau^m{}_{n,r}(\theta_{pv(\xi)})$ and $\pi^m{}_{n,r}(\theta_{pv(\xi)})$ are the row matrixes similar to the matrix $\mathbf{N}_{\zeta mn,r}(\mathbf{s}_{pv(\xi)})$ Eq. 16; $\mu^m{}_{n,r}(\theta_{pv(\xi)}) = z_n(\gamma)n(n+1)\pi^m{}_n(\theta_{pv(\xi)})\sin(\theta_{pv(\xi)})/m$ [20]. Subscripts $(\theta,\varphi,r)_{pv(\xi)}$ implies that the vector spherical functions are given in the orthonormal basis system

$\{\theta_{pv(\xi)}, \varphi_{pv(\xi)}, r_{pv(\xi)}\}$ of the $(XYZ)_{(\xi)}$ coordinate system. Taking into account that $|\mathbf{X}_{v(0a)}| \approx |\mathbf{X}_{v(a)}|$ and that the expression $|\mathbf{X}_{v(a)}| \approx |\mathbf{X}_{pv}| + \mathbf{s}_{v(a)}\mathbf{X}_{p(a)}$ is valid for far field scattering, Eq. (8) for the amplitude-phase factor can be presented in more convenient form from a systematic standpoint [20]:

$$k_{Ne}(|\mathbf{X}_{pv}|) = k_{Ne1}(|\mathbf{X}_{v(0a)}|)\cdot k_{Ne2}(\mathbf{s}_{v(a)}, \mathbf{X}_{p(a)}) \ , \tag{19}$$

$$\textit{where} \quad k_{Ne1}(|\mathbf{X}_{v(0a)}|) = \left[j\,\frac{\exp(jk_a|\mathbf{X}_{v(0a)}|)}{k_a\cdot|\mathbf{X}_{v(0a)}|} \right]^n \ , \qquad k_{Ne2}(\mathbf{s}_{v(a)}, \mathbf{X}_{p(a)}) = \left[\exp(-jk_a\mathbf{s}_{v(a)}\mathbf{X}_{p(a)})\right]^n \tag{20}$$

are the phase factors; $\mathbf{X}_{v(0a)}$, $\mathbf{X}_{p(a)}$ are the position vectors of the V observation point and of the p-sphere center in the corresponding $(XYZ)_{(0a)}$ and $(XYZ)_{(a)}$ coordinate systems.

Thus taking into account the modified coefficients, the electric field vector, scattered to an observation point V on a p-spherical particle illuminated by i-th plane wave, can be expressed for arbitrary (far- or near) zone in the orthonormal basis system $\{\theta_{pv(\xi)}, \varphi_{pv(\xi)}, r_{pv}(\xi)\}$ of the $(XYZ)_{(\xi)}$ coordinate system by the relatively simple formula in which the general (for all PWS plane waves) time- harmonic dependence $f_{sDa}(\omega_{sDa}t) = f_{La}(\omega_a t)\cdot f_{Da}(\omega_{Da}t) = \exp(-j\omega_{sDa}t)$ is suppressed:

$$\mathbf{E}_{sav(\theta v\xi)}(\mathbf{s}_{i(\xi)}, \mathbf{s}_{v(\xi)}, \mathbf{X}_{p(a)}, t) = \begin{bmatrix} E_{\theta,sav(\theta v\xi)} \\ E_{\varphi,sav(\theta v\xi)} \\ E_{r,sav(\theta v\xi)} \end{bmatrix} = A_a(|\mathbf{X}_{(a)}| = 0)\cdot k_{Ne1}(|\mathbf{X}_{v(0a)}|)\cdot$$
$$A_{sav(\theta v\xi)}(\mathbf{s}_{i(\xi)}, \mathbf{s}_{v(\xi)}, \mathbf{X}_{p(a)})\cdot \mathbf{e}_{sav(\theta v\xi)}(\mathbf{s}_{i(\xi)}, \mathbf{s}_{v(\xi)}, \mathbf{X}_{p(a)})\cdot f_{sDia}(\omega_{Dia}, \omega_{Da}, t) \ , \tag{21}$$

where $f_{sDia}(\omega_{Dia}, \omega_{Da}t) = f_{Dia}(\omega_{Dia}t)\cdot f_{Da}(\omega_{Da}t)$; $f_{Dia}(\omega_{Dia}t) = \exp(+j\omega_{Dia}t)$ and $f_{Da}(\omega_{Da}t) = \exp(+j\omega_{Da}t)$ are the coefficients taking into account variation of the Doppler frequencies $\omega_{Dia} = k_a\mathbf{s}_{i(a)}\mathbf{V}_{p(a)} = k_a\mathbf{s}_{i(ia)}\mathbf{V}_{p(ia)}$ for the i-th plane wave and $\omega_{Da} = k_a\mathbf{s}_{a(0)}\mathbf{V}_{p(0)}$ for the "a" beam; $\omega_{sDa} = \omega_a - \omega_{Da}$ is the well known expression of the PDA signal frequency [16];

$$A_{sav(\theta v\xi)}(\mathbf{s}_{i(\xi)}, \mathbf{s}_{v(\xi)}, \mathbf{X}_{p(a)}) = |\mathbf{F}_{sav(\theta v\xi)}(\mathbf{s}_{i(\xi)}, \mathbf{s}_{v(\xi)}, \mathbf{X}_{p(a)})| \ ; \ \mathbf{e}_{sav(\theta v\xi)}(\mathbf{s}_{i(\xi)}, \mathbf{s}_{v(\xi)}, \mathbf{X}_{p(a)}) = \frac{\mathbf{F}_{sav(\theta v\xi)}(\mathbf{s}_{i(\xi)}, \mathbf{s}_{v(\xi)}, \mathbf{X}_{p(a)})}{A_{sav(\theta v\xi)}(\mathbf{s}_{i(\xi)}, \mathbf{s}_{v(\xi)}, \mathbf{X}_{p(a)})} \tag{22}$$

are correspondingly the amplitude and unit polarization vector of the electric scattered field in the above orthonormal basis system;

$$\mathbf{F}_{sav(\theta v\xi)}(\mathbf{s}_{i(\xi)}, \mathbf{s}_{v(\xi)}, \mathbf{X}_{p(a)}) = k_{Ne2}(\mathbf{s}_{v(a)}, \mathbf{X}_{p(a)})\ k_{Pe}(\mathbf{s}_{i(a)}, \mathbf{X}_{p(a)})\ \ \mathbf{F}^{\wedge}_{sav(\theta v\xi)}(\mathbf{s}_{i(\xi)}, \mathbf{s}_{pv(\xi)}) \ , \tag{23}$$

$$\mathbf{F}^{\wedge}_{sav(\theta v\xi)}(\mathbf{s}_{i(\xi)}, \mathbf{s}_{pv(\xi)}) = A^{(1)}_{i(\xi)}(\mathbf{s}_{i(\xi)})[\mathbf{F}^{\wedge}_{sp(\theta v\xi),c}(\mathbf{s}_{i(\xi)}, \mathbf{s}_{pv(\xi)})]_r\,\mathbf{e}^{(1)}_{i(\xi)}(\mathbf{s}_{i(\xi)}) \ , \tag{24}$$

in which $A^{(1)}_{i(\xi)}$ and $\mathbf{e}^{(1)}_{i(\xi)}$ are calculated by using Eq. (3) for the $(XYZ)_{(a)}$ coordinate system ($\xi = a$) or Eq. (4) for the $(XZY)_{(ia)}$ system ($\xi = ia$);

$$[\mathbf{F}^{\wedge}_{sp(\theta v\xi),c}(\mathbf{s}_{i(\xi)}, \mathbf{s}_{pv(\xi)})]_r = [\mathbf{F}^{\wedge}_{xsp(\theta v\xi),c}(\mathbf{s}_{i(\xi)}, \mathbf{s}_{pv(\xi)}) \quad \mathbf{F}^{\wedge}_{ysp(\theta v\xi),c}(\mathbf{s}_{i(\xi)}, \mathbf{s}_{pv(\xi)}) \quad \mathbf{F}^{\wedge}_{zsp(\theta v\xi),c}(\mathbf{s}_{i(\xi)}, \mathbf{s}_{pv(\xi)})] \ , \tag{25}$$

$$F^{\Delta}_{\varepsilon\delta sp(\theta v\xi),c}(s_{i(\xi)},s_{pv(\xi)}) = \begin{bmatrix} F^{\Delta}_{\varepsilon\theta sp(\theta v\xi)m,c}(s_{i(\xi)},s_{pv(\xi)})\Phi_{m,r}(s_{pv(\xi)}) \\ F^{\Delta}_{\varepsilon\varphi sp(\theta v\xi)m,c}(s_{i(\xi)},s_{pv(\xi)})\Phi_{m,r}(s_{pv(\xi)}) \\ F^{\Delta}_{\varepsilon r,sp(\theta v\xi)m,c}(s_{i(\xi)},s_{pv(\xi)})\Phi_{m,r}(s_{pv(\xi)}) \end{bmatrix} ; \quad (26)$$

where the x, y or z vectors (for ε = x,y,z) of the modified matrix of the scattering factor $\mathbf{F}^{\Delta}_{sp(\theta v\xi)}$:

$$\Phi_{m,r}(s_{i(\xi)}) = [\ \varepsilon_{m_{min}}\Phi_{m_{min}}(\varphi_{pv(\xi)}) \quad \varepsilon_{m_{min}+1}\Phi_{m_{min}+1}(\varphi_{pv(\xi)}) \quad \dots \quad \varepsilon_{m_{max}}\Phi_{m_{max}}(\varphi_{pv(\xi)})\ ] \ ; \quad (27)$$

ε_m is the symmetry coefficient of the summing over m ($\varepsilon_m = 1$, for the summing limits $\{m_{min} = -n_{max};\ m_{max} = n_{max}\}$ and arbitrary m or for the $\{m_{min} = 0;\ m_{max} = n_{max}\}$ and $m = 0$; $\varepsilon_m = 2$, for the summing limits $\{m_{min} = 0;\ m_{max} = n_{max}\}$ and $m \geq 0$); $n_{max} = \rho_p + 4\rho_p^{1/3} + 2$ is the total number of terms [17] required for good convergence of the Mie equations; $\rho_p = k_a r_p$ is the Mie parameter; r_p is the radius of a spherical particle;

$$F^{\Delta}_{\varepsilon\delta sp(\theta v\xi)m}(s_{i(\xi)},s_{pv(\xi)}) = [N^{(3)\Delta}_{\delta mn,r}(s_{pv(\xi)})]_r\ [a^{\Delta}_{\varepsilon mn,c}(s_{i(\xi)})]_c \quad (28)$$

is the m-th element of the corresponding column vector $\mathbf{F}^{\Delta}{}_{\varepsilon\delta sp(\theta v\xi)m,c}$ of the modified scattering factor; $\delta = \theta,\varphi,r$;

$$[a^{\Delta}_{\varepsilon mn,c}(s_{i(\xi)})]_c = \begin{bmatrix} a^{\Delta}_{\varepsilon mn,c}(s_{i(\xi)}) \\ b^{\Delta}_{\varepsilon mn,c}(s_{i(\xi)}) \end{bmatrix} = \begin{bmatrix} \alpha_{n,d}(\rho_p,m_p) & 0 \\ 0 & \beta_{n,d}(\rho_p,m_p) \end{bmatrix} \begin{bmatrix} P^{\Delta}_{\varepsilon mn,c}(s_{i(\xi)}) \\ Q^{\Delta}_{\varepsilon mn,c}(s_{i(\xi)}) \end{bmatrix} ; \quad (29)$$

the vectors $\mathbf{a}^{\Delta}{}_{\varepsilon mn}$ and $\mathbf{b}^{\Delta}{}_{\varepsilon mn}$ are the 1*n column matrixes, which elements $a^{\Delta}{}_{\varepsilon mn}$ and $b^{\Delta}{}_{\varepsilon mn}$ are the expansions coefficients for the scattered field modified by using coefficient k_p; $\alpha_{n,d}(\rho_p,m_p)$ and $\beta_{n,d}(\rho_p,m_p)$ are the diagonal matrixes which elements are the familiar Lorenz-Mie coefficients $\alpha_{n,d}(\rho_p,m_p)$ and $\beta_{n,d}(\rho_p,m_p)$ [2]; m_p is the complex refractive index of spherical particle relative to the medium.

Analysis of the equations shows that the calculations of the scattered field vector in the $(XYZ)_{(a)}$ coordinate system (ξ = a) has some difficulties. This is due to the fact that $s_{yi(a)} \neq 0$ and $c_{zi(a)} \neq 0$ for most of the i-th plane waves of the PWS spectrum. This leads to complication the formulas for the expansion coefficients for the incident field and to the necessity to calculate the above matrixes over the wide range of order m and degree n [15]:

$$-n_{max} \leq m \leq n_{max} \ , \quad |m| \leq n \leq n_{max} \ . \quad (30)$$

To decrease the time of simulation we will get at first the unit polarization vector of scattered field in the $(XYZ)_{(ia)}$ coordinate system of the i-th plane wave and then to transform this vector to the $(XYZ)_{(pol)}$ polarizer coordinate system. It is obvious that for the $(XYZ)_{(a)}$ coordinate system $s_{xi(ia)} = s_{yi(ia)} = 0$ and $[\mathbf{P}^{\Delta}{}_{\varepsilon mn,c}(s_{i(ia)})]_c = 0$ for $m \neq 1$. Thus it is enough to solve the 1*n matrixes instead the $m^*n_{max}/2 - m^*n_{max}$ matrixes (see Eq.31) for the $(XYZ)_{(a)}$ coordinate system. It is not difficult to show that the formula for the modified scattering factor in the $(XYZ)_{(ia)}$ coordinate system and in the far scattering zone (in which a photoreceiver of PDA is located) is essentially simplified:

$$[F^{\Delta}_{sp(\theta via)}(s_{i(i-1)},s_{pv(ia)})]_r = [F^{\Delta}_{xsp(\theta via)} \quad F^{\Delta}_{ysp(\theta via)} \quad F^{\Delta}_{zsp(\theta via)}] = \begin{bmatrix} S_2(\theta_{pv(ia)},\rho_p,m_p)\cos\varphi_{pv(ia)} & S_2(\theta_{pv(ia)},\rho_p,m_p)\sin\varphi_{pv(ia)} & 0 \\ -S_1(\theta_{pv(ia)},\rho_p,m_p)\sin\varphi_{pv(ia)} & S_1(\theta_{pv(ia)},\rho_p,m_p)\cos\varphi_{pv(ia)} & 0 \\ 0 & 0 & 0 \end{bmatrix}, \tag{31}$$

where S_1, S_2 are the well known [19] elements of the amplitude scattering matrix for p-spherical particle for which calculation it is necessary to sum only n_{max} terms.

The transformation of the unit polarization vector $\mathbf{e}_{sav(\theta via)}$ obtained by using Eqs. (22) - (24),(31) and the vector of the modified scattering factor $\mathbf{F}^{\Delta}_{sav(\theta via)}$ into the $(XYZ)_{(jpol)}$ polarizer coordinate system can be performed by

$$e_{sav(pol)}(s_{v(ia)},s_{v(ia)},X_{p(a)}) = R_{\Sigma pol}e_{sav(\theta via)}(s_{i(ia)},s_{v(ia)},X_{p(a)}) \quad , \quad F^{\Delta}_{sav(pol)}(s_{i(ia)},s_{v(ia)}) = R_{\Sigma pol}F^{\Delta}_{sav(\theta vi:)}(s_{i(ia)},s_{v(ia)}), \tag{32}$$

where $\mathbf{R}_{\Sigma}$ is the transform matrix given in [13].

Consequently, the electric vector $\mathbf{E}_{sav(pol)}(t)$ of the field scattered to the observation point V taking into account the contribution of all i-th plane waves of the "a" beam angular spectrum can be written as:

$$E_{sav(pol)}(t) = A_a(|X_{(a)}| = 0)k_{Ne1}(|X_{v(ia)}|)\cdot\tau_{pol}\cdot k_{Ne2}(s_{v(a)},X_{p(a)})\cdot f_{sDa}(\omega_{sDa}t)\cdot \iint F^{\Delta}_{sav(pol)}(s_{i(ia)},s_{v(ia)})\cdot k_{Pe}(s_{i(a)},X_{p(a)})\cdot f_{sDia}(\omega_{Dk},\omega_{Da},t)ds_{xi(a)}ds_{yi(a)} \ , \tag{33}$$

where $f_{sDa}(\omega_{sDa}t)$ is the general time- harmonic dependence suppressed in Eq. 21; τ_{pol} is the diagonal vector of the polarizer transmission coefficients.

A similar expression is valid for the trailing incident beam by using subscript "t" instead "a".

Eq. (33) is the basic relationship to obtain the expression of the interference field amplitude of the scattering (practical - the PDA signal) in the observation point V:

$$A_{sv}(t) = \sqrt{(E_{sav(pol)}(t) + E_{sv(pol)}(t))(E^{*}_{sav(pol)}(t) + E^{*}_{sv(pol)}(t))} \ . \tag{34}$$

Comprehensive expressions of the PDA signal are eliminated in this work because it is well known [16].

4 Conclusions

A mathematical formulation is presented to calculate the signal of a generalized optical PDA system that incorporates two elliptically polarized beams with arbitrary profiles and known angular plane wave spectrum. The expressions for the unit polarization vector of the each i-th PWS plane-wave are obtained. It is suggested for essential decreasing of calculation time to express the amplitude and unit polarization vector of the scattered electric field in the coordinate system of the i-th plane wave for the PWS of each incident beam and then to transform this vector in the coordinate system of the receiver polarizer. All transformations are provided with use of the elements of the corresponding unit propagation and position vectors. Thus, practically all non-effective and repeated calculation of trigonometric functions are eliminated.

The technique is valid for far field scattering as well as for near field scattering. It is usable to investigate the signal of a maladjusted PDA systems.

It is shown that variation of the coordinates of the moving spherical particle influence only on the phase-factors expressions of which are located outside of the Mie algorithm (outside of the formula

for the modified scattering factor) and are independent on the i-th plane wave parameters. Using of this factor also simplifies the calculation of the PDA signal in case of the particle movement. Alike to the previous papers this technique allows to estimate the fine effect of influence a particle velocity variation on the frequency and phase of PDA signal by using coefficient $f_{sDia}(\omega_{Dia},\omega_{Da},t)$.

The suggested method is suitable to simulate the electric and magnetic fields scattered by other measurement or control systems with non-Gaussian profile of the incident beams.

References

1. U. Munasse, T. Wriedt, and K. Bauckhage, Phase Doppler sizing of optically absorbent single- and multi component liquid droplets using semiconductor devices.*Sci.Thechnol.*,vol. 4, pp. 369-377,1993.
2. H.C. van de Hulst, *Light Scattering by Small Particles*, Dover, New York, 1981.
3. G. Gouesbet, B. Maheu and G. Grehan, Scattering of a Gaussian Beam by a Sphere Using a Bromwich Formulation : Case of an Arbitrary Location. *Part. Pat. Syst. Charact.*, vol. 5, pp. 1-8, 1988.
4. K.F. Ren, G. Grehan, and G. Gouesbet, Localized Approximation of Generalized Lorenz-Mie Theory: Faster Algorithm for Computation of Beam Shape Coefficients, g^m_n. *Part. Pat. Syst. Charact.*, vol. 9, pp. 144-150, 1992.
5. N. Morita, T. Tanaka, T. Yamasaki, and Y. Nakanishi, Scattering of a Beam Wave by a Spherical Object. *IEEE Trans. Antennas Propagat.*, vol. 16, pp. 724-727, 1968.
6. W.C. Tsai and R.J.Pogorzelski, Eigenfunction Solution of the Scattering of Beam Radiation Fields by Spherical Objects. *J. Opt. Soc. Am.*, vol. 65, pp. 1457-1463, 1975.
7. W.G. Tam and R. Corriveau, Scattering of Electromagnetic Beams by Spherical Objects. *J. Opt. Soc. Am.*, vol. 68, pp. 763-767, 1978.
8. J.S. Kim and S.S. Lee, Scattering of Laser Beams and the Optical Potential Well for a Homogeneous Sphere. *J. Opt. Soc. Am.*, vol. 73, pp. 303-312, 1983.
9. J.P. Barton, S.A. Schaub, and D.R. Alexander, Electromagnetic Field for a Beam Incident on two Adjacent Spherical Particles. *Appl. Opt.*, vol. 30, pp. 4706-4715, 1991.
10. V.I Ovod, Calculation of the Characteristics of Optical Particle Size Analyzer into Account of Convergence of a Non-Uniform Illuminating Beam. *Sov. J. Opt. Technol.*, vol. 53, pp. 1-4, 1986.
11. S. Colak. Focused Laser Beam Scattering by Stationary and Moving Particles: A Theoretical Study, Ph.D. thesis, University of California, Los Angeles, 1978.
12. E.E.M. Khaled, S.C. Hill, P.W. Barber, Scattered and Internal Intensity of a Sphere Illuminated with a Gaussian Beam. *IEEE Trans. Antennas Propagat.*, vol. 41, pp. 295-303, 1993.
13. V. Ovod, T. Wriedt, K. Bauckhage, Modified Fast-Technique of the Increasing Computation Accuracy of Phase-Doppler Spray Analyzers / *Proc. Sixth International Conference on Liquid Atomization and Spray Systems*, Rouen, France, July 1994 (to be published).
14. By D. Mackowski, Analysis of Radiative Scattering for Multiple Sphere Configurations. *Proc.R.Soc.Lond A*, vol.433, pp.599-614, 1991.
15. J.H.Bruning. Multiple Scattering by Spheres. Ph. D thesis, University of Illinois, 1969
16. A.A. Naqwi and F. Durst, Analysis of Laser Light-Scattering Interferometric Devices for in-Line Diagnostics of Moving Particles. *Appl. Opt.*, vol. 32, pp. 4003-4018, 1993.
17. Ru T. Wang and H.C. van de Hulst, Rainbows: Mie Computations and the Airy Approximation. *Appl. Opt.*, vol. 30, pp. 106-117, 1991.
18. V.I.Ovod and V.Ya.Shlyko, Correction of the Characteristics of Laser Microparticle Analyzers Taking Account of the Nonuniformity of the Radiation Flux Density Distribution. *Sov. J. Opt. Technol.*, vol. 52, pp. 261-263, 1986.
19. C.F. Bohren and D.R. Huffman, *Absorption and Scattering of Light by Small Particles*, Willey - Interscience, New York, 1983.
20. A-K.M. Hamid, Electromagnetic Wave Scattering by Many-Sphere Systems With Application to Simulation of Three Dimensional Bodies, Ph.D. thesis, University of Manitoba, Canada, 1991.

These research results were attained with the assistance of the Alexander von Humboldt Foundation.

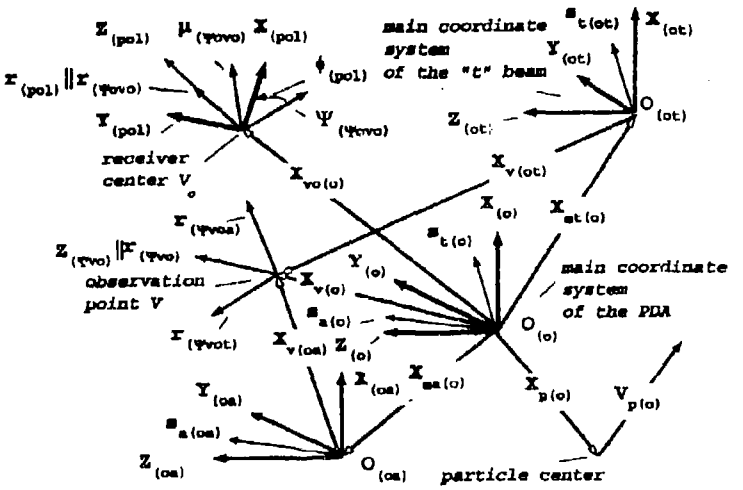

Fig.1. Relative position of the arbitrary located main coordinate system $(XYZ)_{(0)}$ of PDA, intermediate coordinate systems $(XYZ)_{(0a)}$ and $(XYZ)_{(0t)}$ for the approaching and the trailing beams, correspondingly, receiver center V_0 and observation point V.

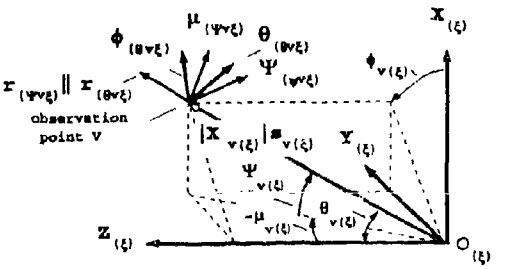

Fig. 2. Two kind of orthonormal basis vectors $\{\theta_{(\theta v\xi)}, \Psi_{(\theta v\xi)}, \Gamma_{(\theta v\xi)}\}$ and $\{\psi_{(\psi v\xi)}, \mu_{(\psi v\xi)}, \Gamma_{(\psi v\xi)}\}$ for calculation and representation of the scattering polarization vector.

TIME-DOMAIN ELECTROMAGNETIC RESPONSES AND MODEL UNCERTAINTIES

R. Inguva
Department of Physics and Astronomy
University of Wyoming
Laramie, WY 82071

C. Ray Smith
Advanced Sensors Directorate
Research, Development, and Engineering Center
U. S. Army Missile Command
Redstone Arsenal, AL 35898-5253

Paul M. Goggans
Department of Electrical Engineering
University of Mississippi
University, MS 38677

and

Dennis J. Andersh
Wright Laboratory
Wright Patterson Air Force Base
Dayton, OH 45433-6543

ABSTRACT

Uncertainties in the geometry of scattering systems may have major implications for system identification based on electromagnetic signatures. We derive a probability distribution to be used for system identification under conditions of model uncertainties; this distribution will allow us to study the effects of such uncertainties on system identification. We investigate in detail the effects of perturbations of the dimensions of an open-ended cavity on its time domain response. We report on numerical results in the high-frequency regime, performed for rectangular and circular geometries using the modal expansion method.

1. INTRODUCTION

In the last few years, considerable effort has been devoted to experimental and theoretical studies of high range-resolution radar returns from metallic targets with complicated geometries. On the experimental side, high range-resolution radar has been

available for some time. On the theoretical side, very sophisticated numerical codes have been developed using the shooting and bouncing ray method (SBR) to study radar returns from complicated geometries [1]. The *XPATCH* computer code is now becoming a standard in the field [2].

In this paper, we address several issues that have not been dealt with before. We are exclusively concerned here with radar returns from open ended cavities. While highly accurate numerical codes are now available, the sensitivity of the results to uncertainties in the various parameters that are input to these codes has not been investigated. For example, unknown variations in geometrical dimensions and surface conditions, such as deformations, roughness and deposited material, represent such uncertainties. One can identify several problem areas requiring analysis: Foremost is the effects of geometrical uncertainties on radar returns, and next is the consequences of deposits of inhomogeneous dielectric coatings on metallic surfaces. The effect of dielectric coatings as a function of thickness on radar range profiles has apparently not been studied before.

In this paper, we concentrate on the effect of geometrical uncertainties on the RCS and range profiles in the frequency and the time domains. In Sec. 2, using Bayes' theorem in probability theory, we present a general procedure for extracting probabilty distributions based on data and the available information on the uncertainties discussed above. In Sec. 3, we consider the case of circular and rectangular geometries and investigate the effect of geometrical uncertainties on the radar range profiles using the modal approach. In Sec. 4, we offer a few concluding remarks.

2. Probability Distribution Functions and Model Uncertainties

Target identification by means of high range-resolution radar (HRR) requires a complete set of signatures (range profiles) of potential targets to be available in the target library. The radar return from an unidentified object could then be matched against the library as part of an identification process [3, 4]. The radar waveform incident on the target will be denoted by $f(t)$. The received signal $g(t)$ is then of the form [4]:

$$g(t) = \int_{-\infty}^{\infty} r(t,t')f(t')dt', \tag{1}$$

where $r(t,t')$ is the target impulse response function. For a given $f(t)$, $g(t)$ is then the target signature. In the study reported in this paper, the point of interest is that the target impulse response function is a function of the geometry of the surface from which the return is observed [5].

In this paper, we assume that the target is stationary and has no moving parts that can modulate $f(t)$. The quantity $r(t,t')$ is then a function of $t-t'$ only, so that Eq.(1) becomes

$$g(t) = \int_{-\infty}^{\infty} r(t-t')f(t')dt'. \tag{2}$$

The surfaces of most targets are complicated and are composed of several contiguous and overlapping surfaces. Let S represent the surface of the target contributing to the return

$g(t)$. In numerical computations, S is specified by an enumeration of a set of parameters (in some cases, the set may be extremely large). Thus, we write

$$S = S(\alpha_1, \alpha_2, \ldots, \alpha_M), \tag{3}$$

where $\alpha_1, \ldots, \alpha_M$ are the M parameters that are required to characterize this surface. In the case of cylindrical geometry, the surface is specified by two parameters: length and radius of the cylinder. In general, we have

$$r = r(t, \boldsymbol{\alpha}, \Theta), \tag{4}$$

where $\boldsymbol{\alpha}$ is a vector set of surface parameters and Θ is the aspect angle. Hence, the target signature $g(t)$ also depends on the surface parameters and the aspect angle.

We give next a brief description of the problem we want to consider in this paper and why it is of interest. Even though a library of target signatures can be prepared in principle, in practice a target may have no correspondent in the library because its surface parameters differ, by an unknown amount, from any used in generating the library. Alternatively, we could say that no two targets of the same class are completely identical with respect to the geometrical surfaces responsible for the returns. Also, the surface of a given target will be subject to deformations and depositions over a period of time. This statement applies to external surfaces and to internal surfaces such as those of a cavity. It would be especially interesting to determine the effects of dielectric coatings on the inner surfaces of cavities; however, we do not consider these perturbations in this paper, even though the formulation to be outlined next is general enough to cover these cases. The problem we consider then is how to incorporate the geometrical uncertainties into the analysis for radar target identification. In the rest of this section we outline a procedure using Bayesian statistical methods [6].

Given data on range profiles, we would like to obtain the probability that one of the model target signatures in the library is true. Thus, we need the following conditional probability: $p(g_k \boldsymbol{\alpha}_k | DE)$, which is the probability for model g_k and parameter set $\boldsymbol{\alpha}_k$ for target class k, given the data D and our prior information E.

The probability distribution that we will be able to assign is $p(D|g_k \boldsymbol{\alpha}_k E)$. This will be used as the likelihood function for the model g_k based on data D. In order to relate $p(g_k \boldsymbol{\alpha}_k | DE)$ to $p(D|g_k \boldsymbol{\alpha}_k E)$, we use Bayes' theorem:

$$p(g_k \boldsymbol{\alpha}_k | DE) = \frac{p(g_k \boldsymbol{\alpha}_k | E)\, p(D | g_k \boldsymbol{\alpha}_k E)}{p(D|E)}. \tag{5}$$

where $p(g_k \boldsymbol{\alpha}_k | E)$ is the prior probability for g_k and $p(D|E)$ is the prior, or global, probability for the data D—here, $p(D|E)$ serves as a normalization constant.

Once $p(g_k \boldsymbol{\alpha}_k | DE)$ has been assigned, inference on the validity of various $\{g_k\}$ can be carried out and a decision can be made as to which target is supported by the data. The above analysis assumes that the underlying model relating $g_k(t)$ to $r_k(t)$ and $f(t)$ is known along with all the parameters. As discussed earlier, we cannot expect to have

accurate information on the α_k. In the statistical literature such parameters, being of no interest beyond the inference, are called *nuisance parameters*. To eliminate the explicit appearance of such parameters, we marginalize over them:

$$p(g_k \alpha_k | DE) = \int d\alpha_k \, p(g_k \alpha_k | DE)$$
$$= \int d\alpha_k \, p(D | g_k \alpha_k E) \, p(g_k \alpha_k | E), \tag{6}$$

which is seen to be a weighted average. Once the likelihood $p(D|g_k \alpha_k E)$ and the prior $p(g_k \alpha_k|E)$ are specified, we can obtain $p(g_k|DE)$, which can be used for radar target identification. Previous work in other areas shows such an averaging over the nuisance parameters leads to significantly better performance than other methods [7]. In most problems, an appropriate choice for $p(D|g_k E)$ is a Gaussian [], given by

$$p(D|g_k E) = (2\pi\sigma^2)^{-N/2} \exp[(d \cdot d - 2d \cdot g_k + g_k \cdot g_k)/2\sigma^2]. \tag{7}$$

In the absence of any further information on α_k, one chooses a uniform prior or a Jeffreys prior for α_k, where the Jeffreys prior [8] is given by $p(g_k \alpha_k|E) \propto (\alpha_1 \cdots \alpha_M)^{-1}$.

In the case of circular cylindrical geometry, $M = 2$, $\alpha_1 = a$, the radius of the cylinder, and $\alpha_2 = L$, the length of the cylinder. In the case of rectangular geometry, $M = 3$ and $\alpha_1 = a$, $\alpha_2 = b$, $\alpha_3 = c$, the sides of the cavity. Determination of $p(g_k|DE)$ based on the analysis presented above would be extremely valuable and work along these lines is in progress. To get an estimate on the potential significance of geometrical uncertainties, we computed the effects of variations in the dimensions of both rectangular and circular cylindrical cavities on their time-domain response functions. These results are presented and discussed in the next section.

3. Effect of Geometrical Uncertainties on Range Profiles for Circular Cavities

Detailed investigations based on the modal solution approach have been carried out by Lee and Chou [9]. These authors computed the RCS for both $\theta\theta$ polarization as well as $\varphi\phi$ polarization as a function of the angle. The geometry used in this work is shown in Fig. 1. Because of circular symmetry the azimuthal angle ϕ can be set to zero. Lee and Chou [9] used the Stratton-Chu approximation in the formulation and kept only the propagating modes at a given wavelength. As the details of the calculations are well documented in the literature, we present only the results using this modal approach.

The RCS as a function of the angle θ is illustrated in Fig. 2 for the $\theta\theta$ polarization and in Fig. 3 for the $\phi\phi$ polarisation for the case $a = 15\,cm$, $L = 90\,cm$ at a frequency of 10CHZ. The results of Figs. 2 and 3 are in complete agreement with the earlier work in the literature [9]. The variation of RCS at any θ with the radius of the circular cavity is illustrated in Figs. 4 and 5 for the two polarizations. We note from these three-dimensional plots that at certain angles there are sharp variations even for a few percent

variation in the radius of the cavity. We have checked numerically that for these cases, new modes that were evanascent become propagating as the radius is varied.

We now turn to the calculation of range profiles. The scattering amplitude as a function of frequency f is defined by

$$G(f) = \int_{-\infty}^{\infty} g(t) e^{-i2\pi ft} dt, \tag{8}$$

where $g(t)$ is the radar return signal as a function of time. Because the incident signal is band-limited, it is only necessary to determine $G(f)$ for frequencies in the passband $F(f)$ in order to calculate $g(t)$. For the purposes of calculation of $g(t)$ any suitable band-limited function $F(f)$ can be chosen; we have used the four-term Blackmann-Harris window for $F(f)$. The function $g(t)$ can then be expressed in the form

$$g(t) = i(t)\cos(2\pi f_0 t) + q(t)\sin(2\pi f_0 t), \tag{9}$$

where $i(t)$ and $q(t)$ are the in-phase and quadrature components of $g(t)$. The four-term Blackmann-Harris window function for $F(f)$ is symmetric about the peak frequency f_0. In this case, the in-phase and quadrature components can be written in the form [5]:

$$\begin{aligned} i(t) + jq(t) &= \int_{-\Delta f/2}^{\Delta f/2} F(f + f_0) G^*(f_0 - f) e^{j2\pi ft} df, \\ g(t) &= p(t)\cos\{2\pi f_0 t + \tan^{-1}[q(t)/i(t)]\}, \\ p(t) &= [i^2(t) + q^2(t)]^{1/2}. \end{aligned} \tag{10}$$

Thus, $p(t)$ is the envelope of the return signal and is referred to herein as the radar profile. The radar profile is computed from Eqs.(8) - (10), where the scattering amplitude $G(f)$ is obtained from the modal formulation.

In Figs. 6 - 9 we plot the radar profile function $p(t)$ of a circular cavity as a function of time and radius and at fixed angles 10° and 19.8°. The bandwidth Δf is 1GHZ at a center frequency of 10GHZ. For the Blackmann-Harris window we chose a bandwidth so as to achieve a time resolution of approximately 1 nsec. We note that the main feature (peak) in $p(t)$ occurs approximately at $t = 2L/c\cos\theta$, where L is the length of the cavity (in these examples $L = 90\,cm$). From Figs. 6 - 9, we notice again a few percent variation in the radius of the cavity can have significant effects on the profile for certain angles. The reasons for this are the same as the corresponding behavior in the RCS.

4. Conclusions

In this paper, we set up a formalism for studying the role of model uncertainties in the radar target identification problem. In particular, using Bayesian statistical methods, we have shown how to incorporate geometrical uncertainties for estimating the return signals from various geometries. As a first step in carrying out the program, we computed the effect of varying the dimensions of rectangular and circular cavities with perfect conducting terminations on the radar range profiles. We have shown that for certain angles

the effects can be striking and thereby that the study of the role of these uncertainties is very important. With the method of moments [10], it is possible to obtain relatively accurate solutions for the time-domain response of a circular cavity. The role of geometrical uncertainties should be investigated using the more accurate methods and compared with the modal solutions presented here, and work along these lines is in progress.

References

[1] H. Ling, R. C. Chou and S. W. Lee, "Shooting and bouncing rays: Calculating the RCS of an arbitrarily shaped cavity," *IEEE Trans. Antennas Propagat.*, vol. AP-37, 1989, pp. 194 - 205.

[2] "User Manual for XPATCH," DEMACO Inc., Sept 15, 1993.

[3] C. Ray Smith, "On Radar Target Identification," in *Physics and Probability*, W. T. Grandy, Jr., and P. W. Milloni, eds., (Cambridge University Press, 1993), pp. 161 - 175.

[4] C. Ray Smith and Paul M. Goggans, "Radar Target Identification," *IEEE Antennas and Propagation Magazine* **35**, 1993, pp. 27-37.

[5] C. Ray Smith, "Theory of Radar Target Identification Including Model Uncertainties," U. S. Army Missile Command Technical Report. In preparation.

[6] Edwin T. Jaynes, *Probability Theory - The Logic of Science*. In preparation. Preliminary copies available from the author (Physics Department, Washington University, St. Louis, MO 63130).

[7] G. Larry Bretthorst, *Bayesian Spectrum Analysis and Parameter Analysis* (Springer-Verlag, Berlin, 1988).

[8] Harold Jeffreys, *Theory of Probability*, (Oxford University Press, Third Edition, 1961).

[9] S. W. Lee and R. C. Chou, "High Frequency RCS of Open Cavities with Rectangular and Circular Cross Sections," *IEEE Trans. Antennas Propag.*, vol. AP-37, 1989, pp. 648 - 654.

[10] R. F. Harrington, *Field Computations by Moment Methods*, (Macmillan, New York, 1968).

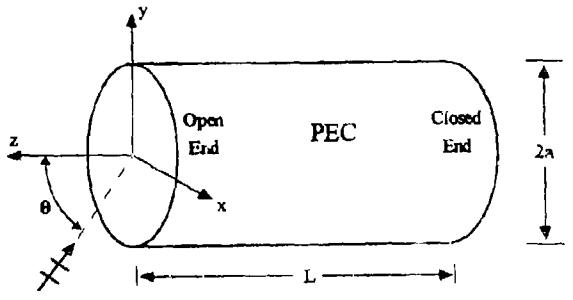

Fig. 1. Typical geometry of a circular cavity with one end open and the other end closed with a perfect electric conductor.

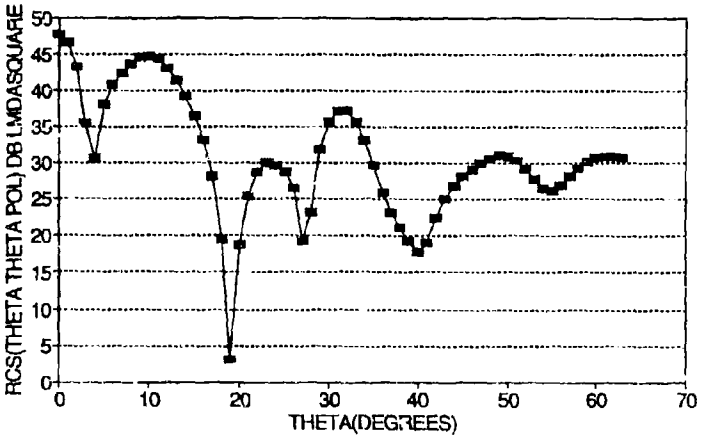

Fig. 2. RCS in $db\,\lambda^2$ as a function of θ for a circular cavity with radius 15 cm and length 90 cm at a frequency of 10 GHZ and for $\theta\,\theta$ polarization.

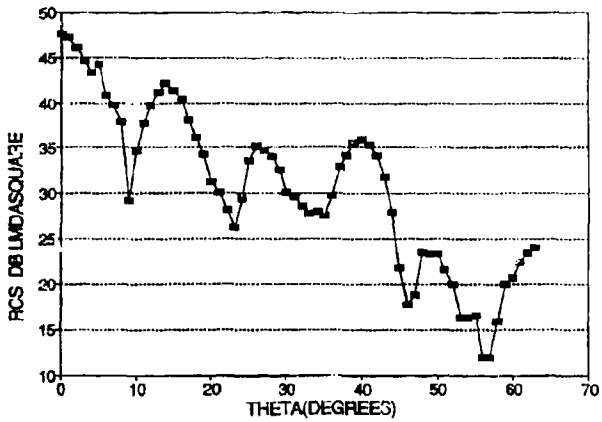

Fig. 3. Same as for Fig. 2, but for $\phi\,\phi$ polarization.

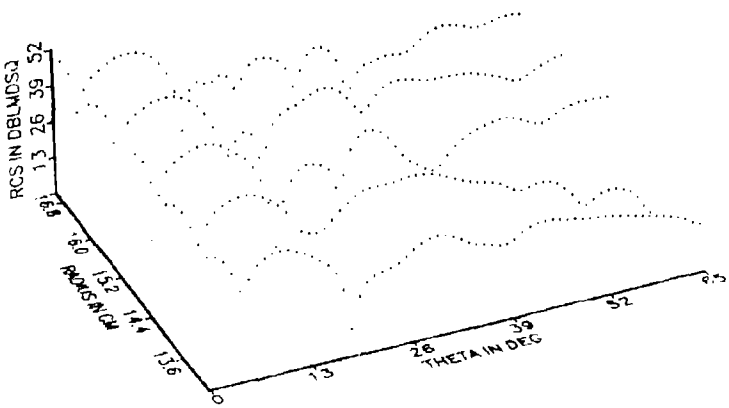

Fig. 4. Plot of RCS in $d\,b\,\lambda^2$ as a function of θ and radius, for $\theta\,\theta$ polarization and frequency 10 *GHZ*.

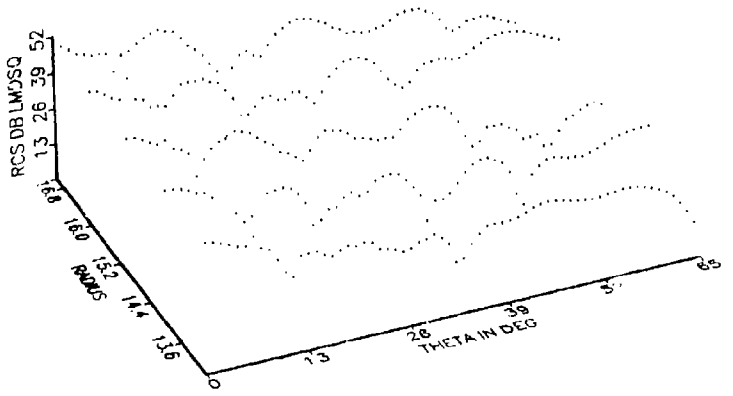

Fig. 5. Same as for Fig. 4, but for $\phi\,\phi$ polarization.

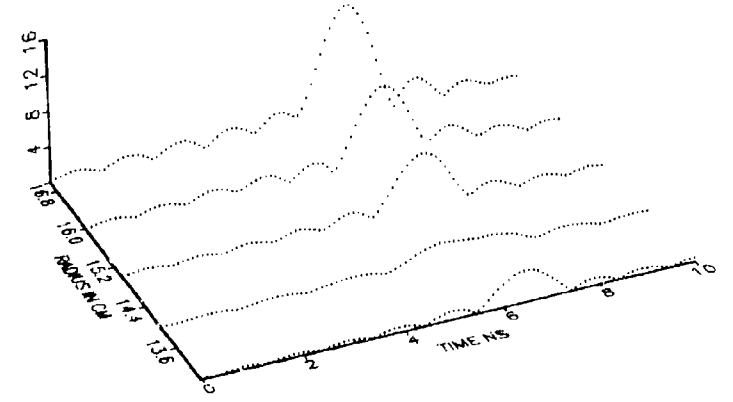

Fig. 6. Range profile $p(t)$ of Eq. (10) as a function of time and radius for $\phi\,\phi$ polarization at central frequency 10 GHZ and with bandwidth 1 GHZ for a circular cavity of length 90 cm and $\theta = 10°$.

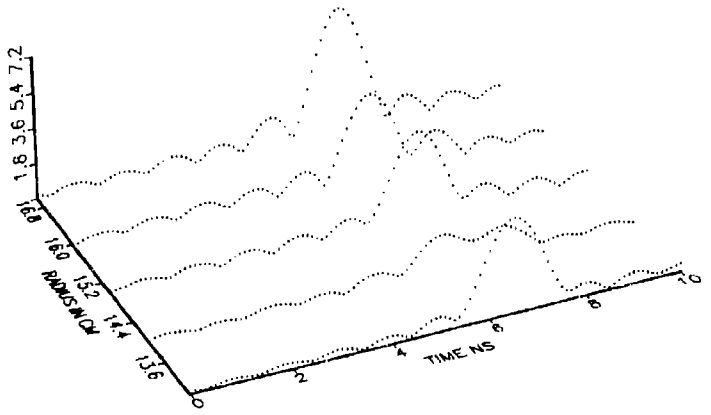

Fig. 7. Same as Fig. 6, but for $\theta = 19.8°$.

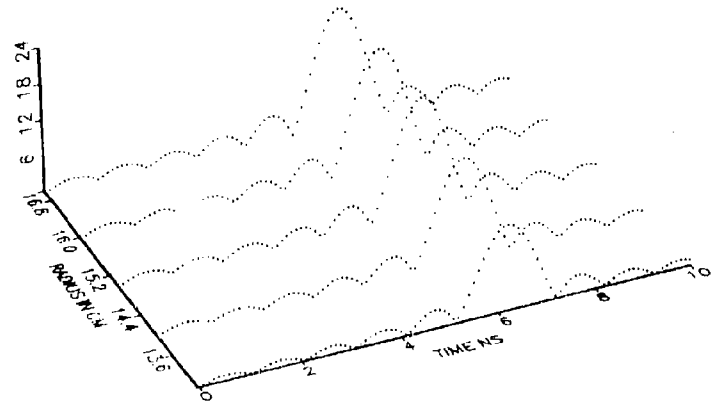

Fig. 8. Same as Fig. 6, but for $\theta\theta$ polarization.

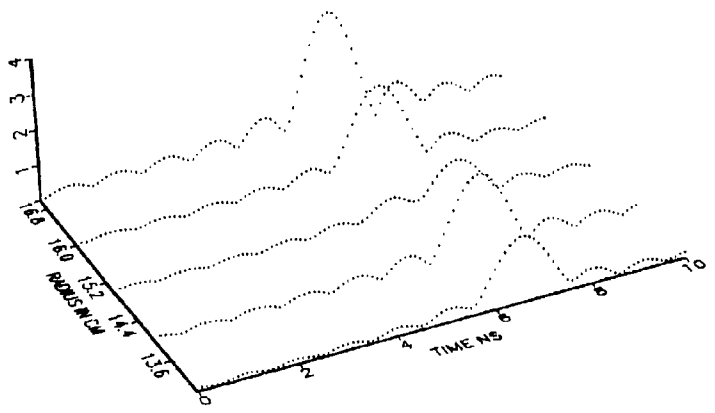

Fig. 9. Same as Fig. 7, but for $\theta\theta$ polarization.

EAM:BSC
AN ELECTROMAGNETIC SCATTERING ANALYSIS TOOL FOR WINDOWS

A. Paul Tsitsopoulos and Malcolm J. Packer
Science Applications International Corporation
Communication Engineering Laboratory
300 Nickerson Road, Marlborough, MA 01752
(508) 460-9500 FAX (508) 460-8100

ABSTRACT

SAIC has developed an electromagnetic scattering analysis tool for Windows™, EAM:BSC, that incorporates the Numerical Electromagnetic Code-Basic Scattering Code (NEC-BSC) with a graphical pre-and post-processor. EAM:BSC allows the user to graphically define a model and save it in standard NEC-BSC format. Windows™ multi-tasking capability is used to perform the NEC-BSC analysis transparently in the background from within EAM:BSC. User-specified output data is obtained directly from NEC-BSC output files and is displayed in color linear plots. Although NEC-BSC has been recompiled to run in Windows™, the analysis algorithms and output files remain unaltered, making EAM:BSC compatible with existing NEC-BSC input and output files.

EAM:BSC is designed to run on a 80386/486 PC with Windows™ 3.0 or higher running in enhanced mode. It requires a mouse, 4 MB of RAM, and about 3 MB of hard disk space. VGA graphics is recommended.

INTRODUCTION

Software tools for predicting the performance of antennas in complex environments have been available for several years. These tools, consisting of rigorous, time-intensive algorithms have, however, traditionally required the speed and processing power of main-frame computers, and have been extremely difficult to use. Now, due primarily to recent advances in computer hardware and software technology, these tools can realistically be applied on a PC as well.

One such tool is the Numerical Electromagnetics Code - Basic Scattering Code (NEC-BSC) [1]. NEC-BSC is a highly recognized code used for predicting antenna patterns and coupling in the presence of scattering structures that are generally greater than a few wavelengths in size. While porting it over to a PC has eased platform requirements, NEC-BSC remains, like most text-based engineering tools, user unfriendly, and requires extensive knowledge and experience to be used correctly and effectively.

In 1992, SAIC started development of a Windows™-based analysis tool for NEC-BSC for the USAF. The Electromagnetic Antenna Modeling System : BSC (EAM:BSC) consists of a customized model definition/drawing processor and a data post-processor. It is intended to be used for antenna analysis targeted at both experienced and novice electromagnetics (EM) engineers. Because of the anticipated broad range of user experience, the application was designed to support all of NEC-BSC's sophisticated antenna analysis features while also being intuitive enough to mitigate the most common deficiency of NEC-BSC, i.e., user error.

EAM:BSC

EAM:BSC is designed to run on a 80386/486 PC with Windows™ 3.0 or higher running in enhanced mode. It is a customized, intuitive, graphical user interface (GUI) for NEC-BSC. EAM:BSC has three main functions: 1) to graphically define the antenna and its environment; 2) to save the model and execute the analysis; 3) to read, process, and display user-specified data. The major components that make up the EAM:BSC include: a main menu, a model pre-processor, a transparent execution interface, a data post-processor, and an on-line help system.

Model Definition

A key feature of EAM:BSC is the model definition window. By design, it has the look and feel of a typical Windows™ vector-based drawing package. EAM:BSC, however, employs additional features for drawing in 3D and automating the tedious work of typing plate, cylinder, cone, etc., coordinates in a DOS text file. As shown in Figure 1, the window contains a model title, drawing area, tool bar for structure and view manipulation, scroll bars, and specific model information.

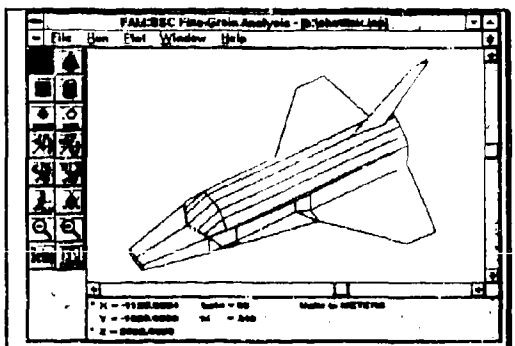

Figure 1. EAM:BSC Model Definition Window

Tool Bar

The major advantage of using EAM:BSC is the ability to define an entire model from within the drawing window. For the most commonly used options, there is no need to use a text editor. Each specific geometric solid that NEC-BSC uses, i.e. flat plate, elliptic cylinders cones, etc., is given a drawing tool. The individual tools, located in the toolbar shown in Figure 2, give you the ability to draw and edit each structure.

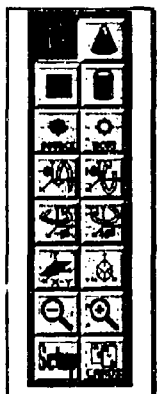

Figure 2. Tool Bar.

Model Building Blocks

There are several functions associated with the "Arrow Tool". Some of these include the ability to draw and edit any model building block, activate a parameters dialog box, change the location of a source or receiver, and, stretch or shrink a plate by "rubber banding" its corners.

The "Cone Frustum Tool" has not been implemented at the time of this paper.

Selecting the "Plate Tool" button activates the plate drawing tool and changes the cursor to a plate cursor. In NEC-BSC, a plate is defined by the number of corners and their location relative to the coordinate system origin. This is accomplished in EAM:BSC using the mouse to define the corner coordinates

of a new plate. For example, the first corner is specified by simply clicking the mouse at the desired coordinates. Each subsequent corner is similarly specified by moving the mouse in the model definition window and clicking at the location of each new corner. To complete a plate, you simply double-click the mouse on the last corner.

Selecting the "Cylinder Tool" button activates the cylinder drawing tool and changes the cursor to a cylinder cursor. Each new cylinder is given default values for specific geometric parameters, i.e. orientation, radius, etc. The only parameter defined with the mouse in the cylinder drawing mode is the location of the cylinder coordinate system origin.

Selecting the "Source Tool" or "Receiver Tool" button activates the source/receiver drawing tool and changes the cursor. Source/receiver position is specified simply by clicking in the model definition window at the desired location. A source/receiver dialog box is used to specify additional pertinent parameters.

View Manipulation

View manipulation is controlled using the following seven tools. These include: "Rotate in Theta", "Rotate in Phi", "Zoom in", "Zoom out", "Rotate to a Standard Plane" configuration, "Isometric View", and "Setup".

Selecting one of these buttons will rotate the entire model so that theta is either decremented or incremented. The curved arrow shows the apparent rotation of the model. The delta for rotation in theta can be customized by setting parameters via the "Set-Up Tool" button.

Selecting one of these buttons will rotate the entire model so that phi is either decremented or incremented. The curved arrow shows the apparent rotation of the model. The delta for rotation in phi can be customized by setting parameters via the "Set Up Tool" button

These tools are all part of a model rotation function that advances each time the button is selected. The first button rotates the model so that the your view is normal to the XY-plane (θ=0°, ϕ=0°). The second button rotates the model so that the your view is normal to the YZ-plane. (θ=90°, ϕ=0°). The third button rotates the model so that the your view is normal to the ZX-plane (θ=90°, ϕ=90°). In other words, with each button click, the next rotation function, and tool button face representative of the function, is called. For example, the first time the button is pressed, the model will be rotated to the XY-plane. If the button is pressed again, the model will be rotated to the YZ-plane. One more press will rotate the model to the ZX-plane, and another back to the XY-plane. This rotation sequence always begins in the XY-plane.

This "Isometric Tool" button rotates the model so that you view it from an isometric perspective (θ=45°, ϕ=45°).

The "Zoom In/Out" tools vary the magnification of the drawing area in the MDW. The magnifying glass with the minus sign reduces the magnification of the drawing area, while the tool with the plus sign increases the magnification of the drawing area.

This button lets you customize various settings for the drawing window. The available options include a maximum

model dimension, snap-to-grid, and theta and phi rotation increments.

The Maximum Model Dimension value controls the maximum model coordinate that can be specified. This setting is primarily to allow for a reasonably sized drawing area to be created.

The Snap-to-Grid resolution value controls the drawing grid resolution. For new models, it is easiest to draw when the maximum grid resolution is used, i.e. use a course resolution for the basic framework and then a finer grid resolution for detailed work. For example, if a model is to be created in 0.5 meter increments, the grid resolution should be set to 0.5. A setting of anything less would be unnecessary, and could even create a more difficult environment to work in. Existing models are automatically scanned for the maximum allowable grid resolution.

Theta and Phi Increment value are associated with the "Rotate Theta" and "Rotate Phi" tools. The values allow you to set the angle of rotation to you preference.

Building Plate Parameter Dialog Boxes

Non-geometric parameters for all structures, including sources and receivers, are specified via customized dialog boxes. To modify the parameters of a the specific existing model structure, you simply double click the cursor on that structure. This activates a dialog box which contains all of the structure's parameters. An example of the parameters dialog box for a plate is shown in Figure 3. From this parameters dialog box, you can modify or delete corner coordinates, modify the plate type, and, if applicable, modify the layer parameters.

In addition, default parameters can be specified for each tool so that all new structures created will exhibit the same parameters, minus the coordinates, of course. An example would be to set the plate tool parameters to always create a perfectly conducting metal plate.

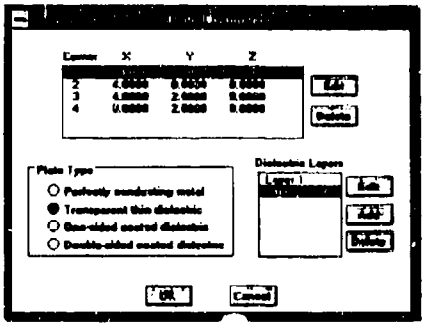

Figure 3. Plate Parameters Dialog Box

Control Line Editor

Upon completion of the model's geometry, program control information such as frequency, antenna movement, field patterns etc., must be specified. EAM:BSC simplifies this process with a control line editor, shown in Figure 4.

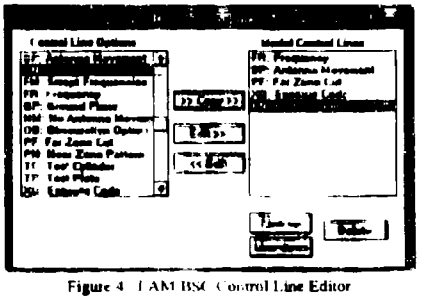

Figure 4. EAM:BSC Control Line Editor

The control line editor can be broken up into two sections: its left side contains all the control line options available in EAM:BSC, and its right side contains all the control lines being applied to the active model in the drawing window. The parameters associated with the control lines can

be quickly and easily modified using the two edit buttons located between the lists. An example of a dialog box used to edit a control line is shown in Figure 5, the Far Zone parameters dialog box. Additional features of the control line editor include the capability to default individual control line parameters to be used on all future models, and to create and save a default "Model Control Line List" to be recalled for use in any model at the click of a button.

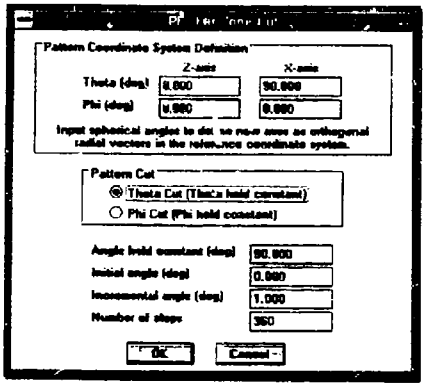

Figure 5. Far Zone Parameters Dialog Box

NEC-BSC Execution

Running a NEC-BSC analysis is accomplished by selecting the *Run* menu item. EAM:BSC automatically creates and saves an input file for the active model definition window, and then transparently executes NEC-BSC. Once an analysis has begun, the cursor changes to a rotating wheel, signifying execution is in process. At this time, you can take advantage of Windows ™ multi-tasking capability and switch to another application. EAM:BSC will notify you when the analysis is through. Figure 6 demonstrates the selection of the *Run* menu item and the prompt dialog box.

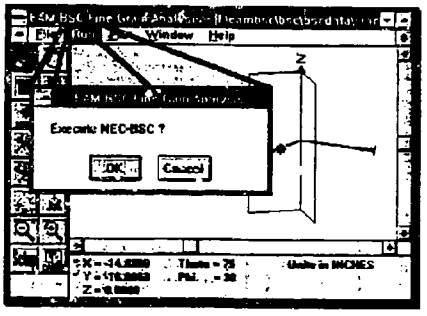

Figure 6. Selecting the ***RUN*** menu item.

Note: EAM:BSC uses NEC-BSC Version 3.2-3 recompiled to run on a PC running Windows™ in enhanced mode. The only modification made to the NEC-BSC code was a redefinition of the file name it executes on. *All algorithms and input/output formats remain unchanged.*

Data Presentation

Presently, EAM:BSC is capable of displaying far-field and radiation data for both angle and frequency sweeps. (An upgrade that incorporates near-field plots is near completion). It does not perform any reformatting or editing of NEC-BSC output files. Instead, it reads the NEC-BSC generated files for desired information and plots the data in the form of color linear plots, as shown in Figure 7. Here, both E-plane and H-plane E-Field patterns are displayed simultaneously on a single plot. The two patterns are distinguished by both line color and texture.

Data obtained from existing output files, including those generated on a main-frame computer can also be graphically displayed. In other words, huge models can be easily created with the EAM:BSC, transferred to a main frame computer for execution, and then transferred back to the PC for graphical display.

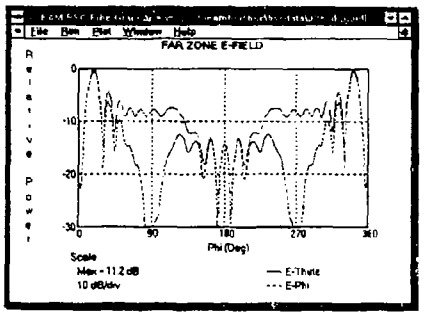

Figure 7. EAM:BSC Linear Plot of Far Zone Electric Field

One of the most useful features of EAM:BSC is the ability to display multiple windows on the screen simultaneously. Figure 8, for example, displays a model and two of its output plots, E-field and radiation intensity.

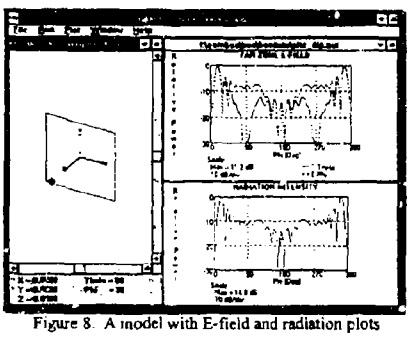

Figure 8. A model with E-field and radiation plots

SUMMARY

SAIC has developed an electromagnetic scattering analysis tool for Windows™, EAM:BSC, that incorporates the Numerical Electromagnetics Code - Basic Scattering Code (NEC-BSC) with a graphical pre-and post-processor. EAM:BSC can be used both by novice and experienced EM engineers and analysts. A user with only a basic understanding of PCs and Windows™ will be able to use this tool to predict the performance of any antenna and environment that can be modeled with NEC-BSC. EAM:BSC automates the otherwise tedious and confusing methods required to specify inputs and to view results. It includes 3D drawing capabilities, easy-to-understand output plots, error checking, and on-line help. It, also is capable of reading and editing existing NEC-BSC input and output files. Presently, EAM:BSC version 1.0 is available.

SAIC has three other Windows™-based graphical tools used for electromagnetics and propagation analyses. One uses closed form and simple MM solutions to perform quick parametric studies of twenty standing wave, traveling wave, and aperture antenna types. Since computationally simple solutions are used, predictions for each of the twenty antenna types can be obtained in under ten seconds. Another Windows™-based software package provides a graphical shell for the Numerical Electromagnetics Code (NEC) [2] called EAM:NEC [3]. NEC uses MoM algorithms to model antenna structures that are less than a few wavelengths in size. The graphical shell is similar to that of EAM:BSC except that it uses wires for model construction. IONWIN, SAIC's latest graphical shell, simplifies the use of IONCAP [4], a High Frequency (HF) skywave propagation code. IONWIN provides input windows, map windows, and plot windows. Input windows provide user-friendly dialog boxes with error checking for defining IONCAP input parameters. Map windows use the Defense Mapping Agency's Digital Chart of the World to display node locations and signal-strength contours on high-resolution maps. Plot windows are used to display IONCAP's numerical output data in the form of nine types of Cartesian and polar plot types.

Interoperability is built into all of SAIC's Windows™-based antenna, propagation. and map software. As a result, complete end-to-end communication system performance can be determined quickly, easily, and accurately.

REFERENCES

Windows™ is a registered trade-mark of Microsoft Corporation.

[1] Marhefka R., Silvestro J., Numerical Electromagnetic Code-Basic Scattering Code-Ver. 3, ElectroScience Laborat y, March 1989.

[2] Burke G.J., Poggio A.J., *Numerical Electromagnetics Code*, Lawrence Livermore Laboratory, January 1981.

[3] Packer M.J. Powers R.A., Tsitsopoulos A.P. *Graphical Shell For Numerical Electromagnetics Code*, Applied Computational Electromagnetics Society Conference, 1993

[4] Teters R.T., Lloyd J.L., Haydon G.W., Lucas D.L., *Ionospheric Communications Analysis and Prediction Program User's Manual*, Institute for Telecommunication Sciences.

SESSION 18:

PRE
AND
POST PROCESSING

Chair: Todd Hubing
C0-Chair: Linda Russell

NEC - MoM Workstation: NEEDS 3.0

L. Russell, D. Tam, J. Rockway, D. Wentworth
Naval Command Control and Ocean Surveillance Center
RDT&E Division
San Diego, CA 92152-5000

J. Eadie
Naval Sea Systems Command
Arlington VA 22242-5160

ABSTRACT

The Numerical Electromagnetic Code - Method-of-Moments (NEC-MoM), Version 4.0 is the principal computational tool for the determination of the shipboard EM environment in the HF through VHF bands. The use of the NEC-MoM for antenna system and electromagnetic environment evaluation is a lengthy, tedious, and error-prone process. NEC-MoM requires rigidly defined inputs and produces large masses of output data. A NEC-MoM Workstation, Numerical Electromagnetic Engineering Design System (NEEDS) 3.0, was developed to assist in making the method-of-moment process less tedious and more error-free.

1.0 INTRODUCTION

The ship electromagnetic (EM) environment today is very complex. In addition the ship EM environment has become a critical design resource as weapons and sensors have become more powerful, more sensitive to upset, and have expanded to make more sophisticated use of the EM spectrum. The task of integrating all the EM radiating and receiving systems into the topside of a Navy ship is very formidable. This task requires a broad and well founded background in electrical and electronics engineering, as well as a practical knowledge of Navy ships, Navy operating procedures, the shipboard operating environment, Navy equipments and required system performance.

Ship designers must address the key issues of (1) predicting the EM environment of new ship designs, major modernizations, or overhauls and (2) assessing the EMI impact of that environment on system performance and hence ship mission capabilities. Recent progress in workstation capabilities and algorithm development has significantly increased the effectiveness of computational electromagnetics (CEM). With the development of the NEC-MoM Workstation, NEEDS 3.0, ship designers can now more effectively apply these tools as an integral part of the ship design process.

NEEDS 3.0 was developed in the X-windows environment using the Motif toolkit for implementation on a UNIX workstation. NEEDS 3.0 currently resides on two UNIX workstations: the Naval Sea Systems Command (NAVSEA) CAD II Intergraph and the

Silicon Graphics (SGI) Iris Workstation. The supporting engineering graphics were developed using SPHIGS (Simple Programmer's Hierarchical Interactive Graphics System). This development approach ensures significant portability between UNIX based machines. Two different model visualization development approaches were used. Model visualization was developed using SPHIGS. An additional capability was developed using SGIs GL (Graphics Library) to make use of the SGI high performance visualization capabilities.

NEEDS 3.0 supports the three major modules of the method-of-moments' process: PROBLEM DESCRIPTION, EXECUTION, and SOLUTION DISPLAY. The main menu bar of NEEDS 3.0 is structured around the concept of the three major modules.

FILE	INPUT	EXECUTE	RESULT	OUTPUT
Open	Geometry description	Problem summary	All	Printer. . .
Save	Electrical description	Diagnostics	Impedance	Plotter . . .
Save as	Solution description	Translation	Admittance	Spreadsheet. . .
New		NEC-MoM Export	Currents	Visualization . . .
Exit		NEC-MoM Import	Charges	
		NEC-MOM execute	Coupling	
			Near fields	
			Patterns	

A filing capability is provided. INPUT consists of defining the geometry of the antenna, specifying the electromagnetic parameters such as frequency and sources, and choosing output products. To support the EXECUTION module NEEDS 3.0 translates the NEEDS problem definition into a NEC 4.0 problem description. The NEC output for a ship modeling problem can be considerable. In support of Solution Display NEEDS 3.0 provides the ability to view the tabular output. The tabular results can also be displayed in user-specified engineering graphs. In addition 3-D visual displays are available to enhance the understanding of the output. The structure of NEEDS 3.0 is shown below in the following pictorial.

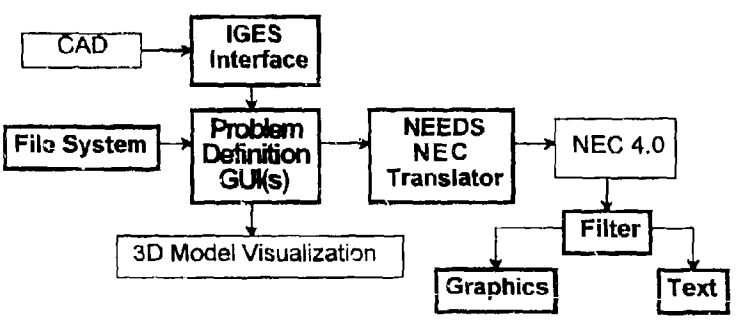

2.0 PROBLEM DESCRIPTION

INPUT consists of three submodules: Geometry description, Electrical description and Solution description. The user develops the PROBLEM DESCRIPTION accessing the series of windows listed in the table below.

GEOMETRY	ELECTRICAL	SOLUTION
Node Coordinates	Frequency	Maximum Coupling Calculation
Straight Wires	Loads	Near Electric Field
Tapered Wires	Voltage Sources	Near Magnetic Field
Catenary Wires	Incident Plane Waves	Radiation Patterns
Wire Arc	Transmission Lines	Print Options
Helix or Spiral	Two Port Networks	
Meshes	Insulated Wire	
Surface Patches	Ground Parameters	
Multiple Patches	Additional Ground Parameters	
Transformations	Upper Medium	
Rotations		
Reflections		
IGES		
Spiral Ordering		

Each window follows the Naval Sea Systems Command (NAVSEA) defined EM Engineering Common User Interface (CUI). An example of a graphical user interface (GUI) used in NEEDS 3.0 is displayed below for the Node Coordinates. In each GUI a list box will appear at the top of the dialog box containing a list of the defined items. Below the list box will be all of the entry fields that define the parameters for one item. Along the right side of the dialog box will be three push buttons; ADD, MODIFY, and DELETE. The user adds an item by filling in the parameter data and pushing the ADD button. Clicking on an item in the list box fills the parameter data for that item. The user modifies that item by editing the parameter data and pushing the MODIFY button. The user deletes an item by clicking on an item in the list box and pushing the DELETE button. At the bottom of the dialog box there will be four buttons. These four buttons and their actions are as follows:

- OK - Accept all of the inputs and dismiss the dialog box,
- APPLY - Accept all of the user inputs and do not dismiss the dialog box,
- RESET - Ignore all of the user inputs since the dialog box appeared or since the user hit the APPLY button (whichever happened last) but do not dismiss the dialog box,
- CANCEL - Ignore all of the user inputs since the dialog box appeared or since the user hit the APPLY button (whichever happened last) and dismiss the dialog box.

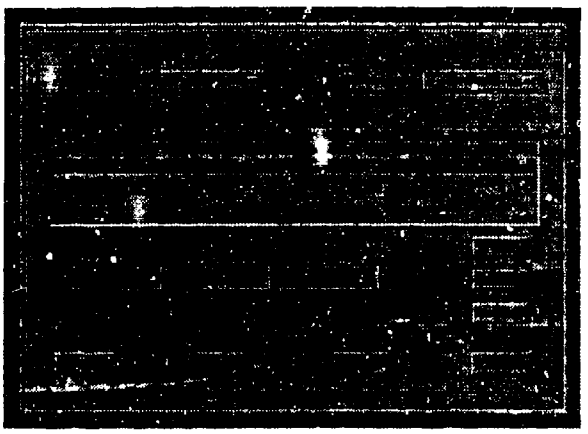

On-line help is available to assist the user in developing the INPUT. Intrinsic diagnostics at the window level improve the quality of the INPUT. As an example, intrinsic diagnostics ensure that wires do not have zero length.

Complex models often require several weeks of effort to specify, check, and correct. NEEDS 3.0 includes the ability to input the geometry from keyboard input. In addition a commercial computer-aided design (CAD) package will be used to support this submodule. It is desired that the commercial CAD product provide the following capabilities:

- 3-D model building
- 2-D model building
- Interface to keyboard, mouse, and digitizer
- Interface to IGES file format
- Automatic meshing for both wire griding and triangular patches
- Generation of 3-D model from a 2-D model description

The first three functions appear to be available in most commercial CAD products. The automatic meshing for both wire griding and triangular patches appear to be available in only some of the products. For complex structures, such as a ship, it is not apparent that the meshing capability is critical. In these cases an automatic mesher will not be able to accommodate the complexity of the model. However, the generation of a 3-D model from a 2-D model is a very important function. In many cases the building of a method of moments geometry data of a complex structure, such as a ship, will be initiated from drawings. The ability to generate a MoM model from a 2-D drawing will be considerably enhanced if the computer can propose an acceptable first guess at the 3-D model from the 2-D inputs. The NRaD developed IGUANA computer code is able to perform this function. The CAD

interface to NEEDS 3.0 will be in the form of an IGES interface. The choice of the commercial CAD package will be left to the individual user. There is some inconvenience to this approach. Two different environments will have to be learned: the commercial CAD package environment and the NEEDS 3.0 environment.

Finally, a spiraling capability is available in NEEDS 3.0. The ability to re-sort wires and patches along selected diagonals will considerably reduce the time required to solve the resulting MoM matrix equation. The amount of time spent partial pivoting during the LU-decomposition of the matrix will be considerably reduced.

3.0 EXECUTION

A problem summary is available to provide a quick overview of the particular problem. Extrinsic diagnostics are available to the user to further improve the quality of the INPUT. The extrinsic geometry diagnostics examine the geometry for conformance to individual wire, wire junction, and patch modeling guidelines. The modeling guidelines reside in a data base which could be modified as experience is gained and improved method of moments are developed. The GUI in NEEDS 3.0 for the geometry guidelines is shown below.

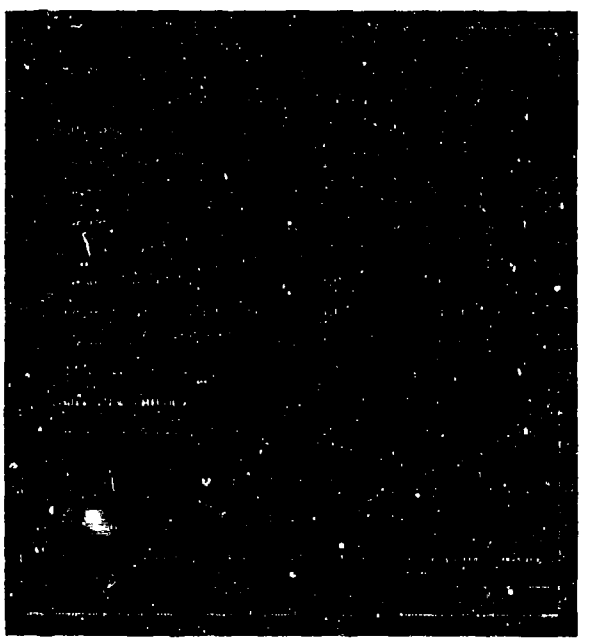

Finally, geometry visualization assists in input validation. In support of wire modeling these geometry visualization windows include: wire segmentation (segment length in meters), wire radius (in meters), wire segment to radius ratio, or wire connectivity (none, one, or both ends connected). All of these windows display the model as a 3-D object. As appropriate to the specific geometry visualization, the data is encoded in the color of each wire segment, using a linear or log color assignment scheme. A color key is displayed in the lower left corner of the window. The available transformations for the model include rotation, translation, and zooming. A sample window shows wire segmentation. Modification of the geometry can be accomplished using an editing capability that is linked to the 3-D model visualization.

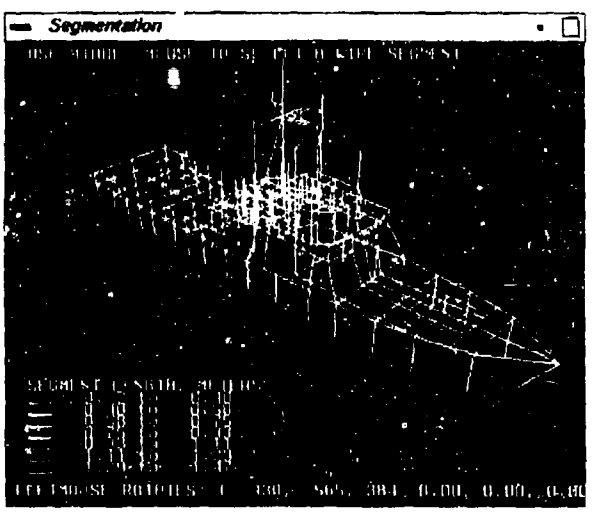

To support the EXECUTION module NEEDS 3.0 translates the NEEDS problem definition into a NEC-MoM problem definition. A capability also exists for editing the NEC-MoM problem definition. It is not necessary to go back to tthe problem definition GUIs to modify a given NEC data set. NEC-MoM is then run using the NEC problem definition. NEEDS can also translate a NEC data set back into a NEEDS problem definition.

4.0 SOLUTION DISPLAY

SOLUTION DISPLAY consists of tabular reports, engineering graphics and "thought enhancing" visualization windows. The availability of the visualization windows and the

quality of the visualization is workstation dependent. Again, an additional capability was developed using the SGIs GL (Grapics Library) to make use of the SGI visualization capability. The NEC output for a ship modeling problem can be considerable. A filter is used to view specific tabular results. These results include "All" of the NEC output and the specific tabular results including impedance, admittance, currents, charges, coupling, near fields and radiation patterns. The filtered tabular output is then available for plotting of engineering graphs. NEEDS 3.0 includes x-y plots, polar plots and the SMITH Chart. The user has only a certain amount of flexibility in defining these engineering graphs. The filtered results are also available in a form for "easy" input to a commercial engineering graphics programs. The user will make use of the commercial engineering graphics programs to provide the more "sophisticated" graphical display.

Solution description visualization is displayed in many different windows. These windows include currents (real component, imaginary component, magnitude, or phase), total near field (electric field, in volts/meter), z-component of near field, theta component of far field, and phi component of far field. Currents on the geometry are displayed using the same technique as was used for the geometry description products: current is color coded on a 3-D display of the model. Since currents are complex, there are four different current data windows that can be displayed: real component, imaginary component, magnitude, and phase. In most cases, it was found that trying to display both components (real and imaginary or magnitude and phase) of a complex data set in one image confused the user unnecessarily. A decision was made to allow the user to display complex data in side-by-side windows if both components needed to be viewed simultaneously. Most users have found the magnitude window to be most useful. Current data are also vectors. For wires the current vector is defined relative to the wire's direction. A satisfactory, straightforward method for displaying a vector's orientation has not been developed. It is felt that the current direction did not have as much value as the magnitude and phase of the current.

The near fields are displayed using a "fog" technique in which the density of activated pixels in the image is linearly proportional to the field intensity at the nearest calculation point. Since the calculation points usually form a 3-D grid, the image contains square blocks of fog varying in density with the field intensity. The fog is color coded in a manner similar to that used for the geometry description products. The 3-D geometry model is drawn using a dark gray color so as not to detract from the near field display. The near field windows also have a thresholding capability. By clicking in the window with the middle mouse button, the user is able to selectively change the threshold at which the fields are displayed. This allows the user to quickly determine what areas surrounding the model have fields above a particular cutoff level. For example, the threshold can be selected to be any of the color key bin levels, HERP (Hazardous Electromagnetic Radiation for Personnel), or HERO (Hazardous Electromagnetic Radiation for Ordnance). HERP and HERO are a function of the frequency at which the NEC model was run. The near field windows also display the value of the frequency.

There are two windows available for the display of far fields. These windows allow the user to display either the theta component or the phi component of the far electric field. The

fields are displayed as a three-dimensional surface. The distance from a point on the surface to the origin is proportional to the field magnitude at that point. The color at the point is determined by the phase of the field at that point. Gouraud shading is used between points to transition the color.

5.0 FUTURE EXTENSIONS

The Numerical Electromagnetic Engineering Design System (NEEDS) Workstation is a concept to address the deficiencies of the present method of moments process. This focus on the method of moments process is the first step toward the development of an overall NEEDS Workstation that will provide user interface to an entire family of numerical modeling algorithms. These algorithms might include method of moments, finite difference, and quasi-optical techniques. This extended NEEDS Workstation will allow the hybridization of a problem to allow the mixing of solution techniques within an individual problem. The initial development of the NEEDS Workstation has focused on a modular approach that allows the incorporation of algorithms beyond the method of moments.

REFERENCES

Russell, L. C. and J. W. Rockway. 1993. "EM Visualization on a SGI 4D Workstation", *9th Annual Review of Progress in Applied Computational Electromagnetics*, March.

Rockwell International Corporation. 1992. "Updated EM Engineering System Architecture Description", *prepared for Weapons and Combat Systems Directorate, Naval Sea System Command, Contract N00024-879-C-5648*, March.

Burke, G. J. 1992. "Numerical Electromagnetics Code - Nec-4 Method of Moments Part 1: User's Manual", *Lawrence Livermore National Laboratory UCRL-MA-109338*, January.

Li, S. T., J. C. Logan, and J. W. Rockway. 1988. "Ship EM Design Technology", *Naval Engineers Journal*, May.

AutoNEC ... A marriage of convenience.

Mr. Alan Nott
Electromagnetics Engineer
Information Systems Division
Engineering Development Establishment
Private Bag 12, Ascot Vale, Victoria, Australia, 3032.

Background:
Engineering Development Establishment (EDE) is the design agency for much of the Australian Army's equipment. Work on radiation hazards (RADHAZ) to explosives and equipment has been performed at EDE for over 20 years. Lately EDE has become increasingly involved in the assessment of biological hazards and propagation prediction. Since 1980, NEC-2 has been run on a mainframe some 500 miles distant from EDE. Access is by means of a terminal and line printer, and the arrangement lacks any graphics capability. On this system running jobs of any complexity presented many problems, particularly those of job creation and interpretation. However, the availability of personal computer (PC) versions of NEC now enables large jobs to be run in house and sophisticated pre- and post- processing of data has became a reality. AutoNEC addresses this area.

AutoNEC is an evolving suite of software which is run both internal and external to AutoCAD to interface it with NEC. It removes much of the trauma associated with the preparation and analysis of large jobs, particularly for multiple runs made over a large number of frequencies. Many attempts have been made by others to provide a user-manageable interface to NEC for large jobs. NEEDS provides for manual as well as digitised data input and supports a variety of output formats including tabulations and plots. Needs provides a moderately friendly environment but requires specific hardware to take full advantage of its capabilities. Lacking this hardware, EDE chose an alternative approach - to develop software to link NEC and AutoCAD, both of which run on a PC - hence the name AutoNEC.

AutoNEC reduces the need for manual preparation and interpretation of large amounts of data. It also makes use of AutoCAD's extensive three dimensional (3D) drafting capability for generation and examination of models to be evaluated and to display of the results of a run. It significantly reduces the need for a user to be familiar with the capabilities, limitations, requirements and idiosyncrasies of NEC. It requires no special hardware, using a mouse or a digitising tablet as a pointing device. AutoCAD is an open architecture drafting package which can be fully customised. It allows the user to write specialist procedures in AutoLISP (and now in C) to control its execution and AutoNEC makes extensive use of this capability. When installed, these procedures merely become extensions to the AutoCAD instruction set. The original AutoLISP procedures were written for AutoCAD Version 10. These were transferred without change to Versions 11 and 12. The enhancements now available with Version 12 offer an almost seamless user interface, and much of the code originally developed as external PASCAL procedures is being rewritten to run within AutoCAD. In addition, Version 12 provides for extended entity data - it is now possible to append additional data to such as wire diameter, segmentation, tag numbers, electrical parameters and textual data to standard drawing entities.

What does AutoNEC do?

AutoNEC provides an efficient means of creation of NEC input files directly from AutoCAD drawings of the structure. As AutoNEC has the ability both to create NEC input files from a drawing and to generate drawings from NEC input files, the structure to be analysed can be edited either as a drawing or text.

During job creation the following functions are provided:

- model integrity checks including zero length, duplicated, unterminated and intersecting wires.
- optional rounding and merging of node (wire end) positions

- recreation of the structure drawing from a NEC input file.
- automatic segmentation of wire elements.
- interactive control card generation.
- automatic creation of multiple NEC input files where segmentation cannot cover the frequency range required.
- automatic creation of a batch file to control processing.
- automatic generation of Sommerfeld files, where required.
- automatic creation of the initial entries in an audit trail.

Following a NEC run the following functions are provided:

- creation of radiation pattern, near field, induced voltage or current data files in a concise format. This includes the removal of superfluous data and merging of files from multiple runs.
- creation of antenna database files for use with the ASAPS and PSYCHIC HF prediction programs.
- maintenance of the audit trail.

AutoNEC can also produce drawings derived from NEC output data. These presently comprise radiation patterns and near field contours. These images can be manipulated as 3D drawings, and multiple images can be generated and run as slide shows within AutoCAD. Images can be further enhanced by rendering and shading, either within AutoCAD or by using packages such as RENDERMAN or 3DSTUDIO.

Structure representation:
Although AutoCAD supports modeling with 3D surfaces, because of the nature of structures of immediate interest to EDE, the development of AutoNEC has so far been confined to wire elements. Wire modeling allows more accurate ground modeling with the Sommerfeld/Norton method, particularly for structures near ground - a method which is not available with surface patches. To maintain accuracy, segment lengths need to be between $10^{-1}\lambda$ and $10^{-3}\lambda$. When a wire model is analysed over a wide frequency range, to remain within these limits the number of segments of a wire element rises with frequency. NEC allows user specification of element segmentation, and AutoNEC will automatically determine segmentation in the NEC pre-processor. Multiple NEC input files are generated, each covering a specific frequency range and with appropriate segmentation and control cards in each.

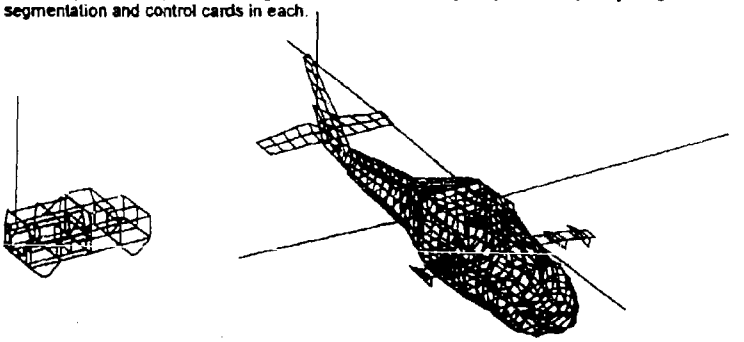

Fig 1: Wire models of a helicopter - 444 and 1458 wires respectively.

NEC input file structure:
The NEC input file consists of the following main sections:

- **Comment section:** AutoNEC initially generates this section within AutoCAD. It contains user comments input through AutoCAD, and the beginnings of the audit trail, including drawing source file names, date of last modification and processing date. NEC transfers the comment section directly to its output file. As subsequent AutoNEC processing expands the audit trail, files produced at various stages contain a complete history of their origins and processing.

- **Geometry section:** This describes the model geometry, segmentation, wire diameter and tag references. Wires selected by the user within AutoCAD are passed with non-zero tag numbers for reference during subsequent processing.

- **Control section:** This contains run parameters such as frequency, excitation, segment loading and the output required. An interactive control card processor inserts control statements as well as adding corresponding 'comment' cards for subsequent control of post-processing.

Preparing a job:
The NEC input file is produced as follows:

AutoCAD is used to draw a 3D wire model of the structure - often by laying wires directly over the existing manufacuring drawings. A number of additional commands have been added to the standard AutoCAD set aimed at the painless generation of accurate models. Duplicate and zero length wires, which can result from carelless use of AutoCAD, can be deleted. A file name is automatically generated from the generic drawing name plus the extension '.GEO' - geometry. This generic file name (with different extensions), is transferred to all subsequent files during the processing through NEC and back to AutoCAD, thus producing a coherent series of files. Audit trail data and user comments are written into the comment area, and this followed by the geometry section.

```
CM BH444RN.GEO
CM 2449357.9469
CM D:\HELIO\CONFIG1\BH444RN.DWG
CM 2449357.0179
CM
CM Helicopter bh444rn
CM less rotors and load carriers
CM
CM Expected unterminated ends = 0
CM Tags referenced = 1
CE
GW,0,0,0.0000,14.2480,-1.4310,-0.6080,14.2510,-1.4250,0.020
GW,0,0,-0.6080,14.2510,-1.4250,-0.5460,14.6580,-1.6720,0.020
GW,0,0,-0.5460,14.6580,-1.6720,0.0000,15.0040,-1.7210,0.020
GW,0,0,0.0000,14.2480,-1.4310,0.0000,13.6470,-0.8050,0.020
GW,0,0,0.0000,13.6470,-0.8850,-0.8120,13.6550,-1.1200,0.020
GW,0,0,-0.8120,13.6550,-1.1200,-0.6080,14.2510,-1.4250,0.020
etc.
```

Fig 2: AutoCAD output file format.

AutoNEC then massages the file into columns for ease of reading. Geometry checks are performed and if the file is error-free, the NEC control statements are generated interactively and appended to the file. Node co-ordinates (wire ends) can be rounded to a user-defined resolution and nodes which lie within a user-defined distance of each other can be merged. Such capabilities have been found invaluable in tidying up large jobs which are badly prepared and contain a multitude of small geometry errors. Checks are performed for unterminated, floating, zero length, intersecting and duplicated wires. Errors are flagged and the user advised. The user can either manually edit the data file, and read the corrected file back into AutoCAD to update the drawing, or correct the drawing and regenerate the NEC input file. With errors flagged, they can be selectively displayed in different colours within AutoCAD.

```
CM File BH444RW.I01 created 08:35 on 4-1-1994 from
CM ACAD output file BH444RW.GEO created 18:30 on 4-1-1994 from
CM Drawing D:\HELIO\CONFIG1\BH444RW.DWG last updated at 08:28 on 4-1-1994
CM **************************
CM Drawing from data Helicopter BH444RW.INC
CM less rotors and load carriers
CM Tags referenced = 1
CM  **************************
CM Unterminated ends expected = 0
CM Unterminated ends found    = 0
CM Wires processed = 244
CM Nodes within 0.01m have been merged
CM Zero length wires = 0
CM Duplicated wires = 0
CM Intersecting wires = 0
CM Floating wires = 0
CM **************************
CM Frequency 1.000 MHz
CM Excitation tag 1, voltage source, 1000 V
CM Free space
CM Antenna gain at 100 km.  azim=360*5, elev=180*5
CM
CM TAG  SEG      X1        Y1        Z1        X2        Y2        Z2      DIA
CE**************************************************************************
GW  0    1     0.000    14.218    -1.430    -0.607    14.251    -1.424    0.002
GW  0    1    -0.607    14.251    -1.424    -0.545    14.658    -1.671    0.002
GW  0    1    -0.545    14.658    -1.671     0.000    15.004    -1.720    0.002
GW  0    1     0.000    14.248    -1.430     0.000    13.647    -0.884    0.002
GW  0    1     0.000    13.647    -0.884    -0.811    13.655    -1.119    0.002
GW  0    1    -0.811    13.655    -1.119    -0.607    14.251    -1.424    0.002
                  *                                     *
                  *                                     *
GW  0    2    -0.719     6.360    -2.569    -0.569     4.710    -2.569    0.002
GW  0    2    -0.569     4.710    -2.569    -0.449     3.590    -2.569    0.002
GW  0    1    -0.449     3.590    -2.569     0.000     2.720    -2.628    0.002
GW  1    1    -1.059     7.640    -2.569    -0.723     7.749    -2.576    0.002
GE
PT -1    1    1    1
FR  0    1              15.0       1.0
EX  6    1    1    0   1000.0       0.0
GN -1
RP  0   19   72 1500      0.0       0.0       5.0       5.0    1000.0       0.0
EN
```

Fig 3: NEC input file format.

If errors are found, the segment field is loaded with the wire reference number. When the geometry is error-free, one or more NEC input files are created. Auto-segmentation is performed at this time, and a batch file to run the job is generated. If an attempt is made to run a file containing errors, NEC cannot process the embedded error messages and aborts quickly. Alternative, if the only errors are zero length or duplicated wires, AutoNEC can generate the required NEC input and batch files with these wires deleted. The user can then regenerate the corrected drawing from any of the NEC input files.

```
CM File BH444RW.I01 created at 08:35 on 4-1-1994 from
CM ACAD output file BH444RW.GEO created 18:30 on 4-1-1994 from
CM Drawing D:\HELIO\CONFIG1\BH444RW.DWG last updated at 08:28 on 4-1-1994
CM **************************
CM Drawing from data Helicopter BH444RW.INC
CM less rotors and load carriers
CM **************************
CM Unterminated ends expected = 0
CM Unterminated ends found    = 0
CM Wires processed = 244
```

```
CM Tags referenced = 1
CM Nodes within 0.01m have been merged
CM Zero length wires = 1
CM Duplicated wires = 3
CM Intersecting wires = 0
CM Floating wires = 0
CM **************************
CM Frequency 7.0 MHz
CM Excitation tag 1, voltage source, 1000 V
CM Free space
CM Antenna gain at 100 km.  azim=360*5, elev=180*5
*****************************************************************
*****                                                       *****
*****            Warning ... 4 unterminated ends found.     *****
*****            Warning ... 2 duplicated wires found.      *****
*****                                                       *****
***** ERROR    GEOMETRY ERRORS ... RUN WILL BE ABORTED    ERROR *****
*****                                                       *****
*****************************************************************
CM
CM TAG   SEG       X1        Y1        Z1        X2        Y2        Z2       DIA
CM*************************************************************************************
GW  0     1     0.000    14.248    -1.430    -0.607    14.251    -1.424     0.020
GW  0     2    -0.607    14.251    -1.424    -0.545    14.658    -1.671     0.020
GW  0     3    -0.545    14.658    -1.671     0.000    15.004    -1.720     0.020
***** Warning ... the next wire duplicates wire 1
GW  0     4     0.000    14.248    -1.430    -0.607    14.251    -1.424     0.020
GW  0     5     0.000    14.248    -1.430     0.000    13.647    -0.884     0.020
GW  0     6     0.000    13.647    -0.884    -0.811    13.655    -1.119     0.020
***** Warning  . the next wire has zero length
GW  0     1    -0.545    14.658    -1.430    -0.545    14.658    -1.430     0.020
                   *                                     *
                   *                                     *
***** Warning ... the next wire duplicates wire 29
GW  0   241    -0.719     6.360    -2.569    -0.569     4.710    -2.569     0.020
GW  0   243    -0.469     3.590    -2.569     0.000     2.720    -2.628     0.020
GW  1   244    -1.059     7.640    -2.569    -0.723     7.749    -2.576     0.020
GE
FR -1     1     1     1
FR  0     1                15.0       1.0
EX  0     1     1     0    1000.0       0.0
GN -1
RP  0    19    72 1500       0.0       0.0       5.0       5.0    1000.0       0.0
EN
```

Fig 4: NEC input file showing flagging of geometry errors.

Running a job:
Once the job has been prepared, it is run by execution of the appropriate batch file. This will create output files for each of the input files, as well as including or creating the necessary Sommerfeld files.

Examining the output:
NEC produces fairly large output files - even with the use of print control, quarter-Mbyte files are not uncommon for a single frequency run. For runs over many frequencies, this data is well into the MegaByte range. Apart from the data aspects of these files, there are indicators of possible inaccuracies arising from a badly conditioned job. AutoNEC keeps an eye open for these and warns the user. However,for most applications, very little of this output may be of interest. AutoNEC contains a post-processor which sumarises the data in a file of friendly structure, reasonable size, and which can be read directly into AutoCAD or printed. AutoNEC also has the capability to merge files resulting from multiple runs at different frequencies.

A number of summary file structures have been developed for different types of run e.g. radiation patterns, near fields, and induced currents. The user can examine the summary files, or can import them into AutoCAD as 3D drawings.

```
File BH444RM.ANT created 14:24 on 4-1-1994 from
File BH444RM.I01 created 08:35 on 4-1-1994 from
ACAD output file BH444RM.GEO created 18:30 on 4-1-1994 from
Drawing D:\HELIO\CONFIG1\BH444RM.DWG last updated at 08:28 on 4-1-1994
**************************
Radiation patterns: azim = 360*5, elev = 180*5

Frequency = 2.000 MHz
                                        Elevation
Azim      0     5    10    15   ...   65    70    75    80    85    90
  0    5.72  5.26  3.85  1.48   ...  7.23  7.16  7.08  7.02  6.98  6.97
  5    5.86  5.42  4.08  1.89   ...  7.25  7.17  7.09  7.03  6.99  6.97
 10    6.10  5.68  4.43  2.42   ...  7.29  7.20  7.11  7.03  6.99  6.97
 15    6.42  6.03  4.85  3.01   ...  7.34  7.23  7.12  7.04  6.99  6.97
 20    6.79  6.42  5.32  3.62        7.39  7.27  7.15  7.05  6.99  6.97
 25    7.19  6.83  5.79  4.22        7.46  7.31  7.17  7.06  7.00  6.97

          *           *                   *                 *
335    6.59  6.13  4.70  2.27   ...  7.35  7.23  7.12  7.04  6.99  6.97
340    6.25  5.77  4.31  1.77   ...  7.30  7.20  7.10  7.03  6.99  6.97
345    5.97  5.48  3.99  1.40   ...  7.26  7.17  7.09  7.02  6.99  6.97
350    5.77  5.29  3.80  1.21   ...  7.23  7.16  7.08  7.02  6.98  6.97
355    5.69  5.21  3.75  1.24   ...  7.22  7.15  7.08  7.02  6.98  6.97

Frequency = 3.000 MHz
                                        Elevation
Azim      0     5    10    15   ...   65    70    75    80    85    90
  0   10.22 10.88 11.28 10.22   ... 13.76 13.57 13.02 12.37 11.87 11.68
  5   10.26 11.15 11.76 10.66   ... 13.81 13.61 13.04 12.38 11.87 11.68
 10   10.35 11.41 12.19 11.06   ... 13.86 13.65 13.07 12.40 11.87 11.68
 15   10.47 11.67 12.55 11.40   ... 13.91 13.69 13.09 12.41 11.88 11.68
 20   10.63 11.91 12.85 11.69   ... 13.96 13.72 13.11 12.42 11.88 11.68
 25   10.82 12.12 13.09 11.92   ... 14.01 13.75 13.13 12.43 11.88 11.68

          *           *                   *                 *
335   10.67  9.95  8.21  7.61   ... 13.56 13.40 12.90 12.31 11.85 11.68
340   10.51 10.05  8.88  8.14   ... 13.59 13.42 12.92 12.32 11.85 11.68
345   10.37 10.21  9.54  8.68   ... 13.62 13.46 12.94 12.33 11.85 11.68
350   10.28 10.40 10.16  9.22   ... 13.66 13.49 12.97 12.34 11.86 11.68
355   10.22 10.63 10.75  9.74   ... 13.71 13.53 12.99 12.36 11.86 11.68
```

Fig 5: Friendly file structure for antenna gain.

Analysis capability:
NEC can perform a variety of different analysis tasks. To date the following general types of evaluations have been considered.

- **Far-field sky-wave and ground-wave antenna gains.** This work has already largely developed and examples of 3D antenna gain plots are included in this paper. As well as a tool for propagation prediction, this technique has considerable potential in electromagnetic visualisation and education.

- **Near field E and H field intensities.** This technique has immediate application in all areas of RADHAZ work. Algorithms are being expanded for plotting 3D contours of field intensities over the original geometry drawing within AutoCAD.

- **Induced currents and voltages.** General purpose graphing routines are being developed to plot safe field strengths against frequency, based on the susceptibility thresholds and induced voltage or current.

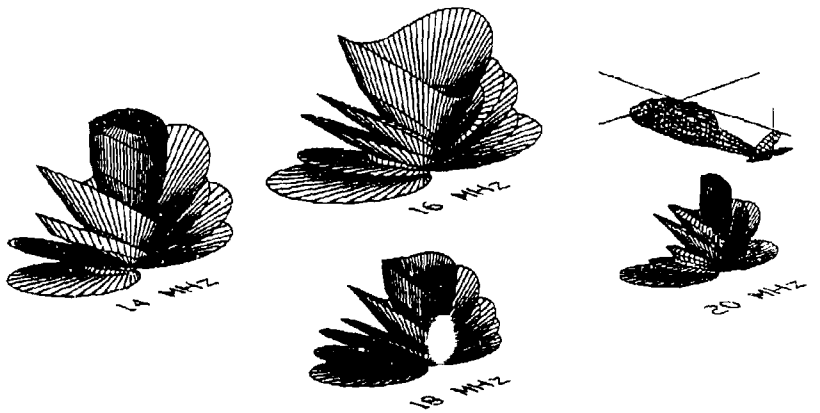

Fig 6: Examples of antenna radiation patterns.

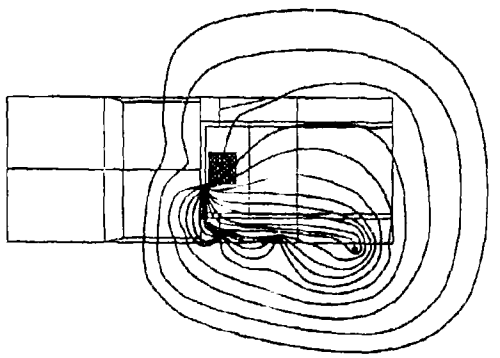

Fig 7: Near field contours in a Landrover.

Using the SLIDE capability of AutoCAD, moving pictures of radiation patterns have been produced. With this technique a series of antenna radiation patterns can rapidly be displayed as the frequency changes, or as the observer moves around the pattern. A series of such images on video tape, particularly when enhanced with rendering and shading, has significant potential as a training aid in antenna theory, and will provide dramatic visualisation of the radiation patterns.

Future development:

Reduction of NEC execution times, particularly with multiple runs of large jobs, is being addressed. A recent acquisition is a ten-transputer 'PC', and it is hoped to have a parallel version of NEC running before the end of 1994. Other areas yet to be addressed include improved scratch file efficiency and the ability to embed comments anywhere in the NEC input file. The latter will provide significant benefits in the interpretation of large NEC files, particularly within the geometry definition section. Methods to automatically assigning wire diameters is also being considered.

The enhanced capability of AutoCAD Version 12 offers the possibility of incorporating most, if not all, of the processing presently done under DOS using stand-alone programs. Further possibilities in the AutoCAD area include:

- Production of a NEC-specific menu structure for AutoCAD.
- Development of procedures for colour plotting of field contours. .
- Conversion of the programs running within AutoCAD from LISP to C for improved speed.
- Development of AutoCAD drawing entities which fully parallel those used by NEC - e.g. wires will have diameters and not merely end points, networks and transmission lines will have electrical parameters, and appropriate information will be associated with tagged wires.
- Conversion between surface patch and wire model topologies where appropriate.
- Shading and rendering of 3D models of radiation patterns and field contours.

Conclusion:
AutoNEC has considerably enhanced the accessibility of NEC, and at the same time reduced problems associated with data preparation and interpretation. With accurate definition of the structure to be analysed, the time for preperation of large NEC input files has been reduced from weeks to days. Examination of the results can now be done visually rather than wading through pages of figures.

It has applications in a wide variety of electromagnetic evaluations including:

- Plotting of 3D radiation patterns and field contours of radiating structures, such as antennas, for both near and far fields.
- Investigation of radiation pattern anomalies from specific antenna configurations.
- Preparation of antenna characteristic data for incorporation in HF prediction programs.
- Estimation of currents coupled from a radiating structure to a system containing sensitive devices such as electro-explosive devices.
- Plotting of safe field profiles for personnel, equipment and explosives, given the knowledge of the victim susceptibility.
- Production of advanced training aids for those involved in electromagnetic training, propagation and analysis.

The techniques and procedures so far developed show considerable potential in many areas of electromagnetic analysis and education. The enhancements available using AutoCAD Version 12 will significantly refine the user interface.

Although input formats differ, GEMACS and other electromagnetic modeling packages use essentially similar types of input and output data, and AutoNEC could readily be adapted to support these codes. It will also be extended to support NEC-4 when it finally becomes available.

Acknowledgments:
The author gratefully acknowledges the enthusiastic and continued support of this work by the Superintendent, Information Systems Division, EDE, and the many and varied contributions and suggestions from other members of the Division.

A Ray Tracer for the NEC Basic Scattering Code

Don P. Davis, R. Paknys; S.J. Kubina
Concordia University Electromagnetic Compatibility Laboratory
7141 Sherbrooke Street W. Montreal Quebéc H4B 1R6
E-mail : don@emc2.concordia.ca

Abstract

This paper will introduce a companion code to the NEC Basic Scattering Code version 2, BSC2. BSC2 is a member of the NEC family of codes used to model the behavior of structures in the presence of electromagnetic fields. BSC2 uses the principles of ray optics and the Geometrical Theory of Diffraction to perform the analysis. The companion code, called the Basic Scattering Code Viewer or BSCV allows the user of BSC2 to view the ray paths chosen by the code. In addition the viewer can draw the radiation patterns computed by BSC2 and preview the object modeled by the code. It is anticipated that the viewer will be a valuable tool in the analysis of models using the BSC2 code as well as a tool in debugging BSC2 itself. The operation of the viewer as well as the requirements for the use of the viewer will be discussed.

INTRODUCTION

The NEC Basic Scattering Code (version 2), developed at Ohio State University , is used to analyze the near and far field radiation patterns of antennas in the presence of scattering structures[1]. The structure to be analyzed is approximated by a model consisting of flat plates and elliptical cylinders. These plates may have a coating of dielectric layers or may be a single perfectly conducting layer. The code allows the user to place transmit and receive antennas or arrays of antennas anywhere around the geometry under question. The analysis techniques are based upon the Uniform Geometrical Theory of Diffraction, UTD. Due to the nature of the analysis technique, this code is used for high frequency analysis. That implies that the scattering structure must have dimensions on the order of a wavelength or greater.

The companion code, BSCV, will preview the scattering geometry and display it on the screen of the terminal or print it as the user desires. The BSCV code allows the user to then plot the radiation patterns as well as draw the ray paths as they are determined from the BSC2 run. The BSCV runs within a MATLAB[2] environment and uses both MATLAB as well as FORTRAN languages to perform the required functions. The BSCV code can also run a subroutine trace and print out the points, as well as the subroutines, used in calculating the various UTD mechanisms used to determine the field at each evaluation point.

NEC BASIC SCATTERING CODE

The NEC Basic Scattering Code uses UTD techniques to characterize the field behavior due to scattering objects. The mechanisms used are the direct rays, reflected rays, edge diffracted rays, corner diffracted rays, and creeping waves. Higher order effects such as: twice reflected rays, diffracted-diffracted rays, reflected-diffracted rays, and diffracted-reflected rays, are also considered by the code. Each mechanism is determined by a separate subroutine. The geometry of the scattering material as well as the source and receiver positions are stored in common data blocks that are shared by all the routines that require the information.

The input of the code contains the required information on the scattering geometry and the data on the form and position of the sources. The measurement points used to form the radiation pattern and any coupling calculations are also specified in the input section. The form of the input section is a text file with the data and the instructions written down following a predetermined format.

The output of the code is a series of electric and magnetic field values, magnitude and phase, at each measurement point. The values of the coupling between antennas would also be given in this section. The output is produced as a text file.

The process by which the BSC2 code arrives at the output is not presented to the user. The diffraction coefficients used by the code and the UTD mechanisms do not come to light during the normal operation of the code. To shed further light onto what happens during the operation of the code the companion code was developed.

THE BASIC SCATTERING CODE VIEWER

The BSCV begins with the same information set that the BSC2 code starts with, namely the geometrical data that is used to represent the system under study. The viewer then translates the input data on the geometry into a three dimensional shape representing what the code perceives as the scattering form. The transmitting antennas are also placed in their proper positions with respect to the scattering object. This is the previewing stage of the BSCV code. The person using the code may check to see if the input geometry is of the correct shape. This affords the user of the code a change to error check the input before running the BSC2 code itself. The previewing section can be used without running the BSC2 code since the only data it requires is the input geometry. The translation of the input data into the image is done in two parts. The input data is first preprocessed by a FORTRAN code into suitable format for MATLAB. The preprocessed data is then sent to MATLAB which will draw the shape on the screen.

The next stage is the running of the BSC2 code itself. The data for the ray tracing and the radiation patterns is extracted from BSC2 as the code runs. The data is tapped from the subroutines as they are calculated and then written to a data file. This data is then used to draw the ray paths as calculated by BSC2. The rays are color coded according to the diffraction mechanism so as to make differentiation easier for complex scattering geometric forms. The rays are then superimposed upon the shape drawn by the previewer so that the person using the viewer can observe the effect of each of the components of the scattering geometry upon the rays forming the total field. The radiation patterns are plotted from the output data file written by BSC2 after it has completed the run. The viewer also traces the subroutines and the data generated by each subroutine. A data trace file is generated from the information extracted from subroutines during the BSC2 run. This along with the radiation pattern and ray path data gives a good picture of what the code did during the run. This can prove to be a valuable set of information when debugging or analyzing the code. The person using the code can now see which rays are affecting the pattern at any chosen point. This will allow the person doing the analysis to see if a certain section of the geometry affects the radiation pattern in the expected way or if the code treats the scattering object differently. The color coding of the different rays will allow easy characterization of the UTD effects being viewed. The translation of the data into the image seen on the screen is done entirely within MATLAB. The data is written to files as soon as it is processed. The data is then extracted from the files by MATLAB and used to draw the ray paths and the radiation patterns.

REQUIREMENTS FOR THE CODES

The BSC2 code is set up on a UNIX workstation and must be compiled by a FORTRAN compiler. The memory requirements are on the order of 300 kbytes of core memory. The BSCV code is set up within a MATLAB 4.0 environment that is supported in turn by X-WINDOWS. This is a UNIX workstation environment. The viewer will also run on a PC windows version of MATLAB 4.0. The viewer has some routines that must be

compiled in the same way as the BSC2 code. The viewer generates a series of scratch files that hold temporary variables used in generating the ray paths and the geometry of the scattering object. These scratch files will require disk space. The size of the scratch files will depend upon the complexity of the geometry and the number of field points chosen. The companion code can be set to delete the scratch files when the user exits the code. This will allow for the disk space to b after this application is terminated. The scratch files may take up from 1 to 50 kilobytes typically. The s scratch files is dependent upon the number of field points chosen, this implies that a large number of ob on points could result in the scratch files taking up more space than the range mentioned above.

RESULTS AND DISCUSSION

The code uses edge diffracti smooth the transition from a region where a direct or reflected ray suddenly turns on or off. The disc nuity in the radiation pattern caused by the sudden appearance or disappearance of one of the above mentioned rays will be smoothed out. The code uses corner diffraction to compensate for the sudden appearance or disappearance of an edge diffracted ray. The corner diffraction will smooth the radiation pattern so that the sudden change in the diffracted field will not cause discontinuities in the radiated field.

The first test run was with a 1x1 meter plate at 299 MHz. The location of the source was (-5,0,5) meters in (X,Y,Z) respectively. The source was a z directed dipole. The radiation pattern was taken in a half circle of radius 10 meters starting above the plate and ending below the plate. The pattern was calculated in increments in theta of one degree. Theta is the angle measured from the Z axis, (perpendicular to the plate), to the X-Y plane, (the plane of the plate). For validation the same calculations were performed using a moment method code, Richmond's THNWR code[3] was used with a wire grid forming the plate with a mesh size of 0.1λ. A sample of the associated ray picture is given by Fig 1. The rays present are the corner diffracted rays and the edge diffracted rays for this particular observation point. The following figure, Fig. 2, is the radiation pattern for the given cut calculated by the two different techniques mentioned above. The position phi=0 corresponds to the positive X axis. The position phi= 90 corresponds to the positive Y axis. The radiation pattern is a yaw plane pattern.

The second run was done on a circular cylinder of length 15 meters and radius 1.35 meters. The run calculated the radiation pattern about a circumferential path of 20 meters radius. Fig 3 shows an associated ray path at one of the measurement points. The radiation pattern itself is shown in Fig. 4. The position of phi equal to zero degrees corresponds to the end of the cylinder opposite to the source. The source is mounted above one end of the cylinder. The source is a radially directed dipole. The position in the Cartesian plane is (-5.054,0,3.1335). The source is again a dipole identical to the one in the first run. The rays present are: the ray diffracted from the endcap of the cylinder as well as the direct ray and the ray reflected from the cylinder side.

The third run was done on a model of the Challenger jet. The Challenger jet is a small commercial aircraft with a length of 15 meters and two engines mounted aft of the midsection of the plane. The body of the plane was modeled as a cylinder with a circular cross-section. The engines were modeled as flat plates as were the fins and wings. The cylinder forming the fuselage of the aircraft is identical to that of the second run. The source is of the same type and has the same position as the source of the second run. The cylinder accounts for an edge diffracted ray from the endcap, as well as a reflected ray from the side of the cylinder. The plates that model the wings allowed edge diffraction as well as diffracted-reflected rays. The greater complexity in the ray picture is mirrored by a more complex radiation pattern. Fig. 5 shows a ray picture of the model with a dipole source at (-5.054 0 3.1335) in the Cartesian coordinate system. The receiver is directly above the center of the aircraft model at (0 0 10) in the Cartesian coordinate system. Fig. 6 shows the radiation pattern associated with a path about the length of the aircraft.

CONCLUSION

The use of the companion code BSCV to handle the input and output of the BSC2 code has several advantages. The input file can be previewed before the running of the BSC2 code. This allows the user of the code to check the input geometry before actually running the code. This visual previewer will allow a quick and easy way to double check the input file. After the code has been run, the companion code will allow the use to draw the radiation patterns. If any abnormality or unexpected value occurs in the radiation pattern, the ray tracing option will allow the persons using the code to see what the ray picture is for that particular field point. This will allow the code user to determine what aspects of the geometry affect that particular field point. If it is suspected that an unexpected GTD mechanism occurs or a GTD mechanism is missing, the color coded rays will show the user what rays are present and allow the code user to determine what mechanisms are present. The companion code will also provide a trace of all the rays and the subroutines that generated them. This will help the code user in debugging or modifying the BSC2 code if there is a need. A PC code which will produce a picture of the input of the BSC2 is commercially available. The commercially available code, EAM:BSC[4] does not have the ray tracing features mentioned above. The EAM:BSC code will only preview the input of the code and not produce any of the other ray tracing or debugging features. While it will produce radiation patterns, the EAM:BSC code does not provide the additional debugging features present in the BSCV code.

It is anticipated that the above features of the companion code will make it a valuable tool in the analysis of models using the BSC2 code as well as a tool in debugging BSC2 itself.

REFERENCES

[1] R.J. Marhefka and W.D. Burnside, "NUMERICAL ELECTROMAGNETIC CODE-BASIC SCATTERING CODE NEC-BSC (VERSION 2) PART II: CODE MANUAL.," The Ohio State University ElectroScience Laboratory technical report 712242-14.

[2] The Math Works inc. " MATLAB High -Performance Numeric Computation and Visualization Software.", user's guide.

[3] J.H. Richmond " Computer Program for Thin Wire Structures in a Homogeneous Conducting Medium."The Ohio State University Electroscience Laboratory technical report 2902-12

[4] SAIC Communication Engineering Laboratory "EAM:BSC Graphical Shell for Basic Scattering Code" promotional advertisement. Science Applications International Corporation Communication Engineering Laboratory 300 Nickerson Road, Marlborogh, MA 01752. (Voice) (508) 460-9500.

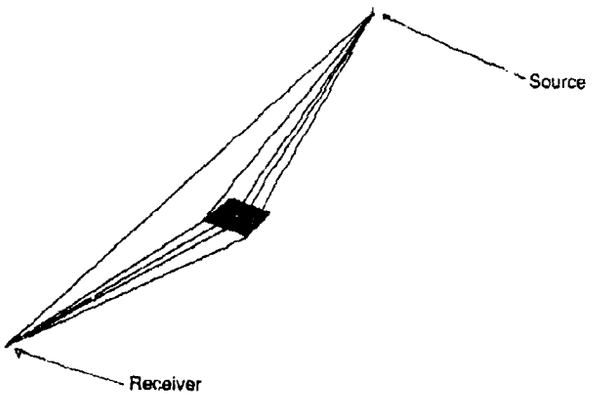

Figure 1: Flat 1x1 plate ray picture

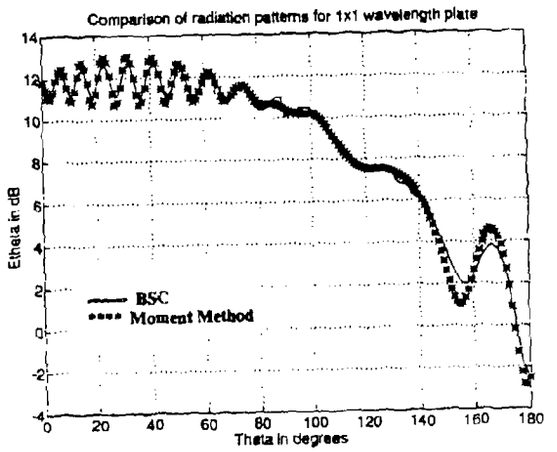

Figure 2: Radiation patter for 1x1 plate elevation plane

Figure 3: Cylinder ray picture

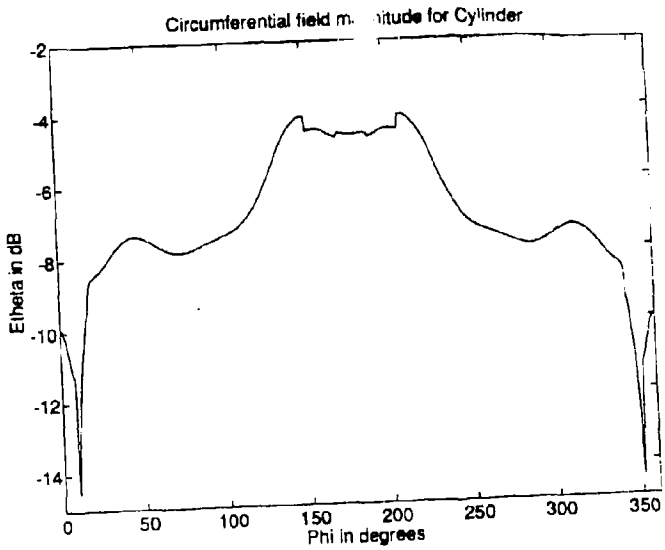

Figure 4: Radiation Pattern associated th cylinder

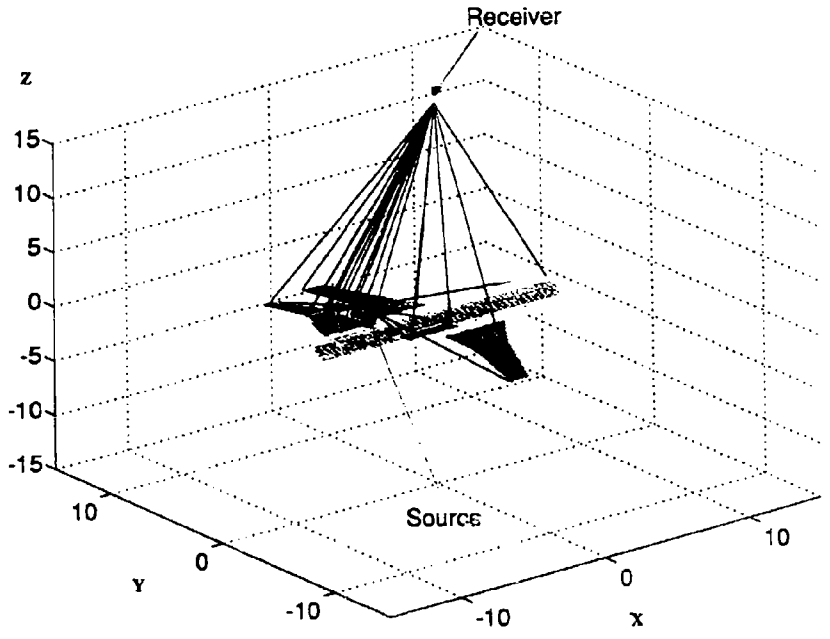

Figure 5: Challenger Jet BSC model ray picture

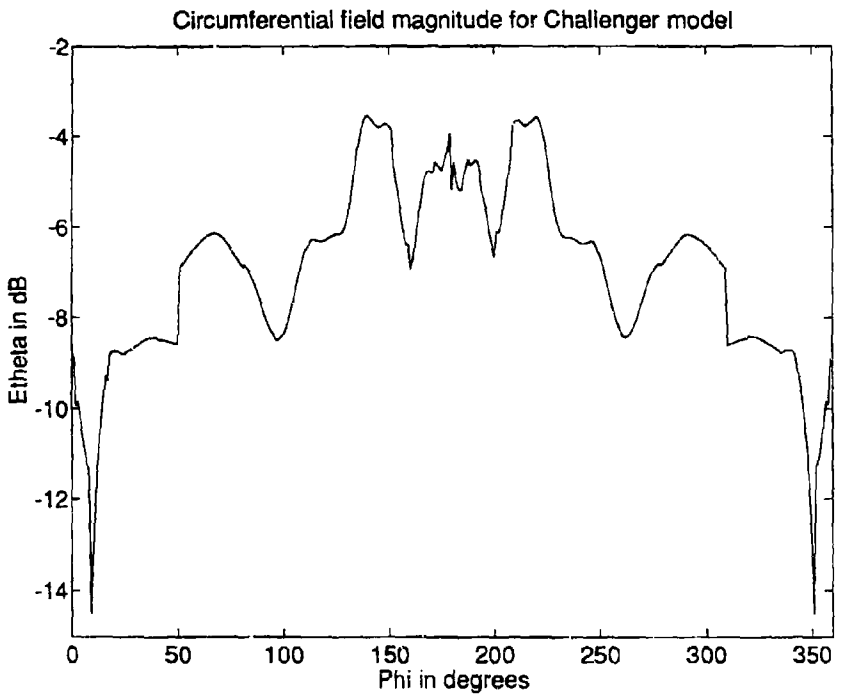

Figure 6:Radiation pattern for model of jet

SOURCE to FIELD, What happens in between?

A New Method for Graphical Display of GTD Scattering

Mr Jeffrey A. Evans
Decision Science Applications, Inc.
1300 Floyd Ave.
Rome, NY 13440
Phone (315) 339-6184
FAX (315) 339-6923

Dr. Edgar L. Coffey
Advanced Electromagnetics
5617 Palomino Dr. NW
Albuquerque, NM 87120
Phone (505) 897-4741
FAX (505) 831-1031

INTRODUCTION

Does the thought of electromagnetic (EM) analysis codes conjure up images of a black box where you feed information in and wait for an answer, hopefully correct, out of the opposite end? If so, you aren't alone. Many engineers are finding today that valuable information can be obtained during the process of solving a problem rather than just from the final output data set. Also, there are educational reasons for viewing intermediate data from an analysis program. A large area of interest in EM analysis involves the scattering of EM energy from an object(s) for antenna placement, radar cross section analysis, etc. This paper describes a new method for displaying Geometrical Theory of Diffraction (GTD) scattering information. The generation and display of the GTD scattering data has been incorporated into the programs the General Electromagnetic Model for the Analysis of Complex Systems (GEMACS), Graphical Aids for the Users of GEMACS (GAUGE) and the Windows version of GAUGE (WinGAUGE©).

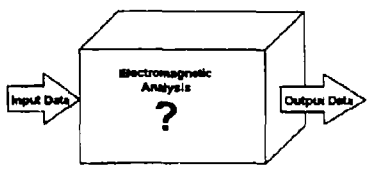

The Black Box of EM Analysis

BACKGROUND

The GTD solution technique in GEMACS is a high frequency ray optics approach that includes diffraction effects from edges and scattering from surfaces as well as diffraction effects from surface discontinuities and waves creeping around smooth structures. These scattering and diffraction effects are shown below.

This work was sponsored by Rome Laboratory under the Expert Science and Engineering Program (BAA 90-04), Contract F30602-93-C-0022

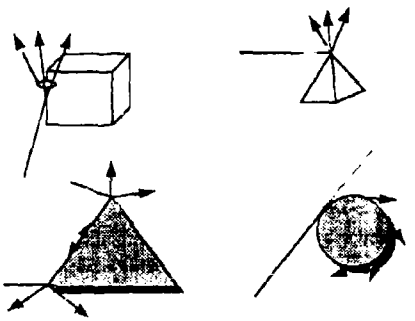

GTD Interactions

The primary method for visualizing the results of a GTD analysis is to plot, in 2 or 3 dimensions, the radiation patterns generated from an analysis. There is a missing component in this display methodology. What happens to the electromagnetic energy in and around the object under analysis? Another more pointed question would be what are the portions of the structure that contribute the most to the shape of the final pattern? Or, what part of the geometry is being shaded in the analysis? The answers to these questions can give greater insight into an EM analysis. The final radiation patterns become more understandable when it is known what part(s) of the structure are affecting portions of the pattern. Looking at this intermediate data can assist in the modeling effort by allowing the analyst to focus the modeling effort on areas of interest with confidence that the other areas are not going to be major contributors to the results.

5. RAY PATH GENERATION AND GRAPHICAL DISPLAY

GEMACS and other GTD analysis programs have always calculated the path the EM radiation will follow from a source to a requested field point. However, this data was typically discarded after the individual ray paths were summed to form the field strength at the requested field point. In the latest version of GEMACS this data can now be saved to an auxiliary data file via the RAYPTH command. The RAYPTH command is a toggle that turns on and off the saving of the individual ray paths. The ray paths in GEMACS are only calculated when a field pattern is requested. Therefore to generate a data file of ray paths the user needs to bracket the GEMACS field command with a set of RAYPTH commands turning on the saving before generating the field and turning it off after the field command. This is done as follows:

```
RAYPTH ON  LU=99
EF1=EFIELD(GEOM)  P1=0  T1=0  DT=1  T2=180
RAYPTH OFF
```

The LU=99 parameter of the RAYPTH command specifies the file number for GEMACS to write the data (e.g. FOR099.USR). This data file will contain all ray paths from all sources to the field points

with in the scope of the RAYPTH command. The number of generated ray paths can become very large based on the requirements of the analysis. For example, if a 10 x 10 array were being simulated with the requirements called for field patterns in THETA and phi at 1° resolution over 180° the final total of direct paths from each array element to each field point would be 18,000 (10 elements X 10 elements X 180 field points X 2 fields). And this does not include the possibility of scattered ray paths from a structure the array may be mounted on. Thus the RAYPTH command should be used judiciously. If there is concern over the appearance of a field within a specified area the analysis can be rerun over the smaller area with the ray paths turned on to help find the cause of the concern without generating huge amounts of data.

Once the ray paths have been generated the data is displayed on the geometry via the CAD programs GAUGE and WinGAUGE. The ray path is depicted as a series of arrows sowing the direction and bounce points of the ray. This method of displaying path information on geometry has been used successfully in the computational fluid dynamics (CFD) field and shows great promise for CEM.

The following figure shows the graphical display of the scattering from a GTD plate model of a cube and cylinder. The ray paths on the cube example include diffractions from the top and bottom edges of the cube and from the four corners on the side nearest to the source and field points. The ray paths on the cylinder example include reflection from the surface, diffraction from the endcap rim and creeping waves around the surface of the cylinder. Within the GAUGE program there are different options for displaying the ray path geometry. These include, numbering the ray segments, displaying rays based on there path number, displaying the strength of the rays as a color code, displaying rays based on the number of times they interact with the structure (bounce), and displaying ray paths based on the source that generated them and the field point they are going to.

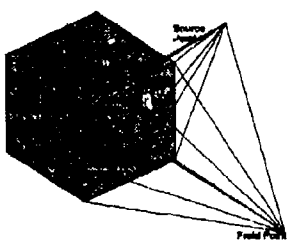

Ray Paths on a GTD Cube

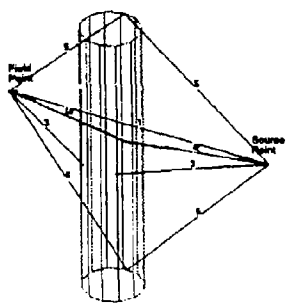

Ray Paths on a GTD Cylinder

EDUCATIONAL USE

This added capability of displaying the intermediate data of an analysis can be very beneficial to students learning about electromagnetics in general and GTD in particular. The use of computer simulation can reduce the amount of time needed in the laboratory by providing a firm understanding of the phenomena associated with electromagnetic waves. The graphical display further facilitates this by giving the student a visual picture of these phenomena.

ENGINEERING EXAMPLE

The following example shows a typical engineering example to evaluate antenna location on an aircraft. The structure is a model of a 707 size aircraft. It is constructed with a cylinder for the fuselage and flat plates for the left wing and control surfaces. The area of interest is along the left side of the aircraft so the right wing and horizontal stabilizer are not modeled.

The goal of this analysis is to view the effects of the trailing edge of the wing on the antenna pattern and to see where the interactions with the wing occurs. This information can then be used to make decisions about the location of the antenna.

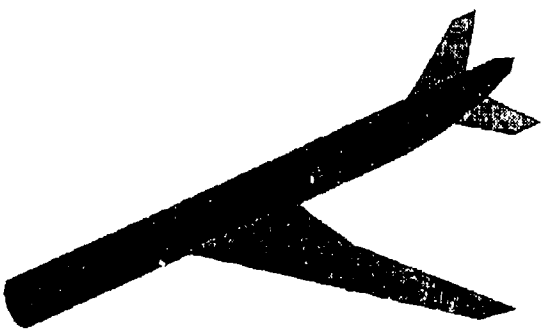

The antenna for the first step of this analysis was located on top of the fuselage approximately centered on the root of the wing. The analysis input data was configured to generate only the field data associated with the diffractions from the trailing edge of the wing. The field pattern of interest is theta=90 and 0≤phi≤180. The following figure shows the ray paths that were generated from the antenna to the trailing edge of the wing. For this presentation only a 5° arc, from phi=130° to phi=135° , was used to generate the ray path data. The field pattern for this antenna is show in the next figure.

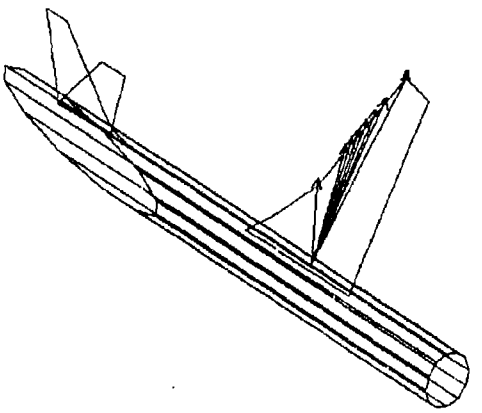

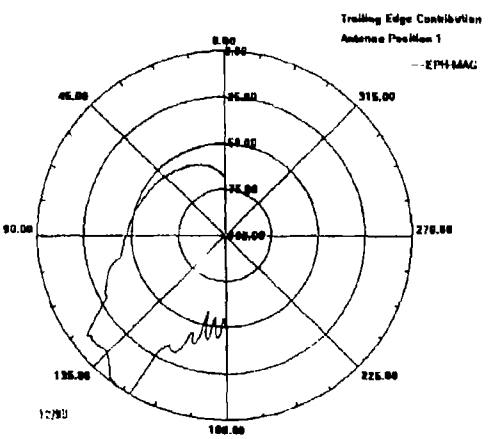

The second step of this analysis was to move the antenna towards the read of the aircraft by 8 meters. Again the analysis input data was configured to generate only the field data associated with the diffractions from the trailing edge of the wing. The following figure shows the ray paths that were generated from this new antenna position to the trailing edge of the wing. The field pattern for this antenna is show in the next figure. This example shows that for the same arc of coverage the amount of interaction with the trailing edge of the wing has been greatly reduced by moving the antenna. Also we can easily observe which parts of the structure contribute to the field of interest through the use of the

ray plotting capability. Additional analysis would need to be completed to see how moving this antenna affected other portions of the field pattern for the antenna.

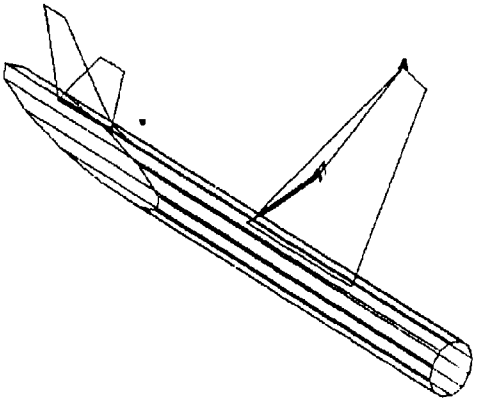

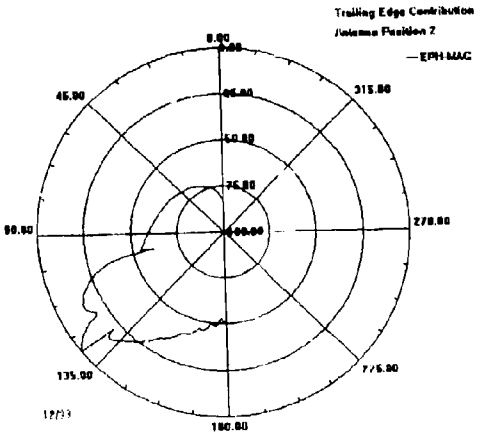

AVAILABILITY

GEMACS and GAUGE are owned by the US. Air Force. Approval to receive the software can be obtained by contacting Mr. Ken Siarkiewicz, Rome Laboratory/ERPT, Griffiss AFB, NY.

WinGAUGE was developed by Decision-Science Applications, Inc. and is being distributed commercially. Commercial versions of GEMACS are also available for personal computers, workstations, and mainframes. Anyone interested in ordering a copy of the code can contact the authors. Government approval, via Rome Laboratory, is still required for receiving the commercial versions of the codes.

REFERENCES

Interactive Numerical Electromagnetics Modeling & Analysis Using Computer-Aided Engineering Software

S. R. Rousselle, S. S. Marlor, and W. F. Perger Electrical Engineering Department
Michigan Technological University
Houghton, MI 49931-1295

1. Introduction

Since most practical electromagnetic (EM) problems are not solvable by analytic techniques, numerical computer codes have become vital to the EM design process. Although codes, such as NEC (Numerical Electromagnetics Code)[2], have become valuable design tools, the overwhelming amounts of numerical data supplied to and received from these codes has seriously impeded their effectiveness. To overcome this pitfall, numerous software packages have been developed to aid in the design and analysis of antenna structures. Their lack of robustness, versatility, and adaptability, however, has limited their use as *engineering* design tools.

Over the years, small steps have been made towards the advancement of EM design tools, but repeatedly these tools fail to encompass the *entire* engineering design process. In addition, the maintenance and upgrading necessary to maintain the state-of-the-art in visualization usually leads to their demise. By using a commercial CAE package, such as I-DEAS[6], a comprehensive, interactive EM design package can been realized without the complications associated with developing and maintaining visualization software[1].

In the past, the sharing of information, from or with other disciplines, has been considered "non-traditional," especially in electromagnetics, because of the uniqueness and specialization required. The advent of computer workstations, however, has bridged this gap in the sense that computer modeling, design, and analysis techniques are interrelated. In addition, economic considerations are forcing engineering towards a shared platform of information (i.e., Concurrent Engineering). With this, and the recommendations for future EM design packages [3][7], it becomes evident that existing Computer Aided Engineering (CAE) software should be employed as the visual interface for numerical electromagnetics.

To demonstrate the power and versatility of this union, I-DEAS is used to generate geometry input files for NEC2. In addition, it is used as a post-processor to aid in the analysis of various EM characteristics such as far-field patterns, current distributions, and polarization. Examples of new modeling techniques that have resulted from using NEW I-DEAS will be presented and compared with measured data. From the examples, it will become obvious that this refreshing approach to EM design meets and/or exceeds the requirements of existing and future numerical EM codes.

2. Modeling EM Structures

The majority of tools developed for numerical EM typically try to mimic commercial CAE/CAD (Computer Aided Design) packages. Therefore it is not necessary to dwell on the specifics of creating a finite-element model in I-DEAS. Instead, listed below are several of the useful features available for developing models of antenna structures.

- Solid Modeler
- Automatic mesh generation
  - Complex surfaces from solid modeling

  - Quadrilaterals or triangular patches
- Material Properties
- Automated Surface Normal Check for Patches
- Duplicate Node & Element Removal
- Programming Language
- Interactive Graphical Display
  - Real-time interactive axes rotation
  - Complex Shading
  - Hidden Line Removal
  - Wire Cross-Section Display

2.1. Concurrent Engineering

By using a CAE design package, the same model is used concurrently throughout the design process by the mechanical, electrical, and manufacturing engineers. This allows the engineers to perform mechanical, EM, and manufacturing simulations to determine the structural stability, EM performance, and manufacturing process to determine product feasibility. In addition, mechanical simulations, and the resulting displacements, can be used to study the effects that external mechanical forces will have on the electromagnetic properties. This is nearly impossible to accomplish using existing EM tools since they were developed for a specific task.

2.2. New Modeling Techniques

Through the use of the NEW I-DEAS technique, several new modeling processes have been developed. To demonstrate these advances, the antenna shown in Figure 1 will be used. It is a 151 wire element Helical antenna with a 3° taper over a reflector made up of 64 patches.

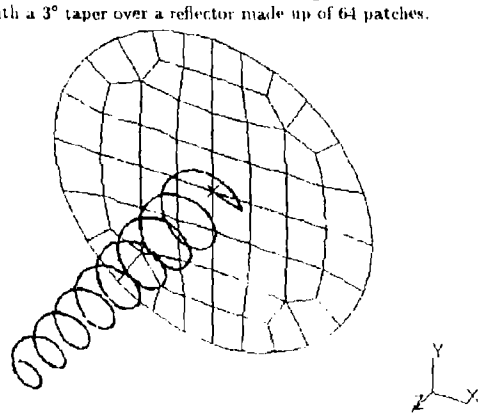

Figure 1: Helical antenna using 150 wire elements and 64 patches.

From Figure 1, it is evident that the antenna is modeled over an open-surface. It has been found that it is possible to model a thin surface with an infinitely thin patches as long as the currents approach zero near the edges[4]. To demonstrate the effectiveness of this modeling technique, Figure 2 compares the measured far-field pattern (solid line) with the results from NEC2 (dotted line) at 1.5 GHz.

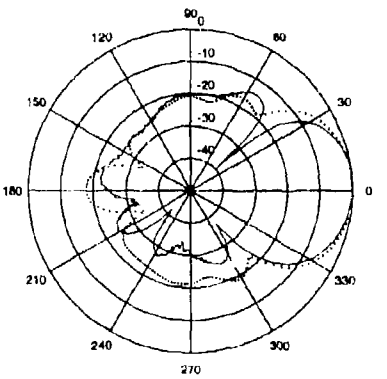

Figure 2: Comparison of modeled far-field pattern and experiment for helical antenna.

When modeling complex surfaces in I-DEAS, it is possible to automatically generate patches to represent the surface. Because it is common to model surfaces using wire grids, which can't be automatically generated on a surface, a method to transfer the patches to NEC2 as wires or patches was developed. This isn't revolutionary, but when the calculated current distribution are displayed for post-processing, they are displayed on the surface instead of on wire elements. This makes it easier for the designer to see how well the wire grid simulates a surface. Figure 3 compares the measured (solid line) with the simulated (dotted line).

The most interesting and useful improvement uses the current distribution on a surface to re-generate a mesh. Figure 4 shows a contour plot of the current distribution on the original mesh. From this information, a second mesh was automatically generated by I-DEAS and is shown in Figure 5. Figure 2(before adaptive mesh) and Figure 6 (after adaptive mesh) show the results (dotted line) compared to the measured (solid line) patterns. After the adaptive meshing, the pattern resulted in a slight improvement over the original simulation. Using this technique, a iterative process could be developed to optimize the model. In addition, adaptive meshing can be used in conjunction with the conversion of patches to wires to adaptively mesh wire-grid models.

3. Post-Processing

Without the aid of color and an interactive display, the post-processing capabilities of I-DEAS cannot be demonstrated. Below is a list of how the data generated by NEC2 can be visualized using I-DEAS. For a complete description of the post-processing features see [5].

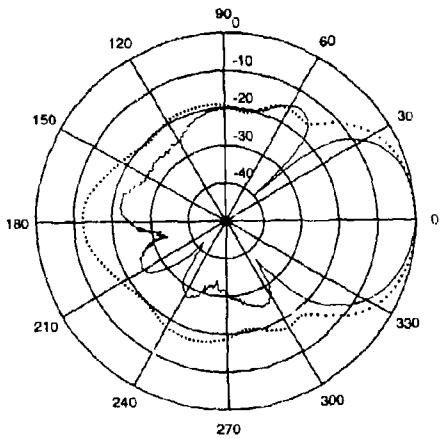

Figure 3: Comparison of measured (solid line) with wire-grid (dotted line) far-field patterns for helical antenna.

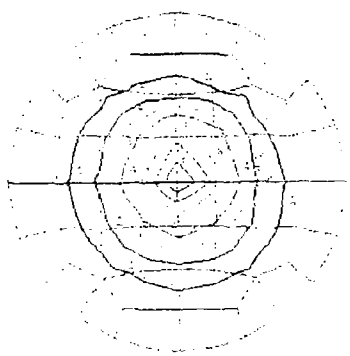

Figure 4 Current distribution on the ground plane of the helical antenna.

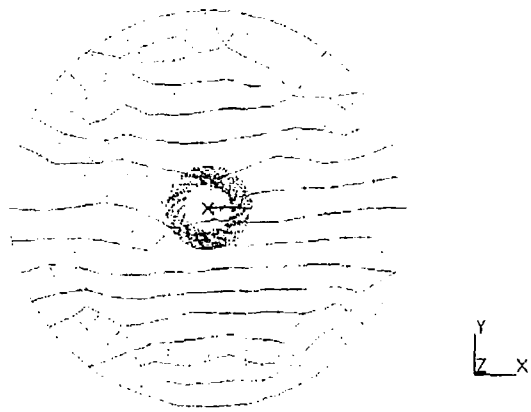

Figure 5: Example of re-meshing using automatic mesh generation.

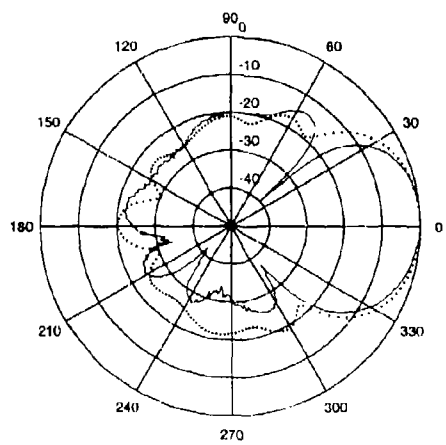

Figure 6: Comparison of experiment (solid line) and simulated (dotted line) far-field patterns for helical antenna using adaptive meshing.

- 3-D far-field patterns
  - Gain
  - Axial Ratio (AR)
- 2-D pattern cuts
  - XY Plots
- Current Distributions

4. Conclusions

An interactive technique for processing large amounts of numerical data for numerical EM codes was demonstrated using NEC2 and I-DEAS. By utilizing I-DEAS relational database, other numerical codes could be added effortlessly.

NEW I-DEAS has resulted in the development of several new modeling techniques that improve the simulation results while reducing the modeling time. In addition, this technique breaks the rigid barriers of cross-disciplinary design. This moves concurrent engineering design practices one step closer to the complete integration of design, analysis, and manufacturing.

References

[1] Matthew Arrott. Perspectiv[illegible] Visualization. *IEEE Spectrum*, 29(9):61–65, September 1992.

[2] G. J. Burke and A. J. Poggio. Numerical electromagnetics code (NEC)- method of moments. Technical document 116, Naval Ocean Systems Center, San Diego, California, 1981.

[3] E.K. Miller and R.P. Kruger. A Proposed Approach for Developing Next-Generation Compuational Electromagnetics Software. In *9th Annual Reviews of Progress in Applied Computational Electromagnetics*, pages 122–138, 1993.

[4] S.R. Rousselle and W.F. Perger. A Hybrid Code for NEC(Numerical Electromagnetics Code). In *1994 ACES Users' Conference Proceedings*, page In Press, 1994.

[5] Steve Rousselle, S. S. Marlor, and Warren F. Perger. An interactive antenna design technique using I-DEAS. pages 77–88. ICCON, ICCON User's Conference Proceedings. May 1993.

[6] SDRC-Ideas. 2000 Eastman Drive, Milford, OH 45150-2789. *IDEAS V*. Copyrighted by Structural Dynamics Research Corporation.

[7] Kenneth R. Siarkiewicz. The Electromagnetic Modeling and Simulation Environment for Systems (EMSES). In *9th Annual Reviews of Progress in Applied Computational Electromagnetics*, pages 114–121, 1993.

A Proposed EM Code Interface Standard

Edgar L. Coffey, III
Advanced Electromagnetics
4516 Stockbridge Avenue NW
Albuquerque, New Mexico 87120

The purpose of this paper is to present ideas that could be used to interface electromagnetic code components in many areas, three of which will be presented: geometry description, physics quantities for MOM and GTD/UTD, and excitation/observables description. The characteristics of several popular EM numerical techniques will be presented and the proposed interface standard critiqued against each one. Should this or a similar standard be adopted by ACES, it would be possible (1) to integrate together the functions of different software packages with diverse characteristics and (2) to avoid "re-inventing the wheel" each time a new code is developed.

Geometry Description There has been a tendency to lump the geometrical description of a structure together with its electromagnetic description. It would be far better to have distinct geometrical and EM databases so that the form of the geometrical data could be accessed by any EM technique. For example, a flat convex polygon could be used by a MOM code as an MFIE or EFIE surface patch (provided it was electrically small) or by a GTD/UTD code as a flat plate (provided it was electrically large enough), or by a finite difference (FD) code as a boundary element. A point-polygon geometrical database (that included curved polygons) would satisfy the needs of most every EM numerical method.

MOM and GTD Physics An object-oriented formalism has been shown to work for GTD in GEMACS version 5 and was presented at ACES in 1993. A similar approach is possible for MOM and strongly recommended. MOM electromagnetic modeling elements (e.g., wire segments and surface patches) are derived naturally from the geometry database elements. Basis and test function objects would devolve naturally from one or more EM modeling objects. The MOM interaction matrix [Z] and excitation vector [V] would be computed by combining basis and test objects appropriately. The advantage of such an approach would be the ease with which a new capability could be added (e.g., a new basis function or a new geometry element) without modifying <u>any</u> of an existing code's structure.

Excitations and Observables By defining excitations and observables in a more general way, the basic EM numerical quantities can be computed more efficiently. For example, in MOM the defining quantities are [Z] [I] + [Vant] = [V] and [G] [I] + [Einc] = [F]. The first equation must be solved for [I]. The second equation uses [I] to compute fields [F]. The quantities [Z], [V], [G], and [Einc] can use identical numerical routines <u>if</u> the excitations and observables are defined appropriately.

A Geometry Description Language for 3D Electromagnetic Analysis Codes

Todd Hubing, Clara Hong-Him Lim, and James Drewniak
University of Missouri-Rolla

With the proliferation of 3D electromagnetic modeling software, many researchers are finding that the process of defining the input and interpreting the output is overly complex and unintuitive. Graphical user interfaces (GUIs) can help the user to visualize input geometries and output current and field distributions, but representing three dimensional data on a two-dimensional computer screen is inherently a complex process. The steep learning curve associated with most user interfaces prevents many EM modelers from experimenting with different EM modeling codes.

An Initial Solution

In a previous paper [1], a user interface (input only) was described that employed commercial Computer Aided Drawing (CAD) software. The idea was to isolate the development of the numerical EM modeling software from the development of the user interface. In this way, EM modeling code developers could concentrate on developing the best modeling software and development of the CAD interface could be left to programmers who specialized in that area. A relatively simple translation code was used to link the CAD software to the EM modeling code. The translation code read the 3D geometry information, prompted the user for any additional information (e.g. source amplitudes or material constants), checked for errors, and wrote a file suitable for exporting to the EM modeling code.

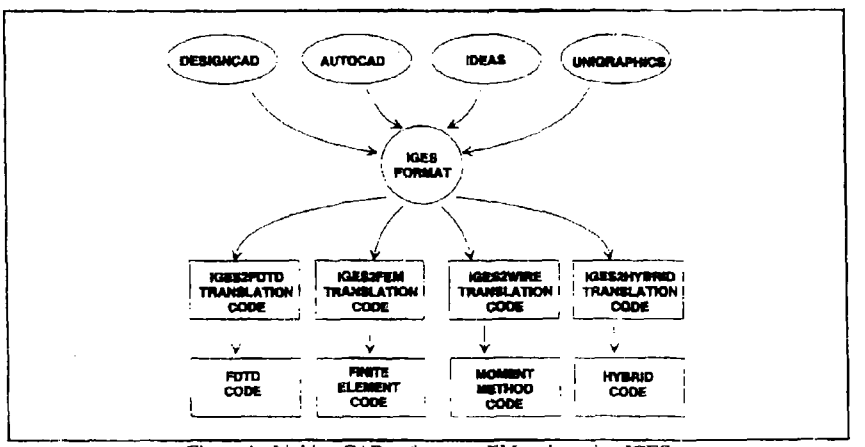

Figure 1: Linking CAD software to EM codes using IGES

In theory, a translation code written to interpret a standard graphics format, such as IGES or DXF, could accept input from a variety of CAD software packages. This approach, illustrated in Figure 1, would allow EM modelers to select the CAD software best-suited to their own needs to use as a graphical front-end to their EM modeling codes. If each 3D EM modeling code used was provided with a similar translation code, the modeler could analyze a given geometry using more than one technique without having to enter the geometry data each time. Also the code user could become proficient with a single CAD package and avoid having to learn a new user interface for every new EM modeling code. Using CAD software to create an IGES file is usually much more efficient than using a text editor and/or special subroutines to create a native format file. With the translation code, the standard graphics format effectively replaces the native input format of the modeling code.

This approach is not without drawbacks however. Currently there is no truly standard graphic format. IGES and DXF files can vary significantly depending on the CAD software used, the computer platform, and the techniques used to create a particular geometry. Also, IGES and DXF files were not optimized for storing the data required by most EM modeling software. The files are long and complex and they contain much information that is unusable by EM modeling codes. In addition, the IGES and DXF formats do not provide a standard method for conveying EM source or material information. In order to store an input geometry that the user may want to modify later, both the CAD file and a file containing the source and material information must be saved.

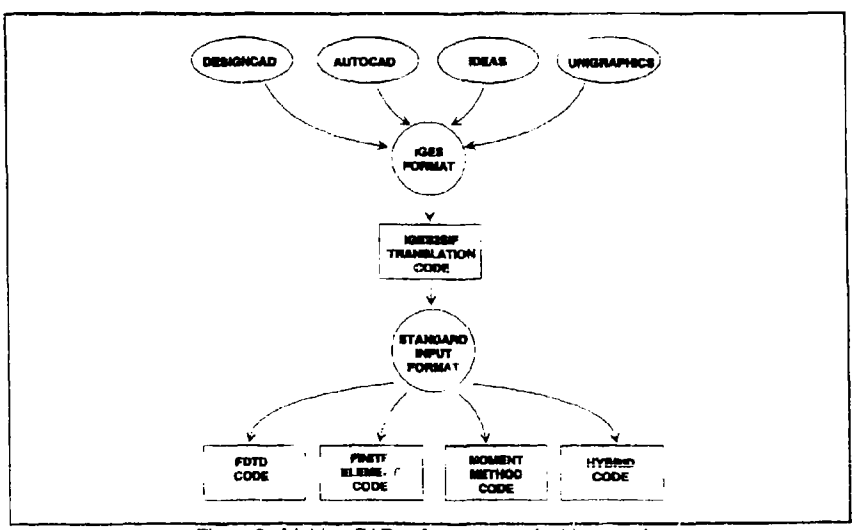

Figure 2: Linking CAD software to standard input codes

A New Approach

If there were a standard input file format that could be read by a variety of EM modeling codes, then only a single translation code would be required to link CAD software to the electromagnetic modeling software as indicated in Figure 2. Furthermore, if the standard input format were concise and simple to understand, then perhaps in many cases, it would be possible to eliminate the graphical user interface altogether.

To some extent, this is the approach used by the Numerical Electromagnetics Code (NEC). The relatively simple text input format employed by NEC allows many users to create and/or edit input geometry information without the aid of a graphical user interface. For complex geometries, a number of graphical interfaces are available all of which generate NEC input files in the same text format. Because of this, the NEC code is relatively platform independent. Code developers can make changes in the NEC code without worrying about the user interface, and users can choose the particular user interface best-suited to their own needs.

Of course, the NEC input format is optimized for the NEC code, which is a surface integral technique. It would not be suitable for another EM modeling code that used a different analysis technique (e.g. a finite element code or an FDTD code).

The remainder of this paper describes a new input file format (or, more specifically, a "geometry description language") that is optimized for use with EM modeling codes, but flexible enough to be used in codes that employ a variety of modeling techniques. This input format is currently used by three separate EM modeling codes at the University of Missouri-Rolla. One is a finite-element modeling code employing nodal elements. One is a hybrid FEM/MOM edge-element code. The third code employs a finite-difference time-domain technique.

The Input File Format

The new input file format was developed with three primary objectives:

1. That it be as simple and intuitive as possible. For simple geometries, the user should be able to visualize the input configuration simply by reading the input file.
2. That it be concise. In most cases, the user should be able to type in the entire input file using only a text editor.
3. That it be flexible. EM codes using different modeling techniques have vastly different capabilities and requirements.

Each line of the input file is either a data line or a comment (blank lines are ignored). Comment lines begin with a # sign and may be ignored or copied to the output file by the modeling code. All data lines consist of a *keyword* followed by space-delimited parameters. The format and the number of parameters depends on the keyword. For example, the line

```
dielectric 1 1 1 8 2 8 4.2 .002 1.0 d
```

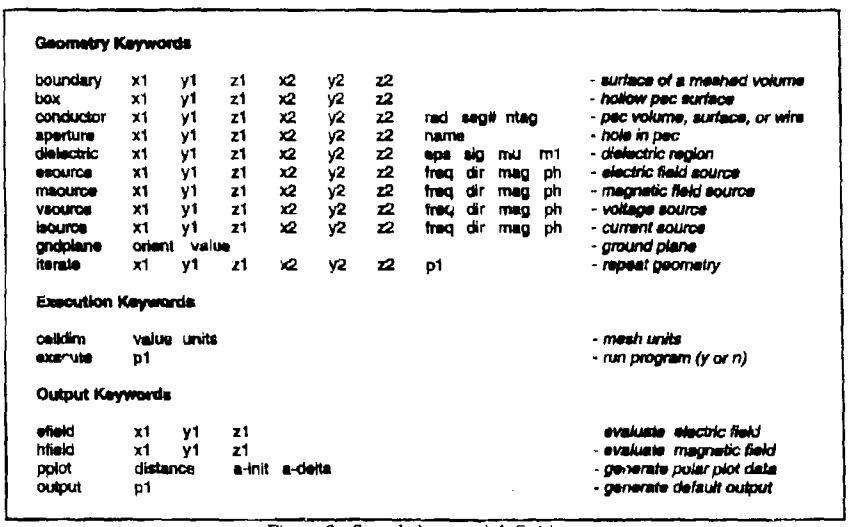

Geometry Keywords

boundary	x1	y1	z1	x2	y2	z2					- *surface of a meshed volume*
box	x1	y1	z1	x2	y2	z2					- *hollow pec surface*
conductor	x1	y1	z1	x2	y2	z2	rad	seg#	ntag		- *pec volume, surface, or wire*
aperture	x1	y1	z1	x2	y2	z2	name				- *hole in pec*
dielectric	x1	y1	z1	x2	y2	z2	eps	sig	mu	m1	- *dielectric region*
esource	x1	y1	z1	x2	y2	z2	freq	dir	mag	ph	- *electric field source*
msource	x1	y1	z1	x2	y2	z2	freq	dir	mag	ph	- *magnetic field source*
vsource	x1	y1	z1	x2	y2	z2	freq	dir	mag	ph	- *voltage source*
isource	x1	y1	z1	x2	y2	z2	freq	dir	mag	ph	- *current source*
gndplane	orient	value									- *ground plane*
iterate	x1	y1	z1	x2	y2	z2	p1				- *repeat geometry*

Execution Keywords

cellsize	value	units	- *mesh units*
execute	p1		- *run program (y or n)*

Output Keywords

efield	x1	y1	z1		*evaluate electric field*
hfield	x1	y1	z1		- *evaluate magnetic field*
pplot	distance		a-init	a-delta	- *generate polar plot data*
output	p1				- *generate default output*

Figure 3: Sample keyword definitions

contains the keyword "dielectric". This keyword must always be followed by at least 8 parameters. The first 6 parameters are integers that define the shape and position of the dielectric. The next 2 parameters are floating point numbers that define the relative permittivity and conductivity of the dielectric. The next parameter is optional and defines the relative permeability. The last parameter, also optional, is a character that, in this case tells the mesh generator to use an extra fine mesh in this region of the geometry.

A number of keywords have been defined, some of which are briefly described in Figure 3. Note that in addition to geometry keywords, there are keywords that affect the execution of the program and keywords that determine the output parameters.

Not all EM modeling codes will take advantage of every keyword. For example, a surface-integral code like NEC would probably ignore any *boundary* statements in its input file. EM modeling codes should be written to accept all valid keywords, but warn the user if any keywords in the input file are being ignored.

The basic keywords described in Figure 3 and their parameters have been chosen so that they are meaningful to EM codes based on a variety of EM modeling techniques. Codes that employ surface grids, codes with fixed volume meshes, and codes that require mesh generators, can all read the same input file and interpret it in a similar manner.

```
#  a shorted waveguide with dielectric loading
box          0 0 0 8 5 20
dielectric   0 0 10 8 5 20  4.0  0
esource      1 1 0 7 4 0 3000 y 1.0 0.0
```

Figure 4: Input file for a dielectric-loaded waveguide

```
# a simple printed circuit board configuration
# two rectangular loops above a ground plane
boundary     0 0 0 10 11 5
conductor    1 1 1 9 10 1
dielectric   1 1 1 9 10 2 4.0 0.0
conductor    2 2 2 8 3 2
conductor    2 4 2 8 5 2
conductor    2 2 2 3 5 2
conductor    7 2 2 8 5 2
conductor    2 6 2 8 7 2
conductor    2 8 2 8 9 2
conductor    2 6 2 3 9 2
conductor    7 6 2 8 9 2
esource      2 3 2 3 4 2 80 y 5.0 0.0
pplot        3 0 180
```

Figure 5: Input file for a printed circuit configuration

Examples

Examples of this geometry description language are provided in Figure 4 and Figure 5. Figure 4 shows the input file corresponding to a dielectric-loaded waveguide that is driven at one end with a uniform electric field and shorted at the other end. An IGES format description of this geometry is 195 lines long and does not include the source information. The input file in Figure 4, on the other hand, is 4 lines long and contains all the information required by the EM modeling code.

Figure 5 shows the input file corresponding to a printed circuit board configuration. The IGES format description requires 159 lines without the source. The input file in Figure 5 is 15 lines. Both

input files in these examples were easily generated with a simple text editor and are intuitive enough to visualize without a graphical user interface.

Conclusions

The geometry description language outlined above allows EM code users to create standard input files that can potentially be used with a variety of EM modeling codes. By establishing a standard input file format, code developers are isolated from user interface issues and they are free to develop codes that are relatively platform independent. Code users also benefit from a standard input format because they are able to choose a single compatible user-interface and use it with a variety of EM modeling codes.

So far, this input format is being used with three different EM modeling codes. One is a finite element code, one is an FDTD code, and the other is a hybrid code. Although a CAD interface that employs this input format has been developed, the authors typically find that simply creating the input files using a text editor is quicker and simpler. Development of this geometry description language is still under way. Enhancements continue to be made as the authors gain experience using the new input format and as they receive suggestions from other code users.

Reference

[1] T. H. Hubing, " Using Commercial CAD Packages to Interface with 3-D EM Modeling Codes," Proceedings of the Eighth Annual Review of Progress in Applied Computational Electromagnetics, Monterey, CA, March 1992, pp. 607-610.

A Geometry Description Language for 3D Electromagnetic Analysis Codes

Todd Hubing, Clara Hong-Him Lim, and James Drewniak
University of Missouri-Rolla

With the proliferation of 3D electromagnetic modeling software, many researchers are finding that the process of defining the input and interpreting the output is overly complex and unintuitive. Graphical user interfaces (GUIs) can help the user to visualize input geometries and output current and field distributions, but representing three dimensional data on a two-dimensional computer screen is inherently a complex process. The steep learning curve associated with most user interfaces prevent many EM modelers from experimenting with different EM modeling codes.

An Initial Solution

In a previous paper [1], a user interface (input only) was described that employed commercial Computer Aided Drawing (CAD) software. The idea was to isolate the development of the numerical EM modeling software from the development of the user interface. In this way, EM modeling code developers could concentrate on developing the best modeling software and development of the CAD interface could be left to programmers who specialized in that area. A relatively simple translation code was used to link the CAD software to the EM modeling code. The translation code read the 3D geometry information, prompted the user for any additional information (e.g. source amplitudes or material constants), checked for errors, and wrote a file suitable for exporting to the EM modeling code.

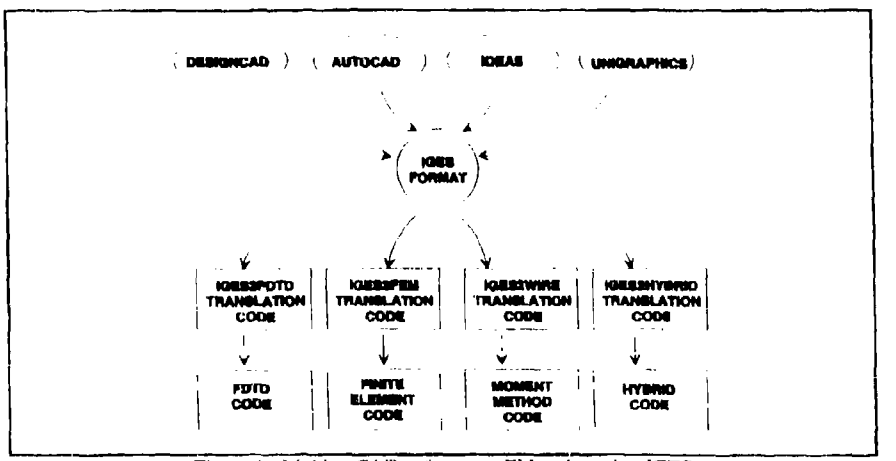

Figure 1: Linking CAD software to EM codes using IGES

In theory, a translation code written to interpret a standard graphics format, such as IGES or DXF, could accept input from a variety of CAD software packages. This approach, illustrated in Figure 1, would allow EM modelers to select the CAD software best-suited to their own needs to use as a graphical front-end to their EM modeling codes. If each 3D EM modeling code used was provided with a similar translation code, the modeler could analyze a given geometry using more than one technique without having to enter the geometry data each time. Also the code user could become proficient with a single CAD package and avoid having to learn a new user interface for every new EM modeling code. Using CAD software to create an IGES file is usually much more efficient than using a text editor and/or special subroutines to create a native format file. With the translation code, the standard graphics format effectively replaces the native input format of the modeling code.

This approach is not without drawbacks however. Currently there is no truly standard graphic format. IGES and DXF files can vary significantly depending on the CAD software used, the computer platform, and the techniques used to create a particular geometry. Also, IGES and DXF files were not optimized for storing the data required by most EM modeling software. The files are long and complex and they contain much information that is unusable by EM modeling codes. In addition, the IGES and DXF formats do not provide a standard method for conveying EM source or material information. In order to store an input geometry that the user may want to modify later, both the CAD file and a file containing the source and material information must be saved.

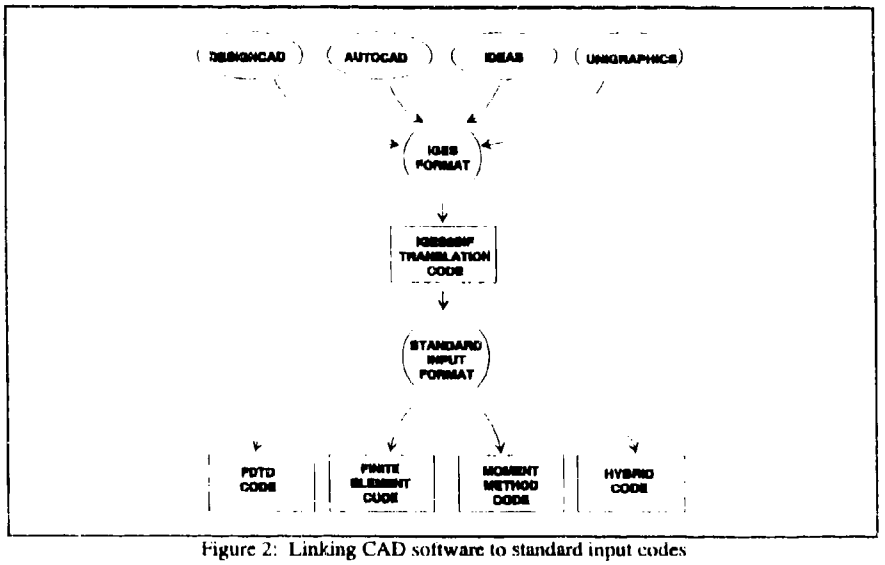

Figure 2: Linking CAD software to standard input codes

A New Approach

If there were a standard input file format that could be read by a variety of EM modeling codes, then only a single translation code would be required to link CAD software to the electromagnetic modeling software as indicated in Figure 2. Furthermore, if the standard input format were concise and simple to understand, then perhaps in many cases, it would be possible to eliminate the graphical user interface altogether.

To some extent, this is the approach used by the Numerical Electromagnetics Code (NEC). The relatively simple text input format employed by NEC allows many users to create and/or edit input geometry information without the aid of a graphical user interface. For complex geometries, a number of graphical interfaces are available all of which generate NEC input files in the same text format. Because of this, the NEC code is relatively platform independent. Code developers can make changes in the NEC code without worrying about the user interface, and users can choose the particular user interface best-suited to their own needs.

Of course, the NEC input format is optimized for the NEC code, which is a surface integral technique. It would not be suitable for another EM modeling code that used a different analysis technique (e.g. a finite element code or an FDTD code).

The remainder of this paper describes a new input file format (or, more specifically, a "geometry description language") that is optimized for use with EM modeling codes, but flexible enough to be used in codes that employ a variety of modeling techniques. This input format is currently used by three separate EM modeling codes at the University of Missouri-Rolla. One is a finite-element modeling code employing nodal elements. One is a hybrid FEM/MOM edge-element code. The third code employs a finite-difference time-domain technique.

The Input File Format

The new input file format was developed with three primary objectives:

1. That it be as simple and intuitive as possible. For simple geometries, the user should be able to visualize the input configuration simply by reading the input file.
2. That it be concise. In most cases, the user should be able to type in the entire input file using only a text editor.
3. That it be flexible. EM codes using different modeling techniques have vastly different capabilities and requirements.

Each line of the input file is either a data line or a comment (blank lines are ignored). Comment lines begin with a # sign and may be ignored or copied to the output file by the modeling code. All data lines consist of a *keyword* followed by space-delimited parameters. The format and the number of parameters depends on the keyword. For example, the line

```
dielectric 1 1 1 8 2 8 4.2 .002 1.0 d
```

Geometry Keywords

boundary	x1	y1	z1	x2	y2	z2						- *surface of a meshed volume*
box	x1	y1	z1	x2	y2	z2						- *hollow pec surface*
conductor	x1	y1	z1	x2	y2	z2	rad	segs	ntag			- *pec volume, surface, or wire*
aperture	x1	y1	z1	x2	y2	z2	name					- *hole in pec*
dielectric	x1	y1	z1	x2	y2	z2	eps	sig	mu	mt		- *dielectric region*
esource	x1	y1	z1	x2	y2	z2	freq	dir	mag	ph		- *electric field source*
msource	x1	y1	z1	x2	y2	z2	freq	dir	mag	ph		- *magnetic field source*
vsource	x1	y1	z1	x2	y2	z2	freq	dir	mag	ph		- *voltage source*
isource	x1	y1	z1	x2	y2	z2	freq	dir	mag	ph		- *current source*
gndplane	orient	value										- *ground plane*
iterate	x1	y1	z1	x2	y2	z2	p1					- *repeat geometry*

Execution Keywords

cellsm	value	units	- *mesh units*
execute	p1		- *run program (y or n)*

Output Keywords

efield	x1	y1	z1		- *evaluate electric field*
hfield	x1	y1	z1		- *evaluate magnetic field*
pplot	distance		a-init	a-delta	- *generate polar plot data*
output	p1				- *generate default output*

Figure 3: Sample keyword definitions

contains the keyword "dielectric". This keyword must always be followed by at least 8 parameters. The first 6 parameters are integers that define the shape and position of the dielectric. The next 2 parameters are floating point numbers that define the relative permittivity and conductivity of the dielectric. The next parameter is optional and defines the relative permeability. The last parameter, also optional, is a character that, in this case tells the mesh generator to use an extra fine mesh in this region of the geometry.

A number of keywords have been defined, some of which are briefly described in Figure 3. Note that in addition to geometry keywords, there are keywords that affect the execution of the program and keywords that determine the output parameters.

Not all EM modeling codes will take advantage of every keyword. For example, a surface-integral code like NEC would probably ignore any *boundary* statements in its input file. EM modeling codes should be written to accept all valid keywords, but warn the user if any keywords in the input file are being ignored.

The basic keywords described in Figure 3 and their parameters have been chosen so that they are meaningful to EM codes based on a variety of EM modeling techniques. Codes that employ surface grids, codes with fixed volume meshes, and codes that require mesh generators, can all read the same input file and interpret it in a similar manner.

```
#  a shorted waveguide with dielectric loading
box          0 0 0 8 5 20
dielectric   0 0 10 8 5 20  4.0  0
esource      1 1 0 7 4 0 3000 y 1.0 0.0
```

Figure 4: Input file for a dielectric-loaded waveguide

```
# a simple printed circuit board configuration
# two rectangular loops above a ground plane
boundary     0 0 0 10 11 5
conductor    1 1 1 9 10 1
dielectric   1 1 1 9 10 2 4.0 0.0
conductor    2 2 2 8 3 2
conductor    2 4 2 8 5 2
conductor    2 2 2 3 5 2
conductor    7 2 2 8 5 2
conductor    2 6 2 8 7 2
conductor    2 8 2 8 9 2
conductor    2 6 2 3 9 2
conductor    7 6 2 8 9 2
esource      2 3 2 3 4 2 80 y 5.0 0.0
pplot        3 0 180
```

Figure 5: Input file for a printed circuit configuration

Examples

Examples of this geometry description language are provided in Figure 4 and Figure 5. Figure 4 shows the input file corresponding to a dielectric-loaded waveguide that is driven at one end with a uniform electric field and shorted at the other end. An IGES format description of this geometry is 195 lines long and does not include the source information. The input file in Figure 4, on the other hand, is 4 lines long and contains all the information required by the EM modeling code.

Figure 5 shows the input file corresponding to a printed circuit board configuration. The IGES format description requires 159 lines without the source. The input file in Figure 5 is 13 lines. Both

input files in these examples were easily generated with a simple text editor and are intuitive enough to visualize without a graphical user interface.

Conclusions

The geometry description language outlined above allows EM code users to create standard input files that can potentially be used with a variety of EM modeling codes. By establishing a standard input file format, code developers are isolated from user interface issues and they are free to develop codes that are relatively platform independent. Code users also benefit from a standard input format because they are able to choose a single compatible user-interface and use it with a variety of EM modeling co .

So far, this input format is being used with three different EM modeling codes. One is a finite element code, one is an FDTD code, and the other is a hybrid code. Although a CAD interface that employs this input format has been developed, the authors typically find that simply creating the input files using a text editor is quicker and simpler. Development of this geometry description language is still under way. Enhancements continue to be made as the authors gain experience using the new input format and as they receive suggestions from other code users.

Reference

[1] T. H. Hubing, " Using Commercial CAD Packages to Interface with 3-D EM Modeling Codes," Proceedings of the Eighth Annual Review of Progress in Applied Computational Electromagnetics, Monterey, CA, March 1992, pp. 607-610.

SESSION 19:

HIGH FREQUENCY

Chair: Janice Karty

XPATCH : A High Frequency Electromagnetic Scattering Prediction Code Using Shooting and Bouncing Rays

Dennis J. Andersh, USAF, WL/AARA-2, WPAFB OH 45433
S. W. Lee, University of Illinois, Urbana IL 61801
Frederick L. Beckner, Cyberdynamics, Palo Alto CA 94301
Michael Gilkey, Veda, Dayton OH 45433
Richard Schindel, Sverdrup, Dayton OH 45433
Michael Hazlett, USAF, WL/AARA-2, WPAFB OH 45433
C. L. Yu, Naval Air Warfare Center, Point Mugu CA 93042

ABSTRACT

This paper describes an electromagnetic computer prediction code for generating radar cross section (RCS), time domain signatures and synthetic aperture radar (SAR) images of realistic 3-D vehicles. The vehicle, typically an airplane or a ground vehicle, is represented by a computer-aided design (CAD) file with triangular facets, curved surfaces, or solid geometries. The computer code, XPATCH, based on the shooting and bouncing ray technique, is used to calculate the polarimetric radar return from the vehicles represented by these different CAD files. XPATCH computes the first-bounce Physical Optics plus the Physical Theory of Diffraction contributions and the multi-bounce ray contributions for complex vehicles with materials. It has been found that the multi-bounce contributions are crucial for many aspect angles of all classes of vehicles. Without the multi-bounce calculations, the radar return is typically 10 to 15 dB too low. Examples of predicted range profiles, SAR imagery, and radar cross sections (RCS) for several different geometries are compared with measured data to demonstrate the quality of the predictions. The comparisons are from the UHF through the Ka frequency ranges.

INTRODUCTION

XPATCH is a general-purpose radar signature prediction code and environment for calculating high frequency electromagnetic scattering from complex objects described by several different computer-aided design (CAD) representations. XPATCH has been developed by the DEMACO in Champaign Illinois under the joint tri-Service sponsorship of Wright Laboratory at Wright-Patterson AFB, Ohio, Phillips Laboratory at Kirtland AFB, New Mexico, the Army Research Laboratory at Ft. Belvoir, Virginia, and the Naval Air Warfare Center at Pt. Mugu, California. The codes and graphical users interface (GUI) are currently available from Wright Laboratory (WL/AARA) for qualified United States users. The codes and tools will be distributed by the DOD/NASA Electromagnetic Code Consortium (EMCC) in 1994 with the same restrictions. The X-Window Motif™ GUI combines CAD geometry pre-processing and analysis tools, along with the XPATCH prediction codes, and post-prediction analysis tools. This GUI allows the user to perform end-to-end predictions analysis all in one package.

XPATCH is based on the high frequency shooting and bouncing ray technique [1,2] that is capable of calculating the fully polarimetric radar return from complex geometries represented by different CAD geometry types. Both the first-bounce Physical Optics (PO) plus the Physical Theory of Diffraction (PTD) contributions and the multi-bounce ray contributions are included in the computation. For the first bounce calculations, the most time-consuming aspect is shadow and blockage checks on the geometry. A hardware and software ray-tracing technique is used in XPATCH for highly accurate and fast calculations. Once the geometry's blocked and shadowed surfaces are determined, the first-bounce contribution is calculated using PO. The first-bounce PO calculation can be accomplished with a fast frequency domain integration [3] or by a time domain technique developed by Sheppard et al [4]. An option exists to include the first order metal edge diffraction by using the Ufimstev-Mitzner incremental diffraction coefficients. Although blockage on edges are taken into account by ray tracing, edge diffractions due to multiple bounce are not included.

To calculate the multi-bounce effects, a set of parallel rays are launched from the incident direction toward the geometry. Each ray is traced as it bounces from one part of the geometry to another, until it exits the geometry. The field

on the ray tube at each bounce point is calculated by the theory of geometrical optics, including the effects of polarization, ray divergence factor, and material reflection coefficients for frequency-dependent, multi-layered materials, and for semi-transparent materials such as radomes and camouflage nets. At the last reflection point on the geometry, a frequency domain or a time domain physical optics integration of the induced surface currents are performed to calculate the far field contribution from each ray tube. Contributions from all rays are then summed up at a far-field observation point to give the final scattered field.

Given the geometry and incident angle, rays are launched from a shooting window determined by the bounding box of the geometry. As an example, consider a typical fighter airplane (F-15) illuminated at an incidence elevation of -15° and azimuth of -15°. The shooting window is 674 λ by 397 λ at 10 GHz. Accuracy using an SBR type technique for radar cross section (RCS) and range profile (time domain) calculations requires a minimum ray density of 10 rays per linear wavelength. Using this minimum ray density, 23 million rays are launched at the target, of which 4 million actually hit the geometry. At millimeter wave frequencies, the XPATCH code has the option of using a different ray tube shape function that allows the user to trace fewer rays per wavelength. The minimum required ray density for synthetic aperture radar (SAR) imagery can also be reduced to two or three rays per linear wavelength, depending upon geometry complexity and the amount of multi-bounce contributions required to accurately calculate the backscattered field from the geometry. An interesting display of the multi-bounce effect is presented in Figure 1 for near broadside incidence of a tank. This figure clearly illustrates the necessity to use the shooting and bouncing ray technique to capture all the multiple bounce effects in backscattering predictions.

Presently, a typical frequency domain range profile computation with 1,024 frequencies (50 bounces, 10 rays/λ, X-band, 100,000 facet vehicle) takes approximately 40 minutes on an HP 720 workstation. Performing the same calculation directly in the time domain on the same HP 720 workstation takes approximately 20 minutes [5], however, this technique is currently valid only for perfect electric conducting targets. Computation times for the narrow angle (3°) X-band SAR imagery of a tank, using the direct time domain approach, takes approximately four minutes on an HP 720 workstation. Similarly, using IGES surface representations increases the frequency domain run time for the same 100,00 facet vehicle to about 400 minutes on an HP 720 workstation. For this reason, a new technique has been developed in XPATCH that incorporates the surface curvature into a flat-faceted geometry file. This hybrid geometry file provides fast computation associated with flat facet targets and accounts for the surface curvature to improve the amplitude calculations by including the ray divergence factor. One drawback of this hybrid approach, depending on the surface curvature, is that 100,000 plus facets are required to represent a typical fighter class vehicle and this means larger core memory requirements.

The XPATCH codes have been parallelized, by Sandia National Laboratories, using a 64-node Intel iPSC 860 Hypercube, 480 node Intel Paragon, and a 1024 nCUBE2 machine. Current production capacity is 3000+ signatures (1024 X-band frequency points) or images per day on a 64-node hypercube, and 14,000+ (1024 X-band frequency points) signatures or images per day on the 480-node Intel paragon. Research is proceeding in several areas to improve performance and accuracy. Optimization of the ray tracer and associated electromagnetic calculations in XPATCH is also an ongoing effort. Research to augment XPATCH with low frequency codes such as finite elements, finite difference time domain, and method of moments solutions is underway. Hybridization is being pursued to improve the XPATCH prediction code suites' accuracy for cavities such as jet engines, antennas, and for vehicle details less than 10 linear wavelengths in size. Research is also ongoing to provide the capability for full vehicle in scene clutter modeling from UHF through the Ka frequency band.

CODE CAPABILITIES

The electromagnetic part of XPATCH consists of roughly 30,000 lines of FORTRAN , the other parts consist of over 150,000 lines mostly in C. XPATCH consists of three parts:

1) Electromagnetics: XPATCH1, XPATCH2, XPATCH3, and XPATCH4.
2) CAD and visualization tools: cifer, XLOOK, Xyplot, McRange, and McImage.
3) Graphical user interface (GUI).

Typical output files from electromagnetic computation are:

1) complex scattered far field or RCS in dBsm (0D signature),
2) range profile (1D signature), and
3) synthetic radar image SAR (2D signature).

A summary of XPATCH capabilities is given in Table 1. Any code in XPATCH can be used individually as an independent unit, or it can be used as a component in the integrated GUI package. The graphical users interface consists of multiple pre- and post- prediction analysis tools: cifer, XLOOK, Xyplot, McRange, and McImage. Cifer is a file translator package that translates CAD formats from one CAD system to another and into the required format for XPATCH. XLOOK is a visualization tool that allows the user to display the CAD geometry and evaluate the physical integrity of the geometry to determine if the proper material assignments have been made to the geometry, normals are correct, and if the surfaces are properly modeled. Xyplot is a plotting package for producing xy-plots of the data. McRange allows the user to display the CAD file with measured and predicted time domain signatures to evaluate the cause and effect of scattering. McImage allows the user to overlay a CAD file with a predicted or measured SAR image and also allows the user to evaluate the cause and effect of the scattering. All of these tools have been integrated into one package with the GUI to allow the user to perform a seamless analysis of a complete electromagnetic prediction task.

Table 1. XPATCH Radar Signature Prediction Code

FEATURE	XPATCH1	XPATCH2	XPATCH3	XPATCH4
Freq/time domain	freq	freq	time	time
Target geometry	facet	CSG/NURB	facet	CSG/NURB
Coating/radome	both	coating	coating[2]	coating[2]
Divergence factor	yes[1]	yes	no	yes
First bounce	PO/z-buffer	SBR	SBR/z-buffer	SBR
Higher bounce	SBR	SBR	SBR	SBR
Edge diffraction	metal	metal	no	no
Best For	RCS/range	RCS/range	SAR	SAR

[1] Divergence factor is calculated from an additional curvature file

[2] Reflection from material is done approximately

The complex object geometry representation for XPATCH radar scattering predictions can be either triangular flat facets, BRL-CAD™ constructive solid geometries, or IGES 128 surface formats. By far, the most popular format is the triangular facet file because the computation time is about 10 times faster than the time for curved surface or solid geometry representations. Figure 2 is a view of a solid model for a typical tank, and Figure 3 is a facet model of an aircraft visualized in the XPATCH analysis tools, XLOOK.

One of the most important aspects of radar predictions is the integrity of the CAD geometry file. To analyze the CAD geometry, tools, such as XLOOK, have been developed to visualize, rotate, evaluate geometry normals, and inspect geometry surface integrity and connectivity (Figure 3). After the geometry has been visualized and evaluated for integrity the next step is to set up the run parameters to compute the electromagnetic scattering from the CAD geometry. The run parameters for XPATCH have all been integrated into a GUI that allows for easy input and assignment of the run parameter. An example input file for XPATCH is illustrated in Figure 4. After the computations with XPATCH insight into scattering causes and effects on targets is provided through another tool, McRange. McRange displays the CAD geometry with its corresponding range profile in the same range coordinate system (Figure 5). User-defined vertical solid lines on the plots illustrate the tie of scatter location to a physical attribute on the geometry. These GUI tools are very useful to evaluate the fidelity of CAD geometries, set up the run parameter, monitor the computational run and analyze the causes and effect of scattering.

VALIDATION RESULTS

XPATCH has been extensively validated against primitive objects and full scale complex vehicles [2, 6, 7]. The results for different geometries are shown in Figures 6 through 9 with a comparison of measured and predicted data. Figure 10 is a McImage rendering of predicted SAR image of a portion of a jet engine exhaust nozzle called turkey. This image was computed with the shooting and bouncing ray technique using the direct time domain method and required a computation time of 4 minutes on a Silicon Graphics workstation. Imagery such as this can be used as a diagnostic tool to study the cause and effect of scattering.

CONCLUSIONS

XPATCH provides realistic RCS, range profiles, and 2-D SAF imagery calculations for complex geometry types from 500 MHz to 100 GHz. Deficiencies in the existing CAD models contribute major errors in the predictions. Model deficiencies include poor or missing detail, inaccurate surface curvature, and improper modeling of small features and materials. The result is incomplete and inaccurate RCS, range profiles, and 2-D SAR images. More accurate CAD geometries can correct the deficiencies, but modeling is time-consuming and difficult. Additionally, the ultimate level of fidelity required for a CAD geometry is unknown. Research is ongoing to quantify the level of fidelity required from CAD models for different frequency ranges and applications.

XPATCH does not currently perform calculations for some of the higher order scattering effects such as traveling waves, surface waves, resonant effects, and creeping waves. Ongoing research to augment XPATCH for these scattering phenomena is currently in progress, with emphasis on new methods and hybridizing the predictions with low frequency methods. The XPATCH prediction code suite is being upgraded to perform full vehicle in scene predictions from UHF through Ka band. The major conclusion thus far is that the predictions created with XPATCH are adequate to use in studying the radar signatures of complex 3-D objects over a wide range of frequencies.

ACKNOWLEDGMENTS

We wish to acknowledge several contributors to this joint effort: Peter Shirley and Kevin Sung for helping us with the ray tracer; Shyh-Kang Jeng for writing the shape functions and facet splitter; Luke Lin, Hao Ling, Ri-Chee Chou, and John Baldauf for their contributions to the early versions of XPATCH; C. Long Yu for his vision on the importance of graphics in RCS predictions; John Ho for assisting in the extension of XPATCH to MMW applications; Robert Bonnor and Cullen Lee for improving the code structure and speed; Howard Nussbaum and Jim Roedder for sharing their methods of fast frequency looping to improve computational speed; Tom Sullivan for sharing his methods of fast time domain computational speed improvements; John Fraschilla and Charlie Thorington for their ideas on radome and material predictions; Rick Bowman and Rich Moore for giving us guidance and support; Phil Dykstra, Charlie Liang, and Richard Shepherd for developing xpatch and the time-domain z-buffer technique; Mike Christensen, Sean Ni, and Mike Gilkey for testing the code and producing application results; the authors of BRL-CAD for providing the CSG and IGES ray tracer and the modeler; Harry Reed for creating accurate geometric models; and Tim Olsen, J. P. Abelanet, and C.S. Liang for their cooperative work with and insight into the ACAD modeling program.

REFERENCES

1. H. Ling, R. Chou, and S. W. Lee, "Shooting and Bouncing Rays: Calculating the RCS of an Arbitrarily Shaped Cavity," IEEE Trans. Antennas & Propagation., vol. 37, 194 : 205 (1988).

2. Users Manual for XPATCH, DEMACO, 100 Trade Centre Drive, Champaign IL (1993).

3. J. M. Rius, M. Ferrando, and L. Jofre, "GRECO: Graphical Electromagnetic Computing for RCS prediction in real time," IEEE Antennas and Propagation Magazine, vol.35, No.2, pp.7-17, 1993.

4. R. A. Sheppard, T. D. Olson, and C. S. Liang, 1992 IEEE Antennas and Propagation's Society International Symposium, Chicago Illinois: 1992 Digest, Volume III, page 1311.

5. H. Ling and R. Bhalla, "Time Domain Ray-Tube Integration Formula for the Shooting-and-Bouncing-Ray Technique," Technical Report NASA Grant NCC 3-273, The University of Texas, Austin Texas (1993).

6. E. M. Miller, D. J. Andersh, A. J. Terzuoli, Jr, IEEE Antennas and Propagation's Society International Symposium, Ann Arbor Michigan: 1993 Digest, Volume III, page 1404.

7. E. M. Miller, D. J. Andersh, A. J. Terzuoli, Jr, 9th Annual Review of Progress at Applied Computational Electromagnetics, 1993 Conference Proceedings, Mar 93, page 610.

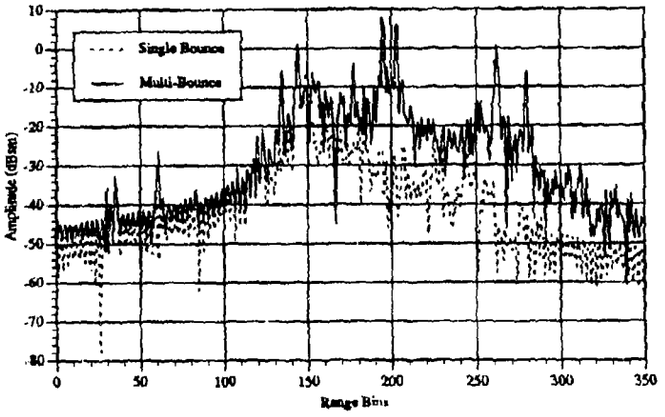

Figure 1. Range Profile Plots as a Function of Range for Single Bounce(Dashed Line) PO Calculations Versus Multi-Bounce (Solid Line) for a Tank at an Off Cardinal Angle of 45° Az and Depression of 45° at 10 GHz.

Figure 2. Solid Model CAD File of a tank Used in Predictions

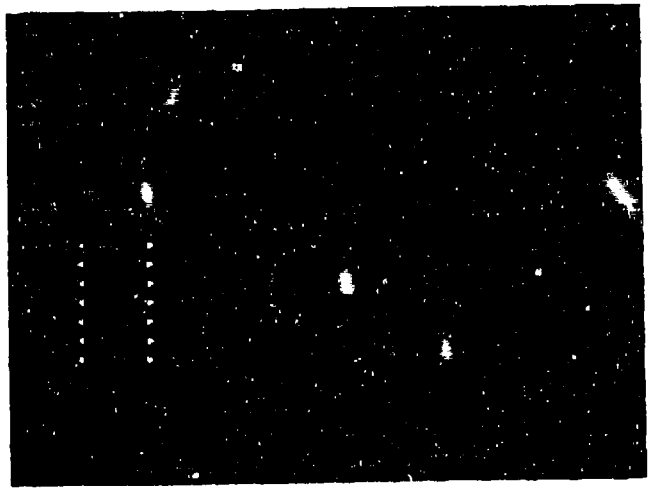

Figure 3. Example of Faceted Aircraft CAD Model Using Visualization Tools (XLOOK) Available in XPATCH.

Figure 4. Input Page of XPATCH Graphical Users Interface for Setting Up Code Run Parameters

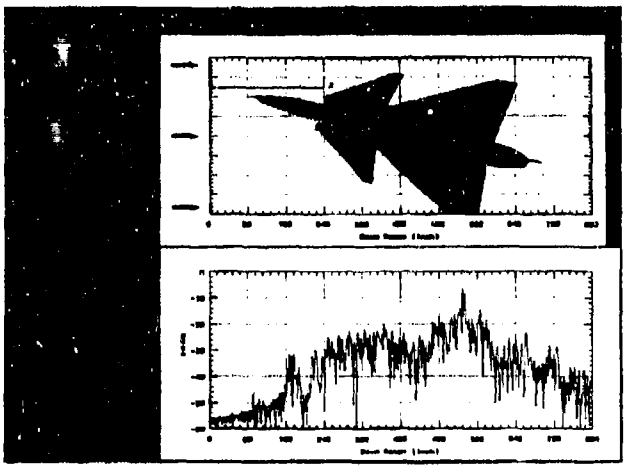

Figure 5. Predicted Range Profile of the vfy218 From an Aspect of Az = 0 and El = - 15.8 at a Center Frequency of 10 GHz Illustrating the Post Prediction Tool (McRange) (Note Solid Lines Can be Drawn From the Bottom Plot Connecting to the Upper CAD File Showing Scattering Cause and Effect)

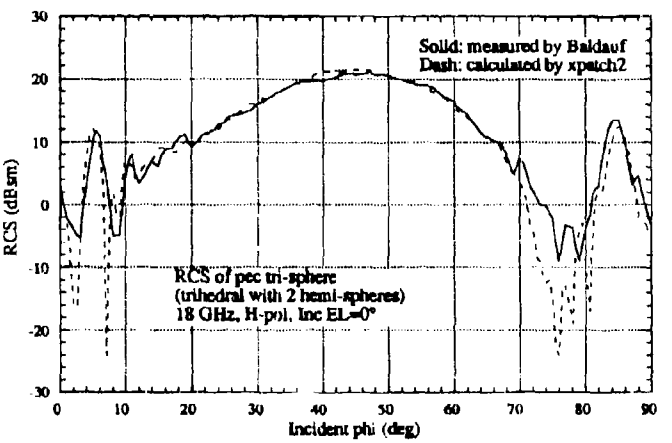

Figure 6. Comparison of Predicted Data to Measured Data for a 1EC Trihedral with Two Hemispheres, f = 18 GHz, HH Pol, $\phi = 0°$.

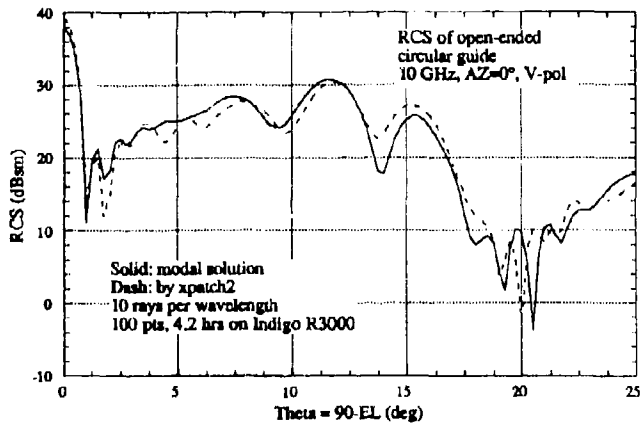

Figure 7. Comparison of Predicted Data to a Modal Solution for a Shorted Cylindrical Duct, f = 10 GHz, VV Pol, $\phi = 0°$, diameter = 95.9 cm, length = 254 cm.

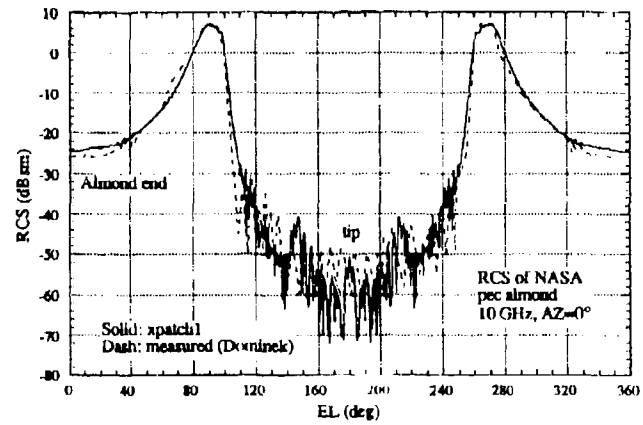

Figure 8. Comparison of Measurements and Predictions for a PEC Almond, VV Polarization, f= 10 GHz, NASA 1 Meter Almond.

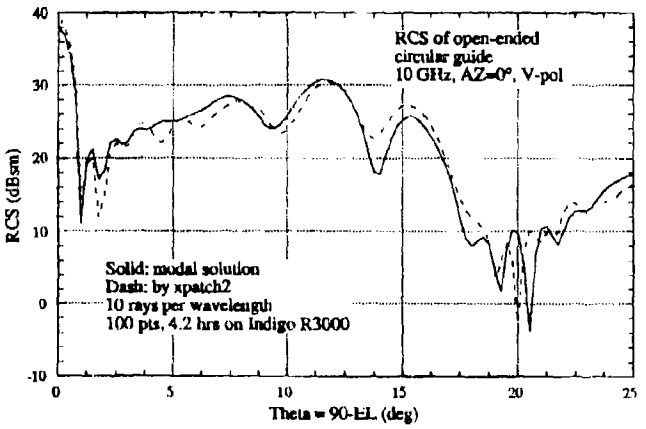

Figure 7. Comparison of Predicted Data to a Modal Solution for a Shorted Cylindrical Duct, f = 10 GHz, VV Pol, ϕ = 0°, diameter = 95.9 cm, length = 254 cm.

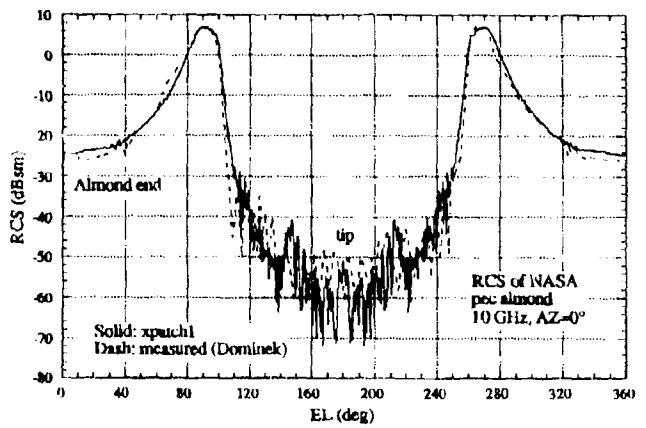

Figure 8. Comparison of Measurements and Predictions for a PEC Almond, VV Polarization, f= 10 GHz, NASA 1 Meter Almond.

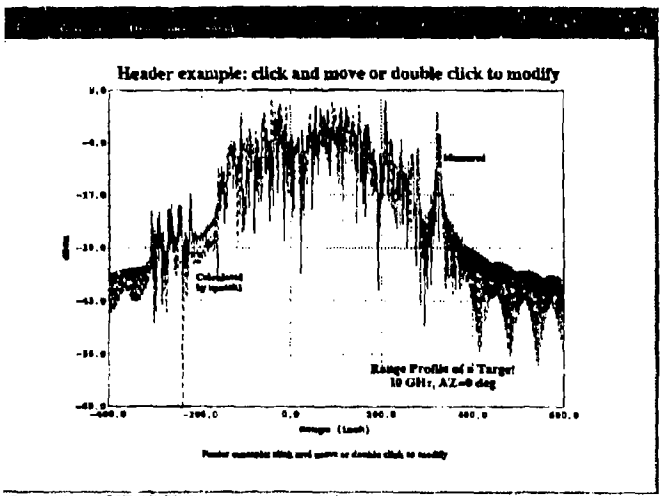

Figure 9. Comparison of XPATCH Range Profile Predictions to Measured Results for an f = 10 GHz, Actual Vehicle, VV Pol.

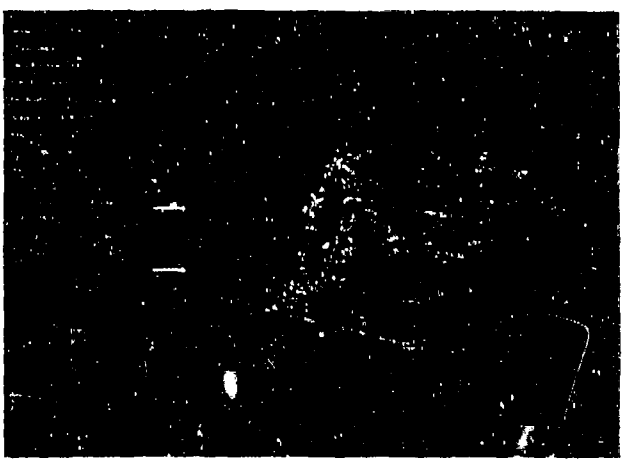

Figure 10. Prediction of a SAR of a Turkey at X-Band and Displayed with CAD Geometry using Analysis tool McImage.

A SIMPLE PHYSICAL OPTICS ALGORITHM PERFECT FOR PARALLEL COMPUTING ARCHITECTURE

W. A. Imbriale and T. Cwik
Jet Propulsion Laboratory
California Institute of Technology
Pasadena, CA 91109

Abstract

A reflector antenna computer program based upon a simple discreet approximation of the radiation integral has proven to be extremely easy to adapt to the parallel computing architecture of the modest number of large-grain computing elements such as are used in the Intel iPSC and Touchstone Delta parallel machines. It has also proven to be very efficient with reasonable size reflectors, parallel efficiencies approaching 98% have been demonstrated.

Introduction

One of the simplest reflector antenna computer programs is based upon a discrete approximation of the radiation integral (Reference 1). This calculation replaces the actual reflector surface with a triangular facet representation so that the reflector resembles a geodesic dome. The Physical Optics (PO) current is assumed to be constant in magnitude and phase over each facet so the radiation integral is reduced to a simple summation. This program has proven to be surprisingly robust and useful for the analysis of arbitrary reflectors, particularly when the near-field is desired and surface derivatives are not known.

Because of its simplicity, the algorithm has proven to be extremely easy to adapt to the parallel computing architecture of a modest number of large-grain computing elements such as are used in the Intel iPSC and Touchstone Delta parallel machines.

For generality, we consider a dual-reflector calculation, which can be thought of as three sequential operations: (1) compute the currents on the first reflector using the standard PO approximation; (2) utilizing the currents on the first reflector as the field generator, compute the currents on the second reflector; and (3) compute the required field values by summing the fields from the currents on the second reflector. The most time-consuming part of the calculation is the computation of the currents on the second reflector due to the currents on the first, since for $N \times N$ triangles on the first reflector, each of the $M \times M$ triangles on the second reflector required an N^2 sum over the first. However, since each calculation requires the identical number of operations, the N^2 triangles can be evenly distributed over the nodes, and the sum done in parallel for each of the M^2 triangles on the second reflector (also evenly distributed over the nodes). In addition, the output field values can be calculated in parallel with each node, summing its respective triangles, and the final output field obtained by summing the field in each of the nodes.

For reasonable size reflectors, parallel efficiencies approaching 98% have been demonstrated.

Physical Optics Algorithm

The analysis method utilized is a straightforward numerical integration of the physical optics radiation integral. Since the incident magnetic field is required to evaluate the PO surface current on the second reflector (see Figure 1), we choose the following form for the radiation integral (although the method is identical if the E field is required):

$$H(r) = -\frac{1}{4\pi}\int_{\Sigma}\left(jk+\frac{1}{R}\right)\hat{R}\times J_s(r')\frac{e^{-jkR}}{R}ds' \tag{1}$$

in which r designates the field point, r' the source point, $R = |r-r'|$ is the distance between them, and $\hat{R} = (r-r')/R$ is a unit vector. The PO current on the surface J_s is expressed as

$$J_s(r') = 2\hat{n}\times H_s(r') \tag{2}$$

with $H_s(r')$ the incident magnetic field.

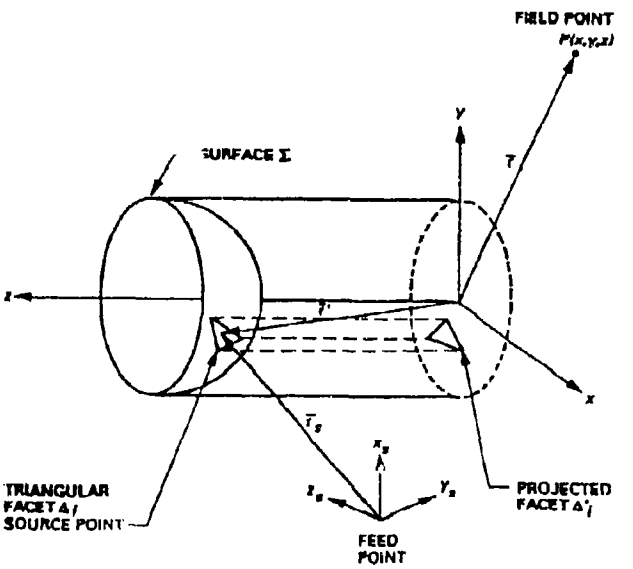

Figure 1. Reflector analysis coordinate systems and a typical triangular facet.

Let (x_s, y_s, z_s) denote the coordinates of the reflector surface. For the purpose of analysis, the reflector surface is subdivided into small triangular regions. Within each triangular region, the actual subreflector surface is approximated by a planar surface, or facet. Now, let R_{k1}, R_{k2}, R_{k3} be vectors directed to the three vertices of the kth facet. Then, vectors along the sides of the facet are given by

$$A = R_{k1} - R_{k2}$$

$$B = R_{k2} - R_{k3}$$

$$C = R_{k3} - R_{k1}$$

and a unit normal n_k may be constructed by the following vector operations:

$$n_k = \frac{A \times B}{|A \times B|}$$

The area Δ_k of the triangle is readily calculated from

$$\Delta_k = \sqrt{S(S-A)(S-B)(S-C)}$$

where

$$S = \frac{|A| + |B| + |C|}{2}$$

With this triangularization established, the PO surface current is approximated by

$$J_s \approx \sum_{k=1}^{N} J_s^{(k)}$$

where $J_s^{(k)}$ is the PO current evaluated at the center of the kth facet. In other words, the PO surface current is assumed to be constant over a facet. Using this expression in Eq. (1) gives the following approximation for the PO radiation integral:

$$H = \frac{1}{4\pi} \sum_{k=1}^{N} \left(jk + \frac{1}{R_k} \right) \hat{R}_k \times J_s^{(k)} \frac{e^{-jkR_k}}{R_k} \Delta_k \tag{3}$$

Notice that a discrete approximation is used for the current as well as the surface. For aid in convergence, the distance R_k is chosen to be on the surface rather than on the triangular facet.

Dual-Reflector Calculation

For generality, we will consider the dual-reflector calculation; the single reflector calculation can be done in the same manner, but the time associated with the calculation is considerably less and may not require the capabilities of parallel computing.

Referring to Figure 2, the dual-reflector case consists of a feed, subreflector surface, and main reflector surface. The field scattered from these surfaces is evaluated at a given field point and the calculation can be thought of as three sequential operations: (1) compute the currents on the first reflector using the standard PO approximation; (2) utilizing the currents on the first reflector as the field generator, compute the currents on the second reflector; and (3) compute the required field values by summing the fields from the currents on the second reflector.

Utilizing the method described in the previous section, each surface is subdivided into small triangular regions, with a typical mesh projected into the x-y plane shown in Figure 3. The currents on the first surface (typically called the subreflector) are evaluated using Eq. (2). For the examples considered in this paper, the incident will be in the form of a cosine to the power Q, although any desired incident field evaluation could be used. Thus the incident field is of the form

$$H_s(r') = \cos^q(\theta)\frac{e^{-jkr'}}{r'}$$

where the feed is assumed to be pointing along the Z_f coordinate and θ is the polar angle. The magnetic field incident on each triangle of the second reflector (typically called the main reflector) is evaluated using Eq. (3). The currents on each triangle are then obtained by using the physical optics approximation of $J = 2\hat{n} \times H$. Observe that to obtain the current for each triangle of the second reflector requires a sum over all the triangles of the first reflector. The field scattered from the second reflector is then evaluated by another application of Eq. (3) (or a similar form of the equation if the E-field is required).

Parallel Algorithm

Observe that the most time-consuming part of the calculation is the computation of the currents on the second reflector due to the currents on the first, since for $N \times N$ triangles on the first reflector, each of the $M \times M$ triangles on the second reflector required an N^2 sum over the first. Since each calculation requires the identical number of operations, the N^2 triangles can be evenly distributed over the nodes, and the sum done in parallel for each of the M^2 triangles on the second reflector. However, since the computation of the currents on the first surface is trivial, little (other than storage) is gained by distributing the N^2 triangles of the first reflector over the nodes. Computation of the currents on each of the M^2 triangles is evenly distributed over the nodes and the computations are done in parallel. Hence each node has a copy of the program for computing the integrand of Eq. (3), and each node computes the H-field and current for its assigned triangles. After each of the nodes computes its M^2/NODES of the currents, the currents are then collected such that each node has all the currents. To compute the field values, each node does M^2/NODES of the sum of Eq. (3) utilizing the currents on the main (second) reflector. The final result is obtained by summing the

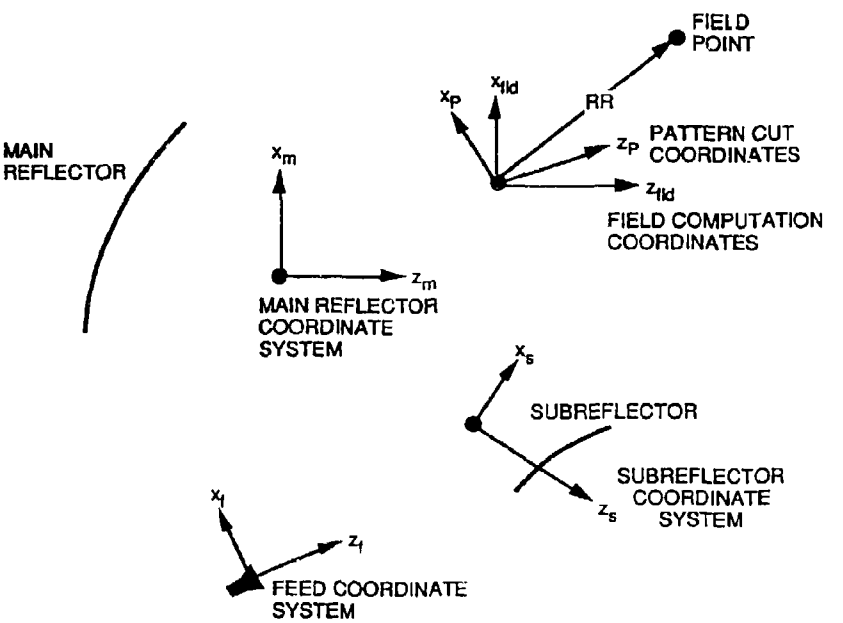

Figure 2. Schematics of the coordinate systems.

fields obtained from each of the nodes. It is possible to improve the algorithm for storage (but only a minor time savings) by not collecting all the currents on the main reflector, since each node only needs its M^2/NODES currents to do the field summation.

Examples and Conclusions

As an example, we consider the two parabola example shown in Figure 4 (Reference 2). This is a portion of JPL beamwaveguide system and is designed to image the input feed pattern to the first parabola at the output focus of the second parabola. The geometry is as shown and for this calculation a $\cos^q(\theta)$ feed pattern with $q = 238.25$ is used as an input. A typical output is shown in Figure 5 with a comparison to measured data included.

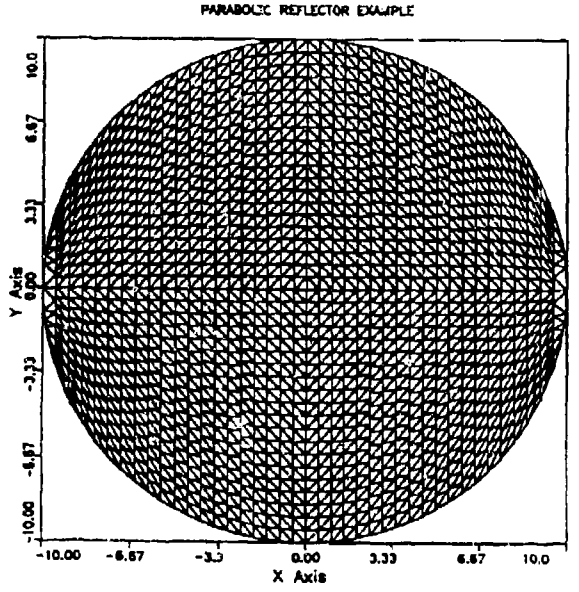

Figure 3. Typical mesh projected in X-Y plane.

The typical time for a small example is shown in Table 1. The only part of the program that was parallelized was the portion which computes the second reflector currents from the first reflector currents. For sufficiently large problems this portion of the code dominates. However, it is possible to parallelize the field evaluation and this will be done in the future. Observe that the efficiency of calculating the currents using 8 nodes is 98.6%.

Table 1. Dual reflector example with 10372 triangles on each surface

# Nodes	1	4	8
Time for first reflector currents	11	12	13
Time for second reflector currents	11,339	2849	1437
Field evaluation	191	192	194
Total (seconds)	11,721	3053	1644

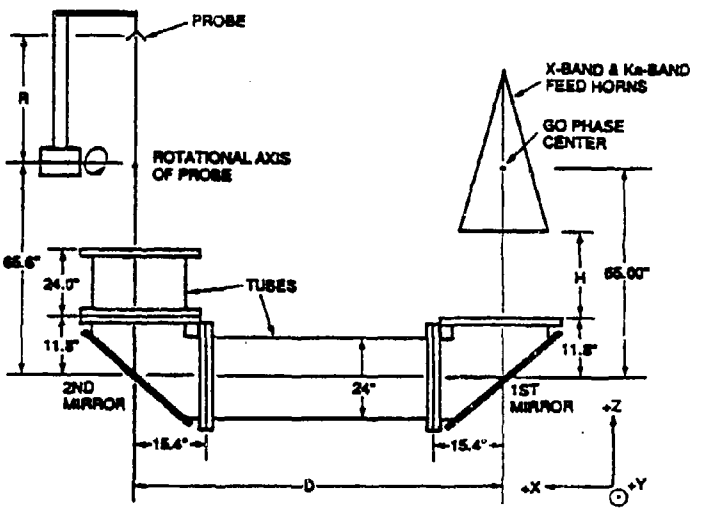

Figure 4. A two-mirror BWG system test setup.

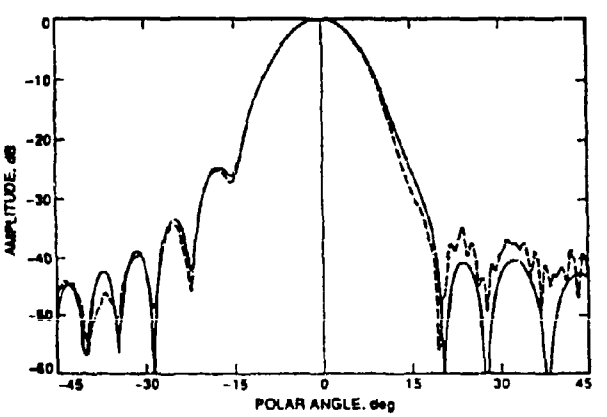

Figure 5. Measured (dashed line) and computed (solid line) data for offset plane (X-band).

Acknowledgment

The research described in this paper was carried out by the Jet Propulsion Laboratory, California Institute of Technology, under a contract with the National Aeronautics and Space Administration.

References

1. W. A. Imbriale and R. Hodges, "Linear Phase Approximation in the Triangular Facet Near-Field Physical Optics Computer Program," *Applied Computational Electromagnetics Society Journal, Vol. 6, No. 2*, Winter 1991.

2. J. R. Withington, W. A. Imbriale, and P. Withington, "The JPL Beamwave Test Facility," *1991 AP-S Symposium Digest*, London, Ontario, Canada, pp. 1194–1197, June 1991.

A UGO/EUTD with Application to Fourth Order Polynomial Strips

Ronald J. Marhefka and Evagoras D. Constantinides
The Ohio State University
ElectroScience Laboratory
1320 Kinnear Road
Columbus, Ohio 43212-1191
Phone: (614)292-5752
Fax: (614)292-7297
E-mail: rjm@tiger.eng.ohio-state.edu

Abstract

The ability to efficiently calculate the far zone scattering from polynomial surfaces is needed when modeling structures using modern CAD packages. A uniform geometrical optics (UGO) and extended uniform geometrical theory of diffraction (EUTD) has recently been developed for polynomial structures. The applications of this theory to two-dimensional fourth order polynomial strips is discussed. The results are validated using moment methods.

I Introduction

The wide availability of CAD packages to engineers has lead to many structures being routinely defined by splines, that is, patches defined by polynomials. There are numerous useful codes for calculating the radar cross section of such objects in use. Most of these codes are based on some form of explicit physical optics and fringe current integrations (PO/PTD). Geometrical optics (GO) [1], geometrical theory of diffraction (GTD) [2], and it uniform version (UTD) [3] has seen limited use for these applications. This is due to the fact that the classical solution fails in caustic regions for surfaces defined by powers greater than two. Yet, it can be desirable to have a solution that retains the efficiency for large objects and the physical insight into the scattering phenomenology that UTD affords.

A solution has recently been developed that extends the GO/UTD to general polynomial defined surfaces. This extended solution, referred to here as UGO/EUTD [4], has been rigorously defined for arbitrary polynomial surfaces for near and far zone cases. The solution is limited in practice by the ability to efficiently calculate the special transition functions. The third order solution is fully worked out for cubic polynomial strips [5] using incomplete airy functions [6]. This discussion will outline the theory, but concentrate on the implementation, in particular for fourth order polynomial strips. The advantages for large sized patches will be discussed.

II Technical Approach

The development of the UGO/EUTD diffraction coefficients is based on the use of spatial domain radiation integrals for the scattered fields obtained from PO. The relevant scattering mechanisms, corresponding to the critical points of the integrals, are extracted using uniform asymptotic procedures, in particular, a generalised form of Chester's expansion [7]. The details of this derivation are given in Reference [4], for the general case, and also [5] for just the third order case. Previous solutions, like in References [10] and [11], do not contain edges.

The surface under consideration here can be defined as

$$\vec{r}(u) = u\hat{x} + Y(u)\,\hat{y},\ a \le u \le b,$$

where

$$Y(u) = a_0 + a_1 u + a_2 u^2 + \cdots + a_n u^n.$$

The geometry is illustrated in Figure 1, in this case, for a fourth order polynomial surface. In general, there will be several reflection points (i.e., Q_1, Q_2, and Q_3), zero-curvature points (i.e., Q_{p1} and Q_{p2}), and two edge diffraction points (i.e., Q_a and Q_b). The form of the solution is designed to correspond to the standard form of the UTD, that is, diffraction coefficients associated with the pertinent rays. The important practical difference is that the new solution includes transition functions composed of complete and incomplete generalised Airy type integrals [4], including standard Airy and Pearcy functions [6, 8, 9]. The following results are for the two-dimensional case, where $\nu = n$ refers to the order of the polynomial.

The reflected field for one of the reflection points may be written as

$$\vec{E}^r(\theta', \theta; \rho) \sim \vec{E}^i(Q_r) \cdot \overline{\overline{\mathcal{R}}}(Q_r) \sqrt{\frac{1}{2}\rho_g(Q_r)\cos\theta^i}\, e^{jkF(Q_r)\cdot\hat{s}^r} \frac{e^{-jk\rho}}{\sqrt{\rho}},$$

where $\vec{E}^i(Q_r)$ is the incident plane wave for the particular reflection point and $\overline{\overline{\mathcal{R}}}(Q_r)$ is the UGO dyadic reflection coefficient given by

$$\overline{\overline{\mathcal{R}}}(Q_r) = \mathcal{R}_s(Q_r)\,\hat{e}_\perp\hat{e}_\perp + \mathcal{R}_h(Q_r)\,\hat{e}_\parallel^i\hat{e}_\parallel^r,$$

$$\mathcal{R}_{s,h}(Q_r) = R_{s,h} e^{j\frac{\pi}{4}} \sqrt{\frac{\nu-1}{\nu}}\, \gamma_{1,2}^{\frac{\nu-3}{2}(\nu-1)}\, e^{-j\left(\frac{\nu-1}{\nu}\right)\gamma_{1,2}^{\frac{\nu}{\nu-1}}}\, I_r^*\left(-\gamma_{1,2}, \nu\right),$$

$$R_{s,h} = \mp 1, \text{ for a perfectly conduting boundary.}$$

The special functions will be discussed below.

The zero-curvature diffracted field from a concave-convex polynomial boundary may be written as

$$\vec{E}^r(\theta', \theta; \rho) \sim E^i(Q_p) \cdot \overline{\overline{D}}^{cc}(Q_p)\, e^{jkF(Q_p)\cdot\hat{s}^p} \frac{e^{-jk\rho}}{\sqrt{\rho}},$$

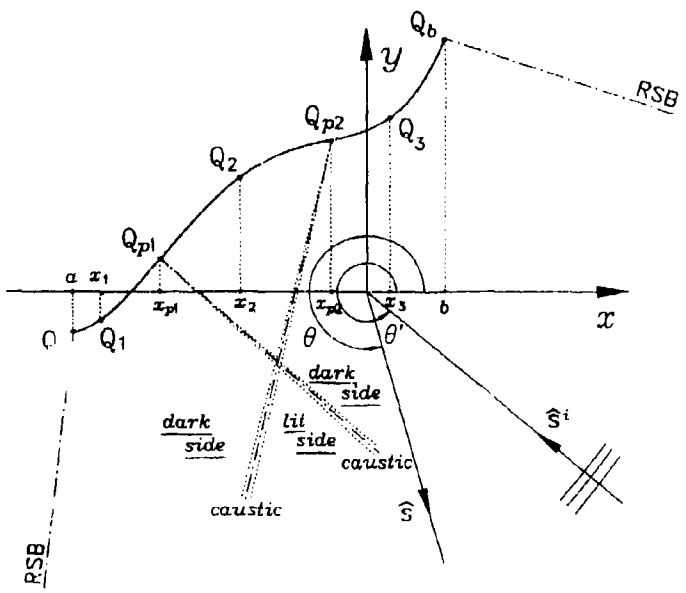

Figure 1: Geometry and relevant parameters for the scattering from a fourth order polynomial strip.

where $\vec{E}^i(Q_p)$ is the incident plane wave at Q_p and $\overline{\overline{D}}^{\infty}(Q_p)$ is the EUTD dyadic odd order zero-curvature diffraction coefficient given by

$$\overline{\overline{D}}^{\infty}(Q_p) = \mathcal{D}_s^{\infty}\left(\varphi_p', \varphi_p; \nu\right) \hat{e}_{\perp}\hat{e}_{\perp} + \mathcal{D}_h^{\infty}\left(\varphi_p', \varphi_p; \nu\right) \hat{e}_{\parallel}^i \hat{e}_{\parallel}^r,$$

$$\mathcal{D}_{s,h}^{\infty}\left(\varphi_p', \varphi_i; \nu\right) = \mp \frac{e^{j\frac{\pi}{4}} k^{\frac{1}{2\nu}}}{\sqrt{2\pi}} L_p\left(\varphi_p', \varphi_p; \nu\right) \begin{cases} I_{pl}(\gamma_p, \nu), \text{(lit side)} \\ I_{pd}(\gamma_p, \nu), \text{(dark side)}. \end{cases}$$

There is a similar expression for even order zero-curvature points, but with a different transition function.

The edge diffracted field may be written as

$$\vec{E}^d(\theta', \theta; \rho) \sim \vec{E}^i(Q_a) \cdot \overline{\overline{D}}^e(Q_a)\, e^{jk\hat{r}(Q_a)\cdot\hat{s}^i} \frac{e^{-jk\rho}}{\sqrt{\rho}},$$

$$\overline{\overline{D}}^e(Q_a) = \mathcal{D}_s^e\left(\varphi_a', \varphi_a; \nu\right) \hat{e}_{\perp}\hat{e}_{\perp} + \mathcal{D}_h^e\left(\varphi_a', \varphi_a; \nu\right) \hat{e}_{\parallel}^i \hat{e}_{\parallel}^d,$$

$$\mathcal{D}_{s,h}^e\left(\varphi_a', \varphi_a; \nu\right) = \frac{-e^{-j\frac{\pi}{4}}}{2\sqrt{2\pi k}} \left[\frac{1}{\cos\left(\frac{\varphi_a' - \varphi_a}{2}\right)} \mp \frac{\mathcal{F}(\gamma_d, \zeta_d, \nu)}{\cos\left(\frac{\varphi_a' + \varphi_a}{2}\right)} \right].$$

The EUTD transition function $\mathcal{F}(\gamma, \zeta, \nu)$ is defined as

$$\mathcal{F}(\gamma, \zeta, \nu) = j\left(\gamma + \zeta^{\nu-1}\right) I_a^*(\gamma, \zeta, \nu)\, e^{j(\gamma\zeta + \zeta^{\nu}/\nu)}.$$

For the cubic polynomial case, $\nu = 3$, the functions I_r^*, $I_{pl} = 0$, and I_{pd} are related complete Airy type integrals. The function I_a^* is an incomplete Airy integral. For the fourth order polynomial strip, $\nu = 4$, the generalized Airy Functions reduce to a special case of the Pearcy integral. In all cases, when the curvature is in a convex region, the complex conjugate versions are used. It should be noted, that when the observation direction is near an optical boundary and far removed from the caustic directions, I_a^*, can be expressed in terms of the Fresnel integral, thereby, the $\mathcal{F}$ function reduces to th normal UTD transition function. To safe space definition of other pertinent parameters can be found in References [4] and [5].

III Numerical Results

The accuracy and limitations of the UGO/EUTD solution is demonstrated by showing the far zone scattering from a fourth order polynomial strip . A two dimensional moment method (MM) solution is used for comparison. The results are also compared with the classical GO/UTD solution to illustrate how the new solution corrects the caustic and composite shadow boundaries.

The results for this discussion are limited to the case where the two first order zero-curvature points, Q_{p1} and Q_{p2}, as shown in Figure 1, are sufficiently far apart. When Q_{p1} and Q_{p2} are close together, the two caustics form a cusp and the UGO/EUTD solution fails. The UGO/UTD solutions does apply when Q_{p1} and Q_{p2} coalesce to form a second order zero-curvature point, however, no results for this case are available at this time. Figure 2 shows the bistatic echo

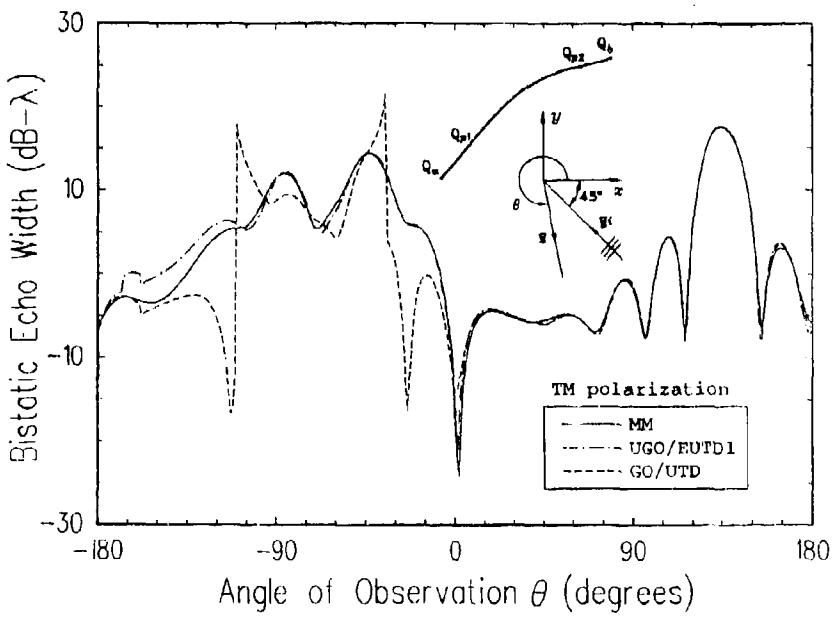

Figure 2: Bistatic echo width (TM case) of a fourth order polnomial strip with $a_0 = 1.0\lambda$, $a_1 = 0.5$, $a_2 = -0.4\lambda^{-1}$, $a_3 = 0.1\lambda^{-2}$, $a_4 = 0.1\lambda^{-3}$, $a = -1.5\lambda$, $b = 1.0\lambda$, and angle of incidence $\theta' = -45°$.

width of a fourth order polynomial strip with $a_o = 1.0\lambda$, $a_1 = 0.5$, $a_2 = -0.4\lambda^{-1}$, $a_3 = 0.1\lambda^{-2}$, $a_4 = 0.1\lambda^{-3}$, $a = -1.5\lambda$, and $b = 1.0\lambda$, illuminated by a TM polarized plane wave incident at an angle of $\theta' = -45°$. The UGO/EUTD results shows good agreement with MM for the TM polarization case. For the TE case, which is not shown here, the agreement is also good, however, near edge on incident requires the addition of higher order diffractions. The classic GO/UTD solution fails dramatically near the caustics ($\theta \approx -112°$ and $\theta \approx -35°$). The solution also works well as the surface goes to a flat strip, that is, it is a uniform solution for different orders of the polynomial.

IV Conclusions

A new extended uniform geometrical optics (UGO) and uniform geometrical theory of diffraction (EUTD) has been developed. It overcomes many of the limitations of the classical UTD solution for polynomial surfaces with order greater than two. It has the advantage that the solution

actually takes less time to compute as the size of the patch gets larger. This is due the fact that the transition functions needs to be calculated more infrequently as the electrical size gets larger. This is in contrast to integration implementations whose calculation time requirements increase with size [12]. It, also, has the advantage of the UTD by providing physical insight into where the scattering emanates. The disadvantage is that it relies on special function evaluation. Efficient algorithms for complete and incomplete Airy Integrals have been developed. Similar studies of the Pearcy Integrals have been under investigation.

The solution has also been investigated for three dimensional patches when the caustics for the two different principal directions are separated. More work is needed for the general case. In any event, this the solution is still useful, since the other dimension can be added through a one dimensional integration. The near zone solution has also been developed but is not discussed here.

The solution has been applied to the far zone scattering from fourth order polynomial strips. Various configurations have been tried and compared with a two-dimensional moment method solution. The results compare very well over the regions that the first order terms included here dominate.

Acknowledgment

This work was supported in part by Grant NSG-1498 from NASA - Langley Research Center, AFEWC/ESAS, and The Ohio State University Research Foundation.

References

[1] M. Kline and I. W. Kay, *Electromagnetic Theory and Geometrical Optics*, Interscience Publishers, Inc., 1965.

[2] J. B. Keller, "Geometrical Theory of Diffraction," *J. Opt. Soc. of America*, Vol. 52, No. 2, pp. 116–130, Feb. 1962.

[3] R. G. Kouyoumjian and P. H. Pathak, "A Uniform Geometrical Theory of Diffraction for an Edge in a Perfectly Conducting Surface," *Proc. IEEE*, Vol. 62, pp. 1448–1461, Nov. 1974.

[4] E. D. Constantinides, "A Uniform Geometrical and an Extended Uniform Geometrical Theory of Diffraction for Evaluating High Frequency EM Fields Near Smooth Caustics and Composite Shadow Boundaries," Ph.D. Dissertation, The Ohio State University, 1993.

[5] E. D. Constantinides and R. J. Marhefka, "A UGO/EUTD Solution for the Scattering and Diffraction from Cubic Polynomial Strips," *IEEE Trans. Antennas Propagat.*, Vol. 41, No. 8, pp. 1088–1098, Aug. 1993.

[6] E. D. Constantinides and R. J. Marhefka, "Efficient and Accurate Computation of the Incomplete Airy Functions," *Radio Science*, Vol. 28, No. 4, pp. 441–457, Jul.-Aug. 1993.

[7] C. Chester, B. Friedman, and F. Ursell, "An Extension of the Method of Steepest Descent," *Proc. Cambridge Phil. Soc.*, Vol. 53, pp. 599-611, 1957.

[8] L. Levey and L. B. Felsen, "On Incomplete Airy Functions and their application to diffraction problems," *Radio Science*, Vol. 4, pp. 959-969, Oct. 1969.

[9] T. Pearcy, "The Structure of an Electromagnetic Field in the neighbourhood of a Cusp of a Caustic," *Phil. Mag.*, Vol. 37, pp. 311-317, 1946.

[10] P. H. Pathak and M. C. Liang, "On a Uniform Asymptotic Solution Valid Across Smooth Caustics of Rays Reflected by Smoothly Indented Boundaries," *IEEE Trans. Antennas Propagat.*, Vol. 38, No. 8, pp. 1192-1203, Aug. 1990.

[11] H. Ikuno and L. B. Felsen, "Complex Ray Interpretation of Reflection from Concave-Convex Surfaces," *IEEE Trans. Antennas Propagat.*, Vol. 36, pp. 1260-1271, Sep. 1988.

[12] W. Ebihara, "Electromagnetic Scattering from Polynomial Surfaces," Ph.D. Dissertation, The Ohio State University, 1993.

Radiation Due To A convex Curvature Discontinuity Of A Dielectric Coated Perfect Conductor

David H. Monteith and Robert G. Olsen
School Of Electrical Engineering and Computer Science
Washington State University
Pullman, WA 99164-2752

Abstract

It is known that surface waves radiate energy at curvature discontinuities. By reciprocity, surface waves will be excited by plane waves incident upon such a discontinuity. Here, the problem of the radiation of a surface wave on a flat dielectric coated perfect conductor which changes abruptly into a cylindrical dielectric coated perfect conductor is considered. The dielectric is assumed to be homogeneous, isotropic and linear. The problem is formulated as an integral equation over the vertical discontinuity in terms of Green's functions of flat and cylindrical coated conductors. This integral equation can be simplified by the use of regular perturbation theory in the case of a large radius of curvature. Thus, perturbation forms of the Green's functions are determined and from these an iterative approximate solution to the integral equation is obtained. Results of a numerical solution of the integral equation for an impedance surface are compared to published results for the same surface and some results for the coated surface are discussed.

Introduction

Bound modes of open wave guides radiate energy at irregularities such as an abrupt change in curvature [1]. By reciprocity, a plane wave incident upon such an irregularity will excite a bound mode. An important problem is to

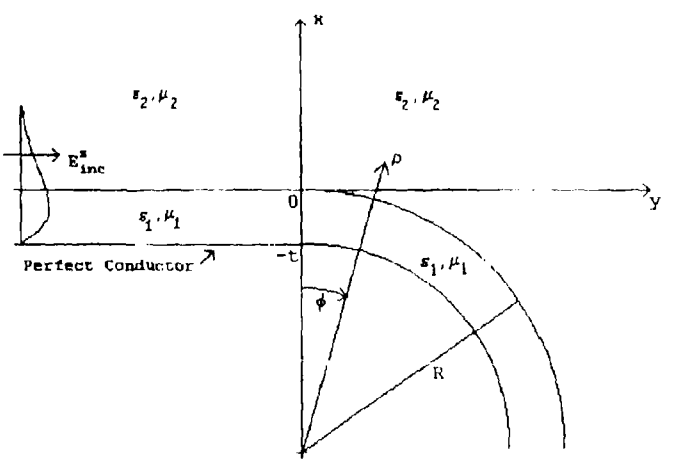

Figure 1 The Problem geometry. The aperture is defined by $y = 0$, $x > -t$.

determine the extent of this coupling and if it is effected by the cutoff frequency of the waveguide. A number of authors, especially [1] and [2], have determined the radiation due to a straight impedance surface abruptly changing to a convex curved impedance surface characterized by a large radius of curvature. To determine how the cutoff frequency affects coupling a more complex structure must be considered. This paper presents a method for determining the unknown magnetic field tangential to an aperture formed by a flat dielectric coated perfect conductor abruptly changing to a curved dielectric coated perfect conductor with a large radius of curvature. Once the unknown tangential magnetic field on the aperture is determined all of the fields are determined [3].

Problem Statement and Formulation

The problem is to solve for the radiation and reflection of a transverse electric surface wave incident upon a convex curvature discontinuity of a dielectric coated perfect conductor. The dielectric is assumed to be homogeneous, isotropic and linear and is characterized by permittivity ε_1, permeabilty μ_1 and thickness t. The region above the dielectric is characterized by the constituitive parameters ε_2, μ_2. The radius of curvature is R. The incident field is a TE surface wave supported by an infinite flat dielectric waveguide, E^{inc}_z. The geometry of the problem is shown in Figure 1. It is assumed that both the flat and curved sections extend to infinity without any deviation so that there are no reflections. Of special interest is the large radius of curvature case. By reciprocity the solution also applies to the excitation of surface waves by plane waves incident upon the curvature discontinuity.

A problem similar to this for an impedance surface was solved by Kuester and Chang [2]. They formulated the problem as an integral equation. This formulation can be generalized to apply to the present problem. Using the aperture shown in Figure 1, defined by the half plane y = 0, x > -t, an integral equation for the unknown aperture fields can be formulated. It can be derived in a similar manner to Rayleigh-Sommerfeld's formulation of diffraction due to an aperture [4]. Applying this technique to the problem results in a Fredholm integral equation of the first kind for f(x) on the aperture, equation (1), in terms of the Green's functions for an infinite flat surface, G_s, and a cylindrical surface, G_c, and the incident field, which is contained in the term $\beta(x)$. The unknown, f(x), is directly related to the tangential magnetic field on the aperture.

$$\beta(x) + 2\int_{-t}^{\infty} G_s(x,0\,;\,x',0)\,f(x')\,dx' + \int_{-t}^{\infty} [G_c(x,0\,;\,x',0) - G_s(x,0\,;\,x',0)]\,f(x')\,dx' = 0 \tag{1}$$

where f(x) and $\beta(x)$ are defined as follows:

$$f(x') = \left.\frac{\partial \Sigma_z}{\partial y'}\right|_{y'=0} \tag{2}$$

$$2\beta(x) = \left\{-2\int_{-t}^{\infty} G_s \frac{\partial E_z^{inc}}{\partial y'}\,dx' + E_z^{inc}\right\}_{y=y'=0} \tag{3}$$

For large radius of curvature it is known that the Green's function for the curved surface will approach the Green's function for the flat surface. Because of this, care must be taken when (1) is solved so that the effect of the second integral is not lost during the numerical solution. An easy way to take care of this is to apply regular perturbation theory [5]. Since

G_s approaches G_c it is possible to derive G_c as G_s plus correction terms. This is formally shown in (4) where ϵ is 1/R and $G_0 = G_s$.

$$G_c(x,0;x',0) = G_0 + (\epsilon^1)\, G_1 + (\epsilon^2)\, G_2 + O(\epsilon^3) \tag{4}$$

Applying (4) in (1) and expanding f(x) as in (5) results in equations (6) and (7) which can be solved recursively for the zero and first order terms of f(x).

$$f(x) = f_0(x) + (\epsilon^1)\, f_1(x) + O(\epsilon^2) \tag{5}$$

$O(\epsilon^0)$:

$$\int_{-\infty}^{\infty} 2\, G_0(x,x')\, f_0(x')\, dx' = -\beta(x) \tag{6}$$

$O(\epsilon^1)$:

$$\int_{-\infty}^{\infty} 2\, G_0(x,x')\, f_1(x')\, dx' = -\int_{-\infty}^{\infty} G_1(x,x')\, f_0(x')\, dx' \tag{7}$$

Closer examination of (6) shows that it is just an equation for an infinite flat surface. This problem has a known solution and does not need to be calculated numerically. Using the known solution for $f_0(x)$ should result in a numerical solution for $f_1(x)$ that is less affected by computing errors due to truncation of the integral equation and truncation of the integrals found in the Green's functions.

The zero and first order terms of the Green's functions for the source, prime coordinate, and field, unprimed coordinate, points both inside and above the dielectric have been calculated. The Green's functions for the source and field points above the dielectric (i.e. x'>0 and x>0) are shown below for an assumed time dependence $e^{j\omega t}$, where ω is the radian frequency.

$$G_0 = \frac{-j}{4\pi} \int_{-\infty}^{\infty} e^{-j\nu|y-y'|}\, e^{-j\gamma_2 x_c} \left[e^{j\gamma_2 x_c} + \Gamma_\beta e^{-j\gamma_2 x_c} \right] \frac{d\nu}{\gamma_2}$$

$$G_1 = \frac{j}{4\pi} \int_{-\infty}^{\infty} e^{-j\nu|y-y'|}\, e^{-j\gamma_2 x_c} \left\{ \left[-\alpha_2(\nu)(x_c^2 - x_c'^2) + \beta_2(\nu)(x_c + x_c') \right] e^{j\gamma_2 x_c} \right.$$
$$\left. + \Gamma_\beta \left[-\alpha_2(\nu)(x_c^2 + x_c'^2) + \beta_2(\nu)(x_c + x_c') + D(\nu) \right] e^{-j\gamma_2 x_c} \right\} \frac{d\nu}{\gamma_2}$$

where:

$$\gamma_1^2 = (k_1^2 - v^2) \qquad \gamma_2^2 = (k_2^2 - v^2)$$

$$x_> = \max(x,x') \qquad x_< = \min(x,x')$$

$$\alpha_1(v) = \frac{v^2}{2j\gamma_1} \qquad \alpha_2(v) = \frac{v^2}{2j\gamma_2}$$

$$\beta_1(v) = \frac{k_1^2}{2\gamma_1^2} \qquad \beta_2(v) = \frac{k_2^2}{2\gamma_2^2}$$

$$\Gamma_b = \frac{j\gamma_2\mu_1\sin(\gamma_1 t) - \gamma_1\mu_2\cos(\gamma_1 t)}{j\gamma_2\mu_1\sin(\gamma_1 t) + \gamma_1\mu_2\cos(\gamma_1 t)}$$

$$D(v) = \frac{\alpha_1\alpha_2(2\gamma_1\gamma_2\mu_1\mu_2) - 2j\gamma_2\mu_1(\mu_1\beta_2 - \mu_2\beta_1)\sin^2(\gamma_1 t)}{\gamma_2^2\mu_1^2\sin^2(\gamma_1 t) + \gamma_1^2\mu_2^2\cos^2(\gamma_1 t)}$$

k_1 and k_2 are the wave numbers for the dielectric and free space respectively.

The Green's functions are valid for $x/R << 1$.

Method of Solution

Now that the Green's functions have been derived, the integral equation for the unknown tangential magnetic field at the aperture can be solved. The equation is solved using pulse Galerkin's method [6] which requires that the integral be truncated so that it is finite. This can be done successfully when the incident field above the dielectric has decayed to a point where it is negligible. This condition results in the further requirement that $1/k_2R << 1$.

The pulse Galerkin's method was used instead of collocation so that the integral involved in calculating the Green's functions would converge more quickly. If collocation were used the integral would decay as $1/\gamma_1$ for large γ_1 but when pulse Galerkin's method is used the integral decays as $1/\gamma_1^2$. This makes the numerical integration easier. Pulse Basis functions were used instead of more complicated basis functions because their relative simplicity allowed integrations over x and x' to be easily calculated analytically.

Results

Kuester and Chang [1] and Shevchenko [4] have solved the problem of a convex curvature discontinuity in an impedance surface. Shevchenko solved the problem by approximating it as a dielectric slab of varying thickness. Kuester and Chang using a slightly different technique derived the same integral equation as was presented earlier. They then solved the exact Green's functions in rectangular coordinates for the slab waveguide and in cylindrical coordinates for the cylindrical waveguide which was then expanded using large argument approximations for the bessel functions. Their results compared favorably to Shevchenko's. Both Shevchenko and Kuester and Chang derive approximate analytical solutions for the unknown magnetic field at the aperture. Their results are favorably compared below with the results obtained by using our method applied to the impedance surface.

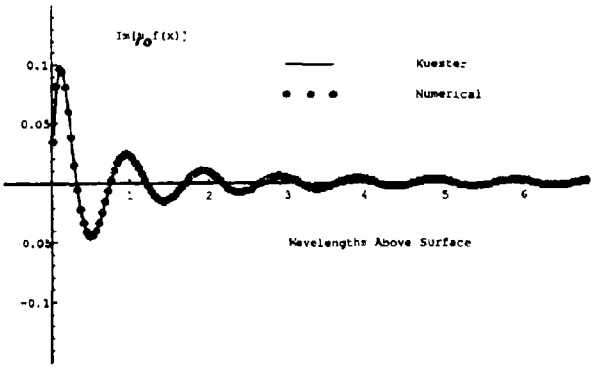

Figure 2 The imaginary part of the first order solution for the impedance surface.

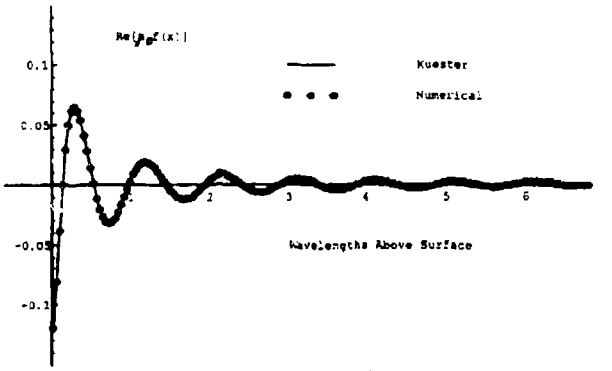

Figure 3 The real part of the first order solution for the impedance surface.

The impedance surface is at x=0 for the straight section and ρ=R for the curved section. The region above the surface is assumed to be free space (wave number k_2) and it is assumed that there are no reflections from the ends. Finally, the radius of curvature is assumed to be large compared to a wavelength. For an impedance surface the Green's function for the zero and first order terms can be written as follows:

$$G_0 = \frac{-j}{4\pi} \int_{-\infty}^{\infty} e^{-jk_2 w \sin\varepsilon} \left[e^{jk_2 w \sin\varepsilon} + \Gamma_0 e^{-jk_2 w \sin\varepsilon} \right] \frac{dv}{w}$$

where

$$w = \sqrt{1 - v^2} \qquad \Gamma_0 = \frac{w - j\gamma_0}{w + j\gamma_0}$$

$$G_1 = \frac{j}{4\pi} \int_{-\infty}^{\infty} e^{-jk_2 w x_>} [-\alpha(v)(x_>^2 - x_<^2) + \beta(v)(x_> + x_<)] e^{jk_2 w x_<} + \Gamma_0 [-\alpha(v)(x_>^2 + x_<^2) + \beta(v)(x_> + x_<) + D] e^{-jk_2 w x_<} \frac{dv}{w}$$

where

$$\alpha(v) = \frac{k_2 v^2}{2jw} \qquad \beta(v) = \frac{1}{2w^2}$$

$$D = \frac{-j}{wk_2(w^2 + \gamma_0^2)}$$

γ_0 is the normalized surface susceptance $-jZ_0/Z_s$.

Figures 2 and 3 respectively show the imaginary and real results of Kuester and Chang (the solid line) and our numerical solution (the dots) for γ_0=.1 and a frequency of 1.0 GHz. As can be seen they compare favorably.

Figures 4 and 5 show a comparison of the exact and numerical solution of the zero order integral equation for the imaginary and real parts respectively. As can be seen the imaginary part compares favorably. The exact solution of the real part is zero. The numerical solution, though not exactly zero, is at least two orders of magnitude smaller than the imaginary part and thus negligible. The real part does show the problem areas in the numerical solution. These occur at the surface of the coating where the Green's functions are difficult to compute and where the integral equation has been truncated. The parameters for the problem shown are $\mu_{r1} = \varepsilon_{r1} = 2$, $\mu_{r2} = \varepsilon_{r2} = 1$, $k_2 = 20\pi/3$, $t = .04566$ and $f = 1$GHz.

Figures 6 and 7 show the imaginary and real part of the solution to the first order problem. The boundary conditions at the dielectric surface, x=0, require that $\mu_1 f(x) = \mu_2 f(x)$ and that their derivatives are also equal. f(x) must also go to zero at the perfect conductor and as x goes to ∞. All of these conditions are met in figures 6 and 7. The coated surface shown was set up to match the impedance surface to the zero order term. A comparison of Figures 2 and 3 to Figures 6 and 7 shows that they have similar shapes but slightly different amplitudes. This is mainly due to the problems not being matched to the first order.

Conclusions

Kuester and Chang [2] and Shevchenko [1] have analytically solved the problem of radiation due to an abrupt but modest change in curvature of an impedance surface. Figures 2 and 3 show that the problem can also be solved using our method. In other words, by first formulating it as an integral equation in terms of Green's functions and the unknown tangential magnetic field at the aperture and then applying regular perturbation theory to these quantities to get a recursive

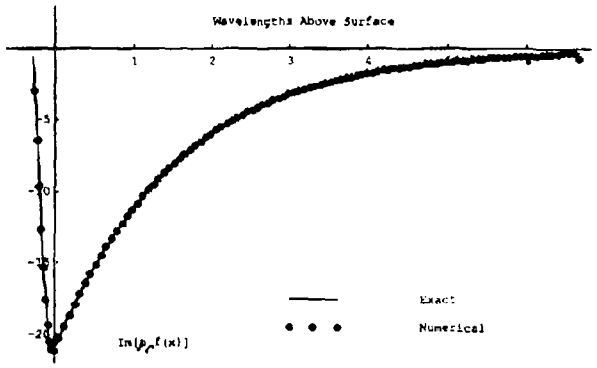

Figure 4 The imaginary part of the zero order solution for the coated surface.

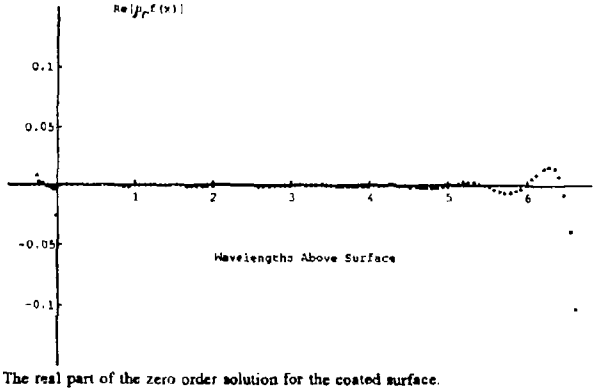

Figure 5 The real part of the zero order solution for the coated surface.

solution that is more robust than just solving the original integral equation. This method was then extended to a dielectric coated perfect conductor for which only the zero order solution is known. Figures 4 and 5 show that the exact and zero order terms compare favorably. The only problems occur at the boundary where numerical calculation of the Green's functions is difficult and where the integral equation was truncated. No published results were found to compare to figures 6 and 7 but they do appear to satisfy the radiation condition and the boundary conditions at the dielectric surface and the perfect conductor.

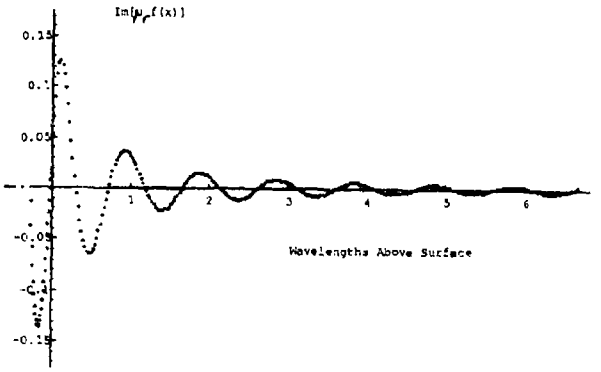

Figure 6 The imaginary part of the first order solution for the coated surface.

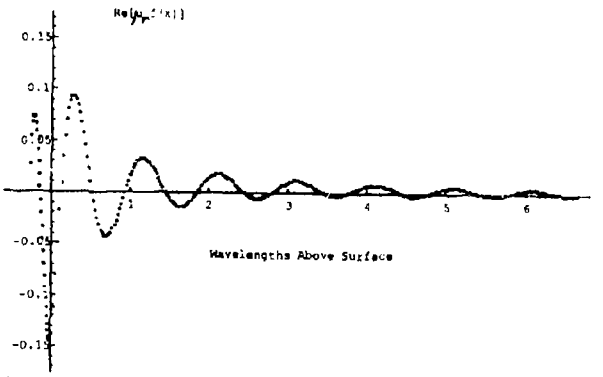

Figure 7 The real part of the first order solution for the coated surface.

References

[1] V.V. Shevchenko, Continuous Transitions In Open Waveguides, Boulder Colorado, The Golem Press, 1971, pp. 65-77.

[2] E.F. Kuester and D.C. Chang, "Scattering of a Surface Wave From a Curvature Discontinuity on a Convex Impedance Surface," IEEE Transactions on Antennas and Propagation, Vol. AP-25, NO 6, Nov. 1977, pp. 796-801.

[3] R.F Harrington, Time-Harmonic Electromagnetic Fields, New York, McGraw Hill Inc., 1961, pg. 120

[4] J.W. Goodman, Introduction To Fourier Optics, New York, McGraw-Hill Inc., 1968, pp. 42-45.

[5] L. Lewin, Theory of Waveguides, New York, John Wiley and Sons, 1975, pp. 91-96.

[6] J.J.H. Wang, Generalized Moment Methods In Electromagnetics, New York, John Wiley and Sons, 1991.

HIGH FREQUENCY SCATTERING BY A CONDUCTING CIRCULAR CYLINDER COATED WITH A LOSSY DIELECTRIC OF NON UNIFORM THICKNESS–TE CASE

S. Gökhun Tanyer, Robert G. Olsen
School of Electrical Engineering and Computer Science
Washington State University
Pullman, WA 99164-2752

1 Introduction

The study of electromagnetic scattering by coated and uncoated scatterers has been of considerable interest to the electromagnetic community. These studies have been motivated by academic interest and by numerous engineering applications. Various methods have been developed to treat cylinders of different shapes, sizes and constituencies.

It is only recently that scattering from a conducting cylinder coated with a dielectric of non uniform thickness has been studied. In 1991, R. P. Parrikar, A. A. Kishk and A. Z. Elsherbeni[1] obtained a series solution for scattering by an impedance cylinder embedded in a non concentric dielectric cylinder. Later, H. A. Raghep, L. Shafai and M. Hamid[2] studied the elliptic cylinder coated by non confocal dielectric coating. These solutions are rapidly converging only for cylinder sizes comparable to or smaller than the wavelength, λ. For electrically larger cylinders, asymptotic solutions are required. This paper presents an analytical solution to high frequency scattering by a conducting circular cylinder coated with a lossy dielectric of non uniform thickness. It is assumed that the coating is thin.

2 Formulation

The problem of electromagnetic scattering from a perfectly conducting circular cylinder coated with a nonuniformly thick dielectric is considered. The cross section of the composite structure (see Fig.1(a)) consists of a perfectly conducting circular cylinder and a lossy isotropic dielectric layer. The dielectric layer is taken to be circular with an axis parallel to but not coincident with the axis of the conducting cylinder. The offset is designated d. The structure is assumed to be illuminated by a transverse electric (TE) plane wave.

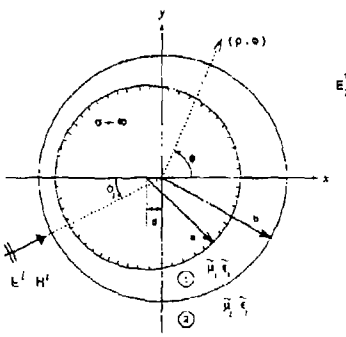

Figure 1: (a) *The cross section of the structure*

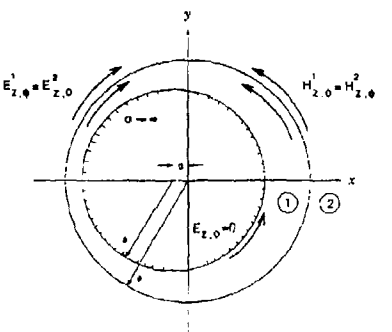

Figure 1: (b) *The boundary conditions*

The z-component of the normalized incident magnetic field can be written in cylindrical form

$$\mathbf{H}_z^i = z\, H_z^i = \sum_{n=-\infty}^{\infty} (-j)^n e^{-jn\phi_i} J_n(k_2\rho) e^{jn\phi} \tag{1}$$

where ϕ_i and ϕ are defined in Fig.1(a). The total fields in both regions are as follows

$$H_z^1 = \sum_{n=-\infty}^{\infty} (-j)^n \left[A_n J_n(k_1\rho) + B_n H_n^{(2)}(k_1\rho)\right] e^{jn\phi} \tag{2}$$

$$H_z^2 = \sum_{n=-\infty}^{\infty} (-j)^n \left[J_n(k_2\rho) e^{-jn\phi_i} + B_n^s H_n^{(2)}(k_2\rho)\right] e^{jn\phi} \tag{3}$$

where 1 & 2 denote the dielectric and the free-space regions, respectively. Note also that

$$H_z^2 = H_z^i + H_z^s \tag{4}$$

where H_z^i and H_z^s are the z components of the incident and the scattered magnetic fields, respectively.

Applying the boundary conditions on two surfaces (see Fig.1(b)), and employing the addition theorem for Bessel and Hankel functions

$$J_n(k\rho) e^{jn\phi} = \sum_{m=-\infty}^{\infty} J_m(kd)\, J_{m+n}(k\rho')\, e^{j(m+n)\phi'} \tag{5}$$

$$H_n^{(2)}(k\rho) e^{jn\phi} = \sum_{m=-\infty}^{\infty} J_m(kd)\, H_{m+n}^{(2)}(k\rho')\, e^{j(m+n)\phi'} \tag{6}$$

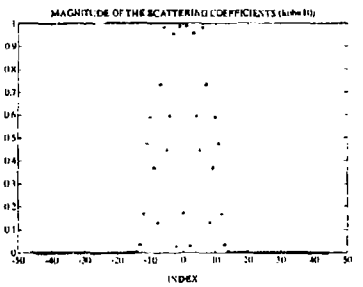

Figure 2: (a) $|B_n^s|$ *vs.* n *for* $k_o b = 10$

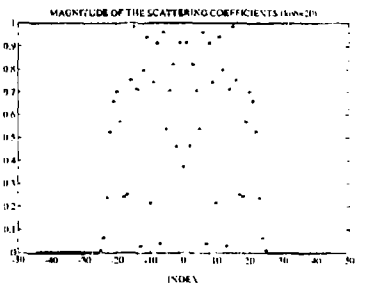

Figure 2: (b) $|B_n^s|$ *vs.* n *for* $k_o b = 20$

yields a set of linear equations in terms of the unknown scattering coefficients B_n^s. By setting B_n^s to zero for n larger than some sufficiently large N

$$\mathbf{Z} \cdot \mathbf{B^s} = \mathbf{I} \tag{7}$$

where $\mathbf{Z}$ in an N×N matrix, and $\mathbf{B^s}$ is the unknown coefficient vector of length N. The value of N can be determined by examining the values of B_n^s for various values of $k_o b$. The coefficients B_n^s have been shown for two values of $k_o b$ in Fig.2. It is clear that N can be chosen to be approximately $k_o b$ without incurring significant error.

The elements of $\mathbf{Z}$, and $\mathbf{I}$ are

$$\Big(\mathbf{Z}\Big)_{mn} = z_{m,n} = \gamma_{m,n} \hat{z}_{m,n} \tag{8}$$

$$\Big(\mathbf{I}\Big)_{n} = \sum_{m=-N}^{N} i_{m,n} = \sum_{m=-N}^{N} \gamma_{m,n} \hat{i}_{m,n} \tag{9}$$

where $(\ )_{mn}$ and $(\ )_n$ denotes the m'th row n'th column element of $\mathbf{Z}$, and n'th vector element of $\mathbf{I}$, respectively and where

$$\gamma_{m,n} = \begin{cases} 1 & \text{for } m = n \\ J_{m-n}(k_1 d) & \text{for } m - n > 0 \\ (-1)^{(n-m)} J_{n-m}(k_1 d) & \text{for } m - n < 0 \end{cases} \tag{10}$$

$$\hat{z}_{m,n} = (-j)^n \left[C_{m,n}\, H_n^{(2)\prime}(k_2 b) + \tilde{C}_{m,n}\, H_n^{(2)}(k_2 b) \right] \tag{11}$$

$$\hat{i}_{m,n} = (-j)^n \left[C_{m,n}\, J_n'(k_2 b) + \tilde{C}_{m,n}\, J_n(k_2 b) \right] e^{-jm\phi_i} \tag{12}$$

where

$$C_{m,n} = k_1 \left[H_m^{(2)\prime}(k_1 a) H_n^{(1)}(k_1 b) - H_m^{(1)\prime}(k_1 a) H_n^{(2)}(k_1 b) \right] \tag{13}$$

$$\tilde{C}_{m,n} = -k_2 \left[H_m^{(2)\prime}(k_1 a) H_n^{(1)\prime}(k_1 b) - H_m^{(1)\prime}(k_1 a) H_n^{(2)\prime}(k_1 b) \right] \tag{14}$$

Direct solution of the equation yields an "exact" solution. Unfortunately however, N becomes very large for electrically large cylinders and a direct solution of Eq.(7) becomes impossible. In this case, perturbation theory can be used to solve for B_n^s provided $k_1 d < 1$. For thin coatings, the offset parameter d is small and the perturbation series

$$B_n^s = \sum_{p=0}^{\infty} \zeta_{n,p} \, (k_1 d)^p \tag{15}$$

is convergent. Coefficients of this series can be found by substitution of Eq.(15) into Eq.(7). Those are

$$\zeta_{n,0} = \frac{C_{n,n} \, J_n'(k_2 b) - \tilde{C}_{n,n} \, J_n(k_2 b)}{C_{n,n} \, H_n^{(2)\prime}(k_2 b) - \tilde{C}_{n,n} \, H_n^{(2)}(k_2 b)} e^{-jn\phi_i} \tag{16}$$

$$\zeta_{n,1} = \frac{\hat{i}_{n,n-1} - \hat{i}_{n,n+1}}{2\hat{z}_{n,n}} - \frac{\hat{z}_{n,n-1}}{2\hat{z}_{n-1,n-1}\hat{z}_{n,n}} \hat{i}_{n-1,n-1} + \frac{\hat{z}_{n,n+1}}{2\hat{z}_{n+1,n+1}\hat{z}_{n,n}} \hat{i}_{n+1,n+1} \tag{17}$$

$$\begin{aligned} \zeta_{n,2} = {} & \frac{\hat{i}_{n,n-2} + \hat{i}_{n,n+2}}{8\hat{z}_{n,n}} \\ & - \frac{\hat{z}_{n,n-2}}{8\hat{z}_{n,n}} \zeta_{n-2,0} - \frac{\hat{z}_{n,n-1}}{2\hat{z}_{n,n}} \zeta_{n-1,1} + \frac{\hat{z}_{n,n+1}}{2\hat{z}_{n,n}} \zeta_{n+1,1} - \frac{\hat{z}_{n,n+2}}{8\hat{z}_{n,n}} \zeta_{n+2,0} \end{aligned} \tag{18}$$

$$\begin{aligned} \zeta_{n,p} = {} & \frac{\hat{i}_{n,n-p} - \hat{i}_{n,n+p}}{p! \;\; 2^p \; \hat{z}_{n,n}} \\ & - \frac{\hat{z}_{n,n-1}}{2\hat{z}_{n,n}} \zeta_{n-1,p-1} + \frac{(-1)^1 \hat{z}_{n,n+1}}{2\hat{z}_{n,n}} \zeta_{n+1,p-1} \\ & - \frac{\hat{z}_{n,n-2}}{8\hat{z}_{n,n}} \zeta_{n-2,p-2} + \frac{(-1)^2 \hat{z}_{n,n+2}}{8\hat{z}_{n,n}} \zeta_{n+2,p-2} \\ & \vdots \\ & - \frac{\hat{z}_{n,n-p+1}}{(p-1)! \;\; 2^{p-1} \; \hat{z}_{n,n}} \zeta_{n-p+1,1} + \frac{(-1)^{p-1} \hat{z}_{n,n+p-1}}{(p-1)! \;\; 2^{p-1} \; \hat{z}_{n,n}} \zeta_{n+p-1,1} \\ & - \frac{\hat{z}_{n,n-p}}{p! \;\; 2^p \; \hat{z}_{n,n}} \zeta_{n-p,0} - \frac{(-1)^p \hat{z}_{n,n+p}}{p! \;\; 2^p \; \hat{z}_{n,n}} \zeta_{n+p,0} \end{aligned} \tag{19}$$

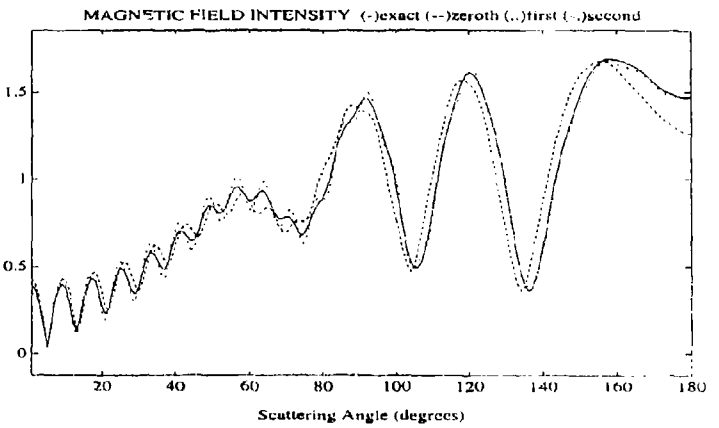

Figure 3: *The approximate perturbation series solutions of order zero, one and two.*

Substitution of Eq.(15~19) into Eq.(3) yields the analytical solution for the fields in Medium 2. Note that the zeroth order solution is equal to the solution for the uniform coating case. The perturbation series solution for the total field in Medium 2 is calculated. The exact series, the zeroth, first and second order solutions are compared in Fig.3 for the coated cylinder. The parameters are

$k_2 b$	=	20	$k_2 t = k_2(b-a)$	=	$0.03\lambda_2$
$k_2 d$	=	$0.03\lambda_2$	$k_2 \rho$	=	30
ϵ_2	=	ϵ_o	ϵ_1	=	$5 - j4$
μ_1	=	μ_o	μ_2	=	μ_o
ϕ_i	=	0^o	*Scattering angle*	=	$\phi - \phi_i$

3 Asymptotic Solution

The perturbation series solution still does not converge well for electrically large cylinders. In addition, it provides no physical insight into the solution. For these reasons, an asymptotic solution is sought. According to *Watson Transform*[3]

$$H_z^2 = \sum_{n=-\infty}^{\infty} (-j)^n B_n^s H_n^{(2)}(k_2\rho)\, e^{jn(\phi-\phi_i)} = \frac{j}{2} \oint_C \frac{(-j)^\nu}{\sin \nu\pi} B_\nu^s H_\nu^{(2)}(k_2\rho)\, e^{j\nu(\phi-\phi_i)}\, e^{-j\pi\nu}\, d\nu \qquad (20)$$

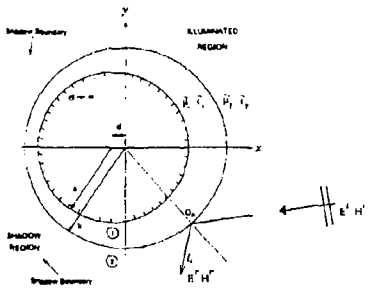

Figure 4: (a) *The geometrical optics*

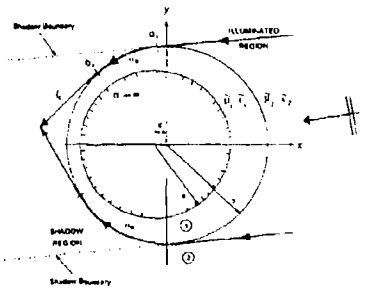

Figure 4: (b) *The creeping wave diffracted rays*

where C encloses the poles of B_ν^s. After some manipulation where the *Cauchy Residue Theorem* and Eq.(15) are employed, one can write

$$H_z^2 \cong H_z^{2,0} + H_z^{2,1} \tag{21}$$

where $H_z^{2,0}$ and $H_z^{2,1}$ are the zeroth and first order correction terms of Eq.(15), and they are

$$H_z^{2,0} = H_z^{GO,0} + \sum_{l=-\infty}^{\infty} \sum_{p=0}^{P} H_z^i(Q_1)\ D_a^0(Q_1)\ D_d^0(Q_2)\ e^{-j\nu_p\alpha_a} \frac{e^{-jk_2 l_c}}{\sqrt{k_2 l_c}} + \sum_{l=-\infty}^{\infty} \sum_{p=0}^{P} H_z^i(Q_1)\ D_a^0(Q_1)\ D_d^0(Q_2)\ e^{-j\nu_p\alpha_b} \frac{e^{-jk_2 l_c}}{\sqrt{k_2 l_c}} \tag{22}$$

$$\begin{aligned} H_z^{2,1} = H_z^{GO,1} + \sum_{l=-\infty}^{\infty} \sum_{p=0}^{P} & H_z^i(Q_1)\big(D_a^{(1,0)}(Q_1)\ D_d^{(1,0)}(Q_1)\ e^{-j\nu_p\alpha_a} \\ & + D_a^{(1,-1)}(Q_1)\ D_d^{(1,-1)}(Q_1)\ e^{-j(\nu_p-1)\alpha_a} \\ & + D_a^{(1,1)}(Q_1)\ D_d^{(1,1)}(Q_1)\ e^{-j(\nu_p+1)\alpha_a}\big) \frac{e^{-jk_2 l_c}}{\sqrt{k_2 l_c}} \\ + \sum_{l=-\infty}^{\infty} \sum_{p=0}^{P} & H_z^i(Q_1)\big(D_a^{(1,0)}(Q_1)\ D_d^{(1,0)}(Q_1)\ e^{-j\nu_p\alpha_b} \\ & + D_a^{(1,-1)}(Q_1)\ D_d^{(1,-1)}(Q_1)\ e^{-j(\nu_p-1)\alpha_b} \\ & + D_a^{(1,1)}(Q_1)\ D_d^{(1,1)}(Q_1)\ e^{-j(\nu_p+1)\alpha_b}\big) \frac{e^{-jk_2 l_c}}{\sqrt{k_2 l_c}} \end{aligned} \tag{23}$$

$H_z^{GO,0}$ and $H_z^{GO,1}$ are the zeroth and first order GO terms, and the total GO contribution is equal to zero in the shadow region and equal to the incident plus reflected field in the illuminated (lit) region(see Fig.4(a)).

The zeroth and first order GO terms in the illuminated region are found to be

$$H_z^{GO,0} = H_z^i(Q_R)\, R_s^0\,(Q_R)\ \frac{e^{-jk_0 l_r}}{\sqrt{l_r}} \tag{24}$$

$$H_z^{GO,1} = H_z^i(Q_R)\, R_s^1\,(Q_R)\ \frac{e^{-jk_0 l_r}}{\sqrt{l_r}} \tag{25}$$

here $R_s^0(Q_R)$ and $R_s^1(Q_R)$ are the zeroth and first order local reflection coefficients at the reflection point Q_R.

$D_a(Q_1)$ and $D_d(Q_2)$ are the attachment and the detachment coefficients for the creeping waves at points Q_1 Q_2, respectively (see Fig.4(b)), and α_a and α_b are the distance that a creeping wave travels along the cylinder surface, clockwise and counter-clockwise, respectively. Summation over l adds all multiple encircling creeping wave contributions, whereas summation over p adds creeping waves with different propagation constants (ν_p), and where $\nu_p \nu_p$ satisfies $\dot{z}_{\nu_p,\nu_p} = 0$. Those coefficients are found to be

$$D_a^0(Q_1) = D_d^0(Q_2) = \left[\sqrt{2\pi}\,\frac{\dot{i}_{\nu+1,\nu+1}}{\frac{\partial}{\partial\nu}\dot{z}_{\nu,\nu}}\Big|_{\nu=\nu_p}\right]^{1/2} \tag{26}$$

$$D_a^{(1,0)}(Q_1) = D_d^{(1,0)}(Q_2) = \left[\frac{\sqrt{2\pi}}{\frac{\partial}{\partial\nu}\dot{z}_{\nu,\nu}}\cdot\left(\frac{\dot{i}_{\nu,\nu-1}\dot{z}_{\nu-1,\nu-1}-\dot{i}_{\nu-1,\nu-1}\dot{z}_{\nu,\nu-1}}{2\dot{z}_{\nu-1,\nu-1}}-\frac{\dot{i}_{\nu,\nu+1}\dot{z}_{\nu+1,\nu+1}-\dot{i}_{\nu+1,\nu+1}\dot{z}_{\nu,\nu+1}}{2\dot{z}_{\nu+1,\nu+1}}\right)\right]^{1/2}\Big|_{\nu=\nu_p} \tag{27}$$

$$D_a^{(1,1)}(Q_1) = D_d^{(1,1)}(Q_2) = \left[\frac{\sqrt{2\pi}}{\frac{\partial}{\partial\nu}\dot{z}_{\nu-1,\nu-1}}\left(\frac{\dot{i}_{\nu,\nu}\dot{z}_{\nu-1,\nu-1}-\dot{i}_{\nu-1,\nu-1}\dot{z}_{\nu,\nu-1}}{2\dot{z}_{\nu,\nu}}\right)\right]^{1/2}\Big|_{\nu=\nu_p+1} \tag{28}$$

$$D_a^{(1,-1)}(Q_1) = D_d^{(1,-1)}(Q_2) = \left[\frac{\sqrt{2\pi}}{\frac{\partial}{\partial\nu}\dot{z}_{\nu+1,\nu+1}}\left(\frac{\dot{i}_{\nu,\nu+1}\dot{z}_{\nu+1,\nu+1}-\dot{i}_{\nu+1,\nu+1}\dot{z}_{\nu,\nu+1}}{2\dot{z}_{\nu,\nu}}\right)\right]^{1/2}\Big|_{\nu=\nu_p-1} \tag{29}$$

$$\alpha = |\phi - \phi_s + 2\pi l| = \cos^{-1}\left(\frac{b}{\rho}\right) \tag{30}$$

$$l_c = (\rho^2 - b^2)^{1/2} \tag{31}$$

The high frequency asymptotic solution for the total field in Medium 1 is calculated. The exact series, the zeroth, first and second order solutions are shown in Fig. 5 for the coated cylinder. The parameters are equal to the case shown in Fig.3, and further details in eqs.(22) and (23)

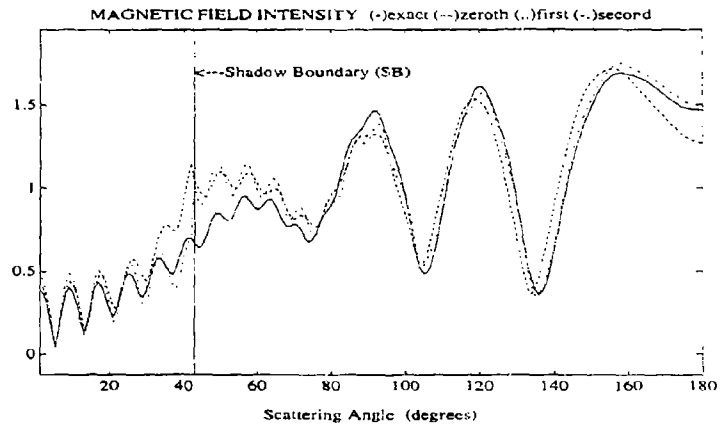

Figure 5: *The asymptotic solutions of order zero, one and two*

Results shown in Fig.5 were found to be sufficiently accurate with three terms of Eq.15 – specially in the forward and backscattering regions. Results can be improved slightly by including more poles in the Watson series. Near the shadow boundary additional corrections are required[4]. For larger cylinders it is expected that more poles will be necessary.

References

[1] R. P. Parrikar, A. A. Kishk, A. Z. Elsherbeni, "Scattering from an impedance cylinder embedded in a non concentric dielectric cylinder". *IEEE Proc.-H*, Vol.138, No:2, April 1991, pp.164-175.

[2] H. A. Raghep, L. Shafai, M. Hamid, "Plane wave scattering by a conducting elliptic cylinder coated by a non confocal dielectric", *IEEE Trans. Ant. Prop.* Vol.39, No:2, February 1991, pp.213-223. solution", *Electromagnetics* 8, 1988, pp.71-83.

[3] G. N. Watson, "The diffraction of electrical waves by the earth", *Proc. Roy. Soc. (London)*, Vol. A95, 1918, pp.83-99.

[4] N. Wang, "Electromagnetic scattering from a dielectric-coated circular cylinder", *IEEE Trans. Ant. Prop.* Vol.AP-33, No:9, September 1985, pp.960-963.

EFFICIENT COMPUTATIONAL TECHNIQUE FOR BACKSCATTERING FROM A DISCONTINUITY ALONG A PIECEWISE CONTINUOUS CURVE ON A PLANAR SURFACE

Jacob J. Kim and Oren B. Kesler

Texas Instruments Incorporated
2501 West University, MS 8019
McKinney, Texas 75070

Abstract

This paper describes an efficient computer algorithm to predict accurate three-dimensional(3-D) backscattering RCS levels from a piecewise continuous contour on a planar surface utilizing simple two-dimensional(2-D) scattered field formulations. The contour can be defined by any localized discontinuities such as small step, slit, groove, dielectric filled gap, bump, impedance discontinuity, conducting wedge, and coated wedge. This technique utilizes a simple geometrical deformation of the piecewise continuous contour on the scattering object so that available 2-D scattered field formulations can be directly applied. The 2-D field formulations can be obtained from high-frequency asymptotic techniques or 2-D full wave analyses. The technique has been validated with other known analytic solutions and extensive measurements. The main advantage of this technique is in its simplicity, computational efficiency, and its vast application to many practical complex 3-D scattering problems.

Introduction

In recent years many asymptotic or numerical techniques were developed to predict RCS levels from steps, gaps, and cracks on a planar surface or flat plate edges. However, their applications are still limited to the simple 2-D geometries or only perfectly conducting materials due to lack of 3-D diffraction coefficients or too many unknowns for matrix inversion.

Recent developments using Incremental Length Diffraction Coefficient(PO ILDC, PTD ILDC, GTD ILDC) techniques[1,2,3] showed significant improvement in scattering prediction from a piecewise continuous contour on a planar surface. However, the applications of the ILDC techniques are still limited to perfectly conducting scatterers due to the lack of diffraction coefficients for nonmetallic materials. The new technique in this paper calculates the 3-D backscattering RCS directly from the 2-D scattered field of the contour on a planar surface through the staircase deformation of the geometry. In the past a similar approach has been used by Sikta *et al* [4] to represent a general shaped plate with a series of strips. However, their Equivalent Current Method(ECM) approach requires formulation of equivalent electric and magnetic currents and actual summation of the scattered field from infinitesimally small strips along the edge to calculate total backscattered field. The new approach does not require actual integration or summation along the piecewise section of the contour in that the integration along the piecewise section is carried out through the analytical evaluation. Another key feature is the computationally efficient use of 2-D scattered field from localized discontinuities. The 2-D scattered field may be obtained by moment methods, finite element techniques, or high-frequency asymptotic techniques.

Uniform Field Integration Method

This paper describes an efficient computational technique, which is referred to as Uniform Field Integration Method(UFIM), to predict accurate backscattering RCS levels from a piecewise continuous contour on a planar surface. The essential feature introduced in this paper is that one can represent a piecewise continuous contour in the limiting case by a series of stairs where the stair step approaches zero and analytical evaluation is used to carry out the line integration. Figure 1(a) shows the geometry of an arbitrary curve on a planar surface and its deformed staircase. The figure also includes a few typical characteristics in EM scattering analyses due to the geometry changes. Figure 1(b) shows a section of a piecewise continuous contour on a planar surface and its deformed staircase for the UFIM calculation. The figure also includes a conventional ECM formula-

tion[5] for the 3-D scattering from a straight edge and a simplified UFIM scattered field formulation for a deformed geometry for comparison. Note that the stair step becomes zero in acual UFIM calculations and the deformed staircase approaches the original piecewise continuous contour in the limiting case. This deforming process actually converts the original scattering problem for a piecewise continuous contour into a simple 2-D scattering geometry which can be readily solved by available 2-D scattered field formulations. To justify the UFIM approach three stair models with different step sizes were tested and the uniform scattered fields from the deformed geometries were compared with the conventional 3-D Equivalent Current Method(ECM) results. Figure 2(a) shows the test model of a square conducting plate(dash line) and a deformed staircase(solid line). Figures 2(b), 2(c), and 2(d) show the elevation RCS patterns for the step sizes of 0.25λ, 0.1λ, and 0.05λ, respectively. The solid line indicates the RCS patterns for the staircase model and the dash line indicates that of 3-D ECM model. The comparison clearly shows the RCS pattern converges to the 3-D ECM results as the step size is reduced.

A computer code has been developed using this technique(UFIM) and validated with other known analytic solutions such as PTD and ECM for a conducting flat plate. Figure 3(a) shows the geometry of a flat conducting plate and and the conical RCS pattern coordinate system. Note that θ_p is the half cone angle of the conical pattern measured from the surface normal. Figures 3(b), 3(c), and 3(d) show the comparison of the conical RCS patterns between the UFIM results and the conventional PTD results for $\theta_p = 30°, 50°$, and $70°$, respectively. The comparison showed excellent agreement between two different approaches. Figures show only the half of the pattern shapes because of the symetrical nature of the test geometry. The comparison shows that the UFIM approach is as accurate as the conventional PTD approach for the perfectly conducting scattering objects. The UFIM predictions were also compared with extensive measurements for continuous steps on a planar surface. Figures 4(a) and 4(b) show Azimuth RCS patterns for a 0.1 cm straight step and a 0.1 cm serrated step on a planar surface at 18 GHz, respectively. The results reveal good agreement between the theoretical UFIM prediction and measurements. The

UFIM predictions were compared with extensive measurements for other frequencies and all showed very good agreements.

Conclusions

An efficient computational technique(UFIM) has been developed to predict the backscattering RCS levels for any piecewise continuous contour on a planar surface utilizing available two-dimensional scattered field formulations. The predicted RCS data were compared with measured data and the comparison showed very good agreements. In this paper this technique was applied to the piecewise contours on a planar surface. However, the application of this technique can be extended to the contours on a curved surface using CAD generated input geometry.

The UFIM technique is computationally efficient and very simple to apply to many practical RCS problems.

References

[1] Robert A. Shore and Arthur D. Yaghjian," Incremental Diffraction Coefficients for Planar Surfaces," IEEE Trans. Antennas and Propaga., vol. AP-36, pp. 55-70, Jan. 1988.

[2] K.M. Mitzner, Incremental Length Diffraction Coefficients, Tech. Rep. No. AFAL-TR-73-296, Apr. 1974.

[3] A. Michaeli, " Equivalent edge currents for arbitrary aspects of observation," IEEE Trans. Antennas and Propagat., vol. AP-32, pp. 252-256, Mar. 1984.

[4] Fathi A. Sikta, Walter D. Burnside, Tai-Tseng Chu, and Leon Peters, Jr., " First-Order Equivalent Current and Corner Diffraction Scattering from Flat Plate Structures," IEEE Trans. Antennas and Propagat., vol. AP-31, pp. 584-589, Jul. 1983.

[5] Y. T. Lo and S. W. Lee, *Antenna Handbook*, New York: Van Nostrand Reinhold Company, 1988.

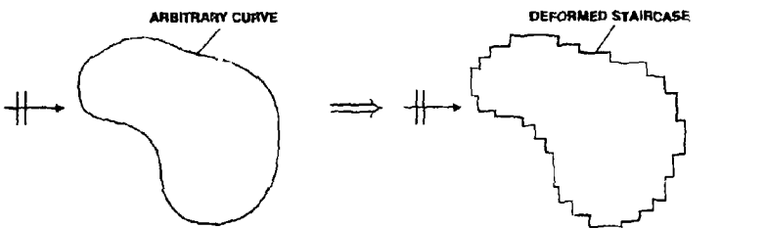

CONVENTIONAL APPROACH

- Requires 3-D analytic solution for the RCS prediction.
- Requires a known expression for the equivalent currents or incremental length diffraction coefficients.

UFIM APPROACH

- Deform the contour of the scattering object so that 2-D scattered field can be directly applied for the 3-D RCS prediction.
- No specific knowledge of the currents or diffraction coefficients is required.
- Not limited to a particular analytic solution.

Figure 1(a). Staircase deformation of an arbitrary curve.

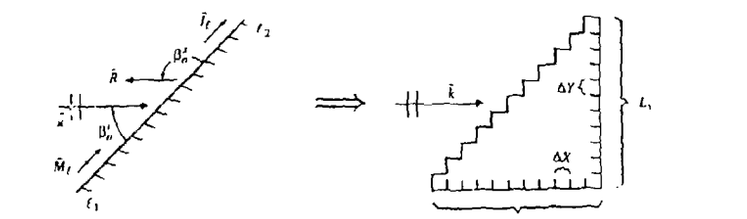

$$\bar{E}^d = \frac{jkZ_0}{4\pi}\int_{\ell_1}^{\ell_2}\left[\hat{R}\times\hat{R}\times\bar{I}_\ell(\ell')\hat{\ell}' + Y_0\hat{R}\times\bar{M}_\ell(\ell')\hat{\ell}'\right]\frac{e^{-jkR}}{R}\,d\ell' \qquad \bar{E}^S_{total} = \lim_{\substack{\Delta X\to 0\\ N\to\infty}}\sum_{n=1}^{N}\Delta\bar{E}^S_n = \bar{E}_{2-D}(Q)L_y\frac{\sin(kL_x)}{kL_x}$$

Figure 1(b). Deformation of a piecewise section of a contour.

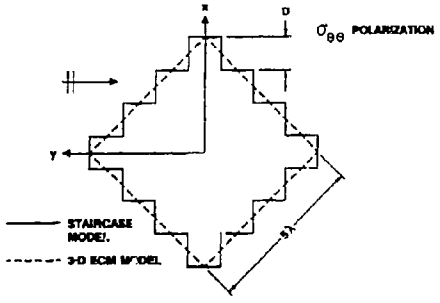

(a). Test model

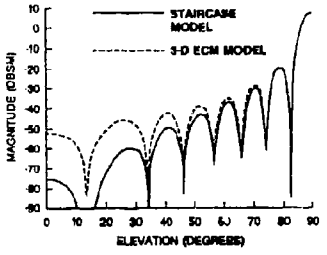

(b). D = 0.25λ

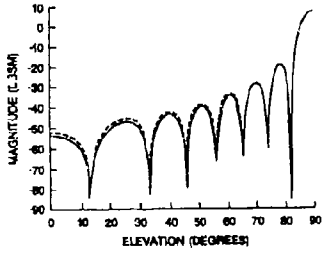

(c). D = 0.1λ

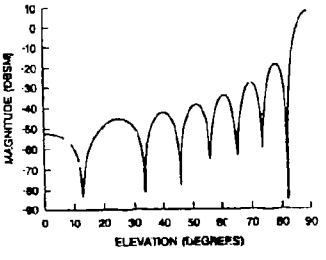

(d). D = 0.05λ

Figure 2. Ele ion RCS patterns for three different step sizes.

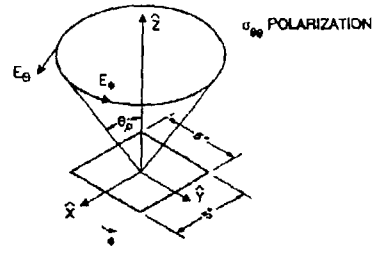

(a). Conical pattern coordinate system

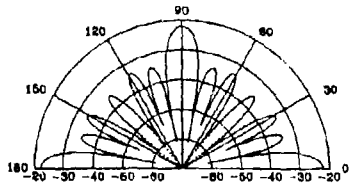

(b). $\theta_p = 30°$

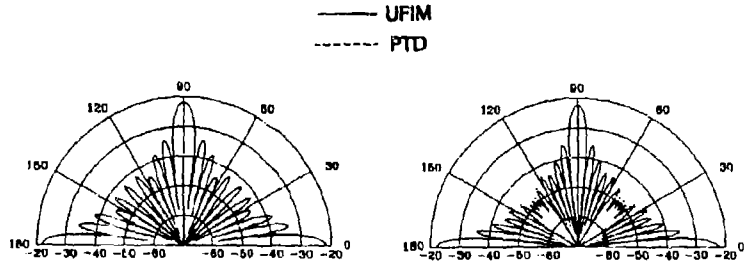

(c). $\theta_p = 50°$

(d). $\theta_p = 70°$

Figure 3. Comparison of the conical RCS patterns between UFIM and PTD.

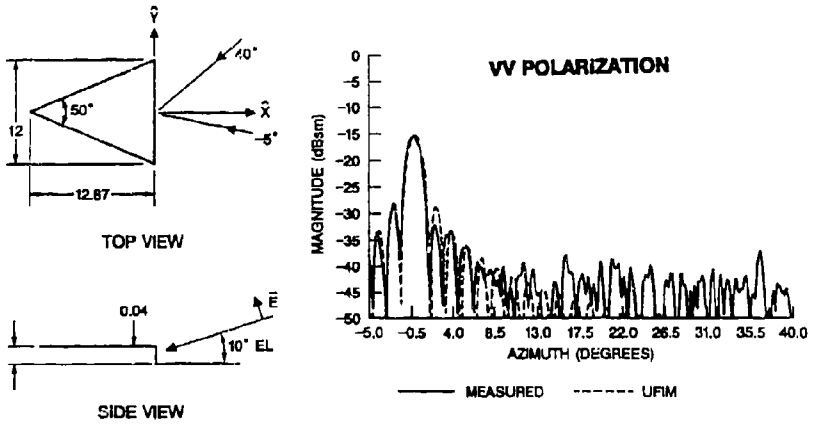

Figure 4(a). Azimuth RCS pattern for a straight step at 18 GHz.

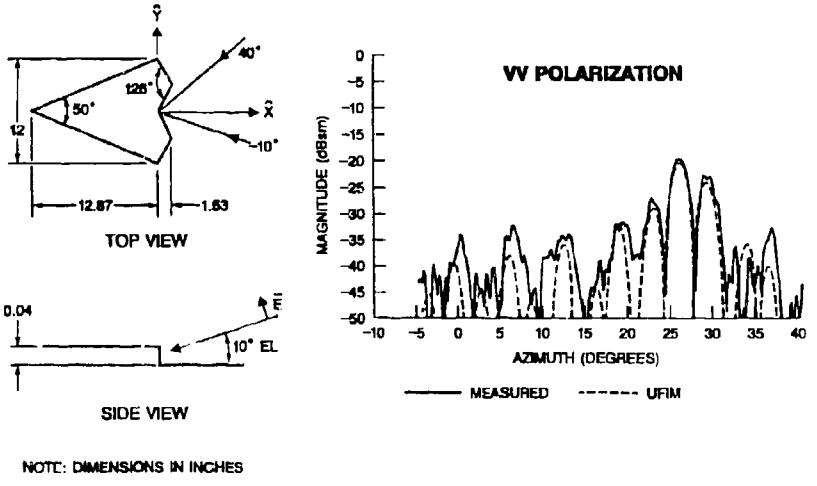

Figure 4(b). Azimuth RCS pattern for a serrated step at 18 GHz.

Computer Simulation of Diffraction and Focusing Processes in Quasioptics

A. V. Popov, Yu V. Kopylov, and A. V. Vinogradov*

Institute of Terrestrial Magnetism, Ionosphere and Radio Wave Propagation
IZMIRAN, 142092
Troitsk, Moscow Region, Russia

FAX: (095) 3340124
E-MAIL: kopyl@anet.sovam.com

*P.N. Lebedev Physical Institute
117924, Moscow, Leninsky
Prospect 53, Russia
FAX: (095) 1357880

ABSTRACT

Here, we describe numerical modeling of the wave fields produced by complex quasioptic elements. The parabolic equation method and exact transparency boundary conditions are used in the computational algorithm. The computer code provides global field visualization using color graphics.

In many branches of electromagnetic theory it is desirable to have a detailed visual representation of the wave field produced by an optical or quasioptical system being designed or used in experiments. The most popular approach to the field calculation is based on approximate Fresnel-Kirchhoff diffraction theory describing spatial field distribution in terms of an integral transformation of its boundary values over the aperture. In the paraxial approximation, the Fresnel transformation arises.

Along with the well known advantages, this method has essential limitations and weak points. The first we mention here is that the obstacles are considered as plane screens with transparent, semi-transparent or phase shifting openings. It is difficult to treat adequately real dielectric elements as lenses, thick diffraction gratings or Fresnel zone plates within the framework of the Kirchhoff approximation. Another shortcoming is a comparatively long time needed for detailed field calculation over a chosen computational mesh.

We suggest another computational approach using the Leontovich-Fock wave parabolic equation (WPE) [1]. In is well known that the Fresnel-Kirchhoff integral is nothing but an exact solution of the WPE governing the slowly varying amplitude $u(x,y,z)=E(x,y,z)\exp(-ikz)$ of a paraxial wave packet in free space. Nevertheless, for calculating the field distribution in a considerable volume, the straightforward numerical integration of the WPE is often much more effective. Moreover, in contrast to the Kirchhoff approximation, the parabolic equation method can be used for the field calculation in the presence of (and inside) dielectric insertions. If the complex dielectric permittivity eps = 1 + alph(x/a,y/a,z/b) satisfies the conditions: kbalph 1, ka /b 1, a modified WPE arises that can be solved by numerical methods.

The parabolic equation method as a powerful computational tool, proposed by G. Malyuzhinets [2] and rediscovered by F. Tappert [3], has been developed rapidly in recent years. We use the finite difference method for solving the WPE. In order to reduce the 2D problem posed in the half-space $z > 0$ to a semi-strip $y<A$, $z>0$ we employ the exact absorbing boundary conditions derived in [4]. For an axially symmetric problem in three dimensions, the boundary condition can be proposed that provides full transparency of an arbitrarily chosen cylindric boundary $r = A$ surrounding all the dielectric insertions.

The developed computer code calculates the complex wave amplitude u(y,z) or u(r,z) starting from the initial values u(O,z) and taking into account all the refractive and diffractive optical elements. The resulting wave field is visualized by means of color graphics in any chosen cross-section of the wave beam. We demonstrate examples of the calculated field intensity distributions produced by focusing lenses and various types of the zone plates. The algorithm can be used for a wide frequency range of EM waves - from microwaves up to the X-ray region.

REFERENCES

1. V.A Fock. Electromagnetic diffraction and propagation problems. Pergamon Press, Oxford, 1965.
2. G. D. Malyuzhinets, A. V. Popov, Yu N. Cherkashin. On development of a numerical method in diffraction theory (in Russian). - Proc. of the 3rd Symposium on diffraction. Nauka, Moscow, 1964, pp. 176-178.
3. F. D. Tappert. The parabolic approximation method, in: Lectures Notes in Physics, 70. J. B. Keller, J. S. Papadakis (eds). Wave propagation and underwater acoustics. Springer, New York, 1977, pp. 224-287.
4. V. A. Baskakov, A. V. Popov. Implementations of transparent boundaries for numerical solution of the Schrodinger equation. - Wave Motion, 14, No 1 1991, pp. 123-128.

SYMBOLIC PROGRAMMING WITH SERIES EXPANSIONS: APPLICATIONS TO OPTICAL WAVEGUIDES

R.L. Gallawa, Arun Kumar[§], and Andreas Weisshaar[¶]

National Institute of Standards and Technology
Electromagnetic Technology Division
Boulder, Colorado 80303

[§] Visiting Scholar, on leave from PLysics Department,
Indian Institute of Technology, New Delhi, 110016, INDIA.

[¶]Department of Electrical and Computer Engineering,
Oregon State University, Corvallis, OR 97331

ABSTRACT

We discuss the utility of symbolic computer languages in the context of optical fiber analysis. The symbolic *Mapping* command, for example, is useful whenever a series expansion approach is used in eigenvalue problems if the basis functions are integrable in closed form. We show how this command allows a simple but accurate evaluation of single-mode fiber parameters in most cases of practical interest. The *Replacement* command is also demonstrated in tracking the variation of fiber operational parameters as a function of the *V*-parameter. The saving in CPU time is substantial.

I. Introduction

This paper addresses the utility and power of symbolic computer routines[1] in the modeling of weakly guiding optical waveguides. The tools that are discussed are of general interest. Indeed, the use of series expansion solutions is known to yield excellent results if the basis functions are properly chosen. We think that the utility of symbolic routines is being overlooked in these cases. Our examples show how to apply some of the tools that are available.

To demonstrate the issues, we concentrate on Galerkin's method of analyzing nonuniform optical waveguides using Laguerre-Gauss basis functions.[2] The method yields the propagation constant and the series expansion approximation to the electromagnetic field for the mode in question. The utility of symbolic programming is demonstrated in evaluating (1) the matrix elements that are called for by the method and (2) important waveguide parameters that depend on integration.

II. Formulation

Consider a circular optical fiber having an arbitrary refractive index $n(r)$ in the fiber core ($r \le b$). The wave equation is

$$\frac{1}{r}\frac{d}{dr}\left(r\ \frac{d\psi}{dr}\right) + \left[k^2\left(n^2(r) - n_e^2\right) - \frac{m^2}{r^2}\right]\psi = 0, \qquad (1)$$

where $\psi(r)$ is the scalar wave function, k is the free space wavenumber, n_e is the unknown effective index for the mode (the single most important parameter), and m is the modal parameter that describes the

azimuthal variation of the field. We have assumed that the electromagnetic field of the form

$$E = \psi(r) \begin{Bmatrix} \cos(m\phi) \\ \sin(m\phi) \end{Bmatrix} e^{-i\beta z}, \tag{2}$$

where $\beta = kn_e$. Let

$$V = kb\, n_1 \sqrt{2\Delta}\,, \tag{3}$$

where n_1 is the maximum refractive index in the fiber core and Δ is the refractive index contrast. Equation (1) can be normalized by defining the parameters,

$$R = r/b, \qquad X = VR^2, \tag{4}$$

$$N^2(R) = \frac{n^2(r) - n_2^2}{n_1^2 - n_2^2}, \tag{5}$$

and

$$B = \frac{n_e^2 - n_2^2}{n_1^2 - n_2^2}. \tag{6}$$

n_2 is the refractive index of the uniform cladding, and B is the normalized propagation constant, which is very sensitive to errors in calculation. Equation (1) then becomes

$$X \frac{d^2\psi}{dX^2} + \frac{d\psi}{dX} + \frac{1}{4}\left[V N^2(X) - VB - \frac{m^2}{X}\right] \psi = 0. \tag{7}$$

We expand the field in terms of M Laguerre-Gauss basis functions,

$$\Psi(X) = \sum_{i=0}^{M-1} a_i \phi_i(X), \tag{8}$$

where a_i are to be determined and

$$\phi_i(X) = \sqrt{\frac{i!}{(i+m)!}}\, e^{-\frac{X}{2}} X^{\frac{m}{2}} L_i^m(X). \tag{9}$$

L_i^m is the associated Laguerre polynomial. The basis functions are normalized so that

$$\int_0^\infty \phi_i(X)\, \phi_j(X) dX = \delta_{i,j}. \tag{10}$$

Substituting Eq. (8) into (7) and multiplying the result by ϕ_j and then integrating over all space, we get

$$- \sum_i a_i \left[\left(\frac{2i + m + 1}{V} + B \right) \delta_{i,j} + \frac{\sqrt{i(i+m)}}{V} \delta_{i-1,j} + \frac{\sqrt{(i+1)(i+m+1)}}{V} \delta_{i+1,j} \right] + \sum_i a_i \int_0^V N^2(X) \phi_i \phi_j \, dX = 0 . \quad (11)$$

The choice of Laguerre-Gauss basis functions has distinct advantages. They form a complete set that satisfies the boundary conditions at the origin and at infinity, and they are everywhere continuous with a continuous derivative; they are valid over the entire range of interest; they are computationally simple; and, finally, they match the field very well and, hence, represent a good choice for the basis functions.

Equation (11) has the form

$$[A - I B][a] = 0, \quad (12)$$

where A is a square M x M matrix and B is a diagonal matrix. The eigenvalues of A are the values of B for which we can find vectors a_i (eigenvectors) such that Eq. (11) is satisfied.

The problem is thus reduced to finding the eigenvalues and the eigenvectors of the matrix A. The method yields M eigenvalues but since the guided modes must have eigenvalues between 0 and 1, the acceptable values of B must be in that range. Having the eigenvalues and associated eigenvectors, we can use Eq. (8) to approximate the field. The accuracy of the results depends on the number of terms used and on the precision of the integration in Eq. (11). The integration is over only the core area.

III. APPLICATION

The initial task is to evaluate the terms that go into the matrix A. Only the last term on the left side of Eq. (11) presents a computational problem. That term contributes to every element of the matrix, so M^2 integrals must be evaluated. For optical waveguides of practical interest, M is often less than 10. Symmetry arguments can be used to approximately halve the integration task but there are, nevertheless, on the order of 50 integrals.

Symbolic programming can be used to simplify the task considerably for all cases of practical interest. In particular, if $N^2(X)$ is a polynomial in X or if it can be approximated as a polynomial in X, a symbolic *Mapping* routine can be used to avoid integration. The simplification comes about because

$$\int_0^V X^q \exp(-X) \, dX = \Gamma(1+q) - \Gamma(1+q, V), \quad (13)$$

where $\Gamma(1+q)$ is the Euler gamma function and $\Gamma(1+q, V)$ is the incomplete gamma function. Both are available as library functions on most machines and can be evaluated as precisely as desired.

The last term on the left side of Eq. (11) has precisely this form for every value of i since $L_i^m(X)$ is itself a polynomial. The integral can thus be evaluated *exactly* using the symbolic *Mapping* routine, as follows. Define the mapping pattern $i \cdot (CX^q)$ according to Eq. (13)

$$\text{int}(CX^q) = C(\Gamma(1+q) - \Gamma(1+q, V)), \tag{14}$$

where C is a constant and q is a real integer. Note that the exponential term is not included because it appears in the same form in every term of the expansion and can, therefore, be suppressed. The integral can then be evaluated as follows:

1. Expand the expression (see Eq. (11))

$$f(X) = \sum (X) \sqrt{\frac{i!}{(i+m)!}} \sqrt{\frac{j!}{(j+m)!}} X^m L_i^m(X) L_j^m(X). \tag{15}$$

This will be a summation of terms, each of which is of the form $C_q X^q$, where C_q is a constant.

2. Invoke the symbolic *Mapping* command

$$D_{i,j}[V] = Map[\text{int}, f], \tag{16}$$

where f is the expansion obtained in step 1. $D_{ij}[V]$ is the contribution to A coming from the last term on the left side of Eq. (11). The *Mapping* command examines each element of the series f and then uses the rule established by *int* in Eq. (14). It examines every term, determines the multiplying constant C_q and the exponent q, and returns a value according to the definition of *int*.

We have conducted tests to determine the saving in CPU time when using the *Mapping* command rather than doing the integration for a step index fiber, for which $N^2(X) = 1$. The test was conducted on a 12.5 MIPS machine for the fundamental mode ($m = 0$ which is the most important case) for a step index fiber. Results are given in Table 1. The simplification due to fiber symmetry was not invoked in this test.

Most symbolic programs treat integrals in the following ways. If the integration can be done in closed form, the exact closed-form solution is used to evaluate the integration. A numerical integration will not be done unless it is specifically asked for. If the limits of integration are fixed but unevaluated, the program will return the result in closed form, if possible, but the unevaluated limit will appear in the result. Thus, it is convenient to let V in Eq. (11) be variable (unevaluated). It is that unevaluated form of the integration that is compared to the symbolic *Mapping* routine in Table 1.

Leaving V unspecified allows evaluation of B as a function of V. Consider a linear fiber taper, for example, where the fiber radius a changes linearly with z. It is of interest to track the variation of B through the fiber taper. We assume that the fiber contrast remains fixed. In that case, V changes in direct proportion to the change in a. The values of B can be found as a function of V by leaving V undefined when establishing the matrix A and then using the symbolic *Replacement* command. Thus, for $V = 3$, for example,

$$B_{V=3} = Eigenvalues[A /. V \to 3]. \tag{17}$$

The symbolic *Replacement* (designated /. in this equation) calls for all terms to be evaluated for $V = 3$. Equation (17) returns the eigenvalues (values of B) for $V = 3$ and stores them at address $B_{V=3}$. The matrix A remains a function of V after Eq. (17) is invoked so the operation can be repeated for other values of V. Thus, the integration is done only once but with V as a variable. The matrix A is then available as a function of V. The *Replacement* command is a vehicle to perform "what if" tests on the result.

This procedure can also be used to track mode loss and mode conversion as functions of position in a taper. In that case the taper is replaced by a series of step discontinuities and the loss and mode conversion are determined at each of the steps. The overlap integral is required at each of the step discontinuities. This

is discussed further below.

The relative speed of the symbolic *Replacement* command was tested in the following way. We concentrated on the integral term of Eq. (11) and we evaluated that integral contribution to the matrix A for 3 values of V. We evaluated it in the following two ways. (1) The contribution to the matrix was established using the *Mapping* command with V left unevaluated. The *Replacement* command was then used to evaluate the contribution for 3 values of V. Values of V between 3.0 and 3.4 were used. (2) The contribution to the matrix was evaluated for the 3 values of V using the *Mapping* command 3 times. The results, given in Table 2, are not surprising. The timing ratio of 3 corresponds to the fact that 3 values of V were used. Thus, in the first method the *Mapping* command, which establishes the form of the contribution, is invoked only once. The same *Mapping* command was used 3 times in the second method. The results show that the *Replacement* command is very fast indeed. Once the matrix was established, it required very little time to evaluate the terms using *Replacement*. Thus, while the *Mapping* command offers considerable simplicity over numerical integration, even more simplicity is introduced when the *Mapping* command is combined with the *Replacement* to find the variation of B, for example, with V.

Fiber dispersion, which is a function of dn_e/dV, limits the bandwidth of the fiber and, hence, is of considerable interest. Dispersion can be determined numerically through the use of the *Replacement* command, using it to determine n_e in the vicinity of the V of interest to find the approximate numerical derivative and, from that, fiber dispersion.

The *Mapping* routine is also useful in determining other fiber parameters such as modal spot size or mode field radius (MFR). Two definitions are important. The first determines splice loss arising from tilt offset and is designated W_0, defined implicitly as

$$W_0^2 = \frac{2\int_0^\infty \Psi^2(r)\, r^2\, dr}{\int_0^\infty \Psi^2(r)\, r\, dr}. \tag{18}$$

The second definition is important in determining splice loss due to transverse fiber offset. It is also a determinant of fiber dispersion; for this reason, it is designated W_d, where

$$W_d^2 = \frac{2\int_0^\infty \Psi^2(r) r\, dr}{\int_0^\infty \left(\frac{d\Psi(r)}{dr}\right)^2 r\, dr}. \tag{19}$$

According to Eq. (8), $\Psi(r)$ is the product of a polynomial in r and the Gaussian function. The derivative that appears in W_d is therefore also the product of a polynomial in r and the Gaussian function. The evaluation of W_0 and W_d will thus require the evaluation of a series, each term of which has the form

$$\int_0^{\infty} r^q \exp\left[\frac{-Vr^2}{b^2}\right] r\,dr = \frac{\left(\frac{V}{b^2}\right)^{-\left(\frac{q+2}{2}\right)} \Gamma\left(\frac{q+2}{2}\right)}{2} . \tag{20}$$

The evaluation of spot size can be accomplished without numerical integration by noting and using the pattern-matching (*Mapping*) algorithm suggested above. The procedure is as already described but now the pattern (*int*) is given as

$$int[Cr^q] = \frac{\left(\frac{V}{b^2}\right)^{-\left(\frac{q+2}{2}\right)} \Gamma\left(\frac{q+2}{2}\right)}{2} . \tag{21}$$

The term b that appears here is the fiber core radius. We revert to the variable r rather than X, use Eq. (8), suppress the exponential term, and expand the integrand in each of these expressions. We then invoke the *Mapping* command as given in Eq. (16). Every term in the series is evaluated from the pattern (or form) of that term as established by *int* rather than by resorting to term-by-term integration. In this sense, the *Mapping* command might be called a transform or form-matching algorithm.

Splice loss between dissimilar fibers or loss and mode conversion in a tapered fiber can be handled in a similar fashion. The overlap integral, which represents mode coupling between fiber modes i and j under weakly guiding conditions, is

$$\int_0^{\infty} \Psi_{k-}^{i} \cdot \Psi_{k-}^{j} \, r\,dr . \tag{22}$$

Ψ^i represents the electromagnetic field of the ith mode and the subscripts $k-$ and $k+$ indicate evaluation on either side of step k. If the expansion is in terms of the same basis functions on either side of the discontinuity, evaluation of this integral reduces to evaluating the inner product of the eigenvectors. In symbolic nomenclature,

$$[a_k^i] \bullet [a_{k+1}^j] , \tag{23}$$

where $[a_k^i]$ is the set of eigenvectors associated with the expansion of the ith mode and the dot represents inner or dot product. Subscript k is associated with evaluation at $k-$ and subscript $k+1$ is associated with evaluation at $k+$. Evaluation of the dot product is very fast and explicit integration is not required.

V. Conclusions

Symbolic programming routines when used in conjunction with Laguerre-Gauss basis functions are seen to be useful in evaluating some of the important single-mode fiber parameters. Parameters that require the integration of the modal field over the fiber's transverse cross section or over an infinite cross section can be handled easily using the symbolic *Mapping* command in most cases of practical interest. Overlap integrals, for example, are amenable to this approach. The *Replacement* command is useful in performing "what if" tests or in tracking operational parameters as a function of V.

VI. References

1. Stephen Wolfram, *Mathematica: A System for Doing Mathematics by Computer*, Addison Wesley Publishing Company, New York, Second Edition (1991).

2. R.L. Gallawa, I.C. Goyal, and A.K. Ghatak, "Modal properties of circular and noncircular optical waveguides," Fiber and Int. Opt., Vol. 11, pp. 25-50, 1992.

Table 1
CPU Timi[illegible]mparison
Integra[illegible] Only

M	Unevaluated Integral (seconds)	Symbolic *Mapping* (seconds)	Timing Ratio
7	111.2	4.3	26
9	234.9	9.5	25
11	422.9	18.1	23
13	686.7	32.0	22

Table 2
CPU Timing Comparison
3 Values of V
Integral Term Only

M	Symbolic *Mapping* with *Replacement* (seconds)	Symbolic *Mapping* Only (seconds)	Timing Ratio
7	7.1	21.0	3
9	15.9	46.8	3
11	30.5	90.4	3
13	53.9	157.2	3

SESSION 20:

LOW FREQUENCY

Chair: John Brauer
Co-Chair: Abd Arkadan

A Comparison of Two Low-Frequency Formulations for the Electric Field Integral Equation

W. Wu, A. W. Glisson, and D. Kajfez
Department of Electrical Engineering
University of Mississippi
University, MS 38677

Abstract

The numerical solution for the Electric Field Integral Equation (EFIE) at low frequency range is investigated. A version of triangular surface patch code which solves the EFIE by the method of moments is modified to implement two low-frequency formulations. The investigation focuses on the stability of the moment matrix in the low frequency range. The condition number of the moment matrix for the two low-frequency formulations is quite different for some cases. Comparisons are also made with data from the original patch code.

I. Introduction

The numerical solution for the Electric Field Integral Equation (EFIE) has been found to become inaccurate in the frequency range where the maximum dimension of the surface is much smaller than a wavelength [1,2]. The inaccuracy occurs at the stage of evaluating the elements of the impedance matrix in the moment method solution procedure, because, for the mixed potential form of the EFIE, one observes that $| j\omega \mathbf{A} | \ll | \nabla \phi |$, as $\omega \to 0$. Thus, the information on the magnetic vector potential A is lost at low frequency, and the remaining information from the electric scalar potential is not sufficient to determine the surface current distribution. Consequently, the solution is numerically unstable.

This problem may be partially overcome by simply increasing the numeric precision used in the computer code. However, to obtain a stable EFIE solution at any frequency, a special method of moments solution procedure must be used. Low-frequency formulations have been applied to rectangular-patch models, bodies of revolution, and triangular patch models in [1-3]. The two different methods used in [1-3] have been applied to extend a version of patch code [4] to the low frequency range. The modifications require the use of different expansion and testing functions that tend to decouple the electrostatic and magnetostatic portions of the solution. The Galerkin testing procedure is used to obtain the system of linear equations.

The two low-frequency formulations are tested and it is found that the condition number of the impedance matrix for the different formulations is quite different for some cases. The results are also compared with results from the original patch code. The outlines for the two low-frequency formulations are given in section II, and numerical results are shown in section III. A brief summary is provided in section IV.

II. Low-Frequency Formulations

The scattering problem of a perfectly electrically conducting (PEC) body subject to illumination by an incident plane wave can be formulated via the EFIE as

$$-\mathbf{E}^i_{tan} = [-j\omega\mathbf{A}(\mathbf{r}) - \nabla\phi(\mathbf{r})]_{tan} \quad , \qquad \mathbf{r} \text{ on } S \tag{1}$$

where $\mathbf{E}^i_{tan}$ is the incident electric field, $\mathbf{A}$ is the magnetic vector potential, and φ is the electric scalar potential. Both potentials can be expressed as functions of the surface current [4].

Many method of moments [5] schemes have been developed to obtain the numerical solution for equation (1). One of these is the triangular patch model [4], which is based on a method of moments solution of the EFIE in conjunction with a planar triangular patch model of the scatterer and a special set of basis functions. In this section, for completeness, we first describe the basis function used in the original patch code [4]; then the two other vector basis function sets that are suitable for low-frequency use are described briefly.

In the method of moments solution procedure, the surface current density $\mathbf{J}$ is approximated as

$$\mathbf{J} \cong \sum_{n=1}^{N} \mathrm{I}_n \mathbf{u}_n(\mathbf{r}) \tag{2}$$

where N is the number of unknowns, I_n is an unknown coefficient to be determined, and $\mathbf{u}_n$ is a vector basis function. In (2) $\mathbf{u}_n$ could be either $\mathbf{f}_n$, $\mathbf{J}_n^c$ and $\mathbf{J}_n^d$, or $\mathbf{J}_n^c$ and $\mathbf{J}_n^l$, as described in following.

The original vector basis function $\mathbf{f}_n$. As defined in [4], $\mathbf{f}_n$ is the vector basis function defined on pairs of adjacent triangles associated with n^{th} edge as shown in Figure 1 and given by equation (3), where l_n is the length of n^{th} edge and $A_n^{\pm}$ is the area of triangle $T_n^{\pm}$.

To extend the original patch code [4] to the low frequency range, vector basis functions are developed based on the ideas in [1-3]. These vector basis functions $\mathbf{J}_n$ are divided

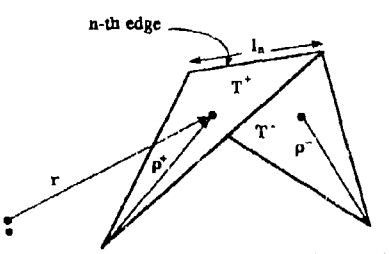

Fig. 1. Local coordinates associated with an edge

$$\mathbf{f}_n(\mathbf{r}) = \begin{cases} \dfrac{l_n}{2A_n^+}\rho_n^+ & , \quad \mathbf{r} \text{ in } T_n^+ \\ \dfrac{l_n}{2A_n^-}\rho_n^- & , \quad \mathbf{r} \text{ in } T_n^- \\ 0 & , \quad \text{otherwise} \end{cases} \tag{3}$$

into two types, $\mathbf{J}_n^c$ and either $\mathbf{J}_n^d$ or $\mathbf{J}_n^t$, with the following properties which make them suitable for use in the magnetic vector and electric scalar potentials at low frequencies:

- $\mathbf{J}_n^c$ is associat[illegible] interior nodes and is divergenceless;
- $\mathbf{J}_n^d$ is associated with faces and is curl-free;
- $\mathbf{J}_n^t$ is equivalent to $\mathbf{f}_n$, but is only associated with the interior edges of the model that lie along a tree [illegible]ructure connecting the centroids of the triangular patches.

The combination of $\mathbf{J}_n^c$ and $\mathbf{J}_n$ is subsequently referred to as the divergenceless/curl-free basis function set, and the combination of $\mathbf{J}_n^c$ and $\mathbf{J}_n^t$ is referred to as the divergenceless/tree basis function set. Each of the basis functions $\mathbf{J}_n^c$, $\mathbf{J}_n^d$, and $\mathbf{J}_n^t$ can be constructed as a linear combination of the vector basis functions $\mathbf{f}_n$ defined in (3).

Vector basis function $\mathbf{J}_n^c$. Figure 2 illustrates the basis function $\mathbf{J}_n^c$ associated with an interior node n^L. $\mathbf{J}_n^c$ has vector direction parallel to the edge opposite to node n^L on each triangle attached to node n^L, and $\mathbf{J}_n^c$ forms a loop around node n^L. In Fig. 2(a), besides the edges which are opposite node n^L, all other edges are connected to node n^L. The currents at the edges connected to node n^L are the unknowns in the original patch code and are associated with the original vector basis functions $\mathbf{I}_n$. Fig. 2(b) shows the edges and local coordinates associated with one of the triangles in Fig. 2(a).

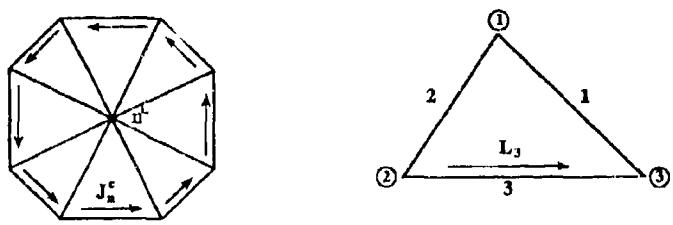

(a) (b)

Fig. 2. Vector basis function associated with interior node n^L

In Fig. 2(b), if node 1 corresponds to node n^L in Fig. 2(a), then $\mathbf{J}_n^c$ in this triangle is parallel to edge 3. As indicated in [4], a constant vector of arbitrary magnitude and direction within the triangle may be synthesized by a linear combination of two of the original vector basis functions. Thus, in conjunction with the definition of the vector basis function in equation (3), a vector $\mathbf{L}_3$ within the triangle of Fig. 2(b) can be formed as

$$\mathbf{L}_3 = \frac{2A}{l_1}\mathbf{f}_1 - \frac{2A}{l_2}\mathbf{f}_2 \tag{4}$$

where l_1 and l_2 are the lengths of edges 1 and 2, respectively, and A is the triangle area.

The basis function $\mathbf{J}_n^c$ in the triangle of Fig. 2(b) is then defined to be

$$\mathbf{J}_n^c = \frac{\mathbf{L}_3}{A} \tag{5}$$

This definition holds for all triangles attached to interior node n^L by using the local coordinate notation in Fig. 2(b) for each triangle attached to n^L. Then the basis function $\mathbf{J}_n^c$ associated with interior node n^L is defined as

$$\mathbf{J}_n^c = \sum_{j=1}^{N_t} \frac{\mathbf{L}_{jop}}{A_j} \tag{6}$$

where N_t is the number of triangles attached to node n^L, $\mathbf{L}_{jop}$ is the vector parallel to the edge opposite to node n^L in the j^{th} triangle, and A_j is the area of the j^{th} triangle.

Vector basis function $\mathbf{J}_n^d$. The vector basis function $\mathbf{J}_n^d$ associated with faces is relatively simple. The $\mathbf{J}_n^d$ associated with face n^f can be constructed as

$$\mathbf{J}_n^d = \sum_{i=1}^{3} S_{ni}\mathbf{f}_{ni} \tag{7}$$

where $\mathbf{f}_{ni}$ is the original vector basis function associated with a non-boundary edge i of face n^f, and S_{ni} is a sign coefficient.

Vector basis function $\mathbf{J}_n^t$. The basis function $\mathbf{J}_n^t$ consists of the $\mathbf{f}_n$'s for the interior edges of the model that lie along a tree structure connecting the centroids of adjacent triangular patches. The definition of *tree* and *branch* for the rectangular-patch model in [Ch.8, 6] is also applied for the triangular patches used here. Once a tree is obtained, $\mathbf{J}_n^t$ can be defined as

$$\mathbf{J}_n^t = \begin{cases} \mathbf{f}_k \text{ , if edge } k \text{ intersects a tree branch} \\ 0 \text{ , otherwise} \end{cases} \tag{8}$$

where $\mathbf{f}_k$ is the original vector basis function associated with a non-boundary edge k.

With these definitions, we use three simple approaches to forming a complete set of basis

functions. The surface current density J is then approximated by either of the three basis function sets. If the original vector basis function $\mathbf{f}_n$ is chosen, i.e. the same basis set as in [4], then

$$\mathbf{J} \cong \sum_{n=1}^{N} I_n \mathbf{f}_n(\mathbf{r}) \tag{9}$$

where N is the number of interior (non-boundary) edges in the triangular patch model. If the divergenceless/curl-free basis function set is chosen, then

$$\mathbf{J} \cong \sum_{n=1}^{N^L} I_n \mathbf{J}_n^{\,c}(\mathbf{r}) + \sum_{n=N^L+1}^{N} I_n \mathbf{J}_n^{\,d}(\mathbf{r}) \tag{10}$$

where N^L is the number of interior nodes, and $N - N^L + 1$ is the number of faces in the triangular patch model. If the divergenceless/tree basis function set is chosen, then

$$\mathbf{J} \cong \sum_{n=1}^{N^L} I_n \mathbf{J}_n^{\,c}(\mathbf{r}) + \sum_{n=N^L+1}^{N} I_n \mathbf{J}_n^{\,t}(\mathbf{r}) \tag{11}$$

where $N - N^L$ is the number of tree branches in the triangular patch model.

With a Galerkin testing procedure, the impedance matrices for these cases may be represented as

$$Z_{orig} = j\omega \langle \mathbf{A}_n, \mathbf{J}_m \rangle + \langle \nabla\phi, \mathbf{J}_m \rangle \tag{12}$$

$$Z_{dlc} = j\omega \begin{bmatrix} \langle \mathbf{A}_n^{\,c}, \mathbf{J}_m^{\,c} \rangle & \langle \mathbf{A}_n^{\,d}, \mathbf{J}_m^{\,c} \rangle \\ \langle \mathbf{A}_n^{\,c}, \mathbf{J}_m^{\,d} \rangle & \langle \mathbf{A}_n^{\,d}, \mathbf{J}_m^{\,d} \rangle + \frac{1}{j\omega} \langle \nabla\phi, \mathbf{J}_m^{\,d} \rangle \end{bmatrix} \tag{13}$$

$$Z_{dlt} = j\omega \begin{bmatrix} \langle \mathbf{A}_n^{\,c}, \mathbf{J}_m^{\,c} \rangle & \langle \mathbf{A}_n^{\,t}, \mathbf{J}_m^{\,c} \rangle \\ \langle \mathbf{A}_n^{\,c}, \mathbf{J}_m^{\,t} \rangle & \langle \mathbf{A}_n^{\,t}, \mathbf{J}_m^{\,t} \rangle + \frac{1}{j\omega} \langle \nabla\phi, \mathbf{J}_m^{\,t} \rangle \end{bmatrix} \tag{14}$$

where the subscript on Z denotes the basis and testing function type, and $\langle\ \rangle$ denotes the symmetric product. Equation (12) uses the original basis and testing functions; equation (13) uses the divergenceless/curl-free basis and testing functions; and equation (14) uses the divergenceless/tree basis and testing functions.

If one compares equations (13) and (14) with (12), it is evident that the magnetic vector potential contribution to the elements of the impedance matrix appears alone in the upper potions of $Z_{d/c}$ and $Z_{d/t}$ is not lost in comparison with $\nabla\Phi$. We also note that the low-frequency formulations described in this section are valid in principle at any frequency.

III. Numerical Results

The two low-frequency vector basis functions described in section II have been incorporated in a version of patch code [4], and several structures have been studied over a wide frequency range. Numerical results are presented in this section comparing the condition numbers of the impedance matrix and current distributions obtained using the different approaches. All scatterers studied are modeled by triangular patches and subject to illumination by an incident plane wave.

The first example is a flat square plate scatterer, as shown in Fig. 3(a). Th condition number obtained for the impedance matrix using the original basis functions is found to start oscillating wildly when L/λ is smaller than 10^{-7}, while the condition numbers obtained using the divergenceless/tree basis functions is an order of magnitude better then that using the divergenceless/curl-free basis functions, but both are essentially constant as a function of frequency for $L/\lambda < 10^{-2}$. The absolute value of the real and imaginary parts of the current coefficient for edge 8 in Fig. 3(a) is shown in Fig. 3(b). Good agreement is observed for the real part of current using two the low-frequency formulations; however, the result obtained using the original basis functions falls apart at the frequency where the impedance matrix becomes unstable. Also, the imaginary part of the current for the divergenceless/tree approach becomes inaccurate for L/λ less than 10^{-7}. Numeric underflows occur in the computation in the latter case, but it is not clear that the underflows are the direct cause of the accuracy loss.

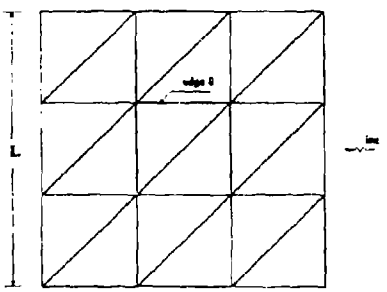

Fig. 3(a)

The next example is a long narrow (L=30W) strip which is bent to form a square, open loop, as shown in Fig. 4(a). Results for the condition number in this case are similar to that of the previous case, except that the condition number for the divergenceless/tree procedure is about three orders of magnitude better than that of the divergenceless/curl-free procedure as, shown in Fig. 4(b). The results for the current on one of the edges shows behaviour similar to that of Fig. 3(b). Results obtained in some other cases, however, indicate that the imaginary part of the current obtained with the divergenceless/curl-free approach may also become inaccurate at very low frequencies. The real part (magnetostatic part) of the current seems to always be stable for both low-frequency formulations.

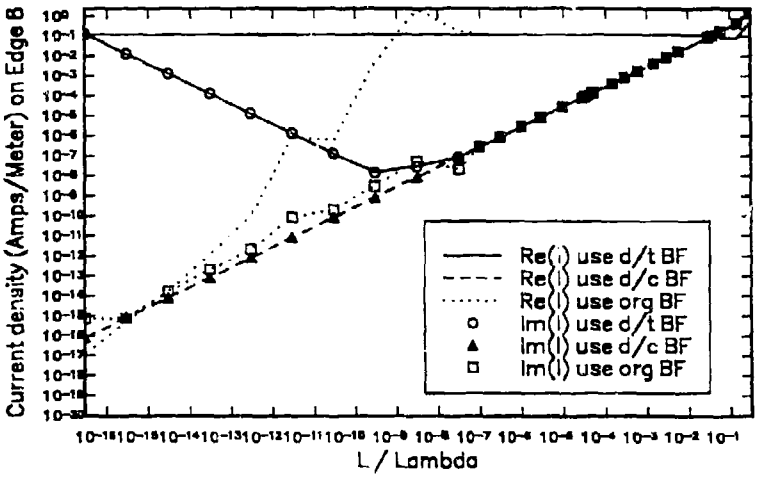

Fig. 3(b)

IV. Summary

Two alternate vector basis functions described in section II have been implemented in a version of the triangular patch code [4] to extend its usefulness to the low frequency range. Numerical results are presented for different structures over a wide frequency range. The condition numbers of the impedance matrix and computed current values as a function of frequency are presented to illustrate the improvement of the EFIE solution in the low-frequency range. While good results have generally been obtained, the investigation has revealed that further work may be necessary to ensure accurate results for the imaginary part of the induced current.

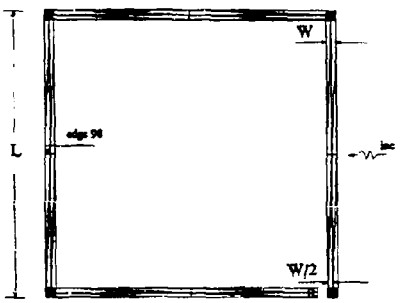

Fig. 4(a)

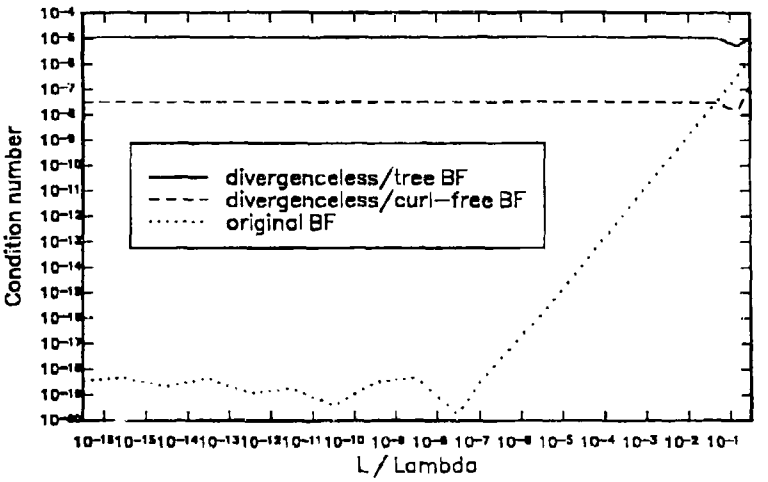

Fig. 4(b)

References

[1] D. R. Wilton and A. W. Glisson, "On improving the electric field integral equation at low frequencies," in *Abstracts, 1981 Spring URSI Meeting*, Los Angeles, CA, June 1981.

[2] J. R. Mautz and R. F. Harrington, "An E-field solution for a conducting surface small or comparable to the wavelength," *IEEE Antennas Propagat.*, vol. AP-32, pp. 330-339, April 1984.

[3] J. S. Lim, S. M. Rao, and D. R. Wilton, "A novel technique to calculate the electromagnetic scattering by surfaces of arbitrary shape," in *Abstracts, 1993 URSI Meeting*, University of Michigan, Ann Arbor, Michigan, June 28-July 2, 1993.

[4] S. M. Rao, D. R. Wilton, and A. W. Glisson, "Electromagnetic scattering by surfaces of arbitrary shape," *IEEE Trans. Antennas Propagat.*, vol. AP-30, pp. 409-418, May 1982.

[5] R. F. Harrington, *Field Computation by Moment Methods*. New York: Macmillan, 1968.

[6] C. M. Butler, D. R. Wilton, and A. W. Glisson, *A Short Course on Fundamentals of Numerical Solution Methods in Electromagnetics*, University of Mississippi, October 15-18, 1984.

COMPUTATIONS OF INDUCED ELECTRIC FIELDS IN BIOLOGICAL CELLS EXPOSED TO MAGNETIC FIELDS

Maria A. Stuchly and Weiguo Xi
Department of Electrical and Computer Engineering
University of Victoria, Victoria, BC, Canada
V8W 3P6

INTRODUCTION

There is considerable evidence that extremely low frequency (ELF) magnetic fields interact with biological systems. That evidence has emerged from studies with laboratory animals and biological cells. The mechanisms of these interactions remain elusive. The critical parameters of exposure responsible for the interactions still remain to be defined. At least some biological experiments indicate that induced electric fields or currents are responsible for the interactions. One of the important research needs is modeling of the induced electric fields and currents in various cell preparations. It is rather elementary to evaluate these parameters in low density cell suspensions. But to model cells growing in a monolayer and forming a confluent colony, as well as to compute the fields at subcellular structures are difficult and demanding tasks.

The three-dimensional impedance method has been successfully used to compute the induced fields and currents in heterogeneous models of man and animals in low frequency electric and magnetic fields. This paper explores this method's utility in microdosimetry (i.e. dosimetry on cellular and subcellular level). The main limitation arises from conflicting requirements between the required resolution to represent geometrical and electrical complexity of a cell and cell colonies and manageability of computations in terms of memory, time and convergence. Some useful results that can be obtained such as an effect of cell density, role of gap junctions in confluent cell monolayer are highlighted.

Computational technique

To evaluate induced currents and electric fields in models of biological cells the three dimensional (3D) impedance network method is used [1,2]. This is an effective computational technique for magnetic fields of sufficiently low frequencies, such that the secondary magnetic field produced by the induced current can be neglected. This conditions is satisfied for frequencies:

$$f << 1/\mu_o \sigma L \tag{1}$$

where: μ_o is the permeability of free space, σ is the conductivity and L is the largest dimension of the geometry analysed.

Another simplifying assumption made is that:

$$\sigma >> 2\pi f \varepsilon' \tag{2}$$

where: ε' is the dielectric constant ($\varepsilon' = \varepsilon'_r \varepsilon_o$). At a frequency of 60 Hz this condition is reasonably well satisfied even for the membrane, assuming its relative dielectric constant of the order of 3. This simplifying assumption needs further evaluation in view of the membrane charge related relaxation phenomena. The assumption given by eq. (2) reduces the impedance network to the resistance network.

When all the loop equations are written up they form a system of equations of the size N^3, where N is the number of computational cells. That system of equations is solved using an iterative process, (in this case the successive over-relaxation technique). All modeling results reported are for an arbitrarily selected value of the magnetic flux density equal to 1T. The results can be scaled linearly for other flux densities.

Cell models

In the random monolayer model biological cells are represented by cubical volumes of zero conductivity. Since cell membranes have the conductivity of the order of 10^{-5} to 10^{-7} S/m such representation is justified as the first order approximation [3]. Cells are placed in a medium of the conductivity typical for cell suspensions, in this case of 1 S/m. The cells are only permitted to occupy positions at the bottom of an exposure container, e.g., petri dish. This simulates the behavior of cells forming a monolayer.

The cells and solute are contained in a cylindrical dish of 5 cm diameter. This volume is modeled by a 102x102x4 cubical grid, where each biological cell occupies 2x2x2 spaces (0.5mm), of the grid. Therefore, the monolayer is two grids thick. This subdivision of biological cells is necessary for correct representation of their behaviour in the numerical algorithm used. The solute above the monolayer is also two grids thick. Two representative threshold distributions of biological cells in the monolayer are considered and cell densities associated with them are estimated. In our model the biological cells are randomly placed (placement generated by computer) but there are restrictions on surface contact between them. In the first case, no contact between any two cells is permitted resulting in 17% cell density within the monolayer. In the second case, cells can make contact with other cells but only at their edges. Cell placement is also random as generated by a computer algorithm. The edge contact effectively obstructs the current flow.

Under this condition an approximate cell density within the monolayer is 34% . In the model of [illegible] gap junctions biological cells are represented by cubes, a confluent monolayer has the side dimension of five biological cells (the total number of cells 25). The small number of biological cells [illegible] is due to computational limitations. Since each biological cell is subdivided into a relatively [illegible] computational grid (a large number of divisions) to facilitate modeling of membranes and gap [illegible] even the cases described result in the number of unknowns approaching 10^6. The [illegible] region consists of 61x61x13 grids, each 10 μm. The applied magnetic flux density is 1 T, [illegible] and its direction is perpendicular to the monolayer. The gap junctions are placed in the centre of [illegible] surfaces adjacent to the neighbouring cells. The area of the junctions is varied from [illegible] approximately 0.4 to 5% of the total surface area of the membrane. The conductivity is varied from 10^{-2} to 1 S/m. The selected parameters of the model gap junction are representative of those reported for actual gap junctions, i.e. conductivity up to 1 S/m and surface area up to 3% [4].

Results and Discussion

The induced current density pattern in a cylindrical dish filled with cells in suspension forming a monolayer closely resembles that of the same dish filled with the medium (solute) for relatively low cell densities. When the density increases to the value at which cells can come in contact with each other, the current density pattern is no longer defined by the dish geometry but depends solely on the spatial distribution of the cells . For a dense (but not confluent) monolayer of cells the current density pattern in the solution just above the monolayer mimics to a large extent the pattern in the monolayer. At larger distances above the monolayer, the current flow depends only on the dish geometry. The average current density for a low cell density in the monolayer is reasonably close to that predicted from the mixture formulae. Its higher value mostly reflects the fact that averaging is only done over the volume where the current flows. If the averaging is done over the whole monolayer volume, the average is

247 $\mu A/cm^2$ which is very close to the mixture theory prediction of 239 $\mu A/cm^2$ (3% difference). For the higher cell density (34%), the differences are significant independently what volume is selected for averaging. The differences between the numerical calculations and analytical for the solute are 2.5%, and can be partly attributed to the computational error of the numerical method, and partly result from the effect of the bottom layer and the existence of a small component of the current in the direction of the magnetic field.

When cells form a confluent monolayer the current flows only inside the individual cells. However, if gap junctions are allowed, increases of both the average and the maximum current densities are observed. The highest current density is in gap junctions. Certain resemblance of the current pattern is maintained to that of an assembly of isolated cells in a confluent monolayer. But this is true only with respect to the amplitude, the prevailing direction of the current flow is the same throughout the monolayer.

The network impedance method has some advantages and a number of serious limitations when used to model induced fields and currents in biological cells exposed to low frequency magnetic fields. The main advantages are its simplicity, convenient formulation facility to include anisotropic properties, and reasonable computational efficiency. However, the method is only suitable and reliable when certain rules are observed. Problems with convergence are encountered when the cell conductivities vary over a few orders of magnitude, as in the case of the monolayers analyzed. These problems deteriorate further when non-uniform size meshes are used. This makes it difficult to model membranes of biological cells at a correct dimensional scale without going to a large number of computational cells. At the same time the total number of computational cells is limited to about 10^6. This limitation results partly from a need to use a large number of iterations (up to 10^5, typically 1-5 x 10^{-4}), for geometries like the monolayer with gap junctions. Solutions for geometries forming circles (or squares) or rings have a tendency to converge to a false solution unless a sufficient number of iterations is forced. Geometries of the type representing a random cell distribution do not pose any computational problems. A typical time to compute data for a random model is 10 minutes and for a monolayer about five hours on workstation HP 9000/730.

Acknowledgement

This work was supported by a Strategic Grant from the Natural Sciences and Engineering Research Council of Canada and a grant from the U.S. National Institute of Environmental Health and Safety (through a contractual agreement with the University of California, Riverside).

References

[1] DeFord, J.F. and O.P. Gandhi, 1985, "An impedance method to calculate currents induced in biological bodies exposed to quasi-static electromagnetic fields". *IEEE Trans. Electromagn. Compat.* 27, pp. 168-173.

[2] Orcutt, N. and O.P. Gandhi, 1988, "A 3-D impedance method to calculate power deposition in biological bodies subjected to time-varying magnetic fields", *IEEE Trans. Biomed. Eng.* 35, pp. 577-588.

[3] Foster, K.F. and Schwan, H.P., 1989, "Electric properties of tissues and biological materials: a critical review". *CRC Crit. Rev. Biomed. Eng.* 17 pp. 25-104.

[4] Bennett, M.V.L., and V.K. Verselis, 1992, "Biophysics of gap junctions", *Cell Biology*, Vol. 3, pp. 29-47.

INDUCED CURRENTS IN BIOLOGICAL BODIES IN LOW FREQUENCY MAGNETIC FIELDS: IMPEDANCE METHOD WITH IMPROVED SPATIAL RESOLUTION

Weiguo Xi and Maria A. Stuchly
Department of Electrical and Computer Engineering
University of Victoria, Victoria, BC, Canada
V8W 3P6

Introduction

The knowledge of the spatial distribution of the electric currents and fields induced in the human body by low frequency magnetic fields is important in the assessment of potential health hazards to people on the basis of experiments with cellular and animal systems [1,2]. This is also very useful in some medical applications, e.g., neural stimulation [3]. Among the methods developed for this type of electromagnetic problems, two differential equation-based methods: the time-domain finite difference method (FDTD) and the impedance or admittance network method, have been found effective for modeling of heterogeneous and complicated 3D bodies representing biological subjects [4]. At low frequencies, the problem is a quasi-static one as the displacement current is negligible compared to the conduction current. This, together with the fact that a biological system does not perturb an exposing magnetic field, makes the impedance network method especially attractive.

With large memories (16-64 Mbytes) increasingly available on computers today up to 1 million cells can be routinely handled. A reasonable representation of the human anatomy and its surroundings can therefore be obtained. However, the computing time increases almost exponentially with the number of unknowns, and an increase in the number of the computational cells beyond 1 million leads to demands of a computing speed not available in most computers. Moreover, to model the detailed anatomy and morphology of a whole human body, one needs much more than 1 million computational cells. There are many practical situations where a high resolution modeling is of interest for only a certain part of the body. For example, such situations arise in case of the exposure evaluation of the head to the magnetic field produced by a hair-drier.

In this paper, a new approach for the sub-region analysis with a high spatial resolution is presented. In this approach, the injection currents on the sub-region boundary are taken into account by using the previously computed results for the whole-body as the sub-region boundary values.

Computational Method

At low frequencies such as power-line frequencies (50 or 60 Hz) the problem can be considered as quasi-static. Additionally, for biological materials, impedances consist of resistances only since $\sigma >> 2\pi f\varepsilon$ (where σ is the material conductivity, f is the frequency and ε is the material dielectric constant). A biological body is represented by a 3D resistance network in which each parallelepiped volume shown in Fig.1a is equivalent to three resistance $R_x^{i,j,k}$, $R_y^{i,j,k}$ and $R_z^{i,j,k}$ associated with the network node (i,j,k) as shown in Fig.1b. The resistances are calculated as [5]:

$$R_m^{i,j,k} = \Delta_m/(S_m\sigma_m^{i,j,k}) \qquad (m=x,y,z) \qquad (1)$$

where Δ_m is the cell length in the m-th direction, S_m is the area of the cell surface perpendicular to the m-th axis, and $\sigma_m^{i,j,k}$ is the cell electrical conductivity in the m-th direction. For each node, three line currents: $\hat{I}_x$, $\hat{I}_y$ and $\hat{I}_z$, and three loop currents: I_x, I_y and I_z are defined in Fig.1c. Once the loop currents are known, the line current through each resistance element can be obtained by summing up the four loop currents which are common to that resistance element. As illustrated in Fig.1d, the line current through $R_z^{i,j,k}$ can be expressed by the loop currents as

$$\hat{I}_z^{i,j,k} = -I_x^{i,j,k} + I_x^{i,j-1,k} + I_y^{i,j,k} - I_y^{i-1,j,k} \tag{2}$$

Similarly, $\hat{I}_x^{i,j,k}$ and $\hat{I}_y^{i,j,k}$ can be found to be

$$\hat{I}_x^{i,j,k} = -I_y^{i,j,k} + I_y^{i,j,k-1} + I_z^{i,j,k} - I_z^{i,j-1,k} \tag{3}$$

and

$$\hat{I}_y^{i,j,k} = -I_z^{i,j,k} + I_z^{i-1,j,k} + I_x^{i,j,k} - I_x^{i,j,k-1} \tag{4}$$

respectively. Applying Kirchhoff's voltage equation to each loop associated with node (i,j,k), say z-loop in Fig.1c, the following relationship is obtained

$$R_x^{i,j,k}\hat{I}_x^{i,j,k}+R_y^{i+1,j,k}\hat{I}_y^{i+1,j,k}-R_x^{i,j+1,k}\hat{I}_x^{i,j+1,k}-R_y^{i,j,k}\hat{I}_y^{i,j,k} = (emf)_z^{i,j,k} \tag{5}$$

where $(emf)_z^{i,j,k}$ is the electromotive force generated by a magnetic field perpendicular to the loop, and

$$emf_z^{i,j,k} = \omega B_z^{i,j,k} S_z \tag{6}$$

Substituting Eqs.(3) and (4) into Eq.(5), $I_z^{i,j,k}$ can be found as

$$\begin{aligned} I_z^{i,j,k} = [&emf_z^{i,j,k} - R_x^{i,j,k}(I_y^{i,j,k-1}-I_y^{i,j,k}-I_z^{i,j-1,k}) - R_x^{i,j+1,k}(I_y^{i,j+1,k}-I_y^{i,j+1,k-1}-I_z^{i,j+1,k}) \\ &-R_y^{i,j,k}(I_x^{i,j,k-1}-I_x^{i,j,k}-I_z^{i-1,j,k}) - R_y^{i+1,j,k}(I_x^{i+1,j,k}-I_x^{i+1,j,k-1}-I_z^{i+1,j,k})] \\ &/[R_x^{i,j,k}+R_x^{i,j+1,k}+R_y^{i,j,k}+R_y^{i+1,j,k}] \end{aligned} \tag{7}$$

Similar equations can be derived for $I_x^{i,j,k}$ and $I_y^{i,j,k}$.

Let's consider a parallelepiped generic region (Fig.2a), representing either a biological body and its surrounding space or a sub-region identified from the whole body for the purpose of a high spatial resolution analysis. On its six surfaces: left (i=1), right (i=nx), bottom (j=1), top (j=ny), rear (k=1) and front (k=nz), line currents are assumed to be known. In the sub-region analysis, the line current density on the boundary can be obtained by interpolating the results from the whole region analysis. The line currents on the boundary are sometimes called injection currents, however, they may also flow outward or parallel to the boundary as shown in Fig.2a.

The loop equations are formulated differently for several outer nodes compared to inner nodes. The y-loop at A(i,j,nz-1), the z-loop at B(nx-1,ny-1,k) and the x-loop at C(i,j,1) are representative. The boundary line currents involved around the loop are indicated by arrows; the unmarked line currents need to be decomposed into the loop currents. To illustrate the formulation of the method, the z-loop current equation at node B is given in detail.

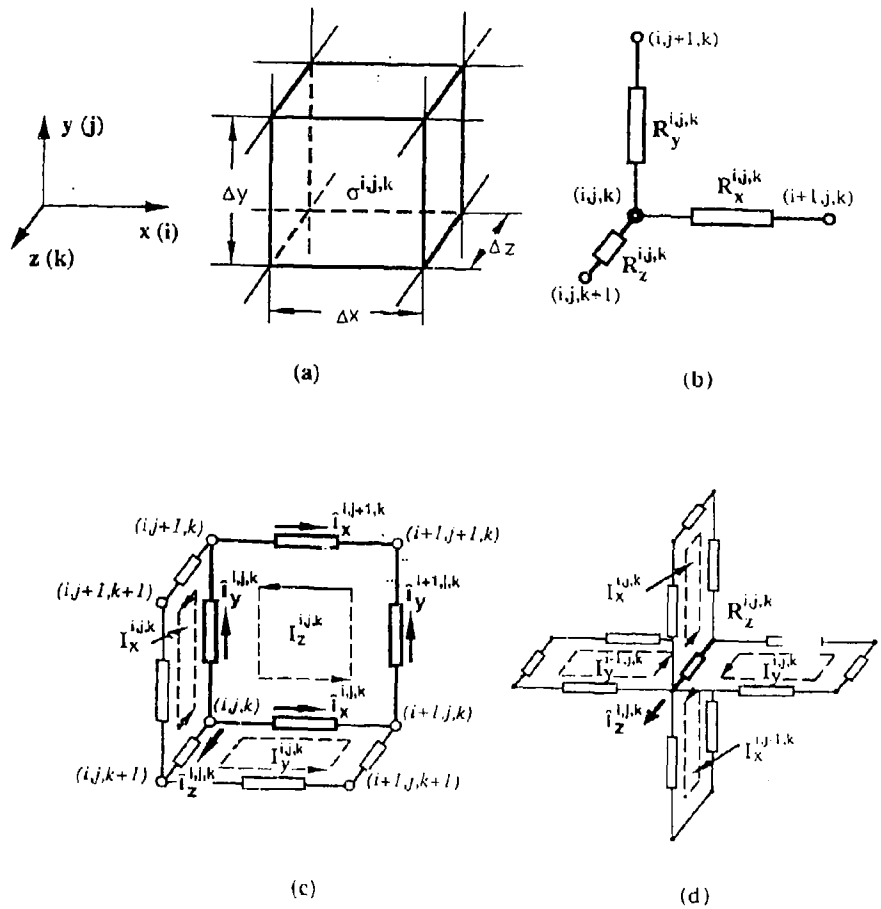

Figure 1 Illustration for the impedance network method.
(a) a parallelepiped tissue volume of the body forming a computation cell of (i,j,k);
(b) three directional impedances associated with node (i,j,k);
(c) three line currents and loop currents, $\tilde{i}_m$ and I_m (m=x,y,z), defined for node (i,j,k);
(d) line current $\tilde{i}_z^{i,j,k}$ shown as a superposition of four loop currents flowing through the resistance $R_z^{i,j,k}$.

From Eq.(5), the z-loop equation at B(nx-1,ny-1,k) is given as

$$R_x^{nx-1,ny-1,k} \hat{I}_x^{nx-1,ny-1,k} + R_y^{nx,ny-1,k} \hat{I}_y^{nx,ny-1,k} - R_x^{nx-1,ny,k} \hat{I}_x^{nx-1,ny,k} - R_y^{nx-1,ny-1,k} \hat{I}_y^{nx-1,ny-1,k} = emf_z^{nx-1,ny-1,k} \quad (8)$$

where line currents $\hat{I}_x^{nx-1,ny,k}$ and $\hat{I}_y^{nx,ny-1,k}$ have known values, and $\hat{I}_x^{nx-1,ny-1,k}$ and $\hat{I}_y^{nx-1,ny-1,k}$ are unknown. Using Eqs.(3) and (4), the unknown currents $\hat{I}_x^{nx-1,ny-1,k}$ and $\hat{I}_y^{nx-1,ny-1,k}$ can be expressed as

$$\hat{I}_x^{nx-1,ny-1,k} = -I_y^{nx-1,ny-1,k} + I_y^{nx-1,ny-1,k-1} + I_z^{nx-1,ny-1,k} - I_z^{nx-1,ny-2,k} \quad (9)$$

and

$$\hat{I}_y^{nx-1,ny-1,k} = -I_z^{nx-1,ny-1,k} + I_z^{nx-2,ny-1,k} + I_x^{nx-1,ny-1,k} - I_x^{nx-1,ny-1,k-1} \quad (10)$$

respectively. After substituting Eqs.(9) and (10) into Eq.(8) and rearranging it, $\hat{I}_z^{nx-1,ny-1,k}$ can be readily found as

$$\begin{aligned} \hat{I}_z^{nx-1,ny-1,k} = {} & [emf_z^{nx-1,ny-1,k} + R_x^{nx-1,ny,k} \hat{I}_x^{nx-1,ny,k} - R_y^{nx,ny-1,k} \hat{I}_y^{nx,ny-1,k} \\ & + R_x^{nx-1,ny-1,k} (I_z^{nx-1,ny-2,k} + I_y^{nx-1,ny-1,k} - I_y^{nx-1,ny-1,k-1}) \\ & + R_y^{nx-1,ny-1,k} (I_z^{nx-2,ny-1,k} + I_x^{nx-1,ny-1,k} - I_x^{nx-1,ny-1,k-1})] \\ & / (R_x^{nx-1,ny-1,k} + R_y^{nx-1,ny-1,k}) \end{aligned} \quad (11)$$

Verification

A solution for a double-layered sphere is used to verify the formulation and accuracy of the sub-region analysis. The sphere has radii of 0.15 m and 0.25 m, and electric conductivities of 1 S/m and 0.5 S/m for its inner and outer layers, respectively, and is placed in a uniform 60 Hz magnetic field in free space. An analytical solution is available for this problem and hence can be used to check the numerical results.

The verification is conducted in three steps. In the first step, computations are performed for the whole sphere. In the second step, one eighth of the sphere is considered for a sub-region analysis where the boundary values in the planes of x=0, y=0 and z=0 need to be assigned. The computational cell size is halved in each dimension, resulting in roughly the same cell number as in step one. To examine the effect due to the error in boundary values, the computation of this eighth sphere is performed in two cases: in the first case, the numerical results from the first step, and in the second case, the analytical results are used as the boundary values. In the final step, a cubical region partially embeded in the eighth sphere is chosen for another stage of sub-region analysis and the cell size is again halved. The boundary values on the six surfaces of this cube are taken from the numerical results from case 1 and 2 of step one, and from the analytical solution. The error evaluation for each step/case is illustrated in Fig.3 for comparison.

Sub-Region Analysis of Human Head

To illustrate the application of the above-described approach of the sub-region analysis, electric currents and fields induced in the human head by a uniform 60 Hz magnetic field of 1 T directed from the back to

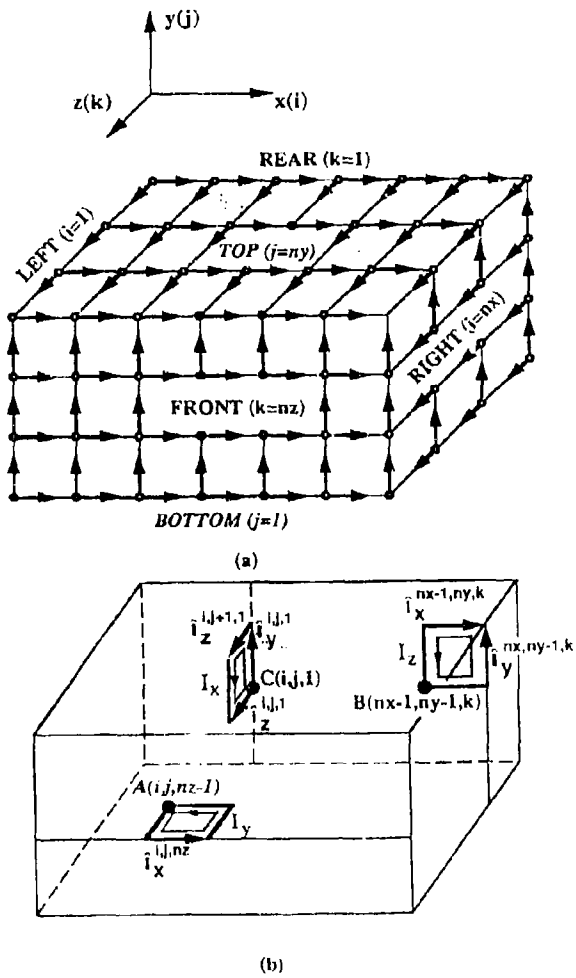

Figure 2 Model for the derivation of iterative loop current equations for the outer nodes of a parallelepiped sub-region.
(a) Line currents on the sub-region boundaries, i.e., left, right, bottom, top, rear and front surfaces;
(b) Three outer nodes: A(i,j,nz-1), B(nx-1,ny-1,k) and C(i,j,1) and the boundary line currents involved in their loop current equations.

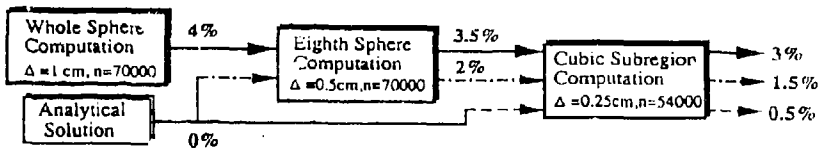

Figure 3 The relative errors in the computations of a double-layered sphere.

the front are computed. The anatomically based man models developed at the University of Utah are used in this computation. The man model consists of quarter-inch grid (0.665cm). An electric conductivity was assigned to each of such cubical cells, according to the tissue type they belong. The obtained conductivity matrix for the body volume and its surrounding space has a size of 90X48X268, i.e., about 1.16 million. Since this requires a memory space too large for most readily accessible computers, the data for 2X2X2 = 8 cells are combined to form a smaller matrix of 45X24X134. This half-inch model is used in the whole body computation, while the quarter-inch model is used in the computation of the head-region starting from the neck. The boundary values on the neck cross-section are obtained by interpolating the line current densities from the whole body computation.

The average and maximum values of the calculated electric currents and fields induced in the head are listed in Table 1 for three computation cases. It can be noted that maximum current density and field intensity for smaller computational cells are 2-3 times higher than those of case 1, though the average values are very close. The ratio of the maximum to the average for both the current and field in the head would be even larger if the head was modeled with finer computational cells. Secondly, the differences for the average and the maximum values between case 2 and 3 are significant, indicating that the current flow between the head and the rest of the body cannot be neglected.

Conclusions

In modeling of the induced electric current distributions in a 3D heterogeneous human body the impedance network method coupled with the sub-region analysis approach is viable. It is effective in dealing with conflicting requirements between the modeling resolution and the computation manageability Using one or multi-stages of sub-region analyses, a body region of interest can be dealt with in a "zoom"-like manner and does not result in an excessively large number of computation cells.

Acknowledgement

This work is supported by a strategic grant from the Natural Sciences and Engineering Research Council of Canada and a grant from the U.S. National Institutes of Health through a contractual agreement with the University of California, Riverside. The authors also wish to thank Dr. O.P. Gandhi and Ms. C. Furse for their generous assistance.

TABLE 1 Comparison of Various Computation Cases of Modeling the Electric Current and Field Induced in the Head by a 60 Hz Uniform Magnetic Field of 1T from the Back to the Front.

Computations Cases	Current Density ($\mu A/cm^2$)		E-Field (V/m)	
	Average	Maximum	Average	Maximum
Case 1: Whole Body Analysis (Δ=1/2", n=144,700)	191	1440	14.0	105
Case 2: Head Sub-Region Analysis (Δ=1/4", n=35,900)	206	2000	13.7	296
Case 3: Detached Head Analysis (Δ=1/4", n=35,900)	161	1050	11.3	65.2

References

[1] G. Theriault, "Cancer risks due to exposure to electromagnetic fields", *Recent Results in Cancer Res.*, Vol.120, pp.166-180, 1990.

[2] S.F. Cleary, "In vitro studies: low frequency electromagnetic fields", *Proc. Sci. Workshop on the Health Effects of Electromagnetic Radiation on Workers*, U.S.Dept. of Health and Human Services, Cincinnati, OH, Publ. No.91-111, pp.47-89, 1991.

[3] M.A. Stuchly, "Applications of time-varying magnetic fields in medicine", *CRC Crit. Rev. Biomed. Eng.*, vol.18, pp.89-124, 1990.

[4] O.P. Gandhi and J.Y. Chen, "Numerical dosimetry at power-line frequencies using anatomically based models", *Bioelectromagn.*, Supplement No.1, pp.43-60, 1992.

[5] N.Orcutt and O.P. Gandhi, "A 3-D impedance method to calculate power deposition in biological bodies subjected to time varying magnetic fields, *IEEE Trans.Biomed. Eng.*, vol.BME-35, pp.577-587, 1988.

THE TWO-DIMENSIONAL FINITE INTEGRAL TECHNIQUE COMBINED WITH THE MEASURED EQUATION OF INVARIANCE APPLIED TO OPEN REGION SCATTERING PROBLEMS

Griffin K. Gothard
Sadasiva M. Rao
Department of Electrical Engineering
Auburn University, AL 36849

ABSTRACT

Static and frequency domain analysis of various scattering PEC bodies is accomplished using the two-dimensional finite integral technique (FIT) combined with the measured equation of invariance (MEI). The resulting FIT/MEI solutions are compared with the well known method of moment (MOM) solutions for validation.

I. INTRODUCTION

The finite integral technique (FIT) uses the integral form of Maxwell's equations applied to a discrete conformal grid. The scattering structure and the surrounding region is subdivided into elements, in this case triangles, and constitutive material parameters are assigned to each triangle thus facilitating the specification of an inhomogeneous body. Then, Maxwell's equations, in the integral form, are applied to each element to generate a sparse matrix. The measured equation of invariance (MEI) is used to truncate the problem space close to the scattering body.

II. THE FINITE INTEGRAL TECHNIQUE

The finite integral technique directly applies the Maxwell's equations in integral form to a discrete grid [1]. The unknown quantities are approximated by explicit basis functions, and therefore the technique is easily derived and implemented. Also, use of the integral form of Maxwell's equations provides a smoothing effect on the problem solution.

Beginning with Maxwell's equations

$$\begin{aligned} \nabla \times \mathbf{H} &= -j\omega\varepsilon\mathbf{E} \\ \nabla \times \mathbf{E} &= j\omega\mu\mathbf{H} \end{aligned} \tag{1}$$

the two-dimensional integral form (no z variation) may be easily derived, given by

$$\begin{aligned} \int \mathbf{H}_t \cdot d\mathbf{l} &= j\omega \int \varepsilon \mathbf{E}_z \, ds \\ \mathbf{E}_z^{i+1} - \mathbf{E}_z^{i} &= -j\omega \int \mu \mathbf{H}_t \cdot \hat{\mathbf{n}} dl \end{aligned} \tag{2}$$

where $\mathbf{H}_t$ is the transverse magnetic field, $\mathbf{E}_z$ is the z-directed electric

field, and E_z^{i+1} and E_z^i are the electric fields at two adjacent node locations i+1 and i in the mesh, respectively.

Applying the appropriate basis functions results in an equation which, if applied to every node in the discrete mesh, generates a FIT matrix that can then be solved for the unknown quantities [1].

IV THE MEASURED EQUATION OF INVARIANCE

The measured equation of invariance [2] technique, applied to the boundary nodes of a discrete grid scheme, enforces the radiation condition for open region scattering problems.

Using the static case as an example, assuming we have an open region PEC with a charge density ρ_v on the body, we can find the potential V at any point in space using

$$V(\rho) = \int_C \frac{\rho_v(\rho')\ln|\rho - \rho'|}{2\pi\varepsilon_o} dc' \tag{3}$$

where ρ' and ρ represent the position vectors to the source and field points, respectively, and ρ_v is the charge density. Also, at each boundary node, an equation relating the boundary nodes potential with the neighboring potentials can be defined as

$$\sum_{i=1}^{N} \alpha_i V_i = 0 \tag{4}$$

where V_i is the unknown voltage at node i, α_i is an unknown weighting coefficient associated with V_i, and N is the number of potentials considered.

By assuming N-1 orthogonal functions for the purpose of representing ρ_v in (2), and then solving for the V_i's in (3), a set of N-1 linear equations with N-1 unknown α_i's can be defined at each boundary node. Solving these equations yields a set of weighting coefficients (α_i, i=1, N-1) associated with each boundary node. Using these weighting coefficients, in place of the finite difference schemes weighting coefficients, implements the MEI method and enforces the radiation condition. Since N is a finite number (in our case equal to 4), the new finite-difference global matrix is still sparse.

IV NUMERICAL RESULTS

Figure 1 shows the predicted charge distribution on the body for a 0.1m infinite PEC strip and an infinite PEC square cylinder, 0.1m on a side, as predicted by FIT/MEI and MOM. For both geometries, the potential on the bodies is raised to a constant 10V. For Figure 1a, the FIT/MEI approach terminates the problem space two layers away from the

strip and has 38 unknowns. For the MOM, the strip is divided into 10 equal segments. For Figure 1b, the FIT/MEI approach terminates the problem space two layers away from the square cylinder, and has 72 unknowns. The MOM problem is divided into 24 equal segments. For both geometries, there is good overall agreement.

Figure 2 shows the predicted normalized current distribution on the body of a 0.1λ infinite PEC strip illuminated by a normally incident TM plane wave as predicted by FIT/MEI and MOM. Figure 2a compares the real part of the current and Figure 2b compares the imaginary part. The FIT/MEI problem space is terminated two layers away from the strip and has 64 unknowns. The MOM strip is divided into 16 equal segments. For 2a-b, agreement is fair in the middle of the strip but not good at the ends.

Figs. 3, 4, and 5 show the predicted normalized current distributions induced on infinite cylinders of circular, square, and bow-tie cross sections, illuminated by a TM plane wave as predicted by FIT/MEI and MOM techniques (dimensions are provided in each figure). In each figure, current is plotted beginning from the middle of the shadow region finishing in the middle of the illuminated region. For all the cases, the FIT/MEI problem space is terminated two layers away from the cylinder. The circular, square and the bow-tie cylinder problems use 40, 84, and 80 equal segments for the MOM solution and 160, 184, and 172 unknowns for the FIT/MIE solution, respectively. Agreement between the FIT/MEI and MOM is reasonably good in all cases.

V. CONCLUSIONS

The thrust of this effort was simply to validate the FIT/MEI method, and no effort was made to minimize the unknowns for either the FIT/MEI or MOM techniques, nor to maximize agreement between the two methods by increasing FIT/MEI or MOM unknowns. However, since the FIT/MEI technique generates a sparse matrix, and easily handles inhomogeneous or anisotropic materials and complex geometries, it is possible that the technique could deal with more complex and electrically larger problems than the MOM. Presently, work is in progress to validate this observation.

REFERENCES

[1] J. E. Wheeler III, *Formulation and investigation of finite integral techniques for computing electromagnetic fields in the presence of arbitrary inhomogeneous objects*, PhD thesis, University of Houston, December 1991.

[2] K. K. Mei, R. Pous, Z. Chen, and Y. W. Liu, "The measured equation of invariance: a new concept in field computation," 1992 IEEE ALS International Symposium, Chicago, USA, pp. 2047-2050.

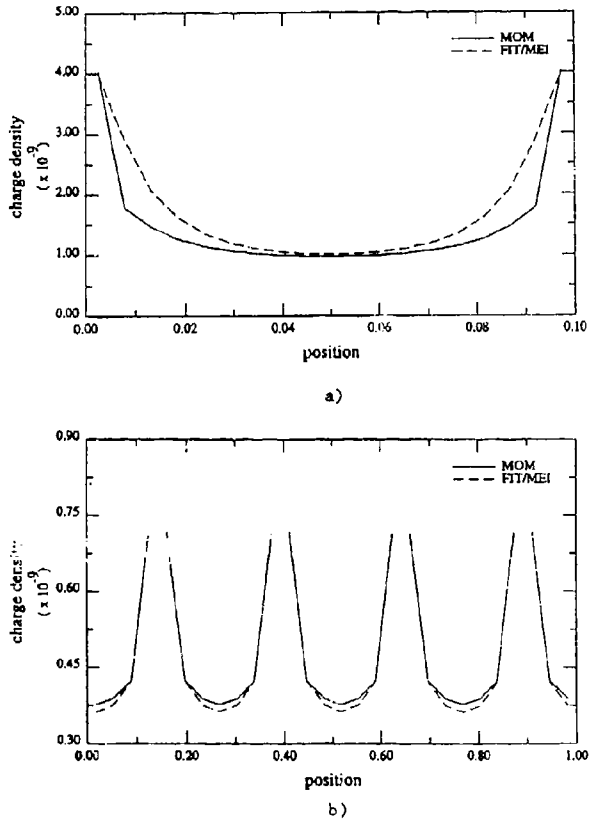

Figure 1. a.) A 0.1m infinite PEC strip is raised to a 10V potential. The charge density on the strip as predicted by MOM and FIT/MEI is then compared. b) An infinite square cylinder, 0.1m to a side, is raised to a 10V potential. The charge density on the square as predicted by MOM and FIT/MEI is then compared.

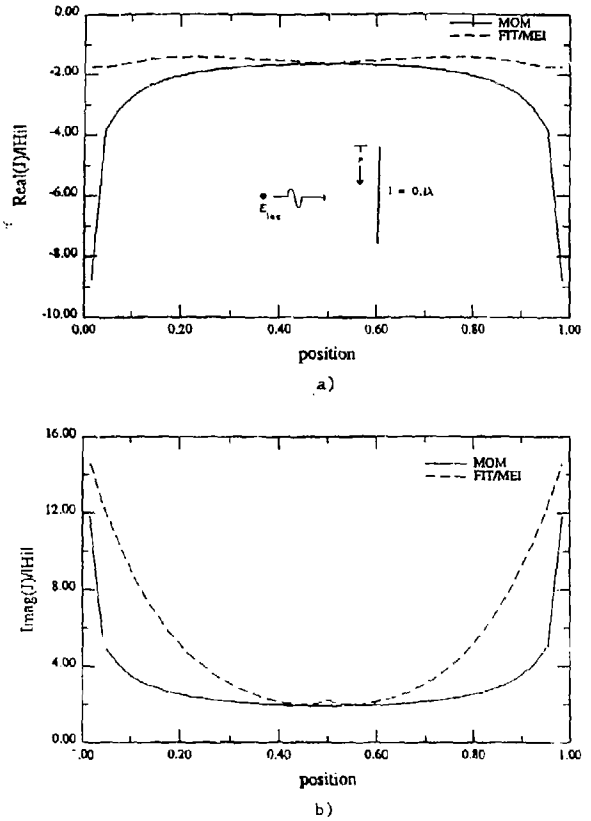

Figure 2. A 0.1λ infinite PEC strip is illuminated (as shown) by a normally incident TM plane wave. The normalized current distribution on the strip is predicted by MOM and FIT/MEI and then compared, where a) compares the real part of the normalized current distribution and b) compares the imaginary part.

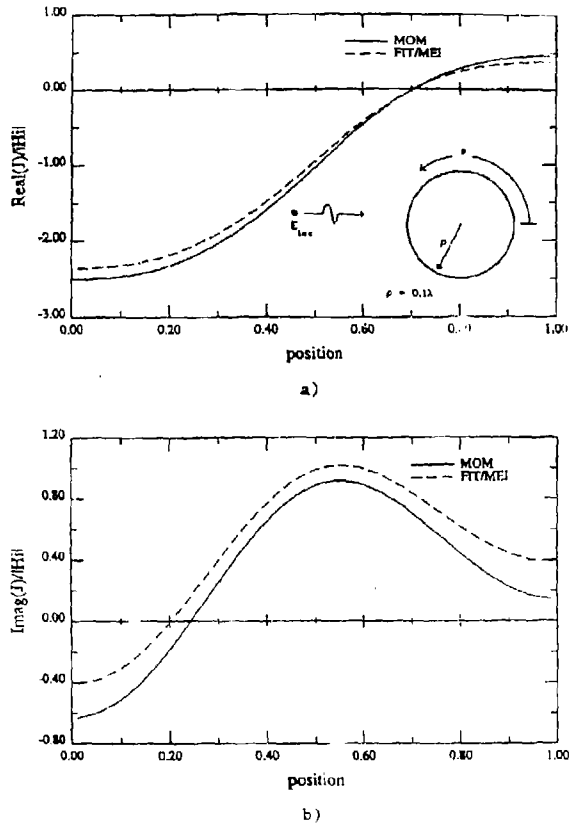

Figure 3. An infinite PEC circular cylinder, with $\rho = 0.1\lambda$, is illuminated (as shown) by a TM plane wave. The normalized current distribution on the body is predicted by MOM and FIT/MEI and then compared, where a) compares the real part of the normalized current distribution and b) compares the imaginary part.

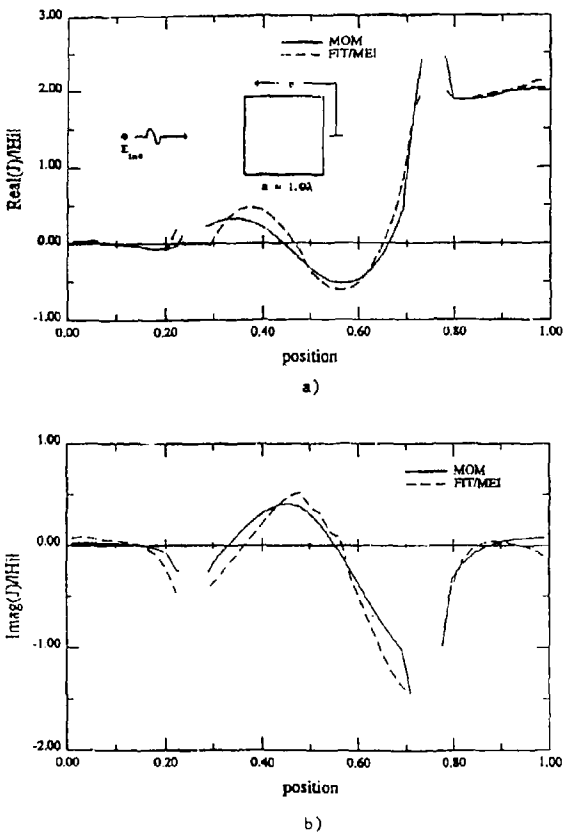

Figure 4. An infinite PEC square cylinder, 1.0λ on a side, is illuminated (as shown) by a normally incident plane wave. The normalized current distribution on the body is predicted by MOM and FIT/MEI and compared, where a) compares the real part of the normalized current distribution and b) compares the imaginary part.

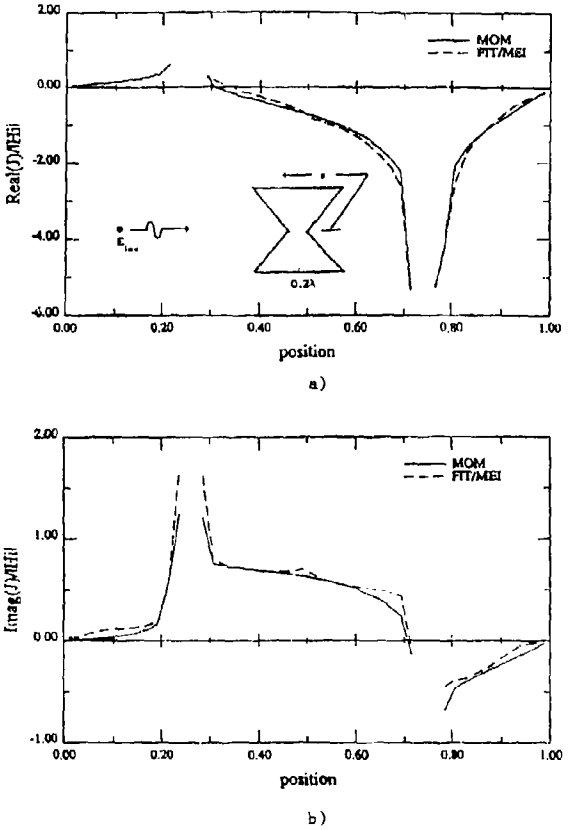

Figure 5. An infinite PEC bow cylinder, 0.2λ by 0.2λ with a gap spacing of 0.02λ, is illuminated (as shown) by a TM incident plane wave. The normalized current distribution is predicted by MOM and FIT/MEI and then compared, where a) compares the real part of the normalized current distribution and b) compares the imaginary part.

A T-Matrix Solution for the Scattering from Dielectric Cylinders

J. Paul Skinner
Air Force Institute of Technology

Abstract

The T-Matrix method (also known as the extended boundary condition method) is a low frequency technique for computing scattered fields which offers advantages relative to the volumetric based method of moments for many dielectric scattering problems. This paper documents the development of T-Matrix solutions in both the TM_z and TE_z polarizations for dielectric cylinders of infinite length. The physical cross-section of the cylinders is any closed contour which can be approximated with flat facets, including both concave and convex shapes. Results indicate T-Matrix solutions can often be derived with many fewer unknowns than with volumetric moment methods, and with much less computation time.

1. INTRODUCTION

The T-Matrix method was first developed by Waterman as an alternative to moment methods for solving low frequency acoustic and electromagnetic scattering problems [1, 2]. Descriptions of the general method are found in several books [3, 4, 5, 6]. The method requires expanding an incident field into a sum of wavefunctions from a complete set, with known expansion coefficients. The scattered field is then postulated to be an unknown expansion of outward propagating wavefunctions, whose coefficients (assuming linear media) must be linearly related to the coefficients of the incident expansion via a transition, or T-Matrix. The challenge is then to set up an analysis procedure to deduce how to fill the elements of this T-Matrix. The analysis procedure requires the use of a null-field integral equation (NFIE), which means the scattering body must be bounded by a closed surface. The approach also requires obtaining an eigenfunction expansion of the free space Green's function. The T-Matrix construction procedure then follows by exploiting of the orthogonality of the eigenfunctions.

The next section outlines the T-Matrix solution for several two dimensional electromagnetic scattering problems. A somewhat detailed explanation is given for the case of an isotropic, homogeneous dielectric cylinder in the TM_z polarization. This is followed by a brief explanation of the necessary modifications for the problems of dielectric cylinders in the TE_z polarization. The third section discusses issues related to the numerical implementation of the solutions. Results are then given in the fourth section.

2. T-MATRIX SOLUTION PROCEDURE

Consider the 2-D geometry depicted in Figure 1. All of space is divided into two regions, separated by the closed boundary S. Region II extends to infinity and is filled with empty space (μ_o, ϵ_o). Region I is filled with a homogeneous, isotropic dielectric (μ_1, ϵ_1). Note the outward normal $\hat{n}$ is directed into Region II. Also note the imaginary circular cylindrical surfaces of radii R_i and R_o, which just inscribe and superscribe the physical boundary S.

2.1 DIELECTRIC CYLINDER, TM_z POLARIZATION

In this polarization with the cylinder of infinite length, the incident, scattered, and total electric

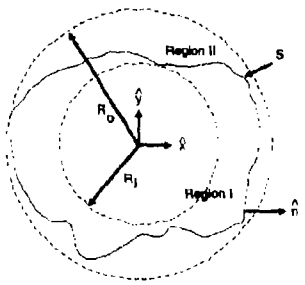

Figure 1: Cross-Section of the Cylinder Geometry (Infinite in z)

fields everywhere must be purely $\hat{z}$ directed. Thus, we start with a scalar form of the NFIE,

$$\left.\begin{array}{ll} \bar{\rho} \text{ in Region I,} & -E_z^I(\bar{\rho}) \\ \bar{\rho} \text{ in Region II,} & E_z^I(\bar{\rho}) \end{array}\right\} = \oint_c \left[E_z^{II}(\bar{\rho}') \frac{\partial G_o}{\partial n} - G_o(\bar{\rho}, \bar{\rho}') \frac{\partial E_z^{II}}{\partial n} \right] dl', \tag{1}$$

where c is the curved line contour of the surface S within the XY plane. The interpretation of the electric field for the line integral is the total electric field that exists infinitesimally away from the boundary into Region II, a fact borne out from the application of the divergence theorem in deriving Green's second identity and subsequently, the NFIE. The 2-D free space Green's function in Eq (1) satisfies

$$(\nabla_t^2 + k_o^2) G_o(\bar{\rho}, \bar{\rho}') = -\delta(\rho - \bar{\rho}'), \tag{2}$$

with the 2-D form of the Sommerfeld radiation condition for $e^{j\omega t}$ time dependence. This Green's function has the well known closed form expression,

$$G_o(\bar{\rho}, \bar{\rho}') = \frac{-j}{4} H_0^{(2)}(k_o|\bar{\rho} - \bar{\rho}'|), \tag{3}$$

but may also be expressed in the eigenfunction expansion,

$$G_o(\rho, \rho', \phi, \phi') = \frac{-j}{4} \sum_{m=0}^{\infty} \epsilon_m J_m(k_o \rho_<) H_m^{(2)}(k_o \rho_>) \cos[m(\phi - \phi')], \tag{4}$$

where we use the Neumann number, $\epsilon_m = 1$ for $m = 0$ and $\epsilon_m = 2$ for all positive integers m.

Now we introduce the even and odd mode scalar wavefunctions of circular cylindrical coordinates, which are:

$$\psi_{e,m}^{(i)}(k\bar{\rho}) = Z_m^{(i)}(k\rho) \left\{ \begin{array}{l} \cos(m\phi) \\ \sin(m\phi) \end{array} \right\} \tag{5}$$

where $Z^{(i)}$ represents Bessel functions of the first kind, second kind, and Hankel functions of the first and second kinds for $i = 1, 2, 3$, and 4 respectively. Using these wavefunctions, we can express the Green's function as

$$G_o(\rho, \rho', \phi, \phi') = \frac{-j}{4} \sum_{m=0}^{\infty} \epsilon_m \left[\psi_{om}^{(1)}(k_o \bar{\rho}_<) \psi_{om}^{(4)}(k_o \bar{\rho}_>) + \psi_{om}^{(1)}(k_o \bar{\rho}_<) \psi_{om}^{(4)}(k_o \bar{\rho}_>) \right]. \tag{6}$$

Noting the completeness of the wavefunctions, we may expand the incident field as

$$E_z^i(\rho) = \sum_{m=0}^{\infty} \left[a_{om} \psi_{om}^{(1)}(k_o \bar{\rho}) + a_{om} \psi_{om}^{(1)}(k_o \bar{\rho}) \right] \tag{7}$$

where the ordinary Bessel functions are chosen to include representing E_z^i at the origin.

Let us now test the NFIE along the circular contour of radius R_i. Here, it is clear that $\bar{\rho}_< = \bar{\rho}$ and $\bar{\rho}_> = \bar{\rho}'$. We can then substitute the expansions of G_o and E_z^i into the NFIE, multiply $\psi_q^{(1)}(k_o \bar{\rho})$ to each term and integrate over the circular circumference at the R_i radius. From the orthogonality of the wavefunctions, we extract

$$a_q = \frac{j}{4} \epsilon_m \oint_c \left[E_z^{II}(\bar{\rho}') \frac{\partial}{\partial n} \psi_q^{(4)}(k_o \rho') - \psi_q^{(4)}(k_o \rho') \frac{\partial E_z^{II}}{\partial n} \right] dl' \tag{8}$$

where q (and later, u and ν) represents the collection of subscripts, ${}^{e}_{o}m$. Note that Eq (8) is a representation of a system of equations indexed by q. To go further, we introduce the boundary conditions for the dielectric interface,

$$E_z^I = E_z^{II} \tag{9}$$

$$\frac{1}{\mu_1} \frac{\partial E_z^I}{\partial n} = \frac{1}{\mu_o} \frac{\partial E_z^{II}}{\partial n}, \tag{10}$$

valid for all points along c. We also choose to expand the total field in Region I as

$$E_z^I = \sum_u c_u \psi_u^{(1)}(k_1 \bar{\rho}) \tag{11}$$

where the coefficients, c_u, are unknown for now. Using the boundary conditions and this latest expansion for E_z^I, we rewrite the system of equations represented by (8) as

$$[a_q] = [Q_{qu}^I][c_u] \tag{12}$$

where the entries of the Q^I matrix are given by

$$Q_{qu}^I = \frac{j\epsilon_m}{4} \oint_c \left[\psi_u^{(1)}(k_1 \bar{\rho}') \frac{\partial}{\partial n} \psi_q^{(4)}(k_o \bar{\rho}') - \frac{\mu_o}{\mu_1} \psi_q^{(4)}(k_o \rho') \frac{\partial}{\partial n} \psi_u^{(1)}(k_1 \bar{\rho}') \right] dl'. \tag{13}$$

Note that the m subscript associated with the Neumann number in the above is part of the q subscript collection (not u). By filling the entries of the Q^I matrix and inverting it, we can now solve for the expansion coefficients for E_z^I if we desire, but this will not be necessary for what follows. Thus, like volumetric moment methods (but unlike surface integral equation approaches) the total field inside the dielectric is readily available from the T-Matrix approach without additional integrations.

Next, we apply the NFIE in Region II along the circular contour of radius R_o. Specifically, for $\rho \geq R_o$, we postulate an expansion of the scattered field of the form,

$$E_z^s = \sum_\nu b_\nu \psi_\nu^{(4)}(k_o\bar{\rho}), \tag{14}$$

substitute it into Eq (1), use the eigenfunction expansion of the Green's function with $\bar{\rho}_< = \rho'$ and $\bar{\rho}_> = \bar{\rho}$, multiply each term by $\psi_\mu^{(4)}(k_o\bar{\rho})$, and integrate over the contour of radius R_o to get the system of equations,

$$[b_\nu] = [Q_{\nu\mu}^{II}][c_\mu]. \tag{15}$$

The entries of the Q^{II} matrix are given by

$$Q_{\nu\mu}^{II} = \frac{-j\epsilon_m}{4} \oint_c \left[\psi_\mu^{(1)}(k_1\bar{\rho}') \frac{\partial}{\partial n} \psi_\nu^{(1)}(k_o\bar{\rho}') - \frac{\mu_o}{\mu_1} \psi_\nu^{(1)}(k_o\rho') \frac{\partial}{\partial n} \psi_\mu^{(1)}(k_1\rho') \right] dl' \tag{16}$$

where m is part of the ν collection of subscripts. Note that if the dielectric media is lossless (ϵ_1, μ_1 and k_1 are real), then the entries of $[Q^{II}]$ may be quickly obtained from the corresponding entries of $[Q^I]$ via

$$Q_{\nu\mu}^{II} = -j \cdot Imag\{Q_{\nu\mu}^I\}, \tag{17}$$

which can be seen by comparing Equations (13) and (16).

Finally, we recognize the solution from Equations (12) and (15), which is

$$[b_\nu] = [T_{\nu q}][a_q] \tag{18}$$

where the T-Matrix is simply

$$[T] = [Q^{II}][Q^I]^{-1}. \tag{19}$$

For an incident plane wave coming from a polar angle ϕ from the $+\hat{x}$ axis within the XY plane, the incident field may be expressed as

$$E_z^i = e^{jk_o(x\cos\phi + y\sin\phi)}, \tag{20}$$

which may be put in the form of the expansion in Equation (7) with the coefficients,

$$a_{zm}^i = \epsilon_m j^m \left\{ \begin{array}{c} \cos(m\phi) \\ \sin(m\phi) \end{array} \right\}. \tag{21}$$

Once the expansion coefficients b_ν are determined, the scattered field pattern is readily found by using Eq (14), avoiding the final step of a radiation integral which typically comes up in moment method calculations.

2.2 DIELECTRIC CYLINDER, TE_z POLARIZATION

The development of the T-Matrix solution for this case is extremely similar to that presented in the previous section. It is no more difficult to derive and execute than the TM_z case, unlike volumetric moment method approaches (which fall into vector current unknowns in $\hat{x}$ and $\hat{y}$, instead of a single

scalar unknown current for the TM_z polarization). The only changes come from a different form of a scalar NFIE, and different boundary conditions which come from an application of duality. The NFIE used here is

$$\left.\begin{array}{ll} \bar{\rho} \text{ in Region I,} & -H_z^I(\bar{\rho}) \\ \rho \text{ in Region II,} & H_z^I(\bar{\rho}) \end{array}\right\} = \oint_c \left[H_z^{II}(\bar{\rho}') \frac{\partial G_o}{\partial \hat{n}} - G_o(\bar{\rho}, \bar{\rho}') \frac{\partial H_z^{II}}{\partial n} \right] dl'. \tag{22}$$

The field expansions used are

$$H_z^I = \sum_q a_q \psi_q^{(1)}(k_o \bar{\rho}) \tag{23}$$

$$H_z^I = \sum_u c_u \psi_u^{(1)}(k_1 \bar{\rho}) \tag{24}$$

$$H_z^I = \sum_\nu b_\nu \psi_\nu^{(4)}(k_o \bar{\rho}) \tag{25}$$

and the necessary boundary conditions are

$$H_z^I = H_z^{II} \tag{26}$$

$$\frac{1}{\epsilon_1} \frac{\partial H_z^I}{\partial n} = \frac{1}{\epsilon_o} \frac{\partial H_z^{II}}{\partial n}. \tag{27}$$

The results are a solution of the form of Eq (18) and (19), where the entries of the Q^I and Q^{II} matrices are

$$Q_{qu}^I = \frac{j\epsilon_m}{4} \oint_c \left[\psi_u^{(1)}(k_1 \bar{\rho}') \frac{\partial}{\partial n} \psi_q^{(4)}(k_o \bar{\rho}') - \frac{\epsilon_o}{\epsilon_1} \psi_q^{(4)}(k_o \rho') \frac{\partial}{\partial n} \psi_u^{(1)}(k_1 \rho') \right] dl' \tag{28}$$

with the m associated with q, and

$$Q_{\nu u}^{II} = \frac{-j\epsilon_m}{4} \oint_c \left[\psi_u^{(1)}(k_1 \bar{\rho}') \frac{\partial}{\partial n} \psi_\nu^{(1)}(k_o \bar{\rho}') - \frac{\epsilon_o}{\epsilon_1} \psi_\nu^{(1)}(k_o \rho') \frac{\partial}{\partial n} \psi_u^{(1)}(k_1 \rho') \right] dl' \tag{29}$$

where m is part of ν. Again, Eq (17) may be used to simplify the calculations of the Q^{II} entries if the scatterer is lossless. The excitation coefficients for the expansion of the incident magnetic field are identical to those in Eq (21).

3. COMPUTER CODING ISSUES

Two important considerations in developing a computer code based on the solutions derived in the previous section are how to input and handle the geometry, and how to compute the necessary special functions. Here, we have chosen to confine the geometry to be a closed surface of flat facets, the size of which are independent of wavelength, but only chosen for geometric fidelity. This choice has the advantages of both making the geometry definition easy and allowing for simple surface normal calculations to be made, which are necessary for the general requirement to numerically perform the normal derivatives. The code developed in this effort reads in a series of x and y coordinates of nodes, which when connected form the flat facets. The nodes are defined sequentially in a counter-clockwise sense, starting at node #1 and finishing with node $\#N$. The code always assumes a facet connection between nodes i and i + 1, with the implicit assumption that node $\#N$ connects with node #1.

Figure 2 shows an example of a cylinder geometry built with five facets. Note that node #i + 1 follows node #i in the counter-clockwise sense. We may designate the connection between these two nodes as facet #i, which has an outward surface normal direction $\hat{n}_i$. No matter what the orientation of this facet, be it part of a concave or convex surface, the normal may be computed via

$$\hat{n}_i = \hat{x}\frac{y_{i+1} - y_i}{d_i} + \hat{y}\frac{x_i - x_{i+1}}{d_i} \tag{30}$$

where the width of the facet is

$$d_i = \sqrt{(x_{i+1} - x_i)^2 + (y_{i+1} - y_i)^2}. \tag{31}$$

This procedure guarantees giving the outward normal direction as long as the nodes were defined sequentially in the counter-clockwise sense.

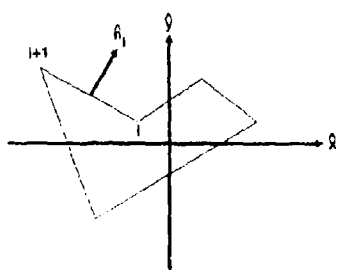

Figure 2: Node and Facet Geometry

The derivatives of the wavefunctions were first attempted to be found numerically by sampling at points a small increment δ away from the facet points in the $\hat{n}_i$ direction. This approach had limited success, as it was difficult to choose a good universal value for δ, even with approaches based on the given dielectric constant of the input geometry. A better way to handle the derivatives is analytically, as follows:

$$\begin{aligned}
\frac{\partial \psi^{(i)}_{e,m}}{\partial n} &= \hat{n} \cdot \nabla \psi^{(i)}_{e,m} \\
&= n_\rho \frac{\partial \psi^{(i)}_{e,m}}{\partial \rho} + \frac{n_\phi}{\rho}\frac{\partial \psi^{(i)}_{e,m}}{\partial \phi} \\
&= n_\rho \left\{ \begin{array}{c} \cos(m\phi) \\ \sin(m\phi) \end{array} \right\} \frac{\partial Z^{(i)}_m(k\rho)}{\partial \rho} \mp \frac{m n_\phi}{\rho} Z^{(i)}_m(k\rho) \left\{ \begin{array}{c} \sin(m\phi) \\ \cos(m\phi) \end{array} \right\}
\end{aligned} \tag{32}$$

where

$$\frac{\partial Z_m^{(i)}(k\rho)}{\partial \rho} = \frac{m}{\rho} Z_m^{(i)}(k\rho) - k Z_{m-1}^{(i)}(k\rho) \quad (33)$$

$$= k Z_{m-1}^{(i)}(k\rho) - \frac{m}{\rho} Z_m^{(i)}(k\rho). \quad (34)$$

The ρ and ϕ components of $\hat{n}$ are merely

$$n_\rho = n_x \cos\phi + n_y \sin\phi \quad (35)$$

$$n_\phi = -n_x \sin\phi + n_y \cos\phi \quad (36)$$

where n_x and n_y are evident in Equation (30).

To compute the special functions, we first made use of the well known 12th order polynomial approximations for the zero and first order Hankel functions [7]. To extend our ability to compute Hankel functions with different large order and argument combinations, we then made use of Somers' modification of Miller's algorithm with auxiliary functions [8]. We also chose to recurse upward for the calculation of $J_n(x)$ whenever $x > n$, which was necessary for stability. This extension greatly expanded the electrical sizes and shapes of cylinders which could be used without numerical difficulty. Since recursion is employed, both $Z_m^{(i)}(k\rho)$ and $Z_{m\pm1}^{(i)}(k\rho)$ could be computed in the same subroutine call with a minimal addition of computation time (i.e., use the appropriate expression for $\frac{\partial Z_m^{(i)}}{\partial \rho}$ for the direction of recursion in the application). This greatly sped up the calculation of the normal derivatives vs. taking numerical derivatives (which require a different argument in the Bessel functions).

4. RESULTS

A single FORTRAN based computer code was written to execute the 2-D cylinder scattering problems discussed earlier, with arbitary flat facet geometry definition. The code can be used for a wide variety of cylinder problems; here we only illustrate a single test case, because of space limitations. The purpose of this example is to demonstrate the validity of the T-Matrix theory and show some advantages the T-Matrix has vs. the moment method.

The test case involves a dielectric cylinder of square cross-section in the TM_z polarization. For this case, we place the origin in the center of the cylinder and define nodes at $x = \pm 0.5\lambda_o, y = \pm 0.5\lambda_o$ (i.e., each side of the square cross-section is $1\lambda_o$ long). The material parameters are $\epsilon_r = 2, \mu_r = 1$. We analyze the bistatic scattering from this cylinder with a fixed incident direction of $\phi = 0$, which is normal to one of the flat faces. Due to the problem symmetry, we recognize that only even mode wavefunctions will contribute to the solution, so we do not use any odd functions in ϕ for the T-Matrix solutions. In Figure 3, we compare T-Matrix solutions for the bistatic echo-width (in units of $dB\lambda_o$) with a volumetric moment method solution using pulse basis/point matching.

Experience with the T-Matrix method indicates that one generally needs to use all wavefunctions up to $m = M$, where M is the closest integer to $2k_oR_o$. This is based on the fact that the "maximum frequency content" of a scattering pattern is proportional to the largest dimension of the target in free space wavelengths. In the present case, $2k_oR_o = 8.89$, which means we expect to need 10 total even mode wavefunctions (counting $m = 0$). Note that exploiting the target and excitation symmetry saves 9 unknowns (the odd modes) here. In Figure 3, we compare the T-Matrix solution

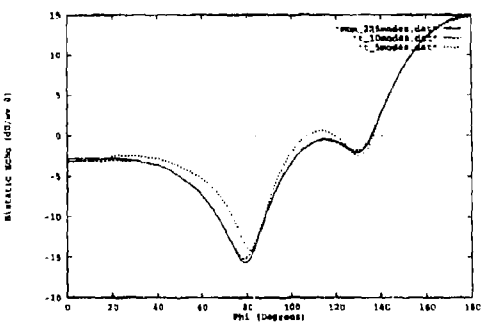

Figure 3: Bistatic Scattering from $1\lambda_o \times 1\lambda_o$ Dielectric Cylinder, TM_z, $\epsilon_r = 2$, Fixed Incidence of $\phi = 0$ (Normal to a face)

using 10 wavefunctions with the moment method solution using 225 unknowns (chosen to maintain 10 pulses per dielectric wavelength). Also shown is a T-Matrix solution with only 5 wavefunctions, which clearly has not converged. We also ran the T-Matrix code with the first 20 even wavefunctions - this only changed the solution from 10 wavefunctions by a maximum of 0.02 dB in the pattern, indicating that 10 unknowns were enough for convergence.

The convergence of the T-Matrix solution for the first test case can also be seen by examining the magnitude of the expansion coefficients for the scattered field, b_n. In Figure 4, we plot these magnitudes for the first 11 even modes. The magnitude of the $m = 10$ term is 1.97×10^{-5}, which is barely significant in the resulting field pattern. An extension to higher terms gives a dramatic fall in coefficient magnitudes; e.g., the $m = 19$ term is only 9.64×10^{-13}. It should also be noted that the wavefunctions have $1/\sqrt{m}$ dependence in the far zone due to the asymptotic behavior of the Hankel functions, which further dampens the effect of higher order terms. In comparing these coefficients in T-Matrix solutions using different mode cutoff criteria, one gets almost the same values for the same modes, with only minor differences associated with interactions between the new modes and the old ones.

Not only does the T-Matrix method often require fewer unknowns than the moment method, but there can also be dramatic savings of CPU time. For the first test case, our solutions took 1141 CPU seconds for the volumetric moment method (granted, a surface integral formulation should be quicker) and only 37.1 CPU seconds for the 10 unknown T-Matrix solution. Both solutions were generated on a VAX 8650 machine using numerical integration sampling which was adjusted until no significant changes occurred. The self-impedance terms in the moment method solution were computed efficiently with an approximate singularity avoidance method developed by Richmond [10]. In addition, one should note that as the dielectric constant increases, moment method solutions

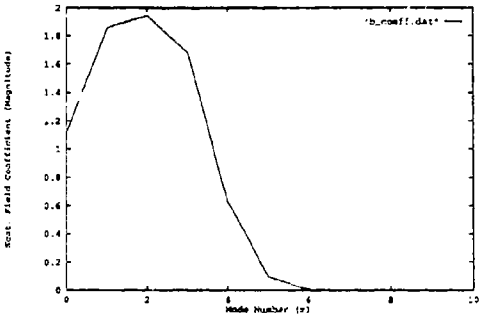

Figure 4: Magnitudes of Scattered Field Expansion Coefficients (Even Modes) for $1\lambda_o \times 1\lambda_o$ Dielectric Cylinder, TM_z, $\epsilon_r = 2$, Fixed Incidence at $\phi = 0$ (Normal to a face)

require more basis functions, but the T-Matrix solution only needs enough unknowns according to the size of the body in free space wavelengths.

An important drawback of the T-Matrix method, however, is the tendency for the solution to become numerically instable for large matrices. This instability comes from the inability to accurately invert the $[Q^l]$ matrix, or to solve Eq (12) by Gaussian elimination. The condition number of the $[Q^l]$ matrix, defined as the absolute value of the ratio of the largest to smallest eigenvalues, is a good indicator of the numerical stability of the solution [9]. For this test case, when 5 modes were used, the condition number for $[Q^l]$ was a mere 1.30. For the case of 10 modes, which was adequate for convergence, the condition number rose to 17.80. For the case run with 20 modes, we obtained the same scattering pattern, but the condition number for $[Q^l]$ grew to 696.36. Thus, as one chooses to solve the problem with more modes than necessary, one may pay the price of dealing with an ill-conditioned matrix. T-Matrix implementation on geometries of high aspect ratios (R_o/R_i from Figure 1 being large) tend also to give ill-conditioned matrices.

5. CONCLUSION

The T-Matrix method proves to be a powerful method relative to some moment methods for certain scattering problems. This paper provides the development of T-Matrix scattering analysis on arbitrarily shaped dielectric cylinders, and gives numerical results for a square cross-section cylinder in the TM_z polarization. These results [illegible] decisive advantages relative to typical volumetric moment method results, though in other cas[illegible] T-Matrix may not be nearly so attractive.

References

[1] Waterman, P.C., "Matrix Formulation of Electromagnetic Scattering," Proceedings of the IEEE, Vol. 53, pp. 805-11, 1965.

[2] Waterman, P.C., "New Formulation of Acoustic Scattering," Journal of the Acoustical Society of America, Vol. 45, pp. 1417-29, 1969.

[3] Mittra, R. (ed.), **Computer Techniques for Electromagnetics**, Hemisphere Pub. Corp., 1987.

[4] Varadan, V.K. and V.V. Varadan (ed.), **Acoustic, Electromagnetic and Elastic Wave Scattering – Focus on the T-Matrix Approach**, Pergamon Press, 1980.

[5] Ishimaru, A., **Electromagnetic Wave Propagation, Radiation, and Scattering**, Prentice Hall, 1991.

[6] Chew, W.C., **Waves and Fields in Inhomogeneous Media**, Von Nostrand Reinhold, 1990.

[7] Abramowitz, M. and I.E. Stegun (ed.), **Handbook of Mathematical Functions with Formulas, Graphs, and Mathematical Tables**, National Bureau of Standards Applied Mathematics Series 55, Washington D.C., 1972.

[8] Somers, G.A. and B.A. Munk, "A Recursive Technique to Avoid Arithmetic Overflow and Underflow when Computing Slowly Convergent Eigenfunction Type Expansions," ACES Journal, Vol. 7 No. 1, 1992.

[9] Strang, G., **Linear Algebra and Its Applications**, 2nd Edition, Academic Press, New York, 1980.

[10] Richmond, J.H., "Scattering by a Cylinder of Arbitrary Cross Section," IEEE Trans. on Antennas and Propagation, Vol. AP-13, May 1965, pp. 334-341.

SESSION 21:

EDUCATION

Chair: Magdy Iskander

EMAG 2.0 -Enhanced 2D Electrostatic and Magnetostatic Solver in MATLAB

David P. Wells and Jovan E. Lebaric
Naval Postgraduate School, Monterey, CA 93943

Introduction

EMAG is a finite difference (FD) MATLAB "toolbox" for solving 2-D electrostatic and magnetostatic field problems that also provides visual representation of electric or magnetic fields and potentials. This paper describes EMAG and its recent extension for rotationally symmetric problems. A method to implement an open boundary for FD problems in Cartesian and cylindrical coordinates, using special equations for the nodes on the FD grid boundary, is also presented. Finally, sample EMAG results for both "z-invariant" and rotationally symmetric problems are presented, comparing these results to analytic solutions where such are available. The theory behind EMAG is outlined using electrostatic equations. EMAG solves magnetostatics problems using magnetostatics duals of the electrostatics equations.

EMAG Description

EMAG solves electrostatic and magnetostatic Poisson equations on a uniform square grid subject to a distant Dirichlet boundary of zero potential. This boundary is imposed far beyond the edges of the computational grid. Users define a problem (media, sources) of their choice on a computational grid using mouse and keyboard. Dielectric and Perfect Electric Conductor (PEC) objects can be defined for electrostatic problems while magnetic and Perfect Magnetic Reluctor (PMR) objects can be defined for magnetostatic problems. The EMAG grid is effectively "surrounded" by free space by employing a technique we refer to as Transparent Grid Termination (TGT). Using TGT to implement an "open boundary", EMAG solves discretized Poisson equations for electric and magnetic potentials on either a coarse (17 by 17) or fine (51 by 51) grid. EMAG provides graphical displays of electric or magnetic fields, equal-potential lines, or mesh plots of electric or magnetic potential. EMAG is also capable of calculating enclosed charge in a user specified area on the electric field plot or enclosed current on the magnetic field plot.

The first version of EMAG solves problems that are invariant along an infinite axis into and out of the computational grid. This implies infinitely long structures and is applicable to solving problems like wires at known potential, lines of charge, parallel strips, etc. The latest version, EMAG 2.0, solves the same z-invariant systems as its predecessor but can also solve problems with rotational symmetry. EMAG 2.0 users solving a rotationally symmetric problem draw the right-hand side of the "meridian" cross section of their problem, thus making the left border of the computational grid the axis of symmetry. Output is displayed in a similar manner so that none of the display area is "wasted" with a mirror image of the plot. EMAG 2.0 has been set up so that the axis of rotational symmetry is exactly between the nodes making up the left side of the computational grid and the nodes making up the left side of the TGT boundary, because of rotational symmetry that requires that potentials be identical at points equidistant from the center line. Consequently, the computational grid for rotationally symmetric problems has a Neumann boundary of zero gradient on its left and a distant Dirichlet boundary with zero potential for its remaining three sides. Since the Poisson equations and the boundary conditions for the left side of the grid for z-invariant and rotationally symmetric systems are different, so are their associated TGT coefficients.

Transparent Grid Termination (TGT)

The TGT expresses the nodal potentials on the computational grid boundary (TGT boundary) as weighted sums of the potentials of the nodes forming the layer just inside the TGT boundary. The equations for the nodes on the TGT boundary are thus of the "global" variety, linking a node on the TGT boundary to each and every node on the layer just inside the boundary, as illustrated in Figure 1. The TGT boundary coefficients *are calculated only once* and stored. These same coefficients are used over and over when solving different user-defined problems. TGT thus eliminates the

need for many free-space "buffer" cells between the sources and the Dirichlet boundary, thereby making it possible to solve open-boundary problems quickly and accurately on a PC. The TGT idea is illustrated by the "system matrix" topology in Figure 2. This depicts the sparsity pattern for the discretized Laplacian operator (using "spiral" node labeling rather than "raster" node labeling)) and represents the "linkage" among the nodes within the EMAG computational grid and on the TGT boundary. Empty areas of the map (zeros) represent pairs of nodes that are unrelated (most nodes are "connected" to just four neighbors). The central tri-diagonal line represents the node "self terms" and the linkage between these "center " nodes and their neighbors to the "right" and "left". The outer diagonal lines represent the links between nodes and their neighbors "above" and "below". Finally, the dense square area in the upper left shows the non-zero TGT coefficients linking each node on the TGT boundary to *every* node on the layer just inside this boundary. The entries in this square region are not problem dependent, since they represent the "compressed" free-space between the TGT boundary and a distant Dirichlet boundary. These entries ("coefficients") depend only on the "thickness" of the compressed free-space, that is on the number of free-space nodes between the TGT and the distant Dirichlet boundary that have been "compressed". The matrix sparsity pattern thus reveals the use of both "local" and "global" relationship between various nodes of the same computational grid.

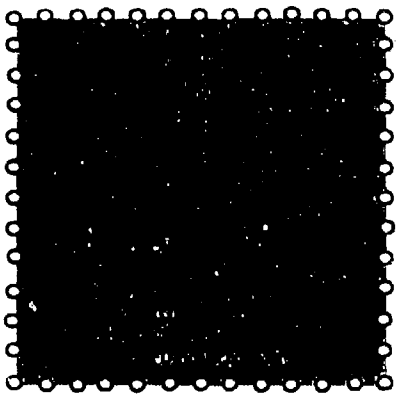

Figure 1: TGT Idea

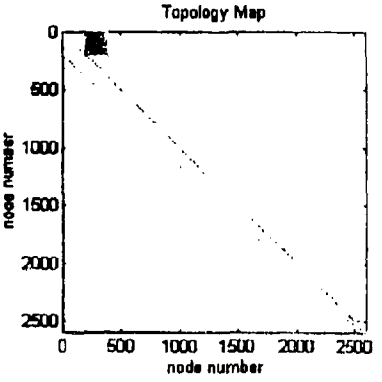

Figure 2: System Matrix Sparsity Pattern

We have developed two different methods to "link" a layer of nodes having a distant Dirichlet boundary to the next inner layer of nodes and so calculate the coefficients of the TGT equations (entries for the dense square region of the system matrix shown in Figure 2.) One is the probabilistic Monte Carlo Method (MCM) while the other method uses matrix approach to "compress" a distant Dirichlet boundary inward. Both approaches are based upon discretized Laplace equations for homogeneous media. Given below are 2) discretized Laplace equations for electric scalar potential:

$$\Phi_l + \Phi_r + \Phi_t + \Phi_b - 4\cdot\Phi_c = 0 \qquad \text{for z-invariant problems}$$

$$\Phi_l\left(1 - \frac{\delta r}{2\cdot r}\right) + \Phi_r\left(1 + \frac{\delta r}{2\cdot r}\right) + \Phi_t + \Phi_b - 4\cdot\Phi_c = 0 \qquad \text{for rotationally symmetric problems}$$

From the above equations, it can be seen that the potential at any given node (subscript c for "center") is a weighted average of the potentials of its neighbors above (top) , below, and to its right or left (subscripts t, b, r and l respectively). Note that for z-invariant problems the weighting factors are constant while for the rotationally symmetric problems the weighting factors are functions of radial distance from the axis of rotation.

Applying the ***Monte Carlo Method*** we developed a MATLAB program to "release" a fixed number of "random walkers" from a starting point on the TGT grid so that they could walk freely about the buffer zone between the computational grid and the distant Dirichlet boundary. At each step in their journey, individual walkers take their next step based on the weighting coefficients (interpreted as probabilities of moving in each of the four possible directions) and the output of a random number generator. For the z-invariant case, the walkers are always given a 1/4 probability of moving up, down, right or left since the Laplace equation states that the potential of any node in the buffer zone has a potential equal to the average of the potentials of each of its four neighbors. The probabilities are unequal for the case of rotational symmetry since Laplace equation coefficients are functions of the walker's radial distance from the axis of rotation. Regardless of the type of problem, the walkers will eventually land on either the zero potential Dirichlet boundary, or on the layer of nodes just inside the TGT boundary. In the former case, our program "discards" the walkers (as if to give them zero potential) while in the latter case the walkers are "trapped" (such that they do not continue walking) and counted. Once all (or some percentage such as 99.99%) of the released walkers have been accounted for (i.e. either trapped or discarded), the number trapped at each inner layer node is divided by the number of walkers originally released. This procedure results in a set of coefficients relating the potential of the walker's initial release node to all nodes on the grid layer just inside the TGT boundary. This process is repeated for each node on the TGT boundary with a matrix of TGT coefficients as the result. Predictably, many walkers must be released from each starting node to get a stable result for the TGT coefficients. Choosing too few walkers results in some of the TGT coefficients being zero. In general, this number is related to the computational grid size and the distance from the TGT boundary to the Dirichlet boundary. We represent this distance as a ratio ("compression" ratio) of the Dirichlet boundary grid size (number of nodes on the Dirichlet boundary) to the computational grid size (number of nodes on the TGT boundary). The compression ratio is an important factor (regardless of the method chosen for calculating the TGT coefficients) since the Dirichlet boundary should ideally be at infinity (infinite compression ratio). We have selected the compression ratio of 15:1 for EMAG (the larger the compression ratio, the better TGT boundary emulates infinite free-space). The number of walkers was chosen to be 500,000 per TGT node based on the speed/memory limitations of the computer (486-class PC) used for the calculation of TGT coefficients. While the computation time using this method increases linearly with the number of walkers chosen, it increases much more rapidly with increasing the compression ratio. Memory required for the computation also varies directly with number of walkers chosen but is completely unaffected by the compression ratio. Furthermore, one can avoid excessive memory use by simply repeating the procedure many times and averaging the results. The advantages of the Monte Carlo method (with respect to the matrix approach) can be fully realized on a massively parallel computer.

The ***matrix solution*** method of developing the TGT coefficients is a more "stable" approach in that it does not involve random events like the Monte Carlo method. While the matrix solution method produces identical results for the TGT coefficients time and time again, the Monte Carlo method in principle never produces the same result twice (although the variations are made small in statistical sense by using large numbers of walkers). The accuracy of the matrix method is limited only by the numerical precision of the computer. However, unlike for the Monte Carlo method, both computation time and memory grow with increasing the compression ratio. Large memory requirement for a large compression ratio is the major drawback of the matrix solution method. The matrix method starts with three matrices. One matrix relates the nodes on a grid layer just inside the Dirichlet boundary (call it layer B) to the nodes on the Dirichlet boundary layer (call it layer A), representing the linkage of the nodes on the B layer to their neighbors "above" (A layer). This matrix has only one non-zero entry per row, since each node has only one neighbor on the layer "above". The second matrix relates the nodes of the B layer to their neighbors on the same layer. This matrix has three non-zero entries per row (center node "self-term" and its linkage to the neighbors to the left and to the right). The third matrix relates the nodes of the B layer to the nodes of the next layer inward (layer C). This matrix also has only one non-zero entry per row since there is only one neighbor on the layer "below". The matrix form of the discretized Laplace equation for the nodes on the B layer as the "center" nodes can be written as:

$$\mathbf{B_b}|b\rangle = \mathbf{B_a}|a\rangle + \mathbf{B_c}|c\rangle \qquad (1.)$$

Next, the matrices relating the nodes of layer C to their nearest neighbors are formed in exactly the same manner. These matrices have the same "pattern" as the B layer matrices but are smaller (as we progress inward there are fewer and fewer nodes per layer).

$$\mathbf{C_c}|c\rangle = \mathbf{C_b}|b\rangle + \mathbf{C_d}|d\rangle \qquad (2.)$$

Since the Dirichlet boundary nodes are at zero potential, we have $|a\rangle = 0$. This allows us to express the nodal potential on the C layer (vector $|c\rangle$) as follows:

$$C_a|c\rangle = C_b(B_b)^{-1} B_a |c\rangle + C_d |d\rangle \quad (3.)$$

$$(C_a - C_b(B_b)^{-1} B_a) |c\rangle = C_d |d\rangle \quad (4.)$$

or, using the matrix inverse:

$$|c\rangle = (C_a - C_b(B_b)^{-1} B_a)^{-1} C_d |d\rangle \quad (5.)$$

Note that this expresses the nodal potentials on one layer (layer C) in terms of the nodes one layer inward (layer D). As this layer elimination progresses inward, the expressions become lengthier so we define "termination" matrices Γ_n for each node layer as follows:

$$\Gamma_b = B_b \quad (6.)$$

$$\Gamma_c = C_a - C_b \Gamma_b^{-1} B_a \quad (7.)$$

This process can be continued inward and, in general, we can write an expression for nodal potentials of a layer (say M-th layer) in terms of the nodal potentials of the layer just "below" (N-th layer) as:

$$|m\rangle = (\Gamma_m)^{-1} M_n |u\rangle \quad (8.)$$

Where the termination matrix for the M-th layer can be expressed *recursively* as:

$$\Gamma_m = M_m - M_l (\Gamma_l)^{-1} L_m \quad (9.)$$

(Note that the layer above the M-th layer is the L-th layer.) When this process is performed iteratively down to the layer of nodes that makes up the TGT boundary (say layer M is the TGT boundary), the TGT coefficients are obtained by:

$$TGT = (\Gamma_m)^{-1} M_n \quad (10.)$$

These TGT coefficients are as close to those obtained from the Monte Carlo Method approach as possible given that the Monte Carlo TGT coefficients are always subject to small random perturbations. In either case, the boundary condition compression goal is achieved and the results using TGT are *exactly the same* as the results obtained by solving a much larger problem on a computational grid in direct contact with the Dirichlet boundary. Furthermore, as will be shown in the next section, EMAG results using TGT are very accurate when compared to analytic solutions. As a demonstration of the two methods of calculating TGT coefficients, the rotationally symmetric problems presented have been solved using Monte Carlo TGT coefficients while the z-invariant problems have been solved using coefficients obtained via the matrix solution method.

EMAG 2.0 Examples

Example 1 The following example is a demonstration of EMAG's accuracy in solving rotationally symmetric problems. On the left is a plot of equal-potential lines for a charged ring (1 nC/m line charge density) of 1 meter radius and positioned 0.4 meters above the bottom side of the TGT boundary. The left edge of the plot is the axis of rotation. The graph on the right shows the magnitude of the electric field on the axis of rotation as a function of position along the axis of rotation for the exact (analytic) solution, EMAG's 17 by 17 grid (coarse) solution, and EMAG's 51 by 51 grid (fine) solution.

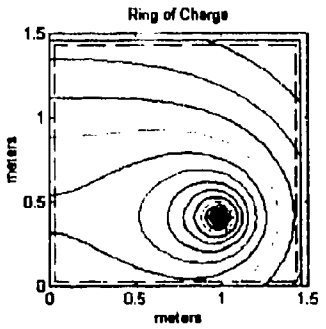

Figure 3: Equal Potential Lines for a Ring of Charge

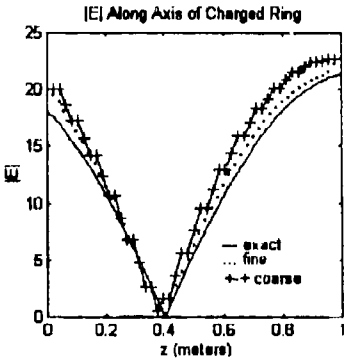

Figure 4: Electric Field magnitude Along the Ring Axis

Example II This example demonstrates EMAG's accuracy in solving a z-invariant problem and illustrates how TGT closely approximates an open boundary. On the left is a cross-sectional potential plot for an infinite line of charge. Note that the lines of equal potential are circles, and are not distorted by the proximity to the TGT boundary as they would be if the Dirichlet boundary were in contact with the computational grid. Note that the source has been placed in the corner of the grid which represents the "worst case" for adverse effect of an "imperfect" open boundary. The graph on the right shows the magnitude of the electric field along a vertical line one meter away from the source as calculated using the analytic solution, EMAG's coarse grid solver, and EMAG's fine grid solver.

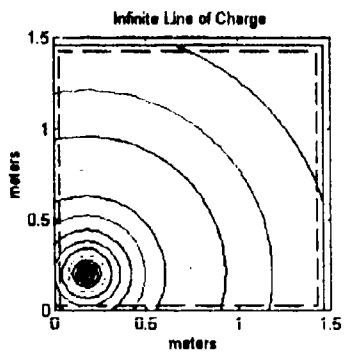

Figure 5: Equal Potential Lines for a Line of Charge

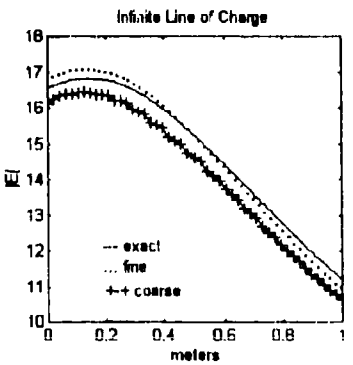

Figure 6: E-field Magnitude vs. Vertical Coordinate

Examples III & IV These examples demonstrate EMAG's utility in solving complicated problems for which there is no analytic solution. The plot on the left depicts the effects of a highly permeable body (a submarine) on the field lines of a uniform magnetic field (relative permeability of the submarine "shell" is 1,000). The plot on the right shows

non-turbulent airflow streamlines around an airplane. (Non-turbulent airflow problems can be described by Poisson equation.)

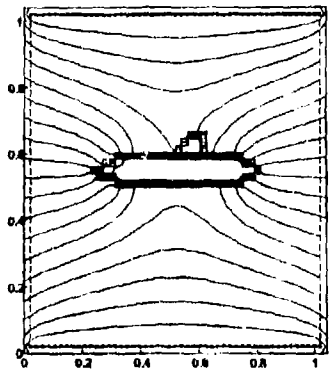

Figure 7: Submarine Perturbing a Uniform Magnetic Field

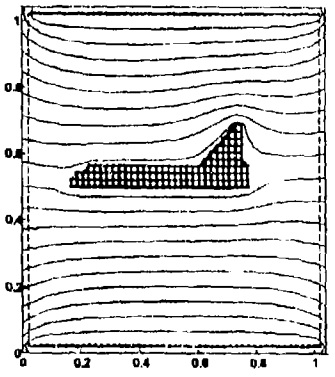

Figure 8: Non-Turbulent Airflow

Example V This final example shows the equal-potential contour plot for two "coupled" microstrip lines at potentials of +1V and -1V. The substrate relative permittivity is 10 and the ground plane is of finite extent (the width of the computational grid). The plot to the left is the mesh-plot of the potential across the grid, with the strips at +1V and -1V clearly visible. Note that the potential along the TOT boundary is not constant, as it would be the case for a Dirichlet boundary. The plot to the right shows the lines of equal potential for the microstrip lines.

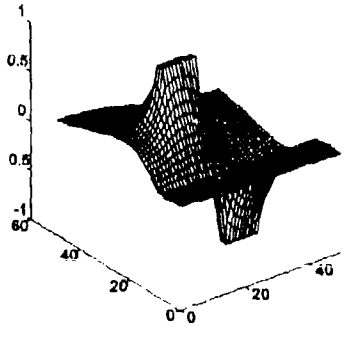

Figure 9: 3-D Mesh Plot of Potential for Coupled Microstrip

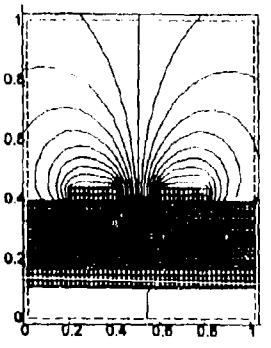

Figure 10: Lines of Equal Potential for Coupled Microstrip

Using Numerical Electromagnetic Code (NEC) to Improve Student Understanding of Monopole Antennas and to Design a Two Element Monopole Array

by Prof. M. E. McKaughan
and LCDR W. M. Randall
USCG Academy

ABSTRACT:

To help a first semester student of electromagnetics visualize radiation patterns or understand reflection coefficients and input impedance is not a challenge for the weak of heart. Some students believe that antennas and electromagnetics are pure magic; others get bogged down in the mathematics; and a few believe these topics are irrelevant to their future as electrical engineers. To dispel this fear of the unknown and to help students understand antennas better, we have developed a unique laboratory experiment for our antennas and propagation class. The experiment uses Numerical Electromagnetic Code (NEC), a network/spectrum analyzer, and an anechoic corner (we could not afford the space or cost of having a full anechoic chamber, so we set up a corner of one of our labs to take field measurements). Last year the idea of having the students design their own antenna array was tested and was a great success. This year the experiment was improved and expanded. It has been divided into three parts:

(A) An introduction to the equipment.
(B) An evaluation of a monopole antenna.
(C) An open ended project to design a two element array with one driven element and one parasitic element. At the conclusion of the project, the arrays are entered into a contest to determine the best design.

The lab combines many of the skills any electrical engineering graduate should possess and helps meet ABET accreditation design requirements. A copy of the lab and ideas for continued improvement are offered.

INTRODUCTION:

Front-to-back ratio, input impedance, matching, reflection coefficient, antenna patterns.... All these terms are foreign to a first semester student of electromagnetics. To help a student visualize radiation patterns or understand reflection coefficients and input impedance is not a challenge for the weak of heart. Some students believe that antennas and electromagnetics are pure magic; others get bogged down in the mathematics, and a few believe these topics are irrelevant to their future as electrical engineers. The Numerical Electromagnetic Code (NEC) software package has provided us with a tool to help the first semester student to understand simple antennas and the terms that describe them. With NEC a student may plot the electric field as a function of ϕ or θ, plot the current vs. length for a variety of frequencies, and examine the impact of frequency on input impedance.

As is the case with many small undergraduate electronic engineering programs, we offer only one course in antennas and propagation. In this course we cover Maxwell's equations, transmission lines, boundary conditions, and antennas. To cover this material in a 16-week semester requires imaginative

tools. At the United States Coast Guard Academy we have developed a laboratory exercise[1] that combines the use of NEC with the use of a network analyzer and an "anechoic corner" (we could not afford the space or cost of having a full anechoic chamber, so we set up a corner of one of our labs to take field measurements). We challenge the students to understand the impact of length, spacing, and frequency on antenna performance and to design a two element Yagi-Uda array. To help in their design process, the students were given several references including **Antennas** by J.D. Kraus, **Antenna Theory, Analysis, and Design** by Constantine Balanis, and **Principles of Radar** from the MIT RADLAB Series.

THE LABORATORY EXPERIMENT:

The laboratory exercise is divided into three parts with a little competition to add some incentive. The three parts are:

(A) An introduction to the equipment.
(B) An evaluation of a monopole antenna. The students are required to plot the input impedances, frequency, current versus length for a variety of frequencies, and the radiation patterns.
(C) An open ended design project to design a two element array with one driven element and one parasitic element. The adjustments to the array are controlled. At the conclusion of the project, the arrays are entered into a contest to determine the best design.

PART A: Equipment Operation

In part (A) the students are introduced to the equipment used for modeling and measuring antenna radiation patterns and antenna driving point impedance.

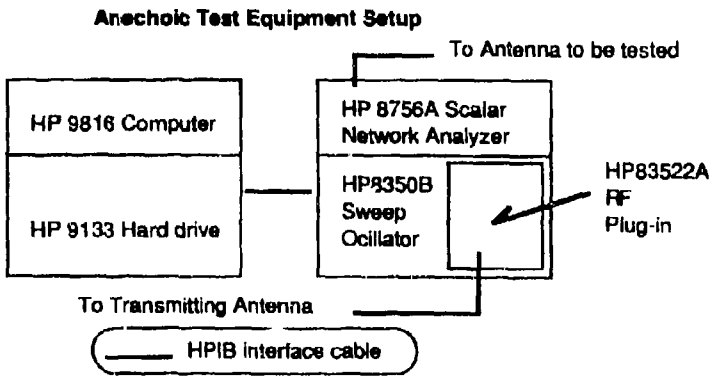

They are introduced to Numerical Electromagnetics Code (NEC) compiled for the Macintosh™, our anechoic corner controlled by an HP 9816 computer, and a Hewlett Packard HP-4195A Network/Spectrum Analyzer for measuring input impedance. Part (A) is not worth many points, but we have found, over the past two years, that if we require the students to write down all of the operating instructions we save ourselves a great deal of time and effort.

[1] A complete copy of our laboratory exercise is included in appendix (A).

Part B: Evaluation of a Monopole Antenna

For this section of the lab the students evaluate a standard commercial antenna. They investigate input impedance as a function of frequency, current vs. length of the antenna for a variety of frequencies, and antenna patterns. For the Coast Guard, the communications antennas in the high frequency (HF) range must work across a full decade (3-30 MHz). This range and the limited space on a ship offer some very real problems. Because of this, we choose a 35 foot whip antenna, one of the Coast Guard's most common HF antennas, for this portion of the lab. The 35' whip is found on every Coast Guard Cutter from the largest polar icebreakers to small coastal buoy tenders. We simplified the model of the antenna by assuming a very thin, constant diameter instead of the tapered design normally seen in use.

Part C: Design a Two Element Array

The last part of the lab is an open ended design project. Design problems are an excellent teaching tool. Using NEC and the anechoic chamber, the students are required to design a two element array with one driven element and one parasitic element for a frequency of 10MHz. They have the option of adjusting the length of both elements and the distance from the origin of the parasitic element. The results are compared using the formula:

$(1-\Gamma)^*[(\text{maximum gain-minimum gain})_{NEC}+(\text{maximum gain-minimum gain})_{AUT}]$

RESULTS:

This lab provides the student to develop their insight of antennas. We did not get very many comments on the first two parts of the lab because of the short answer format we decided to use. We went with short answers to reduce the amount of time they spent on these sections. As we stated above, part (a) was more to save us from answering questions on the equipment than it was to teach them anything about antennas.

After the lab was written and the students had started the work on part (b), we felt that we were missing something. We felt the lab should include some way of looking at the impact of an additional structure. Our solution was to build a small copper house that could be added to the table in the anechoic chamber and have the students look at the pattern with the house "in the way." At first we received comments about the house having no impact. We found that the frequencies students selected for the test were too low. Our solution for next year is to add a summary question to part (b), looking at the impact of the house as a function of frequency.

A second problem we encountered was with our formula to compare the designs.

$(1-\Gamma)^*[(\text{maximum gain-minimum gain})_{NEC}+(\text{maximum gain-minimum gain})_{AUT}]$

The problem was that we did not have enough control over the numbers that went into the formula. In hindsight we should have:

a.) Modified the radiation pattern card in the NEC run file to include the directive gain instead of the power gain and should have used those numbers;

b.) Defined what input impedance should be used to calculate Γ;

c.) Controlled the power supplied to the transmitting antenna in the anechoic chamber.

CONCLUSION:

The insight the students gained from this experiment is best expressed in their own words. Cadet 2/c (a junior) Kevin Carroll wrote, "The knowledge gained in this project helps me dramatically in the understanding some of the material covered in class about chapter 9 (**Electromagnetic Fields & Waves**, by Magdy Iskander)." He added, "I also got an important look at engineering work such as repeat trials and failures....I was able to start putting different concepts together to help solve problems."

We all know that our mistakes are often our best teachers. 2/c Eric Smyth wrote, "We did not keep an accurate log of our design, step by step, in order to follow any trends that might have arisen from our numerical analysis." This is a lesson that we all had to learn. If he has learned it before it impacts anything but his grade, it is a successful lesson.

We will continue to use this lab exercise in our course. One of the most important considerations is to ensure that the students have sufficient time to work through the entire design process with its frustrations and its rewards.

Study of a Monopole Antenna above a Ground Plane & Design of a Two Element Array of Monopole Antennas

Name __ _____ Lab Section & Instructor _____

In this three part laboratory exercise you will learn to:

1.1. (5 points) Use the lab equipment, including:

1.1.1 Numerical Electromagnetics Code (NEC)
1.1.2 Anechoic Chamber w/ Hewlett Packard computer
1.1.3 Network/Spectrum Analyzer

1.2. (30 points)Evaluate a simple antenna:

1.2.1. Look at input impedance as a function of frequency
1.2.2. Look at current as a function of frequency
1.2.3. Look at pattern at the horizon with the test set-up
1.2.4. Look at the pattern as a function of the azimuth angle with NEC
1.2.5. Look at the impact of an additional structure added to the groundplane (either another antenna or some type of box)

1.3. (65 points) Design a two element array using NEC and the anechoic chamber to attain the maximum front to back ratio and the lowest reflection coefficient (G). The formula for comparing the results between groups is:

$(1\text{-}G)^*[(\text{maximum gain-minimum gain})_{NEC}+(\text{maximum gain-minimum gain})_{AUT}]$

First place is worth 5 extra credit points, second place is worth 3 extra credit points, and third place is worth 1 extra credit point.

2.0 REPORTS REQUIRED:

2.1. For parts 1.1 and 1.2. each student is required to answer the questions at the end of this lab handout and to provide the plots requested.

2.2. For part 1.3. a formal write-up is required from each student. The data and results you may share with your partners, but the analysis and conclusions should be your own work. Any assistance a student receives and any references used should be cited. The formal write-up should include: Abstract (5 points), purpose (3 points), theory (20 points), procedure (5 points), data and results (6 points), analysis (20 points), and conclusions (6 points).

3.0 INTRODUCTION:

3.1 You have been provided with a floppy disk which has a copy of this lab and the NEC programs you need to complete this part of the lab. Check to ensure you have the following NEC programs:

Part-A Part-B Part-C

If you are missing any one of these programs, notify your instructor.

3.2 Lab equipment and hard disk space are limited. Please remove your computer files and clean up your antennas when you are not testing. You will be responsible for coordinating among yourselves to ensure that you all have sufficient time to make your measurements.

4.0 PROCEDURES:

4.1 Part A: Equipment Operation

4.1.1 During this part of the lab you will become familiar with the techniques we use for measuring antenna radiation patterns and antenna driving point impedances including:

4.1.1.1 Numerical Electromagnetics Code (NEC). NEC is a program developed by Lawrence Livermore Laboratory for the Department of Defense to model antennas and other structures. The code is designed to calculate the current, and using that current, calculate the electromagnetic field.

4.1.1.2 Anechoic Chamber w/ Hewlett Packard computer for measuring the radiation pattern. The radiation pattern of an antenna tells us something about the spatial electric field about the antenna. This information is useful when one is designing a communication system.

4.1.1.3 Network/Spectrum Analyzer for measuring the driving point impedance. The driving point impedance of an antenna is an important parameter in system design. The driving point impedance can be used to evaluate the reflection coefficient, transmission coefficient, and information about overall system efficiency and bandwidth. If an antenna presents a considerable mismatch, an antenna coupling device may be required.

4.1.2 Operating NEC:

We have a version of NEC that runs on the MAC. After you run NEC please remove input and output files to your floppy. This is a sample NEC program with a description of what the different lines of code mean.

Comment lines - All comments will appear in the output file.	CM 1/4 wave monopole over CM perfect ground
End comments - Must be used	CE
Geometry card - for wire	GW1,25,0.,0.,0.,0.,0., 8.2,.03125
Scaling card - Converts the dimensions from feet to meters.	GS0,0,.3048
End geometry -Must be used	GE1
Perfect ground at Z=0	GN1
Frequency card - in MHz	FR0,1,0,0,30.
Excitation - the feed point	EX0,1,1,0,1.
Radiation Pattern	RP0,91,2,1001,0.,0.,1.,90.
End Card	EN

The only numbers you should have to change as you do this lab are:

A. The last number on the frequency card. As noted above, the frequency is in MHz and you must have a decimal point after the number.

B. the location and length of the parasitic wire in part C. Below is a breakdown of the wire geometry card

GW1, 25, 0., 0., 0., 0., 0., 35., .03125

Wire # | # of segments | X Y Z coordinates of one end | X Y Z coordinates of other end | wire radius

4.1.2.1 Run NEC usi: ; the NEC input file "part-A" and answer the summary questions.

4.1.3 Operating the anechoic chamber:

Operation of the anechoic chamber will be described by your instructor. Careful, precise notes should be taken as they will be needed for parts B and C of this lab.

4.1.4 Operating the Network/Spectrum analyzer:

The network/spectrum analyzer can be used to measure impedances of networks. This is not surprising if you take a moment to consider that impedance is merely the ratio of the voltage to the current. The analyzer will monitor these two parameters and calculate their ratio as a function of frequency. This impedance is then displayed on the screen.

4.1.4.1. Read through the information in the operations manual to become familiar with the techniques for setting up the analyzer and for measuring impedance.
4.1.4.2. Determine the driving point impedance over the specified frequency range for one of the test boxes provided.

4.2 Part B: Evaluate a 35' whip antenna

4.2.1 Antenna Choice: We are working with the 35 foot whip antenna because it is one of the Coast Guard's most common high frequency antennas. You find 35 foot whips on every class of Coast Guard cutter from the 399' WAGB to the 180' WLB.

This part of the lab is designed to:

A. Look at input impedance as a function of frequency
B. Look at current as a function of frequency
C. Look at pattern at the horizon with the test set-up
D. Look at the pattern as a function of the azimuth angle with NEC
E. Look at the impact of an additional structure added to the groundplane (either another antenna or some type of box)

Using the techniques learned in part A of this lab, answer the summary questions at the end of the lab.

4.3 Part C: Design a two element array

Using NEC (input file "Part-C") and the anechoic chamber, design a two element array with one driven element and one parasitic element for a frequency of 10MHz. The formula for comparing the results between groups is:

$(1\text{-}G)*[(\text{maximum gain-mininum gain})_{NEC}+(\text{maximum gain-minimum gain})_{AUT}]$

You may only adjust the length of the driven element and the length and distance from the origin of the parasitic element. Your final report should inc'ude the NEC results needed to show your design approach (not all of your NEC output files), the pattern from the anechoic chamber, and the input impedance measured with the analyzer.

Study of a Monopole Antenna above a Ground Plane & Design of a Two Element Array of Monopole Antennas

Name _____ Lab Section & Instructor _____

Summary Questions for part A:

1. Write the instructions to operate the Hewlett Packard (HP) scalar network analyzer using the HP computer. Provide sufficient detail so that a person not familiar with the lab set-up could obtain an antenna pattern.

2. Write the instructions to operate the Hewlett Packard (HP) network/spectrum analyzer. Provide sufficient detail so that a person not familiar with the lab set-up could obtain an input impedance measurement.

3. For the NEC program (NEC program "Part A") provided (a quarterwave monopole antenna above a perfect ground), how do the results, for the distribution of the current along the antenna from NEC compare with the theoretical values for current distribution: $I=A*\sin[\beta(l-z)]$ where A is a constant, β is the wave number, and l is the length of the antenna.. Plot the calculated and theoretical current distribution.

4. Using the information from NEC, plot the magnitude of the electric field as a function of q. How does that compare with the pattern given in your text.

5. Using the information from NEC, plot the magnitude of the electric field as a function of f. How does that compare with the pattern given in your text.

Summary Questions for part B:

1. How long is the 35 foot whip, in wavelengths, at 2 MHz, 5 MHz, 10MHz, 20 MHz, and 30 MHz.

2. For the NEC program (NEC program "Part B-1") provided (a 35 foot monopole antenna over a perfect ground), plot the magnitude of the current for 2 MHz, 5 MHz, 10MHz, 20 MHz, and 30 MHz.

3. Since we cannot put a 35 foot antenna in the anechoic chamber (please do not try just to prove me wrong) we scale the length of the antennas. The test frequency used in the anechoic chamber is inversely proportional to the scale of the antenna (i.e., if a 21 inch antenna is used to model the 35 foot whip then 40 MHz test frequency is used in place of 2 MHz).

   What are the scaled frequencies for 2 MHz, 5 MHz, 10MHz, 20 MHz, and 30 MHz if we are scaling the antenna by a 20:1 ratio.

4. Antenna plots as a function of ϕ:
   A. Plot the pattern, as a function of ϕ, at 5 MHz (scaled) using the anechoic chamber.
   B. Plot the pattern, as a function of ϕ, at 5 MHz using NEC program "Part B".
   C. Compare the two plots (in writing) and explain if the patterns you get are what is expected. Cite your references.

5. Plot the antenna pattern, as a function of θ, at 5 MHz, 10 MHz, 20MHz, and 30 MHz using NEC program "Part B". Explain (in writing) whether the patterns you get are what is expected. Cite your references.

6. Using the network/spectrum analyzer, measure the impedance of the model antenna as a function of frequency. Scale the frequencies you evaluate so they would be equal, in wave lengths, to a 35 foot whip evaluated from 2 MHz to 25 MHz. Provide the Smith Chart of the plot. Remember that you have to calibrate the meter at the connector on the table.

Finite Difference Analysis with MATLAB and VMAP in Undergraduate Instruction

W. Perry Wheless, Jr. Carolyn S. Wheless
University of Alabama, Tuscaloosa, AL

Abstract— The finite difference method is among the fundamental techniques of computational electromagnetics. Students at The University of Alabama are required to demonstrate basic understanding of finite difference principles by solving project problems which require computer programming. Distraction from the main mathematical concepts is reduced by the use of a high-level interactive software package such as MATLAB™ rather than traditional languages such as Fortran or C. In many cases, however, the visualization of the (electromagnetic) vector fields calculated by MATLAB is better accomplished by exporting the data into the external program VMAP. Plotting 2-d vector fields with VMAP is straightforward and the quality of the field plots is impressive. Example problems are documented here which should be useful to other educators involved in teaching finite difference methods in undergraduate fields courses. The examples are accompanied by ample background discussion and are presented in sufficient detail for direct in-course use.

I. Introduction

Partial differential equations (PDEs) and integral equations (IEs) arise frequently in electromagnetic problems. Steady-state problems with a variety of fields - stress, temperature, flow, as well as electromagnetic - involve Elliptic PDEs of the general form

$$a\frac{\partial^2 U}{\partial x^2} + b\frac{\partial^2 U}{\partial y^2} + c\frac{\partial^2 U}{\partial z^2} + d\frac{\partial U}{\partial x} + e\frac{\partial U}{\partial y} + f\frac{\partial U}{\partial z} + gU = k(x,y,z) \quad (1)$$

where a, b, and c are non-zero and of the same sign. The Poisson and Laplace equations are of this type. In applications, numerical solution of these equations usually is required. The curriculum at most research universities now includes the introduction of electrical engineering undergraduates to basic principles of finite differences (FD), finite elements (FE), and the moment method (MoM) as the most prominent techniques for obtaining reliable numerical solutions. This paper concentrates on the rectangular coordinate system and, specifically, the finite difference method. Two-dimensional example problems from electrostatics are presented, which are suitable for direct in-course use in junior and senior-level fields courses.

Major steps in the finite difference technique include manipulation of the continous governing PDE into a discrete/finite set of linear algebraic equations, and solution of the linear algebraic equation set. This paper excludes detailed discussion of the subject of options and techniques for solution of systems of linear equations: thorough basic treatment is available in numerous texts, including [1] and [2]. Iterative solution remains generally preferable for two and three-dimensional problems, and is employed here.

The so-called Richardson extrapolation [3], [4] is not discussed in this paper, but it is employed in the solution of the second example problem and is worthy of note.

The experience of students with computer-based projects, such as those presented here, is more favorable with a higher-level interactive software package like MATLAB [5] than with traditional languages such as Fortran, Basic, Pascal, or C. Programming is more straightforward with MATLAB, so that distraction from the mathematical concepts of the method is reduced. However, mastering MATLAB graphics for depiction of vector fields is more difficult and time-consuming. This paper features a combination of the programming ease and computational strengths of MATLAB with the convenient and impressive visualization of 2-d vector fields offered by the software package VMAP [6], [7].

II. Finite Difference Method in 2-D Electrostatics

The differential Poisson equation is a point relationship governing potential Φ:

$$-\varepsilon\nabla^2\Phi = \rho_v. \quad (2)$$

For a source-free region of space, Laplace's equa-

tion results; namely,

$$\nabla^2\Phi = 0. \tag{3}$$

For two-dimensional problems, $\Phi = \Phi(x,y)$ and Boundary Conditions (B.C.) must be applied, so

$$\begin{cases} \nabla^2\Phi = \frac{\partial^2\Phi}{\partial x^2} + \frac{\partial^2\Phi}{\partial y^2} = 0 \text{ in } \mathcal{R}\ (\alpha_l \le x \le \alpha_u, \\ \qquad\qquad\qquad\qquad \beta_l \le y \le \beta_u) \\ B.C.: \quad \Phi(x,y) = g(x,y) \text{ on } \mathcal{B} \end{cases} \tag{4}$$

where usually the problem geometry is set so that $\alpha_l = \beta_l = 0$. Eq. 4 is one of the most important PDEs of the Elliptic type.

A given continuous problem is reduced to finite size for computer solution by selecting a set of rectangular mesh points in the solution region, as illustrated in Fig 1. While the spatial separation between nodes with respect to x and y may be different, $\Delta x \neq \Delta y$, it is common practice to take a uniform mesh ($\Delta x = \Delta y = h$) for simple problems. A convenient shorthand notation which gives each node a unique reference 'name' is to use discrete indices i, j so that $\Phi_{i,j} \equiv \Phi(i,j) \equiv \Phi(ih, jh)$. After a grid-point network is set up, the potentials Φ are found are at each mode in the mesh as discussed below, so that the Φ's satisfy Laplace's equation plus the specified boundary conditions on the interfaces and borders in the region.

To compute the potential at the mesh nodes, it is necessary to discretize Laplace's equation by converting it to an equation of differences. The following difference approximations for the first derivative operator are used:

$$\begin{cases} \frac{\partial\Phi}{\partial x} \simeq \frac{\Phi_{i+1,j}-\Phi_{i,j}}{\Delta x} + \mathcal{O}(\Delta x) & \text{forward} \\ \frac{\partial\Phi}{\partial y} \simeq \frac{\Phi_{i,j}-\Phi_{i,j-1}}{\Delta y} + \mathcal{O}(\Delta x) & \text{backward} \\ \frac{\partial\Phi}{\partial x} \simeq \frac{\Phi_{i+1,j}-\Phi_{i-1,j}}{2\Delta x} + \mathcal{O}(\Delta x^2) & \text{central} \end{cases} \tag{5}$$

with the central difference approximation preferred as more accurate because its error is of the order $\Delta x^2 = \Delta y^2 = h^2$ for a uniform mesh, but use of the forward/backward approximations may be necessary near boundaries. The second derivative approximations are

$$\begin{cases} \frac{\partial^2\Phi}{\partial x^2} \simeq \frac{\Phi_{i-1,j}-2\Phi_{i,j}+\Phi_{i+1,j}}{\Delta x^2} + \mathcal{O}(\Delta x^2) \\ \frac{\partial^2\Phi}{\partial y^2} \simeq \frac{\Phi_{i,j-1}-2\Phi_{i,j}+\Phi_{i,j+1}}{\Delta y^2} + \mathcal{O}(\Delta x) \\ \frac{\partial^2\Phi}{\partial x\partial y} \simeq \frac{\Phi_{i+1,j+1}+\Phi_{i-1,j-1}-\Phi_{i+1,j-1}-\Phi_{i-1,j+1}}{4\Delta x\Delta y} \\ \qquad\qquad +\mathcal{O}\left[(\Delta x+\Delta y)^2\right] \end{cases} \tag{6}$$

For a uniform mesh, therefore, the Laplace equation $\nabla^2\Phi = 0$ is converted into

$$\Phi_{i-1,j} + \Phi_{i+1,j} + \Phi_{i,j-1} + \Phi_{i,j+1} - 4\Phi_{i,j} = 0 \tag{7}$$

which is easily remembered by the molecule form suggested in Fig. 2 in a typical mesh. Rearrangement of Eq. 7 gives the difference equation of interest for computer implementation:

$$\Phi_{i,j} = \frac{1}{4}\left(\Phi_{i-1,j} + \Phi_{i+1,j} + \Phi_{i,j-1} + \Phi_{i,j+1}\right). \tag{8}$$

If Eq. 8 is applied at each of the N nodes in a finite difference mesh, clearly the result is a system of N linear algebraic equations. Here, problems with potential Φ specified at all nodes on the boundary (the so-called Dirichlet boundary condition) are considered. As one would expect, a considerable amount of programming effort must be directed toward ensuring correct Φ values for nodes on the boundary, and for carefully computing Φ at interior points neighboring the boundary.

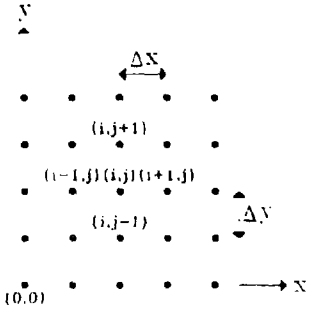

Fig. 1 Typical two-dimensional finite difference mesh, showing node referencing method

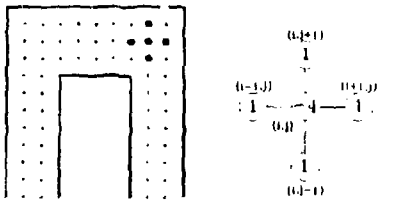

Fig. 2 Basic molecule for discretized Laplace equation

III. Iterative Solution

Iterative Gauss-Siedel solution for Φ at each mesh node, enforcing Eq. 8, is used here. A superscript indicates the iteration number, with superscript "0" denoting the initial values which are arbitrarily assigned (except to the boundary points, which have known value). For example, $\Phi^3(i,j)$ means the potential at node location $x = ih, y = jh$ after the third iteration. The process begins by updating the initial values Φ^0 to those after the first iteration according to

$$\Phi^1_{i,j} = \frac{1}{4}\left(\Phi^0_{i-1,j} + \Phi^0_{i+1,j} + \Phi^0_{i,j-1} + \Phi^0_{i,j+1}\right) \quad (9)$$

and continues repetitively until satisfactory convergence is achieved (that is, the change from one iteration to the next is small enough to satisfy a specified convergence tolerance). Gauss-Siedel iteration merely means that we are using the most recent numbers available in the calculation of the next step.

To improve convergence, the further enhancement of "over-relaxation" [8] can be incorporated into the solution procedure. The RHS of Eq. 7 at the subject node (i,j) is actually some residual and not exactly the target value zero, that is,

$$\Phi_{i-1,j} + \Phi_{i+1,j} + \Phi_{i,j-1} + \Phi_{i,j+1} - 4\Phi_{i,j} = R_{i,j}. \quad (10)$$

For the n-th iteration, applying over-relaxation to Laplace's equation causes Eq. 8 to become

$$\Phi^n_{i,j} = \Phi^{n-1}_{i,j} + wR_{i,j}\left[\frac{1}{4}\left(\Phi^{n-1}_{i-1,j} + \Phi^{n-1}_{i+1,j} + \Phi^{n-1}_{i,j-1} + \Phi^{n-1}_{i,j+1}\right) - \Phi^{n-1}_{i,j}\right], \quad (11)$$

where w is the relaxation parameter. $w > 1$ speeds convergence, but numerical instability results when the value of w is made too large. $w \approx 1.5$ has been found to give good, stable results for Laplace's equation. The first example problem in this paper is solved by explicit Gauss-Siedel iteration without relaxation. Over-relaxation is employed in the second example problem. Once $\Phi(x,y)$ is known, computation of the electric field is straightforward from the basic relationship $\mathbf{E} = -\nabla\Phi$.

Example 1 *To demonstrate the basic method, consider the two-dimensional boundary value problem depicted in Fig. 3. Determine the potential Φ and the electrostatic field $\mathbf{E}$ in the indicated cross-sectional plane with the boundary conditions given in the figure. Note that the top plate is insulated from the other three sides at the upper left and upper right corners, so that it can be maintained at a different potential by the 10 kV dc source. With length = height = L, divide L into four intervals to demonstrate the effectiveness of a low-order solution to this problem. Set the initial potential at all interior nodes to zero. In the computer program, provide for rectangular as well as square geometry and allow user specification of the desired number of intervals.*

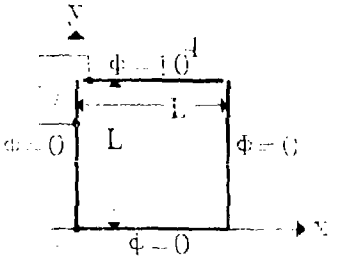

Fig. 3 A two-dimensional boundary value problem

Solution of Example 1: The governing equations are

$$\frac{\partial^2\Phi}{\partial x^2} + \frac{\partial^2\Phi}{\partial y^2} = 0, \tag{12}$$

$$\text{B.C.: } \begin{matrix}\Phi(x,0) = \Phi(0,y) = \Phi(L,y) = 0 \\ \Phi(0 < x < L, L) = 10^4\end{matrix}, \tag{13}$$

and

$$\mathbf{E} = -\nabla\Phi. \tag{14}$$

For 4 intervals, choose $\Delta x = \Delta y = h = \frac{L}{4}$, and number the nodes as indicated in Fig. 4. The interior node starting values are all set to zero, as specified. An explicit Gauss-Siedel interative solution for the potential at each node is obtained.

Students are usually encouraged to take full advantage of symmetry in a given problem, as a way to significantly reduce computer memory requirements and cpu time. However, symmetry is not used to reduce the problem size in this case because the problem is so small.

A representative MATLAB program for solving this problem is listed in Fig. 5. The potential values at the nine interior nodes evolve in the following manner:

$$\begin{bmatrix} (1,3) & (2,3) & (3,3) \\ (1,2) & (2,2) & (3,2) \\ (1,1) & (1,2) & (1,3) \end{bmatrix} \xrightarrow{\text{initial values}} \begin{bmatrix} 0 & 0 & 0 \\ 0 & 0 & 0 \\ 0 & 0 & 0 \end{bmatrix}$$

$$\xrightarrow{\text{iteration 1}} \begin{bmatrix} 2500 & 3750 & 2500 \\ 625 & 1250 & 625 \\ 156 & 156 & 156 \end{bmatrix}$$

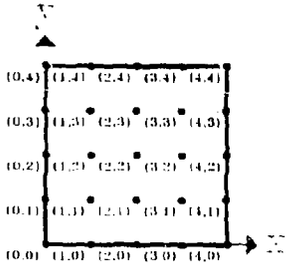

Fig. 4 Node numbering scheme for 2-d boundary value problem

$$\xrightarrow{\text{iteration 5}} \begin{bmatrix} 4207 & 5190 & 4207 \\ 1797 & 2422 & 1797 \\ 675 & 943 & 675 \end{bmatrix}$$

$$\xrightarrow{\text{iteration 25}} \begin{bmatrix} 4286 & 5268 & 4286 \\ 1875 & 2500 & 1875 \\ 714 & 982 & 714 \end{bmatrix}.$$

At later iterations (e.g., iteration 50), the values remain the same as those reported after 25 iterations above. The MATLAB program of Fig. 5 calculates the electric field components at the same nodal points once Φ is determined, and the results are written to file *a:vmap.dat* for export to the separate vector field plotting program VMAP. Apart from a single line of header information, VMAP just requires listing of the E-field x and y components for each of the grid points, proceeding left to right and starting with the node in the lower left hand corner of the figure. The point-by-point data sent to VMAP is shown in Fig. 6, and an electrostatic field depiction from VMAP is presented in Fig. 7.

Example 2 *Fig. 8 shows a cross-sectional view of a shielded long, parallel-plate capacitor with air dielectric. Consider the case* $\frac{w}{d} = 1, \frac{a}{d} = \frac{b}{d} = 3$. *The upper plate potential of* V_0 *in Fig. 8 can be taken to be +1 Volt, with the lower plate then at fixed potential -1 Volt. Calculate and plot the electrostatic field distribution for this problem. What is the capacitance per unit length? Fig. 8 shows a* 7×7 *square grid of finite difference mesh nodes in the first quadrant of the xy plane; the symmetry in the problem is such that a solution in this quadrant solves the complete problem. Note that three metal shield boundaries satisfy Dirichlet conditions (*Φ *is known to be zero at all three boundaries). The x-axis also is at zero potential because it is midway between the capacitor plates.*

Solution of Example 2. Calculation of Φ proceeds in similar fashion to that employed with Example 1, but the requirement for finding the capacitance requires further comment. Taking $\pm V_0 = \pm 1$ V, $C = \frac{Q}{\Delta V} = \frac{Q}{2}$, where Q is the charge on either plate. Q is obtained from Gauss' Law $\oint \mathbf{D} \cdot n dS = Q$, with the integral taken on a surface around the center conductor; using symmetry,

```
fid=fopen('a:vmap.dat','w')
length=input('Input length (m) ... '); height=input('Input height (m) ... ')
disp(' ')
disp(' delta-x and delta-y intervals are the same.')
disp(' calculated from the number of')
disp(' intervals in the larger dimension.')
nint1=input('No. intervals in larger dimension ? ... ')
noit=input('Desired number of iterations ? . . ')
if (length >= height); delta=length/nint1; nint2=height/delta;
  for i=0:nint1;  for j=0:nint2
       if ((j==0) & (i~=0 & (i~=nint1))) phi(j+1,i+1)=10000;
       else phi(j+1,i+1)=0;
end; end; end;
  for x=1:noit; for i=2:(nint1/2)+1; for j=2:nint2
       phi(j,i)=(phi(j-1,i) + phi(j+1,i) + phi(j,i-1) + phi(j,i+1))/4;
       phi(j,nint1-i+2) = phi(j,i);
end; end; end;
fprintf(fid, '%2.0f %2.0f %2.0f ', nint1+1, nint2+1, length);
fprintf(fid, '%2.0f %2.0f %2.0f \n', height, 0, 0);
for j = nint2+1:-1:1; for i = 1:nint1+1;
    if (j==nint2+1); grad(1)=0; grad(2)=phi(j-1,i)/delta;
    elseif (j==1); grad(1)=0; grad(2)=(phi(j,i)-phi(j+1,i))/delta;
    elseif (i==1); grad(1)=phi(j,i+1)/delta; grad(2)=0;
    elseif (i==nint1+1); grad(1)=-phi(j,i-1)/delta; grad(2)=0;
    else; grad(1)=(phi(j,i+1)-phi(j,i-1))/2*delta;
      grad(2)=(phi(j-1,i)-phi(j+1,i))/2*delta; end;
fprintf(fid, '%e  %e \n', grad(1), grad(2));
end; end; end;
if (height > length); delta=height/nint1; nint2=length/delta;
for i=0:nint2; for j=0:nint1;
       if ((j==0) & (i~=0 & (i~=nint2))) phi(j+1,i+1)=10000;
       else phi(j+1,i+1)=0;
end; end; end;
  for x=1:noit; for i=2:(nint2/2)+1; for j=2:nint1;
       phi(j,i)=(phi(j-1,i) + phi(j+1,i) + phi(j,i-1) + phi(j,i+1))/4;
       phi(j,nint2-i+2) = phi(j,i);
  end; end; end;
fprintf(fid, '%2.0f %2.0f %2.0f ', nint2+1, nint1+1, length);
fprintf(fid, '%2.0f %2.0f %2.0f \n', height, 0, 0);
for j = nint1+1:-1:1; for i = 1:nint2+1;
    if (j==nint1+1); grad(1)=0; grad(2)=phi(j-1,i)/delta;
    elseif (j==1); grad(1)=0; grad(2)=(phi(j,i)-phi(j+1,i))/delta;
    elseif (i==1); grad(1)=phi(j,i+1)/delta; grad(2)=0;
    elseif (i==nint2+1); grad(1)=-phi(j,i-1)/delta; grad(2)=0;
    else; grad(1)=(phi(j,i+1)-phi(j,i-1))/2*delta;
          grad(2)=(phi(j-1,i)-phi(j+1,i))/2*delta; end;
fprintf(fid, '%e  %e \n', grad(1), grad(2));
end; end; end;
status=fclose(fid);
```

FIG. 5. *Representative MATLAB program for solving Example 1.*

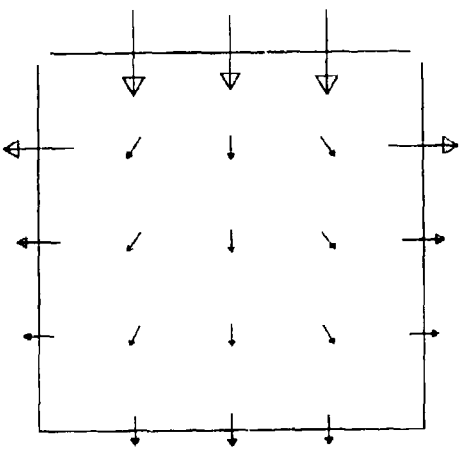

FIG. 6. *Electric field at nodes for Example 1.*

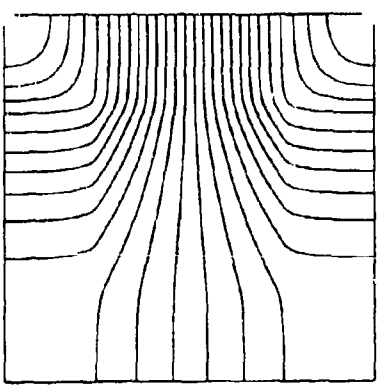

FIG. 7. *Illustration of electrostatic field for Example 1*

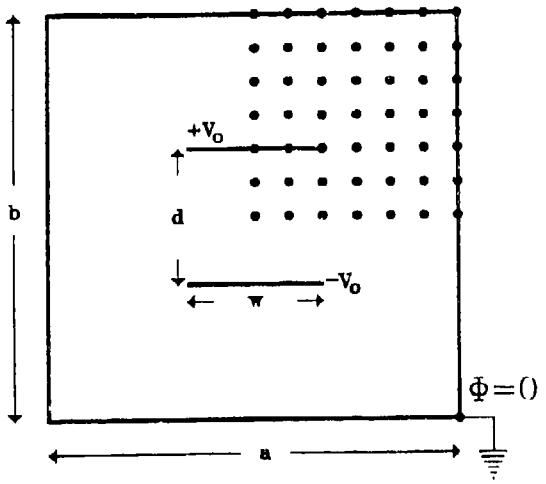

FIG. 8. *Shielded parallel-plate capacitor.*

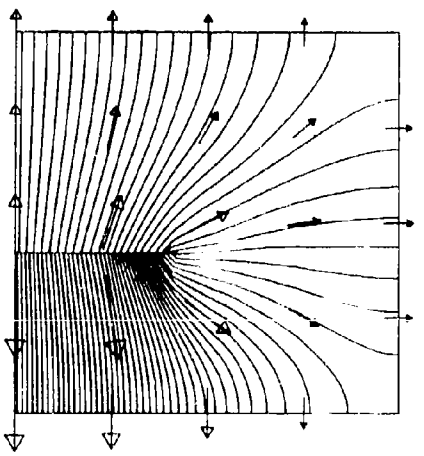

FIG. 9. *Electric field at nodes and field lines for example 2.*

one may double the result of evaluating the integral half-way around the entire conductor. With uniform mesh spacing $\Delta x = \Delta y = h$,

$$\mathbf{D}\cdot\mathbf{n} = D_{normal} = \frac{\varepsilon_0 \Delta\Phi}{h} = \varepsilon_0 \frac{\Phi_2 - \Phi_1}{h}. \quad (15)$$

which simply reduces to $D_{normal} = \varepsilon_0 \frac{\Phi_2}{h}$ if the surface is chosen adjacent to a Dirichlet boundary so that $\Phi_1 = 0$. For a unit length of capacitor, $\ell = 1$, and the integration reduces to summation at the discrete nodes on the 'surface'. Therefore,

$$\frac{C}{\ell} = \frac{\oint \mathbf{D}\cdot\mathbf{n}\,d\hat{\ell}}{2} = \frac{\varepsilon_0}{2}\sum \frac{\Phi_2}{h}. \quad (16)$$

The MATLAB program used to solve this problem is structured similar to the Fortran program in [4]. To solve for $\Phi(x, y)$, it is desirable to have mesh nodes on the capacitor plate. However, because the capacitor plate is taken to be infinitely thin, it is awkward to compute electric field values at nodes precisely on the plate because there are two competing vectors at these nodes. In fact, a 13×13 grid was employed to find Φ and then a 5×5 subset of equispaced nodes was selected to compute $\mathbf{E}$. Nodes on the plate were thus avoided. The resulting field plot from VMAP3[1] is seen in Fig. 9. In addition to an illustration frame which can be turned on/off under user control, VMAP conveniently provides for boundaries. In Fig. 9, note the boundary line which has been drawn to represent the capacitor plate. Most of the electric field lines in Fig. 9 are concentrated toward the lower plate, but the separation between plates is substantial and the shield walls are grounded, with the result that a considerable number of field lines originate on the positive upper capacitor plate and terminate on the shield walls. Finally, the computer analysis concludes that the capacitance per unit length for the situation given in Example 2 is 21.5 ± 0.1 pF.

IV. Conclusions

This paper has demonstrated the feasibility of combining the computational features of MATLAB with the powerful 2-d vector field representation capabilities of VMAP. The combination has proved effective in courses dealing with electromagnetic fields at The University of Alabama.

Two specific examples are documented here that have been found useful in instruction of undergraduates majoring in electrical engineering. Student response to date indicates that computer-based projects involving solution of 2-d electromagnetic field problems are better received by students when MATLAB and VMAP are used rather than traditional programming languages. It appears that exercises of the nature and scope presented here make students more comfortable with numerical methods and increase their interest in more advanced applications. Undergraduates are motivated to learn more about numerical methods and field theory by success with problems such as the ones discussed here.

A significant advantage of the finite difference method is that a number of simple problems are available. Variety can be introduced by the introduction of direct, or other indirect linear equation solution techniques to augment the Gauss-Siedel iteration method used here. Problem complexity can be progressively increased by adding media interface considerations (for instance, placing a dielectric slab between the capacitor plates of Example 2) or treating problems with irregular boundaries so that nodes must occur at un-even intervals. While other educators may devise their own variations and extensions, the examples presented in this paper should remain valuable for teaching the finite difference method in undergraduate fields courses.

[1] VMAP3 presently exists only in Beta test form. One VMAP3 feature is the ability to plot the node vectors and field lines on the same plot.

References

[1] K.E. Atkinson, *An Introduction to Numerical Analysis (Second Edition)*, John Wiley & Sons, New York, NY, 1989.

[2] R.L. Burden and J.D. Faires, *Numerical Analysis (Fourth Edition)*, PWS-Kent Publishing Company, Boston, MA, 1989.

[3] G.I. Marchuk and V.V. Shaidurov, *Difference Methods and Their Extrapolations*, Springer-Verlag, New York, NY, 1983.

[4] R.C. Boonton, Jr., *Computational Methods for Electromagnetics and Microwaves*, John Wiley & Sons, New York, NY, 1992, ch. 1-2.

[5] MATLAB is a registered trademark of The MathWorks, Inc., 24 Prime Park Way, Natick, MA 01760.

[6] D. Kajfez, K. Mahadevan and J.A. Gerald, "PC Software Maps Electromagnetic Fields," *Microwave Journal*, vol. 32, pp. 267-280, May 1989.

[7] D. Kajfez and J.A. Gerald, "PC Program for Plotting the Vector Fields," *Proceedings of the Fourth Annual Review of Progress in Applied Computational Electromagnetics*, Session 4 (pages not numbered), Monterey, CA, March 1988.

[8] G. Carnahan, H.A. Luther and J.O. Wilkes, *Applied Numerical Methods*, John Wiley & Sons, New York, NY, 1969, ch. 5.

SESSION 22:

MICROWAVE

Chair: Richard Booton

Optimization of Microwave Structures using a Parallel TLM Module

Poman P.M. So and Wolfgang J.R. Hoefer

NSERC/MPR Teltech Research Chair in RF Engineering
Department of Electrical and Computer Engineering
University of Victoria
Victoria, British Columbia, V8W 3P6, Canada

Tel: (604) 721-6511/6025
Fax: (604) 721-6230/6052
Email: Poman.So@ECE.UVic.CA

Abstract

The commercially available microwave circuit CAD program OSA90/hope™ has a Datapipe™ feature which allow users to have their own user-defined models for circuit analysis and optimization[i]. We have developed a massively parallel 3D-TLM module for OSA90/hope. This module is more than 30 times faster than its equivalent serial implementation running on a DEC5000/200 workstation. This technique allows optimization of microwave structures using massively parallel 3D-TLM time domain field analysis without the need for equivalent circuits or lookup tables. A comparison of the execution speed of the serial and parallel 3D-TLM simulation modules on three workstations and a DECmpp 12000 have been made. This provides a clear picture of the required computer time for performing 3D-TLM field simulations on various hardware platforms.

Introduction

At present, field theory based microwave circuit CAD/CAM is performed in the frequency domain. This is more a matter of traditional practice and available computer power than a theoretical constraint. This paper reports the first successful combination of a frequency domain CAD program, OSA90/hope, with a massively parallel version of the time domain 3D-TLM electromagnetic field simulator in [1]. This technique increases the speed for the optimization of microwave structures.

The theory of the symmetrical condensed node 3D-TLM[ii] method is well described in [2]. A 3D-TLM mesh is built by cascading a network of these nodes in the three dimensional space. To simulate electromagnetic wave propagation in the mesh, scattering and transfer of voltage impulses must be performed. A massively parallel implementation of this procedure is given in [3]. The parallel 3D-TLM module developed in this paper is divided into 3 programs — two serial and a parallel one; they are *3dtlm-pipe*, *3dtlm-server* and *3dtlm-server*, respectively. *3dtlm-pipe* is executed

i. From now on OSA90/hope and Datapipe will be used for OSA90/hope™ and Datapipe™, respectively

ii. From now on 3D-TLM means symmetrical condensed node 3D-TLM.

locally together with OSA90/hope on a HP 9000 series 700 workstation; *3dtlm-server* is executed remotely on a DEC5000/200 workstation, which is the front-end machine for the DECmpp 12000 massively parallel computer. *3dtlm-server* is executed on a DECmpp 12000 parallel computer. The serial and parallel programs communicate with each other via a few UNIX pipes, [4] and [5]. The serial programs are implemented in C++ to perform serial numerical operations such as discretization of geometrical parameters and computation of discrete Fourier transforms. The parallel program is implemented in MPL, a C like parallel programming language for DECmpp 12000, to perform computer time intensive 3D-TLM simulation.

Datapipe Feature of OSA90/hope

The Datapipe feature of OSA90/hope utilizes UNIX's interprocess communication facility, pipe, to establish high speed data connection between OSA90/hope and one or more external programs. Because UNIX's pipe is used, OSA90/hope can run on its host machine and control external programs running on the same or other machines. This allows CPU time intensive field simulation programs to run on a more powerful computer, such as the DECmpp 12000, [6].

OSA90/hope's Datapipe feature is built on top of the UNIX's pipe and a proprietary communication protocol, [7]. External programs must strictly comply with this protocol in order to work properly with OSA90/hope. Datapipe starts the external program as a child process and sets up a pipe connection between them. Once such a connection is properly established, OSA90/hope and its child process can begin to exchange data. OSA90/hope computes the inputs required by its child process according to their definitions and writes the data to the pipe. The child process reads the inputs from the pipe, carries out the requested calculations, and sends the output back to OSA90/hope. This interaction is illustrated in Figure 1.

The Datapipe feature of OSA90/hope is very good but not yet perfect for our application. One of the problems is that it has to send n requests to its child process if it needs n frequency responses. This is not a problem at all if both OSA90/hope and its child process are executed on the same computer. In our case, OSA90/hope and the parallel 3D-TLM program have to be executed on two different computers which are situated a few kilometers apart. In this case, network delay and overhead cannot be ignored. We have developed *3dtlm-pipe* to circumvent this problem.

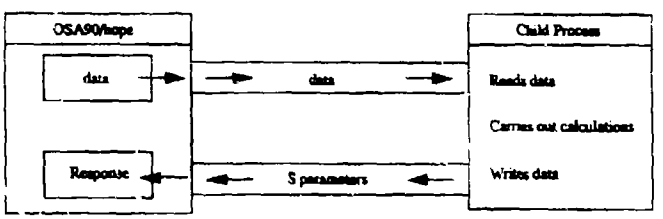

Figure 1 OSA90/hope computes the inputs required by the child process according to their definitions and writes the data to the pipe. The child process reads the inputs from the pipe, carries out the calculations, and sends the output back to OSA90/hope.

The Massively Parallel 3D-TLM Module

The massively parallel 3D-TLM module is divided into 3 programs — two serial and a parallel one; they are *3dtlm-pipe*, *3dtlm-server* and *mpl-server*, respectively. The serial and parallel programs communicate with each other via a few UNIX pipes. The serial programs are implemented in C++ to perform serial numerical operations such as discretization of geometrical parameters and computation of discrete Fourier transforms. The parallel program is implemented in MPL to perform parallel 3D-TLM simulation.

3dtlm-server is based on some source code extracted from the 3D-TLM Simulator in [1]. The graphical user interface module of that program is eliminated. Replacing it is a new module that reads geometrical and control data from the standard input stream; on completion of the requested number of simulations, this module writes time and frequency domain result to the standard output stream if they are requested. The serial 3D-TLM number crunching part of this module is also replaced by a massively parallel program, *mpl-server*, which is based on some source code extracted from [3]. These two programs communicate with each other via UNIX pipes.

3dtlm-pipe is the program that make OSA90/hope and *3dtlm-server*, hence *mpl-server*, work together seamlessly. It provides a fully parameterized 3D-TLM component library for use in microwave circuit analysis and optimization with OSA90/hope. The user of OSA90/hope does not have to interact with *3dtlm-server* at all. He or she only has to work with the Datapipe syntax of OSA90/hope. Currently, the component library of *3dtlm-pipe* includes only three components for the rectangular waveguide environment. They are:

- resonant cavity,
- inductive iris bandpass filter, and
- inductive iris bandpass filter with two tuning screws.

Expanding this library to include more components is an easy task; the prerequisite is a basic knowledge of the 3D-TLM method and the C++ programming language. The interaction of OSA90/hope, *3dtlm-pipe*, *3dtlm-server* and *mpl-server* is depicted in Figure 1.

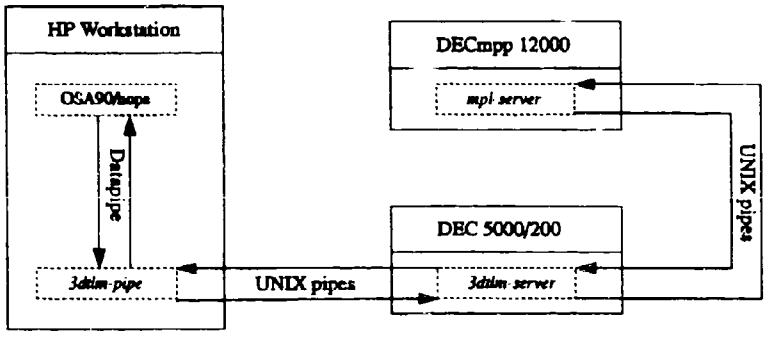

Figure 2 The interaction of OSA90/hope, *3dtlm-pipe*, *3dtlm-server* and *mpl-server*.

Computers	Execution time in seconds
DEC 5000/200 (DECmpp Front-end)	2580
IBM RS6000, Model 350 (42 MHz)	490
HP 9000, Series 7000, Model 755 (99 MHz)	368
DECmpp 12000	75

Table 1 Execution time of the serial and parallel 3D-TLM field simulation modules on three workstations and a parallel computer. The mesh size is 128×64×10; a mesh size of 128×64 in the *xy*-plane represents a full use of a DECmpp 12000 with 8192 processors. The number of time steps and frequency points are both 1000. The execution time shown above include all the network delay due to the piping operations depicted in Figure 1. This provides a clear picture of the required execution time for performing 3D-TLM field simulations on various hardware platforms.

Comparison of Execution Speed of the Serial and Parallel 3D-TLM Simulation Modules

The performance of the parallel 3D-TLM simulation is quite impressive if the mesh dimensions of the problem to be solved are conformed to the processor dimensions of the parallel computer. The processor dimensions of the DECmpp 12000 available to us is 128×64, which gives a total of 8192 processors. Table 1 gives a quantitative comparison of the execution time of the serial and parallel 3D-TLM simulation modules on three workstations and a DECmpp 12000 parallel computer. In the serial cases, there is no *mpl-server* program; the 3D-TLM number crunching operation is done within the *3dtlm-server* program.

Simulation Examples

As a first example, the dimensions of an inductive iris bandpass filter is optimized with the random optimizer of OSA90/hope. The geometry and dimensional parameters of the filter are shown in Figure 3. The design specifications are:

- Center frequency — 33 GHz.
- Pass band — 32.5 to 33.5 GHz.
- Minimize $|S_{11}|$ and maximize $|S_{21}|$ in the passband and vice versa in the stopband

The initial length of the cavities is set to λ_g=11.81mm (rounded off to the nearest Δl). The initial width of the irises is chosen to be small so that the opening will not affect the characteristic of the resonators. The initial response of the filter is shown in Figure 4(a). The random optimizer of OSA90/hope is used to optimize the values of the parameters. The values of the parameters after 30, 60 and 90 simulations are shown in the table in Figure 3; their corresponding responses are shown in Figure 4(b), (c) and (d), respectively. The circuit file used for this optimization process is given in Listing 1.

The second example demonstrates the effect of inserting two tuning screws into the two center cavities of the filter in the above example. The location and depth of insertion are shown in Figure 5 together with the corresponding filter responses.

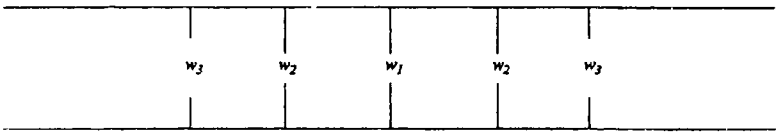

	Initial	30 Random	60 Random	90 Random
w_1 in Δl	2	4	4	4
w_2 in Δl	2	4	6	6
w_3 in Δl	2	10	10	10
d_1 in Δl	23	21	21	21
d_2 in Δl	23	23	22	23

Figure 3 The top view of an inductive iris bandpass filter. The initial and successive optimized values of the parameters are show in the above table, Δl=0.508mm. The desired center frequency is 33 GHz; the passband is from 32.5 GHz to 33.5 GHz. The optimization goal is to have minimum $|S_{11}|$ and maximum $|S_{21}|$ in the passband and vice versa in the stopband.

Circuit Files

The OSA90/hope circuit files for the examples are given in Figure 1.

```
! File: Ind-Iris-Bandpass-Filter-1.ckt
!
Expression
 MF = 9;
 NY = 14;              NX = NY*MF;          NZ = 1;
 Y_DIM = 7.112e-3;
 X_DIM = Y_DIM*MF;
 Z_DIM = NZ*Y_DIM/NY;
 ER = 1.0;             UR = 1.0;            FC = 3;
 N_SIM = 9000;         N_F = 141;
 F_MIN = 26;           F_MAX = 40; ! GHz
 ELEM = 1; ! Inductive iris bandpass filter
 FO = 33;              S11 = 1;             S21 = 2;
 v1 = ? 1   2  6?;
 v2 = ? 1   3  6?;
 v3 = ? 1   5  6?;
 u1 = ?18 21 24?;
 u2 = ?18 23 24?;
 W1 = Y_DIM*floor(v1)*2/NY;
 W2 = Y_DIM*floor(v2)*2/NY;
 W3 = Y_DIM*floor(v3)*2/NY;
 D1 = X_DIM*floor(u1)/NX;
 D2 = X_DIM*floor(u2)/NX;

Datapipe: SIM FILE="3dtlm-pipe"
    N_INPUT =22 INPUT=(NX,NY,NZ,X_DIM,Y_DIM,Z_DIM,
                       ER,UR,FC,N_SIM,N_F,F_MIN,
                       F_MAX,FREQ,ELEM,FO,S11,W1,
                       W2,W3,D1,D2)
    N_OUTPUT=1 OUTPUT=(MAG_S11);

Datapipe: SIM FILE=SAME
    N_INPUT =22 INPUT=(NX,NY,NZ,X_DIM,Y_DIM,Z_DIM
                       ER,UR,FC,N_SIM,N_F,F_MIN,
                       F_MAX,FREQ,ELEM,FO,S21,W1,
                       W2,W3,D1,D2)
    N_OUTPUT=1 OUTPUT=(MAG_S21);

DB_S11 = 20*Log(MAG_S11);
DB_S21 = 20*Log(MAG_S21);

End
```

```
! File: Ind-Iris-Bandpass-Filter-2.ckt
!
Expression
 MF = 9;
 NY = 14;              NX = NY*MF;          NZ = 7;
 Y_DIM = 7.112e-3;
 X_DIM = Y_DIM*MF;
 Z_DIM = NZ*Y_DIM/NY;
 ER = 1.0;             UR = 1.0;            FC = 3;
 N_SIM = 9000;         N_F = 141;
 F_MIN = 26;           F_MAX = 40; ! GHz
 ELEM = 2; ! Inductive iris bandpass filter with
           ! tuning two screws.
 FO = 33;              S11= 1;              S21= 2;
 v1 = ? 1   2  6?;  v2 = ? 1   3  6?; v3 = ? 1 5 6?;
 u1 = ?18 21 24?; u2 = ?18 23 24?;
 sv1= ? 1   2  6?   sv2= ? 1   2  6?
 W1 = Y_DIM*floor(v1)*2/NY;
 W2 = Y_DIM*floor(v2)*2/NY;
 W3 = Y_DIM*floor(v3)*2/NY;
 D1 = X_DIM*floor(u1)/NX;
 D2 = X_DIM*floor(u2)/NX;
 SW1= Y_DIM*floor(sv1)*2/NY;
 SD1= Z_DIM*floor(sv2*NZ;

Datapipe: SIM FILE="3dtlm-pipe"
    N_INPUT =22 INPUT=(NX,NY,NZ,X_DIM,Y_DIM,Z_DIM,
                       ER,UR,FC,N_SIM,N_F,F_MIN,
                       F_MAX,FREQ,ELEM,FO,S11,W1,
                       W2,W3,D1,D2,SW1,SD1)
    N_OUTPUT=1 OUTPUT=(MAG_S11);
Datapipe: SIM FILE=SAME
    N_INPUT =22 INPUT=(NX,NY,NZ,X_DIM,Y_DIM,Z_DIM
                       ER,UR,FC,N_SIM,N_F,F_MIN,
                       F_MAX,FREQ,ELEM,FC,S21,W1,
                       W2,W3,D1,D2,SW1,SD1)
    N_OUTPUT=1 OUTPUT=(MAG_S21);

DB_S11 = 20*Log(MAG_S11);
DB_S21 = 20*Log(MAG_S21);

End
```

Listing 1 The OSA90/hope circuit files for the examples given in this paper. The sweep, specification and control blocks are not shown here. The information for these blocks are given in the previous section.

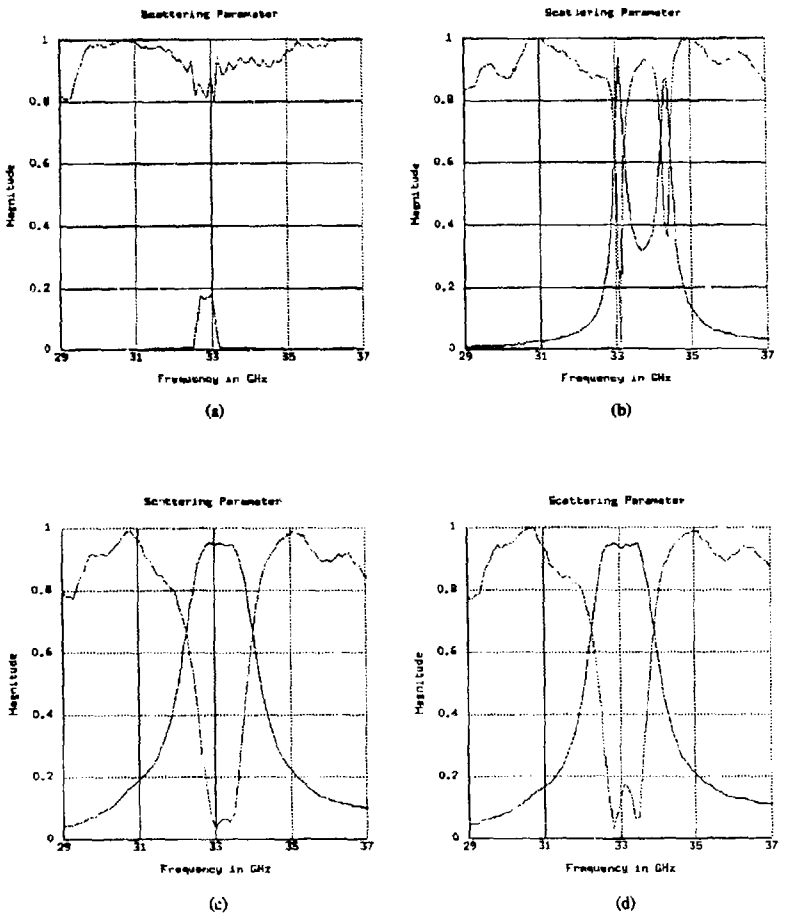

Figure 4 The responses of the inductive iris filter shown in Figure 3. (a) is the initial response; (b), (c) and (d) are the best responses after the 30th, 60th and 90th simulations with parameter values randomly chosen by the random optimizer of OSA90/hope.

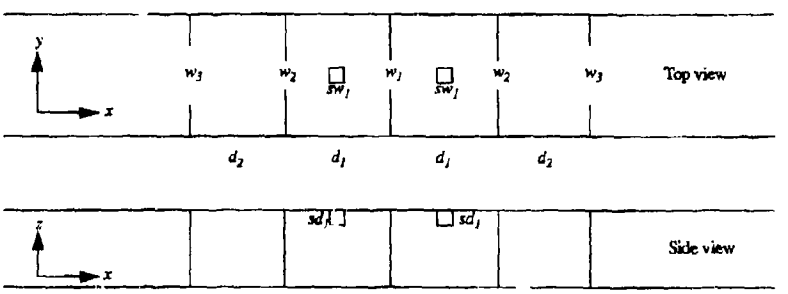

(a)

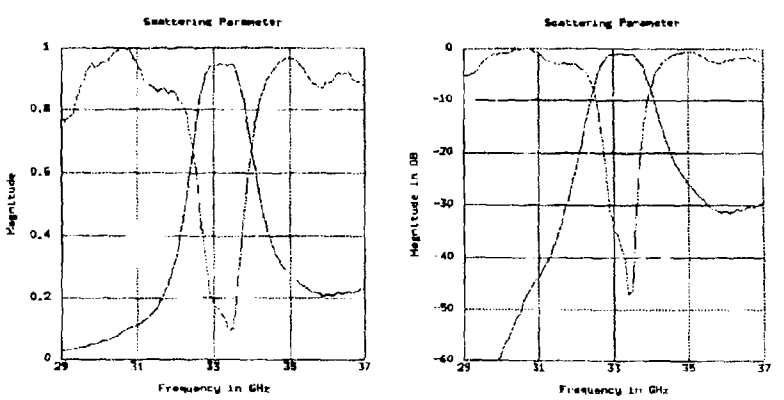

(b)

Figure 5 (a) Top and side views of a rectangular waveguide iris coupled bandpass filter. The values of w_1, w_2, w_3, d_1 and d_2 are given in the last column of the table in Figure 3. sw_1 and sw_1 are both $2\,\Delta l$.
(b) The response of the filter in (a) after 8000 time steps.

Conclusion

A massively parallel 3D-TLM simulation module is developed in this paper to allow the use of the 3D-TLM numerical analysis together with OSA90/hope for microwave circuit analysis and optimization. This massively parallel 3D-TLM module is divided into 3 programs — two serial and a parallel one; they are *3dtlm-pipe*, *3dtlm-server* and *mpl-server*, respectively. The serial and parallel programs communicate with each other via a few UNIX pipes. The serial programs are implemented in C++ to perform serial numerical operations such as discretization of geometrical parameters and computation of discrete Fourier transforms. The parallel program is implemented in MPL to perform computer time intensive 3D-TLM simulation.

A comparison of the execution speed of the serial and parallel 3D-TLM simulation modules on three workstations and a DECmpp 12000 have been made. This provides a clear picture of the required execution time for performing 3D-TLM field simulations on various hardware platforms.

These programs integrate the 3D-TLM method with OSA90/hope via UNIX's pipe. In order to use OSA90/hope to optimize the geometry of microwave circuits, a microwave circuit component library with geometry parameterization in continuous Cartesian coordinates is implemented. Two examples are given to demonstrate the use of *3dtlm-pipe* and its component library.

This massively parallel 3D-TLM module is more than 30 times faster than its equivalent serial implementation running on a DEC5000/200 workstation. Therefore, it is feasible to optimize the geometry of microwave structures using 3D TLM time domain field analysis without the need for equivalent circuits or lookup tables.

References

[1] P.P.M. So and W.J. R. Hoefer, *3D-TLM Time Domain Electromagnetic Wave Simulator for Microwave Circuit Modelling*, IEEE MTT-S, June 1991, Boston, MA.

[2] P. B. Johns, *A Symmetrical Condensed Node for the TLM Method*, IEEE Transactions on Microwave Theory and Techniques, vol. MTT-35, no. 4, pp. 370-377, April 1987.

[3] P.P.M. So, C. Eswarappa and W.J.R. Hoefer, *Transmission Line Matrix Method on Massively Parallel Processor Computers*, in 9th Annual Review of Progress in Applied Computational Electromagnetics Digest, pp.467-474, March 1993, Monterey, CA.

[4] P.P.M. So and W.J.R. Hoefer, *Distributed Computing for Transmission Line Matrix Method*, Second International Workshop on Discrete Time Domain Modelling of Electromagnetic Fields and Networks, October 1993, Berlin Germany.

[5] John J. Valley, *UNIX Programmer's Reference*, 1991, Que.

[6] P.P.M. So, W.J.R. Hoefer, J.W. Bandler, R.M. Biernacki and S.H. Chen, *Hybrid Frequency/Time Domain Field Theory Based CAD of Microwave Circuits*, in 23rd European Microwave Conference Digest, pp.218-219, September 1993, Madrid, Spain.

[7] S.H. Chen, *OSA90/hope™ Version 2.0 User's Manual* — May 1992, Optimization Systems Associates Inc., P.O. Box 8083, Dundas, Ontario, L9H 5E7, Canada.

STATISTICAL RESPONSE OF ENCLOSED SYSTEMS TO HPM ENVIRONMENTS

Richard Holland and Richard St. John
Shield-Rite, Inc., P. O. Box 8250
Albuquerque, NM 87106
(505) 842-6018

Abstract

This paper deals with probabilistic modeling of the EM response of a complex cavity to HMP penetration. Theoretical studies indicate that the field amplitudes squared should have a chi square distribution with two degrees of freedom, but our observations indicate that a log normal fit is empirically better unless the data is first passed through a trend-removing filter. We used this model to simulate cable excitation on an aircraft shell interior. Both the log normal and the chi square field distributions drive the cable in a manner that falls statistically within the experimentally observed spread. However, our simulated response, when filtered for trend removal, does not replicate the observed chi square distribution. There is still an element of autocorrelation missing from our model, which leads to this discrepancy.

Introduction

The problem of as enclosed asset's vulnerability under HPM attack at a frequency where the asset is many (>10) wavelengths on a side (i.e., well overmoded) is all but impossible to treat deterministically. Moreover, even assuming a supercomputer and state-of-the-art finite-volume time-domain (FVTD) code were available, one could logically claim a deterministic solution would be of no value. This claim could be made because, in such a scenario, a 1° rotation of the asset or a 1% shift in frequency would commonly alter the excitation on any given pin or circuit device by 20 dB. Additionally, the interior of a satellite, aircraft, or missile has wiring of almost unbelievable complexity as viewed by a FVTD practitioner who is used to zero or one (two if he is really heroic) conductors passing through each FVTD cell.

Given this dark and bleak outlook on deterministic HPM analysis, the HPM community was thoroughly jolted by the statistical approach worked out by Price and Davis, *et al.*[1] A statistical treatment, unlike a deterministic treatment, actually thrives on complexity. (In many situations, the statistical confidence interval depends on the *inverse* square root of the amount of data provided.) This statistical approach develops a probability density distribution model for the fields inside an asset which is not a hair-trigger function of frequency, attack angle, wiring configuration, or any other parameter.

This work was supported by the U. S. Air Force Phillips Laboratory under Contract F29601-93-C-0047.

A highly elegant derivation accompanied this work, which led to the conclusion that the distribution of the field (squared) versus frequency, projected along any axis, would be chi square with two degrees of freedom; i.e., exponential.[1] This distribution function is characterized by a single parameter μ, the mean value. There is a strong implication that the identical distribution (with the identical μ) would also categorize the field as a function of internal position, attack angle, sensor orientation, or almost any other independent variable one would want to consider.

In order to test the Price-Davis field model and apply it to internal conductor drive, we studied the EMPTAC (727-like) aircraft data for internal fields, surface skin currents, and internal cable currents under illumination by the Ellipticus antenna at frequencies swept from .1 to 1.0 GHz. Data was also provided for frequency sweeps from 3 MHz to .1 GHz, but general belief is that at least some of this low-frequency data is beneath the noise floor. For the low-frequency sweep, the overmoding assumption of the statistical model is not met, and there is even evidence that the EMPTAC fuselage responds like waveguide below cutoff.

It quickly became apparent that the Price and Davis chi square distribution match between experiment and theory was less pristine than we had believed. In particular, their data had been passed through a logarithmic filter designed to factor out a certain amount of "trend" before being compared with experiment. The unfiltered data we saw from the EMPTAC had a distribution much more like log normal than chi square. This same phenomenon, it turned out, had been observed by Price and Davis, who were then kind enough to give us an idea of the filtering which was necessary.

Data Manipulation and Trend Removal

Figure 1 illustrates a low-frequency sweep measurement of $|H_x|^2$, internal to the EMPTAC, where x lies along the aircraft axis. The lower curve with a lot of structure is the actual measured data. The "massage" given this data consists of removing the "trend". We obtain the trend by convolving the raw data with a truncated $(\sin x)/x$ filter function. Figure 2 shows a filter function which takes a 91 point running average of the data. All filtered data we will discuss here was obtained by convolution with this function. Note that we retain the main pulse of the $(\sin x)/x$ function, and also the first negative and positive excursions on each side. If each point in the Figure 1 sweep were separated (in the time domain) by one second from every other point, Figure 2 would correspond to a low pass filter with a cutoff frequency of .033 Hz:

$$f_\omega = \frac{3}{[(N_o - 1)/2] \cdot 2\Delta t} \qquad (1)$$

We tested values of N_o from 3 to 9999, and empirically found that 91 was an optimum value. This rather arbitrary choice does not aesthetically please us, and we do not expect it to please you.

There is one additional twist to our data massage: The filtered data will not be positive definite if the trend is removed in the usual way. Consequently, each data point is passed through a ln () operator before the filtering convolution. Thus, the convolved or filtered data will be negative at some points, but if the result is then passed through an exp() operator, all filtered results will again be positive.

The somewhat smoother overlaid lower curve in Figure 1 is the trend, based on $N_o = 91$, and application of the restoring exp() operator. The upper squiggle in this figure is the result of subtracting the trend from the raw data, and then exponentiating the difference. This squiggle should (and does) fluctuate around 1. If your think for a moment, you will realize (the upper squiggle) x (the trend) will give back the raw data.

We now digress a moment, and indicate our rationale for selecting 91 as N_o. Let us take the $\{|H_x|^2\}$ array and create an associated ln array: $\{\ln |H_x|^2\}$. It can be shown that, if the $\{|H_x|^2\}$ array has been filtered just enough to make it chi square, the associated ln array will have a variance of $\pi^2/6$. Empirically, we have found the $N_o = 91$ corresponds to "just enough"; the ln array associated with the output of this filtering operation has $\sigma_{(\ln H)}^2$ very close to $\pi^2/6$. (The unfiltered array of Figure 1 started with $\sigma_{(\ln H)}^2$ about 1.90 times $\pi^2/6$.)

A probability plot is sort of a visual method for discovering the goodness of fit of a given data set to a proposed distribution model. Roughly speaking, one evaluates the measured cumulative distribution along the x axis and the model's predicted cumulative distribution along the y axis. If the model matches the data perfectly, the resulting probability plot is a straight line at 45°.

We first attempted a normal fit to the unfiltered data. The data was normalized to a standard distribution by the transformation

$$z_i = \frac{|H_x|^2 - \mu}{\sigma} \qquad (2)$$

The probability plot of Figure 3 shows that this fit does not work. We next attempted a log normal fit. This is done by replacing $|H_x|^2$ in Eq. (2) with $\ln |H_x|^2$. Figure 4 shows this model to yield a fairly good probability plot, at least near the critical midpoint where confidence limits become very narrow. (The unillustrated low-frequency counterpart of Figure 4 has an even better fit.) Several other normally based field distributions were considered: $|H_x|^2$ of Eq. (2) was replaced with $(\ln|H_x|^2)^\alpha$ and $\ln(\ln |H_x|^2)$. Neither of these (or other) variants gave improved probability plots.

We also attempted a chi square fit to the unfiltered data. In this case, we made no attempt to normalize the data in the sense of applying some sort of chi square transformation analogous to Eq. (2). The resulting probability plot (Figure 5) does not speak well for the chi square model. (Where σ_N^2 appears in figures or their captions, it denotes the variance of the associated ln array normalized by $\pi^2/6$.) Probability plots were also constructed from the filtered data sets. In general, the normal plot is still very

far off, and the log normal plot is still quite reasonable. However, the probability plot for matching the filtered data to a chi square fit is excellent (Figure 6).

Our problem with this procedure is that we find it really hard to attach a physical meaning to the filtering process. Also, for the synthesis operation, we are totally unformed about the trend which must be folded back into the chi square distribution to drive circuit analysis software with the proper statistical distribution.

In addition to free field data, analysis was also performed on skin current data of the EMPTAC interior. Figure 7 shows an 8-way overlay of six free-field and two skin-current cumulative distributions. (These measuremants pertain to the high-frequency sweep: There the overmoding assumption is met, and hence, EM energy is assumed to be homogeneously and isotropically distributed throughout the EMPTAC interior.) Figure 7 confirms this condition: All fields and surface currents are more or less equal, irrespective of probe orientation or location. (The surface magnetic field H_ϕ, corresponding to circumferential skin current, is slightly depressed. This is not surprising, as the EMPTAC is driven with an axially polarized field, and the internal overmoding may be somewhat shy of complete.)

The EMPTAC cable currents were also scrutinized. Unfiltered cable current distributions also proved to be log normal. Filtered cable currents ($N_o = 91$) came out chi square (see Figure 8). This result was a bit of a surprise, as it is not anticipated by any theoretical work which we have seen.

There is one final necessary observational comment concerning all the cumulative probability distributions: Except for the cable current distribution plots, all the high-frequency data appears to have a longer tail from 0 to .5 than from .5 to 1.0 (see Figure 7). All the low-frequency data and the high-frequency cable current data, on the other hand, turned out to have the two tails about equal in length. This observation may be extremely significant. In particular, it may imply the cable currents, even at high-frequencies, have a higher degree of randomization (look more like noise) than the high-frequency field measurements.

More specifically, it may mean that the upper tail of the cable current distribution is systematically longer than that of the field magnitude distribution. This possibility is highly significant, as it is the upper tail of the cable current distribution that would be the proximate and critical factor for HPM-induced system failure.

This deduction is not apparent solely from study of the probability plots, and may serve as a cautionary signal against relying excessively on the probability plot concept to evaluate system survivability. Probability plots do not necessarily provide critical information about possible distinguishing differences in distributional tails.

Up to now, we have changed distribution models by modifying the independent variable in Eq. (2). However, any function which starts at 0, ends at 1, and never has a negative derivative will work as a cumulative probability distribution. The gaussian cumulative distribution is often denoted $P(x)$. Thus, $P(x)^{\alpha}$ for any $\alpha > 0$ is also a legitimate cumulative probability distribution. Any power series of $P(x)$, where the coefficients of the power series add up to unity, is also a mathematically permitted cumulative probability distribution. Even more generalized distributions may be created by adding a series of sin functions, $\sum a_n \sin n\pi p$, to the power series of gaussian distribution.

We have found that nearly all the EMPTAC data can be described by a cumulative distribution function of the form

$$P_{in}(x) = P_{in}(x) + .1(P_{in}(x) - P_{in}(x)^{10}) + \sum_{n=1}^{3} a_n \sin n\pi P_{in}(x) \qquad (3)$$

where $P_{in}(x)$ is the cumulative log normal distribution. (Equation (3) requires at least one iteration on $P_{in}(x)$ for approximate evaluation of the Fourier correction.) Note that the coefficients of this $P_{in}(x)$ power series add up to unity. The need for the curious correcting term involving $P_{in}(x)^{10}$ can be understood by reference to Figure 7. One may see that this figure is not symmetric about $p = .5$ but rather has a truncated upper tail. The $P_{in}(x)^{10}$ term is almost 0 until $P_{in}(x)$ becomes close to unity at which time the $P_{in}(x)^{10}$ term itself becomes near unity. In this way we provide a method for modeling the upper tail truncation.

We shall next discuss the need and nature of the Fourier corrective term in this model and shall also illustrate the shortcomings of the other log-normal-based models we have attempted to use. Let us first reconsider the consequences of using an unmodified log normal model. Figure 9 shows the 90% confidence limits on the cumulative probability distributions of the internal field $|H_i|^2$. This figure also shows that the measured data does not lie completely inside the 90% confidence limits of the model. We now replot the 90% confidence limits based on the enhanced Eq. (3) model. Figure 10 show that sin series correction alters the model enough to make the entire $|H_i|^2$ sweep lie entirely within the new limits. Figure 11 shows the probability excursion of the sweep from the log normal fit without the Fourier series corrective term. It also the corrective term itself.

Let us lastly, examine the cable current measurements. Figure 12, shows that the cable current can be fit fairly well with a simple log normal model. Figure 13 illustrates the superior results of modeling the cable current by a sin-series enhanced distribution of the form of Eq. (3). While there remains some residual excursion in the enhanced fit, the excursion fr[illegible] at the region of the plot where response is very small. Thus, this excursion does [illegible] have detrimental implications for the enhanced drive model.

Circuit Drive

We here attempted to match the output of a model consisting of a network of segmented cables and the response experimentally observed on cables at the EMPTAC. Our model allows the network to be driven by arbitrary fields at each segment. It yields current or voltage at any place on the cable which may be directly compared to the measurements made by a network analyzer. The network model is calculated in the frequency domain and is composed of up to 200 sections of transmission-line segments; defining equations employ continuity of the current and voltage at each junction and end conditions relating the current and voltage through an impedance.

The line response and drivers are coherent over space and frequency at low frequencies. To mimic the random behavior seen in the EMPTAC data, the excitation over the segments and from one frequency to the next becomes is coherent at intermediate and higher frequencies. At the highest frequencies, the s nent drives are random with respect to each other. To achieve this effect, each seg t is driven with a field of the form

$$E_i = [A(\omega,n)\sin(\omega t) + B(\omega,n)\cos(\omega t)]\cos\theta(\omega,n) \qquad (4)$$

The amplitudes of the sine and cosine terms can be determined from an arbitrary distribution. A log-normal distribution is currently used for $A(\omega,n)$ and $B(\omega,n)$,

$$C(\omega,n) = e^{\mu+\sigma x(\omega,n)} \qquad (5)$$

where μ is the observed average and σ is the observed standard deviation of the logarithms of the observed EMPTAC field amplitudes (μ = -9.0 and σ = .89).

The distribution parameter $x(\omega,n)$ is related to the inverse of the normal distribution and contains parameters to force a frequency- and location-dependent coherence. In the high-frequency limit, there is no spatial or frequency relation between the parameters, and each is determined solely by the chosen random distribution. For a normal distribution and a randomly chosen number R between 0 and 1, $x_{\omega n}$ is found from

$$R = \frac{1}{\sqrt{2\pi}} \int_{-\infty}^{x_{\omega n}} e^{-t^2/2}\,dt \qquad (6)$$

The spatial and frequency coherence is added through a linear combination of dimensionless variables. The spatial correlation has the form

$$x_{space} = \frac{\frac{\lambda}{\Delta l} x_{-1} + f_{space} x_{fm}}{\frac{\lambda}{\Delta l} + f_{space}} \tag{7}$$

where x_{-1} is the value of x for the adjacent line segment, Δl is the separation between segments, and f_{space} is a number near 10. Varying f_{space} between 0 and infinity allows $x(\omega,n)$ to vary from exactly that used by the adjacent segment to a value determined solely by the random distribution. Similarly, the correlation between frequencies is found from

$$x_{freq} = \frac{x_f \frac{\lambda^2}{L\Delta\lambda} + x_{space} f_{freq}}{\frac{\lambda^2}{L\Delta\lambda} + f_{freq}} \tag{8}$$

where x_f is the x for the segment at the last frequency, L is the linear dimension of the network, and $\Delta\lambda$ is the change in the wavelength from one frequency to the next. The actual $x(\omega,n)$ appearing in Eq. (5) is x_{freq} of Eq.(8).

The f_{freq} and $\frac{\lambda^2}{L\Delta\lambda}$ parameters are used to give a frequency-dependent correlation between the $x(\omega,n)$ values at different frequencies. Whenever the wavelength is large compared to the linear dimension of the network or when the wavelength is large compared to the change in the wavelength, the $x(\omega,n)$ parameter is similar to that used at the previous frequency. Similarly, varying f_{freq} between 0 and infinity allows the $x(\omega,n)$ to vary from exactly that used at the previous frequency to the random value resulting from the spatial-coherence calculation.

The $\theta(\omega,n)$ polarization angle in Eq. (4) is determined from a similar procedure, except that the random part of all angles are allowed to be uniformly distributed over all possible directions.

Cable Responses

Previously, we have shown that the currents have unfiltered distributions that are approximately log normal (see Figure 12). It was not obvious what the previously described 91-point trend-removing filter would do to these observed distributions. Figure 8 demonstrates that this filter transforms the observed cable current distributions from log normal to chi square (with two degrees of freedom), just as it transformed the field distributions. The physics and mathematics underlying this result for the cable currents is unclear; in fact, this result was unexpected.

We first simulated the cable drive as described in the previous section of this report. The first run was made with x_{lim} of Eq. (6) log normally distributed. Both f_{space} and f_{freq} were selected to be 100 (minimal coherence), and x_{space} and x_{freq} were evaluated as in Eqs. (7) and (8). For this run, both ends of the cable were terminated in 30 Ω.

Figure 14 shows the resulting cable current response with and without the trend removed. Figure 15 show that, unlike the real data, this cable simulation does not reduce the chi square when the trend is removed, but rather stays log-normal like. This is a distribution problem which we are going to have to fix in our coherence model: An incorrect cable current correlation with respect to frequency is probably not intrinsically serious, but it implies the model's spatial cable current correlation will also be incorrect. The latter deficiency will have all kinds of negative ramifications on our simulation model.

Figure 16 shows that the model's unfiltered cumulative distribution for the cable currents does lie within the experimental scatter when the *f*s are set to 100 and x_{lim} has a log normal distribution.

The next run was made with x_{lim} having a χ^2 distribution in the drive definition. The f_{space} and f_{freq} parameters were here selected to be both 30 (moderate coherence); x_{space} and x_{freq} were evaluated as in the log normal test and again were not averaged. Again, both ends of the cable model terminated in 30 Ω.

Figure 17 shows the resulting cable current verses frequency with and without the trend removed. There is no subjective difference between the log normal and the chi square cable response. Figure 18, shows that the χ^2 cable drive produces a cable-current simulated distribution which looks even more log normal than th se produced by log normal drive. This underlines the previously made point that we have a problem with our simulation *vis-a-vi* coherence.

Figures 19 shows, however, that the model's unfiltered cumulative distribution for the cable currents again lies within the experimental scatter if the *f*s are set to 10 and x_{lim} has a χ^2 distribution.

Summary and Conclusions

We have tried a number of different concepts to model the statistical distribution of the fields inside the EMPTAC enclosure when illuminated by the Ellipticus antenna. There models have included normal, log normal (x replaced by ln x), modified log normal (x replaced by ln (ln x)^a, log log normal (x replaced by ln (ln x)), and chi square. They have also included power series of the log normal distribution, $\Sigma a_n P_{ln}(x)^n$ where $\Sigma a_n = 1$, and modifications to the power series distribution where trigonometric terms of the form $\Sigma b_n \sin(m\pi p)$ are added to the normal power series. Power series variations of the other options, such as of the normal model have also been investigated. Excluding the esoteric trigonometrically-enhanced forms, the log normal power series fit best matches raw data. This occurs with the coefficient of the first power being 1.1, of the tenth power being -.1, and of all other powers being 0. The next best match to raw data taken directly

from the probes is the simple log normal model.

There is a very strong theoretical evidence that this distribution should be chi square of freedom with two degrees not log normal or some variant thereof. We, however, have found it necessary to pass the raw data through a rather *ad hoc* trend-removing filter to extract this theoretical chi square distribution. This is not a pleasing denouement, as it provides no help in telling us how to insert a trend back into a randomly generated chi square field distribution for use in driving the circuitry of an asset whose response to at best we wish to simulate.

There is also a problem with the upper tail of a log normal distribution, as it has a propensity for yielding occasional outliers of absurdly great amplitude. (The chi square distribution does not do this. The log normal power series with a_1 of 1.1 and a_{10} of -.1 *may* also have the impossible outliers inhibited, although this supposition has not been checked.)

It also may be possible to merge a log normal distribution into a chi square distribution at the upper amplitude end, although this idea has also not yet been investigated. Surface currents induced on the EMPTAC interior look very much like free-field measurements of H, although there is a tendency for surface reflection to have a doubling effect on H_{tan} right at the conductor walls. Even observed currents on cables interior to the EMPTAC have response distribution which look log normal in the raw form, but to turn chi square upon judicious trend removal. (The chi square fit of filtered cable current distributions was not expected, and has not been theoretically anticipated or explained.)

There is one, apparently major, miscomprehension about statistical electromagnetics. When one samples a waveform (field or current) and places the results in scoring bins, the coherence, autocorrelation, and spectral energy distribution information are all destroyed. A statistical representation of a waveform does not, in itself permit reconstruction of that waveform. This coherence information destruction has had some negative impact on our statistical-drive and cable-response modeling effort.

In particular, we have made attempts to simulate cable drive using both log normal and chi square models for the field distribution used to drive the cabling. In both cases, the unfiltered cable response data of this simulation is log normal. (Even a chi square field distribution model result in a log normal simulated cable response.) However, if these simulated cable responses are screened through a trend-removing filter, they never reveal a masked chi square behavior. In this sense, our cable drive model, thus, fails to replicate a feature we know the cable currents of the real world posses. It is our conception that this failure occurs because we have destroyed the coherence information of the real world by our statistical binning, and never restored it adequately in our several modeling attempts. This is a problem of real concern at present, and will have to be fixed before statistical EM methodology comes to maturity as a tool for understanding (and simulating) asset response to an HPM threat.

Let us now close on a highly positive note. For a given cable in the EMPTAC, there is a position-dependent spread factor in current response of about five. If the EMPTAC cable drive simulation is overlaid on a graph showing this empirical spread, the simulated distribution lies completely inside this experimentally observed spread. We saw this same pleasing result whether the statistical field drive model was log normal or chi square.

Acknowledgement

In this report, we have made some critical statements about the work of our mentors, Bob Price and Burt Davis. We wish to make it totally clear, however, that without their efforts, the philosophy behind this effort would never have occurred to us, and without their personal willingness to explain new concepts to us, we would never have been able to implement this study.

REFERENCES:

1. Price, R. H., *et al*, "Determination of the Statistical Distribution of Electromagnetic Field Amplitudes in Complex Cavities," 88JAL129, JAYCOR, 1 June 1988.

2. Zelen, M. and N. C. Severo, "Probability Functions," pp. 925-995 (see especially p. 933), in **Handbook of Mathematical Functions**, M. Abramowitz and I. A. Stegun, editors, National Bureau of Standards, Applied Mathematics Series, No. 55, Washington, DC, June 1964.

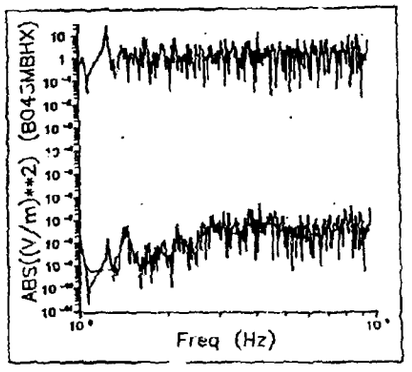

Figure 1. Bottom curves: measured high-frequency raw-data free-field $|H_x|^2$ inside the EMPTAC middle bay, and $|H_x|^2$ trend. Top curve: $|H_x|^2$ with the trend factored out.

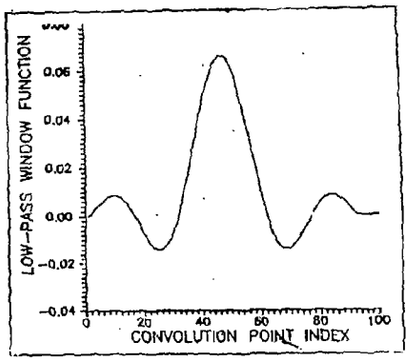

Figure 2. 91-point low-pass filter function used to separate the trend from the raw data by convolution. This filter corresponds to $f_o = .033$ Hz.

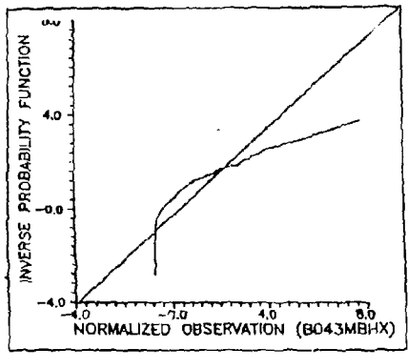

Figure 3. Probability plot for fitting the observed, unfiltered high-frequency $|H_x|^2$ to a gaussian distribution. Essentially, there is no fit.

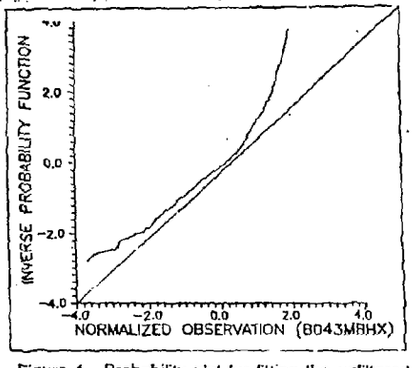

Figure 4. Probability plot for fitting the unfiltered high-frequency $|H_x|^2$ to a log normal distribution. This fit is not bad at the graph midpoint where the 90% confidence limits are tight. The raw data for this plot was characterized by a $[\ln |H_x|^2)$ array with a variance of 3.158.

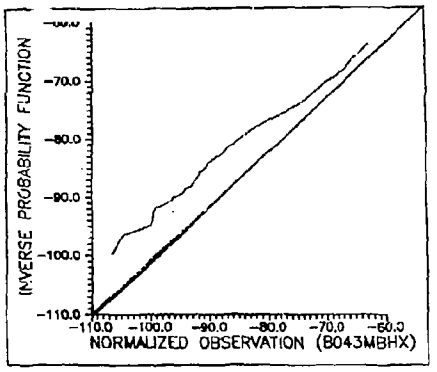

Figure 5. Probability plot for fitting the unfiltered high-frequency $|H_i|^2$ to a chi square distribution. The fit of this model is considerably poorer than that of the log-normal model. For this data set, σ_N^2 is 1.919.

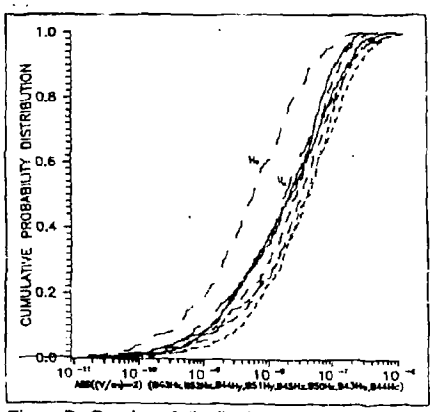

Figure 7. Overlay of distributions for both scans of the free field $|H_i|^2$, i = 1 - 3, at an interior point, plus the distributions for the axial (H_a) and the circumferential (H_c) surface magnetic fields. The tails from 0 to .5 are significantly longer than the tails from .5 to 1 on these distribution plots.

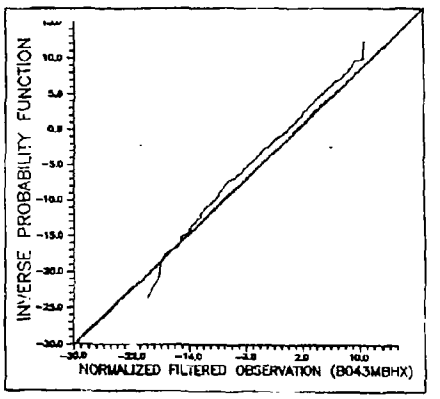

Figure 6. Probability plot for fitting the filtered high-frequency $|H_i|^2$ to a chi square distribution. The fit of this model is excellent, but the rationale for filtering is unclear. For the filtered data set plotted here, σ_N^2 is .8403.

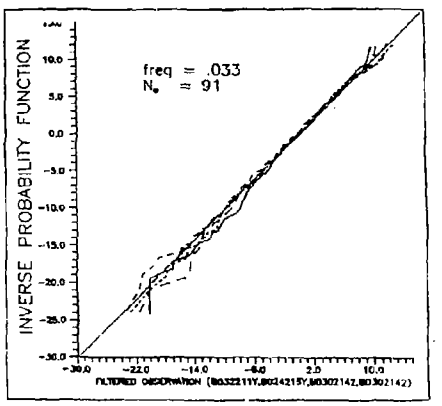

Figure 8. The observed cable currents have a χ^2 distribution after trend-removing filtering.

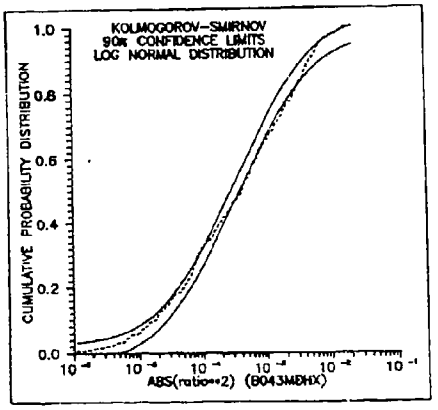

Figure 9. Cumulative probability distribution for the EMPTAC free-field measurement $|H_x|^2$. Also shown on this plot are the Kolmogorov-Smirnov 90% confidence limits for the assumption that this distribution is log normal. This data set has some excursion from the assumed distribution.

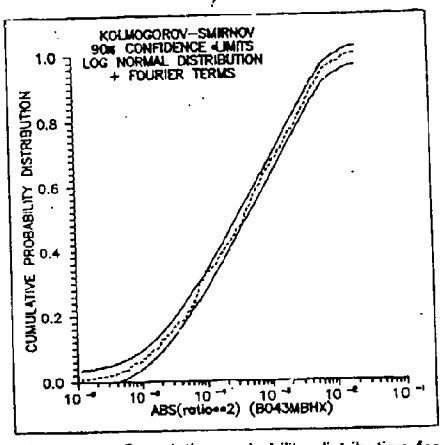

Figure 10. Cumulative probability distribution for the EMPTAC free-field $|H_x|^2$. Also shown are the Kolmogorov-Smirnov 90% confidence limits for the assumption that this distribution is log normal with a Fourier correction . The assumed distribution passes the Kolmogorov-Smirnov test.

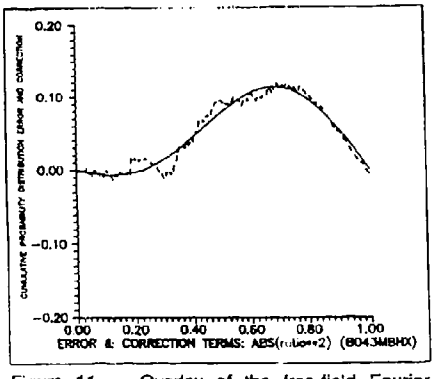

Figure 11. Overlay of the free-field Fourier correction (solid line) and the discrepancy between the data and the log normal power series distribution (solid line) to be nulled out by the Fourier correction. The confidence limits in Fig. 10 include this correction to the assumed $|H_x|^2$ distribution.

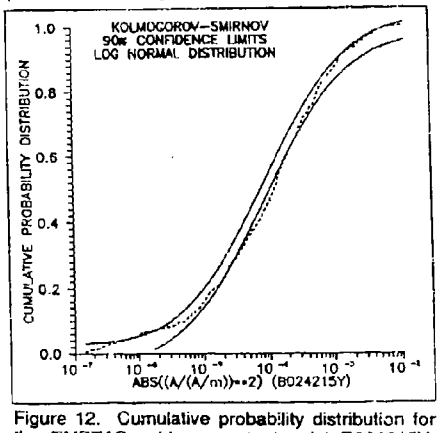

Figure 12. Cumulative probability distribution for the EMPTAC cable current at point B024215Y. Also shown on this plot are the Kolmogorov-Smirnov 90% confidence limits for the assumption that this distribution is log normal. The data is in some disagreement with the assumed distribution.

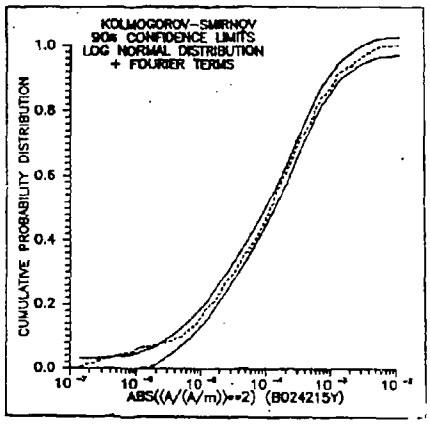

Figure 13. Cumulative probability distribution for the EMPTAC cable current at point B024215Y. Also shown on this plot are the Kolmogorov-Smirnov 90% confidence limits for the assumption that this distribution is log normal with a Fourier

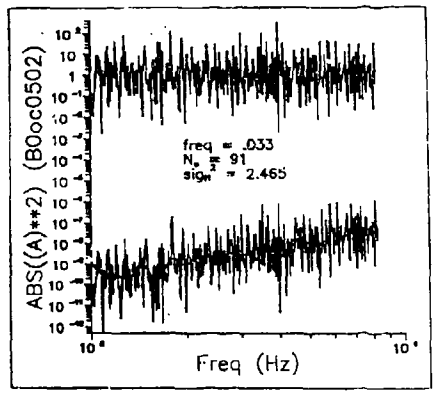

Figure 14. Bottom curves: unfiltered cable current $|I|^2$ and $|I/f^6$ trend. Top curve: $|I|^2$ with the trend factored out: $|I|^2/|I_{trend}|^2$. This figure is based on f_{space} and $f_{ex,7}$ both set to 100, and the assumption that x_{bm} obeys a log normal distribution. Cable ends terminated in 30 Ω.

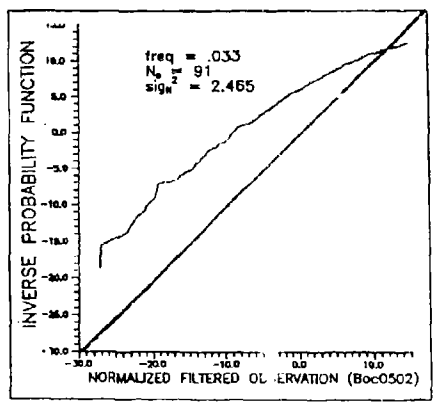

Figure 15. Probability plot from an attempt to fit the filtered data of Fig. 14 to a chi square distribution. The fit does not work.

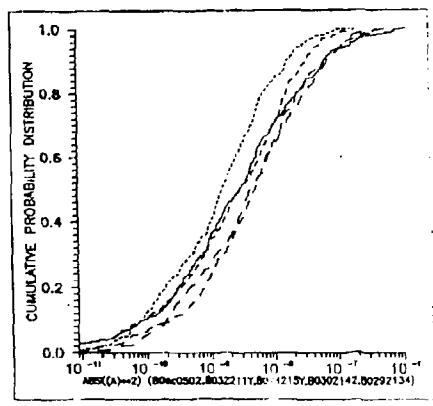

Figure 16. Five way overlay of the simulated data from Fig. 14 (solid line) and the observed cable current from four EMPTAC tests. The calculated current lies within the experimental spread.

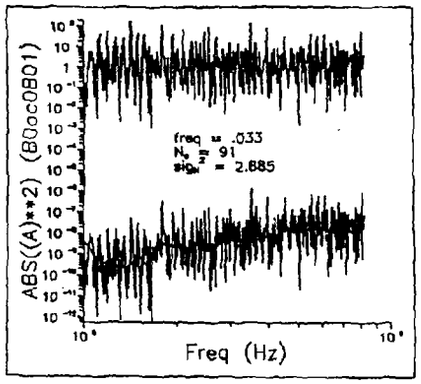

Figure 17. Bottom curves: unfiltered cable current $|I|^2$ and $|I|^2$ trend. Top curve: $|I|^2$ with the trend factored out: $|I^2/I_{trend}|^2$. This figure is based on f_{space} and f_{freq} both set to 30, and the assumption that x_{ijm} obeys a chi square distribution. Cable ends terminated in 30 Ω.

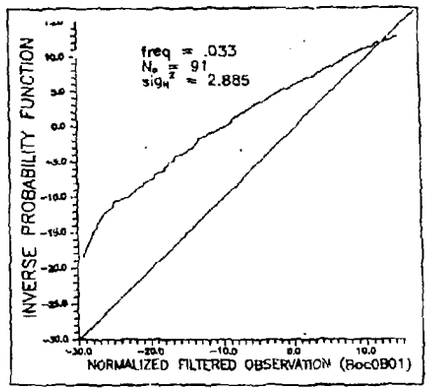

Figure 18. Probability plot from an attempt to fit the filtered data of Fig. 17 to a chi square distribution. The fit does not work.

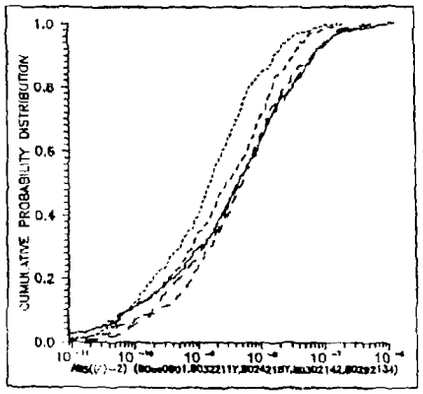

Figure 19. Five way overlay of the simulated data from Fig. 17 (solid line) and the observed cable current from four EMPTAC tests. The calculated data lies within the experimental spread.

A time-domain technique for the analysis of nonlinear devices and circuits

N. Marin[1], K. Fobelets, J. Genoe, G. Borghs
IMEC, Kapeldreef 75, B-3001 Leuven, Belgium

1. Introduction

Many techniques for the analysis of nonlinear circuits, namely time-domain or frequency-domain techniques, have become popular in recent years.

Time-domain techniques are most practical for the analysis of circuits that include lumped elements, while frequency-domain techniques, as harmonic balance analysis or Voltera-series are applicable to strongly or weakly nonlinear circuits [1].

In this work we propose a time-domain technique that can be used for both large signal analysis of devices and lumped-element circuits.

In existing time-domain techniques [2-3], the nonlinear active device characteristics are divided into a large number of linear segments, while the technique we present, uses the nonlinear characteristic of the active device.

Based on the proposed technique, we will present some results obtained by modeling a Resonant Tunneling Diode (RTD) oscillator and a Schottky Diode Detector.

2. Proposed Time-domain Technique

The proposed technique is based on the fact that the response of the physical circuit must be either a periodic or a continuous signal. It is rather difficult to construct a general program for the analysis of nonlinear circuits because of its diversity. The following classification is useful for the proposed solution technique:

1. Self-oscillating circuits.
2. Non self-oscillating circuits.
   2a. With one single frequency input signal.
   2b. With two or more input signals with different frequencies.

In self-oscillating circuits, often two or more oscillation frequencies exist (usually low and high frequencies). For non self-oscillating circuits, the output frequency signal depends on the input frequencies. In the case of one single frequency input signal with a period T_{in}, the period of the output signal is $T_{out} <= T_{in}$ and when two input signals exists with frequencies f_{in_1} and f_{in_2}, the possible frequencies of the output signals are given by $mf_{in_1} + nf_{in_2}$ (with m and n integers).

[1] Institute for Microtechnology, Bucharest, Romania

The proposed time-domain technique includes the following steps:

a) The large signal equivalent circuit for the active device must be constructed.
   - For unipolar devices, the relaxation of the carriers and transit time effects have to be taken into account. When these times are much smaller than the period of the signal, the DC measured characteristics can be used in the equivalent circuit, because the current follows instantaneously the voltage (quasi-static model).
   - For bipolar devices, the quasi-static model can only be used when the generation-recombination times of the carriers are much smaller than the period of the signals.
   - The equivalent circuit of the device must be completed with nonlinear capacitances, resistances, inductances and parasitic elements.

b) Differential equations for this large signal equivalent circuit must be written down.

c) The analysis period T must be larger or equal than the maximum signal period (T_{max}) that can appear in the circuit. For self-oscillating circuits T_{max} is the period determined by the low frequency oscillation, while for non self-oscillating circuit, T_{max} is determined by the highest common factor of the frequencies of the input signals (for one single frequency input signal, T_{max} is the input signal period). For self-oscillating circuit, the analysis period $T > T_{max}$ while for non self-oscillating circuits $T = T_{max}$.

d) The time step Δt is chosen as $\Delta t = T / N_s$. The number N_s must be chosen such that for the minimum signal period in the circuit we will have a sufficient number of points (> 500).

e) To solve the differential equations, the following steps are necessary :
   - The m_k-th order derivatives in point t_1 are replaced by:

$$\left.\frac{d^{m_k} V_k(t)}{dt^{m_k}}\right|_{t_1} = V_k\left(t_{m_k+1}\right) - C_{m_k}^1 V_k\left(t_{m_k}\right) \ldots (-1)^{m_k} C_{m_k}^{m_k} V_k(t_1) \qquad (1)$$

   - Starting from the initial values :

$$V_{k1} = V_k(t_1), V_{k2} = V_k(t_2) \ldots\ldots V_{km_k} = V_k\left(t_{m_k}\right) \qquad (2)$$

   the next voltage in time are found $V_{km_k+1} = V_k\left(t_{m_k+1}\right)$, with $t_{m_k+1} = t_{m_k} + \Delta t$. These solutions will then be used to calculate the following voltages in time and this is done N_s times. Some analysis periods are necessary to reach a steady state solution.

   - The stop conditions are different for the self- or non self-oscillating circuits. When the analysis period is equal to the maximum period ($T = T_{max}$, non self-oscillating circuits), the stop condition is written as:

$$\left|V_k(t_p) - V_{k_{old}}(t_p)\right| \le E_{rr}\left|V_k(t_p)\right| \qquad (3)$$

   with E_{rr} the relative error and $V_k(t_p)$, $V_{k_{old}}(t_p)$ the indexed variables for current and previous iteration.

   For self-oscillating circuits, the condition (3) can not be used and wave form visualization of the analysis period is necessary.

3. Examples

3.1. Resonant Tunneling Oscillator

A detailed analysis of millimeter range Resonant Tunneling Diode (RTD) oscillators is made in [4]. The large signal equivalent circuit of the oscillator is presented in Fig.1 [4]. Lumped-elements for the long lines, necessary for matching the load (radiation resistance R_r) and for the filter, are used (L_{l1},L_{l2},C_l for the load line and L_{f1},L_{f2},C_f for the filter line). C_{DP} is the diode capacitance (including parasitic capacitances), R_{los} is the losses resistance from the diode and the circuit. L_c,L_e are the inductances due to respectively the connection of the diode and the bias to the circuit. C_e,R_e and R_c

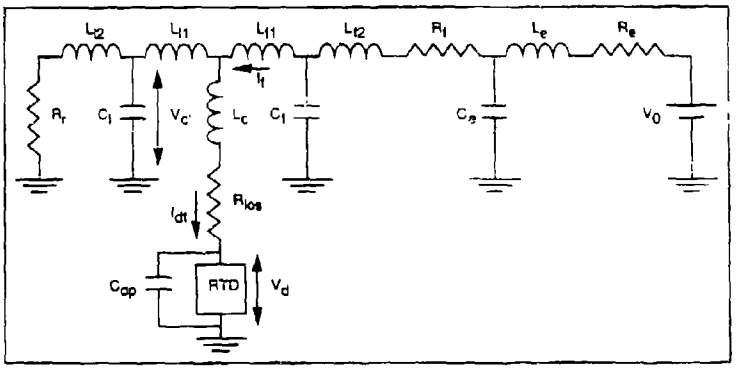

Figure 1 : Large signal equivalent circuit of an RTD oscillator

An RTD is an unipolar device so that the measured nonlinear I_{d0} - V_{d0} characteristic can be used in the numerical simulation.

The differential equations described the circuit given in Fig.1 are:

$$\frac{dI_{DT}}{dt} = \frac{L_{l1}V_{cf} + L_{f1}V_{cl}}{AA1} - \frac{(L_{l1}+L_{f1})(V_D + R_{los}I_{DT})}{AA1}$$

$$\frac{dI_f}{dt} = \frac{(L_{l1}+L_c)V_{cf} - L_cV_{cl}}{AA2} - \frac{L_{l1}(V_D + R_{los}I_{DT})}{AA2}$$

$$V_{cl} = -R_l(I_{DT} - I_f + C_l\frac{dV_{cl}}{dt}) - L_{l2}(\frac{dI_{DT}}{dt} - \frac{dI_f}{dt} + C_l\frac{d^2V_{cl}}{dt^2}) \qquad (4)$$

$$V_{cf} = V_{ce} - R_f(I_f + C_f\frac{dV_{cf}}{dt}) - L_{f2}(\frac{dI_f}{dt} + C_f\frac{d^2V_{cf}}{dt^2})$$

$$V_{ce} = -R_e(I_f + C_f\frac{dV_{cf}}{dt} + C_e\frac{dV_e}{dt}) - L_e(\frac{dI_f}{dt} + C_f\frac{d^2V_{cf}}{dt^2} + C_e\frac{d^2V_{ce}}{dt^2})$$

$$I_{DT} = I_D + C_{DP}\frac{dV_D}{dt}$$

Where $AA1 = L_{el}L_c + L_{f1}(L_{l1} + L_c)$.

In the set of differential equations (4), V_d, V_{cf}, V_{oe}, V_D are the AC signal voltages and I_{DT}, I_f the AC currents.

The AC diode current, I_D is obtained from the measured characteristic as :

$$I_D = I_{d0}(V_{d00} + V_D) - I_{d00} \tag{5}$$

where I_{d00}, V_{d00} are the DC diode current and voltage.

To find the optimum value for analysis signal period T, a study of the oscillations which can possibly appear in the circuit is necessary.

The condition for oscillation is given by:

$$-\frac{1}{wC_{DP}} + wL_c + X_{lf} = 0 \tag{6}$$

$$R_D + R_{los} + R_s = 0$$

where R_D is the large signal equivalent diode (negative) resistance, X_{lf}, R_{lf} are the reactance and resistance of the parallel load-filter impedances (being : $Z_{lf} = Z_l \| Z_f = R_{lf} + jX_{lf}$).

At a useful frequency, the filter impedance Z_f must be much larger than the load impedance Z_l. This frequency is then determinsd by :

$$-\frac{1}{wC_{DP}} + wL_c + X_l = 0 \tag{7}$$

Other oscillation frequencies (given by (5)) can appear in the circuit. These frequencies can be stopped by a filter resistance $R_f \geq 3\Omega$ [4].

Another possible oscillation that can appear in the circuit of Fig.1, is a low frequency oscillation given by the resonance between C_c and L_c. This oscillation can be stopped with a low value for external series resistance ($R_c \geq 1\Omega$) [4].

All the derivatives in equation (4) are replaced by discrete time depending expressions as given in (1).

To solve this set of differential equations, nine starting values are necessary, two for each second derivatives (V_{d1}, V_{cf}, V_{oe}) and one for each first derivative

$$V_{d1}, V_{d2}, V_{cf1}, V_{cf2}, V_{ce1}, V_{ce2}, V_{D1}, I_{f1}, I_{DT} \tag{8}$$

Usually, all the starting variables are zero, except one (or more) for which a small perturbation appears.

The results of the numerical analysis of oscillator circuit (Fig.1), for different values of the circuit elements are shown in Fig.2.

For large values of the filter and external resistances ($R_f = 5\Omega, R_c = 2\Omega$), only the useful oscillation frequency given by (6) is possible in the circuit. Simulations generate a sinusoidal wave form (with a frequency of $f_h = 21.1$GHz) (see Fig.2a).

The analysis period used in the simulations is around T = 400ps, and the number of steps is N_s=20000. In this way the signal period T_s = 45ps includes a number of points larger than 1000. With arbitrary starting values (7), (being : $V_{d2} = 0.1\text{mV}; V_{cf2} = 0.1\text{mV}; V_{oe2} = 0.01\text{mV}$,etc.), the same wave form (Fig.2a) is obtained. The steady state solution is obtained after 40-80 iterations.

The result of the simulations for $R_f = 0\Omega$ ($R_e = 2\Omega$) is shown in Fig.2b. For different starting values (7), a different wave form can appear in the circuit. For $V_{\alpha 2} = 0.1\text{mV}$, a sinusoidal wave form ($f_h \approx 21.1\text{GHz}$) appears in the circuit. For $V_{\alpha 2} = 0.01\text{mV}$, a non sinusoidal wave form (Fig.2b) appears in the circuit ($f = 11\text{GHz}$).

The analysis period is $T = 2400\text{ps}$, and the number of steps is N_s=120000. After 10-20 iterations, the steady state solution is obtained.

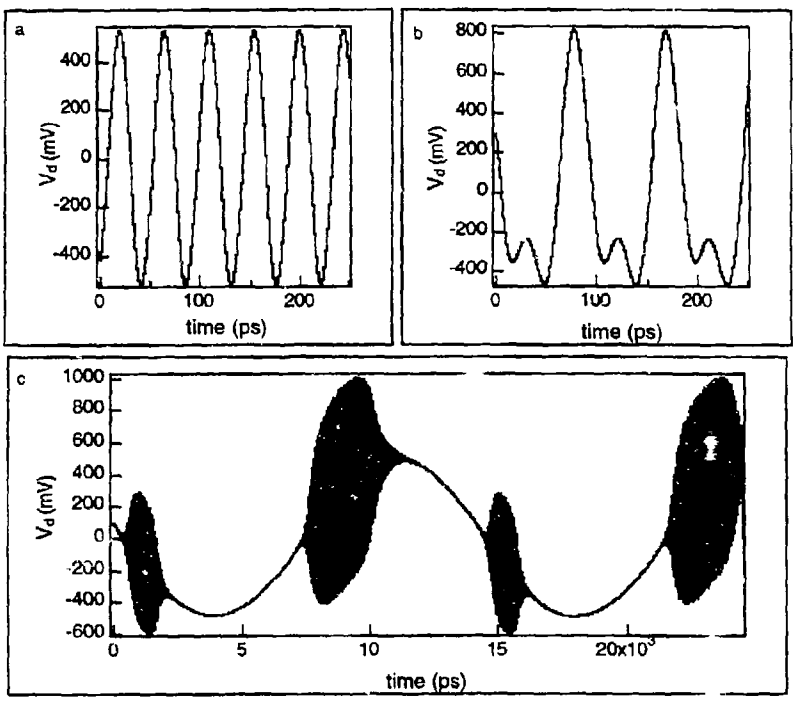

Figure 2 : a) AC diode voltage as a function of time for $R_e = 2\Omega$ and $R_f = 5\Omega$.
b) AC diode voltage as a function of time for $R_e = 2\Omega$ and $R_f = 0\Omega$.
c) AC diode voltage as a function of time for $R_e = 0\Omega$ and $R_f = 5\Omega$.

A similar result is obtained for an external resistance $R_e = 0\Omega$ ($R_f = 5\Omega$) as shown in Fig.2c. Two oscillation frequencies appear. A low frequency oscillation ($f_l \approx 70\text{Mhz}$, which is determined by the resonance of L_cC_c) is obtained and a high frequency oscillation given by the resonance of the diode and the load ($f_h \approx 21.1\text{GHz}$). The starting value (7) is $V_{\alpha 2} = 0.01\text{mV}$. The analysis period is $T = 30\text{ns}$, and the number of steps is N_s=500000. After 3-4 iterations the steady state solution is obtained.

An interesting result obtained by the simulations is presented in Fig.3, where the useful frequency f_h vs. DC bias is given (R_f = 5Ω and R_e = 2Ω). An oscillator with variable frequency (Δf_h = 100MHz) can be obtained.

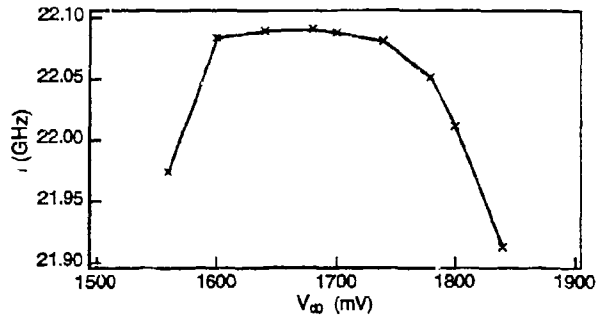

Figure 3 : Oscillation frequency as a function of the DC bias voltage across the diode.

3.2. Schottky diode detector circuit

Using the proposed analysis technique, a simple diode detector circuit with a schottky diode is analyzed.

The large signal equivalent circuit is presented in Fig.4. R_{ka},L_c are respectively the diodes' series resistance and connection inductance, while C_e,R_e are the external elements necessary for detection of the signal. A schottky diode is an unipolar device and the DC measured characteristics can be used in the simulations. The nonlinear diode capacitance C_{DP} of the diode is used in the simulations.

$$C_{DP} = \sqrt{\frac{V_{bi}}{V_{bi} - V_{d0} - V_D}} \tag{9}$$

where, V_{bi} is the built-in diode voltage, V_{d0},V_D are respectively the DC and AC diode voltage.

The differential equations describing the circuit of Fig.4 are:

$$\frac{V_g - V_D}{R_e} + C_c \frac{d(V_g - V_D)}{dt} = (I_D + I_{CD})(1 + \frac{R_{ka}}{R_e}) + (C_e R_{ka} + \frac{L_c}{R_e})(\frac{dI_D}{dt} + \frac{dI_{CD}}{dt}) + C_e L_c (\frac{d^2 I_D}{dt^2} + \frac{d^2 I_{CD}}{dt^2})$$

$$I_D = I_{d0}[\exp(\frac{qV_D}{nkT}) - 1] \tag{10}$$

$$I_{CD} = C_D \frac{dV_D}{dt}$$

where I_{d0} is the DC current of the diode and V_g the AC input voltage.

For a sinusoidal input voltage with a period T_s, the analysis period is $T = T_s$. The set of differential equations (10) can be easily reduced to one third order differential equation.

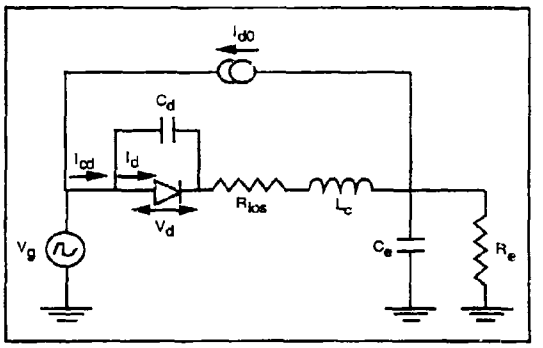

Figure 4 : Large signal equivalent circuit of a detector with a schottky diode

Three starting values for diode voltage V_{D1}, V_{D2}, V_{D3} are necessary. The step number $N_t \geq 1000$ gives good results for the numerical simulation. The output voltage wave form (V_{R_e}) obtained by the simulations is presented in Fig.5. A very large range for starting values can be used.

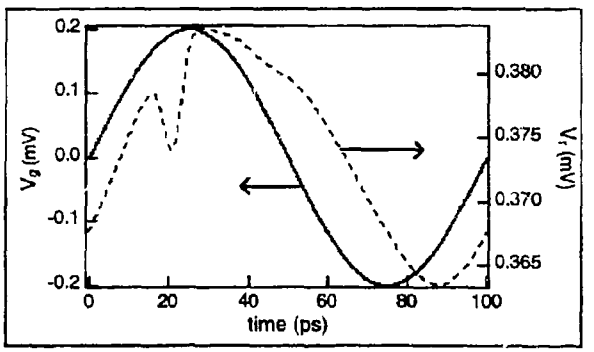

Figure 5 : Input and output voltage for the diode detector

The stop condition (3) is fulfilled (relative error E_r=1%) after 20-100 iterations.

4. Conclusions

A new time-domain technique for the analysis of nonlinear devices and circuits is presented. Using the proposed technique, numerical results of the analysis of a resonant tunneling diode oscillator circuit and a simple schottky diode detector circuit are presented.

The program was developed in the Pascal programming language, for PC computer and Macintosh. Very good convergence of the numerical solutions was obtained.

Full-Wave Analysis of Coplanar Waveguide Discontinuities by a Partial Wave Synthesis

R. Schmidt[1], P. Russer[1,2]

[1]Institut für Hochfrequenztechnik, Technische Universität München, Arcisstraße 21, 80290 München, Germany
[2]Ferdinand-Braun-Institut für Höchstfrequenztechnik, Rudower Chausee 5, 12489 Berlin, Germany

Abstract

Partial wave synthesis is applied to model the discontinuities of shielded coplanar waveguides. This method allows a self-consistent computation of the conductor loss without a surface impedance approximation of the skin-effect. Numerical results for a step discontinuity of a MMIC coplanar transmission line are presented. The influence of the metallization thickness on the propagation characteristics of coplanar waveguides and on the scattering characteristics of coplanar waveguide discontinuities is investigated. The convergence behaviour of the scattering parameters as a function of the number of modes is discussed.

Introduction

In monolithic microwave integrated circuits (MMIC's) the strip width and metallization thickness of transmission lines may range in the skin depth's order of magnitude. Conductor loss becomes significant in these transmission lines and may not be neglected in the circuit design [3].

Most common approaches are based on field modelling assuming perfect conductors, and the conductor losses are evaluated using a surface impedance description. However, the surface impedance description is only valid for a metallization thickness considerably larger than the skin depth. In order to determine accurately the conductor loss and its effect on the propagation constant for waveguides with transverse dimensions in the order of the skin depth, a full-wave analysis is required considering also the electromagnetic field inside the conductor. Partial wave synthesis fulfills these requirements. However, this method has been applied up to now only to the calculation of the propagation characteristics of transmission lines [2,3]. In this paper partial wave synthesis is extended to determine the scattering parameters of coplanar transmission line discontinuities.

Method of Analysis

Analyzing discontinuities by partial wave synthesis requires the calculation of the dominant eigenmode, which is the only propagating mode at the considered frequency, and the evanescent eigenmodes on both sides of the discontinuity. Fig. 1 shows a coplanar waveguide (CPW) with finite metallization thickness inside a rectangular box with perfect electric conducting walls.

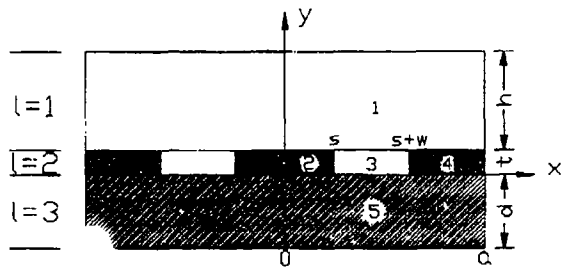

Figure 1: coplanar waveguide cross section

Due to the symmetry with respect to the plane $x = 0$, only half of the structure has to be considered. In the symmetry plane a magnetic or electric wall is placed. The cross section depicted in Fig. 1 is divided into three layers and five regions. In each of the homogeneous regions i the electromagnetic field is expanded into a series of partial waves consisting of a combination of LSE_x and LSH_x longitudinal section waves, respectively [2]. The Helmholtz equations for these waves are

$$\Delta\Pi_{xi} + \omega^2\mu_i\epsilon_i\Pi_{xi} = 0 \tag{1}$$
$$\Delta\tilde{\Pi}_{xi} + \omega^2\mu_i\epsilon_i\tilde{\Pi}_{xi} = 0 \tag{2}$$

with

$$\epsilon_i = \epsilon_0\epsilon_{ri}(1 - j\tan\delta_i) + \frac{\sigma_i}{j\omega} \tag{3}$$

In each region i, the Helmholtz equation is satisfied by the following ansatz of the partial waves.

$$\begin{aligned}\Pi_{xi} &= \sum_n A_{in}\{e^{jk_{xin}x} + B_{in}e^{-jk_{xin}x}\}\{e^{jk_{yin}y} + C_{in}e^{-jk_{yin}y}\}e^{j(\omega t - k_z z)} \\ \tilde{\Pi}_{xi} &= \sum_n \tilde{A}_{in}\{e^{j\tilde{k}_{xin}x} + \tilde{B}_{in}e^{-j\tilde{k}_{xin}x}\}\{e^{j\tilde{k}_{yin}y} + \tilde{C}_{in}e^{-j\tilde{k}_{yin}y}\}e^{j(\omega t - k_z z)} \qquad i = 1,\ldots,5\end{aligned} \tag{4}$$

with

$$\begin{aligned}k_{xin}^2 + k_{yin}^2 + k_z^2 &= \omega^2\mu_i\epsilon_i \\ \tilde{k}_{xin}^2 + \tilde{k}_{yin}^2 + k_z^2 &= \omega^2\mu_i\epsilon_i\end{aligned} \tag{5}$$

The field components are obtained by a superposition of LSE_x waves and LSH_x waves:

$$\begin{aligned}E_x &= \frac{\partial^2\Pi_x}{\partial x^2} + \omega^2\mu\epsilon\Pi_x & H_x &= \frac{\partial^2\tilde{\Pi}_x}{\partial x^2} + \omega^2\mu\epsilon\tilde{\Pi}_x \\ E_y &= \frac{\partial^2\Pi_x}{\partial x\partial y} - j\omega\mu\frac{\partial\tilde{\Pi}_x}{\partial z} & H_y &= j\omega\epsilon\frac{\partial\Pi_x}{\partial z} + \frac{\partial^2\tilde{\Pi}_x}{\partial x\partial y} \\ E_z &= \frac{\partial^2\Pi_x}{\partial x\partial z} + j\omega\mu\frac{\partial\tilde{\Pi}_x}{\partial y} & H_z &= -j\omega\epsilon\frac{\partial\Pi_x}{\partial y} + \frac{\partial^2\tilde{\Pi}_x}{\partial x\partial z}\end{aligned} \tag{6}$$

In the homogeneous layer $l = 1$ and $l = 3$, the coefficients B_{in}, B_{5n} and the separation constants k_{x1n}, $\tilde{k}_{x1n}$, k_{x5n}, $\tilde{k}_{x5n}$ can be determined straightforward using the vertical wall boundary condition at $x = 0$ and $x = a$. This does not apply, however, to the plane of metallization.

because we are dealing here with a structure layered in $x-$direction. Consequently the LSE_x and LSH_x partial waves have to be derived using the field continuity condition at $x = s$ and $x = s + w$ and the boundary condition at the vertical walls at $x = 0$ and $x = a$. We obtain for each partial wave a nonlinear eigenvalue equation

$$[A_n(k_{xin})]\,[x_n] \;=\; 0 \tag{7}$$

with the column vector $[x_n] = [A_{2n}, B_{2n}, A_{3n}, B_{3n}, A_{4n}, B_{4n}]^T$. The eigenvalue k_{xin} corresponds to the separation constant at one of the regions in the the metallization plane. The separation constants of the other regions in this plane are determined by (5) and the condition $k_{yn}^{(l=2)} := k_{y2n} = k_{y3n} = k_{y4n}$, which is a consequence of the continuity condition. Thus each partial wave in a region of the inhomogeneous layer $l = 2$ is matched via the continuity condition to a partial wave in its neighbouring regions. We can now write an unified ansatz of the LSE_x partial waves of the three layers $l = 1, 2, 3$:

$$\Pi_x^{(l)} = \sum_n A_n^{(l)} \cdot \Pi_{xn}^{(l)} = \sum_n A_n^{(l)} \cdot X_n^{(l)}(x) \cdot \left(e^{jk_{yn}^{(l)} y} + B_n^{(l)} \cdot e^{-jk_{yn}^{(l)} y} \right) \tag{8}$$

The factor $e^{j(\omega t - k_z z)}$ is suppressed in the ansatz (8), because it is the same for all partial waves. Note that the separation constants k_{xin} and in the next step the functions $X_n^{(l)}$ are known from (7) while the $k_{yn}^{(l)}$ are determined togather with the propagation constant k_z. The LSH_x partial waves are established correspondingly:

$$\tilde{\Pi}_x^{(l)} \;=\; \sum_n \tilde{A}_n^{(l)} \cdot \tilde{\Pi}_{xn}^{(l)} = \sum_n \tilde{A}_n^{(l)} \cdot \tilde{X}_n^{(l)}(x) \cdot \left(e^{j\tilde{k}_{yn}^{(l)} y} + \tilde{B}_n^{(l)} \cdot e^{-j\tilde{k}_{yn}^{(l)} y} \right) \tag{9}$$

The propagation constant k_z and the coefficients $A_n^{(l)}$, $B_n^{(l)}$, $\tilde{A}_n^{(l)}$, $\tilde{B}_n^{(l)}$ of the ansatz (8) and (9) are determined by applying the boundary condition of the horizontal walls at $y = -d$ and $y = t + h$ and by applying the continuity equation for the transverse fields at the horizontal boundaries of the layers.

$$E_x^{(l=1)}(x) - E_x^{(l=2)}(x) = 0 \qquad E_z^{(l=1)}(x) - E_z^{(l=2)}(x) = 0 \qquad at \quad y = t \tag{10}$$

$$H_x^{(l=1)}(x) - H_x^{(l=2)}(x) = 0 \qquad H_z^{(l=1)}(x) - H_z^{(l=2)}(x) = 0 \qquad at \quad y = t \tag{11}$$

$$E_x^{(l=2)}(x) - E_x^{(l=3)}(x) = 0 \qquad E_z^{(l=2)}(x) - E_z^{(l=3)}(x) = 0 \qquad at \quad y = 0 \tag{12}$$

$$H_x^{(l=2)}(x) - H_x^{(l=3)}(x) = 0 \qquad H_z^{(l=2)}(x) - H_z^{(l=3)}(x) = 0 \qquad at \quad y = 0 \tag{13}$$

Using the corresponding field components of the partial waves of the homogeneous layers $l = 1$ and $l = 3$ as test functions the method of moments [1] applied to the continuity equations (10)-(13) leads to a homogeneous system of equations:

$$[B(k_z)]\,[x] \;=\; 0 \tag{14}$$

Its eigenvalues represent the resulting complex propagation constants and the column vector $[x]$ the unknown coefficients of the ansatz (8) and (9). The electric field $\boldsymbol{\xi}$ and the magnetic field $\boldsymbol{\eta}$ of the partial waves are deduced from the potentials in the ansatz (8) and (9) by means of eq. (6). Thus, one can rewrite the field of the eigenmode m using a simplified notation:

$$\mathbf{e_m} \;=\; \sum_n c_{mn} \boldsymbol{\xi}_{mn} \tag{15}$$

$$\mathbf{h_m} \;=\; \sum_n c_{mn} \boldsymbol{\eta}_{mn} \tag{16}$$

The partial waves are referred to the subscripts mn, because each mode m is an expansion of its own characteristic partial waves. For the normalized eigenmodes $\mathbf{e_m}$, $\mathrm{h_i}$, the orthogonality relation

$$\int_S \mathbf{e_m} \times \mathbf{h_i}\, d\vec{s} = \delta_{mi} \tag{17}$$

holds, where S is the cross section of the box area, and δ_{mi} is the Kronecker delta function. Analyzing the characteristics of discontinuities the incident and scattered fundamental modes as well as higher-order modes must be taken into account on both sides of the junction.

$$\begin{aligned} \mathbf{E} &= \sum_m (A_m + B_m)\, \mathbf{e_m} \\ &= \left([A]^T + [B]^T\right)\, [\mathbf{e}] \end{aligned} \tag{18}$$

$$\begin{aligned} \mathbf{H} &= \sum_m (A_m - B_m)\, \mathbf{h_m} \\ &= \left([A]^T - [B]^T\right)\, [\mathbf{h}] \end{aligned} \tag{19}$$

with

$$[\mathbf{e}] = [\mathbf{e_1} \ldots \mathbf{e_m} \ldots \mathbf{e_M}]^T \tag{20}$$

$$[\mathbf{h}] = [\mathbf{h_1} \ldots \mathbf{h_m} \ldots \mathbf{h_M}]^T \tag{21}$$

The vectors $[A]$ and $[B]$ represent the amplitudes of the incident and scattered modes, respectively. The transverse fields $\mathbf{E_t}$ and $\mathbf{H_t}$ are continuous across the junction plane between two waveguides I and II. Therefore, one has

$$\begin{aligned} [\mathbf{E_t^{(I)}}(x,y)] &= [\mathbf{E_t^{(II)}}(x,y)] \\ [\mathbf{H_t^{(I)}}(x,y)] &= [\mathbf{H_t^{(II)}}(x,y)] \end{aligned} \tag{22}$$

Performing the modal expansion of the fields in equation (22) yields:

$$\left([A^{(I)}]^T + [B^{(I)}]^T\right)\, [\mathbf{e_t}^{(I)}] = \left([A^{(II)}]^T + [B^{(II)}]^T\right)\, [\mathbf{e_t}^{(II)}] \tag{23}$$

$$\left([A^{(I)}]^T - [B^{(I)}]^T\right)\, [\mathbf{h_t}^{(I)}] = \left(-[A^{(II)}]^T + [B^{(II)}]^T\right)\, [\mathbf{h_t}^{(II)}] \tag{24}$$

In order to determine the amplitudes in equations (23), (24) a suitable product is defined [4]:

$$\langle \mathbf{e}(x,y) \times \mathbf{h}(x,y) \rangle = \int_S \mathbf{e}(x,y) \times \mathbf{h}(x,y)\, ds \tag{25}$$

Using the magnetic field of the modes in waveguide I as test functions in eq. (23), and the electric field of the modes in waveguide II as test functions in eq. (24), and making use of the orthogonality relation (17), we arrive at a linear system of equations, which reads in matrix notation:

$$\begin{aligned} [A^{(I)}] + [B^{(I)}] &= [R_1]\left([A^{(II)}] + [B^{(II)}]\right) \\ [R_2]\left([A^{(I)}] - [B^{(I)}]\right) &= -[A^{(II)}] + [B^{(II)}] \end{aligned} \tag{26}$$

The elements of the matrices $[R_1]$ and $[R_2]$ are given by:

$$R_{1mn} = \sum_i \sum_j c_{ni} c_{mj} \langle \boldsymbol{\xi}_{\mathbf{ni}}^{(\mathbf{II})} \times \boldsymbol{\eta}_{\mathbf{mj}}^{(\mathbf{I})} \rangle \tag{27}$$

$$R_{2mn} = \sum_i \sum_j c_{mi} c_{nj} \langle \boldsymbol{\xi}_{\mathbf{mi}}^{(\mathbf{II})} \times \boldsymbol{\eta}_{\mathbf{nj}}^{(\mathbf{I})} \rangle \tag{28}$$

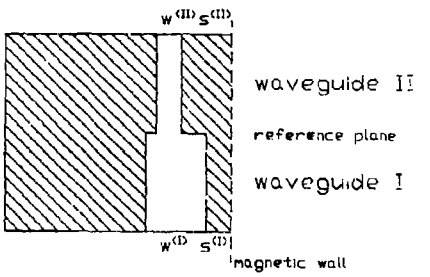

Figure 2: coplanar waveguide discontinuity

From eq. (26), the generalized scattering matrix of the eigenmodes can be written in the form

$$\begin{aligned} [B^{(I)}] &= [S_{11}]\,[A^{(I)}] + [S_{12}]\,[A^{(II)}] \\ [B^{(II)}] &= [S_{21}]\,[A^{(I)}] + [S_{22}]\,[A^{(II)}] \end{aligned} \tag{29}$$

with

$$[S_{11}] = ([I] + [R_1][R_2])^{-1}\,([R_1][R_2] - [I]) \tag{30}$$

$$[S_{12}] = ([I] + [R_1][R_2])^{-1}\,2\,[R_1] \tag{31}$$

$$[S_{21}] = ([I] + [R_2][R_1])^{-1}\,2\,[R_2] \tag{32}$$

$$[S_{22}] = ([I] + [R_2][R_1])^{-1}\,([I] - [R_2][R_1]) \tag{33}$$

where $[I]$ is the identity matrix.

Numerical Results

We calculated the reflection and transmission coefficients of a CPW step discontinuity Fig. 2 using the same parameters as Kuo et al [5], who considered the conductor to be perfect. The results of both calculations are plotted in Fig. 3.

As a second example, a CPW step discontinuity typical for MMIC's is treated. The following results refer to a coplanar transmission line, which has a 600 μm thick substrate with a dielectric constant of 12.9 and a dielectric loss factor of $1.0 \cdot 10^{-3}$. The gold conductor is assumed to have a conductivity of $3.0 \cdot 10^7$ S/m. The frequency is 10 GHz. The skin depth is $0.9\mu m$. The dependance of the propagation constant and the attentuation on the metallization thickness t is plotted in Fig. 4. As could be expected, the attenuation constant α grows significantly for smaller values of t. For metallization thickness lower than the skin depth the effective dielectric constant of the CPW is greater than $(\epsilon_r + 1)/2$. This behaviour can only be described using the full-wave modell also inside the conductor. Fig.(5) shows the scattering parameters $|S_{11}|$ and $|S_{21}|$ of a CPW discontinuity. The parameters were calculated with 4 eigenmodes in each waveguide. The relative error if more eigenmodes were used was below 0.1%. In this case we use the structure functions of the magnetic field in waveguide (I) and the electric field in waveguide (II) as the test function. If we choose the test functions vice versa the convergence rate is much worse, as Fig. 6 demonstrates.

Conclusion

The propagation characteristics and the scattering parameters of CPW step discontinuites have been calculated by using partial wave synthesis. Conductor loss is taken into account rigorously It was found that the attenuation and also the effective dielectric constant of CPW's are very sensitive to metallization thickness, if the line geometries are in the order of the skin depth. Also the reflection and transmission coefficients of a CPW discontinuity are calculated as a function of metallization thickness. A convergence study shows that it is of great importance to choose the proper test functions in the field matching at the discontinuity in order to obtain accurate solutions with a minimum number of modes.

Acknowledgement

This work has been supported by the Siemens AG, Munich. The authors thank Dr. W. Heinrich for a critical reading of the paper.

References

[1] R.F. Harrington. *Field Computation by Moment Methods*. New York: Macmillan, 1968

[2] J. Kessler, R. Dill, P. Russer, "Field Theory Investigation of High-T_c Superconducting Coplanar Waveguide Transmission Lines and Resonators". *IEEE Trans. Microwave Theory Tech.*, vol. MTT-39, pp. 1566-1574, September 1991

[3] W. Heinrich, "Full-Wave Analysis of Conductor Losses on MMIC Transmission Lines". *IEEE Trans. Microwave Theory Tech.*, vol. MTT-38, pp. 1468-1472, October 1990

[4] Q. Xu, K.J. Webb, R. Mittra, "Study of Modal Solution Procedures for Microstrip Step Discontinuities". *IEEE Trans. Microwave Theory Tech.*, vol. MTT-37, pp.381-386, February 1989

[5] C.W. Kuo, T. Itoh, "Characterization of Shielded Coplanar Type Transmission Line Junction Discontinuities Incorporating the Finite Metallization Thickness Effect". *IEEE Trans. Microwave Theory Tech.*, vol. MTT-40, pp. 73-80, January 1992

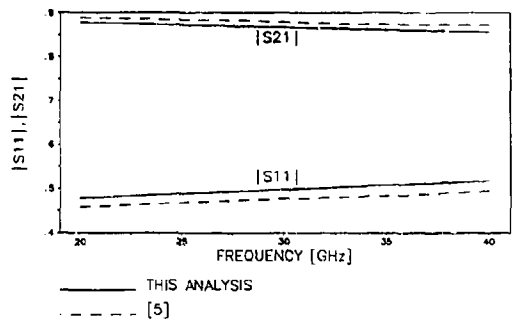

Figure 3: Comparison of scattering parameters ($s^{(I)} = 100\mu m$, $w^{(I)} = 600\mu m$, $s^{(II)} = 400\mu m$, $w^{(II)} = 100\mu m$, $t = 10\mu m$, substrate thickness=$254\mu m$, ϵ_r=9.6)

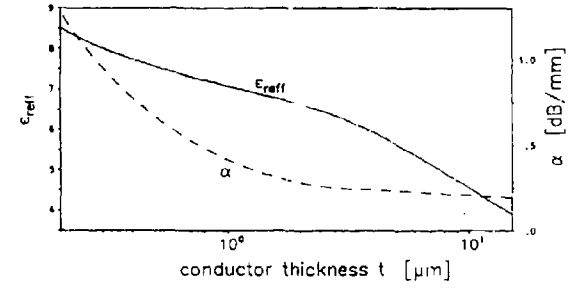

Figure 4: Effective dielectric constant and attenuation ($s = 10\mu m$, $w = 5\mu m$, substrate thickness=$600\mu m$, $\epsilon_r = 12.9$, f=10GHz)

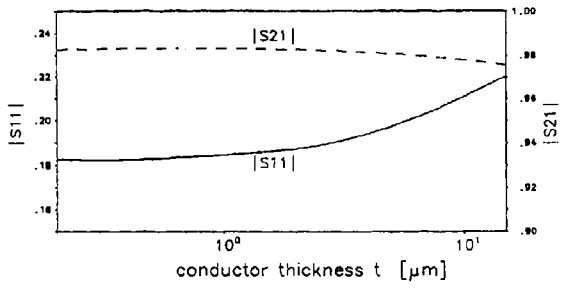

Figure 5: Scattering parameters ($s^{(I)} = 5\mu m$, $w^{(I)} = 10\mu m$, $s^{(II)} = 10\mu m$, $w^{(II)} = 5\mu m$, substrate thickness=$600\mu m$, $\epsilon_r = 12.9$, f=10GHz)

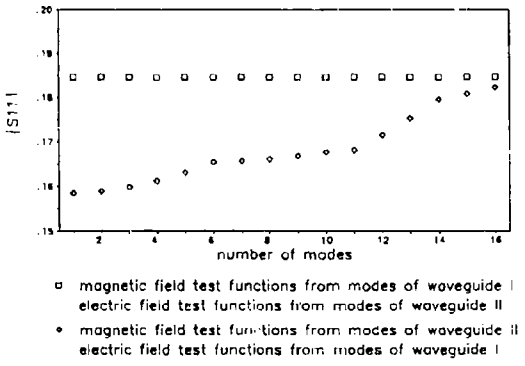

Figure 6: Convergence of the reflection coefficient ($s^{(I)} = 5\mu m$, $w^{(I)} = 10\mu m$, $s^{(II)} = 10\mu m$, $w^{(II)} = 5\mu m$, substrate thickness=$600\mu m$, $\epsilon_r = 12.9$, t=$1\mu m$, f=10GHz)

SESSION 23:

MATERIALS
AND
SIMULATION METHODS

Chair: Fabio Cavallini

Modeling transverse electromagnetic waves in conducting anisotropic media by a spectral time-domain technique

Jose' M. Carcione and Fabio Cavallini

Osservatorio Geofisico Sperimentale
P.O. Box 2011 Opicina, 34016 Trieste, ITALY.

Abstract. This work presents a spectral algorithm for simulating TEM waves (transverse electric and magnetic fields) in the plane of mirror symmetry of a conducting monoclinic medium. Assuming homogeneous material properties in the y-direction, we obtain a two-dimensional model where H_y, E_x and E_z are uncoupled from the other three components. Maxwell's equations are solved by using a technique based on an expansion of the wavefield in optimal basis functions. The algorithm solves the electromagnetic equations in differential form by computing the spatial derivatives with the Fourier pseudospectral method, and expanding the time evolution operator spectrally, to balance spatial and time accuracy. The technique possesses spectral accuracy and is suitable for treating complex morphologies.
From the correspondence principle and the explicit knowledge of the frequency-domain solution in non-conducting media, we get a semi-analytical solution for propagation in unbounded homogeneous media. This novel solution is found for a monoclinic medium where both the conductivity and the permittivity tensors have, in principle, four independent components. The modeling technique is successfully tested against this solution and, as expected, the results show velocity anisotropy and anisotropic attenuation. Finally, the modeling algorithm is applied to wave propagation through a perfectly isotropic and dielectric quarter space embedded in an anisotropic conducting background. Snapshots of the wavefield are interpreted in the light of plane wave analysis made with homogeneous electromagnetic waves.

Maxwell's equations

In 3-D vector notation, the Maxwell equations are (e.g., Chew, 1990)

$$\nabla \times \mathbf{E} = -\frac{\partial \mathbf{B}}{\partial t} + \mathbf{M}, \tag{1a}$$

$$\nabla \times \mathbf{H} = \frac{\partial \mathbf{D}}{\partial t} + \mathbf{J}, \tag{1b}$$

where **E**, **B**, **H** and **D** are the electric intensity, the magnetic flux density, the magnetic intensity and the electric flux density, respectively, while **J** and **M** are the electric and magnetic current densities, respectively. In general, they depend on $\mathbf{x} = (x,y,z)$, the Cartesian coordinates, and t, the time variable. Equations (1a) and (1b) constitute six scalar equations with 12 scalar unknowns since **J** and **M** are known. The six additional scalar equations are the constitutive relations, which for anisotropic media can be written as

$$\mathbf{D} = \boldsymbol{\varepsilon} \cdot \mathbf{E}, \tag{2a}$$

$$\mathbf{B} = \boldsymbol{\mu} \cdot \mathbf{H}, \tag{2b}$$

FAX: +39-40-327307, e-mail: carcione AT ilsogs.bitnet.

where ε and μ are the permittivity and permeability matrices, respectively. The dot in the r.h.s. of (2a) and (2b) denotes ordinary matrix multiplication. Moreover, the current density is

$$\mathbf{J} = \sigma \cdot \mathbf{E} + \mathbf{J}_s, \tag{3}$$

where σ is the conductivity matrix and $\mathbf{J}_s$ is the contribution of the sources. The first term of the r.h.s. of (3) is the conduction current density. Substituting the constitutive relations and the current density into equations (1a) and (1b) gives

$$\nabla \times \mathbf{E} = -\mu \cdot \frac{\partial \mathbf{H}}{\partial t} + \mathbf{M}, \tag{4a}$$

$$\nabla \times \mathbf{H} = \sigma \cdot \mathbf{E} + \varepsilon \cdot \frac{\partial \mathbf{E}}{\partial t} + \mathbf{J}_s. \tag{4b}$$

In general, a realistic medium is described by symmetric anisotropic permittivity and conductivity tensors. Consider, for instance, that

$$\varepsilon = \begin{bmatrix} \varepsilon_{11} & 0 & \varepsilon_{13} \\ 0 & \varepsilon_{22} & 0 \\ \varepsilon_{13} & 0 & \varepsilon_{33} \end{bmatrix} \quad \text{and} \quad \sigma = \begin{bmatrix} \sigma_{11} & 0 & \sigma_{13} \\ 0 & \sigma_{22} & 0 \\ \sigma_{13} & 0 & \sigma_{33} \end{bmatrix}. \tag{5a,b}$$

Tensors (5a,b) correspond to a monoclinic medium with the y-axis perpendicular to the plane of symmetry. There always exists a coordinate transformation that diagonalizes these symmetric matrices. This transformation is called the principal system of the medium and gives the three principal components of these tensors. In cubic and isotropic media the principal components are all equal. In tetragonal and hexagonal materials two of the three parameters are equal. In orthorhombic, monoclinic, and triclinic media, all three components are unequal. The permeability tensor is, for most materials, isotropic. Then, $\mu = \mu 1$, where μ is the scalar permeability, and 1 is the 3×3 identity matrix. Now, assume that the propagation is in the (x,z)-plane, and that the material properties are invariant in the y-direction. Then, E_x, E_z and H_y are decoupled from E_y, H_x and H_z. In absence of electric currents, the first three fields obey the TEM (transverse electric and magnetic fields) differential equations:

$$\frac{\partial E_z}{\partial x} - \frac{\partial E_x}{\partial z} = \mu \frac{\partial H_y}{\partial t} - M_y, \tag{6a}$$

$$-\frac{\partial H_y}{\partial z} = \sigma_{11} E_x + \sigma_{13} E_z + \varepsilon_{11} \frac{\partial E_x}{\partial t} + \varepsilon_{13} \frac{\partial E_z}{\partial t}, \tag{6b}$$

$$\frac{\partial H_y}{\partial x} = \sigma_{13} E_x + \sigma_{33} E_z + \varepsilon_{13} \frac{\partial E_x}{\partial t} + \varepsilon_{33} \frac{\partial E_z}{\partial t}. \tag{6c}$$

Numerical solution algorithm

Maxwell's equations (6a-c) can be written in matrix form as

$$\frac{\partial \mathbf{V}}{\partial t} = \mathbf{D}\mathbf{V} + \mathbf{M}, \tag{7}$$

where

$$\mathbf{V} = \begin{bmatrix} E_x \\ E_z \\ H_y \end{bmatrix}, \qquad \mathbf{M} = \begin{bmatrix} 0 \\ 0 \\ M_y/\mu \end{bmatrix}, \tag{8a,b}$$

and $\mathbf{D}$ is a spatial differential operator matrix given by

$$\mathbf{D} = \frac{1}{\gamma}\begin{bmatrix} -\varepsilon_{33}\sigma_{11} + \varepsilon_{13}\sigma_{13} & -\varepsilon_{33}\sigma_{13} + \varepsilon_{13}\sigma_{33} & -\varepsilon_{33}\partial_z - \varepsilon_{13}\partial_x \\ \varepsilon_{13}\sigma_{11} - \varepsilon_{11}\sigma_{13} & \varepsilon_{13}\sigma_{13} - \varepsilon_{11}\sigma_{33} & \varepsilon_{13}\partial_z - \varepsilon_{11}\partial_x \\ (-\gamma/\mu)\partial_z & (\gamma/\mu)\partial_x & 0 \end{bmatrix}, \tag{9}$$

with $\gamma = \varepsilon_{11}\varepsilon_{33} - \varepsilon_{13}^2$. Equation (7) is solved by a spectral time integration technique introduced in Tal-Ezer et al. (1990). Its formal solution is

$$\mathbf{V}(t) = \int_0^t e^{\theta \mathbf{D}}\mathbf{M}(t-\theta)d\theta, \tag{10}$$

where zero initial conditions have been assumed. In equation (10), $\exp(\theta\,\mathbf{D})$ is called the evolution operator of the system. Most frequently, an explicit or implicit finite-difference scheme is used to march the solution in time. This technique is based on a Taylor expansion of the evolution operator. In Tal-Ezer et al. (1990), the approach is based on a polynomial interpolation of the exponential function in the complex domain of the eigenvalues of the operator $\mathbf{D}$, over a set of points which is known to have some maximal properties. These points should lie on a T-shape set defined by the imaginary axis and the negative real axis of the complex frequency plane. In this way, the interpolating polynomial is 'almost best'. In the isotropic case, the eigenvalues $\lambda = i\omega$ (ω is complex frequency) of $\mathbf{D}$ satisfy the following characteristic equation:

$$\left(\lambda + \frac{\varepsilon}{\sigma}\right)\left[\lambda\left(\lambda + \frac{\sigma}{\varepsilon}\right) + \frac{1}{\varepsilon\mu}\kappa^2\right] = 0, \tag{11}$$

where κ is the real wavenumber. The solutions of (11) are: a static mode corresponding to the eigenvalue $\lambda = -\varepsilon/\sigma$, and two propagating modes lying close to the imaginary axis, corresponding to the other eigenvalues. Note that ε/σ is the relaxation time of the system, and $1/\varepsilon\mu$ is the square of the phase velocity at high frequencies. It can be seen that in the anisotropic case the eigenvalues also lie on the T-shape domain.

The set of interpolation points, known as Fejer points, is found through a conformal mapping between the unit disc and the domain of the eigenvalues T. Let $\chi(u)$ be a conformal mapping from the u-plane to z-space (with z a complex variable), which maps the complement of a disc of radius δ to the complement of T, where δ is the logarithmic capacity of T, given by the limit $\delta = |\chi'(\infty)|$, the prime denoting derivative with respect to the argument. The analytic expression for $\chi(u)$ corresponding to the domain T can be found in Tal-Ezer et al., (1990). The same function $\chi(u\delta)$ maps the complement of the unit disc to the complement of the domain D.

Then, the Fejer points are $z_j = \chi(u_j)$, $j = 0, ..., m-1$ where u_j are the m roots of the equation $u^m = \delta$, with m the degree of the polynomial. The set $\{z_j;\ j = 0, \ldots m-1\}$ has maximal properties of convergence. Then, the sequence of polynomials $P_m(z)$ of degree m found by interpolation to an arbitrary function $f(z)$, analytic on T at the points z_j, converge maximally to $f(z)$ on T. The interpolating polynomial in Newton form is

$$P_m(z) = a_0 + a_1(z - z_0) + a_2(z - z_0)(z - z_1) + \ldots + a_m(z - z_0)\ldots(z - z_{m-1}), \tag{12}$$

where $a_j = f[z_0, \ldots, z_j]$, $j = 0, \ldots, m-1$, are the divided differences. The approximating polynomial is given by $P_m(\mathbf{D}t)$ with $f(z) = e^z$.

To balance time integration and spatial accuracies, the spatial derivatives are computed by means of the Fourier pseudospectral method. This is a pseudospectral or collocation algorithm in which the magnetic field $H = H_y(w)$, ($w = x$ or z, $N = N_x$ or N_z) is approximated by a truncated series

$$H_N(w) = \sum_{r=0}^{N-1} \tilde{H}_r \phi_r(w) \tag{13}$$

of known expansion functions ϕ_r, where the expansion coefficients are chosen such that the approximate solution H_N coincides with the solution $H(w)$ at a discrete set $w_0, w_1, \ldots, w_{N-1}$ of sampling (or collocation) points,

$$H_N(w_j) = H(w_j), \qquad j = 0,\ldots,N-1. \tag{14}$$

The collocation points are defined by equidistant sampling points

$$w_j = jD_w, \tag{15}$$

where D_w is the grid spacing. The expansion functions are defined by

$$\phi_r(w) = e^{i\kappa_r w}, \tag{16}$$

with

$$\kappa_r = \frac{2\pi r}{ND_w}, \qquad r = 0, \ldots, N-1 \tag{17}$$

the wavenumber, whence

$$\phi_r(w_j) = e^{2\pi ijr/N}. \tag{18}$$

Since the functions ϕ_r are periodic, the Fourier pseudospectral method is appropriate for problems with periodic boundary conditions (for example, a wave which exits the grid on one side, reenters it on the opposite side). The coefficients $\tilde{H}_r$ are implicitly defined by

$$H(w_j) = \sum_{r=0}^{N-1} \tilde{H}_r e^{2\pi ijr/N}, \qquad j = 0, \ldots, N-1. \tag{19}$$

The sequence of $H(w_j)$ is the inverse discrete Fourier transform of the sequence of $\tilde{H}_r$. This set of equations is equivalent to

$$\tilde{H}_r = \frac{1}{N}\sum_{j=0}^{N-1} H(w_j) e^{-2\pi ijr/N}, \qquad r = 0, \ldots, N-1. \tag{20}$$

The computation of differential operators by the Fourier method conveniently reduces to a set of multiplications of the coefficients $\tilde{H}_r$ with factors $i\kappa_r$, since

$$\frac{\partial \phi_r(w)}{\partial w} = i\kappa_r \phi_r(w) \tag{21}$$

so that

$$\frac{\partial H_N(w)}{\partial w} = \sum_{r=0}^{N-1} i\kappa_r \tilde{H}_r \phi_r(w). \tag{22}$$

The spectral coefficients $\tilde{H}_r$ are computed by the Fast Fourier Transform (FFT). This algorithm is based on a vectorized version of the mixed-radix FFT (Temperton, 1983). The steps of the calculation of the first partial derivative are as follows:

$$H(w_j) \overset{FFT}{\rightarrow} \tilde{H}_r \rightarrow i\kappa_r \tilde{H}_r \overset{FFT^{-1}}{\rightarrow} \frac{\partial H}{\partial w}(w_j). \tag{23}$$

The method is infinitely accurate up to the Nyquist wavenumber, which corresponds to a spatial wavelength of two grid points. This means that if the source is band-limited, the algorithm is free of

numerical dispersion provided that the grid spacing is chosen such that $D_W \leq c_{min}/2f_{max}$, with f_{max} the cut-off frequency of the source and c_{min} the minimum phase velocity in the mesh.

Plane wave analysis

A brief plane wave analysis helps to understand the physics of wave propagation in this type of media. Let the magnetic field H_y be associated with the following homogeneous plane wave of slowness s and attenuation α

$$H_y = H_0 e^{i\omega t} e^{-i(\omega s - i\alpha)\hat{\mathbf{s}}\cdot\mathbf{x}}, \tag{24}$$

where ω is the angular frequency and $(\omega s - i\alpha)\hat{\mathbf{s}} = \mathbf{k}$ is the complex wavenumber vector with $\hat{\mathbf{s}} = (l_x, l_z)$ defining the propagation direction. Note that for homogeneous plane waves attenuation and propagation directions coincide.
The dispersion relation is obtained by replacing the plane wave solution into Maxwell equations (6). This yields

$$p_{33}l_x^2 + 2p_{13}l_x l_z + p_{11}l_z^2 - \mu\left(\frac{\omega}{k}\right)^2 = 0, \tag{25}$$

where

$$\begin{pmatrix} p_{11} & p_{13} \\ p_{13} & p_{33} \end{pmatrix} = \begin{pmatrix} \varepsilon_{11} - \frac{i}{\omega}\sigma_{11} & -\varepsilon_{13} + \frac{i}{\omega}\sigma_{13} \\ -\varepsilon_{13} + \frac{i}{\omega}\sigma_{13} & \varepsilon_{33} - \frac{i}{\omega}\sigma_{33} \end{pmatrix}^{-1}. \tag{26}$$

This relation defines a complex velocity

$$V \equiv \frac{\omega}{k} = \left(\frac{p_{33}l_x^2 + 2p_{13}l_x l_z + p_{11}l_z^2}{\mu}\right)^{1/2}. \tag{27}$$

The slowness and attenuation vectors can be expressed in terms of the complex velocity as

$$\mathbf{s} = \mathrm{Re}\left[\frac{1}{V}\right]\hat{\mathbf{x}} \quad \text{and} \quad \boldsymbol{\alpha} = -\omega \mathrm{Im}\left[\frac{1}{V}\right]\hat{\mathbf{x}}, \tag{28a,b}$$

respectively. The velocity of the energy (wavefront) is defined by the average power flow density divided by the average energy density and results to be

$$\mathbf{V}_e = \frac{V_p}{\mathrm{Re}[V]}\left\{\mathrm{Re}\left[\frac{1}{\mu V}[(p_{33}l_x + p_{13}l_z)\hat{\mathbf{e}}_x + (p_{11}l_z + p_{13}l_x)\hat{\mathbf{e}}_z]\right]\right\}, \tag{29}$$

where $V_p = 1/\mathrm{Re}[1/V]$ is the phase velocity.

Analytical solution

The analytical solution for the conducting case can be obtained by means of the correspondence principle (e.g., Ben-Menahem and Singh, 1981) in analogy with viscoelastic wave propagation. This requires to know the explicit expression of the perfectly dielectric solution in the frequency domain. Then, the dielectric constants can be replaced by the corresponding complex dielectric constants, and the dissipative solution obtained by an inverse time Fourier transform.
It can be shown that time harmonic TEM waves obey the following Helmholtz equation

$$(p_{11}\partial_{zz} + p_{33}\partial_{xx} + 2p_{13}\partial_{xz})H_y + \omega^2\mu H_y = i\omega M_y. \tag{30}$$

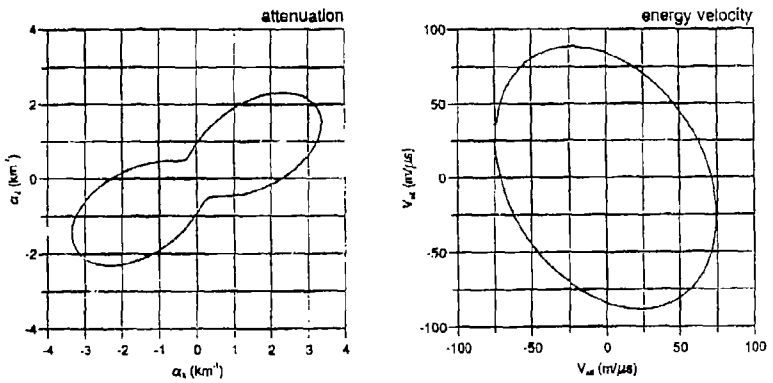

Figure 1. Polar representations of the attenuation and the energy velocity.

The solution to this equation is (Carcione and Cavallini, 1993)

$$H_y(x,z,\omega) = \pi\omega M_y H_0^{(2)}(\omega q), \tag{31}$$

where $H_0^{(2)}$ is the Hankel function of second kind, and

$$q = (p_{33}z^2 + p_{11}x^2 - 2p_{13}xz)/p, \tag{32}$$

with $p = p_{11}p_{33} - p_{13}^2$. To ensure a time-domain real solution, we take for $\omega < 0$

$$H_y(\omega) = H_y^*(-\omega), \tag{33}$$

where the superscript * denotes complex conjugation.

Simulations

We consider a monoclinic medium with $\varepsilon_{11} = 12.5\,\varepsilon_0$, $\varepsilon_{33} = 17.5\,\varepsilon_0$, $\varepsilon_{13} = -4.3\,\varepsilon_0$ and $\sigma_{11} = 3 \times 10^{-5}\,S\,m^{-1}$, $\sigma_{33} = -7 \times 10^{-5}\,S\,m^{-1}$, $\sigma_{13} = -3.46 \times 10^{-5}\,S\,m^{-1}$. The magnetic permeability has been taken equal to that of vacuum. The source central frequency is 300 KHz with a cutoff of approximately 600 KHz. The numerical mesh has $N_x = N_z = 165$ with a uniform grid spacing $D_x = D_z = 20$ m. The solution is propagated to 22.72 μs with a first time step of 9.92 μs corresponding to the duration of the source and two subsequent time steps of 6.4 μs.

Figure 1 displays polar diagrams of the attenuation and energy velocity curves at a frequency of 600 KHz. The orientation and shape of the curves depend on the dielectric and conductivity tensors. As can be seen, the attenuation is highly anisotropic with maximum dissipation at approximately 30° from the horizontal axis. Analogously, the energy velocity (wavefront) has an anisotropic character.

Figure 2 compares numerical and analytical solutions at three different receivers whose locations (x,z), relative to the source, are indicated in the pictures. The distance between the source and each receiver is 600 m. As can be appreciated, the agreement between solutions is virtually perfect despite the anomalous behaviour of the phase velocity at low frequencies. In first place, comparing the different onset values at each receiver reveals the anisotropic character of the wavefield, as predicted

by the energy velocity curve represented in Figure 1. Finally, the anisotropic character of the dissipation is in agreement with the attenuation curve displayed in Figure 1.

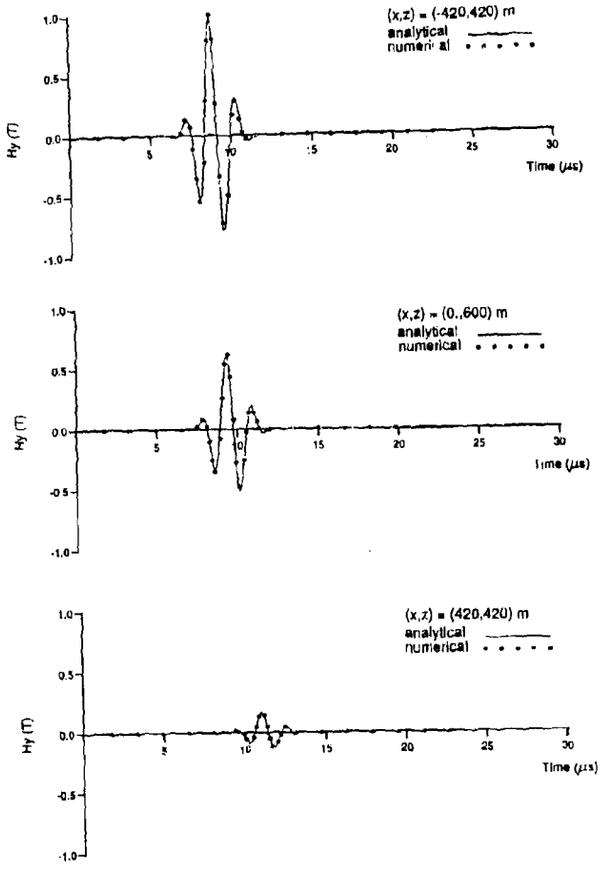

Figure 2. Comparison between analytical and numerical solutions.

The last example simulates wave propagation through a steplike structure consisting in an isotropic perfectly dielectric step with $\varepsilon = 8\varepsilon_0$ and $\mu = \mu_0$, embedded in an anisotropic conducting medium whose properties are the same as in the previous example. The mesh, the source and the time steps are as before. Two snapshots of the magnetic field are represented in Figure 3. As can be observed, wave propagation far from the interfaces agrees with the results seen in the homogeneous case. Moreover, the wavefront inside the step has cylindrical shape and shows no directional attenuation.

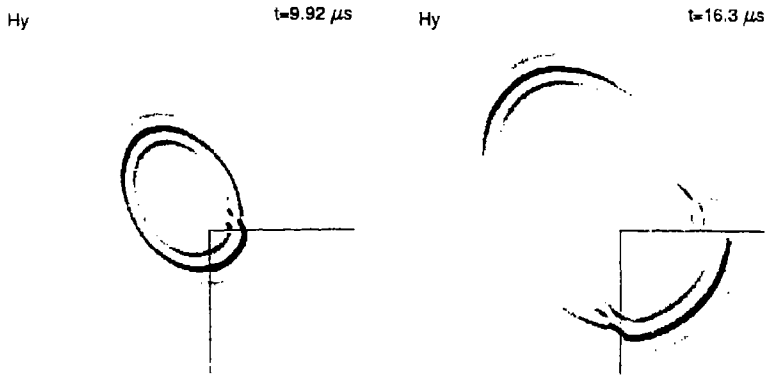

Figure 3. Snapshots at two successive propagation times.

Finally, the wave diffracted by the edge can be appreciated together with a lateral wavefront connecting the refracted and reflected wavefields.

Acknowledgment. This work was supported in part by the Commission of the European Communities under the GEOSCIENCE project.

References

Ben-Menahem A. and S. G. Singh. 1981, Seismic waves and sources, Springer Verlag, New York.

Carcione J. M. and F. Cavallini, 1993, A semi-analytical solution for the propagation of pure shear waves in dissipative monoclinic media, submitted to Acoustics Letters.

Chew, W. C., 1990, Waves and fields in inhomogeneous media: Van Nostrand Reinhold, New York.

Tal-Ezer, H., Carcione, J.M., and Kosloff, D., 1990, An accurate and efficient scheme for wave propagation in linear viscoelastic media, Geophysics, 55, 1366-1379.

Temperton, C., 1983, Fast mixed radix real Fourier transforms, J. Comp. Phys., 52, 340-350.

CCM: CIRCULAR CYLINDERS MODELER FOR ELECTROMAGNETIC SCATTERING FROM COMPOSITE TWO DIMENSIONAL OBJECTS

Atef Z. Elsherbeni and Clayborne D. Taylor Jr.
Department of Electrical Engineering, University of Mississippi
University, MS 38677

Abstract - CCM is a new electromagnetic software package developed to facilitate the scattering and radiation from composite two dimensional scatterers. Composite two dimensional scatterers are modeled by a collection of circular cylinders of different types. The cylinders are made of either homogeneous isotropic dielectric material, perfectly conducting material, material characterized by a surface impedance, or a combination thereof. The method of solution is based on a rigorous analysis for the scattering of electromagnetic waves from multiple cylinders. In this technique the appropriate boundary conditions due to the initial source of excitation and all infinite interactions of scattered waves between the cylinders are applied on the surface of each cylinder. The original source of excitation can be a plane wave or a line source field with either TM or TE type of polarization. The CCM program provides a graphical display of the modeled scatterers and rectangular or polar plots for different components of the associated fields.

INTRODUCTION

Computation of electromagnetic scattered or radiated fields from complex two dimensional scatterers can be a slow and expensive process. Quicker results may be obtained through geometrical approximation of the actual scatterers by smaller objects for which efficient techniques can be used. Following this procedure, the cross-section of two dimensional scattering objects is discretized into segments represented by circular cylinders. The scatterer is then transformed into a collection of circular parallel cylinders of arbitrary radii and positions. The solution of the scattering from such arbitrary array of parallel cylinders can be achieved by applying the appropriate boundary conditions on the surface of each cylinder. However, in order to obtain a rigorous solution for such a problem, one must consider the multiple interaction components of the fields between the cylinders. This type of analysis is reported in details elsewhere [1-4] and briefly summarized in the following section. This paper addresses the circular cylinder modeler (CCM) software package that simplifies the simulation of composite two dimensional scatterers by circular cylinder, implements the scattering algorithm, and finally provides a graphical representation for the computed patterns.

SCATTERING ALGORITHM

Consider an E-polarized incident wave (TM with respect to z axis) where the electric field has a z component only with all vectors independent of z of the circular cylindrical coordinates (ρ,ϕ,z). A time dependence $e^{j\omega t}$ is assumed and suppressed throughout. The incident plane wave is expressed in terms of the cylindrical coordinates of the i^{th} cylinder, whose center is located at (ρ_i', ϕ_i'), as

$$E_{zi}^{inc}(\rho_i,\phi_i) = E_0\, e^{jk_0\rho_i'\cos(\phi_i'-\phi_0)}\, e^{jk_0\rho_i\cos(\phi_i-\phi_0)}$$
$$= E_0\, e^{jk_0\rho_i'\cos(\phi_i'-\phi_0)} \sum_{n=-\infty}^{\infty} j^n J_n(k_0\rho_i)\, e^{jn(\phi_i-\phi_0)} \quad (1)$$

where $k_0=2\pi/\lambda$ which is the free space wave number, λ is the wavelength, and ϕ_0 is the angle of incidence of the plane wave with respect to the negative x. The corresponding scattered electric field component from the i^{th} cylinder can be expressed as,

$$E_{zi}^{s}(\rho_i,\phi_i) = E_0\sum_{n=-\infty}^{\infty} c_{in}\, H_n^{(2)}(k_0\rho_i)\, e^{jn\phi_i} \quad (2)$$

and the transmitted field component inside the dielectric material of the i^{th} cylinder is given by

$$E_{zi}^{d}(\rho_i,\phi_i) = E_0\sum_{n=-\infty}^{\infty} b_{in}\, J_n(k_i\rho_i)\, e^{jn\phi_i} \quad (3)$$

while the ϕ components of the magnetic field are obtained from Faraday's law. The c_{in} and b_{in} are unknown expansion coefficients. The superscripts s and d refer to the scattered fields in free space and the fields transmitted in the dielectric material, respectively. In the above equations, $J_n(x)$ and $H^{(2)}_n(x)$ are the Bessel and the Hankel functions of order n and argument x.

From the above expressions, one notices that the scattered and internal fields associated with the i^{th} cylinder are based on its local coordinates (ρ_i,ϕ_i). Furthermore, for an array of M cylinders, the interaction between the cylinders in terms of multiple scattered fields will require a representation of the scattered field from one cylinder in terms of the local coordinates of another. Therefore, The addition theorem for the Bessel and Hankel functions is used to transfer field components from one cylinder coordinates to the other [3,4].

In this technique, the unknown coefficients related to the i^{th} cylinder c_{in} and b_{in} in (3) and (4) are assumed to include the effect of all interactions between the cylinders. The solution for c_{in} and b_{in} can be obtained by applying the appropriate boundary conditions on the surface of all cylinders. The boundary conditions on the surface of the i^{th} cylinder is then given by

$$E_{zi}^{inc} + \sum_{s=1}^{M} E_{zs}^{s} = E_{zi}^{d} \quad , \quad \rho_i = r_i,\ 0\le\phi_i\le 2\pi \quad (4)$$

$$H_{\phi i}^{inc} + \sum_{g=1}^{M} H_{\phi g}^{s} = H_{\phi i}^{d} \quad , \quad \rho_i = r_i,\ 0 \le \phi_i \le 2\pi \tag{5}$$

Before substituting the field expressions into (4) and (5), it is required to express the scattered electric field from the g^{th} cylinder in terms of the local coordinates of the i^{th} cylinder and obtain an expression for the scattered magnetic field component from cylinder g in terms of the local coordinates of the i^{th} cylinder. This latter requirement is done in two steps. First, the scattered electric field component from cylinder g is transferred to the local coordinates of cylinder i, then the magnetic field component is obtained in terms of the electric field component from Faraday's law. Next one should use the orthogonal property of the exponential function $e^{jn\phi}$ for the resulting expressions from (4) and (5). After some mathematical manipulations, the following relation from the application of the boundary conditions on the surface of the i^{th} cylinder is obtained

$$v_i^{\ell} = \sum_{g=1}^{M} \sum_{n=-\infty}^{\infty} c_{gn}\, s_{ig}^{\ell n} \tag{6}$$

where

$$v_i^{\ell} = e^{j k_0 \rho_i' \cos(\phi_i' - \phi_{v'})}\, j^{\ell}\, e^{-j\ell\phi_{v'}} \tag{7}$$

$$s_{ig}^{\ell n} = \begin{cases} H_{\ell-n}^{(2)}(k_0 d_{ig})\, e^{-j(\ell-n)\phi_{ig}} , & i \neq g \\ \dfrac{\eta_{ri} H_{\ell}^{(2)\prime}(k_0 r_i)\, J_{\ell}(k_i r_i) - H_{\ell}^{(2)}(k_0 r_i)\, J_{\ell}'(k_i r_i)}{J_{\ell}(k_0 r_i)\, J_{\ell}'(k_i r_i) - \eta_{ri} J_{\ell}'(k_0 r_i)\, J_{\ell}(k_i r_i)} , & i = g \text{ and } n = \ell \\ 0 , & \text{otherwise} \end{cases} \tag{8}$$

The normalized intrinsic impedance and the wave number for the dielectric medium of the i^{th} cylinder are $\eta_{ri} = \sqrt{\mu_{ri}/\varepsilon_{ri}}$ and $k_i = k_0\sqrt{\varepsilon_{ri}\mu_{ri}}$, respectively, while μ_{ri} and ε_{ri} are the relative permittivity and relative permeability, respectively. The integers $n,\ell=0, \pm1, \pm2, \ldots, \pm N_i$ and $i,g=0, 1, 2, \ldots, M$. Theoretically, N_i is an integer which is equal to infinity; however practically it is related to the radius and type of the i^{th} cylinder by the relation $N_i = 3k_0a_i$. The prime denotes the derivative of the function with respect to its argument. The elements $s_{ig}^{\ell n}$ and $s_{ii}^{\ell\ell}$ represent the interaction (mutual) and non-interaction (self) terms, respectively.

The application of the same boundary conditions on the surface of all remaining M -1 cylinders, results in similar expressions to (8) except i=1,2,3, ...M. All these M equations are then cast into a matrix form such as

$$[V] = [S]\ [C] \tag{9}$$

The solution of the truncated matrix equation yields the unknown coefficients c_{in}. Once the scattering coefficients are obtained the coefficients b_{in} can be readily evaluated. Thus the scattered (near and far) and transmitted fields can be computed in the presence of the array of cylinders.

The special case of scattering from perfectly conducting cylinders can be analyzed by letting η_{ri} in equation (8) to be equal to zero. The solution for the TE polarization, however, is obtained by replacing η_{ri} by $1/\eta_{ri}$. The analysis for imperfectly conducting or impedance cylinders, is very similar and straight forward. The basic difference is that the impedance boundary condition on the surface of each cylinder must be satisfied instead of the conditions represented by equations (4) and (5).

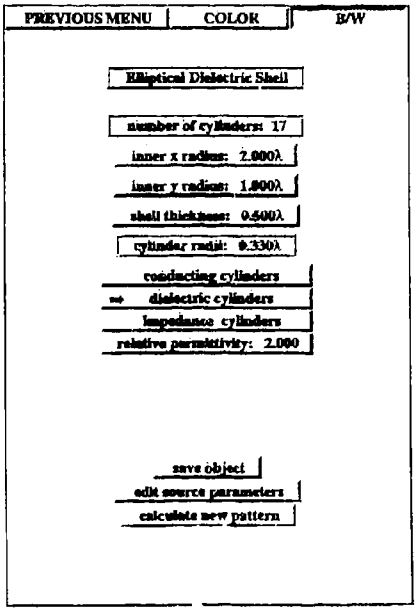

Fig. 1: Parameter view window.

PROGRAM DESCRIPTION

The CCM program runs on an IBM or compatible personal computer with Intel 486DX processor, or compatible, DOS operating system 8 Mbytes of RAM, SVGA graphics display and a Microsoft Mouse or compatible pointing device. For quality hard copies, a postscript compatible printer output is supported. The CCM user interface is mouse driven and contains user selectable areas that appear as buttons with yellow color. Two basic screens are displayed throughout the operation with the program. The first is the opening screen which contains a set of buttons that represent the basic geometries or building blocks for modeling a composite structure. The basic geometries available in CCM are: circular conducting cylinder, circular dielectric shell, elliptical conducting cylinder, elliptical dielectric shell, *thin strip, rectangular shell, and parabolic reflector.* In addition to these basic geometries, the user can model a complex scatterer by using the *arbitrary configuration*

of cylinders or the *macro design editor* options. The geometrical data for any of the modeled geometries can be saved on a disk file for future use. The second screen (the simulation screen) is divided into three sections, or view windows. The left half of the screen is the parameter window and is used to display the scatterer and source parameters as shown in Fig. 1. Selection of the source parameter button in the parameter window displays a new set of buttons in the parameter window from which the user can define the desired source of excitation type (line source or plane wave), position, and polarization (TE or TM). The right half of the simulation screen is divided into two sections, the bottom right corner illustrates the two dimensional representation of the modeled scatterer and the source of incident wave as shown in Fig. 2 for a simulated elliptical dielectric shell, and the top right corner displays the computed pattern, either in a cartesian or a polar format, (see Fig. 3). A complete description of the program components and operation can be found in [5].

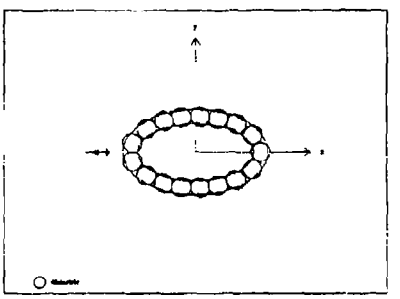

Fig. 2: The simulation of an elliptical dielectric shell.

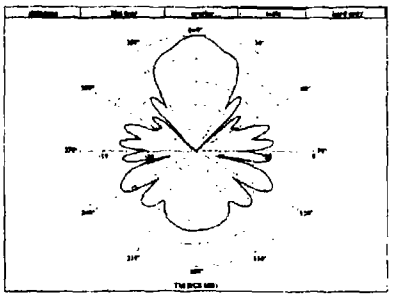

Fig. 3: The TM bi-static RCS in the plot view window.

MODELING OF COMPOSITE SCATTERERS

An example showing the capabilities of the CCM program in simulating composite scatterers is shown in Fig. 4. In this figure the scatterer is composed of conducting, dielectric, and impedance cylinders. The simulation of this scatterer starts from the opening screen by selecting the *elliptic dielectric shell* option. Edit the inner x, y radii and the thickness of the shell to read .3λ, .2λ, and .025λ, respectively, and change the permittivity to 5. Use the *save object* button to save this geometry in a file named ELLIPSE.GEO, for example. The next step is to go to the opening screen and select the thin strip option. Change the strip length and width, as .17λ, and .011λ, respectively. Select the cylinders type to be impedance as shown in Fig. 5. Save this geometry to a file in this exampl named STRIP.GEO. From the first screen select the *circular conducting cylinder* option. Change the number of cylinders to 39, the cylinder radii to 0.01λ, and the big cylinder radius to 0.124λ, as shown in Fig. 6. The user can then select the save option button to save this geometry

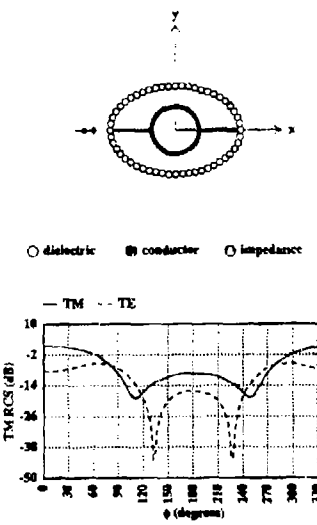

Fig. 4: TM and TE RCS of an incident plane wave on a simulated composite scatterer.

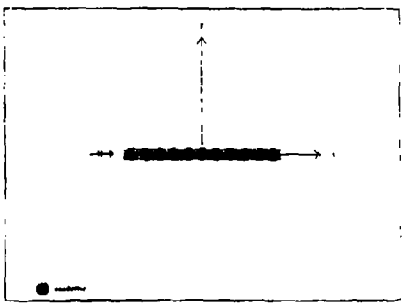

Fig. 5: simulation of an impedance strip.

in a file and name it CYLINDER.GEO. From the opening screen select the arbitrary configuration option. Now go to the opening screen and select the *macro design editor* and load CYLINDER.GEO. Next load the strip geometry from the file STRIP.GEO and shift it to the right by setting the radial distance to 0.209λ. Again, load STRIP.GEO, however, at this time shift the strip to the left by the same amount by changing the angular position to 180° as shown in Fig 7. Now, by loading the ELLIPSE.GEO file, the

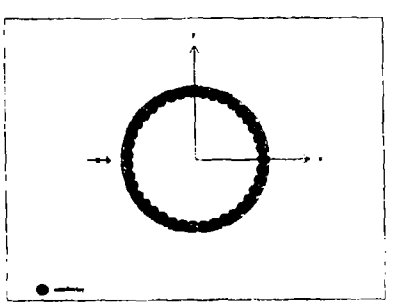

Fig. 6:Simulation of a perfectly conducting cylinder.

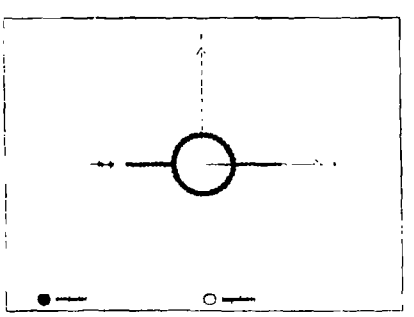

Fig. 7: Simulation of a perfectly conducting cylinder and two impedance strips.

geometry view window should now display the scattering geometry in Fig. 4. Next select the source parameter button to define the source of the incident field as a plane wave with incident angle 180°. Select the TE excitation, and select the calculate new pattern button. Use the *write* button from the *overlay* menu list to save this pattern in a file named TE.DAT. Change TE to TM in the source parameters window, and again select the calculate new pattern button. When the TM pattern is displayed, use the *file 1* button from the *overlay* menu list to load the TE pattern from the file TE.DAT. Use the scale menu list (*min y*, *max y*, and *y tics* buttons) to change the minimum y to -50 dB and the maximum y to 10 dB. Select the *y tics* button to change the number of y tic marks to 6. The resulting TM and TE patterns should look like those in Fig. 4. It is worthwhile to mention that the CPU time required to compute the patterns (180 observation points) in Fig. 4 was approximately 1 and 3.8 minutes for the TM and TE modes respectively, using a 486/66MHz personal computer. Figure 4 is produced on Laserjet postscript printer using the *hard copy* button option in the plot view window.

CONCLUSION

Growth in computational and graphics potentials of present computers allows for a new generation of simulation tools. The developed CCM program is a simulation tool that provides an interactive design procedure for composite two dimensional scatterers using circular cylinders. The flexibility of adding, removing, or editing each individual cylinder or object, using simple mouse and keyboard strokes makes CCM suitable for investigating many different variations of scattering geometries. CCM requires a very small time on IBM or compatible personal computer to compute the scattered data from complex two dimensional objects. This rapid simulation and analysis of scattering from composite objects can be used to gain a better understanding of field interactions in complex geometries.

REFERENCES

[1] A. Z. Elsherbeni and A. A. Kishk, "Scattering from Multiple Imperfectly Conducting Circular Cylinders." In Proceedings of the *Progress in Electromagnetic Research Symposium-PIERS* ,Cambridge, MA, p. 344, July 1989.

[2] A. Z. Elsherbeni and A. A. Kishk, "Modeling of Cylindrical Objects by Circular Dielectric or Conducting Cylinders." *IEEE Trans. Antennas Propagat.*, vol. AP-40, no. 1, pp. 96-99, 1992.

[3] A. Z. Elsherbeni and A. A. Kishk, Author's reply on comments on "Modeling of Cylindrical Objects by Circular Dielectric or Conducting Cylinders." *IEEE Trans. Antennas Propagat.*, vol. AP-41, no. 9, pp. 1343-1344, 1993.

[4] A. Z. Elsherbeni, " A Comparative Study of 2-D Multiple Scattering Techniques," Radio Science. (in press)

[5] A. Z. Elsherbeni and C.D. Taylor, Jr., "Interactive Modeling of Composite Two-Dimensional Scatterers Using Dielectric, Conducting, and Impedance Circular Cylinders: CCM Program (version 1)." Technical Report No. TR-93-5, Department of Electrical Engineering, University of Mississippi, University, MS, Sept. 1993.

DETERMINATION OF VELOCITY AND ATTENUATION OF SURFACE ACOUSTIC WAVES IN LAYERED PIEZOELECTRIC MEDIA

R. Weigel[1], U. Rösler[1], H. Meier[2], P. Russer[1,3]

[1] Technische Universität München, Lehrstuhl für Hochfrequenztechnik,
Arcisstr. 21, D–80333 München, Germany
[2] Siemens Matsushita Components, OFW ENT,
Balanstr. 73, D–81617 München, Germany
[3] Ferdinand Braun Institut für Höchstfrequenztechnik,
Rudower Chaussee 5, D–12489 Berlin, Germany

Abstract – A method for computing the phase velocity and the attenuation of surface acoustic waves (SAW's) under a non–piezoelectric, conducting layer on a semi–infinite piezoelectric substrate is presented. The method consists of a combination of matrix–, partial wave– and simplex–analysis. As an example, we compute the phase velocity and the attenuation constant per wavelength for the SAW mode on a YZ–lithium niobate ($LiNbO_3$) substrate with a layer of amorphous silicon (a:Si) at a frequency of 450 MHz in dependence of the silicon conductivity and film thickness. We found that a properly designed a:Si/$LiNbO_3$–structure may be used as an absorber and replace bulky adhesives.

I. INTRODUCTION

Surface acoustic waves (SAW's) can be generated and guided at the surface of an elastic solid. Over the past twenty five years, this phenomenon has led to a considerable host of SAW devices and systems for consumer, commercial and military applications in modern electronics to carry out particular signal processing functions with great technical facility and cost–effectiveness [1–4]. To suppress unwanted reflections at the chip edges, absorbing strips consisting usually of silicon adhesives (with about 1 mm width) are deposited at certain locations on top of the substrate. The attenuation constants achieved are in the order of 1 dB/λ (λ: wavelength). As a technology, silk–screen printing is used which is incompatible with the photolithographic thin–film techniques used for the fabrication of the other SAW components. Further shortcomings of the adhesive approach are in the areas of long–term stability and chip space requirements. A second mechanical attenuation method is the use of polyimide films having attenuation constants of up to 0.6 dB/λ [5]. Basically different approaches are based on the evaporation of thin films having finite conductivity. The interaction of SAW's propagating on a piezoelectric substrate with charge carriers in thin conducting films deposited on the substrate involves changes in both attenuation and dispersion. Metals such as gold and aluminum [6,7] as well as semiconductors [8,9] have been investigated. The major drawback of metal films is caused by the very small film thicknesses in the order of one nanometer which are required to attain the proper sheet conductivity σ_s of about 10^{-6} $\square\Omega^{-1}$. On the other hand, the use of semiconducting films allows for moderate thicknesses which can easily be fabricated. This is due to the fact that the conductivity of semiconductors is much less than that of metals and can largely be varied by doping.

II. SOLUTION OF WAVE EQUATIONS

In what follows, we consider a half–space of a piezoelectric material with a thin layer of an isotropic semiconducting material, of thickness h, on top, as shown in Fig. 1. A Cartesian coordinate system is introduced so that the SAW's travel in the x_1 direction along the surface whose normal is in the x_3 direction with the substrate being in the lower halfspace $x_3 < 0$. This coordinate system may have an arbitrary orientation with respect to the crystal axes provided the tensors describing the media are properly transformed to the (x_1,x_2,x_3) coordinates. Formulas which govern this transformation may be found in [10].

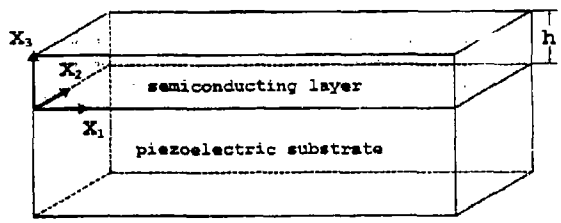

Fig. 1 Piezoelectric half–space coated with a thin isotropic semiconducting film

Elastic wave propagation in a piezoelectric medium (which must of course be anisotropic) is generally governed by the mechanical equations of motion and Maxwell's equations. Since the velocities of the surface acoustic waves are many magnitudes less than those of electromagnetic waves, the quasistatic approximation of Maxwell's equations can be used. The analysis includes the effects of mass–loading and coupling with the charge carriers in the semiconducting layer. Each region of the layered structure is characterized by its own set of constants which are as follows: elastic stiffness, piezoelectric and dielectric tensors c_{ijkl}, e_{kij} and ϵ_{ik}, respectively, and mass density ρ. The elements of the dielectric tensor ϵ_{ik} are complex numbers with the imaginary parts accounting for the ohmic losses. In general, the three particle displacements u_i and the potential ϕ must satisfy the following set of four coupled wave equations in each medium:

$$\sum_i \sum_k \left[\sum_l c_{ijkl} \frac{\partial^2 u_k}{\partial x_i \partial x_l} + e_{kij} \frac{\partial^2 \phi}{\partial x_k \partial x_i} \right] = \rho \frac{\partial^2 u_i}{\partial t^2} \tag{1}$$

$$\sum_k \sum_i \left[\sum_l e_{ikl} \frac{\partial^2 u_k}{\partial x_i \partial x_l} - \epsilon_{ik} \frac{\partial^2 \phi}{\partial x_k \partial x_i} \right] = 0 \,. \tag{2}$$

The indices in equations (1) and (2) change from 1 to 3. For the wave solutions in the substrate s, the layer l, and the superstrate v the following partial wave ansatz is made:

(i): superstrate $x_3 > h$:

$$\phi^v = B^v \exp(jk\gamma x_3) \exp[jk(\delta x_1 - vt)] \tag{3}$$

(ii): semiconducting layer $0 \leq x_3 \leq h$:

$$u_{in}^{l} = A_{in}^{l} \exp(jk\eta_n x_3) \exp[jk(\delta x_1 - vt)] \quad i=1,2,3 \tag{4}$$

$$\phi^{l} = B_{n}^{l} \exp(jk\eta_n x_3) \exp[jk(\delta x_1 - vt)] \tag{5}$$

(iii): piezoelectric substrate $x_3 < 0$:

$$u_{in}^{s} = A_{in}^{s} \exp(jk\alpha_n x_3) \exp[jk(\delta x_1 - vt)] \quad i=1,2,3 \tag{6}$$

$$\phi^{s} = B_{n}^{s} \exp(jk\alpha_n x_3) \exp[jk(\delta x_1 - vt)] \tag{7}$$

Here, A_{in} and B_n are the normalized partial amplitudes, and γ, η, α are the transverse decay constants in x_3–direction. The parameter $\delta = 1 + j\delta_1$ describes the wave propagation in x_1–direction, and k and v designate wavenumber and velocity, respectively. Substituting the formulation of the solution into equations (1) and (2) we obtain for each medium (in general) a set of four homogenoues equations for the relative amplitudes A_{in} and B_n, i.e each region is described by a 4x4 system matrix. The system matrices have a nontrivial solution if their determinants of coefficients vanish. This condition leads to polynomial equations of the 8th order in the transverse decay constants. For given values of velocity v and attenuation constant δ_1 we obtain in general four eigenvalues α_n for a physical substrate solution (α–solutions with a negative imaginary part only) and eight eigenvalues η_n for a physical layer solution. For every set of eigenvalues we find the eigenvector of normalized amplitudes.

The superposition of the partial waves (four in the substrate and eight in the layer) leads to the general physical solution of equations (1) and (2):

(i): superstrate $x_3 > h$:

$$\phi^{v} = B^{v} \exp(jk\gamma x_3) \exp[jk(\delta x_1 - vt)] \tag{8}$$

(ii): semiconducting layer $0 \leq x_3 \leq h$:

$$u_{in}^{l} = \sum_{n=1}^{8} W_n A_{in}^{l} \exp(jk\eta_n x_3) \exp[jk(\delta x_1 - vt)] \tag{9}$$

$$\phi^{l} = \sum_{n=1}^{8} W_n B_{n}^{l} \exp(jk\eta_n x_3) \exp[jk(\delta x_1 - vt)] \tag{10}$$

(iii): piezoelectric substrate $x_3 < 0$:

$$u_{in}^{s} = \sum_{n=9}^{12} W_n A_{in}^{s} \exp(jk\alpha_n x_3) \exp[jk(\delta x_1 - vt)] \tag{11}$$

$$\phi^{s} = \sum_{n=9}^{12} W_n B_{n}^{s} \exp(jk\alpha_n x_3) \exp[jk(\delta x_1 - vt)] \tag{12}$$

with W_n being weighting factors, i.e. normalized amplitudes. These equations have to fulfill the mechanical and electrical boundary conditions at the interfaces $x_3 = 0$ and $x_3 = h$ which are as follows (i = 1,2,3):

(i): at the interface $x_3 = 0$:

$$u_i^s = u_i^l \tag{13}$$

$$T_{3i}^s = T_{3i}^l \tag{14}$$

$$(\vec{E}^l - \vec{E}^s) \times \vec{n} = \vec{0} \tag{15}$$

$$(\vec{D}^l - \vec{D}^s) \cdot \vec{n} = \rho_{s1} \tag{16}$$

(ii): at the interface $x_3 = h$:

$$T_{3i}^l = 0 \tag{17}$$

$$(\vec{E}^v - \vec{E}^l) \times \vec{n} = \vec{0} \tag{18}$$

$$(\vec{D}^v - \vec{D}^l) \cdot \vec{n} = \rho_{s2} \tag{19}$$

Herein, T, $\vec{E}$, $\vec{D}$, and ρ_s denote mechanical stress, electrical field strength, electrical displacement, and surface charge density, respectively [1,2]. The surface charge density ρ_s can be derived from

$$\frac{\partial \rho_s}{\partial t} = -\vec{\nabla} \cdot (\sigma_s \vec{E}_{tan}) , \tag{20}$$

with σ_s being the sheet conductivity. The explicit formulation of the boundary conditions are given in [11].

These conditions can be combined to form a 12x12 matrix – the boundary matrix. For a physical solution, the determinant of the boundary matrix must also vanish. The general solution must cause the determinants of the system matrices as well as the determinant of the boundary matrix to vanish. Because of their complicated structures these matrices cannot be transformed into equations for the velocity v, the attenuation constant δ_l and formulas for the decay constants α, η, and γ. Thus, the following numerical procedure has been used. For a chosen set of values for v and δ_l the eigenvalues and eigenvectors from the set of equations for the relative amplitudes A_{in} and B_n are found and substituted into the determinant of the boundary matrix. If this determinant is zero with a prescribed accuracy the chosen and computed parameters are correct. Then the weighting factors W_n are computed and after the substitution in equations (8) to (12) we obtain the solution. The absolute amplitudes can be determined from the power flow. In the second case, if the determinant of the boundary matrix has a nonzero value, we vary the phase velocity v and the attenuation constants δ_l (using a simplex algorithm), and the procedure must be repeated unless the determinant of the boundary conditions is zero.

III. NUMERICAL RESULTS

Let us consider the fundamental SAW mode propating on a YZ–lithium niobate (YZ- $LiNbO_3$) substrate coated with a thin layer of amorphous silicon (a:Si). As a reference frequency, we chose 450 MHz, i.e. the free substrate wavelength is 7.75 μm. In our calculations, we used the following material data [12,13]:

YZ–$LiNbO_3$: $c_{11} = 1.98432 \cdot 10^{11}\,Nm^{-2}$, $c_{12} = 0.54775 \cdot 10^{11}\,Nm^{-2}$
$c_{13} = 0.65190 \cdot 10^{11}\,Nm^{-2}$, $c_{14} = 0.07884 \cdot 10^{11}\,Nm^{-2}$
$c_{33} = 2.27965 \cdot 10^{11}\,Nm^{-2}$, $c_{44} = 0.59645 \cdot 10^{11}\,Nm^{-2}$
$e_{15} = 3.7159\,Asm^{-2}$, $e_{22} = 2.4365\,Asm^{-2}$
$e_{31} = 0.3062\,Asm^{-2}$, $e_{33} = 1.7847\,Asm^{-2}$
$\epsilon_{11} = 46.3847\,\epsilon_0$, $\epsilon_{33} = 26.702\,\epsilon_0$
$\rho = 4628.0\,kgm^{-3}$

a:Si: $c_{11} = 1.50 \cdot 10^{11}\,Nm^{-2}$, $c_{12} = 0.56 \cdot 10^{11}\,Nm^{-2}$, $c_{44} = 0.47 \cdot 10^{11}\,Nm^{-2}$
$\epsilon = 11.9\,\epsilon_0$
$\rho = 1831.0\,kgm^{-3}$

We compare four different theoretical models for the space charge density distribution in the layer:

1. In a "thick" film model, we assume the entire space charge being concentrated at $x_3 = 0$ ($\rho_{s1} = \rho_s$; $\rho_{s2} = 0$).

2. In a "thin" film model, we assume the space charge to be divided into two equal parts ($\rho_{s1} = \rho_{s2} = \rho_s/2$) which are located at the interfaces $x_3 = 0$ and $x_3 = h$, i.e. we substitute $\sigma_s/2$ in equation (20).

Since physically the space charge is distributed along the x_3 direction in the layer and not located exclusively at the interfaces, both models are only approximative. Thus, we developed a third model which is as follows:

3. To account for the finite conductivity σ, we introduce in equation (2) a "complex permittivity" of the layer as

$$\epsilon^1 = \epsilon + j\frac{\sigma}{2\pi f}. \tag{21}$$

(The plus sign is due to the time harmonic ansatz $\exp(-j\omega t)$ which we use in the above partial wave formulations.)

4. In another model formulated by *Ingebrigtsen* the interaction of the SAW mode with the carrier waves is expressed in terms of a TM–wave impedance of the layer [14]. As material parameters, we use $K^2 = 4.12\,\%$, $D_n = 35 \cdot 10^{-4}\,m^2s^{-1}$, and $D_p = 12.5 \cdot 10^{-4}\,m^2s^{-1}$ with K^2 being the electromechanic coupling coefficient, and D_n and D_p being the diffusion constants of electrons and holes in crystalline silicon, respectively.

Using these models, we compute the phase velocity and the attenuation constant per wavelength in dependence of the silicon conductivity for different film thickness values h. In Figs. 2 and 3 the curves are plotted for the thickness of the silicon layer being 200 nm. Curve 1 is due to our "thick" film model, curve 2 due to our "thin" film model, curve 3 due to our "complex permittivity" model, and curves 4 and 5 are due to *Ingebrigtsen*'s model for both negative and positive carriers, respectively. In all models, we found a maximum attenuation constant near $\sigma_s = 1.6 \cdot 10^{-6}\,\Omega^{-1}$. However, the models differ considerably in amplitude. Which of the theories fits best to the phenomenon of interaction between the SAW mode and the carriers in the layer has to be distinguished by measurements.

Now, let us account for the shielding of the electric field due to the carrier accumulation in the layer by introducing a complex sheet conductivity in our "thick" film model according to [15]

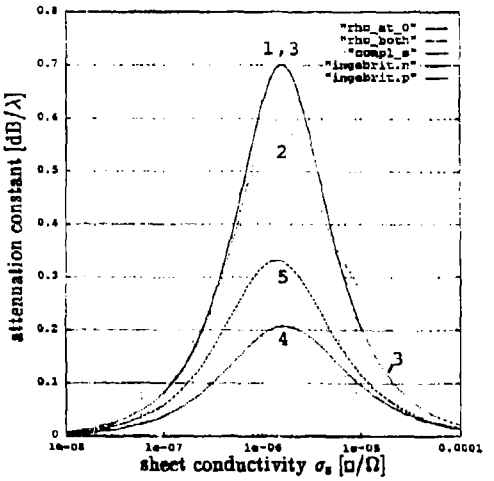

Fig. 2 Computed variation of attenuation constant in a a:Si/$LiNbO_3$–structure in dependence of the conductivity of the layer (h = 200 nm; f = 450 MHz)

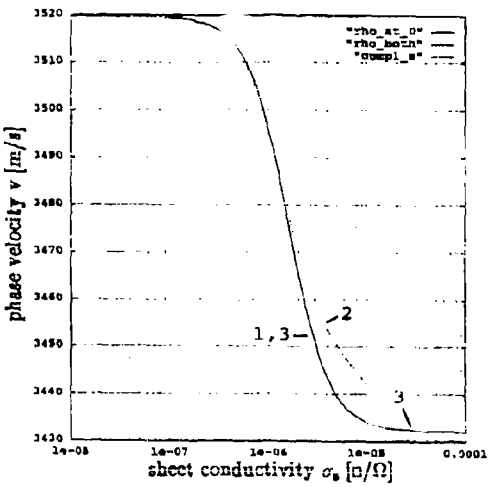

Fig. 3 Computed variation of phase velocity in a a:Si/$LiNbO_3$–structure in dependence of the conductivity of the layer (h = 200 nm; f = 450 MHz)

$$\sigma_s^* = \sigma_s\,(1-j\varkappa)\,. \tag{22}$$

Figs. 4 and 5 demonstrate the influence of the imaginary part x. Herein, *Ingebrigtsen*'s model is depicted as a reference. As is seen in Fig. 4, the curves approach these of *Ingebrigtsen* for increasing x values.

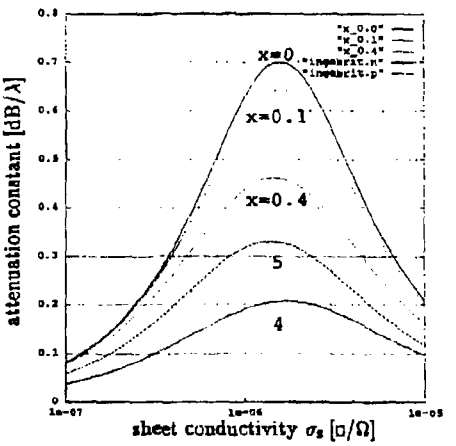

Fig. 4 Computed variation of attenuation constant in a a:Si/$LiNbO_3$–structure in dependence of the conductivity of the layer for different imaginary parts of sheet conductivity (h = 200 nm; f = 450 MHz)

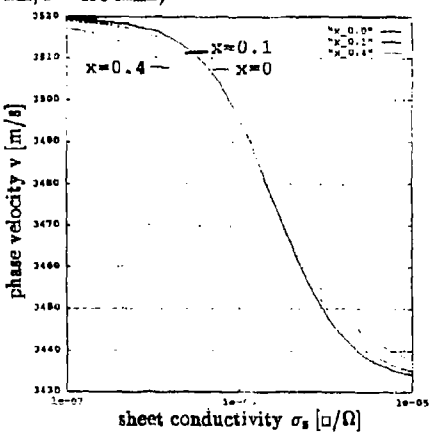

Fig. 5 Computed variation of phase velocity in a a:Si/$LiNbO_3$–structure in dependence of the conductivity of the layer for different imaginary parts of sheet conductivity (h = 200 nm; f = 450 MHz)

An Application of Mini-Max Criterion for LSM-LSE Modes Determination in Ferrite-Dielectric Loaded Waveguides

B.Yu.Kapilevich, Tharek Abd.Rahman

Faculty of Electrical Eng. University Technology of Malaysia
54100, Jl.Semarak,UTM, Kuala Lumpur, MALAYSIA

T.N.Fedotova

Faculty of Radio & TV, Novosibirsk Telecommunication Institute, Kirov St. 86, Novosibirsk-102, RUSSIA

A B S T R A C T

A simple method is proposed for solving the complex transcendental dispersion relation of LSM-LSE modes in rectangular waveguides loaded by a lossy dielectric or magnetized ferrite slabs. The complex propagation constants have been calculated by means of a minimax procedure. The main feature of this method is good accuracy if even standard minimax procedures have been used.

1.INTRODUCTION

Waveguide structures with a nonuniform filling of dielectric or ferrite materials have been of interest from many points of view,especially for applications to a variety of microwave components. Propagation constants of LSM-LSE modes may by calculated in many cases from dispersion relations for rectangular waveguides loaded by dielectric or ferrite slabs [1,4]. Many authors have dealt with structures when the losses were neglected or small. In this paper more common case will be considered namely losses are taken into account without any limitations.

2.BASIC FORMULATION

The general form of dispersion relations for a loaded waveguide may be given as the following scalar equation

$$F([\Gamma(\omega)],[\eta],[\xi]) = 0, \qquad (1)$$

where:$[\Gamma(\omega)]$ is a vector having components of real and imaginary parts of the propagation constant; $[\eta]$ is a vector having components of geometrical parameters of dielectric or ferrite slabs loading a waveguide; $[\xi]$ is a vector having components of complex permittivity of materials filing the waveguide.

Equation (1) is equivalent to a pair of nonlinear coupled equations in the complex plane of Γ

$$\begin{aligned} &\mathrm{Re}\left\{F([\Gamma(\omega)],[\eta],[\xi])\right\} = 0 \\ &\mathrm{Im}\left\{F([\Gamma(\omega)],[\eta],[\xi])\right\} = 0. \end{aligned} \qquad (2)$$

For the given vectors $[\eta]$, $[\xi]$ and radian frequency ω it's necessary to find the vector $[\Gamma]$ satisfying (2). That can be made if

the minimum of the modulus of the function F can be found

$$\text{Min } |F| = \text{Min}\{(\text{Re } F)^2 + (\text{Im } F)^2\}^{1/2}. \qquad (3)$$

The positive feature of such approach is that the vector [Γ] has only two components, namely, Γ′ and Γ″ being real and imaginary parts of Γ respectively. Therefore, high efficiency of calculations can be expected when standard methods of nonlinear programming will be used [5]. In the general case the solutions of (3) must be determined at whole complex plane of Γ.

3. APPLICATION TO LSM-LSE MODES DETERMINATION

This concept is universal and may be used for the determination of complex propagation constants of loaded waveguide modes. As examples, the following cases are considered:

Lossy waveguide. Propagation constants of rectangular waveguide uniformly filled by lossy dielectric can be calculated directly by using of the known analythical expressions [3]. Therefore this case is discussed as a simple illustration of the technique proposed. The propagation constants of TE_{n0}-modes should satisfy to the following dispersion relation:

$$F(\Gamma',\Gamma'') = \sin(k_0 a[\epsilon_r' - j\epsilon_r'' - (\Gamma' - j\Gamma'')^2]^{1/2}), \qquad (4)$$

where a is the width of wavoguide, ϵ', ϵ'' are the real and imaginary parts of permittivity, $k_0 = 2\pi/\lambda$ is the wave number of a free space.

A common behaviour of contour lines is illustrated by Fig.2 (non dissipated medium, $\epsilon_r = 1 - j0$, $a/\lambda = 0.7$, TE_{10} mode), Fig.3 (non dissipated medium, $\epsilon_r = 1 - j0$, $a/\lambda = 1.05$, TE_{10} and TE_{20} modes) and Fig.3 (dissipated medium $\epsilon = 1 - j0.5$, $a/\lambda = 0.7$, TE_{10} mode)

Referring to Fig.2 - 4 we can state that the contour lines of $|F|$ converge in the point of minimum $|F|$. This point corresponds to the solution of dispersion relation (4). By means of minimax procedures there is a possibility to correct this solution with any given accuracy. The minimization on the basis of the well-known method of Hook-Jeevs [5] can be made to determine more exactly the propagation constants of waveguide modes. It should be noticed that the point of trivial solution $\Gamma = \epsilon^{1/2}$ must be removed before starting of calculations.

LSM-modes exist in a rectangular waveguide loaded by a dielectric slab, as shown in Fig.1a. The propagation constants of LSM-modes in this structure must satisfy to the following dispersion relation [2]:

$$F\{[\Gamma(\omega)],[\eta],[\xi]\} = k_{y1}\epsilon_{r2}\sin(k_{y1}b_1)\cos(k_{y2}b_2) +$$

$$+ k_{y2}\epsilon_{r2}\cos(k_{y1}b_1)\sin(k_{y2}b_2) = 0, \qquad (5)$$

where

$$[\Gamma(\omega)] = [\Gamma'(\omega), \Gamma''(\omega)], \qquad [\eta] = [a, b_1, b_2],$$

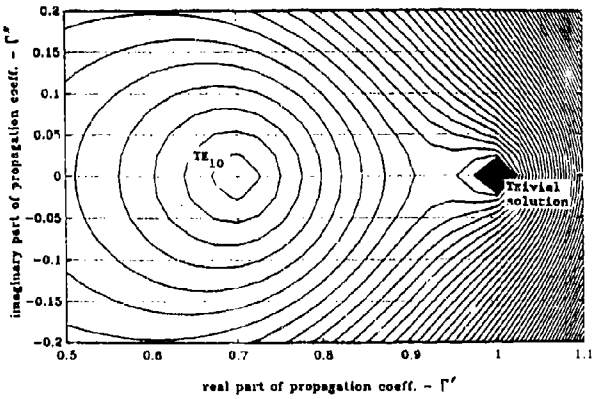

FIG.2 Behaviour of contour lines for non dissipative TE_{10}-mode: $\epsilon_r = 1\text{-}j0$, $a/\lambda = 0.7$

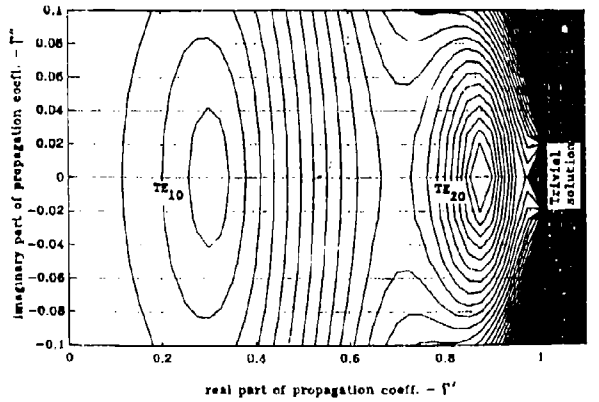

FIG.3 Behaviour of contour lines for non dissipative TE_{10} and TE_{20} mode: $\epsilon_r = 1\text{-}j0$, $a/\lambda = 1.05$

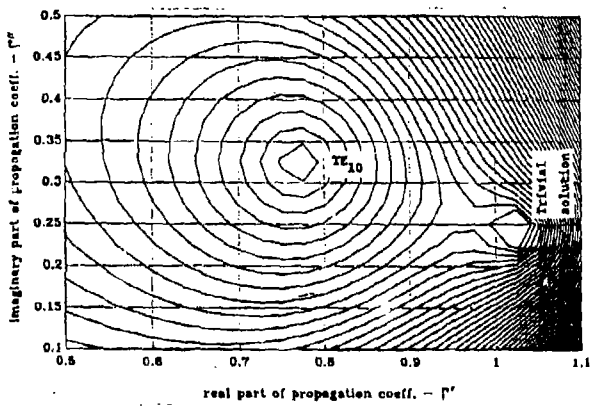

FIG.4 Behaviour of contour lines for dissipative TE_{10} mode:
$\epsilon_r = 1-j0.5$, $a/\lambda = 0.7$

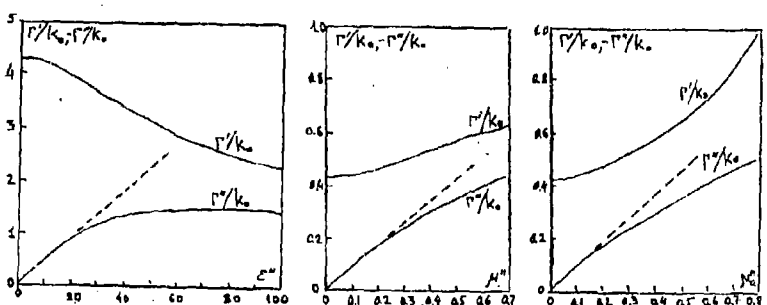

FIG.5 Calculated dependances of Γ'/k_0 and Γ''/k_0 for various imaginary parts of permittivities: approximate solution (dotted line) and minimax approach (solid line)

AUTHOR INDEX

VI = Volume I
VII = Volume II